Sulfur Isotopic Ratios at 67P/Churyumov-Gerasimenko and Characterization of ROSINA-DFMS FM & FS

Inauguraldissertation
der Philosophisch-naturwissenschaftlichen Fakultät
der Universität Bern

vorgelegt von

Ursina Maria Calmonte

von Därligen BE

Leiterin der Arbeit:
Prof. Dr. Kathrin Altwegg
Physikalisches Institut der Universität Bern

Von der Philosophisch-naturwissenschaftlichen Fakultät angenommen.

Copyright Notice

Sulfur Isotopic Ratios at 67P/Churyumov-Gerasimenko and Characterization of ROSINA-DFMS FM & FS

Inauguraldissertation
der Philosophisch-naturwissenschaftlichen Fakultät
der Universität Bern

vorgelegt von

Ursina Maria Calmonte

von Därligen BE

Leiterin der Arbeit:
Prof. Dr. Kathrin Altwegg
Physikalisches Institut der Universität Bern

Von der Philosophisch-naturwissenschaftlichen Fakultät angenommen.

Bern, den 17.12.2015

Der Dekan:
Prof. Dr. G. Colangelo

Genau in dem Moment, als die Raupe dachte, die
Welt geht unter, wurde sie zum Schmetterling.
Peter Benary

Abstract

Comets are thought to be the most pristine bodies present in the Solar System. In consequence of spending the majority of their existence beyond 30 AU, their composition can give insights on the physical and chemical conditions during their formation. Since August 2014 the European Space Agency spacecraft Rosetta accompanies the Jupiter family comet 67P/Churyumov-Gerasimenko on its way to perihelion and beyond. In this study the isotope fractionation of ^{34}S are reported in H_2S, OCS, SO_2, S_2, and CS_2 at 67P. In addition for the first time the isotope fractionation for ^{33}S is presented for cometary volatiles. The ratio $^{32}S/^{33}S$ is given for H_2S, SO_2 and a tentative value is given for CS_2. With a mean value of -50 ± 22‰ and -306 ± 31‰ for $\delta^{34}S$ and $\delta^{33}S$ respectively, H_2S shows a significant depletion in both ^{34}S and ^{33}S. For SO_2 the depletion is less distinct with $\delta^{34}S$ and $\delta^{33}S$ being -67 ± 40‰ and -130 ± 53‰, respectively. The strongest depletion is present for CS_2 with -114 ± 21‰ and -276 ± 55‰, respectively. For OCS and S_2 only $\delta^{34}S$ could be determined which is -252 ± 77‰ and -357 ± 145‰, respectively. A comparison with sulfur isotopic ratios measured in SiC grains revealed that both SiC grains and the five volatile species have similar sulfur isotopic ratios. However, it is beyond the scope of this work to investigate the possibility of a link between SiC grains and cometary ices. Nevertheless, mass-dependent or mass-independent fractionation due to photo dissociation can be ruled out as sole cause of the seen depletion of ^{33}S and ^{34}S. Furthermore, an upper limit of $(9.64 \pm 0.19)\cdot 10^{-4}$ for D/H in HDS has been determined. This value is about a factor two higher than D/H in H_2O for the same comet reported by (Altwegg et al., 2015). Besides the investigation concerning isotopic ratios of sulfur bearing species in this work the calibration and characterization of ROSINA/DFMS has been continued. Here it is reported about the deviation of the mass scale for MCP/LEDA low resolution spectra and the calibration measurements performed in the laboratory. Furthermore the outcome of the attempt to describe the sensitivity of DFMS with an empirical function will be discussed. The last part of the characterization of DFMS is dedicated to determine the so-called individual pixel gain for the laboratory and the flight model. Moreover, correlation between the depletion's manifestation of the MCP with respect to the applied voltages has been investigated for both models. It has been found that further measurements are needed to understand the manifestation of depletion at the laboratory model. For the model on board of Rosetta it could be shown that most of the present feature are due to the usage of the MCP and suggestions have been made in order to answer the remaining question considering the depletion of the MCP.

Contents

List of Figures

List of Tables

1. Introduction

This chapter is dedicated to introduce the instruments used for this work as well as to give brief summaries on comets, meteorites and so-called presolar grains which will be important in the discussion of the scientific results. In addition to this, the importance of isotopic ratios will be explained followed by the presentation of the state of art knowledge concerning sulfur isotopic ratios in comets, meteorites, and so-called presolar grains. Finally the European Space Agency mission Rosetta and its target the comet Churyumov-Gerasimenko are presented.

In this work characterization of the measurement device and scientific research were realized in equal amount which led to different experimental setups and data reduction procedures. As a consequence the presentation and discussion of the results is divided into two parts; first with focus on characterization of the measurement device and second with focus on the scientific results. In the conclusion the most important findings concerning the characterization of the instruments and the sulfur isotopic ratios measured in the sulfur bearing volatiles of Churyumov-Gerasimenko are summarized.

1.1 Aim

Partly the aim of this thesis is to continue the characterization and calibration of the laboratory and the flight model of the ROSINA Double Focusing Mass Spectrometer (DFMS). A comprehensive characterization of this instrument is essential in order to derive meaningful results from the survey of comet 67P/Churyumov-Gerasimenko that started in August 2014 and goes on till mid 2016. On the other hand the aim was to determine the sulfur isotopic ratios in the five most abundant sulfur bearing species in the coma of comet Churyumov-Gerasimenko and to relate the results of this work to what is known about sulfur isotope fractionation in cometary volatiles.

1.2 Comets

By definition of the International Astronomical Union (IAU) “a comet is a body made of rock and ice, typically a few kilometers in diameter, which orbits the Sun” [1].

Although the formation regions of comets can not yet be exactly located an accepted consensus is that comets spent the majority of their ’life’ in either the Oort cloud (OC), a cloud of icy bodies located around heliocentric distances (R_h) of 10’000 - 50’000 AU, or the Kuiper belt (KB), a disk of icy bodies around 30 - 100 AU(Mumma and Charnley, 2011). Those two regions could be determined as the storage region of comets based on orbit observations and determination of the orbital elements. Their hibernation at the edge of the Solar System at temperatures below the sublimation temperature of most species made comets a highly coveted object for observations because they are supposed to be the most primitive and preserved bodies present in the Solar System. Therefore it is a common consensus that in determining the molecular and isotopic composition give an insight on the chemical and physical conditions and processes occurring in the protoplanetary disk, the gas and dust disk surrounding the newborn sun.

---

[1] `https://www.iau.org/public/themes/naming/#comets`

Regardless of formation origin the evolution of a comet goes as follows: after formation the comets arrive in one of the two main reservoirs where they spent the majority of their existence in hibernation. Due to gravitational perturbation the orbit of a comet can change in such a way that it enters the outer Solar System, where an encounter with a giant planet can lead to the injection into the inner Solar System. Approaching the sun the ice starts to sublimate depending on the energy input and the sublimation temperature of the ice components and at a certain point the gas drag will be large enough to lift up so called dust particles. With decreasing heliocentric distance the activity increases and therefore the gas and dust cloud around the comet the so called coma becomes more distinct.
The coma can be up to ~10^5 km and due to motion, solar radiation pressure (dust) and solar wind (ions) a dust tail and an ion tail can be formed (Brownlee, 2014). A schematic drawing of the tails with respect to the sun is shown in fig. 1.2.1. The coma produced through sublimation of different ices is not a gravitational bound atmosphere and while the comet is moving on its orbit it leaves behind a trail of dust and gas. In addition to this tail there is the ion tail consisting of ions produced in the coma. The ion tail is always directed anti-sun ward due to interactions with the solar wind. The size of the coma depends among others on the outgassing rate, which species is looked at i.e. the hydrogen coma can extent over 10^7 km because of the high velocity and long lifetime of hydrogen atoms while the water coma is then 10^5 km. The life-time of a comet in the inner Solar System depends mainly on the orbit, the size, and the ratio between dust and ice. However, its end depends mainly on its dynamical evolution: i) it stays on a stable orbit and loses the majority of its volatile material thus it becomes invisible for observation and cease to exist, ii) it stays on a stable orbit but its surface becomes inert and therefore again stops to exist from the observational perspective, iii) it splits up either due to a close encounter with a giant planet or the sun resulting in a gas and dust cloud or as impactor on either sun or a giant planet or it splits up due to thermal stress. Famous ends of comets were the distribution and impact of Shoemaker-Levy 9 on Jupiter in July 1994 or comet ISON which was disrupted at his perihelion passage in 2013.

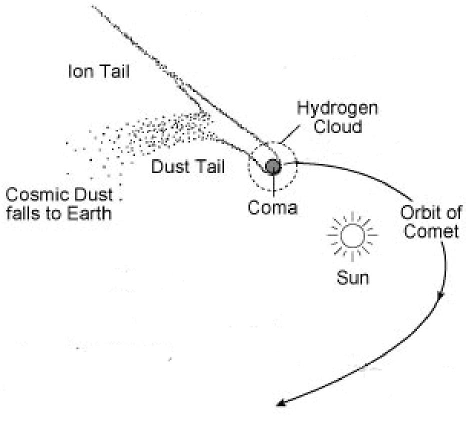

Fig. 1.2.1: Schematic morphology of a comet approaching the sun. The graph has been adapted from `http://www.techknow.org.uk/wiki/index.php?title=Comets`

Most of the knowledge about comet's nature is due to ground based observations of the coma and the tails, since only a handful spacecrafts ever flew to a comet. In addition, the in-situ measurements provided only snapshots of distinct comets allowing to qualitatively understand comets on the basis of a handful in situ measurements. Therefore ground based observation of the coma and model how the coma composition could reflect the composition of the nucleus were essential. A very brief summary of cometary composition with focus on volatile materials is given in the following section. Furthermore the 3 common taxonomies are presented. For a very long time it has been tried to classify comets and despite the tremendous developments in observation techniques in the last 100 years there is no unified classification for comets.

1.2.1 Molecular Composition of Comets

The present knowledge of the composition of cometary nuclear ices is based mainly on investigations of the coma that is built by ice sublimating when comets approach the sun. In the coma water is the main species (about 80 % (Bockelée-Morvan, 2011)) followed by CO, CO_2, CH_3OH, CH_4, H_2S, and NH_3 whereas the relative abundance can vary from less than 0.5% to 20 % relative to water among comets. In addition the relative abundance decreases for increasing complexity of parent molecule. In contrast to this tendency is the detection of complex hydrocarbons like methyl formate and ethylene glycol (Bockelée-Morvan, 2011). An overview on cometary parent molecules is given in fig. 1.2.2 where the range of the relative abundance of a species is given in red and the number of comets in which this species has been detected is on the right edge.

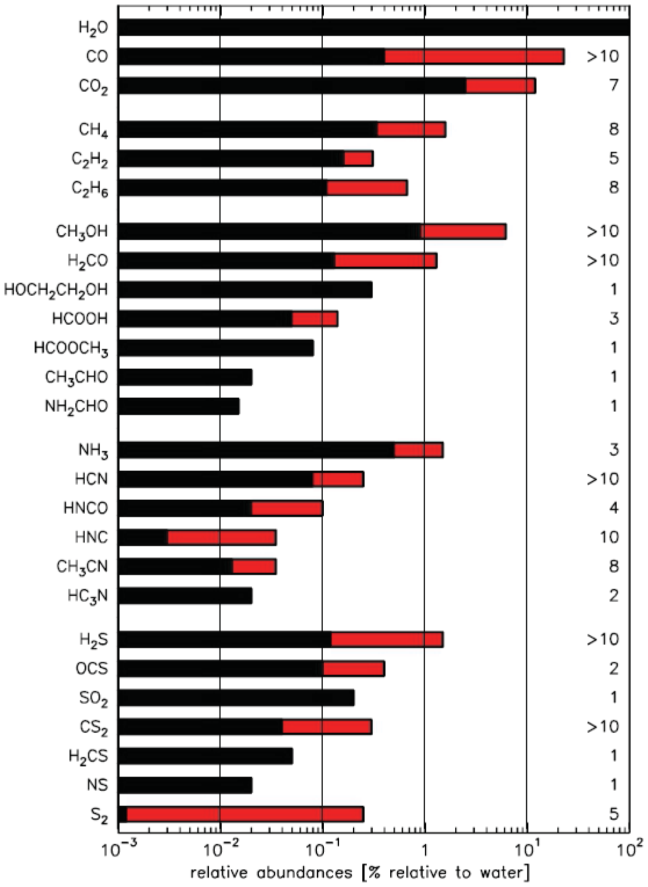

Fig. 1.2.2: Abundance relative to water of 21 species detected in cometary coma. the red bar display the range of measured abundances in comets while the number of comets in which the species was detected is given on the right side Bockelée-Morvan (2011)

1.2.2 Taxonomies

Dynamical Classification Up to date three reservoirs of comets are established, the Oort Could, the Kuiper Belt, and the asteroid main belt whereas the latter is still under debate (Mumma and Charnley, 2011). As soon as a comet is ejected from its reservoir to the inner Solar System due to gravitational perturbation it is classified by its dynamic. A tool to do classifications is the so called Tisserand parameter (T_J) with respect to Jupiter that is defined as

$$T_J = \frac{a_J}{a} + 2 \cdot \sqrt{\frac{a}{a_J}(1 - e^2)} \cdot cos(i) \tag{1.2.1}$$

where a is the semimajor axis of a small body, e its eccentricity, and i its inclination while a_p is the semimajor axis of Jupiter. Comets with $T_J > 2$ are called ecliptic because they all have small inclinations. Comets with $T_J < 2$ are called nearly isotropic comets because of their nearly isotopic inclination distribution. Elliptic comets can further be divided into 3 sub groups, Jupiter family comets with $2 < T_J < 3$, centaur-type comets with $T_J > 3$ and $a > a_J$, and Encke-type comets with $T_J > 3$ and $a < a_J$. Jupiter family comets mainly cross Jupiter orbit and are dynamically dominated by Jupiter. Encke-type comets have their aphelion inside of Jupiter orbit and therefore their orbits are less dominated by this planet (Duncan et al. (2004) and references therein). For ecliptic comets the Kuiper Belt has been identified as reservoir while for nearly isotropic comets the Oort Cloud is thought to be the reservoir.

There are two major theories about the link between forming region and reservoir of comets. The first one formed in the 90‘s when it was thought that most of the Jupiter family comets formed further away of the sun ($R_H > 30$ AU) in the Kuiper belt region and that the Oort Cloud comets were formed between the giant planets at heliocentric distance smaller than 30 AU. The other hypothesis is the so called Nice model introduced in 2005 by Gomet and Morbidelli. It claims that Jupiter and Saturn changed their position in the Solar System due to a resonance which led to a gravitational perturbation that kicked out all smaller bodies to the outer Solar System. The Nice model predicts that comets formed beyond ~15 AU were displaced either to the Oort Cloud or to the Kuiper belt and it is unclear in which proportions. Comets that formed between 5-14 AU, that means in the giant planet feeding zone, are supposed to have entered the Oort Cloud region. So the Oort cloud seems not to consist of only one type of comets formed at one place/heliocentric distance and it is not clear to which extend the Kuiper belt is a mixture of bodies from different forming regions ((Mumma and Charnley, 2011) and reference therein).

C Depletion in Product Volatiles As a second type of taxonomy Mumma and Charnley (2011) mention the classification done by A'Hearn et al. (1995) established on the basis of photometric data of 85 comets. A'Hearn et al. (1995) searched for a relation between the amount of five product species (OH,CN,C_2,C_3, and NH) and dust. The major findings were: i) that a significant amount of the set are so called depleted in carbon-chain molecules (C depletion) which is linked to the production rate ratio of C_2/CN, and ii) that almost all members of the C depleted class are Jupiter family comets although not all of those were depleted. In summary Mumma and Charnley (2011) point out that although the sample set of 85 comets provided adequate statistics to establish a taxonomy based on the carbon depletion the emerged classification might be incomplete because measurements were done at a limited range of heliocentric distances and production rates vary with cometary distance not the same way for all radicals.

Primary Volatiles Besides the classification due to the dynamics and the carbon depletion (Mumma and Charnley, 2011) present a third type of classification: group comets based on to their relative abundance of primary volatiles. Due to solar UV irradiation volatiles in the coma undergo photodissociation resulting in secondary volatiles which can be observed i.e. $HCN + \gamma \rightarrow CN + H$.
To study the primary volatiles in the coma from earth either infrared (IR) or radio wavelength telescope are used. With radio the following primary volatiles have been measured: CO, H_2CO, CH_3OH, HCOOH, HCN, HCNO, CH_3CN, HC_3N, NH_3 and H_2S. However, at least two of them (CO, H_2CO) are both primary and secondary volatiles. Measuring in IR has the advantage that one can measure trace elements together with H_2O and therefore be able to determine the relative abundance based on measurements acquired in the same conditions i.e heliocentric distance . At least 10 primary volatiles can be then followed together with water for different comets (H_2O, CO, H_2CO, CH_3OH, CH_4, C_2H_2, C_2H_6, HCN, NH_3, OCS) in IR.

In their paper Mumma and Charnley (2011) suggest a new cataloging based on the organic composition of primary volatiles. They took the database of 16 comets where species have been measured simultaneously in infrared and divided them into 3 groups:

Group 1 6 Oort Cloud comets with similar relative abundances for C_2H_6, CH_3OH, HCN, and C_2H_2

Group 2 2 comets seem to be enriched in organics (one is an OC and the other one is a KB)

Group 3 Organic depleted, again 2 comets, one is a OC and the other one a KB

However, not all 16 comets could be categorized and even within one group (no. 1) still significant variations are present. Anyhow a larger data set is needed to establish a classification based on primary volatiles and more sensitive telescopes are needed to sample as well faint comets.

1.3 Meteorites

Meteorites are solid extraterrestrial bodies that manage to penetrate the Earths atmosphere and to reach the Earths surface while solid extraterrestrial bodies which only penetrate into the atmosphere are called meteors. Meteorites are divided into the two major categories chondrites and Nonchondrites depending on their bulk composition and their texture. Chondritic compositions is characterized by the presence of round grains so-called chondrules, FeNi-metal, refractory inclusions like calcium aluminum rich inclusions (CAIs), and fine grained matrix material. As a consequence nonchondrites do not show chondritic texture and they are thought to be formed by partial or complete melting of their parent body e.g an asteroid or a larger planetary body as Mars. Based on their composition and texture one can tell that chondrites never experienced melting or igneous differentiation like for instance Earth that consists due to differentiation of layers with different densities. The two major categories can then be divided into first classes and then groups as it can be seen in fig. 1.3.1. Here the following classes will be briefly introduced: the carbonaceous,

ordinary,and enstatite chondrites, the primitive and the differentiated nonchondrites. For further information about the classification of meteorites the author refers to the review of Krot et al. (2007) on which this subsections bases.
Although they are called carbonaceous chondrites only three groups (CI, CM, and CR) of this class show a significant enrichment in carbon relative to noncarbonaceous chondrites. Thus it is not the relative carbon content which differs the three classes of chondrites. Ordinary chondrites are called like this because they are the most common ones and enstatite are nearly pure magnesium silicate (enstatite). Primitive nonchondrites represent an intermediate step between chondrites and differentiated nonchondrites because because their bulk composition is close to chondritic but their texture shows as well characteristics originated in melting processes which implies only a partial melting. In contrast achondrites a group of the differentiated nonchondrites are the product of the entire melting of the parent rocky body. Besides the achondrites the group of the differentiated nonchondrites consists of the stony iron meteorites that contain similar proportions of silicate minerals and metal and the iron meteorites that contain mostly metals.
Due to the lack of melting signatures in chondrites it is commonly supposed that they represent the solar nebula before planets were formed and after the disk accretion. Therefore they are for similar reasons as comets a coveted object of investigation.

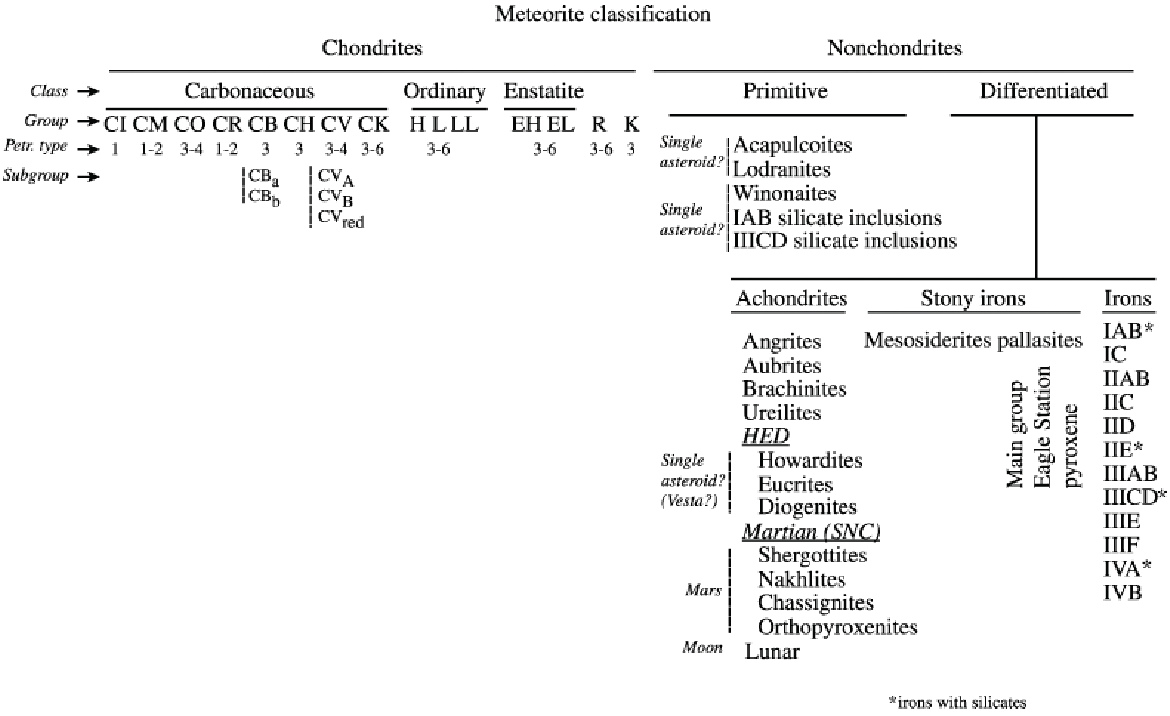

Fig. 1.3.1: Classification of meteorites taken of from (Krot et al., 2007).

1.4 Presolar Grains

Presolar grains are mineral grains which are believed to be formed outside of our Solar System and to be incorporated unaltered in a parent body. First hints of the presence of presolar material were given by the isotopic heterogeneity in noble gases measured in meteorites between 1954 and 1972 ((Zinner, 2014) and references therein). However only after the discovery of oxygen anomalies in primitive meteorites the concept of presolar material embedded in solar material was widely accepted and isotopic anomalies in other elements such as magnesium, calcium, carbon, and nitrogen were detected in the following years. Between 1987 and 1990 three carriers of the detected anomalies could be identified: diamond, silicon carbide (SiC), and graphite. Here only silicon carbide grains will be introduced in more detail.

Silicon carbide grains can have a size between 0.1-20 µm and can have an abundance up to 150 ppm. They have been found in carbonaceous, ordinary, and enstatite chondrites so far. Based on their carbon, nitrogen, and silicon isotopic composition SiC grains are divided into 7 groups: mainstream grains (~93% of the total), AB, C, X,Y,Z, nova grains, and U. It is believed that the majority of the SiC grains originate from so called carbon stars. Those are stars of low mass (1-3 $M\odot$) in their asymptotic giant branch (AGB) phase. In his review Zinner (2014) give two reason why SiC grains are linked to carbon stars: i) both have similar $^{13}C/^{13}C$ ratios, and ii) AGB stars are believed to be the main source of the slow neutron-capture nucleosynthesis (s-process) which results in distinct isotopic patterns seen in SiC grains. In fig. 1.4.1 a) the relation between $^{12}C/^{13}C$ and $^{14}N/^{15}N$ for the different grain types is shown and b)-d) show the three isotope plot with ^{28}Si, ^{29}Si, and ^{30}Si. The data for both graphs can be found in the presolar database (Hynes and Gyngard, 2009).
Silicon carbide grains are a type of presolar grains which are thought to form in stellar outflows of late-type stars (e.g red giants) and as condensates of of stellar explosions like super novae (SNe). Based on their anomalous isotopic ratios in C, S, N and O they were identified to have not formed in the solar system. For a review see (Zinner, 2014). Besides the SiC grains there are 7 other types of grains with presolar origin identified: diamond, graphite, oxides, silicon nitride, Ti-/Te-/Zr-/Mo-carbides, kamacite/iron, and olivine (Zinner, 2007). Before presolar grains were embedded in solar system bodies like meteorites, interplanetary dust particles, Antarctica meteorites, and cometary matter (Xu et al., 2015) they traveled through interstellar matter and were exposed to cosmic galactic rays, could experience sputtering by stellar wind and could be evaporated by SN shocks (Zinner, 2014). At some point they became part of the dense molecular cloud where the formation of our solar system took place. Most of those grains became destructed during the formation process of the solar system bodies but some could survive and preserve their presolar signature because they are embedded in almost non-processed bodies like carbonaceous chondrites (e.g. CM2 Murchison).

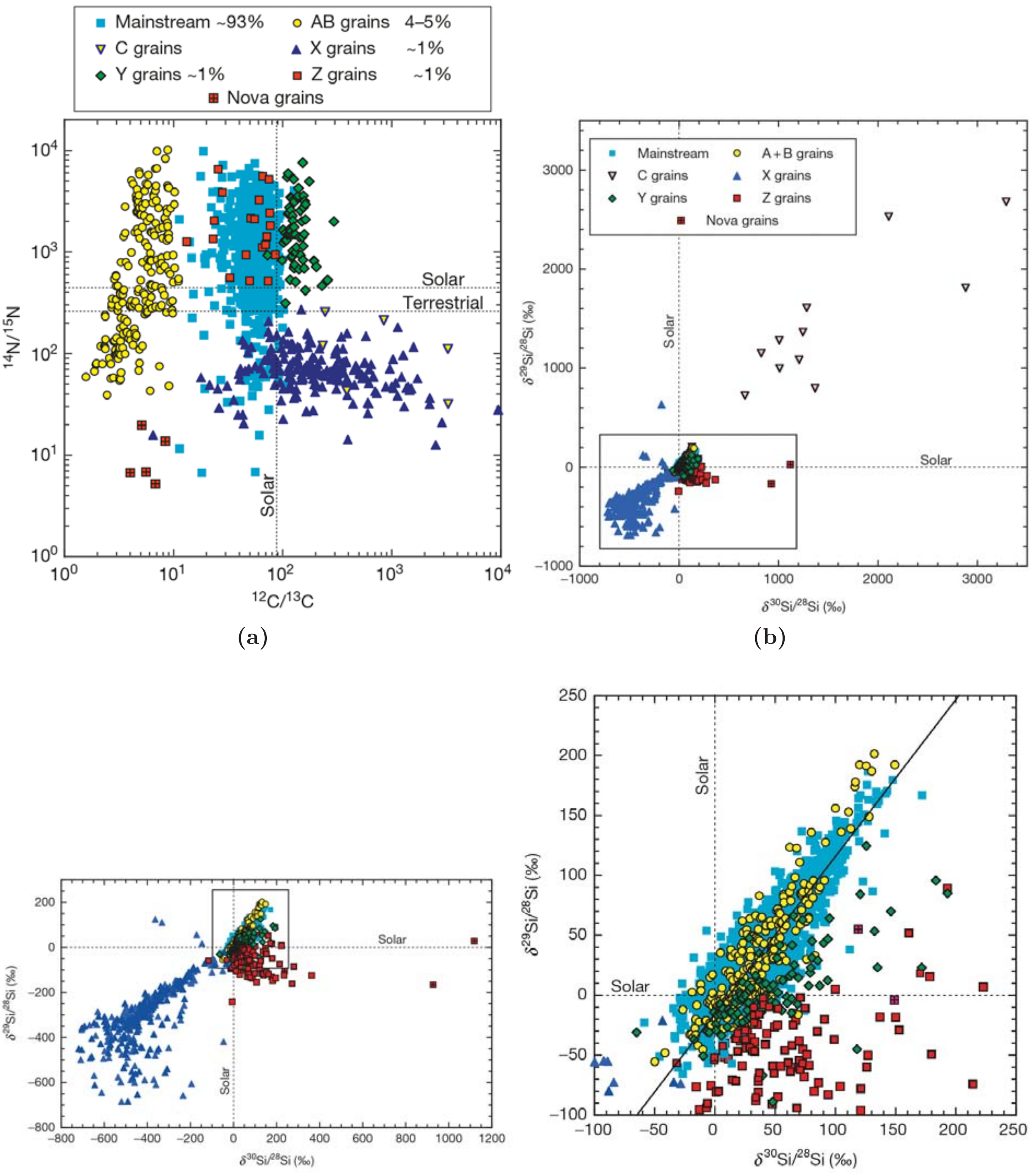

(a) (b)

(c) (d)

Fig. 1.4.1: Carbon, nitrogen, and silicon isotopic composition of silicon carbide grains. a) shows the relation between $^{12}C/^{13}C$ and $^{14}N/^{15}N$ and b)-d) show the three isotope plot with ^{28}Si, ^{29}Si, and ^{30}Si with different scaling (Zinner, 2014)

1.5 Isotopic Ratios

Isotopic ratios are often referred to be the only true key to the question at which chemical and physical conditions comets and therefore planetesimals formed. Here the term isotopic ratio and its importance will be briefly introduced.

The term isotope is used for atoms which have the same number of protons in the nucleus but differ in the neutron number i.e. carbon can be found in nature either as ^{12}C or ^{13}C, both have 6 protons but ^{13}C has 7 neutrons instead of 6 and due to the difference in the nucleus physical properties such as the sublimation temperature differs slightly. Isotopes can be divided into two fundamental kinds: stable or unstable. Unstable isotopes like ^{13}C decay after a certain time in order to reach an energetic lower ground state. Isotopes are a common thing; between mass 1 u (H) and 83 (Bi) only 21 are pure elements meaning only one stable isotope exist (Hoefs, 2009). The others are a mixture of different isotopes, whereby for the light elements one isotope is dominant (e.g O) and for heavier ones differences in abundances are smaller. The isotopic composition of an element is given by the ratio of the isotopes relative to the most abundant one. Molecules built up by different isotopes are called isotopologues and they differ in their physochemical properties because isotopes have different physical properties i.e. exchanging H in water with D leads to different chemical reactions rate.

There are three distinct mechanism that can change the isotopic abundances of an element: first radioactive decay, second isotope fractionation, and third nucleosynthesis.

Radioactive decay occurs when a nucleus is unstable and has to change its nucleus configuration in order to reach stability. Nucleosynthesis can occur when a target material is exposed to high energetic particles or to slow neutrons i.e. among others a meteorite that is exposed to the galactic cosmic rays will change its isotopic abundance of ^{40}Ar. Isotopic fractionation can occur due to evaporation-condensation processes, due to kinetic effects and can be divided into mass dependent and independent process. For the later one the mass difference between isotopes influences the change in isotopic abundance i.e. the enrichment of D with respect to H in water in cold molecular clouds.

Knowing the processes and the quantitative change in isotope abundance of an element can help to constrain the physical and chemical conditions of a system i.e. D/H ratio is lower for earth than for comets indicating that both did not form at the same location and that the region were the Earth formed was warmer then the comet forming region.

1.5.1 Comets

So far the isotopic ratios D/H, ^{14}N/^{15}N, ^{16}O/^{18}O, ^{12}C/^{13}C, and ^{32}S/^{34}S have been reported for several comets and in different species. By far most values are reported for D/H ranging from $1.61 \cdot 10^{-4}$ in water measured at 103P/Hartley2 to $2.6 \cdot 10^{-3}$ in HCN at Hale-Bopp (Bockelée-Morvan et al., 2015). A compilation of the D/H ratio in water is shown in Fig. 1.5.1. Compared to the installer medium, the gas and dust clouds present in space, cometary material show a significant enrichment in deuterium while in so called cold molecular clouds and for low and high- mass protostars an even larger enrichment in D has been observed (see (Bockelée-Morvan et al., 2015) and references therein). In the review Bockelée-Morvan et al. (2015) give two possible explanations for the measured D/H in comets; i) the D/H ratio in comets could have been lowered by ion-molecule reactions in the outer solar nebula cloud, and ii) the D/H seen in H_2O could be due to a mixing of a

D enriched component originating from the presolar cloud with material processed in the inner hot solar nebula. In addition, the models describing the latter process can explain the terrestrial D/H in water, the bulk meteorite value, the enrichment in Enceladus plume, and the mean D/H ratio of $\sim 3 \cdot 10^{-4}$ in water. However; it is not possible to explain the roughly terrestrial value of D/H in water for two of the three measured Jupiter family comets (Bockelée-Morvan et al., 2015) with the current models of formation of comets and of the mixing of a deuterium rich and poor component in the protoplanetary disk. Besides D/H and 14N/15N none of the reported isotopic ratios differ significant from the terrestrial value and a widely accepted consensus is that no strong fractionation occurred for S, O, and C in the Solar System. Isotopic measurements of CN and HNC pointed to a enrichment in 15N with 14N/15N about 150 and a reanalysis of NH2 data done by Rousselot et al. (2014) pointed to 14N/15N of 127 ± 32 (1 σ) but taking into account the average uncertainty the value could lay within ~90 to ~180. For further information about isotopic ratios in comets the author refers to the reviews of Jehin et al. (2009) and Bockelée-Morvan et al. (2015).

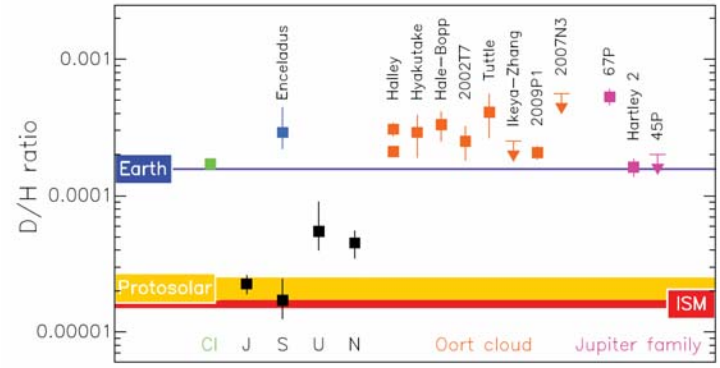

Fig. 1.5.1: The D/H ratio in water for different bodies of the Solar System; for carbonaceous chondrites (CI), the reference value for D/H (VSMOV), Enceladus, 8 Oort cloud comets, and 3 Jupiter family comets. Besides the D/H ratio in H_2 is displayed for Jupiter, Uranuns, Neptun, and the Sun. The graph is taken from Bockelée-Morvan et al. (2015).

1.6 Sulfur Isotopic Ratios in the Solar System and Beyond

In this section the state of art regarding sulfur isotopic ratios in comets, meteorites, and SiC grains will be presented. In addition laboratory work concerning mass independent fractionation in sulfur due to photodissociation will be discussed. However, first the conventional ways of presenting isotopic fractionation will be shown. There are four conventions depending on the field how to display isotopic ratios or isotope fractionation:

1. Give the isotopic ratio with respect to the major isotope:
   $^{3i}\mathrm{S}/^{32}\mathrm{S} \quad \text{with i} = 3,4,6.$

2. Give the isotopic ratio with respect to the minor isotopes (mostly used for isotopic ratios in comets):
   $^{32}\mathrm{S}/^{3i}\mathrm{S} \quad \text{with i} = 3,4,6.$

3. As isotope fractionation relative to a standard:
   $\delta^{3i}S = [\ (^{3i}S/^{32}S)_{\text{sample}}/(^{3i}S/^{32}S)_{\text{standard}} - 1\ ] \times 1000$ with i = 3,4,6.

4. As deviation from mass dependent fractionation:
   $\Delta^{33}S = \delta^{33}S - 1000 \times [\ (1 - \delta^{34}S)^{0.515} - 1\ ]$
   $\Delta^{36}S = \delta^{36}S - 1000 \times [\ (1 - \delta^{34}S)^{1.91} - 1\ ]$

The standard for sulfur was since 1962 the Cañon Diablo Troilite (CDT) which was replaced by the Vienna Cañon Diablo Troilite (V-CDT) (Ding et al., 2001) because it had been proven that CDT is slightly inhomogeneous regarding the sulfur isotopic abundances. V-CDT differs from CDT only in $\delta^{34}S$ by a value of 0.3‰ (Coplen and Krouse, 1998). For oxygen and hydrogen the international measurement standard is the so called Vienna Standard Mean Ocean Water (SMOV), for carbon it is the so called Vienna Pee Dee Belemnite, and for nitrogen the standard is called air nitrogen. The isotopic ratios of the standards mentioned are given in table 1.6.1.

Table 1.6.1: Absolute isotope ratios of international standards.

Standard	Ratio	Accepted value ($\cdot 10^{-6}$)	Reference
SVMOW	D/H	155.75 ± 0.08	(Werner and Brand, 2001)
	$^{18}O/^{16}O$	2005.2 ± 0.45	(Werner and Brand, 2001)
	$^{17}O/^{16}O$	373 ± 15	(Hoefs, 2009)
VPDB	$^{13}C/^{12}C$	11180.2 ± 2.8	(Werner and Brand, 2001)
Air nitrogen	$^{15}N/^{14}N$	3678.2 ± 1.5	(Werner and Brand, 2001)
VDCT	$^{34}S/^{32}S$	44150.9 ± 11.7	(Ding et al., 2001)
	$^{33}S/^{32}S$	7877.24	(Ding et al., 2001)

1.6.1 Photodissociation of Sulfur Bearing Volatiles

Concerning mass independent sulfur fractionation (MIF) only a few studies have been done yet; the photo polymerization of $(CS_2)_x$ and the photodissociation of H_2S, SO_2, and OCS.

The photo polymerization by solar irradiation in the gas-phase of $^{12}CS_2$ and $^{13}CS_2$ to $(^{12}CS_2)_x$ leads to a fractionation of $\delta^{34}S$ = 45.85‰, $\delta^{33}S$ = 28.31‰, and $\delta^{36}S$ = 37.6‰ resp. and to $(^{13}CS_2)_x$ leading to a fractionation of $\delta^{34}S$ = 32.48‰, $\delta^{33}S$ = 16.98‰, and $\delta^{36}S$ = 56.7‰ (Zmolek et al., 1999).

For H_2S photo dissociation by solar vacuum UV photon experiments have been done by Chakraborty et al. (2013) at four different wavelength including Lyman α in the range of $2\cdot10^{-2}$mbar - 0.2mbar and different photolysis time resulting in a mass independent fractionation for Lyman α of $\delta^{33}S$ = 0.27-6.94‰, $\delta^{34}S$ = 1.95-13.87‰, and $\delta^{34}S$ = 5.95-26.60‰.

Very recently the dependence of pressure and 'third body' effects during photolysis of SO_2 has been studied by Masterson et al. (2011). With a D_2 lamp providing a broadband UV continuum peaking at ~200 nm gas mixtures of SO_2 and He with mixing ratios between 1:0 - 1:26 have been irradiated at different pressures (only SO_2: ~20 mbar - 880 mbar; mixtures with He: ~125 mbar - 700 mbar). The MIF with only SO_2 leads to $\delta^{34}S$ =

127.42-160.98‰, and $\delta^{33}S$ = 65.80-106.82‰ while the mixture of SO_2 and He leads to $\delta^{34}S$ = 133.55-177.55‰, and $\delta^{33}S$ = 71.92-102.56‰.

For OCS the the mass independent fractionation has been examined under the following conditions; for OCS alone and mixtures of N_2 at pressures of 3.7 mbar to 501 mbar samples were exposed to a Xe ar lamp (150 W) for different time periods. The isotopic ratio has been determined for the produced S and the remaining OCS resulting for S in $\delta^{33}S$ -0.19‰ (501 mbar, 48 hrs) - 2.48‰ (6.9 mbar, 30 min), in $\delta^{34}S$ -0.37‰ (501 mbar, 48 hrs) - 4.43‰ (6.9 mbar, 30 min) and for OCS in $\delta^{33}S$ -3.14‰ (501 mbar, 48 hrs) - -4.85‰ (6.9 mbar, 30 min), in $\delta^{34}S$ -5.77‰ (501 mbar, 48 hrs) - -9.49‰ (6.9 mbar, 30 min).

Table 1.6.2: Isotope fractionation for sulfur bearing volatiles due to photodissociation using UV.

Species	Slope in $\delta^{34}S$,$\delta^{33}S$ space	Reference
H_2S	0.64 - 0.7	(Chakraborty et al., 2013)
CS_2	0.485 ± 0.005	(Zmolek et al., 1999)
SO_2	0.649 ± 0.006	(Farquhar et al., 2000)
SO_2	0.76 ± 0.05	(Masterson et al., 2011) *
SO_2	0.68 ± 0.05	(Masterson et al., 2011) †
OCS	0.534 ± 0.005	(Lin et al., 2011)

* only SO_2 at different pressures, † SO_2 & He different pressures

1.6.2 Comets

So far four values for $^{32}S/^{34}S$ in volatile species are reported in four different comets. The first value has been measured in the short period comet 1P/Halley in 1986 during the flyby of the spacecraft Giotto. The isotopic ratio was determined with ^{+34}S and is 23 ± 3 (Altwegg, 1996). Then two values are reported for the long period comet Hale-Bopp. The ratio $^{32}S/^{34}S$ in CS is 27 ± 6 (Jewitt et al., 1997) and in H_2S 16 ± 3 (Crovisier et al., 2004). The most recent result has been measured for the Jupiter family comet 17P/Holmes and accounts for 16 ± 3 determined in $C^{34}S$ (Biver et al., 2008).
The results for Halley and in $C^{34}S$ at Hale-Bopp agree within 1 σ with the standard V-CDT. However, the $^{32}S/^{34}S$ ratio in H_2S at Hale-Bopp and in CS at 17P Holmes differ from V-CDT and lay only within 2 σ with V-CDT. So far no explanation could be given for the enrichment in ^{34}S as well as it is not clear why there is such a significant difference between CS and H_2S originating from the same comet. A compilation of the $^{32}S/^{34}S$ isotopic ratio and its conversion into the δ notation is given in table 1.6.3.

Besides the attempts to sample the coma by in-situ measurements and via remote sensing the National Aeronautics and Space Administration (NASA) mission Stardust collected in January 2004 the first samples of cometary matter and brought them back to Earth in 2006. The sample were collected during a flyby at 234 km distance to the Jupiter family comet Wild 2 in January 2004. They were collected with the Aerogel Sample Collectors which consist mostly of a silica aerogel and of ~15% aluminum (frame to hold aerogel). Impact craters contained melted and sometimes unmelted residues of the impactor (Brownlee et al., 2006). From those 24 dust aluminum impact residues were analyzed by Heck et al. (2012) for their four sulfur isotopic composition. In these data set only one impact crater residue showed a small depletion for ^{33}S and ^{34}S ($\delta^{34}S$ -41 ± 17‰ and $\delta^{34}S$ -57 ± 17‰ resp.) while the rest lays within 2σ of bulk meteorite data. Heck et al. (2012) state that the small anomaly might be the result of a mixture between a small presolar grain and a larger grain formed in the Solar System and that the relatively large uncertainties are due to topographic effects and impact fractionation.

Table 1.6.3: ^{32}S/^{34}S isotopic ratio in comets.

^{32}S/^{34}S	δ^{34}S	Comet	Species	Reference
23 ± 6	-15 ± 257	1P/Halley *	$^{34}S^{+}$	(Altwegg, 1996)
27 ± 3	-161 ± 93	(C/1995 O1) Hale-Bopp †	C^{34}S	(Jewitt et al., 1997)
16.5 ± 3.5	372 ± 291	(C/1995 O1) Hale-Bopp ‡	$H_2{}^{34}S$	(Crovisier et al., 2004)
16 ± 3	415 ± 265	17P/Holmes ‡	C^{34}S	(Biver et al., 2008)

* Mass spectrometry (Giotto), † radio spectrometry (JCMT), ‡ radio spectrometry (30m IRAM),

1.6.3 Meteorites

Chondrites For seven carbonaceous meteorites sulfur isotopic measurements of soluble and insoluble organic compounds were done by Gao and Thiemens (1993a) (fig. 1.6.1). They reported internal sulfur isotopic composition variations and all results are consistent with mass dependent fractionation. Internal variations in δ^{34}S, relative to CDT, were reported for Orgeuil (CI) (~6.5‰ - 7.1‰), Murchison (CM) (~3‰- 8.5‰), and Mighei, ALHA84029 (~8.36‰).

Besides carbonaceous meteorites Gao and Thiemens as well studied ordinary and enstatite chondrites for their sulfur isotopic composition (Gao and Thiemens, 1993b). For the ordinary chondrites Bjurbole and Chainpur the variation in δ^{34}S between matrices and chondrules is 0.14‰ and 0.91‰. However, in Bjurbole chondrules posse the heavy isotopic composition while in Chainpur the matrices is carrier of the heavy isotopic composition which was suggested to be the result of either the process of chondrule formation or the chondrules formed from two distinct reservoirs. For the enstatite meteorites Abee, Qingzhen, and Indarch internal isotopic variations in the range of 0.2‰ - 2.0‰ are reported which may be a sign for regional heterogeneity in the solar nebula. Apart from studying meteorite internal variations Gao and Thiemens (1993b) pointed out that between different chondrite groups is a difference in δ^{34}. Going from depletion relative to CDT to enrichment the average δ^{34}S are for enstatite -0.26 ± 0.07‰, ordinary chondrites -0.02 ± 0.06‰, and carbonaceous chondrites 0.49 ± 0.16 ‰.

A thorough study of sulfur isotopic composition in Fe-Ni sulfide grains in two CI and six CM carbonaceous chondrites has been done by Bullock et al. (2010) using secondary ion mass spectrometry (SIMS), which allows to do petrographic analysis before and after isotopic analysis. Thus the matrix type can be verified unambiguous after the measurement unlike in the study of Gao and Thiemens (1993a) were chemical extraction and gas mass spectrometry was used. Remarkably Bullock et al. (2010) got different results for the range of enrichment and depletion of large (~300µm) sulfide grains in chondrules embedded in the matrix and in the rim while previous studies (Gao and Thiemens, 1993a; Monster et al., 1965; Kaplan and Hulston, 1966) showed only an enrichment in δ^{34}S for CI chondrites. CM chondrites the majority of grains showed in average a depletion of δ^{34}S -0.9‰while McSween et al. (1997) reported a enrichment in sulfide grains of Kaidun (CM1). Possible cause for the inconsistency is a bias in the samples since in this study nano phase sulfide grains and sulfur bearing minerals could not be measured which might have been part of the sample for previous studies as the samples were chemically extracted (Bullock et al., 2010).

Achondrites Achondrites have been studied for their sulfur isotopic composition by Rai et al. (2005) revealing an enrichment in ^{33}S in sulfides. In their study they extracted sulfid phases from 4 groups (howardite-eucrite-diogenite (HEDs), acapulcoite-lodranites, aubrites, ureilites, and two ungrouped ones) and measured the isotopic composition. In this set HEDs, acapulcoite-lodranites, and aubrites show an enrichment in ^{33}S of δ^{33}S = 0.227 ± 0.049‰, δ^{33}S = 0.034 ± 0.028‰, and δ^{33}S = 0.119 ± 0.167‰ respectively and an enrichment as well in ^{34}S δ^{34}S = 0.373 ± 0.170‰, δ^{34}S = 0.015 ± 0.147‰, and δ^{34}S = 0.319 ± 0.747‰ respectively (with respect to CDT). Cosmic spallation and stellar nucleosynthesis are ruled out as source of the enrichment because: (i) achondrites have not enough target Fe and too short cosmic ray exposure ages to produce the needed amount of ^{33}S through spallation, (ii) ^{36}S/^{32}S is constant within the uncertainties of the measurements while ^{32}S/^{33}S and ^{32}S/^{34}S are not constant which can not be the case since 32,33,34 are produced in similar star types while 36 is not and since 36 is the least abundant its isotopic ratio is very sensitive to changes.

Ureilites (Farquhar et al., 2000) analyzed 22 samples from 17 ureilites, a type of chondritic meteorite, for their sulfur isotopic composition and reported a small enrichment in ^{33}S relative to carbonaceous chondrites. The average was δ^{34}S = 0.44 ± 0.30‰ (1σ) and δ^{34}S = 0.28 ± 0.15‰ (relative to CDT) and their data lays on a mass-independent fractionation line (see fig fig. 1.6.1). The conclusion was that the enrichment is pristine leaving the question why the ureilite parent body should have a non chondritic sulfur isotopic composition.

Iron Meteorites An excess in ^{33}S and ^{36}S has been reported by Gao and Thiemens (1991) in the metal phase (FeNi alloy) and schreibersite of 4 iron meteorites and it has to be accounted as a result of spallogenic nuclear reactions. Sulfur isotopic composition of troilites (FeS) extracted from the same set of iron meteorites was consistent with mass dependent fractionation.

1.6.4 Possible Link between Meteorites and Photodissociation

Recently a study about the sulfur isotopic composition of magmatically differentiated meteorites has been published by Antonelli et al. (2014). They investigate the possible processes which could lead to the same isotopic composition as measured in those meteorites. As cause for this study the authors recall the conclusion done by Rai et al. (2005): i) that the sulfur isotopic composition was not homogenous among the material which later formed the early Solar System planetesimals, and ii) the 182Hf-182 ages laying within 1-3My of Solar System formation of magmatic irons implying that those are the oldest rocks formed in the Solar System. Therefore 61 troilite (FeS) nodules from 58 iron meteorites covering eight different groups (IAB,IC,IIAB,IIE,IIIAB,IIIF,IVA, and IVB) have been analyzed resulting in -0.799 - 1.289 ‰ for δ^{34}S and δ^{33}S = -0.562 - 0.532‰ respectively leading to a slope of ~0.516 ± 0.009. In their report Antonelli et al. (2014) discuss different possible processes which could lead to the measured Δ^{33}S of 0.042‰ ± 0.007‰ (magmatic processes, kinetic processes, mixing of distinct reservoirs, and Rayleigh distillation) here we will only debate the impact of nucleosynthesis, cosmic ray exposure, and effects of photochemistry.

For Antonelli et al. (2014) nucleosynthesis seems to be unlikely the cause for the variations seen in $\Delta^{36}S$ and $\Delta^{33}S$ because (i) nucleosynthesis would affect most $\Delta^{33}S$ since ^{36}S is thought to be produced in different reactions and circumstances then ^{32}S, ^{33}S, and ^{34}S (ii) a mixture of Solar System reservoir with a reservoir distinguished by a large 32 excess (as it is measured in some SiC grains, see later) would lead to a unidirectional depletion in all minor isotopes. Additionally the case of injection with such material requires a non-chondritic sulfur isotopic composition at the beginning and that the amount of sulfur carried by the SiC grains is not negligibly relative to the total sulfur content in the early Solar System stage. The authors argue against cosmic ray exposure because: (i) there is no correlation between exposure age products due to neutrons and the measured sulfur isotopic ratios, and (ii) the slope for $\Delta^{36}S/\Delta^{33}S$ obtained in this study diverges from theoretical predictions($\Delta^{36}S/\Delta^{33}S$ ~-7 ± 4 and $\Delta^{36}S/\Delta^{33}S$ ~8). As a possible cause Antonelli et al. (2014) suggest gas-phase photochemistry during the T-Tauri phase of the sun. They assume that H^2S, the most abundant S-bearing gas, is within ~2 AU distance to the sun and near to the surface of the disk. Due to Lyman-α radiation photolysis of H_2S would occur resulting in a mass independent fractionation similar to what has been observed for achondritic and iron meteorites. They model the H_2S photolysis with time-dependent mid plane temperature and disk surface density but isothermal vertical temperature profile. Based on the yield in the laboratory work done by Chakraborty et al. (2013) it is estimated that ~2% of the total H_2S is photolyzed and present in the region were parent bodies of achondritic and iron meteorites formed. The authors report that enough it is possible to photolyze ~2% of H_2S in the time span of the T-Tauri phase for high mass and a low mass ($0.24M_\odot$) disk type.

1.6.5 SiC grains

Although silicon carbide grains have been discovered more than twenty years ago only during the last five years extensive studies of single grains could be performed because of the significant improvements of analysis techniques (Hoppe et al., 2010, 2012; Xu et al., 2015; Hoppe et al., 2015). Here we concentrate on sulfur isotopic ratios in this type of grains. Almost all presented data here were retrieved of SiC grains from Murchison meteorite which contains on average the largest grains sizes. This makes it possible to examine single grains instead of a collection of grains. Thus the likely origin of a single grain can be determined from its isotopic ratios.

Recently two studies examined SiC grains from Murchison meteorite for their isotopic composition; C,Si,N, S, Mg-Al, and Ca-Ti isotopic composition by (Xu et al., 2015), and Si, C, and S isotopic composition by Hoppe et al. (2015). For their analysis (Xu et al., 2015) used SiC grains of the separates KJE (described by Amari et al. (1995)) which have a typical diameter between 0.5 and 0.8 µm. With the Cameca NanoSIMS 50 ion microprobe an automatic isotopic imaging was done to find rare SiC grains. The selected grains were then measured with negative ion images to obtain isotopic abundances. They report for 16 X grains, 1 C grain, 1 Y grain, 5 Z grains, and 2 silicon nitride grains isotope fractionation in ^{33}S and ^{34}S (fig. 1.6.2). Z, Y and silicon nitride grains show isotope fractionation of ~± 100‰ for ^{34}S and almost no spread for ^{33}S, X grains show a larger spread with ~±200‰ and ~± 400‰ respectively whereas the C grain shows the largest

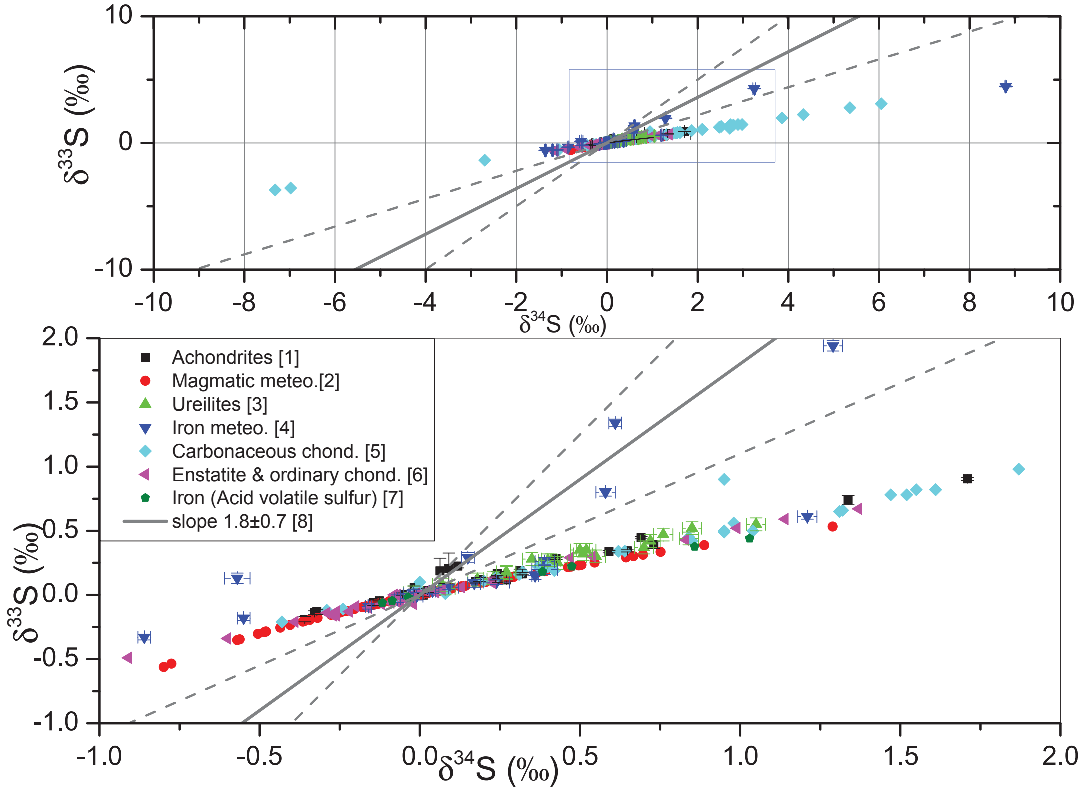

Fig. 1.6.1: Sulfur three isotope plot of meteorite data with δ^{33}S relative to δ^{34}S. Meteorite data are from [1] (Rai et al., 2005), [2] (Antonelli et al., 2014), [3] (Farquhar et al., 2000), [4] (Gao and Thiemens, 1991), [5] (Gao and Thiemens, 1993a), [6] (Gao and Thiemens, 1993b), and [7] (Franz et al., 2010). The slope [8] bases on a fit done by Hoppe et al. (2015) for SiC grains (see section 1.6.5).

depletion in ^{33}S and ^{34}S with -944‰ ± 33‰ and -941‰ ± 14‰, respectively. They conclude that the large ^{32}S excess comes more likely from decay of short-lived ^{32}Si than from the fractionation model established by Hoppe et al. (2012) because the excess is larger than what is predicted for the Si/S zone of core-collapses SNe. Besides comparing models of super novae Xu et al. (2015) addressed two main problems for S isotope studies; first low intrinsic concentration since S does not readily condense into SiC, and second some contamination with isotopically terrestrial S during the separation process i.e. for the C grain the negative ion image most of the S was located at the rim and the depletion was less there than for the center part (for more details see (Xu et al., 2015)). The mean over the entire image would be δ^{34}S -703 ± 14‰ and δ^{34}S -714 ± 24‰.

Hoppe et al. (2015) studied 14 presolar SiC mainstream grains for their C, Si, and S isotopic composition. They prepared a ~48 g sample of Murchison meteorite following a similar procedure which was used for the separate KJE by Amari et al. (1995) and developed by Besmehn and Hoppe (2003) To minimize a bias in the results due to S contamination only grains with smooth surface and a compact appearance were selected for this study. Additionally the grains and their surroundings were cleaned with a Cs^{+} ion beam via presputtering. However, not all the surface contamination could be removed. Isotopic abundances were calculated from negative ion measurements of -^{33}S and -^{34}S. The result for 14 mainstream SiC grains for sulfur isotopic composition lay on a line with slope

1.8 ± 0.7 (see fig. 1.6.2) and the authors stated that this correlation for mains stream grains may come rather from galactic chemical evolution (GCE) than from local stellar nucleosynthesis. For further details about GCE see Hoppe et al. (2015) and reference in there.

Besides SiC grains form Murchison meteorite there is are two reports of sulfur isotopic composition of SiC grains from enstatite meteorite Indarch (Gyngard et al., 2010; Orthous-Daunay et al., 2012). Gyngard et al. (2010) analyzed a C type grain resulting in a depletion of δ^{33}S -331 ± 129‰ δ^{34}S -323 ± 56‰, respectively. In Orthous-Daunay et al. (2012) a so called U/C grain has been identified and it showed a depletion in ^{33}S and ^{34}S of δ^{33}S = -203 ± 84‰ and δ^{34}S = -51 ± 39‰, respectively. Unfortunate no further measurements of the sulfur isotopic composition of SiC grains from this meteorite are available.

From the compilation in fig. 1.6.2 one can see that δ^{33}S in different SiC grains range in average from ~-400 to 300‰ while the spread in δ^{34}S is smaller with a range of ~-200 to 200‰. The data set is too small in order to see distinct types populate in distinct regions.

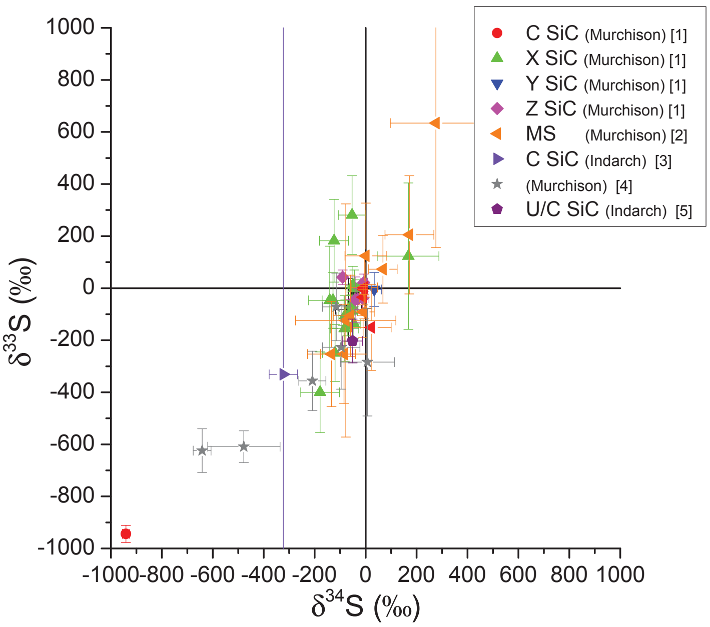

Fig. 1.6.2: Sulfur three isotope plot of SiC grain data. The grains have been sorted due to their type and their parent body is given in brackets. Data from [1] (Xu et al., 2015) , [2] (Hoppe et al., 2015), [3] (Gyngard et al., 2010) , [5] (Hoppe et al., 2012), and [5] (Orthous-Daunay et al., 2012) have been used for this graph.

1.7 Rosetta

Rosetta is an international space mission under the lead of the European Space Agency (ESA) aiming to accompany a comet from close to aphelion past its perihelion. Rosetta was launched in 2004 with a Ariane 5 G+ on March 2nd and encountered its target comet 67P/Churyumov-Gerasimenko beginning of August 2014. During the 10 year of cruise phase Rosetta did several swing-bys at Earth and one at Mars. In addition it did a flyby at the main belt asteroids Steins (2008) and Lutetia (2010) before going into hibernation in July 2011. Hibernation was inevitable because Rosetta gets its power from solar panels and being further away than ~4.4 AU the energy input via solar radiation would have not

been sufficient. More information about the milestones and the space craft itself can be found on the ESA web page `http://sci.esa.int/rosetta/`.
The motive to undertake such a demanding mission is: understanding the origin of comets and learn more about the origin of the Solar System. Consequently the scientific goals of the mission are: i) the global characterization of the nucleus e.g. size, shape, density to name some, ii) characterization of the coma e.g composition of neutrals and ions, the dynamics, and dust, iii) studying the isotopic composition of gas and refractory phase, iv) study the change of activity, surface properties, and the coma composition with decreasing heliocentric distance, and v) study the interaction of the solar wind and the arising coma through out the mission (Glassmeier et al., 2009). To achieve its goals Rosetta has 12 different experiments and a landing unit on board. Here only a short summary about the kind of instruments on board of Rosetta will be given and for further information the author refers to Glassmeier et al. (2009). Besides the camera system OSIRIS also VIRTIS can observe the nucleus in the visible and infrared. Additionally VIRTIS can observe like ALICE (ultra violet) and MIRO (microwave) the coma via spectroscopy. Some sort of combined experiment is ROSINA because it can determine the neutral and ion gas density and determine the velocity of neutral particles. Dust is observe on board of Rosetta by the instruments GIADA, COSIMA, and MIDAS which measure the dust velocity and impact momentum, the dust composition via secondary ion mass spectrometry, and the grain morphology respectively. The solar wind and its interaction with the coma can be observed with the plasma consortium (RPC). As a counterpart to the orbiter the lander PHILAE was designed with 10 small experiments on board. Among them are besides the two cameras CIVA (panoramic camera and microscope) and ROLIS (descent camera), two mass spectrometer PTOLEMY (determination of isotopic ratios) and COSAC (determination of elemental and molecular composition), a α-p-X Ray spectrometer (APXS), a magnetometer with a plasma monitor (ROMAP), an experiment to perform electric and acoustic sounding of the surface (SESAME), MUPUS that measures among others the temperature gradient, and CONSERT a nucleus sounding experiment to measure density distribution in the nucleus (Glassmeier et al., 2009). In more detail only ROSINA will be introduced since this study presents results achieved whit this experiment.

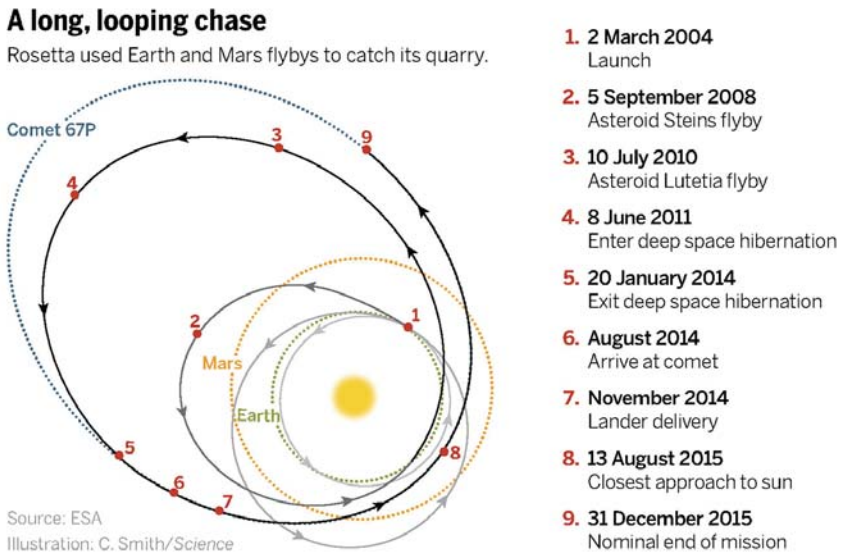

Fig. 1.7.1: Rosettas 10 year long lasting journey to its target Churyumov-Gerasimenko. Credit:ESA

1.8 ROSINA

ROSINA stands for Rosetta Orbiter Spectrometer for Ion and Neutral Analysis and consist of three instruments, a Double Focusing Mass Spectrometer (DFMS), a Reflectron-type Time-Of-Flight mass spectrometer (RTOF), and a COmetary Pressure Sensor (COPS). COPS and RTOF are briefly introduced in this section while DFMS is presented in more details in section 1.9.

1.8.1 Reflectron-type Time-Of-Flight

RTOF is a time of flight (TOF) mass spectrometer and thus has a different principle to do the mass analysis. For such an instrument ions given the same energy with different mass to charge (m/z) are dispersed in time during their flight along a field-free drift path of known length. Assuming that the ions have all the same start time or at least start within a sufficient short time interval, the lighter an ion is the earlier it will arrive at the detector. In order to have a velocity the ions have to be accelerated which is done by applying a voltage U thus the energy of an ion with mass m_i is:

$$E_U = qU = ezU \tag{1.8.1}$$

q is the charge, which can be expressed in units of the electron charge e and an integer z, then $q = ez$. The gained potential energy is transformed into a kinetic energy

$$E_U = ezU = \frac{1}{2} m_i v^2 = E_{kin} \tag{1.8.2}$$

Providing that the ions were at rest before the acceleration the velocity of the ions is given by

$$v = \sqrt{\frac{2ezU}{m_i}} \tag{1.8.3}$$

Knowing the drift length s the mass to charge ratio of the incoming ions can be calculated via:

$$t = \frac{s}{\sqrt{\frac{2ezU}{m_i}}} = \frac{s}{\sqrt{2U}} \sqrt{\frac{m_i}{ez}} \propto \sqrt{\frac{m_i}{q}} \tag{1.8.4}$$

The derived equation holds only under the condition that the particles were at rest before the acceleration and that no further acceleration is present (adapted from Calmonte (2011).

In order to enhance the resolution the flight time thus the flight path has to be enhanced which has been done at RTOF with a reflectron lens. In addition RTOF has two ion sources types a so-called storage source, where continuously produced ions are stored till their extraction, and the so-called ortho-source which is supposed to be used for ion measurements. Like DFMS ions are either produced via electron impact ionization in the ion source or they are produced outside of the instrument in the surrounding gas and measured with special ion operation modes.The RTOF detector consists of a MCP and can be operated in counting or analog mode. Thus it is able to measure single ion and bunches up to 10^5 ions. RTOF is operated that it can measure at least up to m/z 300 in one spectra which takes 200 sec acquisition time and it has a resolution of 400 at 50 % peak height.

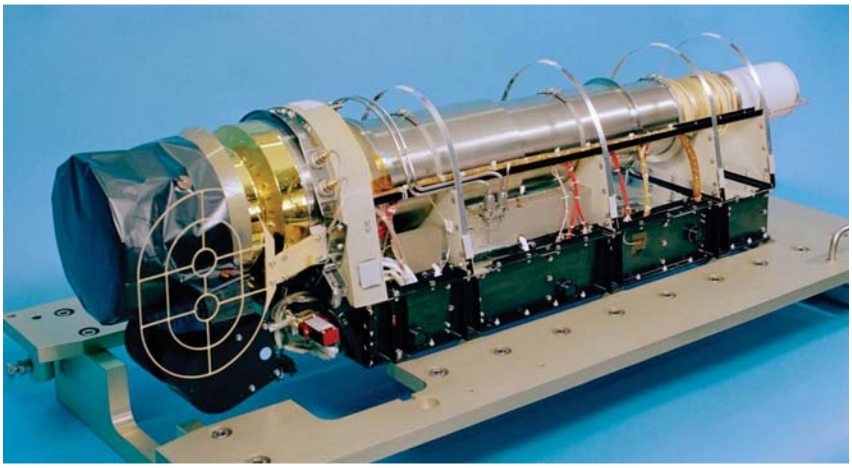

Fig. 1.8.1: RTOF without MLI and covered ion source.

1.8.2 COmetary Pressure Sensor

COPS consists of two pressure gauges the so-called nude gauge which measures the overall gas density and the so-called ram gauge measuring the ram 'pressure' which is a particle flux from a certain direction. At the nude gauge ions are created via electron impact ionization between the filament and the grid and accelerated to the cathode at the base of the cylindrical grid. The measured ion current is directly proportional to the particle density. At the ram gauge ions are generated also with electron impact ionization but the filament has been exchanged by so called microtip field emitters. This had to be done because in front of the ionization part of the ram gauge is an equilibrium chamber where the neutral gas is thermalized. A hot cathode filament would lead to a non isotropic temperature distribution on the equilibrium chamber and make it impossible to analyze the data (Balsiger et al., 2007; Schläppi, 2011). Those measurements allow to calculate the cometary gas velocity and thus the gas temperature. Besides its scientific benefit COPS density measurements are used by various instruments on board of Rosetta and the spacecraft itself as a safety element. Meaning that they shut off if a certain density is exceeded.

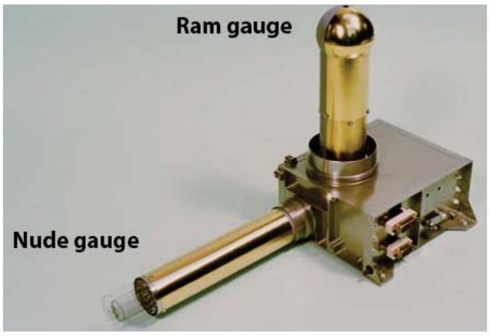

Fig. 1.8.2: COPS

1.8.3 Data Processing Unit

In order to command and control the three instruments ROSINA has a so-called Data Processing Unit (DPU) as it is presented fig. 1.8.3. Except the instrument interfaces all DPU functions are duplicated and organized into two independent branches. Within the

DPU all measurement modes for any of the three instrument are stored and can be changed by either software patches/updates or direct commanding. Besides the operation and observation the three ROSINA instruments the DPU is the interface for communication between ROSINA and the spacecraft.

Fig. 1.8.3: Flight DPU

1.9 DFMS

The main characteristics of DFMS are a high mass resolution of $m/\Delta m$ 3000 at 1% peak height on mass to charge 28 u/e ($m/\Delta m$ 9000 at 50% peak height) and its dynamic range of 10^8 making it possible to measure minor species. Besides this, DFMS is designed in such a way that covers a mass range from m/z 12 - 140 u/e, has a good energy focusing properties in order that $\Delta E/E$ is up to 1 %, and a high mass dispersion in the focal plane making in possible to use a position sensitive detector.

Figure 1.9.1 shows DFMS with closed cover to protect the ion source, with a gas inlet let on the right side for measurement purposes in the lab, and without the so-called Multi Layer Insulation (MLI). The MLI are needed to insulate DFMS against heat loss by thermal radiation and it shields DFMS against electrical charged particles. The main components of DFMS are an electronic box, a ion source protected by a cover during launch, the mass analyzer constituent of a electrostatic analyzer (ESA) and a magnet, zoom optics, a detector head containing three different detector types, and a gas calibration unit (GCU). DFMS is able to measure both neutrals and ions present in the ambient gas although not simultaneously. When DFMS is operating in neutral mode neutral particles in the ion source get ionized and then guided to the mass analyzer while a potential is applied on a grid outside of the ion source (the golden ring structure around the cover) to avoid already charged particles to enter the ion source. In ion mode the grid has a positive potential applied to attract negative ions which are then guided into the ion source. The following process is the same regardless the origin of the ions in the ions source. After leaving the ion source the ions enter the mass analyzer and mass separation takes place in such a case that only particles with a certain mass to charge ratio and a certain energy will be guided to the zoom optics. There the ion beam can be widened resulting in a higher resolution before it hits one of the three detectors. This process and how it is established will be explained in the following sub sections in more detail.

When DFMS was built it was thought that the evolution of sensitivity could be followed via on board calibration. Therefore it has been equipped with a gas calibration unit containing 1/3 in mass of Ne, CO_2, and Xe.

Unlike other instruments used in space ROSINA has for every instrument a twin on Earth

with its own DPU in order to characterize the instrument and to simulate incidents in space. The instrument with the better performance was labeled Flight Instrument (FM) and the other one was the Flight Spare (FS). However, after the postponed launch it turned out that the FS had the better performance and thus it became the instrument flying now in space. In order to not enlarge the confusion the label stayed although the meaning of the names are not true anymore.
After the description of the mass analyzer and the detectors a peculiarity of DFMS will be introduced, the so-called individual pixel gain, and a brief introduction on the sensitivity of DFMS will be given.

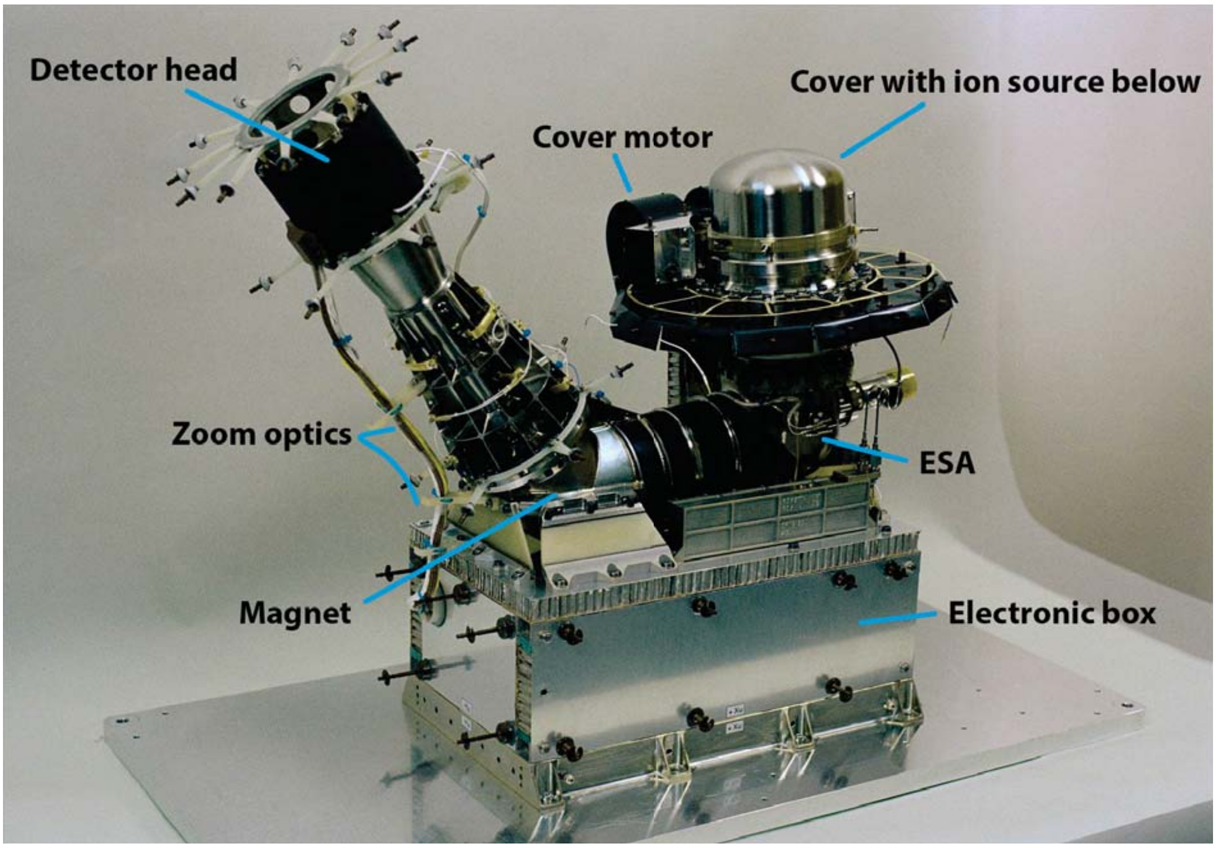

Fig. 1.9.1: Double Focusing Mass Spectrometer (DFMS) with closed cover, a gas inlet on the right end, and without the Multi Layer Insulation (MLI).

1.9.1 Ion Source and Transfer Optics

In fig. 1.9.2 the ion source assembly of DFMS FM is shown, with the ion source, one of the two entry slits, and the grid. DFMS has two entrance slits for particles on top of the ion source and an orthogonal to the ion source axis pointing towards the image plane in fig. 1.9.2. The first one has a field of view (FOV) of ± 20° and the second one has a FOV of ± 2°. As already mentioned DFMS can be operated in ion or neutral mode. In neutral gas mode the grid is positive charged to repel ions from the ambient gas while neutral particles can enter the ion source where they get ionized via electron impact ionization with an electron energy of $E_{e^-} = 45$ eV. The electrons are provided from one of two filaments and guided through a magnetic field of 200 G in such a way that an electron beam orthogonal to the ion optical axis is established. Two filaments are built in for redundancy and thus the not emitting filament can be used as electron trap to observe the emission current that can be regulated to 2, 20 or 200 µA dependent on the pressure to reach best sensitivity. The electron energy can be varied between 10-90 eV. Schläppi (2011) showed that for DFMS at 45 eV less multiple charged ions and less molecule fragments are produced than at 70 eV which is usually used for such a type of ion source.

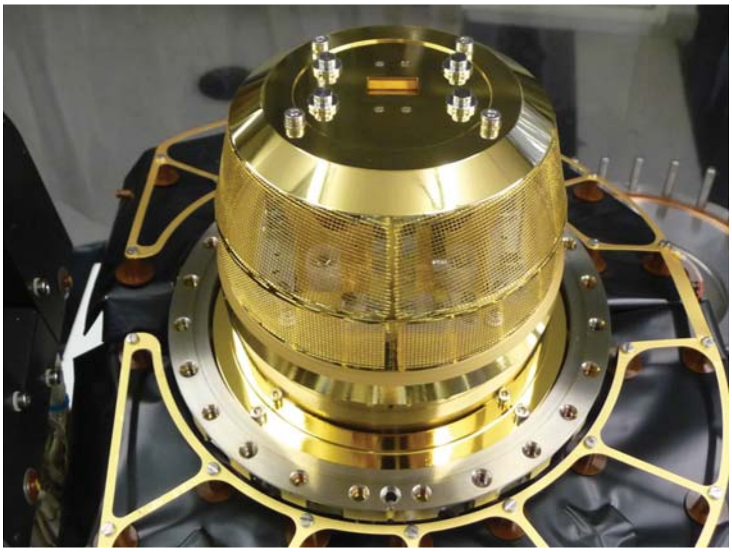

Fig. 1.9.2: DFMS FM ion source assembly; the rectangular opening is one of the two ion source openings, the golden grid below is during neutral modes negatively charged to repel ions from the ambient gas and during ion modes it is positively charged to attract ions.

Electron impact ionization is a violent process which can split up, for a certain percentage, more than one electron leading to multiple charged ions or which can split a certain amount of the molecules into ionized fragments. The production rate of byproducts is dependent on the molecule properties and the energy of the impacting electrons. In addition to the positive grid potential the ion source bias is floated to +200 V and thus external ions present in the ion source are accelerated different from the produced ones in the ion source. With this additional potential it is taken advantage of the energy acceptance of ± 1% of the electrostatic analyzer (ESA). The extraction of the ions is done via two source lenses which deflect the ion beam in to the plane of the ion trajectories and the source exit slit potential which is at -1kV relative to the ion source bias.
In ion mode the grid and some electrodes in the ion source are used to first attract external positive charged ions and then focus them into the ionization zone of the ion source. The grid can be charged ± 5, 10, and 20 V and thus can be used to compensate the space craft potential. During ion modes the filament is in submission meaning the filament stays hot but no current is emitted. Like this an accretion of gas particles on the filament can be prevented. For a more detailed description of the ions source the author refers to the thesis of Schläppi (2011) on which the above paragraph bases.
Since a permanent magnet is part of the mass analyzer a mass scan can only be achieved by varying the ion energy. Thus the extracted ions have to be accelerated or decelerated in order to have the correct energy for analysis which is done with applying the voltage V_{accel}. Besides the adjustment of the ion energy the ion beam has to be focused on one of two selective resolution slits and the ion beam has to be corrected for the axial tilt of 6° between the ion source and the transfer optical axis (see fig. 1.9.3). The narrow slit corresponds to high resolution mode and has a width of 14µm while the wide slit corresponds to low resolution and has a width of 200 µm. The tilt has been introduced

to prevent dust particles falling onto the narrow slit and then possible enter the analyzer section. Thus an ion beam coming from the ion source is first brought to the required energy and transferred to the double entrance slits. After this the ion beam alignment can be adjusted with a rotational quadrupole it enters the entrance slit switch (ESS) region containing the low and high resolution slit. In low resolution the ion beam is deflected by the ESS potentials to the wide slide and afterward the beam is guided back to the so-called alpha slide. For high resolution mode no deflection is needed because the narrow and the alpha slit are aligned on the nominal optical axis (Schläppi, 2011; Riesen, 2007).

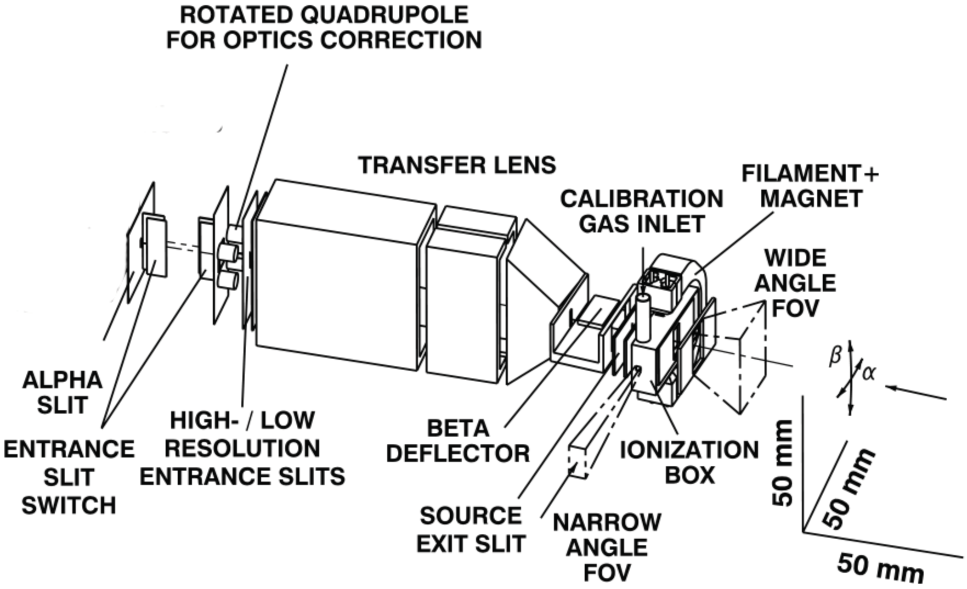

Fig. 1.9.3: Ion source and transfer optics (Balsiger et al., 2007)

1.9.2 Mass Analyzer and Zoom Optics

The mass analyzer of DFMS is designed according the so-called Nier-Johnson configuration (Johnson, E. and Nier, A., 1953) where a electrostatic analyzer deflect charged particles for π/2 followed by a magnet with a deflection of π/3. The ESA consists of two toroidal shaped deflection plates, a pair of Matsuda-plates which close the deflection plates on each side, and fringing fields shunts at the entrance and exit sides (see fig. 1.9.4 (a)). The Matsuda-plates can be used to adjust the image point of the ESA (Wüthrich, 2007) while the shunts ensure that the electric fields are terminated and that the deflection angle is exactly π/2.

The ion population extracted from the ion source is not monoenergetic and shows a spacial spread due to different ionization locations and differences in the start velocities. Therefore the ESA is used to focus the ion population in angle and energy onto the energy slit between the ESA and the magnet. Like this ions entering the ESA at the same point with the same energy but different entrance angles are focused on the image point after the ESA while ions entering the ESA with similar entrance angles but different energies will be spatially separated. The energy slit allows only ions with a deviation of ± 1% in the ion energy to pass. An ion of mass m, charge q, and velocity v that moves on the middle equipotential surface between the electrodes of a toroidal condenser flies on a circular arc of the same curvature as the ion optical element. Therefore the centrifugal force F_{cent} and the electrostatic force F_{el} have to compensate each other like

$$F_{cent} = \frac{mv^2}{r_{esa}} = qE_{esa} = F_{el} \tag{1.9.1}$$

whereas E_{esa} is the electric field applied over the ESA, and $r_{esa} = 60$ mm is the radius of the middle equipotential surface. The the kinetic energy $\frac{mv^2}{2}$ can be exchanged with the potential energy of the particle qV_{accel} which leads to

$$F_{cent} = \frac{2qV_{accel}}{r_{esa}} = qE_{esa} = F_{el} \tag{1.9.2}$$

After the passing trough the ESA the remaining ions enter the magnet analyzer at a distance of 99.5 mm from the energy slit. The magnetic analyzer consists of two permanent 60° sector magnets made of Samarium-Cobalt alloy while the pole pieces and yokes are made of an Iron-Cobalt alloy. The radius is 10 cm, the sector borders are tilted by 5° relative to the perpendicular of the ion trajectory, and it has an average magnetic field of 0.35 T depending on the magnet temperature. The magnetic field B is then:

$$B\left(T_{Mag}\right)_{FM} = 0.3563 - 1.2969 \cdot 10^{-4} \cdot \left(T_{Mag} - T_0\right) \tag{1.9.3}$$

$$B\left(T_{Mag}\right)_{FS} = 0.3550 - 1.7262 \cdot 10^{-4} \cdot \left(T_{Mag} - T_0\right) \tag{1.9.4}$$

where $T_0 = 22°\mathrm{C}$ for which the coefficients have been determined. The ions leaving the ESA are monoenergetic spatially separated rays and when they pass the magnet the will be separated in momentum due to the Lorentz force F_L. In addition the ions are then on a circular flight path which can be determined via balancing the Lorentz force with the centrifugal force:

$$F_L = qvB = \frac{mv^2}{r} = F_{cent} \;\Rightarrow r = \frac{mv^2}{qvB} \tag{1.9.5}$$

and combining this with $v = \frac{2qV_{accel}}{m}$ leads to the refraction radius r dependent on the acceleration voltage which can be adjusted, the magnetic field, and the mass to charge ratio:

$$r = \sqrt{\frac{m}{q}\frac{2V_{accel}}{B}} \tag{1.9.6}$$

In order to have ions after the passing of the magnet the acceleration voltage and mass to charge ratio have to be adjusted to get the same curvature radius for the ion flight path through the magnet as the magnet has.

After passing the mass analyzer the ions pass through a hexapole which is used to rotate the focal plane perpendicular to the ion optical axis. The hexapole is followed by two quadrupoles which are used to magnify the image scale on the detector up to a factor of 6-7 therefore they are called 'zoom system'. A schematic drawing of this system is given in fig. 1.9.4 (b). The effective gain in resolution has been estimated by Riesen (2007) and is ≈ 20%.

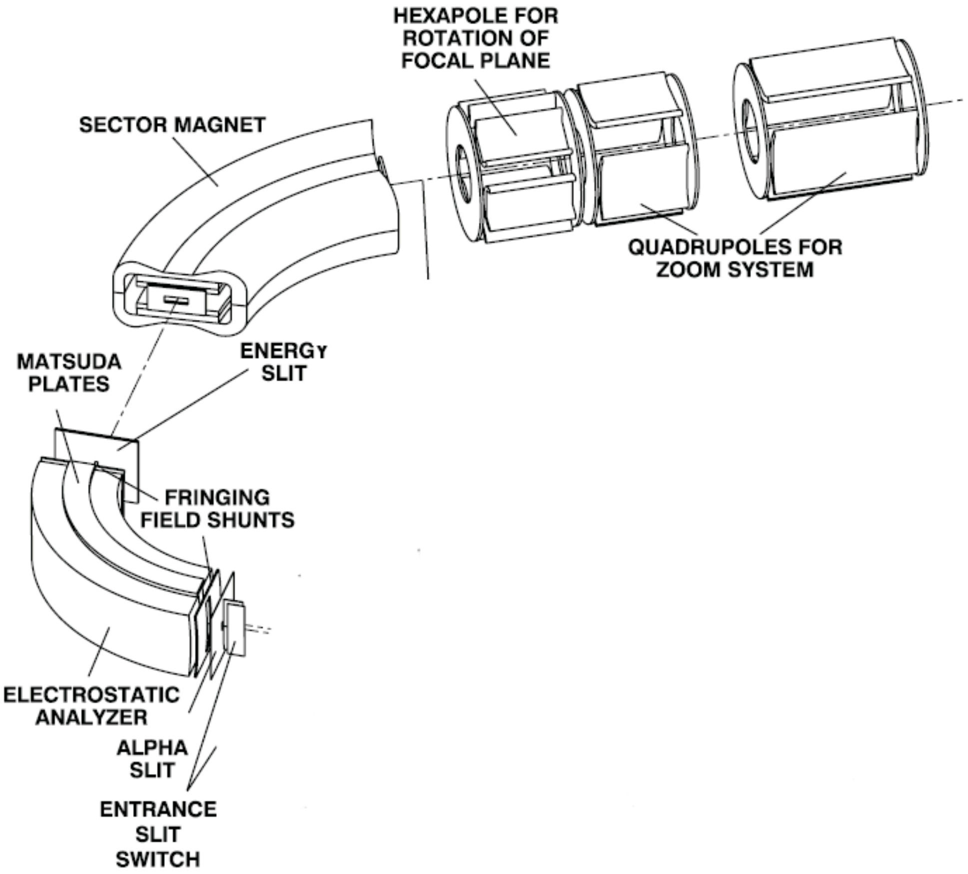

Fig. 1.9.4: Mass analyzer and zoom optics of the double focusing mass spectrometer (Balsiger et al., 2007).

1.9.3 Detector Head

The DFMS detector package consists of a position sensitive detector composed of a multi channel plate (MCP) and Linear Electron Detection Array (LEDA), a Channel Electron Multiplier (CEM), and a Faraday cup. In fig. 1.9.5 the profile of the detector head perpendicular to the ion optical axis is shown and as one can see the opening of CEM and Faraday lay on the focal plane while focal plane crosses the MCP/LEDA in the middle. Thus the detectors are aligned on the focal plane which is nominal tilted by 28.3° towards the ion optical axis. The MCP/LEDA is intended to be the main detector and thus it is positioned at the intersection of the focal plane with the nominal ion optical axis. When either CEM or the Faraday Cup are used an adjustment of V_{accel} will lead to the correct diffraction radius in the magnet to guide the ions to the right detector.

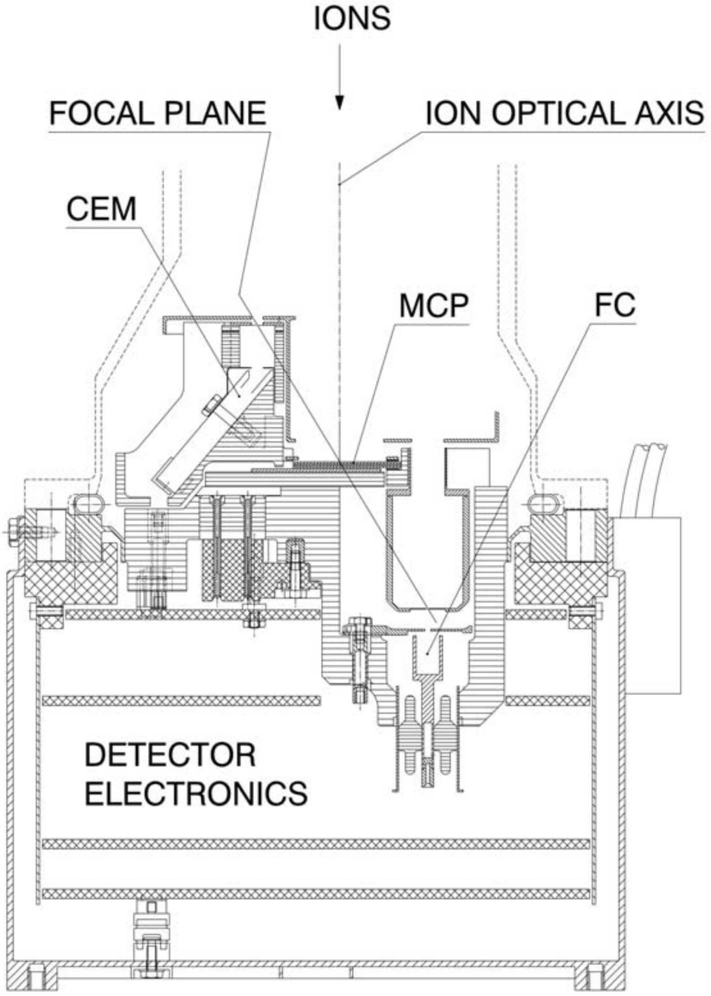

Fig. 1.9.5: Profile of the detector head (Balsiger et al., 2007). In this view pixel 1 is left and pixel 512 on the right side.

1.9.3.1 MCP/LEDA

The position sensitive detector MCP/LEDA is a Linear Electron Detection Array which has in front two micro channel plates. The plates are in a Chevron configuration with a inclination of the tubes of 13°, the thickness is 0.33 mm, the pore diameter is 6 µm, and the surface of one MCP is 26.5 x 18.4 mm^2 (Schläppi, 2011). Micro channel plates amplify the incoming signal by creating a secondary electron avalanche in the pores. The gain can be influenced by applying an electrical field over the MCP because then the secondary electrons are accelerated and will release more electrons from the MCP tube surface. For DFMS the potential at the back side is always at +200 V while on the front side a variable potential can be applied. It is possible to apply 16 different potentials which will vary the the gain in signal between 10^0 to 10^6. The secondary electrons produced in the MCP are then accelerated with 200 V to the LEDA, which is at local ground, in order to prevent a widening of the electron cloud between the creation in the MCP and the detection at the LEDA. The LEDA consist of two independent Linear Electron Detection Arrays (Nevejans et al., 2002) labeled row A and row B. Each row is built up of 215 anodes each covering an area of 8 mm x 22 µm with gap size between the anodes of 3 µm. Since the amplification can be varied with changing the MCP front voltage the LEDA is working in analog mode.

The secondary emission yield of an MCP is energy and species dependent as it has been shown by (Meier and Eberhardt, 1993) for similar set up. As a consequence ions with a low energy and therefore a low V_{accel} would be less efficient detected and to counteract this for mass to charge ratios larger than 69 u/e an additional acceleration voltage is applied on the front face of the detector head that is shown in fig. 1.9.6. The voltage is named post-acceleration (PA), it is either -1kV or 3kV, and it is applied on the gold coated anode in front of the detectors. Due to the asymmetric anode shape for the post acceleration the ion beam is distorted (Wüthrich, 2007; Riesen, 2007; Schläppi, 2011). This effect has already been studied by Wüthrich (2007); Riesen (2007) and further studies are planned.

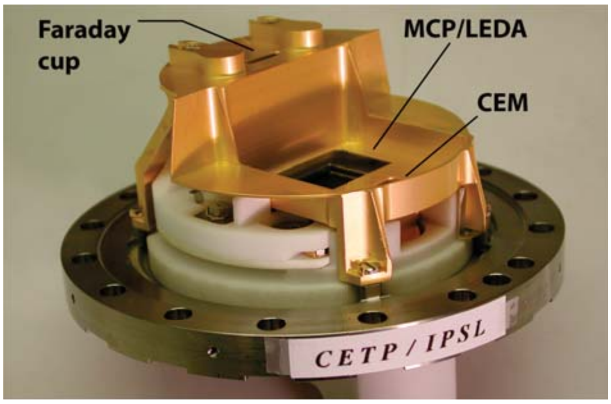

Fig. 1.9.6: Detector head without electronics.

1.9.3.2 CEM

The CEM is located on the left side of the MCP/LEDA in fig. 1.9.5 and a mass spectra is achieved by sweeping the ion beam for a certain mass to charge in steps over the 25 µm entrance slit. Unlike the LEDA the CEM can operate simultaneously in a counting mode and in two (high gain and low gain) analog modes with a nominal potential of -2337V applied over its detector. Since the zoom system can not be used with CEM high resolution and low resolution spectra are achieved by doing different step sizes for the beam. For low resolution the the relation is $\Delta m = \frac{m}{1000}$ and for high resolution $\Delta m = \frac{m}{1000}$. However in high resolution mode the step overlap and have of to be mathematical unfolded Schläppi (2011). Due to the measurement procedure to acquire a spectra with CEM is significantly longer than the recording time of a MCP/LEDA spectra.

1.9.3.3 Faraday Cup

The third detector is a common faraday cup which measures the incoming ion current without any amplification. In order to get a mass spectra the ion beam is like for the CEM shifted over the entrance slit (right side of MCP/LEDA in fig. 1.9.5) whit a step size of $\Delta m = \frac{m}{2000}$. The faraday cup is designed to measure currents between 10^{-14} - 10^{-8} A and therefore is not useful for highly sensitive measurements. Nevertheless is was planed to use the faraday cup in order to check the long term stability of the sensitivity of the other two detectors.

1.9.4 Operation

The operation of DFMS in space is done via so called modes (denoted with M) implemented in the board computer of ROSINA. Each measurement mode has a distinct emission, resolution, used detector type, and mass selection. Since DFMS measures single mass spectra masses sampled during one mode can be arranged as desired thus one can built a measurement mode sampling m/z 18, 28, 30, 44 u/e which takes roughly 4 minutes to be acquired while measuring the range from 13-100 u/e in steps of 1 u/e takes ~40 min. In order to acquire mass spectra a mass to charge ratio has to be set which is supposed to be in the middle of the spectra; this value is denoted with m_0. Based on the desired m_0 all voltages of the ion optics are adjusted to have m_0 in the center of the spectra. A a consequence the commanding in space is done in sequences of modes selected depending on the configuration Rosetta-67P-sun.

1.9.5 Individual Pixel Gain

As it has been explained previously the gain of the signal for the LEDA is achieved with a MCP at which 16 different voltages on the back and front side can be applied. Each voltage difference results in a distinct gain of the ingoing signal and is therefore called gain step (GS). Consequently the raw signal has to be corrected for the gain and a second MCP related correction, the so called individual pixel gain, has to be applied. The individual pixel gain reflects the difference in gain between pixels, due to the manufacturing of the MCP and due to the uneven exposure of pixels to incoming ions. The depletion of certain areas of the MCP are due the efficiency to liberate electrons from the inner wall of a channel drops with number of already released electrons. As may be imagined to have the main amount of a signal always on the same few ten pixels in the center of the LEDA will lead to a strong depletion in the center of the MCP and almost none at the edges. Hence an accurate characterization of this effect is vital for the understanding the measurements at the comet and therefore this section gives a compilation of previous work done by Riesen (2007); Schläppi (2011); Hässig (2013) and results achieved with further measurements with FM and FS.

A first exhaustive determination of the magnitude and thus the importance of the individual pixel gain has been carried out and described by Riesen (2007). DFMS was operating in high resolution, however the zoom was set to 1 and per pixel 5-6 spectra were acquired. The main findings were a modulation of ≈21 pixel with a variation of 34%, the decreasing peak height due to defocusing of the peak for pixel farther away from the ion optical axis, and the individual pixel gain is a function of the applied voltages at the MCP and not of measured species. The described dependence of peak width however seems to have changed since Riesen did this work.

In order to decrease the measurement time of the individual pixel gain factors for one gain step Schläppi (2011) studied the influence of the step width in pixel on the modulation. Measurements were done with a step width of 1-6 and 12 pixel and no significant difference in the individual pixel gain factor could be found in term of size and kind of modulation for 1-6 pixel per step. In contrast a step width of 12 pixels leads up to 6 times larger variations between minima and maxima and frequency of the modulation enlarges. This finding is not surprising taking into account the peak shape in HR mode because the main contributing peak in the signal has a full width at half the maximum (FWHM) of ~ 5 pixels at mass to charge 18 u/e. In consequence the sampling of the peak shape is coarse and thus can not represent the depletion due to the impinging ion beam. Based on this finding the step width was fixed to 4 pixel per step and three measurement modes for the three emissions were implemented in the software executing and controlling measurements. Measurements with FS in 2009 did not show a modulation as seen for FM as it has been expected from preflight calibrations (Nevejans et al., 2002) because the MCP used in FS is not built of hexagonal substructure.

For the calibration campaign carried out by Hässig (2013) measurements of the individual pixel gain factors were done for GS 7-16 where for GS 14 and 10, two data sets are available. A comparison of 2009 and 2012 showed a depletion of roughly 40% which is well understood since in this period DFMS was measuring for ~3000 h.

1.9.6 Sensitivity

The sensitivity for the detection of a neutral particle with DFMS MCP/LEDA is dependent on three parameters:

$$S_i \propto \sigma_{EII} \cdot \tau \cdot yield \tag{1.9.7}$$

where S_i is the sensitivity for the species i, σ_{EII} the ionization cross section, the sensor transmission τ, and the detection efficiency given by the so called *yield* (Hässig, 2013) and and they have in turn particles specific dependencies: i) σ_{EII} depends on the species and the electron energy, which is for DFMS 45 eV, ii) the transmission τ depends on the mass to charge ratio of the particle and the resolution mode because the particles have a different flight path, and iii) the *yield* depends on the species and the energy of the incident particle (Meier and Eberhardt, 1993).

The sensitivity to detect a particle with CEM or Faraday differs only in the detection efficiency from MCP/LEDA which is not species dependent and therefore has been set to 1 (Hässig, 2013).

1.10 Churyumov-Gerasimenko

Initially 46P/Wirtanen was the target of the Rosetta mission but after a failure of an Ariane rocket in 2002 ESA was forced to postpone the launch of Rosetta and thus a new target had to be found. Like Wirtanen the new target 67P/Churyumov-Gerasimenko is Jupiter family comet and it was selected due to orbital considerations. Before the launch of Rosetta only little was known about G-Cs physical properties although it has been discovered by Svetlana Ivanovna Gerasimenko already 1969 (Lamy et al., 2009). After Rosetta had been re targeted a world wild coordinated observational campaign started to characterize 67P as good as possible and thus be prepared as good as possible for the encounter in 2014. A first review has been given by Lamy et al. (2009) and the following short portrait of Churyumov-Gerasimenko bases manly on this review.

When 67P/C-G was discovered by Svetlana Ivanovna Gerasimenko and Klim Ivanovich Churyumov of the Kiev Shevchenko Natonal University it was already on its second orbit after been disturbed by Jupiter from its previous orbit. The change in orbit occurred in 1959 when 67P/C-G and Jupiter had a close encounter which lead to an orbit change for the comet: the perihelion moved from 2.74 AU to 1.28 AU, the eccentricity increased from 0.36 to 0.63, and the orbital period was reduced from 8.97 to 6.55 yr. Besides being a Jupiter family comet (Tisserand parameter $T_J = 2.75$) it is as well a so called Near-Earth comet because model calculations predict encounters with Earth within 0.019

AU and it had already an encounter within 0.4 AU in 1982. In order to characterize C-Gs physical properties measurements at the Hubble Space Telescope could be performed and analyzed by Lamy et al. (2006) on March 1st and 13th when 67P was at 2.52 AU outbound. The characteristics based on those measurements and several assumptions (for more details see (Lamy et al., 2006)) are as follows: a mean radius of 1.98 ± 0.02 km with an assumed albedo of 0.04 and phase coefficient of 0.04 mag/deg, a three dimensional shape of 4.56x3.81x3.44 km, a rotational period of 12.41 ± 0.41 hrs but not clear then whether the rotations is pro- or retrograde, and a color index (V-R) = 0.52 ± 0.05.

A few days before launching Rosetta in 2004 thermal images of 67P were acquired with the Multiband Imaging Photometer for SIRTF (MIPS) of Spitzer when the comet was at 4.48 AU outbound from the Sun Unfortunate the resulting parameters did not converge and further observations were done. Thus a three night observing run was done with the New Technology Telescope (NTT) in May 2005 by Lowry et al. to sample the full light curve of the comet. Since the comet was then at 5.6 AU there were no signs of out gassing or a coma. The results were as follows (personal com. between Lamy and Lowry 2006): a rotational period of 12.72 ± 0.05 hrs thus a bit longer than what Lamy et al. (2006) had, a mean effective radius of 2.26 ± 0.03 km assuming the same albedo and phase coefficient as (Lamy et al., 2006), a mean R absolute magnitude of 15.34 ± 0.03, and a color index (V-R) = 0.41 ± 0.04. Later based on additional measurements at NTT two possible shape models were presented by Lamy et al. (2009) which differed only in the x length. Thus the comets size was predicted to be in x-y-z 5.10 x 4.18 x 3.44 km for prograde rotation and 4.40 x 4.16 x 3.38 for retrograde rotation. A reconstruction of the nucleus of 67P based on Hubble Space Telescope observations is shown in fig. 1.10.1 (a). Further observations and analysis about the nucleus and the activity of C-G were performed by Lowry et al. (2012) and Snodgrass et al. (2013) and here only the part about the activity will be summarized since the results about the nucleus did not change significantly.

For their study Snodgrass et al. (2013) did not only consider their own measurements done at the Very Large Telescope between July 2007 and March 2008 but they took into account the large archival data set of 67P, which ranges from October 1982 to August 2010 and consists of ~200 individual nights. Thus Snodgrass et al. (2013) discovered that activity starts already around 4 AU heliocentric distance and that latest at 3.4 AU “the comets morphology shows activity”. The dust flux shows a slight pre/post-perihelion asymmetry and he suggest that only 1.4% of the surface area is active considering water and it has to be even less for CO_2 (0.04% - 0.09%). In addition Snodgrass et al. (2013) made some predictions for the years 2014/2015 when Rosetta is supposed to be at the comet of which the most important one is that the comet is likely to be active already before the encounter with Rosetta.

Although there was an effort to determine the physical properties of C-G before the encounter with Rosetta only little was known about its composition. In his paper (Schleicher, 2006) mentions studies done by Cochran et al. (1992); Weiler et al. (2004); Schulz et al. (2004) which only studied radicals like C_2 or OH. (Schleicher, 2006) evaluated data of 16 nights acquired at the Lowell Observatory via narrowband photometry during the apparitions in 1982/83, 1995/96, and one night near perihelion in 1996. The heliocentric distance for those measurements ranges from 1.48 to 1.34 AU before perihelion and from 1.30 to 1.86 after perihelion passage. Based on the measurements production rates for OH, NH, CN, C_3, and C_2 were determined and for all of them a pre/post-perihelion asymmetry was present. OH had a pre/post-perihelion ratio of ~2 while the minor species and the dust showed a larger symmetry going up to a factor of 8. In addition Schleicher (2006) estimate the peak productions ratios to be roughly a month after perihelion passage. Due to their sampling interval it was not possible to determine the time of the peak production rate more precise. Following the classification established by A'Hearn et al. (1995) Schleicher (2006) characterized C-G as mildly C depleted because the average log of the C_2-to-CN ratio is -0.21 ± 0.27 which gives a factor of ~2.2 of C_2 with respect to CN. In their summary (Schleicher, 2006) states that "Churuymov-Gerasimenko can be considered a 'proto-typical' Jupiter-family comet, having a large pre/post-perihelion asymmetry, steep r_H-dependencies, moderate depletion of C_2 and C_3, and coma morphologies likely due to one or more jets. ... Each of these characteristics is exhibited by many if not most comets believed to have originated in the Kuiper belt." Furthermore they estimate that only 3-4 % of the surface can be active based on their measurements of OH and the nucleus radius determined by Lamy et al. (2003).

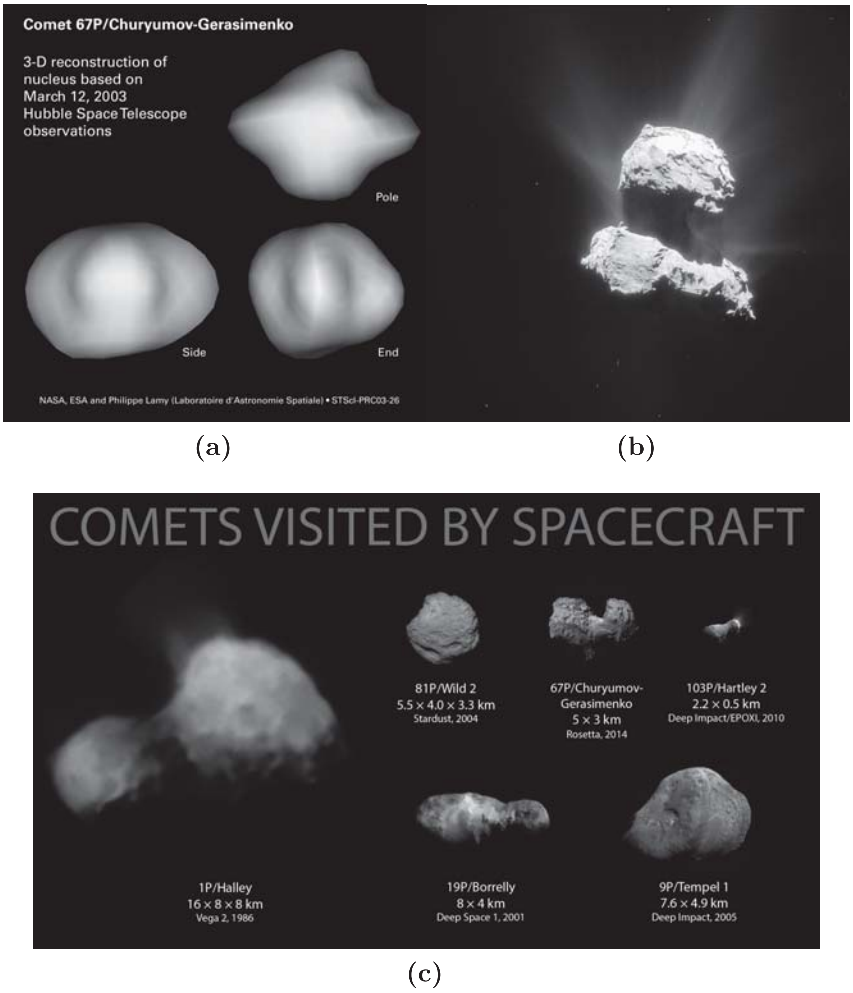

(a) **(b)**

(c)

Fig. 1.10.1: (a) shows the shape model of 67P based on light curves measured with the Hubble Space Telescope in 2003 while (b) shows the nucleus of 67P in April 2015. In (c) a compilation of the comets visited yet by spacecrafts is shown. Credits: (a) NASA ESA and Philippe Lamy (Laboratoire d'Astronomie Spatiale) STScl-PRC03-26, (b) ESA/Rosetta/NAVCAM, CC BY-SA IGO 3.0, and (c) Image credits: Halley: Russian Academy of Sciences/Ted Stryk. Borrelly: NASA/JPL/Ted Stryk. Tempel 1 and Hartley 2: NASA/JPL/UMD. Churyumov-Gerasimenko: ESA/Rosetta/NavCam/Emily Lakdawalla. Wild 2: NASA/JPL. Montage done by Emily Lakdawalla.

One of the first surprises was the actual shape of the nucleus of 67P. The difference between the true shape and the model shown in fig. 1.10.1 (b) and (a) reps. is significant. Instead of a rhombus like object Churyumov-Gerasimenko appears to consists of two lobes similar to the comets Hartley 2 and Borelly as it can be seen from fig. 1.10.1 (c).
The most important findings of ROSINA in the coma of Churyumov-Gerasimenko are:

- Soon after the encounter in August 2014 diurnal and most likely seasonal variations could be observed in the abundance of the major volatile species H_2O, CO, and CO_2. However, it was not possible to draw any conclusion with regarding the origin of this coma heterogeneity (Hässig et al., 2015).

- The D/H in water at 67P was found to be $(5.3 \pm 0.7) \cdot 10^{-4}$ (Altwegg et al., 2015) and thus about 3 times higher than the terrestrial value. This value exceed what has been reported for Jupiter family comets so far - namely $(1.61 \pm 0.24) \cdot 10^{-4}$ in Hartely 2 (Hartogh et al., 2011) and an upper limit of $2.0 \cdot 10^{-4}$ in comet 45P/Honda-Mrkos-Pajdusakova (Ceccarelli et al., 2014). The finding of Altwegg et al. (2015) indicates that there is no distinct value for D/H in Jupiter family comets.

- The first detection of N_2 in comets was reported by Rubin et al. (2015) based on measurements performed in October 2014. For N_2/CO a mean value of $(5.70 \pm 0.66) \cdot 10^{-3}$ has been reported. However, the N_2/CO ratio varies between 0.17 to 1.6% depending on the position of Rosetta with respect to the nucleus. The origin of the variation could not be identified. Based on the depletion of N_2/CO with respect to the solar value Rubin et al. (2015) propose that the ice containing those species formed below~30 K.

- The first detection of a noble gas in comets has been reported by (Balsiger et al., 2015). From measurements performed in October 2014 the range of (0.1 - 2.3)·10−5 $^{36}Ar/H_2O$ was determined. In addition a correlation between the abundance of N_2 and ^{36}Ar could be seen resulting $^{36}Ar/N_2$ of $(9.1 \pm 0.3) \cdot 10^{-3}$ while for carbon monoxide not a significant correlation could be found although all three species have similar volatility. Due to the values of D/H and $^{36}Ar/H_2O$ (Balsiger et al., 2015) concluded that comets like 67P could not be the major source of Earth's major volatiles.

- A first compilation of volatile species revealed that every species measured so far in a cometary coma is present in the coma of 67P (Le Roy, L. et al., 2015). However, the study bases on data acquired at heliocentric distances around 3 AU when the activity is still low making it difficult to compare it with results form other comets.

- The first detection of molecular oxygen in the coma of 67P/Churyumov-Gerasimenko has been reported by (Bieler et al., 2015). Moreover it turned out that molecular oxygen with an abundance relative to water of 3.80 ± 0.85% is one of the major coma compounds. Furthermore the ratio O_2/H_2O is stable with changing spacecraft position relative to the comet and heliocentric distance and therefore Bieler et al. (2015) ruled out a formation due to radiolysis of H_2O and they suggest that O_2 was incorporated during the formation of the comets material.

2. Experimental Methods

2.1 Experimental Set up - FM

The measurements with DFMS FM on ground were done with two different set ups first at the vacuum chamber CASYMIR, and second a direct gas inlet to DFMS was used. Restricted by the availability of the vacuum chamber CASYMIR but in the need of the possibility to do calibration measurements the direct gas inlet has been developed and built by two members of the institute staff (A. Etter and H. Mischler).

2.1.1 CASYMIR

CASYMIR is a calibration facility to simulate cometary coma. It has been developed and built at the University of Bern by Christian Westermann and Wolfram Luithardt (Westermann, 2000) between 1997 and 2000. The purpose is to produce either a neutral particle beam which covers a wide range of velocities and intensities similar to what is expected near a comet or to do measurements at a static pressure.

CASYMIR consist of four connected volumes with dedicated tasks: in V3 after the nozzle the gas expands and transits into molecular flow, between V3 and V2 is a skimmer which let pass only a fraction of the gas, in V2 1D and 2D beam scans can be done, between V2 and V1 the beam size can be changed with an iris, and at the end of V0 is the instrument interface. Thus for measurements with an neutral beam all volumes are needed but for static measurements one can close a slide between V1 and V2 in order to not contaminate V2 and V3. The gas for dynamic and static measurements can be mixed in the so called Gas Mixing Unit (GMU no.1). Currently the available gases are He, Ne, Ar, Kr, Xe, H, CO_2 and N_2. In order to achieve a good vacuum during measurements the chambers V0-V3 are pumped by four turbo molecular pumps (TMP) (fig. 2.1.1). Due to this setting the background pressure in the chamber V0 is in the range of 10^{-10} mbar (this part has been adapted from (Calmonte, 2011)).

For the measurements done in this work CASYMIR was used only in static mode meaning that through the leak valve (no. 2) gas was let in and via a thermal controlling valve a constant pressure was established. When CASYMIR was built only gaseous species could be measured however during the past few years the need to measure either a liquid like methanol or even a solid like naphthalene loomed therefore CASMIYR was equipped with an additional gas inlet shown in fig. 2.1.2. The new gas inlet is mounted between leak valve (no. 2) and GMU in order to not contaminate the GMU with condensates of the measured species. Between the tube coming from the gas mixing unit (no. 1) and the leak valve is a cross which has on the left side an adapter to mount small gas bottles (no. 4) and on the right a pressure sensor to monitor (no. 3). On the right side are two tubes at which the sample glass tube can be plugged. The inlet system and the glass tubes can be heated till 80° in order to vaporize the sample and prevent condensation in the metal tube. A constant pressure in the vicinity of the instruments entry can be established by regulating the leak valve with respect to a pressure sensor right after the leak valve in V4 or on a pressure sensor in V0.

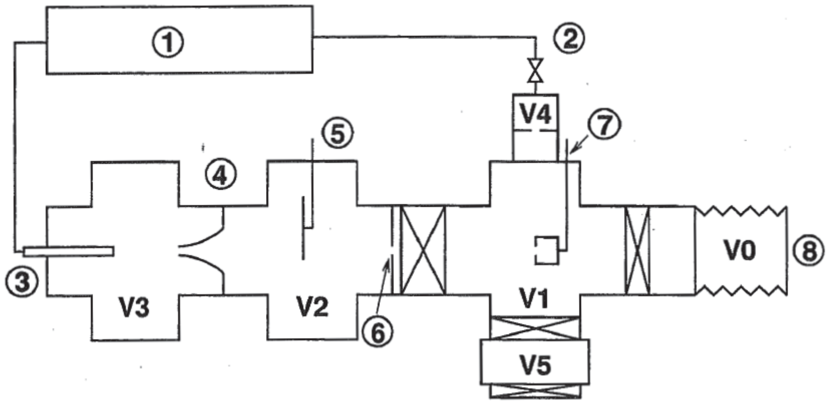

Fig. 2.1.1: CASYMIR contains several chambers, denoted by **V**. Shown are the bellow chamber V0, the main chamber V1 the collimator chamber V2, the expansion chamber V3, the reference chamber V4, and the chamber V5 which contains a titanium sublimation pump. The other parts are 1. the gas mixing unit (GMU), 2. the leak valve used for the static mode, 3. the nozzle used for the dynamic mode, 4. the skimmer, 5, the chopper mechanism, 6. the adjustable iris (⌀ 0-25 mm), 7. the molecular beam analyzer and 8. the docking plate for the instrument interface. (Westermann, 2000)

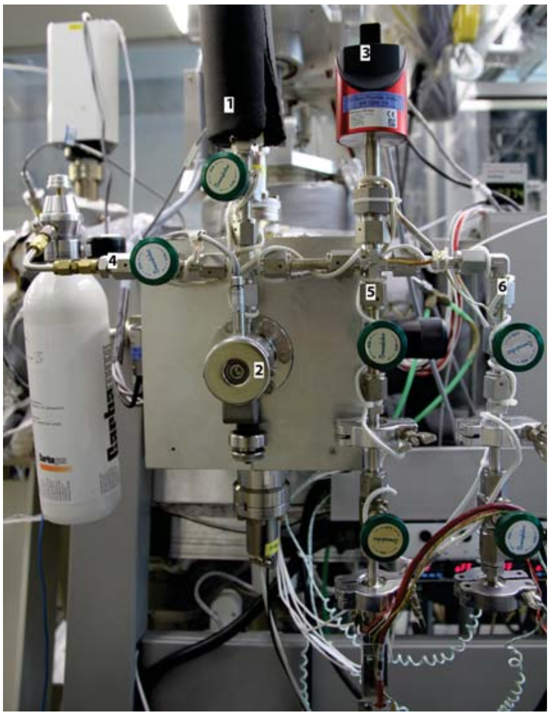

Fig. 2.1.2: Additional gas inlet at CASYMIR for liquid and solid compounds. Gas inlet between leak valve (no. 2) and the gas mixing unit at CASYMIR. Shown are in front the tube going to the GMU (no. 1), the leak valve (no. 2), the pressure sensor (no. 3), the adapter to mount small gas bottles (no. 4), two lines for the sample tubes (no. 5 & no. 6).

DFMS is connected with CASYMIR at the instrument interface (no. 8 in fig. 2.1.1) such that the ion source opening is aligned with the beam line (fig. 2.1.3 (a)). Integrated in the flange (fig. 2.1.3 (b)) which works as an adapter between DFMS and CASYMIR is a GranVille Phillips hot cathode ion gauge to monitor the pressure in the vicinity of the ion source. This ion gauge is calibrated on N_2 and gives the reference pressure for any calibration measurements done with DFMS. Typical pressure for DFMS connected with V0 and V1 of CASYMIR is ~$5\cdot10^{-10}$ mbar and typical pressure if the leak valve to the tube system is open but closed to the GMU is ~$5\cdot10^{-9}$ mbar.

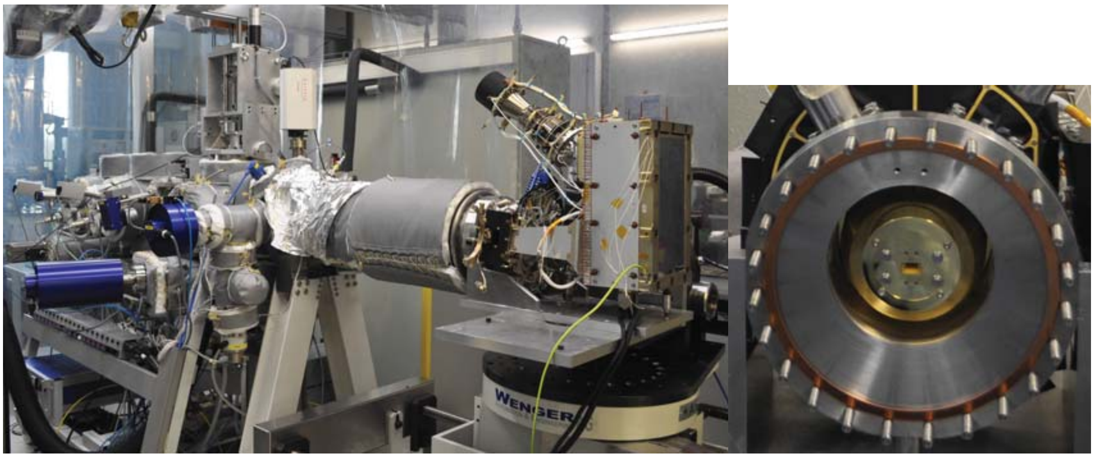

(a) (b)

Fig. 2.1.3: (a) show how DFMS FM is mounted onto CASYMIR and (b) gives a view on the ion source assembly inside the adapter flange.

2.1.2 Clean Room

When DFMS is not mounted at CASYMIR it is either in a clean bench or installed in a clean room depending on the planned measurements till it goes back to CASYMIR. The set up in the clean room was initially built to measure a HCN-polymer. In order to measure this polymer it was heated up and produced $(HCN)_x$. Due to the high toxicity of HCN it was essential to guide the exhaust air of the pumps attached to DFMS outside. The only possibility to do this besides at CASYMIR was in the clean room since only there the problem with the exhaust air of the pumps could be handled and a constant air flow from the ceiling to the floor would in case an incident prevent the gas to distribute in the room. At some point the gas inlet built to measure the HCN-polymer was adapted in such way that small gas bottles could be attached. The adapted gas inlet is shown in fig. 2.1.4: on the right side one can see partially DFMS, on the left side a turbo pump (no. 6) to establish an ultra high vacuum, in the middle is the flange that works as an adapter between DFMS and either a pump or a vacuum chamber. Inside the flange is the ion source of DFMS (see fig. 2.1.3 (b)). Towards the wall mounted at the flange is the GranVille Phillips hot cathode ion gauge which monitors the pressure in the vicinity of the ion source and gives the reference pressure for any calibration measurement done with DFMS. The inlet system can be pumped from the gas bottle (no. 1) to the leak valve (no. 4) via the valves no. 2 and no. 3 with a membrane pump. This set up makes it possible to flush the inlet system and to pump it in order to achieve a small background level and to reduce air contamination. Typical pressure for this set up with closed leak valve is ~$2\cdot10^{-10}$ mbar.

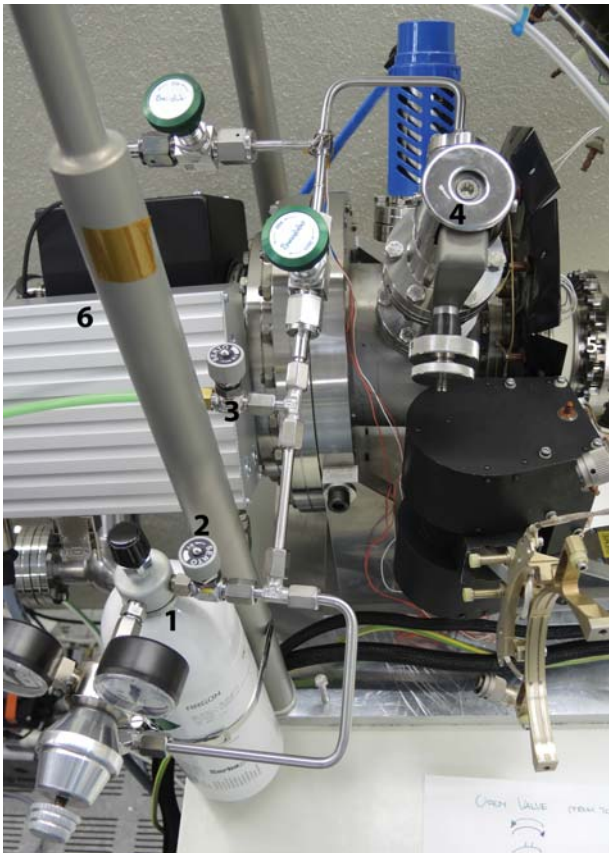

Fig. 2.1.4: Gas inlet: valve to bottle no. 1, bypass valve no. 2, valve to membran pump no. 3, leak valve no. 4, DFMS no. 5, turbo molecular pump no. 6.

2.2 Measurement Procedure

In this work the results of four measurement series with DFMS FM will be presented: first so-called dispersion measurements, second so-called pixel gain measurements, third calibration of NH_3, and fourth calibration of H_2S. In the following the measurement procedure for the four measurement series are presented. Then the measurement conditions for pixel gain measurements performed with FS in space will be annotated in detail as well as for the measurements of sulfur bearing species in the coma of 67P.

2.2.1 Dispersion - FM

Evaluating low resolution spectra of known gases it has been noticed that the mass scale deviates at the beginning and end of the spectrum (for more details see section 3.1). To study this deviation low resolution measurements of a gas mixture consisting of 25% neon, argon, krypton, and xenon each were performed. The measurements were done at CASYMIR and the mass range from 13 to 140 u/e was sampled in steps of 1 u/e. Like this it could be ensured that first for different mass ranges several peaks are spread all over the LEAD, and second that per mass range multiple spectra are available with different peak distributions. Besides ensuring a stable thermal environment no further provisions had to be taken care of. However, preliminary evaluation showed that around m_0 40 u/e the peaks due to doubly charged krypton only covered a small range of the LEDA therefore the low resolution measurements done by Hässig (2013) for the calibration of DFMS have been used.

2.2.2 Pixel Gain Measurement - FM

Measurements to follow the evolution of the individual pixel gain were done at CASYMIR between April and June 2015. Nominal procedure after DFMS is moved to CAYSIMIR is to head CASYMIR up to 80-100°C to reduce the water content in the vacuum chamber. Since DFMS is not allowed to be heated when the GCU is attached the slide between V1 and V0 is closest to prevent adsorption of the released water at and in CASYMIR.
The of the pixel gain determinations is to measure the same ion current on each LEDA pixel and then normalize it to the borders where the least depletion is present. In reality it is rather difficult because: i) the ion beam is larger than one pixel (~40 pixels at $m_0 = 18$) and thus each pixel samples the beam several times at different sections, ii) the gas density around DFMS has to be stable during the entire measurement procedure, and iii) DFMS has to be stable in terms of temperature specifically at the magnet and at the ESA.

For the application in space three measurements modes (M600, M601, M602) were developed and implemented in the software controlling ROSINA. The difference is in the emission current (2, 20, 200 µA). First a spectrum of m_0 18.5 u/e is acquired in LR mode to determine the gain, then the beam is swept over the LEDA in steps of 4 pixels which is achieved by commanding a slightly higher m_0 for every step. As a result one gets 138 spectra with the same gain and the peak at different locations on the LEDA. The step width has been set to 4 pixel per step being aware that one has to find a balance between the degree of determination of the depletion and the use of precious measurement time at the comet for no-scientific measurements (Schläppi, 2011).

To determine the individual pixel gain factors for the FM in the lab a so-called batch has been used because unlike the implemented modes one can measure different species. A batch is a script of commands that can be executed by the DPU. The measurement procedure is as follows when when DFMS is attached to CASYMIR:

1. DFMS is acquiring spectra in a neutral gas measurement mode for 2 hours to establish a thermal equilibrium.

2. GMU at CASYMIR is filled with ~120 mbar gas. For this measurements neon has been used in order to have an inert gas with a mass close to 18 u.

3. Neon is leaked into the chamber via the leak valve and the pressure is regulate.

4. After ~10 min, when the pressure is stable, start DFMS manually and measure spectra in LR mode with 200µA emission at mass to charge 20.9 u/e. Then adjust the front voltage in such a way that the peak is ~80% below the linear limit. With shifting the peak of interest away from the center one avoids exceeding the linear limit of the ADCs during the sweep e.g. in the case the determination of the GS is done with the peak of interest in the center where the MCP has its largest depletion the signal will be underestimated by roughly a factor of 2. If in such a case the GS is chosen in a way that the peak is almost at the linear limit it will exceed it for measurements when the peak is on an area with less depletion.

5. Adjust the batch for pixel gain measurements for the evaluated GS and start it. The batch differs for 3 points from M60x: first the gain determination is done

manually, second the data is automatically stored , and third M60x takes ~70 min while measurements with the batch last ~2 h. The difference in duration arises from automatic storage of the spectra due to the batch.

2.2.3 Calibration of NH_3 - FM

Measuring ammonia (NH_3) requires certain security precautions because it is toxic. The lethal dose is 1.5-2.5[1] g/m^3 in one hour and already short contact can lead from irritation of the respiratory tract and the eyes up to chemical burn. In addition, metals like copper and iron corrode in contact with NH_3. As a consequence the calibration of NH_3 was carried out in the clean room with the gas inlet with a mixture consisting of 99% Ar and 1% NH_3. The use of the set up in the clean room had two advantages: first the exhaust was guided outside and second only a small and easy exchangeable set up was under the influence of NH_3.

The last measured compound before the NH_3 calibration was the HCN-polymer which contained as well NH_3 which even after a few months could be still seen in the instruments background. In order to reduce the this background DFMS has been heated the vicinity of the instruments entry up to 70° over 5 days. In order to heat DFMS a customized heating tent is available and the GCU has to be detached. Background measurements were done for CEM and MCP/LEDA for all three emissions and both resolutions. The background pressure was $2.3{\cdot}10^{-10}$ mbar relative to N_2.

The calibration measurements were done for MCP/LEDA and CEM at 4 different pressures for all three emissions and both resolutions. To not have several background measurements all three pressure measurements series were done sequently. The total pressures relative to N_2 were $1.10{\cdot}10^{-9}$ mbar, $1.22{\cdot}10^{-8}$ mbar, $5.14{\cdot}10^{-8}$ mbar, and $1.21{\cdot}10^{-7}$ mbar. The four partial pressure of NH_3 were $7.47{\cdot}10^{-10}$ Pa, $8.29{\cdot}10^{-9}$ Pa, $3.51{\cdot}10^{-8}$ Pa, and $8.22{\cdot}10^{-8}$ Pa (9.8% uncertainty).

2.2.4 Calibration of H_2S - FM

Due to the availability of CASYMIR calibration measurements of H_2S could be done at there. As NH_3 H_2S is toxic, highly flammable, and corrodes metals as copper therefore the same precautions are required. For calibration a mixture of 99% Ar and 1% H_2S has been used. In order to not contaminate and damage the GMU the additional gas inlet (see fig. 2.1.2) has been used for those measurements. For background measurements the leak valve was open, the valve to the GMU closed, the valve to the sample tubes were closed, and the valve to the gas bottle (no. 4) was closed. The reference pressure relative to N_2 during back ground measurements was $8.02{\cdot}10^{-9}$ mbar and as for NH_3 measurements were performed for both resolutions and all three emissions for CEM and MCP/LEDA. Like for NH_3 measurements with the sample gas were done sequently for total pressures relative to N_2 of $1.37{\cdot}10^{-8}$ mbar, $4.76{\cdot}10^{-8}$ mbar, and $1.37{\cdot}10^{-7}$ mbar. The partial pressures for H_2S were $6.13{\cdot}10^{-9}$ Pa, $2.13{\cdot}10^{-8}$ Pa, and $6.13\ {\cdot}10^{-8}$ Pa (9.8% uncertainty).

2.2.5 Pixel Gain Measurements - FS

To do measurements to determine the individual pixel gain factor in space is challenging because one can not establish a stable environment e.g. the neutral gas density can vary.

---

[1] `http://www.materialarchiv.ch/detail/1139/Ammoniak#/detail/1139/ammoniak`

In addition, a lack of experience in doing such measurements surrounding a comet led to different measurement procedures and to the implementation of six additional measurement modes during a software update in March 2015. The first set, M62x with x = 1,2,3, have all modes high emission but the determination of the GS and the peak to sweep are different than for M60x (for details see table 2.2.1). The second set (M63x) differs only in the set mass for GS determination from M60x. The motivation to have additional modes was to learn whether the resulting measurements are depending on the way of operation.

Table 2.2.1: Compilation of the different modes for measuring the individual pixel gain. All of them are LR modes and with a different combination of emission, m_0 as the swept peak, and m_0 ratio for the GS determination it is tried to ensure that different GS are measured.

mode number	emission (µA)	m_0 (u/e) (sweep)	m_0 (u/e) (GS determination)
600	2	18	18.5
601	20	18	18.5
602	200	18	18.5
620	200	16	16
621	200	16	17
622	200	16	18
630	2	18	17.29
631	20	18	17.29
632	200	18	17.29

The first individual pixel gain measurements after hibernation were performed in the so called commissioning phase on April 24th in 2014. After 3 hours of neutral gas measurement mode M600 was run while RTOF and COPS were off-state. Two hours later interrupted by other neutral gas measurements the modes M601 and M602 were run. Due to this procedure there is no information about the stability of the water signal. However, it is assumed that the measured water is part of Rosettas background and thus is stable. Unfortunately the gain algorithm was not disabled in the mode definition and the GS changed in the middle of the measurement resulting in only one complete data set instead of three. The cometary distance was about 2.7x10^6 km and the neutral gas was due to spacecraft background (for more details see (Schläppi et al., 2010)).

The next measurements were executed on July 25th during the comet approach phase with a distance of about 3000 km to the nucleus. A software update should ensure no further disturbances of the pixel gain measurements. Still the measured water was assumed to originate from the background and to be stable. In addition, COPS was measuring, DFMS was on for 2 hours beforehand.

The third session of pixel gain measurements was done on November 14th and 15th 2014 after lander delivery. DFMS was on for 4 hours sampling neutral gas and COPS was in science mode measuring with both gauges. The modes M600-M602 were measured sequently and the cometary distance was about 46.5 km. Thus the signal was dominated by the cometary activity.

A fourth attempt to measure the individual pixel gain was done on January 3rd when Rosetta was at a cometary distance of ~28.5 km. All three sensors were on; DFMS was in mode M600, COPS measured with both gauges in science mode, and RTOF measured in a neutral gas mode to cover the evolution of water.

To increase the number of pixel gain measurements at different gain steps another set was measured on February 3rd after DFMS has been measuring for 1 hrs and 40 min. In addition, COPS was in science mode with nude gauge only (Ram gauge could not be used due to a technical problem) and RTOF was again measuring neutral gas to cover the evolution of water. The cometary distance was around 30 km and the following modes were measured sequently M600, M601, M602, and M600.

With the same motivation another series of measurements were done on March 15th. DFMS was operational for already more than 2 hrs and the modes M601, M602, and M601 were performed while COPS acquired data with the nude gauge in science mode. Unfortunately, RTOF had some sensor errors and therefore off-state. Rosetta was at a cometary distance of 74 km.

After a software upload, in middle of March, six new pixel gain modes were available and functionality tests were done on March 18th and 19th. Again COPS was measuring with nude gauge in science mode. DFMS measured after 2h 30 min of different measurements the modes M620, M621, M622, and M602. In addition, on March 21st a test was performed to learn more about possible temperature dependence of FS. Since the test was directly after a maneuver during which all instruments are off-state for about 3 1/2 hour, DFMS was supposed to be cold and the aim was to measure the same mode during the warm-up period. Therefore DFMS measured the evolution of water for ~30 min before the pixel gain measurements started. During the next ~10 hrs DFMS measured mode M602 5 times with always 20 min of neutral gas measurements in between. The aim of these measurements was to follow the evolution of H_2O, CO, and CO_2. COPS was in science mode measuring with nude gauge.

Based on the experiences we had so far the following measurements, a procedure was established:

1. COPS is in the so called science mode with the nude gauge running. Compared to normal operation COPS generates every 2 seconds a mean of the previous 10 s thus a better time resolution is achieved.

2. DFMS is acquiring spectra for 2 hours after a wheel off-loading to prevent thermal instabilities.

3. The evolution of H_2O, CO, and CO_2 has to be followed at least for 20 min before and after a pixel gain measurement mode. In addition, RTOF is preferentially measuring neutrals if the gas density is sufficient.

On March 21st and 22nd pixel gain measurements following the above described procedure were executed with this set of pixel gain modes: M602, M622, M632 , M602, M600, M620, M630, M600, M601, M621, M631, and M601.

2.2.6 Measurements of Sulfur Bearing Species - FS

ROSINA has been acquiring data since the comet approach phase in July 2014. During October 2014 Rosetta was at 10 km distance to the comets center as it can be seen from fig. 2.2.1 for almost 14 days which is equivalent of 28 cometary days and five orbits. The data during this period are predestined for studying isotopic ratios since the measured gas densities were at its peak for the mission so far apart from a few short time flybys. Thus making it possible to do an analysis covering a large range of latitude and longitudes. During this 14 days DFMS measured most of the time in a high resolution mode in which single mass spectra are acquired from mass to charge ratio 13 u/e up to 100 u/e in single mass steps. One cycle lasts roughly 40 min resulting in ~400 spectra per mass for the period when Rosetta was at 10 km distance. Rosettas orbit was constrained to be within -60° and 60° latitude due to operational issues thus no data is available outside this range. For determination of sulfur isotopic ratios only species were taken into account which are unlikely to be a fragment due to the ionization process in the ion source. For example H_2S has been analyzed but not HS or S since the latter two are fragments of various parents. Thus H_2S, OCS, S_2, SO_2, and CS_2 have been analyzed.

In fig. 2.2.1 are drawn in the uppermost panel the signal of H_2S, OCS, SO_2, and C_2S, the three panels below show sub satellite latitude and longitude, nadir of pointing and phase angle, and the distance Rosetta-comet and Rosetta-Sun basing on the coordinate system developed by Scholten et al. (2015).

In order to determine the isotopic ratios of sulfur in the sulfur bearing molecules H_2S, OCS, SO_2, S_2, and C_2S a cometary day was selected which is at the end of the 10 km period and with maximum signal for H_2S. The first constraint is due to the individual pixel gain factor correction because the closest measurement of those factors is in November 2014 and with the second constraint it was tried to make sure that the signal height for the heavy isotopologues of H_2S would be as large as possible. Therefore data from 11:00 UTC 23.10.2014 till 04:00 UTC 26.10.2014 was used for H_2S and C_2S and this range covers a bit more than 1 terminator orbit as it can be seen in fig. 2.2.1. A preliminary analysis of this period has shown that the signal of the isotopologues with ^{33}S and ^{34}S for OCS, S_2, and SO_2 is rather low and only sufficiently high during a small period of time when the main isotopologue had its daily maximum. Therefore the data of all the daily maxima in the 10 km orbit were analyzed for OCS, S_2, and SO_2 to raise the number of points in the three isotope space.

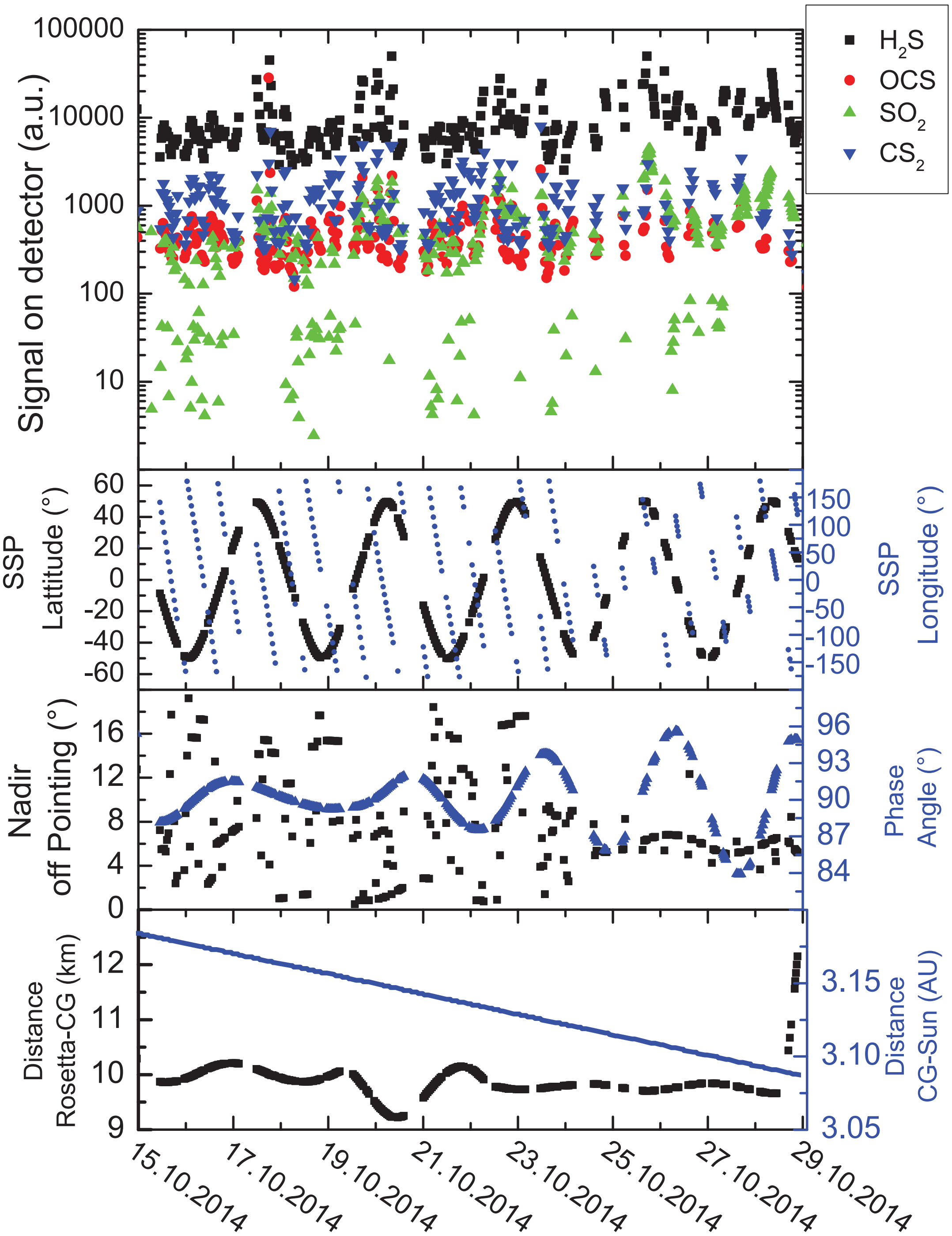

Fig. 2.2.1: The upper most panel shows the evolution of H_2S (black squares), OCS (red dots), SO_2 (green triangles), and CS_2 (blue triangles) during the period when Rosetta was within ~10 km to the center of the nucleus. The remaining three panels give information about the orbit of Rosetta around Churyumov-Gerasimenko which are the sub satellite latitude and longitude, the nadir off pointing and the phase angle between comet Rosetta and sun, and in the last panel the evolution in distance for the comet to the sun and for Rosetta to the comet.

2.3 Data Reduction

2.3.1 Conversion to Ions and Mass to Charge for MCP/LEDA

The MCP/LEDA measures an electron current which is converted to a digital signal by an Analog-to-Digital-Converter (ADC) therefore certain corrections have to be applied in order to have the incident ion current on the MCP :

1. LEDA offset subtraction
2. Correction for individual pixel gain
3. Correct for gain, the ADC conversion (c_{ADC}), and the anode capacity of the LEDA (c_{LEDA}) to get the charge on the detector
4. Determine the number of ions per spectra and the ion current
5. Apply mass scale

Offset Correction In order to measure any signal the LEDA has already a charge applied depending on the internal chip reference level Nevejans et al. (2002) which is temperature dependent (for more details about the LEDA see (Nevejans et al., 2002) and see fig. 2.3.1 (b)-(c)). This is done for every read-out cycle and thus the offset level depends on the number of accumulations in spectra. Consequently the recorded signal has to be corrected for this offset. In fig. 2.3.1 (a) an exemplary spectra of the offset acquired on ground with number of accumulations of 3000 and an integration time of 6.6 ms per cycle is shown. As one can see the offset level is for row A higher than for row B and the curvature at the beginning is larger for A than for B. In addition, it can be seen that the offset can be fitted by a 3rd order polynomial. The differences in offset level and curvature are due to slight different resistances in the LEDA rows (Hässig, 2013). The offset correction can be done for each spectra individually or as it has been suggested by Hässig (2013) with a function for the offset that demands at the end a correction for a constant offset (d_A,d_B). The parameters in the following fits deduced by Hässig (2013) for both rows and both instruments base on the mean of ~50 spectra (personal communication).

$$O_{FMrowA} = -2 \cdot 10^{-6}x^3 + 0.0017x^2 - 0.5268x + 4091.1 - d_A \tag{2.3.1}$$

$$O_{FMrowB} = -1 \cdot 10^{-6}x^3 + 0.0013x^2 - 0.5058x + 3363.2 - d_B \tag{2.3.2}$$

$$O_{FSrowA} = -3 \cdot 10^{-6}x^3 + 0.0022x^2 - 0.5290x + 4771 - d_A \tag{2.3.3}$$

$$O_{FSrowB} = -2 \cdot 10^{-6}x^3 + 0.0015x^2 - 0.249x + 5530 - d_B \tag{2.3.4}$$

where x is the pixel number. In this work the offset function has been determined for every spectra individually.

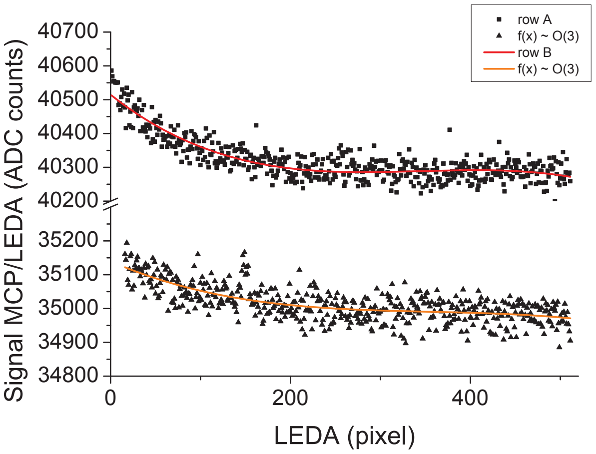

(a) FM

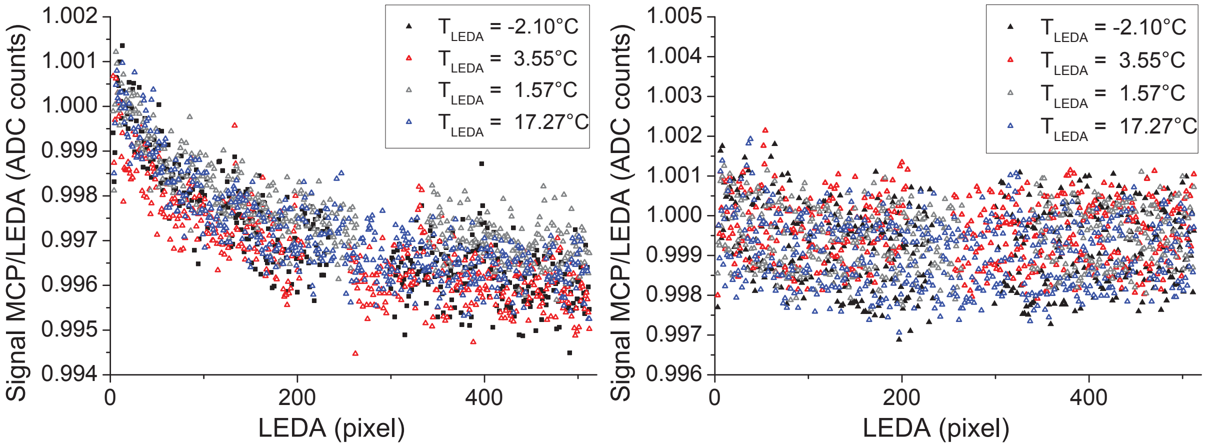

(b) FS - row A **(c)** FS - row B

Fig. 2.3.1: (a)-(c) show the LEDA offset for FM both rows, for FS row A normalized to the first ten pixels, and for FS row B again normalized to the first ten pixels. For all measurements the integrations time was $t_{int} = 6.6$ ms and the number of accumulations was 3000 resulting in 19.8s total integration time.

Individual Pixel Gain Correction As it has been already discussed in section 1.9.5 the individual pixel gain is dependent on the MCP and the degradation which is dependent on the amount of measured particles and the location where they impinged on the MCP. To correct for the individual pixel gain the signal after offset correction has to be divided by the individual pixel gain $pg_{GSj}(x)$ of the gain step at which the spectra was acquired:

$$Data_{Px.corr}(x) = \frac{RawData(x) - Offset(x)}{pg_{GSj}(x)} \tag{2.3.5}$$

where x is the pixel number, and GS j the gain step of the to be corrected spectra.

For this study space data were always corrected with the closest pixel gain in sense of time and the calibration data was corrected with the pixel gain determined in summer 2015.

Conversion to Charge per Pixel In order to obtain the charge on the detector per pixel $Q_{MCP}(x)$ the correction for the ADC conversion, the detectors capacity, the MCP gain, and the MCP secondary electron yield have to be applied:

$$Q_{MCP}(x) = \frac{Data_{Px.corr}(x) \cdot c_{ADC} \cdot c_{LEDA}}{Gain(GSj)\ \cdot y} \tag{2.3.6}$$

where $c_{ADC} = \frac{2.5}{2^{12}-1}$V and $c_{LEDA} = 4.22{\cdot}10^{-12}$ F (Neefs et al., 2002b). The gain is dependent on the gain step, the model, and for FS dependent on the row. The FS gain has been measured and determined first by Neefs et al. (2002a) and during the preflight campaign refurbished by Langer (2003a). For FM the gain has been measured and first determined by Neefs et al. (2002b), refurbished by Langer (2003b), and a second time measured and refurbished by Hässig (2013). As reason for a further refurbishment Hässig (2013) mentioned a correction factor introduced by Riesen (2007) in order to compare measurements at different gain steps. The values given in table 2.3.1 are the most recent ones determined by Langer (2003a) for FS and by Hässig (2013) for FM. The uncertainties are 6% for the FM values (Hässig, 2013).

Table 2.3.1: Gain of the MCP of MCP/LEDA for FS and FM dependent on the gain step.

	FS			FM	
Gain Step	ΔU_{MCP} [V]	Gain row A	Gain row B	ΔU_{MCP} [V]	Gain row A
1	-900	6.93E+00	1.71E+00	-1300	1.41E-01
2	-938	9.48E+00	3.47E+00	-1342	3.88E-01
3	-975	1.46E+01	7.23E+00	-1382	1.01E+00
4	-1012	2.49E+01	1.56E+01	-1425	2.79E+00
5	-1052	4.85E+01	3.67E+01	-1468	7.63E+00
6	-1095	1.07E+02	9.35E+01	-1514	2.20E+01
7	-1138	2.48E+02	2.38E+02	-1562	6.48E+01
8	-1185	6.40E+02	6.52E+02	-1612	1.94E+02
9	-1232	1.65E+03	1.73E+03	-1665	5.97E+02
10	-1280	4.25E+03	4.48E+03	-1722	1.90E+03
11	-1328	1.04E+04	1.10E+04	-1785	6.41E+03
12	-1380	2.57E+04	2.69E+04	-1855	2.25E+04
13	-1450	7.50E+04	7.86E+04	-1932	7.84E+04
14	-1528	2.01E+05	2.16E+05	-2025	2.89E+05
15	-1630	5.30E+05	6.08E+05	-2140	1.02E+06
16	-1770	1.37E+06	1.68E+06	-2300	2.78E+06

The correction of the secondary electron yield proves to be difficult since it cannot be determined for DFMS via calibration measurements (see section 2.3.5). However, the species and energy dependence on the gain of a MPC has been investigated by (Meier and Eberhardt, 1993) and the following relation resulted:

$$y = G_0 \cdot \sum_i z_i \cdot a_i \cdot v \cdot arctan(b_i(v - v_0)) \tag{2.3.7}$$

where G_0 is the reference gain, z_i is the number of atoms i in the molecule, a_i and b_i are the characteristic coefficients for the atoms i, v_0 it she species independent threshold velocity, and v is the velocity of the molecules.

Since the MCP in both FM and FS are is operated at the same voltage as the MCP used in the study of (Meier and Eberhardt, 1993) the relation obtained has to be adapted for the calculation of the amount of ions impinging on the detector during one spectra n_{ions}. For calibrated species the yield is part of the sensitivity and therefore the factor is set to 1 and for uncalibrated species work is in progress to adapt the relation found by Meier and Eberhardt (1993).

Conversion to Ions per Spectra and Ion Current The ion current for one pixel is be obtained by dividing equation (2.3.6) with the total integration time of a spectrum. The total integration time is the product of the integration time for one spectrum and the number of accumulations. The nominal values are $t_{int} = 6.6$ ms, $n_{accu} = 3000$ and thus $t_{total} = 6.6 \text{ ms} \cdot 3000 = 19.8$ s:

$$Ix = \frac{Q_{MCP}(x)}{t_{total}} \tag{2.3.8}$$

The number of ions per pixel in a spectrum is obtained by dividing equation (2.3.6) with the electron charge $e = 1.60217662\ 10^{-19}$ C:

$$n_{ions}x = \frac{Q_{MCP}(x)}{e} \tag{2.3.9}$$

Conversion from Pixel to Mass per Charge The conversion from pixel to a mass scale in the mass per charge space is done via:

$$m(x) = m_0 \cdot e^{(x-x_0)\frac{s}{D \cdot z}} \tag{2.3.10}$$

where m_0 is the commanded mass, x_0 the pixel on which m_0 lays, the distance between two pixels $s = 25$ µm/pixel, D the dispersion factor 127'000 µm (Wüthrich, 2007), and z the zoom factor. This relation has been deduced by Stefan Graf and Sandra Wüthrich. Due to the change of the zoom polynomial by Schläppi (2011) the zoom factor for mass to charge below 20 u/e in HR modes changed and has been determined by Hässig (2013). For low resolution measurements the zoom factor is $z = 1$ for all m_0 and for high resolution between m_0 20 - 69 u/e $z \approx 6.4$. The values for m_0 below 20 u/e are given in table 2.3.2. For m_0 greater than 69 u/e the zoom has not been determined yet although preliminary results show a decrease in zoom due to the additional acceleration via PA (nominal PA = -1000 V). The level of decrease is dependent on the applied voltage because measurements with PA = -3000 V show a larger mass range for the same mass as nominal measurements. Further calibrations to determine the relation between the zoom factor and PA are planned.

Table 2.3.2: Zoom factor z for DFMS FM (Hässig, 2013)

m_0 (u/e)	z ± 0.2
13	5.8
14	5.3
15	6
16	6.3
17	6.4
18	6.3
19	6.6
20	6.2

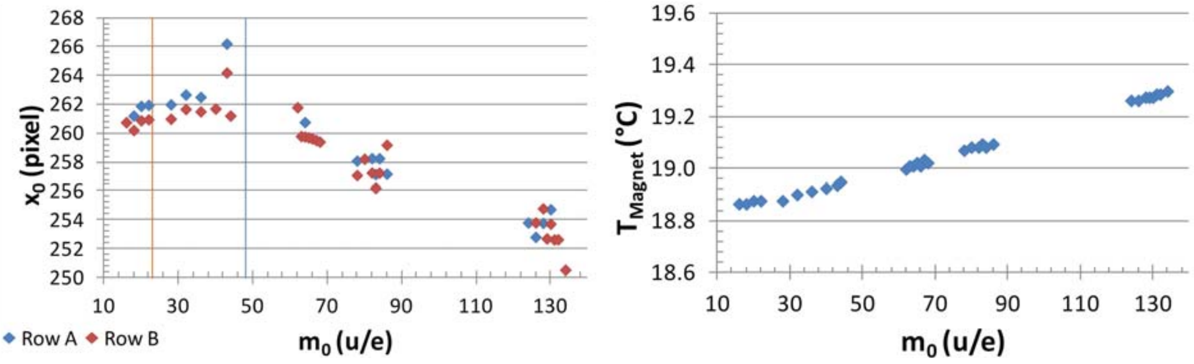

(a) (b)

Fig. 2.3.2: Relation between m_0 and x_0 for DFMS FM determined for low resolution; (a) shows the relation while (b) shows the increase of the magnet temperature during the measurement.

The difficulty of applying the mass scale is that x_0 is not exactly known. Due to the construction it is supposed to be around pixel 250. However, there is a difference between high and low resolution of ~50 pixel. Beside this offset in the nominal position of m_0, x_0 depends on the magnet temperature i.e. when T_{Magnet} is lower than the reference temperature of 20° then x_0 goes towards higher pixel numbers, on m_0, and on how accurate the voltages of the ion optics can be produced in the electronics of DFMS. As a consequence the determination of species bases on a combination of knowing in which range x_0 can lay for a certain m_0 and the method of elimination. The relation between m_0 and x_0 is shown in fig. 2.3.2 (a) for low resolution measured at 20° room temperature. The change of the magnet temperature during the measurement is shown in (b). For low masses the possible number of species in a spectrum is rather small e.g. on m_0 13 u/e it can be ^{13}C, CH, or doubly charged CN and therefore it is easier to determine x_0. The higher m_0 is the more molecules built by C,N,O,S, and H are possible and therefore the determination of x_0 becomes more complicated. For such cases one needs to know in what range x_0 can be for this m_0 and the estimation of the range bases on the values for x_0 of spectra where the species can be unambiguously determined like on m_0 18 u/e (H_2O) or 28 (CO and CH_2O). If the peaks cannot be assigned to a species then one has to search for patterns in the available mass scan i.e. check for fragments, doubly charged particles, and isotopologues.

2.3.2 Dispersion - FM

The deviation between the calculated mass to charge of a peak and the actual mass for the ion is defined as dm. The data has been corrected for the LEDA offset, pixel gain, gain, and then converted from ADC counts to ions as it has been shown previously. In order to calculate the mass scale x_0 in such a way that in the neighborhood of m_0 with D = 125000 $dm \approx 0$. Afterward the mass scale is calculated for 7 values of D in the interval [120000, 130000]. For each value the following procedure has been executed:

1. Each peak in the spectra is fitted with a Gaussian function with respect to the errors of the data. Considering that the interest lies in the location of the peak center a Gaussian peak shape is a sufficient description of the peak.

2. Knowing the exact mass of the ion and the peak center in the spectra the deviation (dm) is calculated.

2.3.3 Determination of Individual Pixel Gain Factors - FM

Previous studies of the individual pixel gain have been analyzed with a computer program written in C by B.Schläppi which unfortunately stopped to work for unknown reasons. Since the calculations done in this code were rather simple, the code has been transferred to Matlab (see section C.1). The compatibility has been checked by analyzing the FS data from 2009 and comparing the results obtained for the two codes. The resulting individual pixel gain factors for row A are showed in fig. 2.3.3, where the C code results are drawn in blue and the Matlab code results in red. There are 3 differences of various importance; first the edges are not the same due to different handling in the codes, second there is a dip around pixel 300 for the red data set which does not appear in the other one, and third the curves do not perfectly overlay. The difference at the edges is not important because it concerns pixels which can not be used for the calculation of the individual pixel gain and so none of these values are relevant for our purpose. The dip around pixel 300 is due to a missing spectrum. In contrast to the C program, such cases have to be treated manually with the Matlab code and more information will be given in section 2.3.4. The results obtained with the Matlab code are in good agreement with the previous C program, the difference between the two codes being less than 1%.

Due to the measurement procedure, each pixel gets theoretically the same signal. The outcome are 138 spectra which are then treated following these steps:

1. Correct the data for LEDA offset like in section 2.3.1 on page 44.

2. Get the maximum value of the peak of interest and its position ($x_c(i)$) for each step (i).

3. Store the counts in the interval [$x_c(i)$-20:$x_c(i)$+20] in the corresponding pixel array.

4. Calculate individual pixel gain for pixel i:

$$pg(i) = \frac{\sum\limits_{j=x_c(i)-20}^{x_c(i)+20} c_{ij}}{\sum\limits_{n=21}^{491} \frac{c_n}{492-21}} \tag{2.3.11}$$

   with c_{ij} is the offset corrected number of counts detected at pixel i in step j, and $c_n = \sum\limits_{j=x_c(n)-20}^{x_c(n)+20} c_{nj}$ the total number of counts detected at pixel n during the sweep.

This procedure results in the pixel gain factors for the pixel 21 to 491 whereby the individual pixel gain for the first and last 20 pixels is not determined. It is not needed to know the individual pixel gain at this locations since it was never intended to do measurements at the edges of the LEDA where the beam is unfocused most.

In addition, to the individual pixel gain the step width in pixel between two steps has been determined in the same Matlab code by:

1. Calculate the deviation from the nominal step size for step i $\delta(i) = x_c(i+1) - x_c(i+1) - 4$.

2. Set a flag for steps which deviate from the previous and subsequent steps.

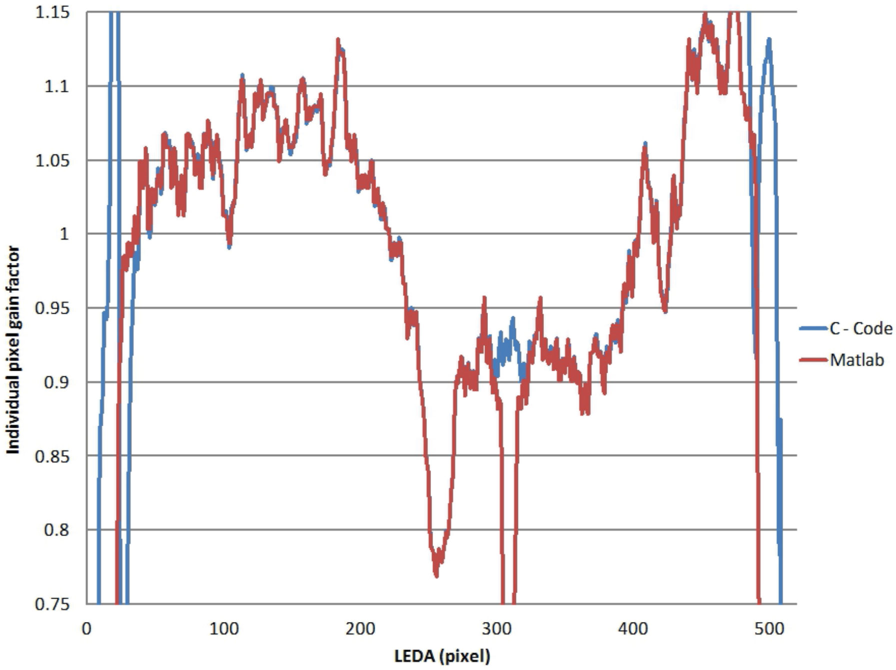

Fig. 2.3.3: Comparison of a pixel gain measurement done in space once analyzed with a C code in blue and analyzed with a Matlab code in red.

2.3.4 Determination of Individual Pixel Gain Factors - FS

To evaluate space data the Matlab code had to be adapted in order to apply corrections for the not stable water signal. The procedure to determine the individual pixel gain for space data is as follows:

1. Correct the data for LEDA offset like in section 2.3.1 on page 44.
2. Get the maximum value of the peak of interest and its position ($x_c(i)$) for each step (i).
3. (electively) Correct data for COPS pressure, or evolution of water peak before and after measurement, or evolution of water relative to the main species (H_2O, CO, and CO_2)
4. Store the counts in the interval [$x_c(i)$-20:$x_c(i)$+20] in the corresponding pixel array.
5. (since November 2014) Interpolate linearly in between the peak maxima for every step
6. Calculate individual pixel gain for pixel i:

$$pg(i) = \frac{\sum\limits_{j=x_c(i)-20}^{x_c(i)+20} c_{ij}}{\sum\limits_{n=21}^{491} \frac{c_n}{492-21}} \qquad (2.3.12)$$

with c_{ij} is the number of counts detected at pixel i in step j, and $c_n = \sum\limits_{j=x_c(n)-20}^{x_c(n)+20} c_{nj}$ the total number of counts detected at pixel n during the sweep.

7. Norm the results to the edges thus to the part of the LEDA where almost no depletion should have occurred:

$$pg_r(i) = \frac{pg(i)}{\sum\limits_{n=440}^{462} \frac{c_n}{462-440}} \tag{2.3.13}$$

The correction for COPS pressure, the evolution of water, and the evolution of water relative to the main species can be done only for certain data sets since the needed data are not available for all of them.

COPS Pressure Correction COPS measures the ion current at nude and ram gauge every 2 seconds and converts it into a pressure. For nominal operation the mean of the last ten seconds is stored every minute in the DPU, and the mean of the last ten seconds is saved every two seconds when COPS is in science mode.
First the COPS data are fitted with a polynomial least square fit for the period of the DFMS mode. The degree of the polynomial depends on the COPS signal. The approach of fitting COPS and then correct DFMS data based on the COPS fit was chosen because of two reasons. First DFMS and COPS measurements might be shifted in the order of seconds and second COPS measurements shows sometimes large variations on a short time scale due to a change in the spacecraft attitude (for more details see fig. C.3.8). The signal in the DFMS spectra were corrected the following way for COPS signal:

$$Data_{corr.\ COPS}(t) = \frac{Data(t)}{\sum\limits_{i=\tilde{t}-1}^{\tilde{t}+7} \frac{COPS_{fit}(i)}{8}} \tag{2.3.14}$$

where $Data(t)$ stands for the spectrum, t is the time after half of a DFMS spectrum is acquired, and $\tilde{t}$ the closest time stamp of COPS to t. By using the time interval $[\tilde{t}-1 : \tilde{t}+7]$, it is assured that the only COPS data used are those which were measured during the data acquisition of DFMS spectra (visualization see fig. 2.3.4).

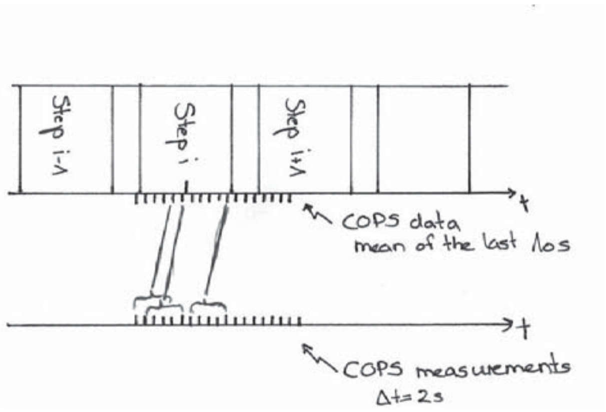

Fig. 2.3.4: Visualization of the overlap between COPS and DFMS measurements.

Correction for Evolution of Water First attempts to follow the evolution of water with RTOF to correct then the pixel gain measurements did not succeed because the gas density was not sufficient to obtain a decent signal whit RTOF. Besides the low density

RTOF had as well problems with sudden changes of the offset level in a spectra which then could cover the peaks. For more details the author refers to the thesis of Sébastien Gasc about RTOF. Thus it was decided to follow the evolution of water before and after the pixel gain measurements with DFMS and then use so-called smoothing splines to calculate the missing part when the pixel gain measurements were performed.
Besides m/z 18 u/e as well m/z 28 and 44 u/e were followed thus the evolution of the most abundant species (H_2O, CO, CO_2) could be determined. Those data were analyzed with the nominal data treatment for MCP data as described in section 2.3.1. Then they were fitted in Matlab using smoothing splines. A spline is a piecewise polynomial fit where the fit is smoothed at the data points. The Matlab option of the fit function does, depending on the input parameter p, either a linear least square fit for p = 0 or a cubic spline interpolant for p = 1, while minimizing the following problem:

$$p\sum_i w_i(y_i - s(x_i))^2 + (1-p)\int \left(\frac{d^2 s}{dx^2}\right)^2 dx \tag{2.3.15}$$

where w_i are the weights, y_i the data, and $s(x_i)$ is the spline evaluated at x_i. Based on the spline the DFMS measurements were corrected according to

$$Data_{corr.\ m18}(t) = \frac{Data(t)}{\sum\limits_{i=\tilde{t}-1}^{\tilde{t}+7} \frac{m18_{spline}}{8}} \tag{2.3.16}$$

The value p has been chosen individually for each case by looking at the data and the resulting spline.

Correction for Evolution of $\mathbf{H_2O/(H_2O+CO+CO_2)}$ This correction is achieved by determine the ratio $H_2O/(H_2O+CO+CO_2)$ before and after the pixel gain measurement, fitting it with smoothing splines, and then correct the spectra for fit and the evolution seen at COPS:

$$Data_{corr.\ ratio\ main}(t) = \frac{Data(t)}{\sum\limits_{i=\tilde{t}-1}^{\tilde{t}+7} \frac{main\ species_{spline}}{8} \cdot \sum\limits_{i=\tilde{t}-1}^{\tilde{t}+7} \frac{COPS_{fit}(i)}{8}} \tag{2.3.17}$$

2.3.5 Sensitivity Relation

The sensitivity measures of how much the instrument can detect from the available amount of particles. In case of DFMS the sensitivity is dependent on how efficient particles are ionized, how much are transmitted through the mass analyzer, and how the detector discriminates the signal. However, it is only possible to determine the all over sensitivity for the species i which is has been defined by Hässig (2013) as the ratio between the total measured ion current (sum of the signal of all fragments and the multiple charged particles) and the density times the emission current:

$$S_{total,i} = \frac{I_{ion}}{\rho \cdot I_{emi}} \tag{2.3.18}$$

while the sensitivity of the fragment j ($S_{j,i}$) is given through

$$S_{j,i} = S_{total,i} * Q_{i,j} \tag{2.3.19}$$

whereas $Q_{i,j}$ is factor of the fragmentation for the fragment j. The density is determined by using the ideal gas law

$$pV = Nk_BT \;\Rightarrow \rho = \frac{N}{V} = \frac{p}{k_BT} \tag{2.3.20}$$

where ρ is the particle density in cm^{-3}, p the pressure in the vicinity of the ion source in Pa, k_B is the Boltzmann constant ($1.38 \cdot 10^{-23}$ J/K), and T is the temperature in the lab which is regulated to 20°C thus $T = 293$ K. In order to calculate the sensitivity the following procedure was performed:

1. Convert ADC counts to ion current with yield = 1
2. Apply mass scale and identify the peaks due to the measured compound
3. Determine the peak area
4. Correct for the background calculated via step 1.-3.
5. Execute a linear least-square fit to determine the sensitivity

Step 1. and 2. are discussed in the previous paragraphs. The peak area can be determined in two different ways: first for single peaks one has to sum up the counts for the peak, and second in case of overlapping peaks the signal has to be fitted to determine the peak are for each of the peaks. For both FM and FS a peak consists the sum of two Gauss peaks; a dominating narrow and a wide one dominating in the percent level. The width of the peak is given among others through the resolution and since this decreases with increasing m_0 the width in u/e increases. However, the increase in width is negligible for $\Delta m_0 = 1$ u/e. In order to have a relation between the measured signal and the amount of gas around the detector the sensitivity only dependent on the mass to charge ratio several correction have to be applied on the sensitivity:

Pressure Correction For calibration of neutral species a Bayard-Alpert gauge (GranVille Phillips pressure gauge) has been used which is calibrated for N_2. For some species a correction factor of the pressure value is given in the manual (Automation, 2007) but by far not for all species considered in our calibration. The difference in sensitivity of the ion gauge is theoretically due to the ionization cross section. Thus the ratio of ionization cross sections of the desired species with respect to N_2 should give the correct factor. In table 2.3.3 a comparison of this calculation and experimental values gathered by Summers (1969) is done. The values for the ionization cross section σ_{EII} for 150 eV are from NIST database[2]. Remarkably for all hydrocarbons the calculated correction factor is between 10-40% lower than the factors reported by Summers (1969).

---

[2] `http://www.nist.gov/pml/data/ionization/index.cfm`

Table 2.3.3: Comparison of pressure correction factor derived by ratio of electron impact cross section (3rd column), values given in an compilation of empirical observations done by (Summers, 1969) (4th column), and the correction factors given in the manual of the ion gauge (5th column). If not stated differently values for the ionization cross section base on NIST.

	σ_{EII} (150eV)	Correction Factor		
Species	(cm^2)	$\sigma_i/\sigma_{N_2}(150eV)$	(Summers, 1969)	(Automation, 2007)
Ne	6.67E-17*	0.38		0.30
Ar	2.29E-16*	1.31		1.29
Xe	3.89E-16*	2.22		2.87
Kr	2.98E-16*	1.70		1.94
N_2	1.75E-16	-	-	1.00
CH_4	1.38E-16	1.23	1.4-1.8	-
C_2H_4	4.43E-16	1.79	2.2-2.5	-
C_2H_6	5.50E-16	2.22	2.5-2.8	-
C_3H_8	7.49E-16	3.02	3.6-4.2	-
C_4H_{10}	1.03E-15†	4.16	4.6-4.9	-
H_2O	2.22E-16	0.89		1.12
NH_3	2.74E-16	1.10		
H_2S	3.40E-16	1.37		
CO_2	3.60E-16	1.45		1.42

* `http://www.ruf.rice.edu/~atmol/index.html`

† there was no data available for C_4H_{10} therefore the cross section of C_4H_8 was taken

Table 2.3.4: Electron impact cross section at 45 eV for noble gases, some basic hydrocarbons, N-bearing molecules, and H_2S.

Species	$\sigma_{EII}(45eV)$ (cm^2)
Ne	2.50E-17 ± 1.25E-18 *
Ar	2.49E-16 ± 1.25E-17
Kr	3.38E-16 ± 1.69E-17 *
Xe	4.60E-16 ± 2.30E-17 *
N_2	1.52E-16 ± 7.60E-18
CH_4	3.18E-16
C_2H_4	4.62E-16
C_2H_6	5.86E-16
C_3H_8	2.76E-16
C_4H_{10}	7.74E-15
H_2O	1.88E-16
NH_3	2.67E-16
H_2S	4.10E-16
CO_2	1.84E-16 ± 9.20E-18

The sensitivities for the measured hydrocarbons in Hässig (2013) have to be corrected according to:

$$S_{total,i}(N_2) = \frac{I_{ion}}{\rho I_{emi}} = \frac{I_{ion}}{\frac{p_i(N_2)}{k_B T} I_{emi}} = \frac{I_{ion}}{\frac{p_i \frac{\sigma_{N2}}{\sigma_i}}{k_B T} I_{emi}} \Rightarrow S_{total,i} = S_{total,i}(N_2) \cdot \frac{\sigma_i(150eV)}{\sigma_{N2(150eV)}} \tag{2.3.21}$$

Correction Due to Ionization in Ion Source On instrument side as well a correction due to the ionization process has to be applied in order to reduce the sensitivity on transmission and the detection efficiency. In Table 2.3.4 the values for the ionization cross section at 45 eV, the electron energy in DFMS, are given.

Another instrumental dependence at least for the MCP is the detector yield (Meier and Eberhardt, 1993) which can not be corrected for since yield data available are not sufficient to do so as it has been already explained.

Fragmentation of Incident Particle in the Ion Source The sensitivities given in Hässig (2013) do not reflect the transmission sensitivity of a particle with a distinct mass to charge ratio because the ion current due to all fragments has been taken into account for the calculation of the sensitivity. however the sensitivity of a fragment j of the species i can be calculated due to equation (2.3.19).

2.3.6 Uncertainties

Depending on the type of end result different uncertainties become important meaning if the abundance of a species is calculated the uncertainty due to the sensitivity has to be taken into account while for isotopic ratio calculations the sensitivity is not needed and no additional uncertainty is introduced. In the following the composition of the uncertainties for the some of later presented results are discussed. The exception are the individual pixel gain results for which the uncertainties will presented in the corresponding discussion.

Dispersion The uncertainties for dm the deviation between true and calculated mass are given through the uncertainty for the peak center of the peak fit.

Calibration The uncertainty of the density is 6% due to the pressure sensor. The uncertainty of the ion current is given by the statistical uncertainty, the uncertainty of the used pixel gain set which accounts for 6% for each row, and the uncertainty of the gain values which are as well 6%.

For the linear least square fit between the density and the ratio of ion and emission current the uncertainties have been taken into account. The uncertainties of the sensitivities are resulting from the linear least square fit considering the uncertainties of the data.

For the fragmentation and the isotopic ratios first the amount of ions was determined and thus the uncertainties are due to pixel gain, gain, and the ion statistic. Based on those the uncertainties for the fragmentation and the isotopic ratios were calculated using the uncertainty propagation law.

Abundance of S-Bearing Species Relative to $\mathbf{H_2S}$ The uncertainty of the resulting signal for the sulfur bearing molecules is composed of the statistical error, correction due to individual pixel gain factor, and fit of the peaks. Based on the results in section 3.4.2.4 the uncertainty introduced by correction for the individual pixel gain is estimated to be not more than 10%. The uncertainty of the fit is estimated to be 7% because 2% are already introduced from the definition of the peak and then fitting overlapping peaks increases this value. An additional uncertainty is introduced by the conversion from ions to density. Since all measurements were performed at the same gain step no further error is introduced by the gain correction. For none of the species the sensitivity's uncertainty has been taken into account since for all except H_2S because they can go up to 100% as it will be shown in section 3.3.

Isotopic Ratios of S-Bearing Species The isotopic ratios were calculated using the amount of ions for one species in a spectrum. Its uncertainty composes of the statistical error given by $\sqrt{no.\ ions}$, the uncertainty due to fitting accounts for 7%, and for the pixel gain the uncertainty is assumed to be 10% for each row (for more details see section 3.4.3). The uncertainties of the isotopic ratios are given by applying the Gaussian uncertainty propagation. Since all measurements were performed at the same gain step no further error is introduced by the gain correction.

2.3.7 Weighted Mean

Since the acquired data do not have all the same uncertainties this has to be taken into account by the mean calculation. There are two main methods how such a data set can be handled either one exclude outliers or the difference in uncertainties is taken into account. Here the later is done via the weighted arithmetic mean which calculates as the following (Bronstein et al., 2001):

$$\bar{x}^g = \frac{\sum_{i=1}^n g_i x_i}{\sum_{i=1}^n g_i} \tag{2.3.22}$$

with g_i the weight based on the distribution of uncertainties, $\tilde{\sigma}$ the minimum uncertainty in the set, $v_i = x_i - \bar{x}^g$ the deviation from the mean.

$$g_i = \frac{\tilde{\sigma}^2}{\sigma_i^2} \tag{2.3.23}$$

The uncertainty of the weighted mean is calculated via:

$$\tilde{\sigma}^{(g)} = \frac{\sqrt{\sum_{i=1}^n g_i v_i^2/(n-1)}}{\sqrt{g_i}} \quad \tilde{\sigma}_{wm}^{(g)} = \frac{\sqrt{\sum_{i=1}^n g_i v_i^2}}{(n-1)\sum_{i=1}^n g_i} \tag{2.3.24}$$

3. Characterization of DFMS FM and FS

In this chapter the results considering the change of dispersion, the calibration of NH_3 and H_2S, and all the over sensitivity relation for MCP/LEDA and CEM will be presented and discussed. Then the presentation of the results of the numerous pixel gain measurements performed in space follow after the results section for the individual pixel gain measurements of DFMS FM.

Although the detectors of DFMS measure ions the charge is not denoted for the measured species unless it is a multiple charged ion. For example if measurements were performed with nitrogen the peak in the spectrum will be labeled with N_2 although ${N_2}^+$ has been measured by the detector.

3.1 Dispersion

As it has been already mentioned in the introduction it has been found that in for MCP/LEDA spectra acquired in low resolution mode the calculated mass ratio differed from the mass of the target peak. For illustration of this effect an exemplary spectrum with Xe as test gas is shown in fig. 3.1.1. For this spectra $m_0 = 130$ u/e and thus the peaks due to the major isotopes are spread over the LEDA more ore less symmetrically. The location of the isotopes are indicated by dashed lines and already from the entire spectrum it can be seen that there is a difference between the center of the peak and the dashed line at least for 136 and 136 u/e. Next to the spectrum is a section going from 133.5 to 134.5 u/e shown and from ti can be seen that the difference between the dashed line and the peak center is significant. In the following sub section the results of the investigation regarding the dispersion in low resolution modes are presented and discussed and upper limits for the accuracy of the mass scale in u/e are given at the end of the discussion.

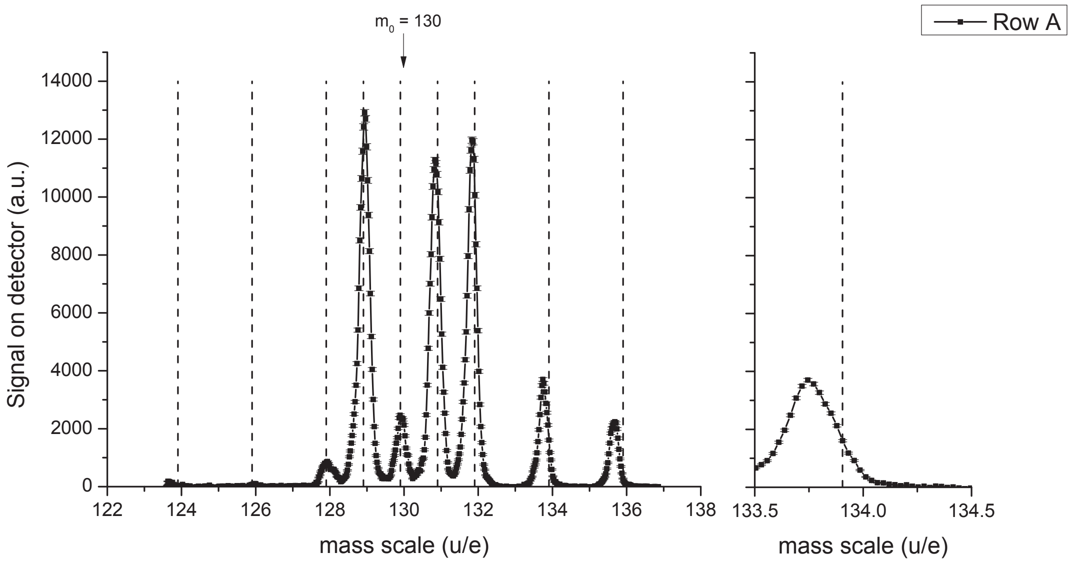

Fig. 3.1.1: Low resolution spectrum with $m_0 = 134$ u/e and Xe as test gas. The left panel shows the entire spectrum where the location of the isotopes of Xe are indicated with a dashed lines. The right panel shows the section going from 133.5 to 134.5 u/e and one can see that there is a significant deviation between the peak center and the theoretical location.

3.1.1 Results

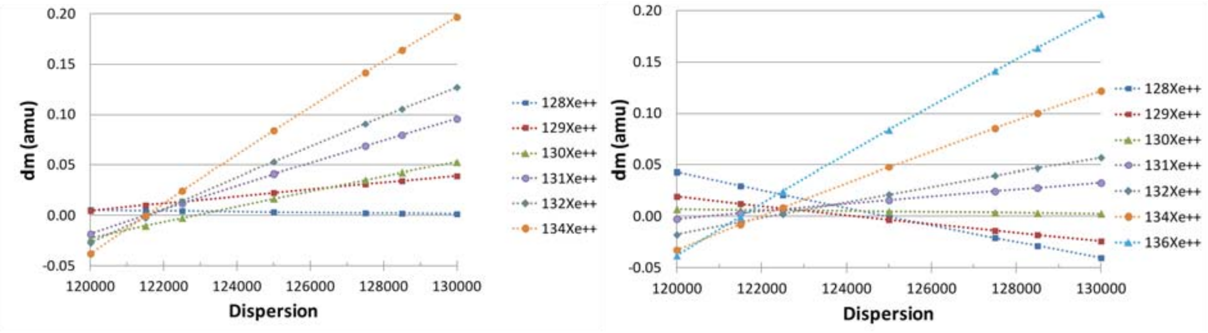

(a) m/z 64 u/e **(b)** m/z 65 u/e

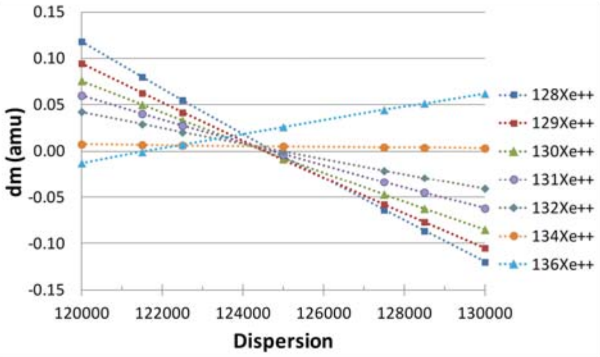

(c) m/z 67 u/e

Fig. 3.1.2: Relation between dispersion and deviation (*dm*) in mass for doubly charged xenon for MCP/LEDA low resolution spectra.

The relation between the dispersion and *dm* (u/e) is shown on the basis of doubly charged Xenon. The graphs for CO_2, Kr, and Xe are shown in section A. For the low resolution spectra with m_0 64, 65, and 67 u/e the deviation between real mass and determined mass based on the procedure described in section 2.2.1 has been calculated. In fig. 3.1.2 is *dm* relative to the dispersion shown for the three spectra. The data is indicated with a symbol and the line was added in order to see were possible cross sections lay. At m_0 64 u/e 6 peaks due to the isotopes of Xenon are present in the spectra (a). For $^{128}\mathrm{Xe}^{++}$ *dm* is almost zero while the peaks with m/z > m_0 have a positive slope which increases with increasing m/z of the peak i.e. $^{134}\mathrm{Xe}^{++}$ has the largest m/z - m_0 and the steepest slope. However, all peaks in the spectra have m/z $\geq m_0$ and therefore lay on the right half of the LEDA. In addition, one can see that between D = 121'500 - 122'500 the range of *dm* for all peaks is the smallest. In order to observe the behavior of the slope for peaks with m/z $\leq m_0$ one has to have a look at spectra with a larger m_0. Increasing m_0 by 1 u/e results in two peaks on the left half of the LEDA and in (b) one can see that those two peaks show a decrease in *dm* with increasing dispersion. For D ≈ 122'500 the spread in *dm* seem to be smallest. In (c) one can see that increasing m_0 to 67 u/e leads for all peaks but one to have m/z $\leq m_0$ and the same trend as in (a) can be seen the larger the difference m/z - m_0 the steeper is the slope however for peaks on the left side of the central peak the slope is negative. In addition, it can be seen: that the smallest spread in *dm* is between D = 124'000 - 125'000. The linear trend and the dependency of the slope on the relative distance of the peak to the center peak can be seen as well for the other three mass ranges around m/z 44 u/e (CO_2), 84 u/e (Kr), and 132 u/e (Xe) though the size on the intersection region changes.

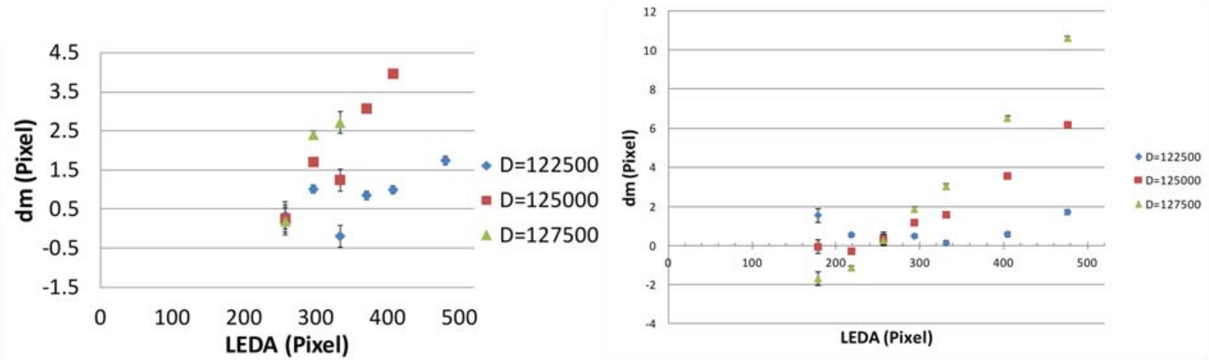

(a) m/z 64 u/e **(b)** m/z 65 u/e

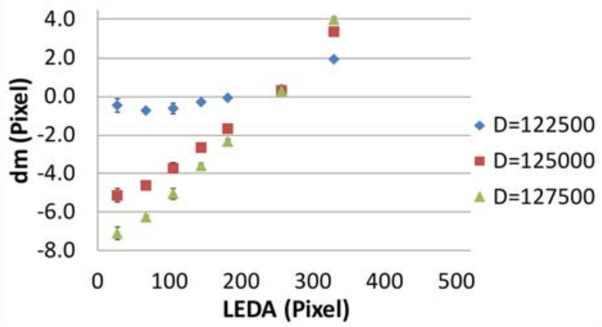

(c) m/z 67 u/e

Fig. 3.1.3: Relation between location on the LEDA and deviation in mass (*dm*) given in pixel for doubly charged xenon in MCP/LEDA for low resolution spectra.

In figure 3.1.3 the relation between the position on the LEDA and *dm* (in pixel) is shown for m_0 64, 65, and 67 u/e for D 122’500 (blue), 125’000 (red), and 127’500 (green). For m_0 64 u/e in graph (a) one can see that the peaks are all on the right half of the LEDA and that the further away the peak form the peak with m_0 (around pixel 250) is the large *dm*, as it already has been seen in the previous paragraph. In addition, it can be seen that for D = 122’500 $dm \approx 2$ pixel for the most distant peak while for D = 1250’000 *dm* is already ≈ 6 pixel and for D = 127’500 *dm* is ≈ 10 pixel. Graph (b) shows the results for m_0 65 u/e and the same features can be seen on the right half of the LEDA and in addition two data points are present on the left half. From this graph it seems as if for D = 122’500 and D = 125’000 the slope changes; for m $\leq m_0$ with D = 122’500 the sign of the slope seems to change and for D = 125’000 it seems as if *dm* is constant for $\leq m_0$. Graph (c) shows the relation between *dm* in pixel and the location of the peak on the LEDA for m_0 65 u/e. Similar as in (a) the slope for D = 127’500 is the steepest and at the left boarder $dm \approx 7$ pixel while $dm \approx 5$ pixel for D = 125’000 and for D = 122’500 *dm* is between 0 and 1 pixel. The characteristics that the further away a peak is from the central peak the large *dm* is is present as well for the three other mass ranges (for the graphs see section A).

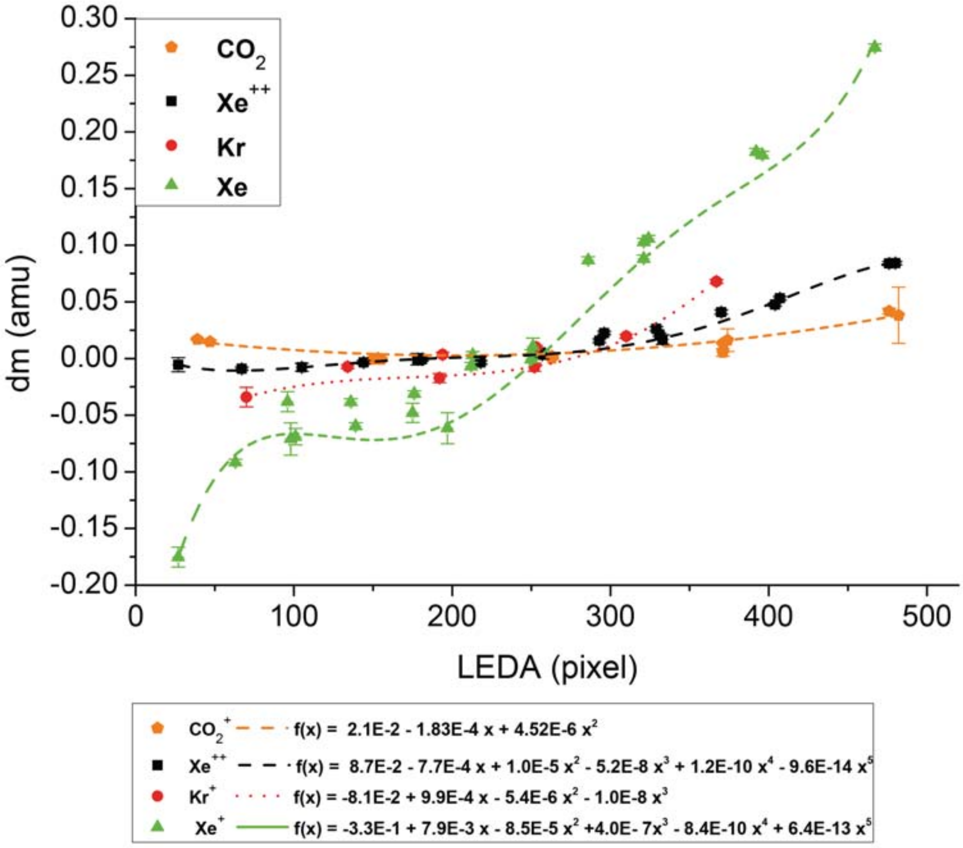

Fig. 3.1.4: Relation between location on the LEDA and deviation in mass per charge for peaks around m_0 44, 64, 83, and 130 u/e. For each data set a least square fit has been performed and is illustrated in the corresponding color and the fit parameters are given in the panel below the graph.

In figure 3.1.4 the relation between location of the peak on the LEDA and dm in u/e is shown for the 4 different mass ranges given by the molecule resp. atom looked at for D = 125'000. For CO_2 measurements were done at m_0 44, 45, 46, and 47 u/e (orange pentagram), for Xe^{++} at m_0 64, 65, and 67 u/e (black square), for Kr at m_0 83 and 86 u/e (red circle), and for Xe at m_0 130, 132, and 134 u/e (green triangle). In addition, each data set has been fitted by a polynomial for which the equation is given in the graph. For CO_2 dm is between 0 and 0.05 u/e, for Xe^{++} the range is already larger going from -0.011 to 0.085 u/e and in addition the curve shape does not look anymore like a polynomial of second order. Around m_0 83 only two measurements could be used and only 3-4 peaks which did not cover the entire range of the LEDA were present. Therefore only the range in dm from pixel 50 to ~350 can be given which is -0.034 - 0.069 u/e. The set with $128 \leq m_0 \leq 132$ shows a significant spread in dm for similar locations at the LEDA i.e. around pixel 100 are two points with $dm \approx$ -0.066 u/e and one with $dm \approx$ -0.038 u/e. In addition, the curve shape seems to be again of a higher order than polynomial of 2nd or 3rd order. Each set was fitted taking into account the uncertainties and the fit with the highest adjusted R^2 has been selected resulting in 2nd order polynomial for around m/z 44 u/e, a 5th order polynomial around m/z 65 u/e, a 3rd order polynomial for around m/z 83 u/e, and a 5th order polynomial around m/z 130 u/e.

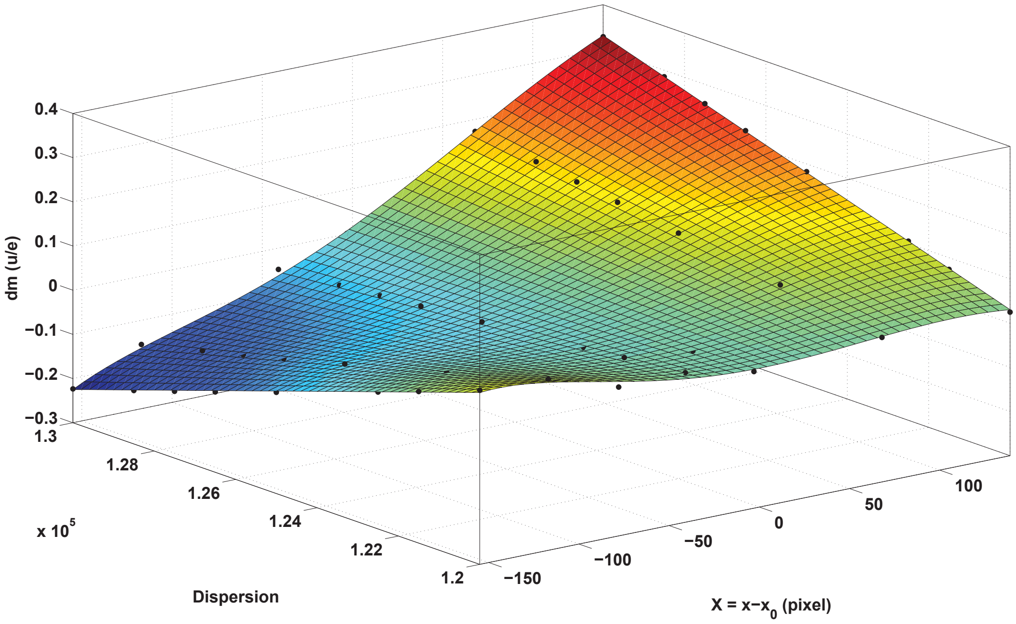

Fig. 3.1.5: The deviation in mass to charge ratio for Xe in low resolution mode as a function of the dispersion and the location of the peak relative to x_0.

For m_0 132 u/e an exemplary surface fit in the space dispersion, x-x_0, dm has been done. The fit is shown as a surface in fig. 3.1.5 and the data are indicated by black dots. The data could be fitted with polynomial of 5th order in X and of 1st degree in D. The parameters and the function are given in table A.0.1.

3.1.2 Discussion

Based on the previous shown results it can be concluded that three parameters influence dm: the position on the LEDA (x_{peak}), m_0, and the value of D. The following characteristics could be observed:

- With changing x_0 the patterns described in the data section moves on linearly.
- The sign and the steepness of the slope s at a fixed D are linked to position of the peak relative to the center peak. However, from fig. 3.1.4 it is clear that it is not a linear relation.
- The curve shape changes with m_0 as it has been illustrated in fig. 3.1.4.
- Between dm can be described with linear function of D.

As a consequence of this small study low resolution spectra should be given always with uncertainties depending on x_{peak}. An estimation of the uncertainties for different x_{peak} and mass ranges for m_0 can be given basing on fig. 3.1.4 :

44 u/e $<$ m_0 $<$ 47 u/e:

pixel 30 $< x_{peak} <$ pixel 400 $\Rightarrow$ $dm \leq 0.02$ u/e
pixel 400 $< x_{peak} <$ pixel 512 $\Rightarrow$ 0.02 u/e $\leq dm \leq 0.05$ u/e

64 u/e < m_0 < 67 u/e:

$x_{peak} > x_0 \quad \Rightarrow 0.01 \text{ u/e} \leq \quad dm \quad \leq 0.09 \text{ u/e}$
$x_{peak} < x_0 \quad \Rightarrow -0.01 \text{ u/e} \leq \quad dm \quad \leq 0.005 \text{ u/e}$

83 u/e < m_0 < 84 u/e:

pixel 400 $> x_{peak} > x_0 \Rightarrow \quad dm \quad \leq 0.1 \text{ u/e}$
$x_{peak} > 400 \quad \Rightarrow 0.1 \text{ u/e} \leq \quad dm \quad \leq 0.15 \text{ u/e}$

128 u/e < m_0 < 134 u/e:

pixel 1 $< x_{peak} <$ pixel 100 $\Rightarrow -0.2 \text{ u/e} \leq \quad dm \quad \leq -0.1 \text{ u/e}$
pixel 100 $< x_{peak} <$ pixel 300 $\Rightarrow -0.1 \text{ u/e} \leq \quad dm \quad \leq 0.1 \text{ u/e}$
pixel 300 $< x_{peak} <$ pixel 400 $\Rightarrow 0.1 \text{ u/e} \leq \quad dm \quad \leq 0.2 \text{ u/e}$
pixel 400 $< x_{peak} <$ pixel 512 $\Rightarrow 0.2 \text{ u/e} \leq \quad dm \quad \leq 0.3 \text{ u/e}$

The cause of the change in dispersion for m_0 below 69 u/e is most probably due to the angle between the plane of the detector and the ion optical focus plane which. For m_0 a further distortion of the ions beam is caused by the asymmetric electrical fields in the vicinity of the detector. The asymmetrical fields are caused by the electrode shape where the post acceleration of -1000 V is applied (for more details see section 1.9.3.1). Although for m_0 below 69 u/e as well a voltage of -50 V is applied on this electrode it is assumed to have a minor affect for lower masses which have a higher energy and are thus more difficult to be deflected.

3.2 Calibration

In the following two sub sections the results for the calibration of NH_3 and H_2S for MCP/LEDA HR are presented and then discussed.
All the measurements were performed with FM as it has been described in section 2.2.3 and section 2.2.4. For both compounds first the obtained sensitivity factors will be presented, then the fragmentation pattern and finally the isotopic ratio of the considered species. All the fingerprints and isotopic ratios measured with DFMS are compared with those found in the online mass spectrum data base of the National Institute of Standards and Technology (NIST).
Although measurements were done as well for CEM the data is not evaluated yet. The reasons is the the low priority for MCP/LEDA LR and CEM sensitivities since in space almost only MCP/LEDA HR is used and CEM data from FS has not been analyzed yet.

3.2.1 Results

3.2.1.1 NH_3 - MCP/LEDA HR

Measurements done at a total pressure relative to N_2 of $1.1 \cdot 10^{-9}$ mbar could not be used for calibration because the signal marginal exceed the background.
Figure 3.2.1 shows the relation between the species density and the ratio between measured ion current and emission current of DFMS. From the graph one can see that ratio of the currents is linear proportional to the neutral density in the vicinity of DFMS as is ha already been shown by (Riesen, 2007; Hässig, 2013). Therefore the data was fitted for each emission with a linear least square fit as well drawn in the figure and a compilation

of the sensitivities for both species is given in table 3.2.2. In addition, one can see that the lower the emission the higher the sensitivity ranging from $(4.57 \pm 0.48)\cdot 10^{-19}$ cm ^{3} to $(2.01 \pm 0.21)\cdot 10^{-18}$ cm ^{3} for 200 µA and 2 µA, respectively.

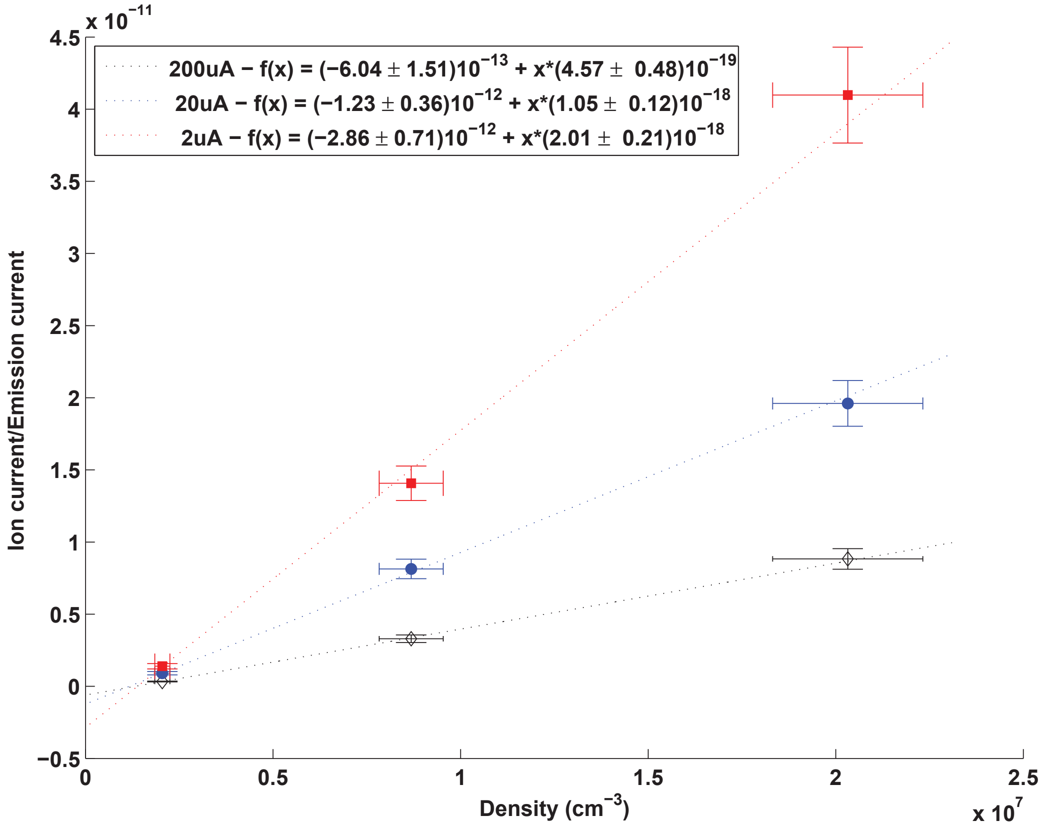

Fig. 3.2.1: Relation between density (m^{-3}) and ion current over emission current for NH_3 measured with DFMS MCP/LEDA in high resolution mode.

Figure 3.2.2 (a)-(c) show the ratio of the different fragments to NH_3 for different pressures and emissions; in blue are the results of this work and in red values from NIST. The amount of NH_2 relative to NH_3 is between 0.7-0.85 thus close to NIST (fig. 3.2.2 (a)). Taking into account the error bars, the relative ratio of NH_3 is in good agreement with NIST. In detail it has been observed that the set 200 µA - $1\cdot 10^{-8}$ mbar and all 2 µA have a lower value than NIST. In contrast the fragmentation to NH and N do not agree with NIST. For NH, the 200 µA data spreads around 0.035 while at 20 µA the amount NH is around 0.027 and for 2µA only at the highest pressure could be detected resulting in NH/NH_3 0.008 ± 0.02 (fig. 3.2.2 (b)). For N/NH_3 (fig. 3.2.2 (c)), the values for $1\cdot 10^{-8}$ mbar are 0.937 ± 0.077 at 200 µA and 0.236 ± 0.027 at 20 µA (they exceed the scale of the graphs). Not taking into account those two values it can be seen that for 200 µA the ratio N/NH_3 for $1\cdot 10^{-7}$ mbar is in good agreement with NIST while for $5\cdot 10^{-8}$ mbar the value is about a factor of 1.5 higher. For 20 µA a similar pattern is present: for the highest pressure N/NH_3 is smaller than for $5\cdot 10^{-8}$ mbar however both values do not agree within 1 σ with NIST. For the emission of 2 µ, the peak relative to N was present only for the highest two pressures ($1\cdot 10^{-7}$ and $5\cdot 10^{-8}$) and for both the fragmentation does not agree with NIST. The values for the fragmentation seem to be dependent on the emission (mean of fragmentation at different pressures) and the mean of all are given in table 3.2.1. For N/NH_3 the values at $1{\cdot}10^{-8}$ mbar were not considered because of the large deviation from the other values. As well the value for $1{\cdot}10^{-7}$ mbar at 2 µA has not taken into account because on m_0 14 u/e the peak was only present on row A but not B.

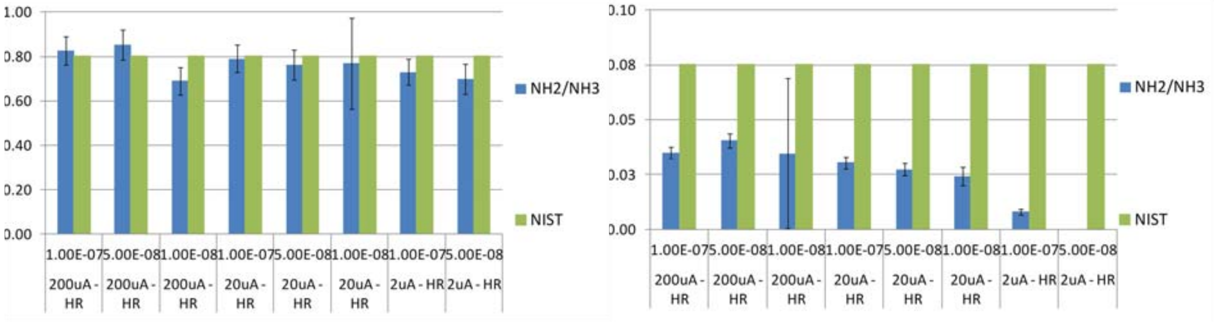

(a) NH_2/NH_3 **(b)** NH/NH_3

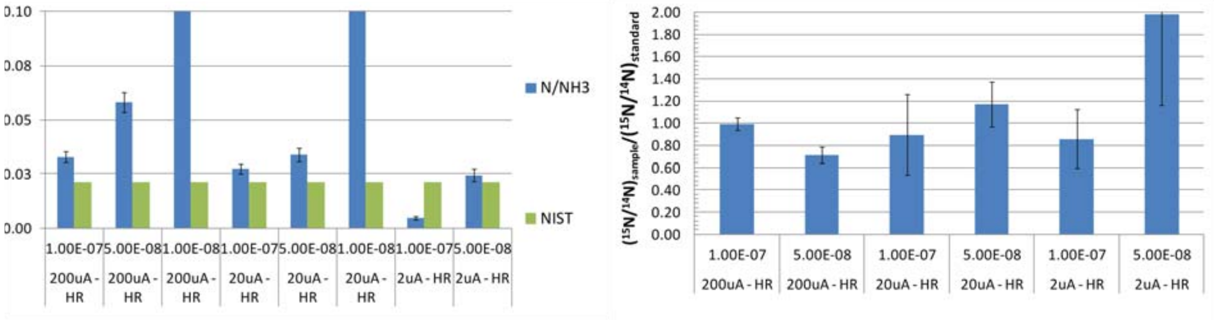

(c) N/NH_3 **(d)** $\frac{(^{15}N/^{14}N)_{sample}}{(^{15}N/^{14}N)_{standard}}$ in NH_2

Fig. 3.2.2: a)-c) show the amount of fragments N, NH, and NH_2 relative to NH_3 in the cases a signal was present. d) shows $\frac{(^{15}N/^{14}N)_{sample}}{(^{15}N/^{14}N)_{standard}}$ in NH_2 for the cases the signal was present.

Figure 3.2.2 (d) show the $^{15}N/^{14}N$ ratio in NH_2. The isotopic ratio could only be determined in NH_2 because: i) $^{15}NH_3$ was overlapped by H_2O, ^{15}NH was overlapped by NH_2, and for ^{15}N not sufficient signal was present. Although the peak of $^{15}NH_2$ could not be seen a change in the curvature of the shoulder was present which is assumed to be to $^{15}NH_2$ (exemplary mass spectra are shown in section B). The ratio of $^{15}N/^{14}N$ of the sample relative to the isotopic ratio of the standard (air-nitrogen) is shown in fig. 3.2.2 (d). For all three emissions at the pressures $1{\cdot}10^{-7}$mbar and $5{\cdot}10^{-8}$mbar it has been tried to determine the isotopic ratio and the results show strong variations and rather large uncertainties (up to 50% for 2µA - $5{\cdot}10^{-8}$ mbar). Except for 200 µA and 2 µA ,both at $5{\cdot}10^{-8}$ mbar, the determined ratios lay within 1σ of the standard however the uncertainties are rather large. The best agreement shows the data set 200 µA - $1{\cdot}10^{-7}$ mbar with $\frac{(^{15}N/^{14}N)_{sample}}{(^{15}N/^{14}N)_{standard}}$ 0.99 ± 0.09.

Table 3.2.1: Fragmentation of NH_3. The upper panel is the fragmentation relative to NH_3 while the lower panel is the fragmentation relative to the sum of fragments is. For each emission and fragment the mean of the available data (expect N see text) is listed below the over all mean value.

Emission (µA)	NH_3/NH_3	NH_2/NH_3	NH/NH_3	N/NH_3
mean	1	0.766 ± 0.022	0.025 ± 0.001	0.028 ± 0.001
200	1	0.791 ± 0.037	0.037 ± 0.002	0.027 ± 0.002
20	1	0.774 ± 0.038	0.027 ± 0.002	0.031 ± 0.002
2	1	0.715 ± 0.043	0.004 ± 0.001	0.024 ± 0.005
	f NH_3	f NH_2	f NH	f N
mean	0.520 ± 0.016	0.399 ± 0.013	0.013 ± 0.001	0.015 ± 0.001
200	0.475 ± 0.022	0.381 ± 0.018	0.018 ± 0.001	0.014 ± 0.001
20	0.527 ± 0.030	0.408 ± 0.023	0.014 ± 0.001	0.017 ± 0.001
2	0.577 ± 0.034	0.413 ± 0.025	0.002 ± 0.000	0.014 ± 0.003

Table 3.2.2: Nitrogen isotopic ratio determined in NH_2. The first column give the emission current, the second the pressure range of the total pressure relative to N_2, and in third column is the $^{15}N/^{14}N$ ratio of the sample relative to the standard (air nitrogen).

Emission (µA)	pressure range (mbar)	$\frac{(^{15}N/^{14}N)_{sample}}{(^{15}N/^{14}N)_{standard}}$ in NH_2
200	$1.00 \cdot 10^{-7}$	0.99 ± 0.09
200	$5.00 \cdot 10^{-8}$	0.72 ± 0.10
20	$1.00 \cdot 10^{-7}$	0.90 ± 0.14
20	$5.00 \cdot 10^{-8}$	1.17 ± 0.24
2	$1.00 \cdot 10^{-7}$	0.86 ± 0.28
2	$5.00 \cdot 10^{-8}$	1.98 ± 0.75

3.2.1.2 H_2S - MCP/LEDA HR

Like for NH_3 the sensitivity for MCP/LEDA in high resolution mode was derived from a linear least square fit of the ratio between ion and emission current and the particle density around the ion source. The resulting fit and the data are shown in fig. 3.2.3. And similar to the results for NH_3 the sensitivity increases for decreasing emission ranging from $(7.03 \pm 0.86) \cdot 10^{-20}$ cm ^{3} to $(5.48 \pm 0.69) \cdot 10^{-19}$ cm ^{3} for 200 µA and 2 µA respectively.

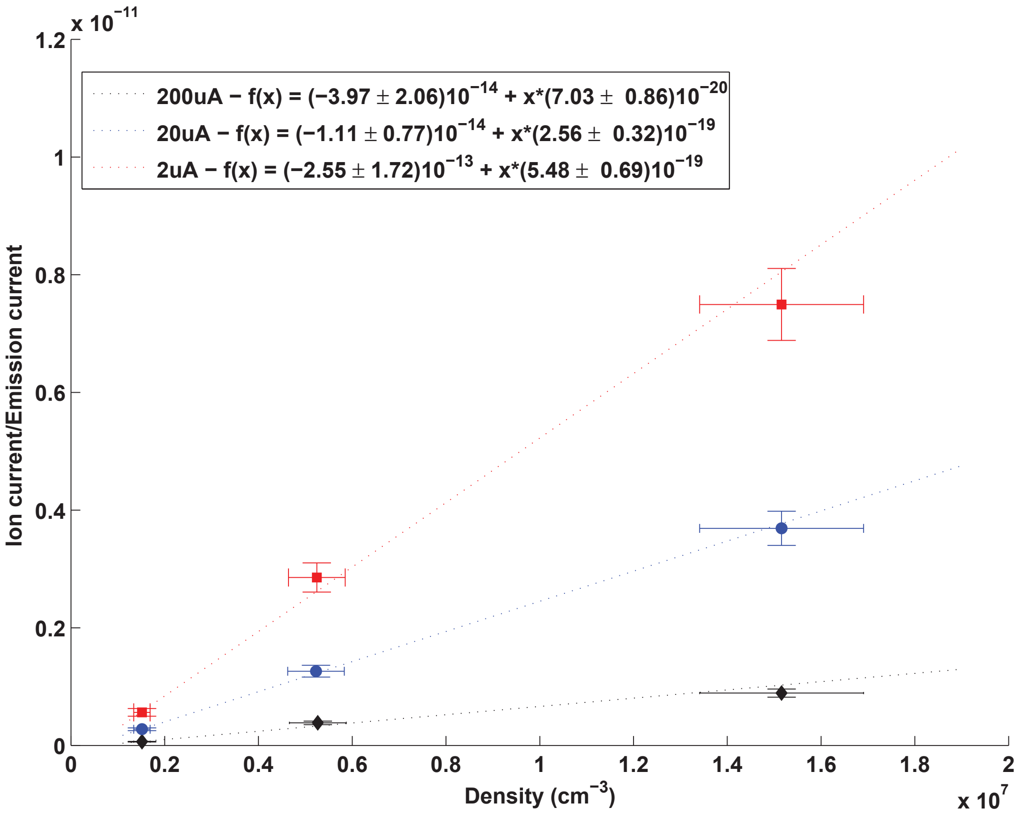

Fig. 3.2.3: Relation between density (m^{-3}) and ion current over emission current for H_2S measured with DFMS MCP/LEDA in high resolution mode.

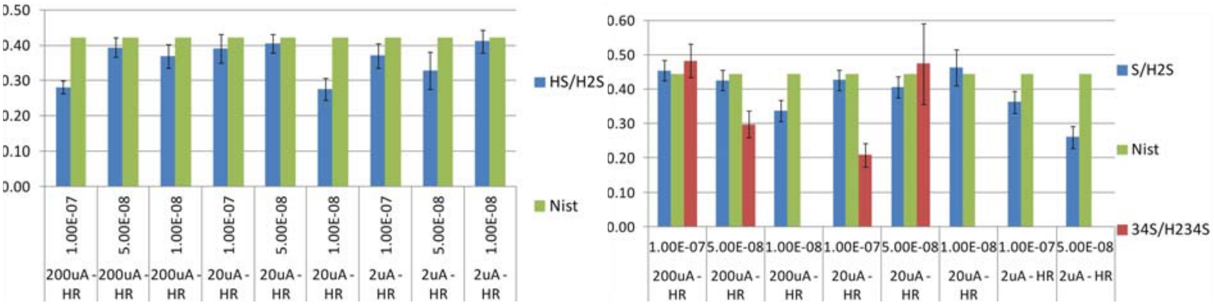

(a) HS/H_2S (b) S/H_2S

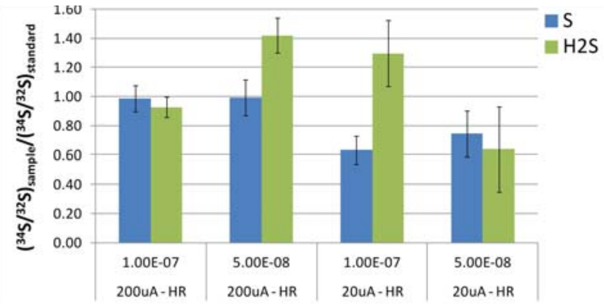

(c) HS/H_2S

Fig. 3.2.4: Fragmentation of H_2S to S and HS for different emissions at different pressures and ratio of $^{34}S/^{32}S$ with respect to the sulfur standard V-CDT.

Figure 3.2.4 (a) and (b) show the ratio of S to H_2S and of H_2 to H_2S for different pressures and emissions during the calibration measurement compared to NIST. The color code is the similar then for the fragmentation patter of NH_3; the blue and red bars correspond to this work wile the green bars correspond to NIST. It can be seen for HS/H_2S (fig. 3.2.4 (a)) that for most of the measurements the value of S/H_2S lays below NIST however it is still within uncertainties. The exceptions are the sets 200 µA - $1{\cdot}10^{-7}$ mbar, 20 µA $1{\cdot}10^{-8}$ mbar, and 2 µA $5{\cdot}10^{-8}$ mbar which all lay distinctly below NIST. The value for the fragmentation to S from H_2S is shown in fig. 3.2.4 (b). For half of the set the ratio S/H_2S lays within 1σ away from NIST. However, the sets 200 µA - $1{\cdot}10^{-8}$ mbar, 20 µ- $5{\cdot}10^{-8}$ mbar, 2 µA - $1{\cdot}10^{-7}$ mbar, and 2 µA - $5{\cdot}10^{-8}$ mbar do not agree with NIST and the remaining data set. Nevertheless the entire data set has been used to determine the mean fragmentation for the all emission (see table 3.2.3).

Table 3.2.3: Fragmentation of H_2S. The upper panel is the fragmentation relative to H_2S while the lower panel is the fragmentation relative to the sum of fragments is. For each emission and fragment the mean of the available data is listed below the over all mean value.

	H_2S/H_2S	S/H_2S	HS/H_2S
mean	1	0.393 ± 0.012	0.352 ± 0.011
200µA	1	0.406 ± 0.017	0.348 ± 0.016
20µA	1	0.432 ± 0.022	0.357 ± 0.018
2µA	1	0.314 ± 0.023	0.352 ± 0.025
	f H_2S	f S	f HS
mean	0.574 ± 1.040	0.224 ± 0.239	0.202 ± 0.145
200µA	0.571 ± 0.925	0.231 ± 0.207	0.198 ± 0.134
20µA	0.559 ± 2.615	0.242 ± 0.603	0.199 ± 0.353
2µA	0.602 ± 0.107	0.187 ± 0.030	0.211 ± 0.024

The isotopic ratio could be determined only for $^{34}S/^{32}S$ in S and H_2S for the highest two pressures because for $H^{34}S$ the signal was too small and for the isotopologues with ^{33}S the signal was too low. The resulting isotopic ratio with respect to the sulfur standard (V-CDT) is shown in fig. 3.2.4 (c) in S and H_2S. For 200 µA the results for S are in good agreement with the standard while for H_2S the result for $1{\cdot}10^{-7}$ mbar plus 1 $\sigma$is scarce below the standard and for $5{\cdot}10^{-8}$ mbar it is about a factor 2 too high. For 20 µat $1{\cdot}10^{-7}$ mbar the values derived for S is about a factor 2 too low and for H_2S it is about a factor of 2 too high. In contrast the values at $5{\cdot}10^{-8}$ mbar are both below the standard however they are still within the error. The isotopic ratio relative to the standard for $^{34}S/^{32}S$ at $1{\cdot}10^{-7}$ mbar are 0.99 ± 0.09 and 0.93 ± 0.0.12 for S and H_2S respectively while for S at $5{\cdot}10^{-8}$ mbar it is 0.99 ± 0.12.

3.2.2 Discussion

In order to check whether the received sensitivities for H_2S and NH_3 are reasonable they can be compared with results achieved by Hässig (2013) for molecules with similar masses. Thus NH_3 can be compared with H_2O while H_2S can be compered with N_2. However, they first need to be corrected for the ionization sensitivity which is given through the ionization cross section. A compilation of the considered sensitivities and the ionization cross section is given in table 3.2.4. For showing purposes the resulting corrected sensitivities are shown in fig. 3.2.5; data acquired at 2 µA is given in blue, at 20 µA in red, at 200 µA in green, and the sets for NH_3 and H_2S are indicated by an arrow. From the graph one can see the following: first except for water the sequences of corrected sensitivities with respect to the emission is inverse proportional to the emission, second NH_3 and H_2O cover a similar range, third for NH_3 and H_2O the result for one emission - 2 µA for NH_3 and 200 µA for H_2S - is significant different from the remaining two emissions, forth the results for N_2 and H_2S overlap only little, and fifth abundance within one species relative to 2 µA is not constant.

The revealed differences can have multiple causes depending on the seen difference and in this paragraph each of them will be discussed. The change in sequence of the sensitivities with respect to the emission seen for water is puzzling since the majority of the calibrated species shows an increasing sensitivity with decreasing emission current. This effect can not be explained by the detector or the transmission sensitivity because they are dependent on the mass to charge ratio and the energy and the composition of the particles respectively. Therefore either it is a particularity of DFMS or a bias in the results for H_2O. That the corrected sensitivities for H_2O and NH_3 cover the same implies that the difference in m/z and energy is compensated by the detection sensitivity resulting in similar corrected sensitivities. The difference in relative sensitivity between 2 µA and 20 µA is not clear to the author and either it is a peculiarity of DFMS or the resulting sensitivity for 2 µA is overestimated. The difference in m/z between of H_2S and N_2 is ~6 u/e which results in a difference in energy of about 20% and might be the major cause for the difference in the corrected sensitivities of N_2 and H_2S. Last but not least the change in abundance within a species relative to 2 µmight indicate a correlation between relative abundance and species i.e. that the yield of ionized particles is not only dependent species and the electron energy but on the emission current or it might point to a bias in the calibration of either sensitivity.

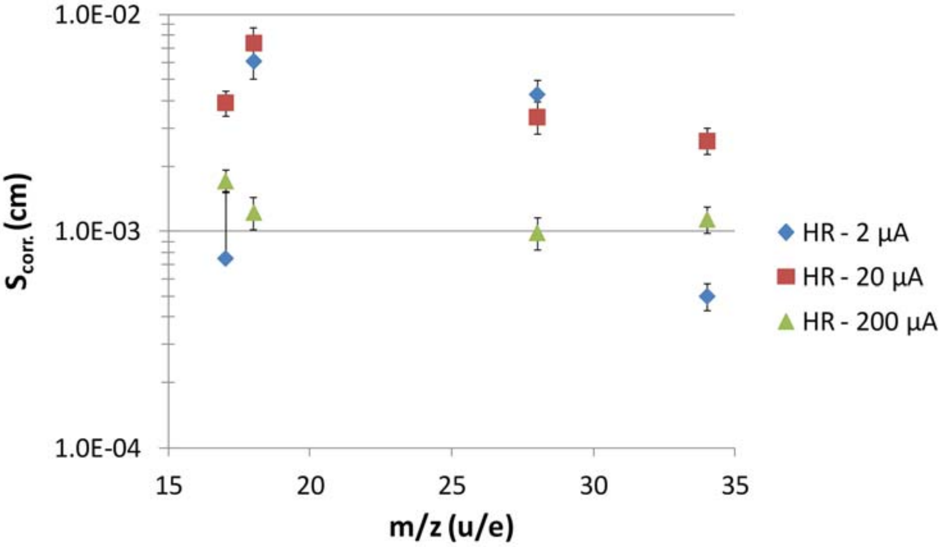

Fig. 3.2.5: Comparison of the high resolution sensitivities at 2, 20, and 200 µA of NH_3, H_2O, N_2, and H_2S corrected for the ionization efficiency given by the ionization cross section (see table 3.2.4).

Table 3.2.4: Compilation of the sensitivities, the electron impact cross section, and the sensitivities corrected for the ionization efficiency for the species NH_3, H_2O, N_2, and H_2S measured at 2, 20, and 200 µA with MCP/LEDA.

Molecule	σ^{*}_{EII} (45 eV) cm ^{2}	Sensitivity (cm^3) HR - 2 µA	HR - 20 µA	HR - 200 µA
$NH_3{}^1$	2.664E-16	$(2.01 \pm 0.21)10^{-18}$	$(1.05 \pm 0.12)10^{-18}$	$(4.57 \pm 0.48)10^{-19}$
H_2O^2	1.879E-16	$(1.15 \pm 0.18)10^{-18}$	$(1.40 \pm 0.22)10^{-18}$	$(2.31 \pm 0.37)10^{-19}$
$N_2{}^2$	2.008E-16	$(8.64 \pm 1.38)10^{-19}$	$(6.80 \pm 0.10)10^{-19}$	$(1.99 \pm 0.32)10^{-19}$
H_2S^1	4E-16	$(5.48 \pm 0.69)10^{-19}$	$(2.56 \pm 0.32)10^{-19}$	$(7.03 \pm 0.80)10^{-20}$
	integer mass (u)	Sensitivity corrected for ionization cross section (cm^3)		
$NH_3{}^1$	17	$(7.55 \pm 7.90)10^{-4}$	$(3.94 \pm 0.51)10^{-2}$	$(1.72 \pm 0.21)10^{-3}$
H_2O^2	18	$(6.13 \pm 1.05)10^{-3}$	$(7.43 \pm 1.27)10^{-3}$	$(1.23 \pm 0.21)10^{-3}$
$N_2{}^2$	28	$(4.30 \pm 0.72)10^{-3}$	$(3.38 \pm 0.57)10^{-3}$	$(9.91 \pm 1.66)10^{-4}$
H_2S^1	34	$(5.03 \pm 0.70)10^{-4}$	$(2.63 \pm 0.36)10^{-3}$	$(1.14 \pm 0.16)10^{-3}$

[1] this work

[2] Hässig (2013)

* NIST Electron-Impact Cross sections for Ionization and Excitation

For both H_2S and NH_3 the fragmentation show some inconsistencies. While for NH_3 the odd one out is the ratio between N/NH_3, both fragments of H_2S have large deviation from the bulk for half of the data points. In addition, not the same measurements show the same trends concerning the variation i.e. at 20µA $5 \cdot 10^{-8}$ mbar the ratio HS/HS2 is within the error the same as NIST while for S/H_2S the ratio between this work and NIST is about a factor 4. Last but not least there is a correlation between the ratio N/NH_3 and the pressure of the calibration gas.

The cause for the variation of the ratio N/NH_3 might be an additional source of N i.e. remaining of the HCN polymer despite heating DFMS to clean or N_2 due to air contamination. The deviation in the ratio of HS/H_2S from the bulk value for the sets 200 µA - $1 \cdot 10^{-7}$, 20 µA - $1 \cdot 10^{-8}$, 2 µA - $1 \cdot 10^{-7}$, and 2 µA - $5 \cdot 10^{-8}$ is most likely due to an overestimation of the signal due to H_2S on m/z 34 u/e. However, one would expect to see a deviation form the bulk ratio of S/H_2S for the same data sets which is not the case. nevertheless a bias in the determination of the peak for all fragments is still the most likely explanation considering difficulties at fitting the peaks due to low signal height and overlapping of peaks. Neglecting the considerable variation of N/NH_3 it seems as the fragmentation is slightly dependent on the emission. It seems as if the amount of fragments decreases with decreasing emission current although always the same electron energy of 45 eV is used. Due to the variation seen in the fragmentation of H_2S it is not possible to check for this possible dependence on the emission and no information is given about this in Hässig (2013) therefore it is not possible to say whether this is a characteristic of DMFS or whether it points to an inconsistency of this calibration work.

The variation seen for both $^{15}N/^{14}N$ in NH_2 and $^{34}S/^{32}S$ can be explained by that at least one peak was overlapped considerably by another species; in the case of NH_2 it was NH_3 that covered almost all of NH_2 so that only an elevation of the shoulder could be seen in the spectra (spectra are in fig. B.0.1), and for H_2S there was an interference for $H_2{}^{34}S$ on m/z 36 u/e with ^{36}Ar. Since there seem to be no correlation with pressure or emission for both $^{15}N/^{14}N$ in NH_2 and $^{34}S/^{32}S$ the variations seen in the ratios are most likely a bias of the area determination.

3.3 Sensitivity Relation

Although not all species present in a coma can be calibrated since they are either lethal or damage the instrument and the calibration facility it has been attempted to find a correlation between the mass to charge ratio and the sensitivity. As it has been already explained in section 2.3.5 several corrections had to be applied to the existing data set in order to get rid of inferences like the ionization efficiency or the fragmentation of a species. In the following the sensitivities for MCP/LEDA and CEM corrected for the ionization and fragmentation are presented. After a comparison of the obtained results for both sensors they will be discussed. A guide on how to to calculate the sensitivity for a not calibrated species can be found in the appendix in section B.1.

3.3.1 Results

In Fig. 3.3.1 and Fig. 3.3.2 the results of attempt to reduce the measured high resolution sensitivities on their mass to charge dependence is shown for MCP and CEM respectively , the results for low resolution are shown in section B.1. For both MCP and CEM data this leads not to a clear correlation between m/z and corrected sensitivity ($S_{i,corr}$) besides the the general decrease with increasing m/z till m/z 70. Remarkably is that for MCP: i) the resulting values for 2 µA and 20 µA overlap for about two third of the measures species, ii) for almost all species the values with 200 µA are significant lower than for the other two emissions, iii) there is a sudden increase of the level between m/z 58 u/e and m/z 84 u/e, and C_2H_4, C_2H_6, and $C_3H_8$are about a factor of 10 lower than the other points for all three emissions. In contrast the reduced sensitivities for CEM have a smaller spread than seen for the MCP, for all species the sensitivities are in a sequence according to the emission, and the difference between C_2H_4, C_2H_6, and C_3H_8 is not as large as seen for MCP.

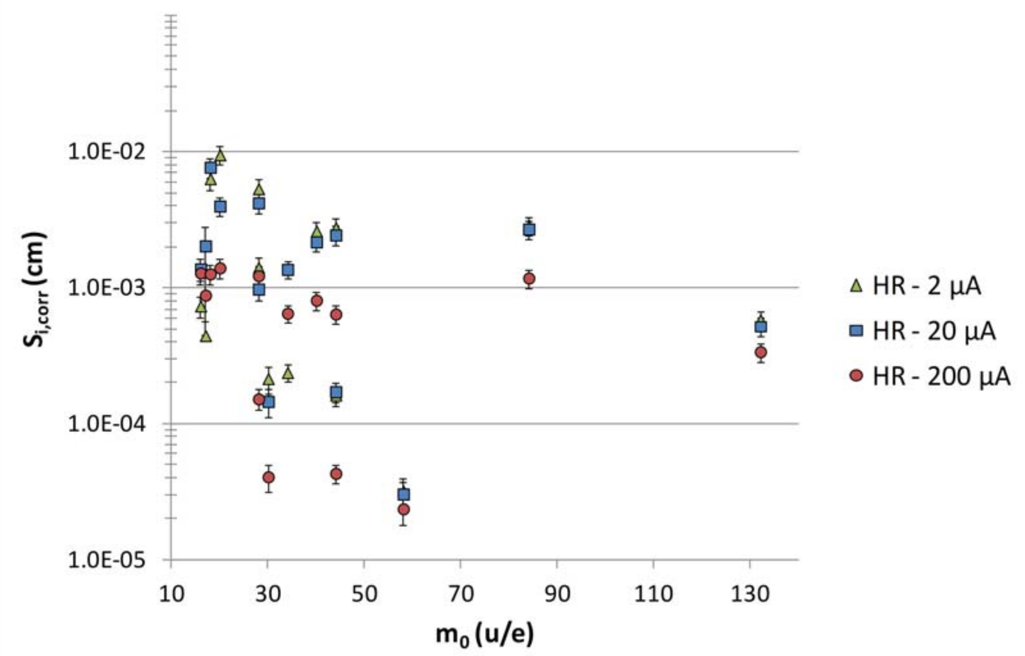

Fig. 3.3.1: Sensitivity ($S_{i,corr}$) of MCP corrected for ionization cross section at 45 eV, pressure (only for hydrocarbons), and fragmentation.

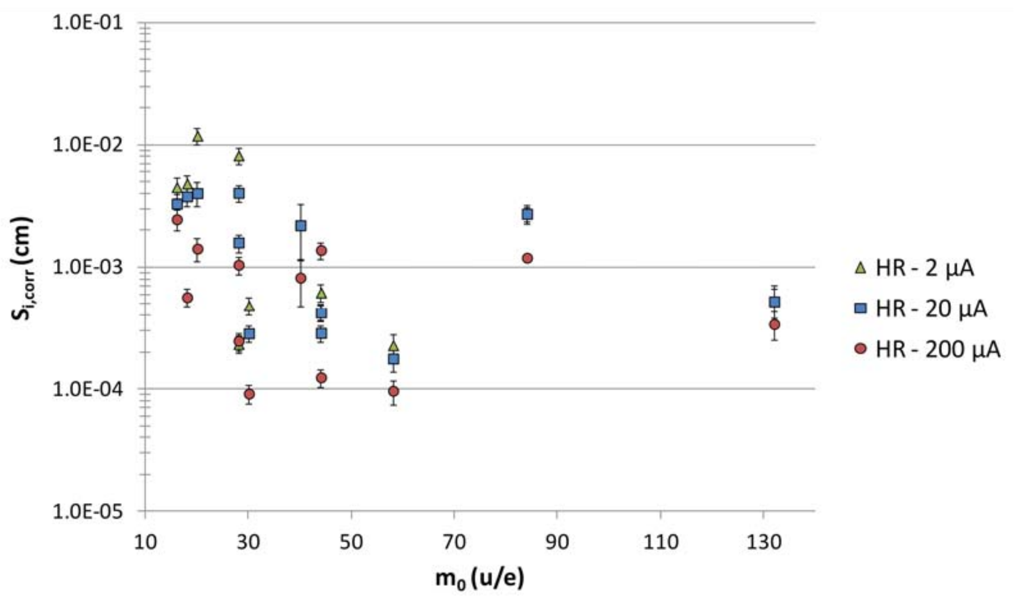

Fig. 3.3.2: Sensitivity ($S_{i,corr}$) of CEM corrected for ionization cross section at 45 eV, pressure (only for hydrocarbons), and fragmentation.

The spread in both CEM and LEDA data indicates that the data is dependent on more than only the mass to charge ratio therefore a reduced data set will be used for further analysis. The data set is reduced on noble gas sensitivities because noble gases are inert and we have data for both ion and neutral measurements. Even though different electron emissions lead to different absolute sensitivities the mass dependence should be independent of emission. Thus the fragmentation is supposed to be independent of the emission and the influence of the transmission is independent of the processes in the source as long as the particles get the same energy. Therefore all data set (1 set: 1 detector, 1 emission, 1 resolution) are normalized to the sensitivity of neon and are drawn in Fig. 3.3.3 and Fig. 3.3.4 for MCP and CEM respectively.

Comparing MPC neutral and ion relative sensitivities leads to 3 observations: i) high resolution data sets do not behave as the ion sensitivities while the relative sensitivities for low resolution lays close to the relative ion sensitivities, ii) the relative sensitivity for high resolution seems to depend on the emission and the mass to charge ratio, and there is no increase for the relative Kr ion sensitivity as is it is present for the neutral data. The sole similarity between CEM and MCP relative sensitivities is the decrease with increasing m/z furthermore the CEM data shows the following characteristics: i) a large spread of the relative sensitivities at m/z 40 where for HR 200 µA, HR 20 µA, and LR 2 µA is above 1, ii) there is no order left due to the emission for a distinct m/z, and iii) in general the relative CEM sensitivities are above the relative ion sensitivities of MCP/LEDA.

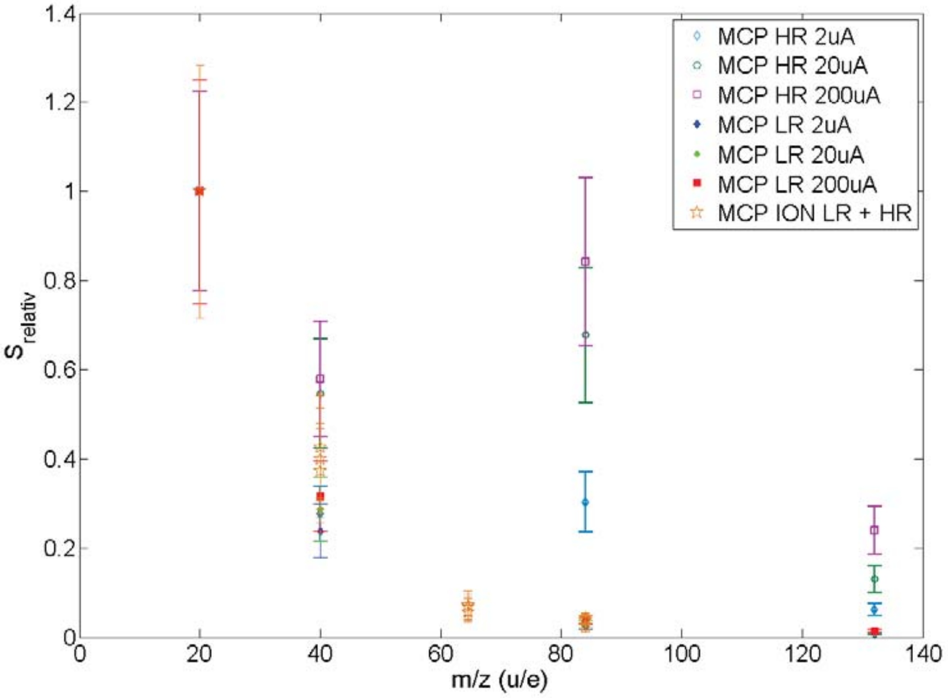

Fig. 3.3.3: Displayed are ion and neutral MCP relative sensitivities of the noble gases Ne, Ar, Kr, Xe normed to neon for both low and high resolution.

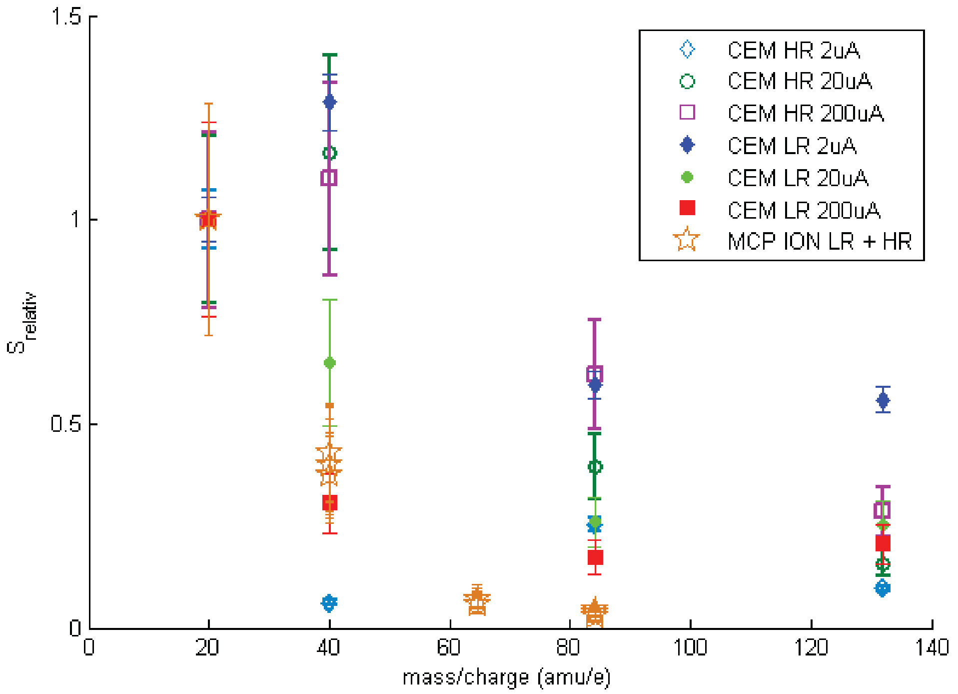

Fig. 3.3.4: Displayed are neutral CEM and ion MCP relative sensitivities of the noble gases Ne, Ar, Kr, Xe normed to neon for both low and high resolution.

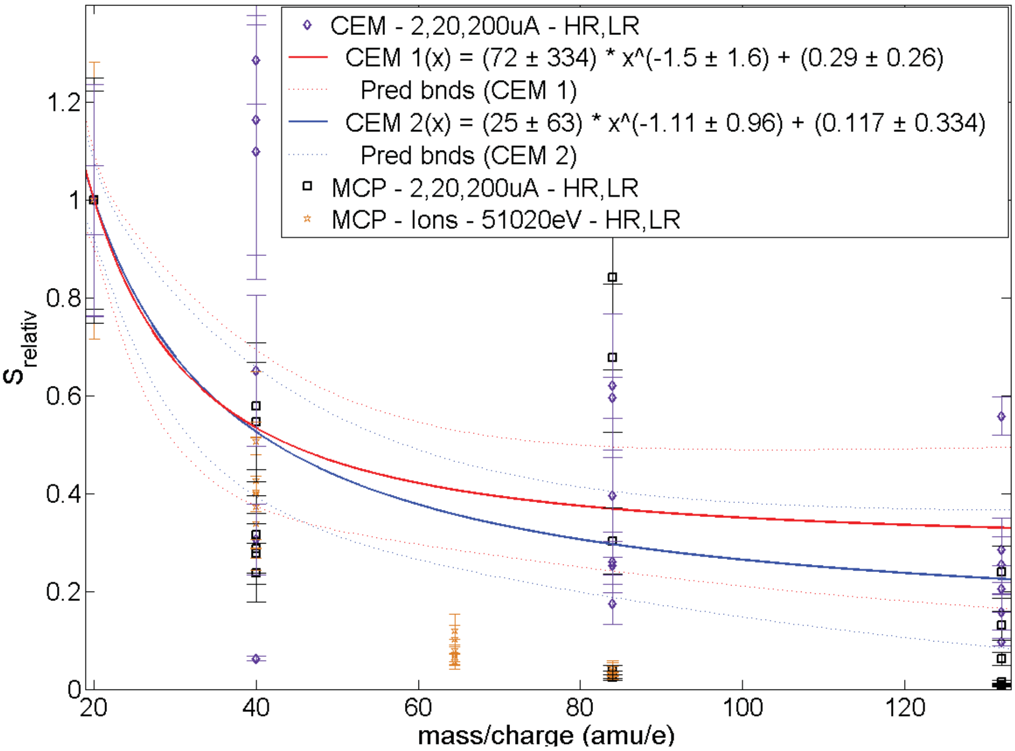

Fig. 3.3.5: Fit of the neutral noble gas relative CEM sensitivities. For CEM 1 all HR data and all data with m/z 20 u/e were omitted while for fit CEM 2 all HR data with m/z > 69 u/e and the results for 2 µA were omitted.

Considering the size of the data set it has been decided that the neutral relative sensitivities for MCP/LEDA, CEM, and the ion relative sensitivity are put together to have 3 larger set for applying a fit. Each of those 3 sets has been fitted with a function of the form $f(x) = a \cdot x^b + c$ where x is m/z. Since for m/z > 69 u/e PA = -1000 V is nominally applied in high resolution this data has been omitted for the fit of MCP neutral measurements. However data above m/z 69 u/e could be used for the relative ion sensitivities because PA was at the same value for the entire mass range and therefore no bias due to this voltage is present. The CEM data were fitted twice: first with omitting all HR data and the values at m/z 20 u/e, and second omitting all HR data above m/z 69 u/e and the data measured with 2 µA. The data together with the corresponding fit are displayed in fig. 3.3.5, fig. 3.3.6, and fig. 3.3.7 for CEM (neutrals), MCP (neutrals), and MCP (ions), resp. and the resulting fit parameters are given in table 3.3.1.

Table 3.3.1: Parameters of the fits for relative neutral noble gas sensitivities of CEM and MCP/LEDA and for the relative ion noble gas sensitivities for MCP/LEDA.

	a	b	c
CEM - 1	72 ± 334	-1.5 ± 1.6	0.29 ± 0.26
CEM - 2	25 ± 63	-1.11 ± 0.96	0.117 ± 0.334
MCP - neutrals	16 ± 40	-0.82 ± 1.19	-0.34 ± 1.37
MCP - ions	15.1 ± 8.7	-0.776 ± 0.254	-0.47 ± 0.29

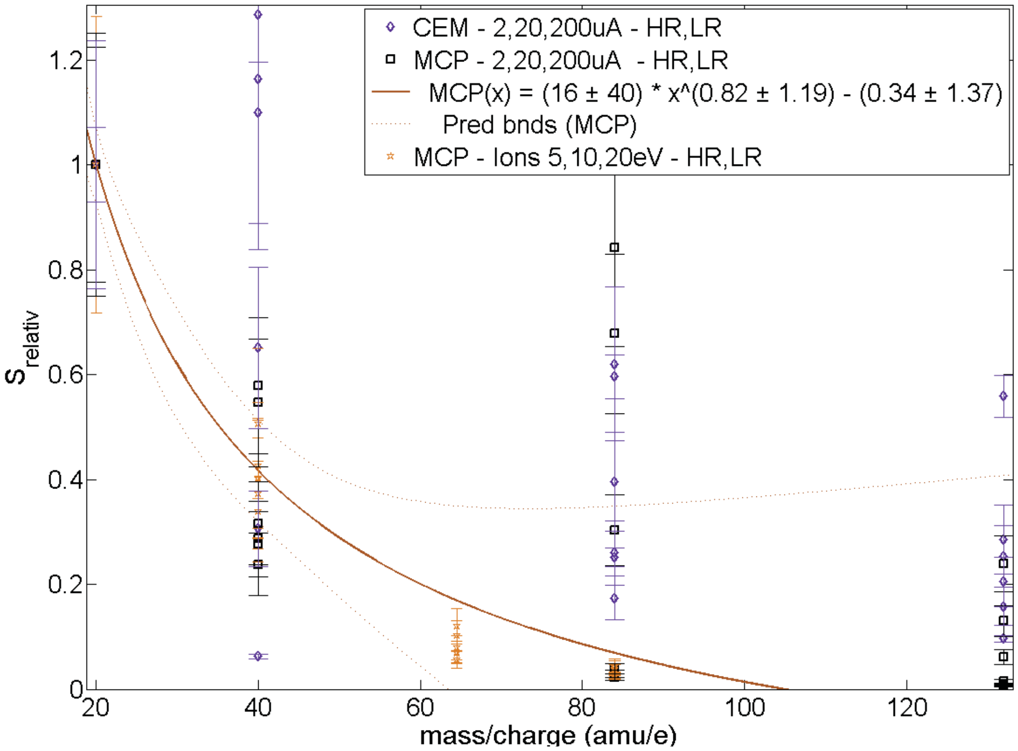

Fig. 3.3.6: Fit of the neutral noble gas relative MCP sensitivities for which all HR data with $m_0 > 69$ u/e were omitted.

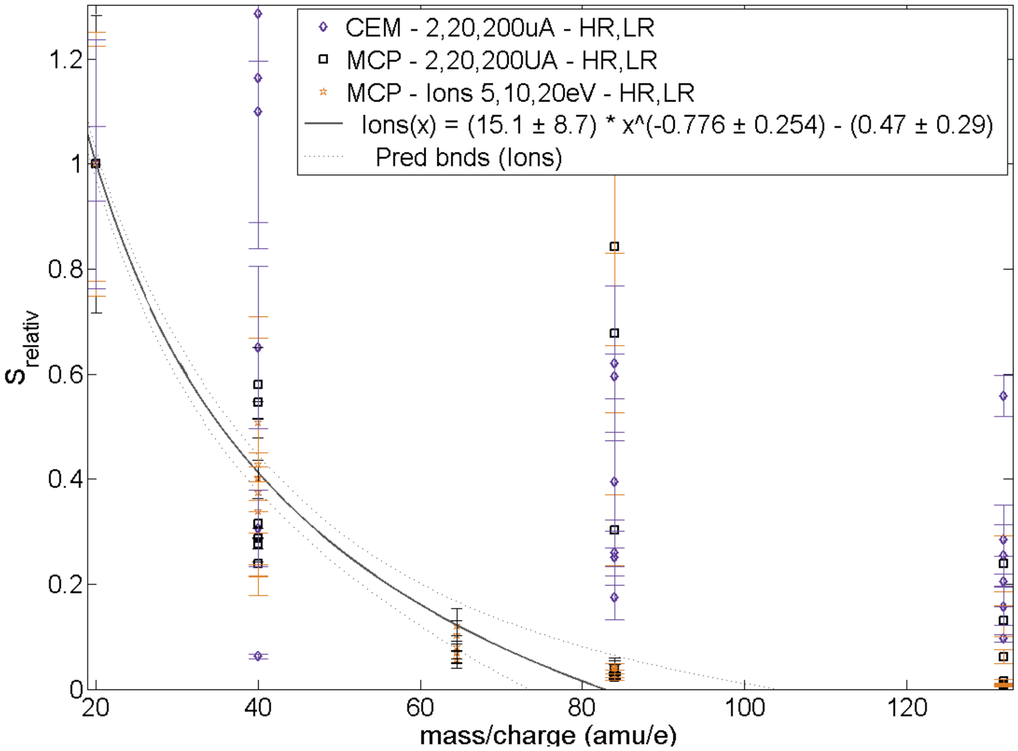

Fig. 3.3.7: Fit of the ion relative noble gas MCP/LEDA sensitivities.

3.3.2 Discussion

Only one of the features seen for the relative sensitives presented in the previously can be explained by the measurement procedure namely the increase in level for m/z > 80 u/e. This increase seen only for the neutral relative sensitivities for CEM and MCP is due to the additional acceleration with PA = - 1000 V and one can see from fig. 3.3.3 and fig. 3.3.4 that it is a considerable increase. the difference seen between neutral and ion relative sensitivity for MCP implies that the applied corrections were not sufficient in particular that there is a dependency on the emission which has not been considered so far. The inconsistencies seen for neutral relative sensitivities, namely spread and the change in sequence depending on the emission within CEM data and the inconsistency comparing them with MCP, imply that some of the CEM sensitivities are not correct. Possible causes are variations of the gas density during the acquisition, and inconsistencies in the data analysis procedure namely back ground correction, peak identification, and deconvolution of the CEM peaks. In order to achieve a fit not biased by the inconsistencies some restrictions based on the patterns seen for the MCP neutral relative sensitivities were applied resulting in the two fits for CEM.

3.4 Individual Pixel Gain

As it has been explained in section 1.9.5 the MCP suffers from located depletion due to the impinging ions. It is inevitable and had the depletion has to be determined on a regular bases in order to obtain meaningful results for densities. First the individual pixel gain factors for FM determined in 2015 are presented and compared to the last set from 2012. Second the results of the numerous measurements performed in space are presented. In addition to this for both FM and FS the manifestation of depletion with respect to the gain step has been investigated. Since the individual pixel gain can lead to crucial changes in the spectra if not properly corrected the effect of a not proper pixel gain correction has been investigated on the basis of the individual pixel gain factors measured at gain step 16 in November 2014 with FS.
For both FM and FS the presentation of the results is done in distinct sub sections. However, the discussion has been combined since a comparison between the findings at FM and FS is done.

3.4.1 Results - FM

3.4.1.1 Individual Pixel Gain Factors

In spring 2015 measurements for individual pixel gain factor calculation of FM were performed with neon as target mass. A compilation of the resulting individual pixel gain factors is given in fig. 3.4.1 (a) and (b) for row A and B, respectively. Measurements were performed from GS 07 to GS 16 and in addition for GS 15 and GS 16 were repeated once and twice, respectively. Comparing the compilation of both rows one can see two distinct differences: first on row A a peak is visible around pixel 430 is a peak which does not appear on row B. Second on row B there is a dip around pixel 320 for GS 13 which is not present on row A. The first one is due to a bad pixel of the LEDA which is not masked and the second one is due to a bad spectrum for row B, that has not been take into account for the pixel gain determination. This leads to a dip in the pixel gain curve similar to the one produced by depletion of the MCP. The individual pixel gain curves for both row have in common: i) a major dip around pixel 260, ii) a larger dip depth for smaller gain step, and iii) a linear slope over the LEDA dependent on the gain step. Checking the data set from 2012 (see fig. 3.4.1 (c)) the three common features appear as well and in addition three changes compared to 2015 can be seen. First the central dip has a more symmetric shape in 2015, second in the same set several additional dips appear between pixel 50-150 as well as 370-471 for both row A and B, respectively. Third the depletion increased. A direct comparison of the individual pixel gain factors for GS 07 gave an enlargement of the depletion in the central part from 0.298 to 0.183 relative to the mean individual pixel gain which is an increase in depletion of 0.115. For GS 16 and GS 15 it is difficult to quantify the change in depth because the 2015 data lays almost within the statistical uncertainty of the 2012 data.

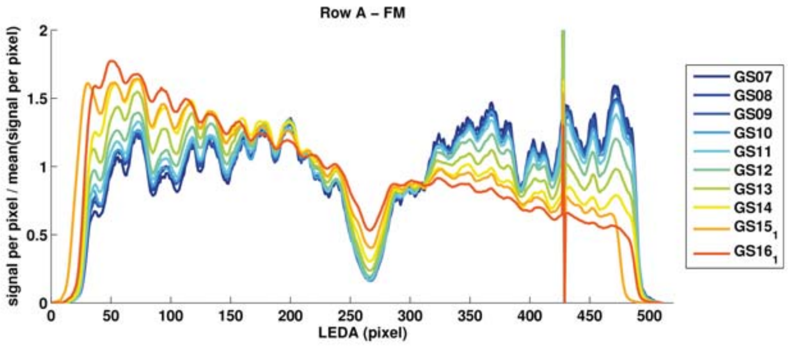

(a) FM row A 2015

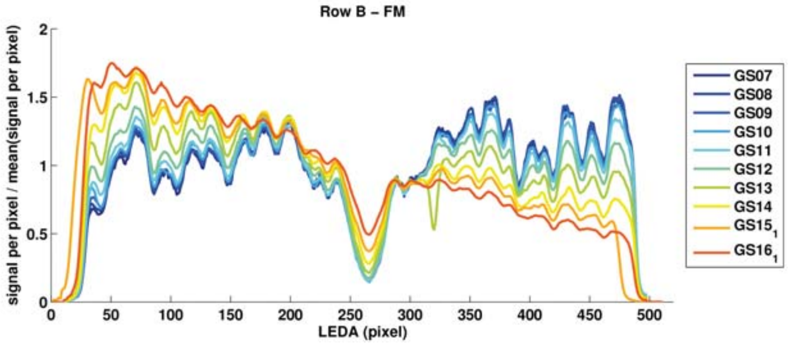

(b) FM row B 2015

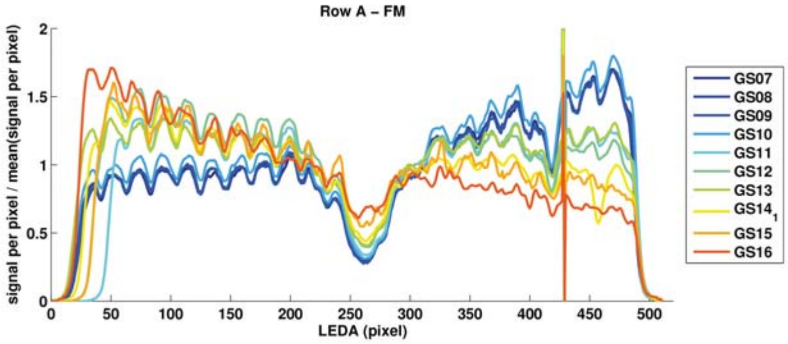

(c) FM row A 2012

Fig. 3.4.1: (a)-(c) show the compilation of the individual pixel gain factors of GS 7 to GS 16 for row A 2015, row B 2015, and row A 2012, respectively.

In addition the normalization seems to be incoherent, because the signal of the supposedly undepleted pixel do not overlap in particular on the left half of the LEDA as it can be seen fig. 3.4.2 (b)). For GS 14 the uncertainties in the data from 2012 is smaller and the change in depletion is about 13%. Except for one, all features seen in the individual pixel gain can be explained by either the quality of the data sets or by natural depletion of the MCP. The one exception is the linear slope of the individual pixel gain factors over the LEDA which is dependent on the applied potential between back and front side of the MCP. This feature has been already observed in previous data sets but no explanation has been found. To rule out mistakes in the measurement procedure GS 16 has been remeasured once with ~10 less signal intensity and once with the inverse sweep i.e. starting on the right side of the LEDA. In fig. 3.4.3 the results following the nominal measurement procedure (in blue), the results for the smaller signal (in red), and the results if the sweep direction is reversed (in black) are shown. The uncertainties due to statistics are not drawn because they are smaller than the line width for all three cases. Remarkably the difference between the three cases at the central dip is almost zero while for both rows the largest difference (~0.02) is present on the left half.

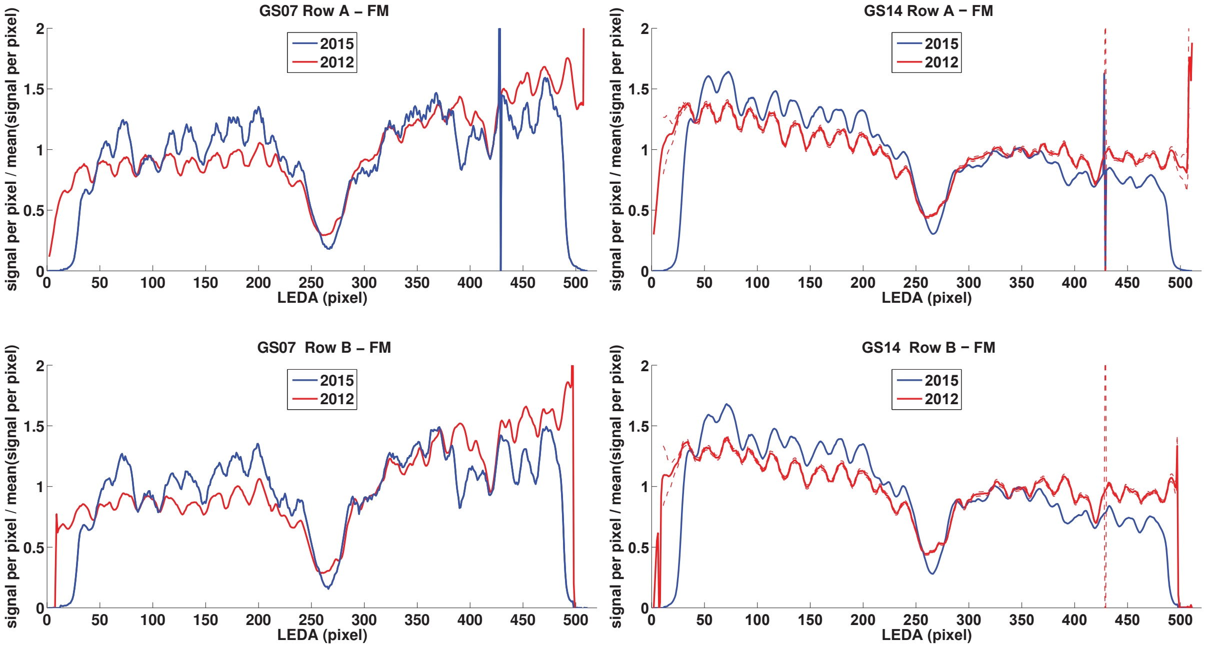

(a) GS 07 FM 2012 vs. 2015 **(b)** GS 14 FM 2012 vs. 2015

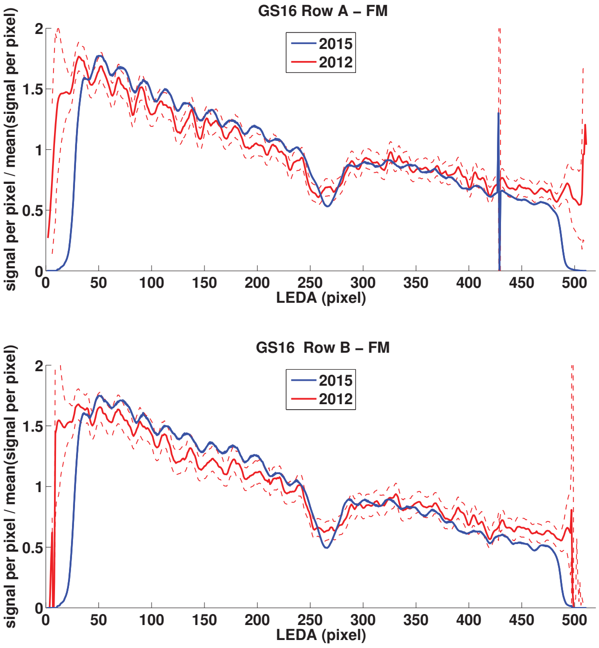

(c) GS 16 FM 2012 vs. 2015

Fig. 3.4.2: Comparison of individual pixel gain factors between 2012 and 2015. (a)-(c) show a comparison of the gain steps 7, 14 and 16 between 2012 (in red) and 2015 (in blue). Uncertainties due to ion statistic are indicated by dashed lines. It can be seen that for three gain steps the depletion in the center of the LEDA increased and five new dips appeared. In addition the normalization seems to be incoherent, because the signal of the supposedly undepleted pixel do not overlap in particular on the left half of the LEDA.

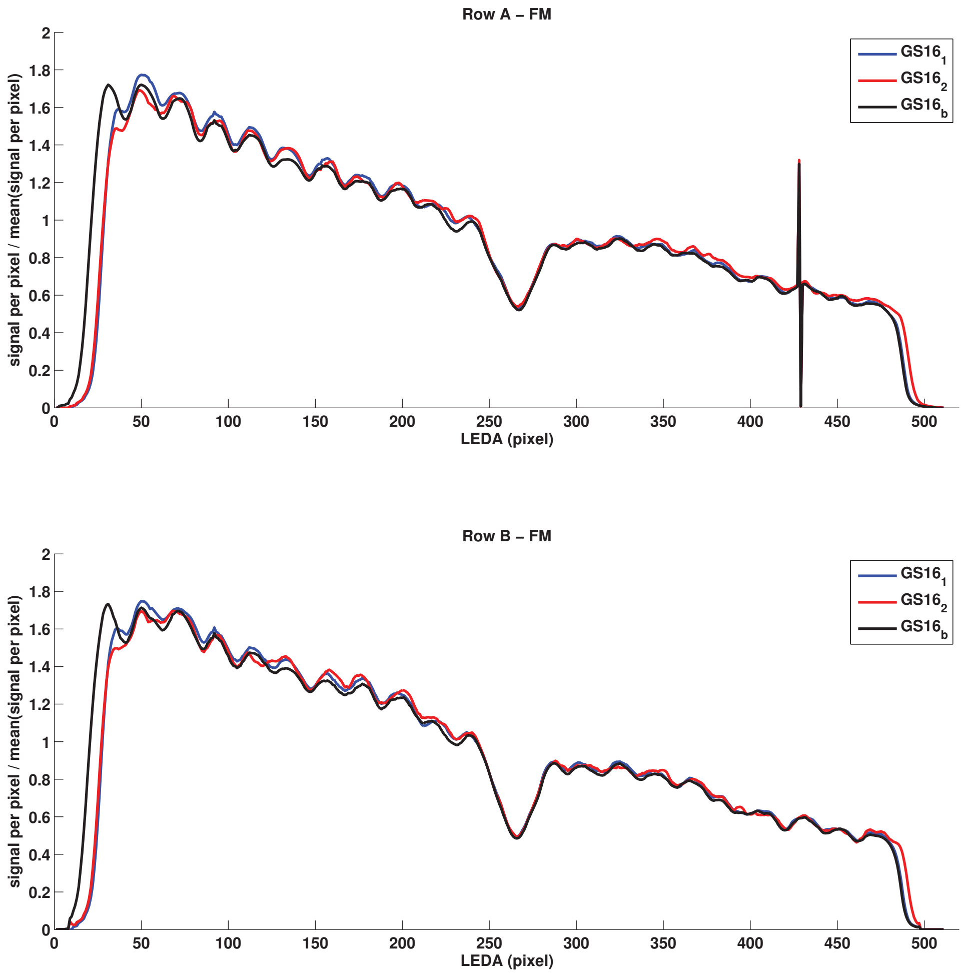

Fig. 3.4.3: Displayed are three data sets for GS 16 acquired in 2015. For blue the nominal measurement procedure was performed, for red the signal was a factor ~10 smaller than for the blue curve, and for the black curve the direction of the sweep has been inverted.

The figures 3.4.4 (a)-(c) show in each upper panel the peak width of every sweep step and in the lower panel the peak maximum for GS 07, GS 11, and GS 16. To obtain the peak width for every step the peak of interest has been fitted with a Gaussian function. The peak maximum shows the same trend seen for the individual pixel gain factors - the change of linear slope with different gain step. Remarkably the peak width decreases for all three shown gain steps with increasing number pixels from ~3 pixels to ~2 pixels. A reanalysis of the 2012 data shows the same pattern which is present for all measured gain steps. As a consequence a linear fit has been made for the 2012 and 2015 data set to determine the slope of the changing width and to check whether there is any correlation with the gain step. In fig. 3.4.5 only the resulting fit curves for 2015 (upper panel) and 2012 (lower panel) are shown. There is no significant difference between all fitted slopes for they are all places within their error margins. However the 2012 data show three different slopes for 3 sets of gain steps. The steepest slope, similar to the one of the 2015, data is seen for GS 11 and 12, the second steepest is for gain step 15 and 16, and almost no change over the LEDA in the peak width can be observed for GS 07- GS 10 and GS 14.

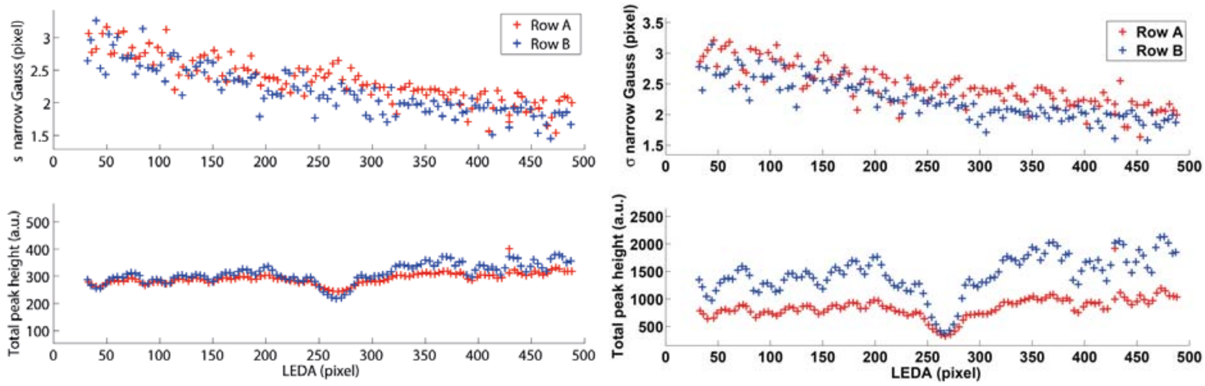

(a) GS 07 2015 **(b)** GS 11 2015

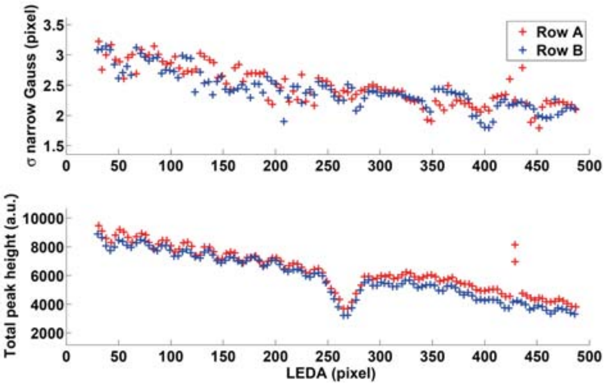

(c) GS 16 2015

Fig. 3.4.4: (a)-(c) in the upper panel show the peak width at different locations on the LEDA and in the lower panel the peak maximum of the neon peak for GS 07, GS 11, and GS 16.

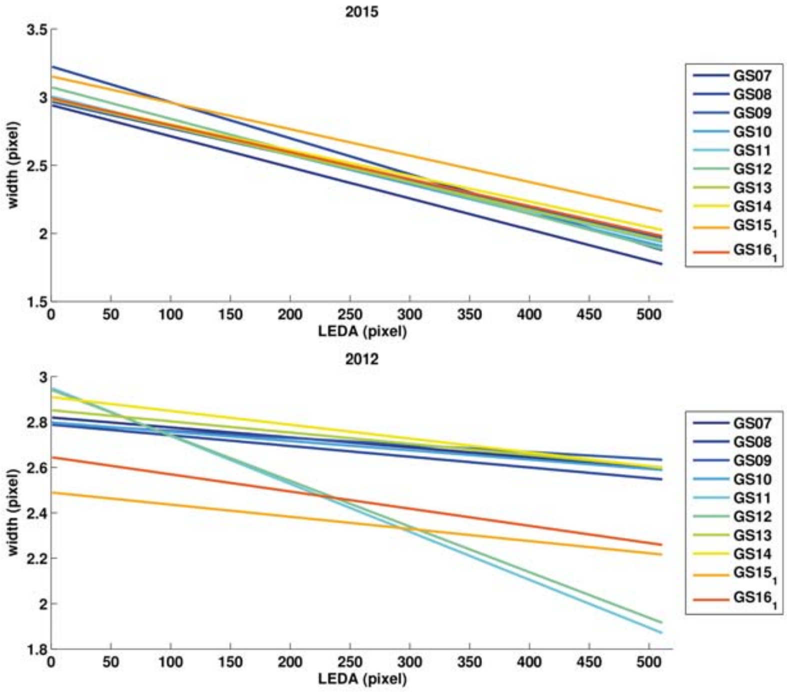

Fig. 3.4.5: Compilation of linear fits of the width size with respect to the peak location on the LEDA for row A FM. The upper panel shows the 2015 set and the lower the set from 2012

3.4.1.2 Manifestation of Depletion

As a consequence of the dependency of dip depth on the voltages applied on the MCP, it has been tried to determine a function for the dip depth considering the GS as a variable. A difficulty in this process was posed by the fact that there is no common level in the individual pixel gain at different gain steps for supposedly undepleted areas of the MCP and in addition to this the sign of the linear slope changes with GS. To be biased as less as possible by this 'offset' divergence, the dip depth has been defined as the difference of the maximum of the last/first bump before the dip starts and the minimum of the dip. Those two locations on the LEDA have been selected because they show the smallest change in 'offset' for different gain steps. The calculation of the dip depth has been done both data set in order to check a depletion dependency. Based on the pattern seen in the data a weighted least square fit for both rows of the 2012 and 2015 data set has been carried out with the functions being:

$$f(x_{norm}) = a \cdot exp(-b \cdot x_{norm}) + c \cdot x_{norm}^2 + d \tag{3.4.1}$$

$$h(x_{norm}) = a \cdot exp(-b \cdot x_{norm}) + c \cdot x_{norm} + d \tag{3.4.2}$$

Figure 3.4.6 shows the dip depth relative to GS 16 in 2012 (red) and in 2015 (blue), $f(x)$ is indicated with a line and $h(x)$ is represented by the dashed line with corresponding colors. The uncertainties shown are due to statistics and observed variations seen for multiple measurements of one gain step. Fig. 3.4.6 (a)-(d) show the relation for relative dip depth for the configurations: (a) dip depth relative to left shoulder for row A, (b) dip depth relative to right shoulder for row A, (c) dip depth relative to left shoulder for row B, and (d) dip depth relative to right shoulder for row B. In order to achieve better fit results, the x axis had to be normalized by $x_{norm} = (x - mean(x))/std(x)$ where x = [7,16]. In addition the adjusted R^2 is given in the legends of fig. 3.4.6 (a)-(d). The parameters for $f(x_{norm})$ for the 2015 data set are given in table 3.4.1.

Table 3.4.1: Resulting parameters of a least square fit with $f(x_{norm}) = a \cdot exp(-b \cdot x_{norm}) + c \cdot x_{norm}^2 + d$ of the dip depth in the 2015 individual pixel gain set.

	a	b	c	d	adj. R^2
Row A - 1	-0.06 ± 0.02	-1.69 ± 0.14	-0.02 ± 0.06	1.74 ± 0.14	0.992
Row A - 2	0.26 ± 0.32	0.93 ± 0.34	-0.34 ± 0.89	1.71 ± 0.34	0.991
Row B - 1	0.05 ± 0.02	1.50 ± 0.06	-0.21 ± 0.06	1.50 ± 0.07	0.928
Row B - 2	0.28 ± 0.03	0.97 ± 0.15	-0.39 ± 0.08	1.79 ± 0.16	0.990

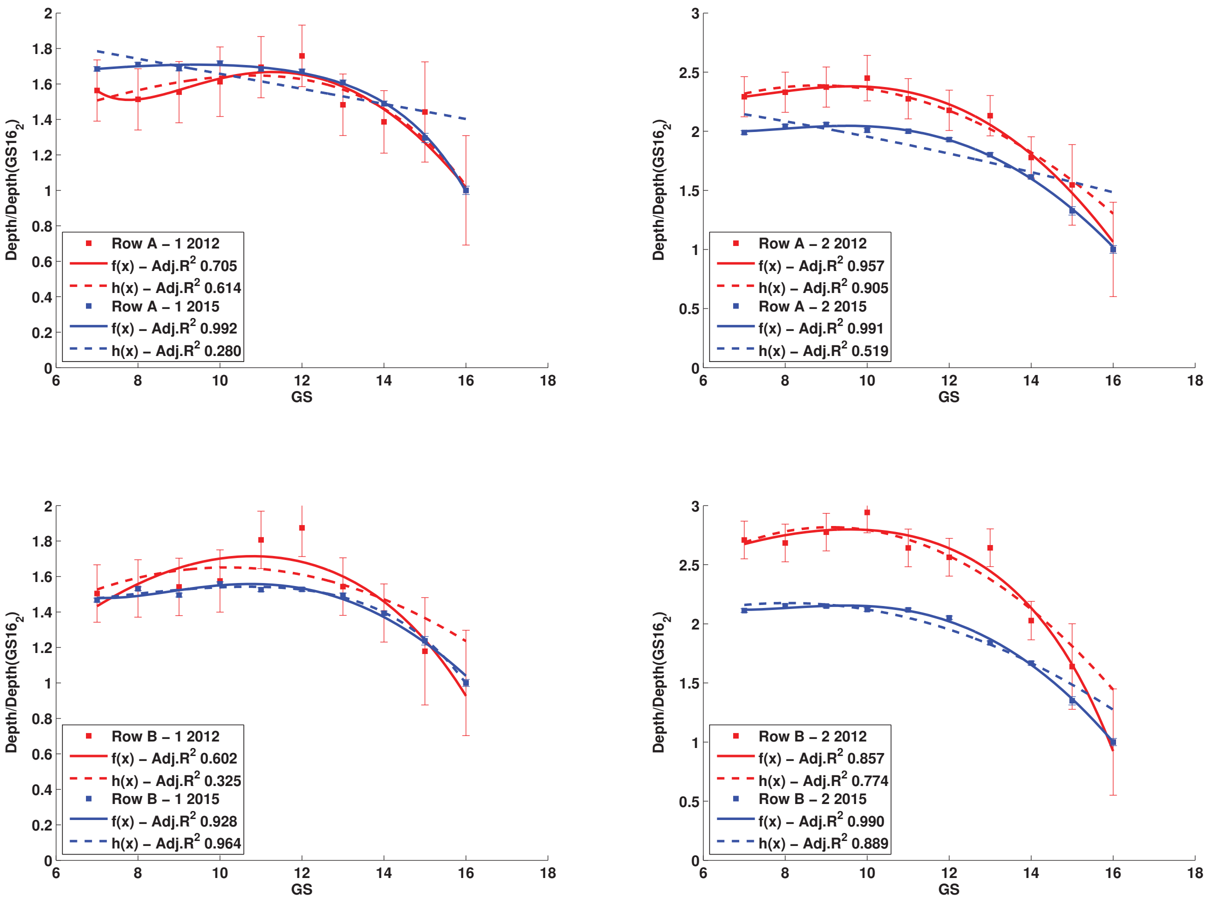

Fig. 3.4.6: Fit of relative dip depth with the functions $f(x) = a \cdot exp(-b \cdot x) + c \cdot x^2 + d$ and $h(x) = a \cdot exp(-b \cdot x) + c \cdot x + d$. Shown in blue are fits and the resulting dip depth of 2012 and in red data of 2015.

3.4.2 Results - FS

A compilation of the evaluated pixel gain measurements performed in space till end of March 2015 is given in table 3.4.2. In total 42 pixel gain measurements were done since end of hibernation and out of these only 4 measurements could not be used due to failures during the measurement procedure. The first two - acquired on April 25 - did not have a fixed gain step during the sweep due to a wrong commanding at the software which has been fixed in an update in March 2014. The two other modes contain incomplete sweeps caused by a so-called Fil2Bias error which turned of the filament instantaneously. In the other mode a so called MCPFront error occurred at the beginning and thus the front voltage of the MCP was set zero. In this case the electric field in the MCP is inverted and no electron avalanche will occur. There were other measurements with a MCPFront error, but since it was after step number 70 of 138 the main part of the MCP was covered and the data could be analyzed. In the this part the results based on the previous described data reduction of all pixel gain measurements after end of hibernation till end of March 2015 will be presented. In contrast to nominal result presentation the all overall uncertainties are not quantified for every measurement and will be discussed in section 3.4.3. However, the uncertainties due to ion statistics are smaller than 1%.

Table 3.4.2: Overview on pixel gain measurements done in space till end of March 2015.

Date	Time (UTC)	Mode	GS	T_{LEDA} (°C)	T_{Magnet} (°C)
22.09.2009		601	13/14/(16)		
26.04.2010		600	15		
26.04.2010		601	13		
25.04.2014	03:48 - 04:48	600	16	-8.7/ -6.1	-23.23/ - 21.39
25.04.2014		601	15/16	-1.3 / 0	-16.64/-14.78
25.04.2014		602	12/14	0/-1.5	-14.78/-12.75
25.07.2014	10:41 - 11:46	600	16	-12.2 / -9.8	-27.25/-25.25
25.07.2014	11:57 - 12:58	602	12	-9.8 / - 7.5	-25.17/-23.15
25.07.2014	13:12 - 14:21	601	15	-7.5 / -5.5	-22.74/-20.80
14.11.2014	23:12 - 00:21	600	16	6.3/6.5	-3.56/-3.25
15.11.2014	00:32 - 01:37	601	14	6.5/6.6	-3.21/-2.94
15.11.2014	01:49 - 02:51	602	9	6.6/6.7	-2.91/-2.71
03.01.2015	00:01 - 01:10	600	16	9.3/9.4	0.41/0.49
03.02.2015	18:06 - 19:09	600	16	10.3/10.3	1.36/1.37
03.02.2015		601		Fil2Bias occurred	
03.02.2015	20:34 - 21:46	602	9	10.3/10.2	1.36/1.32
03.02.2015	21:54 - 23:09	600	14	10.2/10.2	1.31/1.28
15.03.2015	08:58 - 09:55	601	12	3.6	-6.22
15.03.2015		602		MCPFront occurred	
15.03.2015	11:31 - 12:33	601	12	3.6	-6.17/-6.10
18.03.2015	12:41 - 13:52	620	13	1.3/1.9	-10.03/-9.03
18.03.2015	13:59 - 15:01	621	11	2.0/2.5	-8.92/-8.03
18.03.2015	15:16 - 16:17	622	13	2.6/3.1	-7.97/-7.18
18.03.2015	16:33	602	10	3.1/3.5	-7.90/-6.42
18.03.2015	23:40 - 00:47	630	16	4.7/4.8	-4.40/-4.18
19.03.2015	00:55 - 02:04	631	13	4.8/4.9	-4.17/-3.98
19.03.2015	02:10 - 03:21	632	10	4.9	-3.97
19.03.2015	03:26 - 04:28	602	10	5	-3.79/-3.69
21.03.2015	11:05 - 12:09	602	10	-20.1/-15.2	-22.17/-21.88
21.03.2015	12:49 - 13:50	602	11	-12.6/-9.4	-21.42/-20.29
21.03.2015	14:25 - 15:28	602	10	-7.7/-5.4	-19.44/-17.75
21.03.2015	16:11 - 17:11	602	10	-4.0/-2.4	-16.68/-14.97
21.03.2015	17:53 - 18:52	602	11	-1.5/-0.2	-13.94/-12.30
21.03.2015	22:19 - 23:21	602	10	2.5/2.8	-8.54/-7.66
22.03.2015	00:04 - 01:08	622	13	3.1/3.4	-7.27/-6.60
22.03.2015	01:44 - 02:50	632	11	3.7/3.9	-6.27/-5.72
22.03.2015	03:28 - 04:32	602	10	4.1/4.3	-5.51/-5.15
22.03.2015	07:42 - 08:48	600	16	4.6/4.5	-4.68/-4.69
22.03.2015	09:23 - 10:31	620	14	4.5/4.3	-4.71/-4.75
22.03.2015	11:07 - 11:58	630	16	4.4/4.4	-4.79/-4.83
22.03.2015	12:54 - 13:54	600	16	4.3/4.2	-4.88/-4.94
22.03.2015	17:39 - 18:55	601	14	4.2/4.0	-5.23/-5.34
22.03.2015	19:39 - 20:40	621	12	4.0/3.8	-5.40/-5.42
22.03.2015	21:34 - 22:39	631	13	3.9/3.8	-5.41/-5.34
22.03.2015	23:36 - 00:36	601	13	4.0/4.0	-5.25/-5.12

3.4.2.1 Individual Pixel Gain Factors - 2014

The data acquired in April and July 2014 have not been corrected for COPS pressure since Rosetta did not yet reach the comet and the water signal was assumed to be stable. The introduction of the four possible types of correction is given in section 2.3.4. The resulting pixel gain factors for April and July 2014 are shown in fig. 3.4.8 and will be discussed later. Following the nominal data reduction procedure, without applying further corrections, the results for all three measured gain steps in July 2014 differ as it can be seen in fig. 3.4.7. In the same graph the last individual pixel gain factors determined before hibernation are shown. The two pixel gain sets should show the same curve shape since only a few measurements were performed in the meantime. However, they should not show the same dip depth in the center because the measurements were performed at different gain steps. The downward spikes are due to missing steps. In fig. 3.4.8 the corrected data for the measurements performed in April and July 2014 are shown. In order to compare pixel gain measurements done at different gain steps the data is normalized to the right most pixels. This is done under the assumption that the MCP is not depleted at the borders since this region is rarely hit by ions. However a slope appeared on the left side (fig. 3.4.8) for GS 15 and 16 which was not present in 2010 at GS 13. Consequently the left side is not used for normalization. Comparing the individual pixel gain factors from 2010 with the ones acquired in April and July 2014 in fig. 3.4.8 highlight the following features:

- A slope appears on the left side (pixel ~20 till 200) for GS 15 and GS 16 in July as well as for GS 16 in April but this slope is not present for GS 12 in July and not before hibernation (GS 13).
- An increase from 0.8 to 1 between pixel 400 - 460 is present for all sets and the lower the gain step the larger is the change of level between pixel 400 and 460.
- The dip in the center does not have the same amplitude in July and April 2014 for GS 16. The depletion in the center increased from roughly 20% to almost 40%.
- For the July set the dip depth around pixel 264 is larger the smaller the gain step.

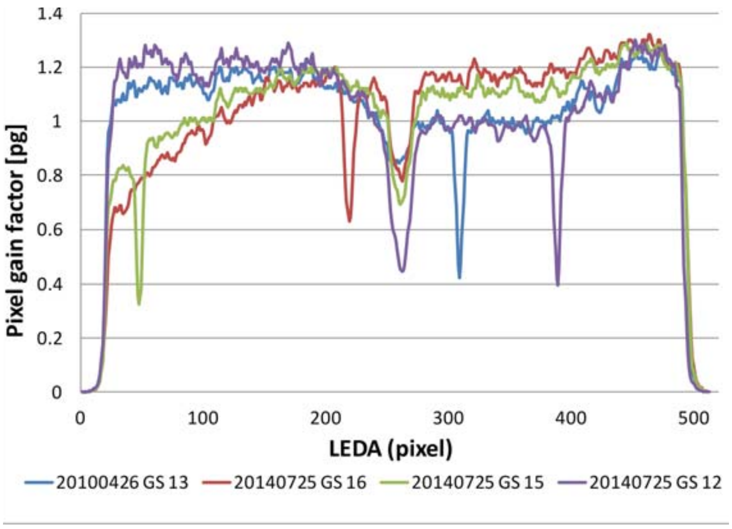

Fig. 3.4.7: Comparison of pixel gain factors of 2010 and July 2014. Data is not corrected for missing measurement steps which leads to downward spikes in the curve and the factors have not been renormalized to the rightmost pixels.

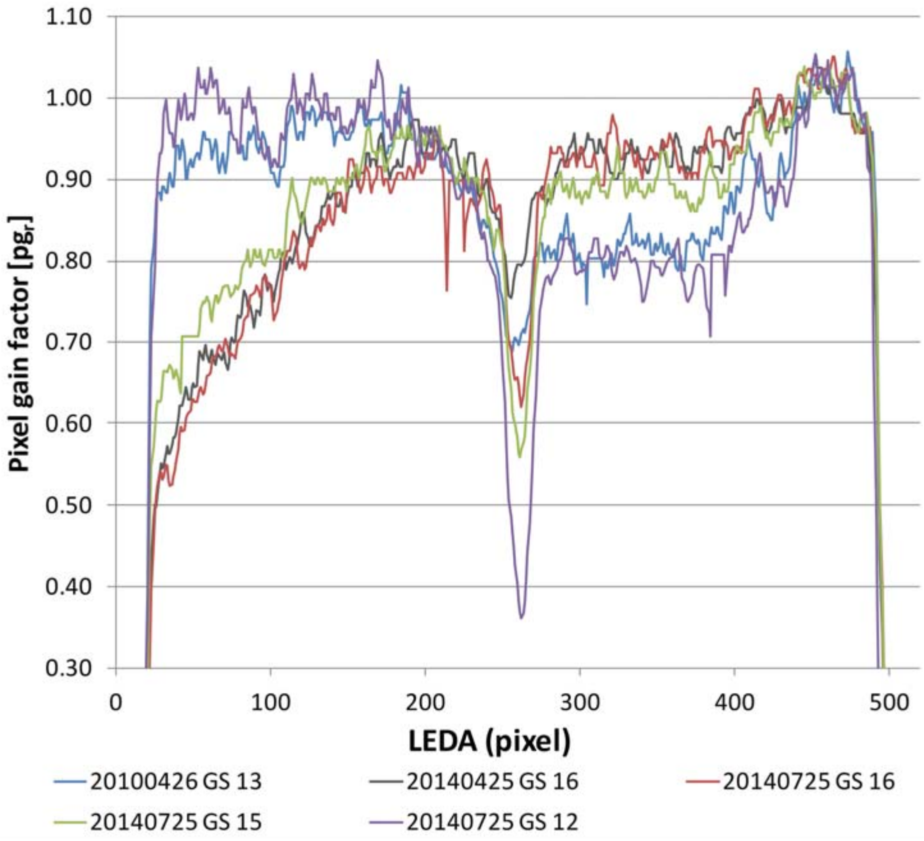

Fig. 3.4.8: Comparison of pixel gain factors of 2010, April 2014 and July 2014. In contrast to fig. 3.4.7 the data are corrected for missing steps and are normalized to the rightmost pixels.

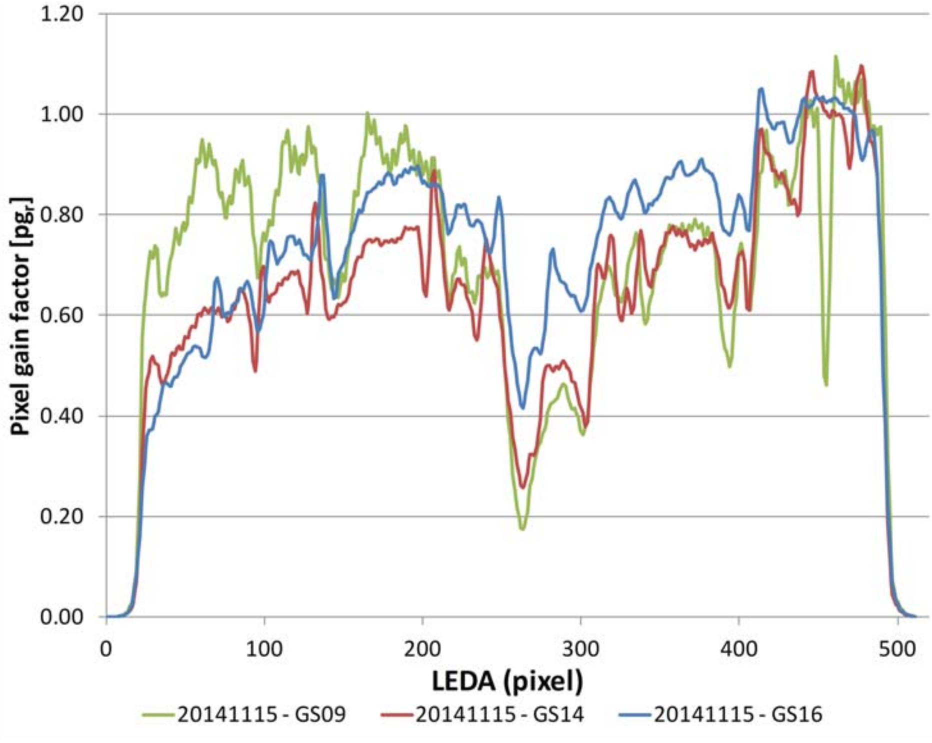

Fig. 3.4.9: Pixel gain factors on the basis of the measurements acquired in November 2014 nominally calculated, corrected for the evolution of COPS pressure, and normalized to the rightmost pixels for GS 9, 14, and 16.

Next set of pixel gain measurements was performed just after Lander delivery in November 2014. This time window has been selected because Rosetta was again further away from the comet and thus the signal of the water was expected more stable. After nominal data reduction, correction for COPS pressure, and normalization to the rightmost pixels, the pixel gain factors seemed to have changed dramatically as it can be seen from fig. 3.4.9. First of all more dips appeared within the first and last 150 pixels, second the central dip for GS 16 increased again to a depletion of about 50%, and third the three curves do not show the same features. After investigating the data sets, the conclusion was drawn that the steps of the sweep were not equidistant ($\Delta x = 4$ pixels) which is shown exemplarily for row A GS 14 in fig. 3.4.10. Drawn in blue are individual pixel gain factors due to nominal data reduction, in red a linear interpolation between the peak maximum of every of the 138 steps, and the maximum values of each step is indicated by green dots. Furthermore the steps which have a non-nominal Δx to their neighbors have a violet cross at the peak location on the LEDA. Moreover it can be seen that a non-equidistant stepping offsidely the central dip is going together with a strong fluctuation in the resulting individual pixel gain factors i.e. around pixel 100 is a step with $\Delta x \neq 4$ pixels and the individual pixel gain factors vary about 0.2 while in the center around pixel 300 are nut such a variation is seen although non equidistant stepping is indicated. In figure 3.4.11 the resulting individual pixel gain factors for row A in November 2014, based on a linear interpolation of the pressure corrected peak maximum of every sweeping step, are shown. The remaining features present for all three GS (9, 14, and 16) can be categorized in “known” and “new”. The slope between pixel 0 and 200, a step in the level around pixel 420, and the central dip around pixel 250 were already present in July 2014 for GS 16 and 15. New features are a second central dip around pixel 300 and at least 10 additional dips spread all over the LEDA (labeled in the graph).

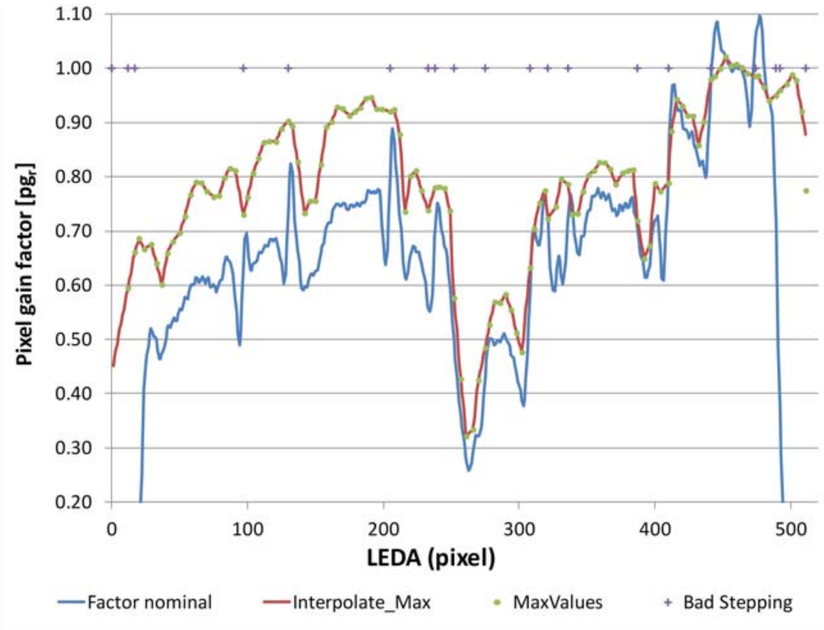

Fig. 3.4.10: At M601 acquired on November 15th 2014 on GS 14 the influence of not equidistant stepping and missing steps is shown. In blue is the individual pixel gain nominal calculated and corrected for COPS pressure. In red is the individual pixel gain calculated by linear interpolation between the peak maximum corrected for COPS pressure of every step, the green dots indicate the peak maximum corrected for COPS at one step, and with pale violet crosses at 1 no-equidistant stepping is indicated.

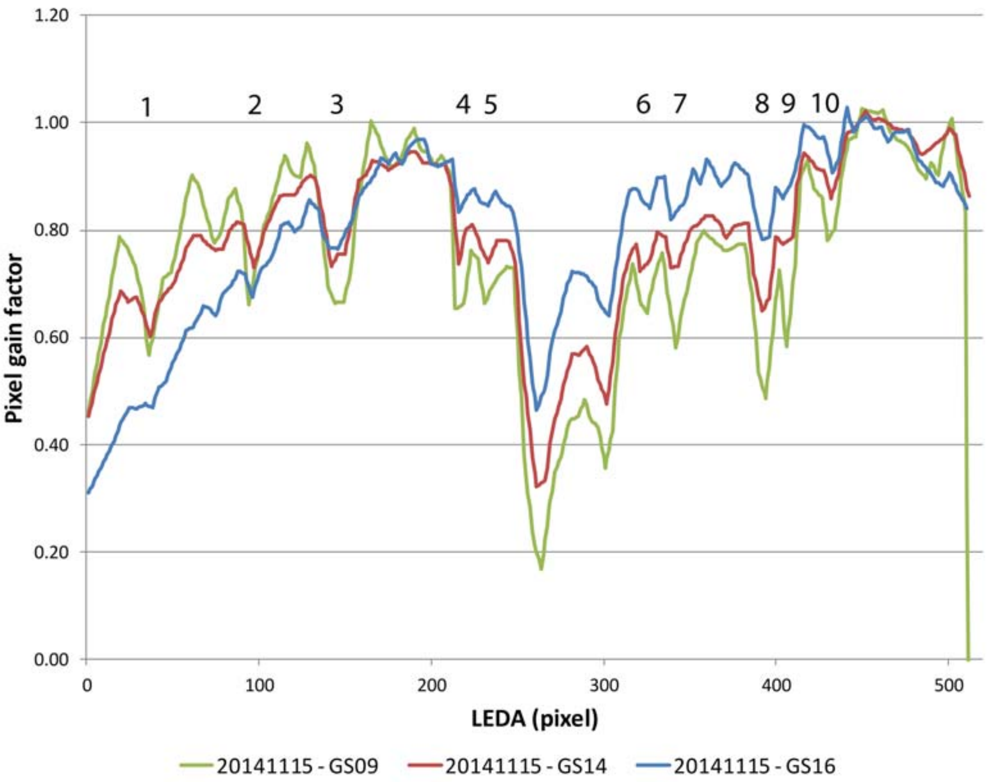

Fig. 3.4.11: Compilation of individual pixel gain data calculated via interpolation procedure and COPS pressure correction of the November 2014 data sets acquired at GS 9, 14, and 16.

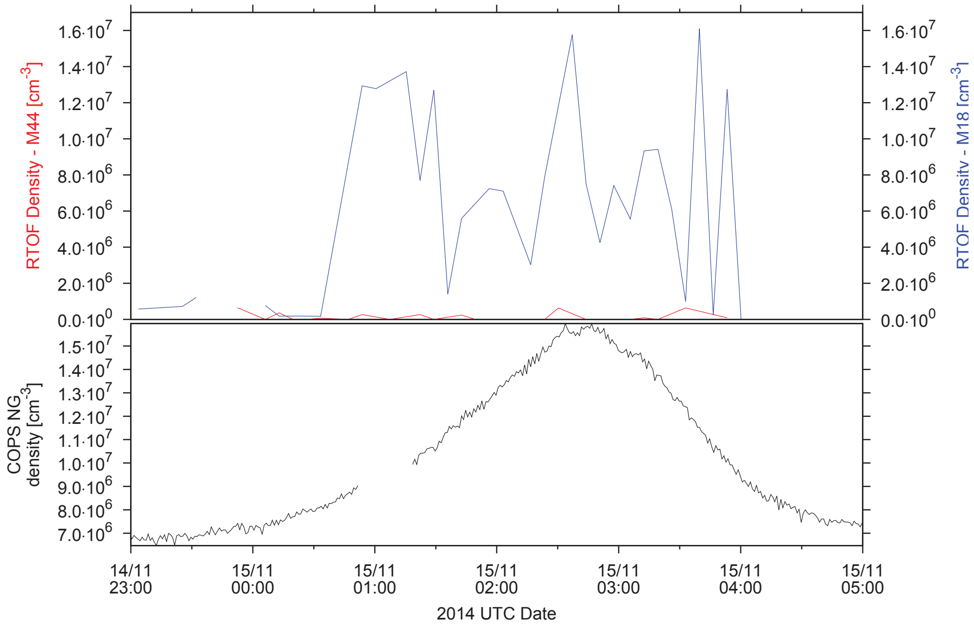

Fig. 3.4.12: The upper panel shows RTOF H_2O and CO_2 densities during the pixel gain measurements of DFMS (14.11 23:12 - 15.11 02:51 UTC) courtesy S. Gasc and in the lower panel COPS nude gauge density courtesy C.-Y. Tzou.

Already since the Lutetia flyby it is known that a change of spacecraft attitude can lead to a sudden change in the measured gas density. It is assumed that this is due to sublimation of ice on the spacecraft which gets suddenly sunlit. To rule out any influence due to the spacecraft background a comparison of the peak maxima in every step with the nude gauge and ram gauge pressure, and the nadir-off-pointing has been made. As it can be seen in fig. 3.4.13 the nadir off-pointing is constant for almost the entire duration of mode 600 which was measuring at GS 16. Moreover the ram and nude gauge pressure do not show any sudden changes nor an increase of signal comparable to the slope seen in the peak maxima respectively the individual pixel gain factors. COPS nude gauge pressure increases from ~$2.7 \cdot 10^{-10}$ mbar to ~$3.1 \cdot 10^{-10}$ mbar, which is an increase of a factor of ~1.15, while the slope variation in the pixel gain for this measurements is about a factor 2. The change in COPS ram gauge pressure is smaller than for the nude gauge and it even decreases slightly. The measurements of the neutral gas done with RTOF were not used for further corrections because neither H_2O nor CO_2 showed some correlation with COPS nude gauge density as it can be seen from fig. 3.4.12.

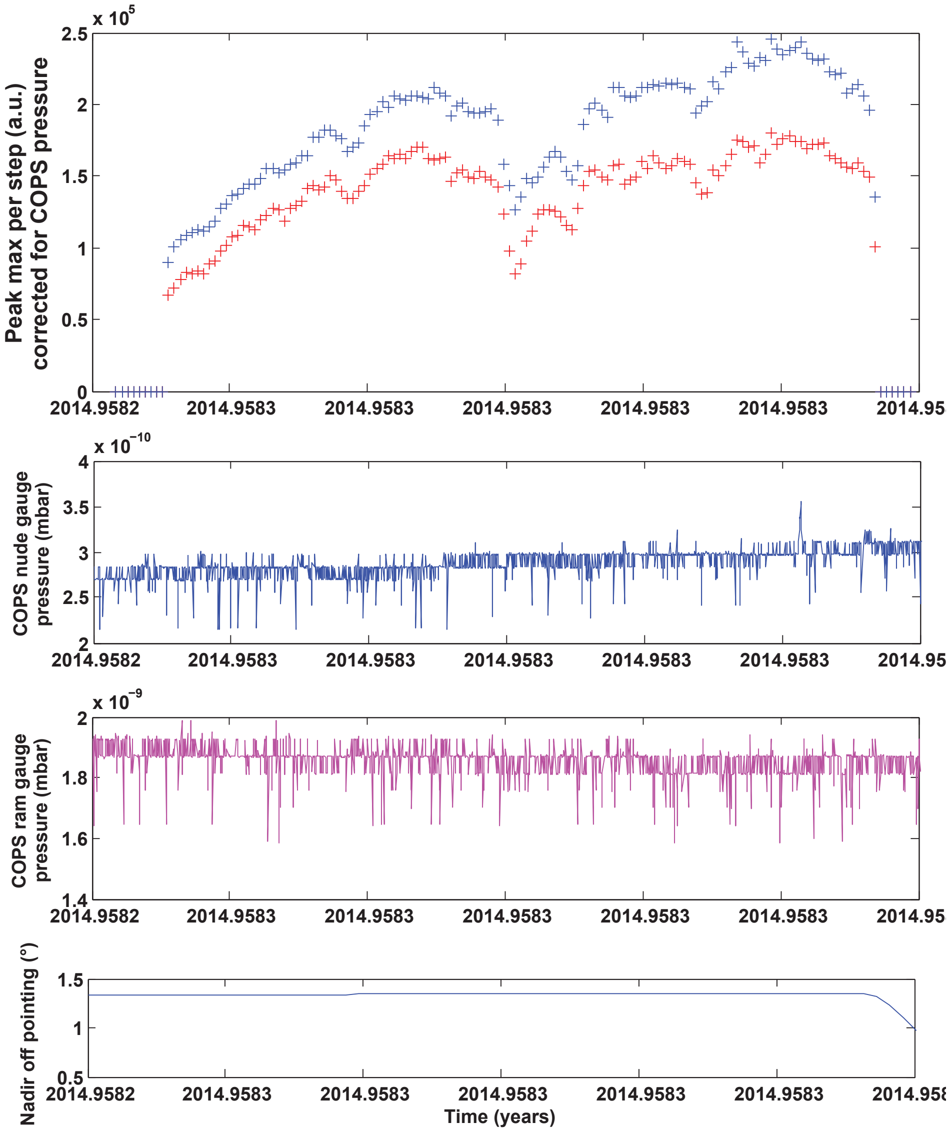

Fig. 3.4.13: The uppermost panel shows the measured water peak during the pixel gain measurement of M600 on November 14th to November 15th, COPS nude and ram gauge pressure in mbar (raw data) in the second and third panel, and Rosetta nadir-off pointing in the last panel.

3.4.2.2 Individual Pixel Gain Factors - 2015

In order to confirm the presence of eleven additional dips the pixel gain mode M600 was commanded and executed on January 3rd. The data has been nominally treated and COPS pressure correction was applied based on nude gauge measurements. Unlike the November measurements where the individual pixel gain factors have been determined the data acquired in January shows less irregularities in the stepping. Only in 6 cases the difference in peak location between two steps is less than 4 pixel. A comparison of individual pixel gain factors for GS 16 from end of hibernation till January 2015 is done in fig. 3.4.14 for row A. In green is the result form March 2014 where no correction was applied and the data was treated nominally (see section 2.3.4), in red the results from July 2014 is shown for which a correction due to COPS pressure evolution was applied. Drawn in dark blue are the results of the linear interpolation of the COPS pressure corrected peak maxima for every step from the measurements in November 2014. In grey the nominal treated and COPS pressure corrected results from January 2015 are illustrated. All of them have a slope on the left side and the central dip around pixel 250 in common. Besides a change of level data both, November and January pixel gain factors, show the same features, namely the second central dip and the recently discovered dips.

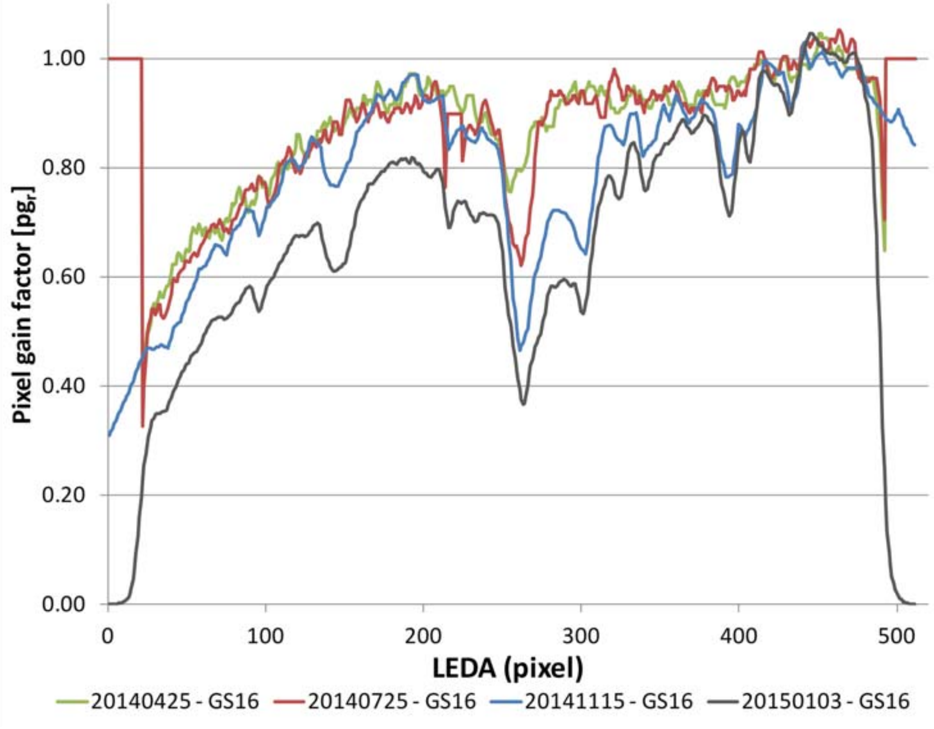

Fig. 3.4.14: A compilation of the individual pixel gain factors for GS 16 of row A between March 2014 and January 2015 is shown. Unfortunately each data set had to be treated differently according to the measurement circumstances - for more details see text or section 2.3.4.

The measurements performed in February 2015 had the same gain steps as the one in November 2014 and thus allowing a direct comparison that is shown in fig. 3.4.15. The February data has been nominally treated and corrected for COPS pressure evolution, but unfortunately the signal density was too low for RTOF to follow the evolution of water (see fig. C.3.4). Similar to January data, almost all measurements show an equidistant stepping and thus the nominal computed values could be used. In fig. 3.4.15 the November data are indicated with a dotted line; GS 09 is in green, GS 14 in red, and GS 16 in blue. Comparing the individual pixel gain factors in graph fig. 3.4.15 one observes notable differences between November and February. In November GS 09 shows a slope in the left half of the LEDA which is not present in the February data. In addition, the increase around pixel 400 is roughly twice as high as in February than in November. For GS 14 the differences are less at the borders and except for the central dip the overall shape is preserved. In the February data the central dip is at 0.27 of the maximal possible gain while in November it has been at 0.33. The second dip around pixel 300 has been at value of 0.47 in November while in February it is at 0.41. The decrease of the individual pixel gain is for both 0.06. For GS 16 the major difference between the two data sets is a change of level in the February values starting at pixel 20 and ending around pixel 375. The difference for the two main dips are 0.10 and 0.12, respectively. However there seems to be an inconsistency about the level for the curves because the regions offside the dips to not overlap for the same gain steps.

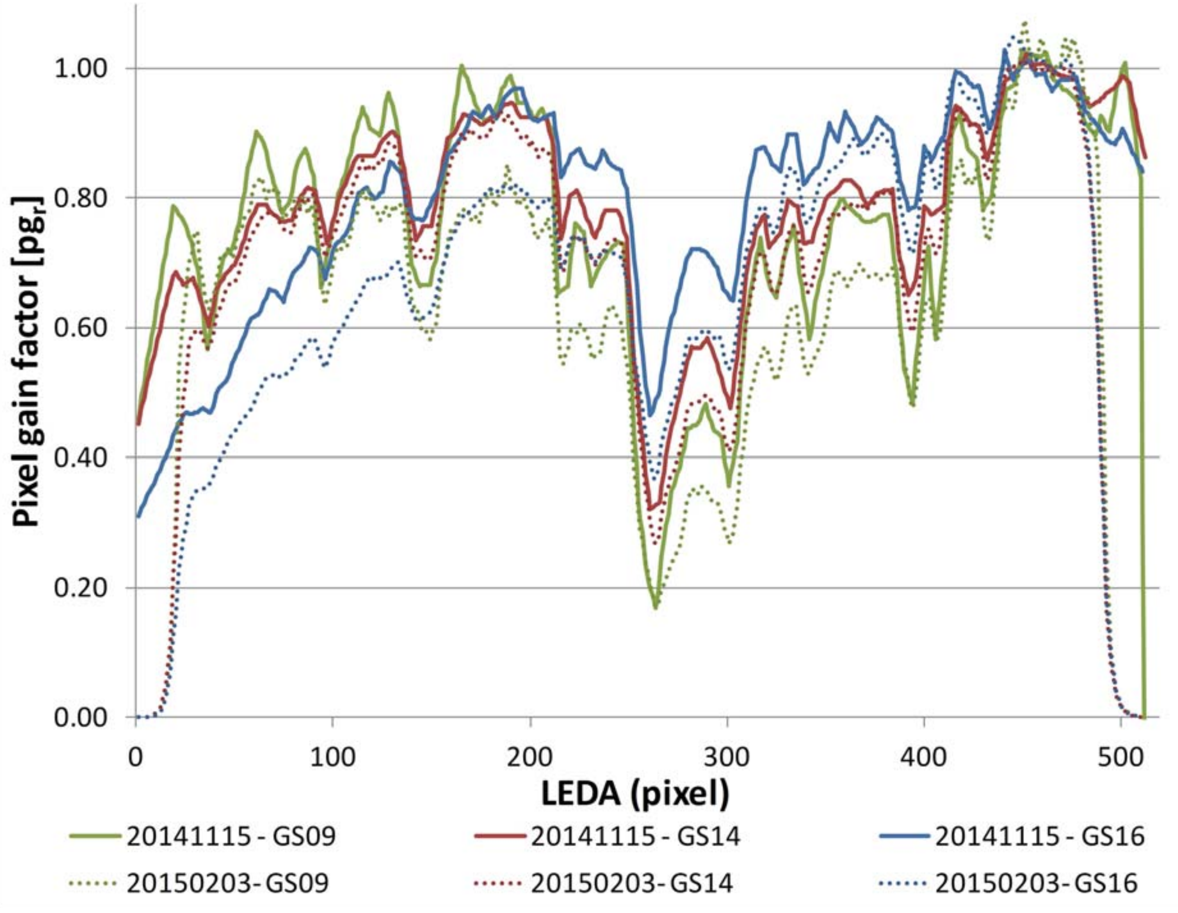

Fig. 3.4.15: Comparison of the individual pixel gain based on November 2014 data (dashed line) and February 2015 (solid line) for GS 09 in green, GS 14 in red, and GS 16 in blue.

In the period between lander delivery (12.11.2014) and mid March 2015 Rosetta was within a cometary distance of ~27 - 150 km and COPS nude gauge density ranged from low to mid 10^8 cm^{-3}, whereas before Rosetta was within 10 km for 2 weeks and the density ranged from mid 10^8 cm^{-3} to low 10^9 cm^{-3} as it can be seen in fig. 3.4.16 (courtesy C.-Y. Tzou). After the end of January it was planned to stay out of bound orbits because it was assumed that the activity would increase significantly (Schulz et al., 2015) and bound orbits would be impossible. Thus it was planned to do so-called close flybys with different scientific goals i.e. a fast and close ($d_{67P\text{-Rosetta}} \approx 8$ km) and a co-rotational flyby to study the influence of insolation on a specific area on the comet. From the planned flybys, two were within 50 km distance to the comet and COPS densities reached ~$8{\cdot}10^8$ cm^{-3} as it can bee seen in fig. 3.4.16 (b). Expecting a high signal at the flyby on February 14th, which was not only very close to the comet but going over the sub solar point, another set of pixel gain measurement was planned. Thus right after the flyby when Rosetta was between ~84 km and 102 km to the comets nucleus, in order to have less variations of the water signal and to check the depletion after the expected high signal of the flyby, pixel gain measurements were performed. Of the three planned measurements two could be used and both had the same gain step as last measured on July 25th 2014. A comparison of the 3 data sets nominally computed and for March COPS pressure corrected is drawn in fig. 3.4.17. Colored in green are the individual pixel gain factors based on the July 2014 data set and in red and blue the two data sets from March 15th 2015. First of all, a significant difference in level between the two March data sets is present only on the left half of the LEDA. Second there is no slope present in the same region for both March data sets and in addition the dips are at the same location. In comparison with the individual pixel gain determined with data of July 25th a distinct change in the overall curve shape is visible due to several additional dips. From this comparison it can be seen that the depletion increased between July 2014 to March 2014 fro GS 12 from ~0.37 to ~0.25 which is an increase of 12%.

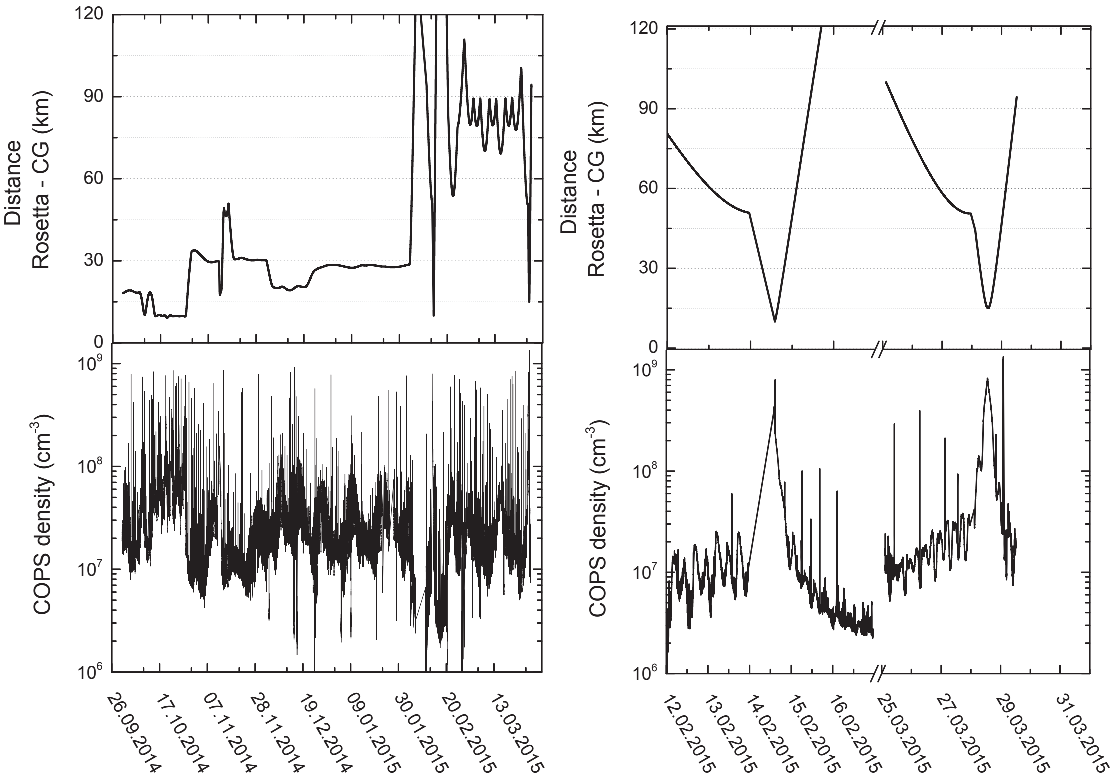

(a) **(b)**

Fig. 3.4.16: (a) and (b) show in the upper panel the distance between Rosetta and the center of mass of 67P while in the lower panel is shown the COPS nude gauge density with spikes due to reaction wheel off loadings (courtesy C.-Y. Tzou). (a) covers the time period from beginning of October 2014 till end of March 2015 and (b) shows the period of the two flybys going closer than 50 km after December 2014.

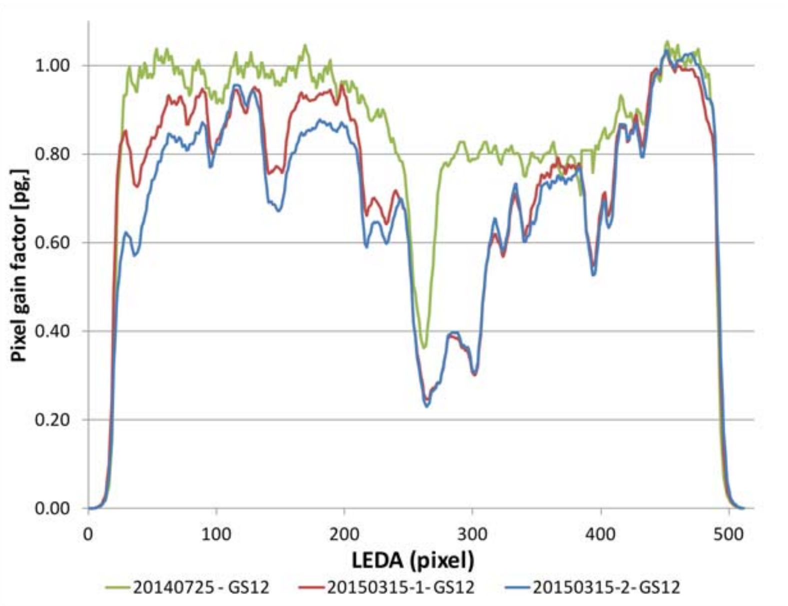

Fig. 3.4.17: Comparison of individual pixel gain at GS 12 before being at comet 67P in July 2014 in green and staying more than 7 months in the vicinity of the nucleus of 67P in blue and red.

Based on the experience we gained during July 2014 and beginning of February 2015, new pixel gain modes were implemented in the on board software and it was decided to follow the evolution of water with DFMS before and after the pixel gain measurements since RTOF was not sensitive enough. In total 25 pixel gain measurements were carried out and an overview is given in section 2.2.5. For every data set, which had 20 min measurements of H_2O, CO, and CO_2 before and after the pixel gain measurements, nominal and interpolation between peak maximum with no correction were computed, then with both COPS pressure correction, water correction, and with correction of the water ratio over main species. In section C.3 all the results are presented in detail and here the further proceeding is described at five exemplary cases. In fig. 3.4.18 (a)-(e) are shown in each graph the results of the four types of correction for M601-20150322-2-GS13, M601-20150322-1-GS16, M600-20150322-2-GS16, M622-20150322-1-GS13, and M601-20150322-1-GS14 (measurement mode-date-number-GS). Comparing the four types of correction for GS 13 in (a) one can see that correction of m18 and no correction have the most overlap while the correction of the main species ratio is most off all over the LEDA and the COPS correction is of for the first half of the LEDA thus the first half of the pixel gain measurement. For GS 16 in displayed in (b) the four corrections do not overlap within the first half of the LEDA but they seem to group for the second half into correction of COPS pressure and no correction and the other two together. In (c) again the individual pixel gain for GS 16 is displayed but measured roughly 4 1/2 hrs afterwards. Again there is a grouping into two corrections; first group is correction COPS with ratio of mean species correction and the second group consists of no correction and m18 correction. The fourth example, (d), shows GS 13 and again there is a grouping however into no correction and COPS correction, and ratio of mean species correction and m18 correction. The first four examples showed throughout some type of grouping of the corrections which is not always the case as it is illustrated in e). This graph shows the resulting individual pixel gain for M601 acquired in GS 14 and one can see no grouping over a large range of the LEDA, thus during most of the duration of the mode, occurred at all.

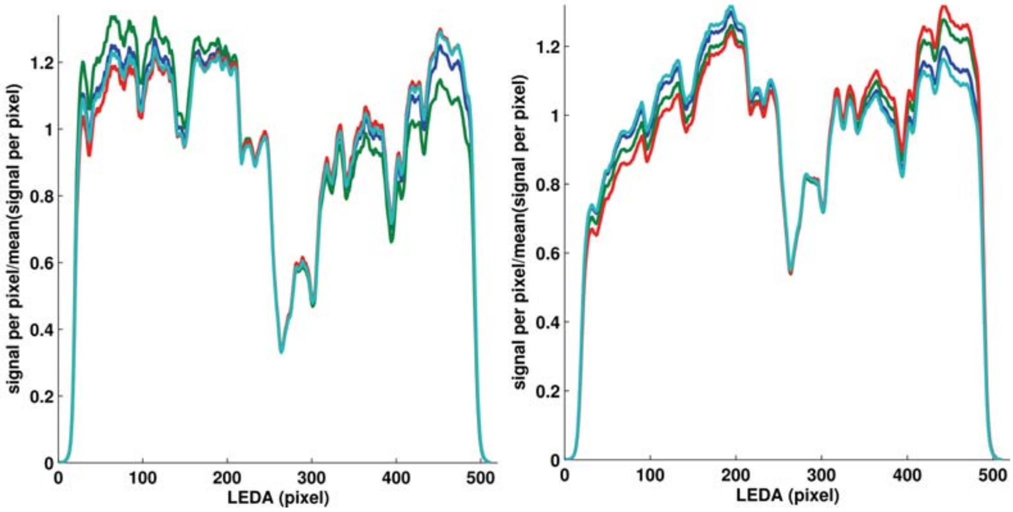

(a) M601-20150322-2-GS13 **(b)** M600-20150322-1-GS16

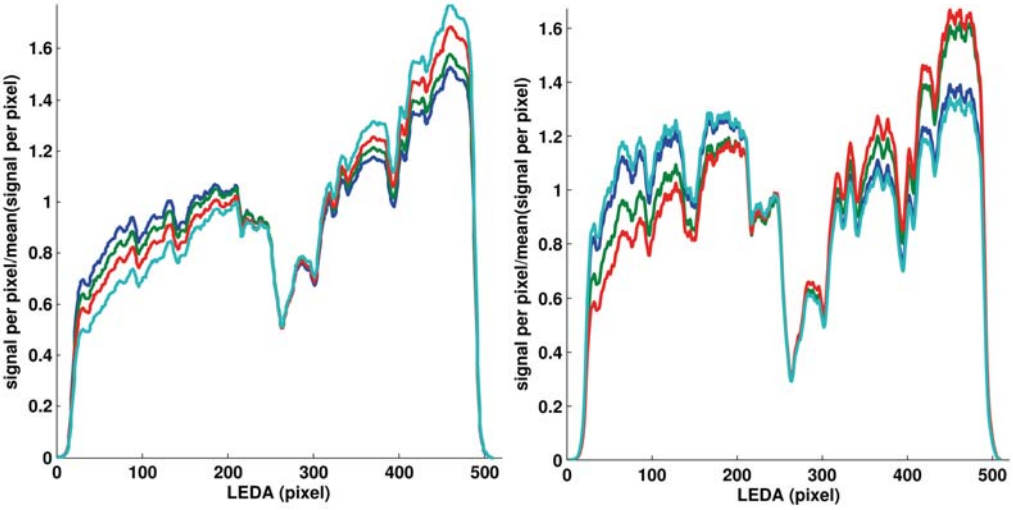

(c) M600-20150322-2-GS16 **(d)** M622-20150322-1-GS13

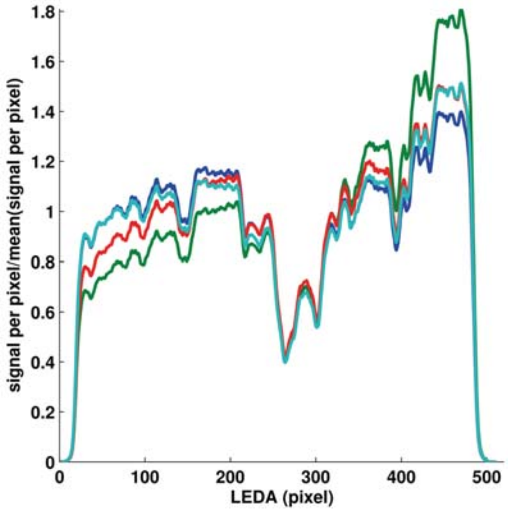

(e) M601-20150322-1-GS14

Fig. 3.4.18: (a)-(e) show a comparison of the different correction types to determine the individual pixel gain described in section 2.3.4 for five exemplar measurements done with row A all acquired on March 22nd. The values were nominal computed and normalized to the mean signal.

In order to compare individual pixel gain values for different gain steps a selection of the most likely correction had to be done for every measurement between beginning of 2015 till mid March (for more details see section C.3). So as to chose the correction which is supposed result closest to the true values of the individual pixel gain the following rules were applied:

1. **No overlap of the four curves** The curve which has the smallest slope on the left side and which has values closest to 1 is chosen.

2. **Mostly overlap between correction for COPS and m18** In this case correction COPS is taken because the overlap indicates that water was the dominate species and for such cases the evolution of water is documented by the COPS measurements.

3. **Mostly overlap between no correction and m18** Here no correction was chosen because the overlap indicates that water signal was fairly constant.

4. **Mostly overlap between no correction and correction COPS** This overlap implies first that water was the dominate species, second that it stayed fairly constant and third that the correction of m18 is not correct. Therefore no correction is used.

5. **At least two corrections overlap mostly and have unusual steep slopes** The curve which has the smallest slope over the LEDA and which has values closest to 1 is chosen.

In order to check the influence on the individual pixel gain of temperature changes at the LEDA and the magnet a series of five pixel gain measurements was done almost immediately after DFMS was off for ~3 1/2 hrs. This procedure ensured that both LEDA and magnet would be around -20°C and then slowly warm up by having DFMS in measurement mode. In addition the same mode was done a few hours later when DFMS was supposed to be in thermal equilibrium. Four out of those six measurements were done at GS 10 and two at GS 11. In fig. 3.4.19 the upper panel shows individual pixel gain for the most likely correction for GS 10 on row A and the lower panel shows GS 11 row A. For gain step 10 the LEDA temperature ranges from -20.1°C to 2.8°C and the magnet temperature ranges from -22.2 °C to -7.7 °C. None of the four curves overlap for wide ranges of the LEDA however the first (red) and the third (green) show the most overlap. The sudden changes of the pixel gain curve in red around pixel 100 is due to a missing step of the measurement procedure. For GS 10 no correlation between the level change over LEDA and the LEDA or/and magnet temperature can be seen. For gain step 11 the first measurement was done when T_{LEDA} was ranging from -12.6 °C to -9.4 °C and the second one when T_{LEDA} was ranging from -1.5 °C to -0.2 °C. Remarkably is the almost perfect overlap over the entire range of the LEDA despite the significant differences in temperature.

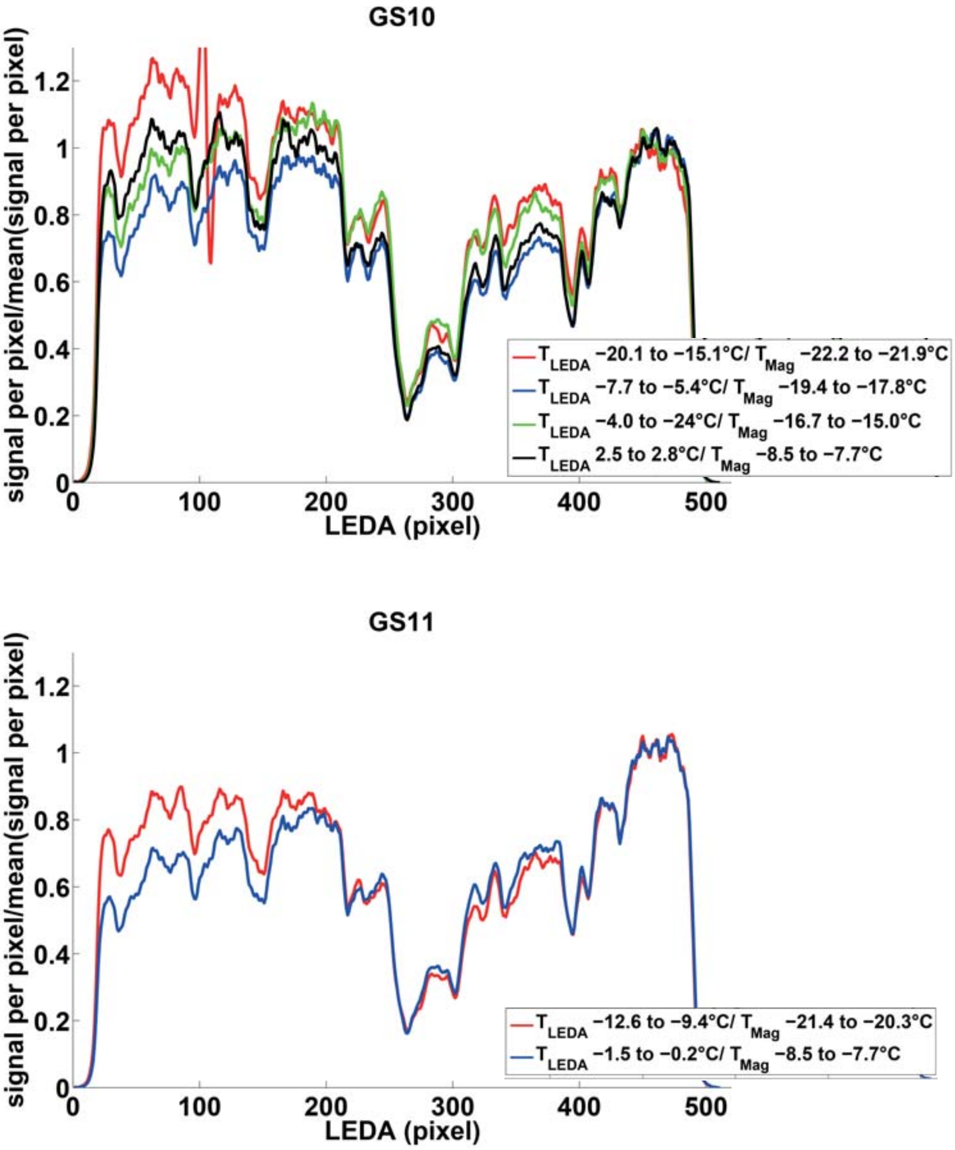

Fig. 3.4.19: Comparison of individual pixel gain at GS 10 and 11 at different T_{LEDA} and T_{Magnet}. The upper panel shows GS 10 and the lower GS 11. The values have been determined following the nominal procedure and the selection of the best correction has been done in section C.3. For both panel only row A is shown normalized to the rigthmost pixels.

For most gain steps more than one data set was available in the period begin 2015 till march 2015 and in the following a comparison of all set per gain step is show in fig. 3.4.20 to fig. 3.4.25. The type of correction has been selected due to the rules described above and more information can be found in section C.3.

For GS 10, 7 measurements are available between March 19th and 21st and all except one are measured with M602 which means water is the peak to be swept, gain step determination was done at $m_0 = 18.5$ u/e, and the emission is at 200 µA. The remaining one is measured in M632 which differs from M602 only in the gain step determination which was done at $m_0 = 17.29$ u/e. The first four curves are the same as seen in fig. 3.4.19 in the upper panel. Comparing the different measurements on both rows allows to see that first all show the same dip features at the same locations and second that the measurements M602-20150321-6 and M602-20150322-1 mostly overlap all over the LEDA. Close by are for some parts M602-20150321-4 in green (pixel ~100-175) and M632-20150319-1 in yellow (pixel ~110 - 135, 157 - 384) while M602-20150321-1, M602-20150321-3, and M602-20150319-1 are off all over the LEDA except the region (pixel 440-462) which has been use to normalize the curves. In (c) an exemplary comparison for GS 10 between both rows has been done on the basis of M602-20150322-1. The level height and most of the dip locations have both rows in common but on row B there seems to be at least four additional dips around pixel 53, 115, 198, and 365 and the variation around the all over shape seems to be larger.

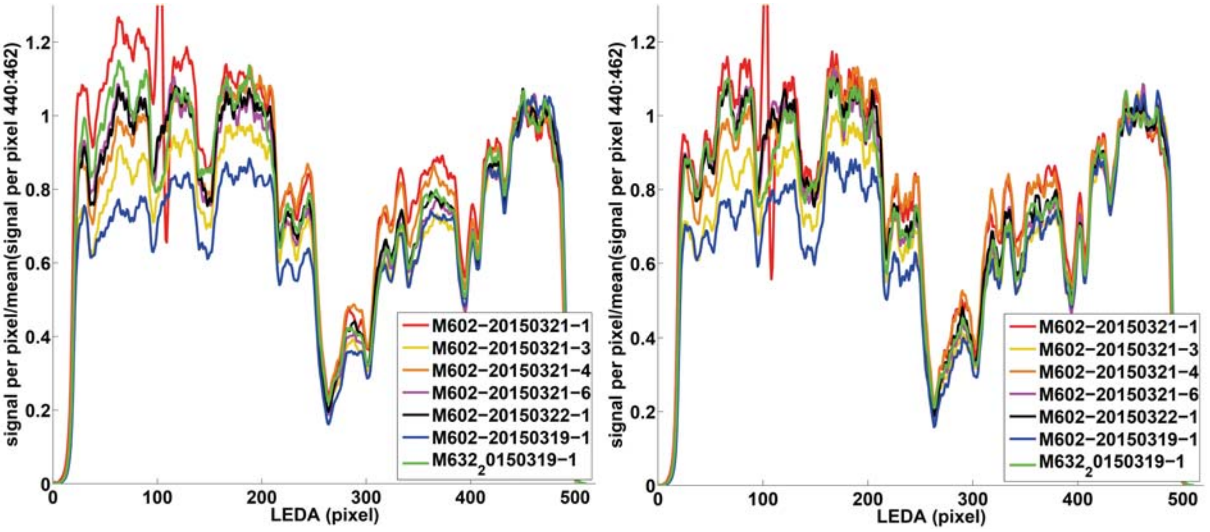

(a) Row A **(b)** Row B

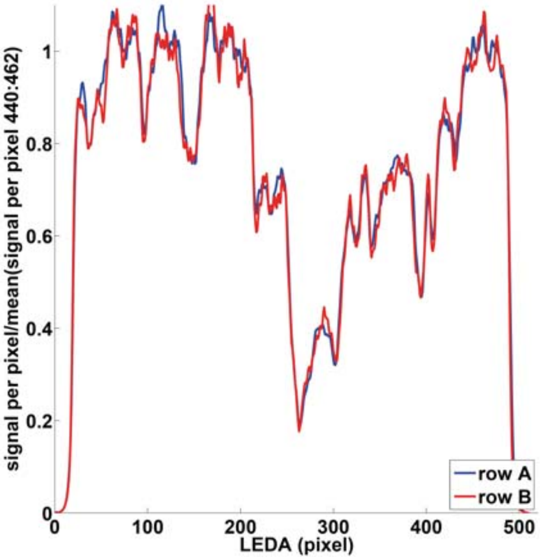

(c) M602-20150322-1

Fig. 3.4.20: Comparison of pixel gain factors for measurements with GS 10 executed between January 2015 and end March 2015. (a) and (b) show row A, B, respectively. The values have been determined following the nominal procedure and the selection of the best correction has been done in section C.3. In (c) a comparison of the individual pixel gain for row A and B is done for the measurement M602-20150322-1.

In fig. 3.4.21 (a)-(b) the comparison of the different measurement is done for GS 11 for row A and B and it can be seen that M621-20150318-1 and M632-20150322-1 group for almost the entire range of the LEDA while the other two overlap only for pixel 204 - 279 and pixel 386 - 484. The comparison of both rows based on M621-20150318-1 in (c) reveals first that on row A the individual pixel gain seems to be higher for the first half of the LEDA and second at least five additional dips located around pixel 52, 178, 199, 367, and 451 are present on row B.

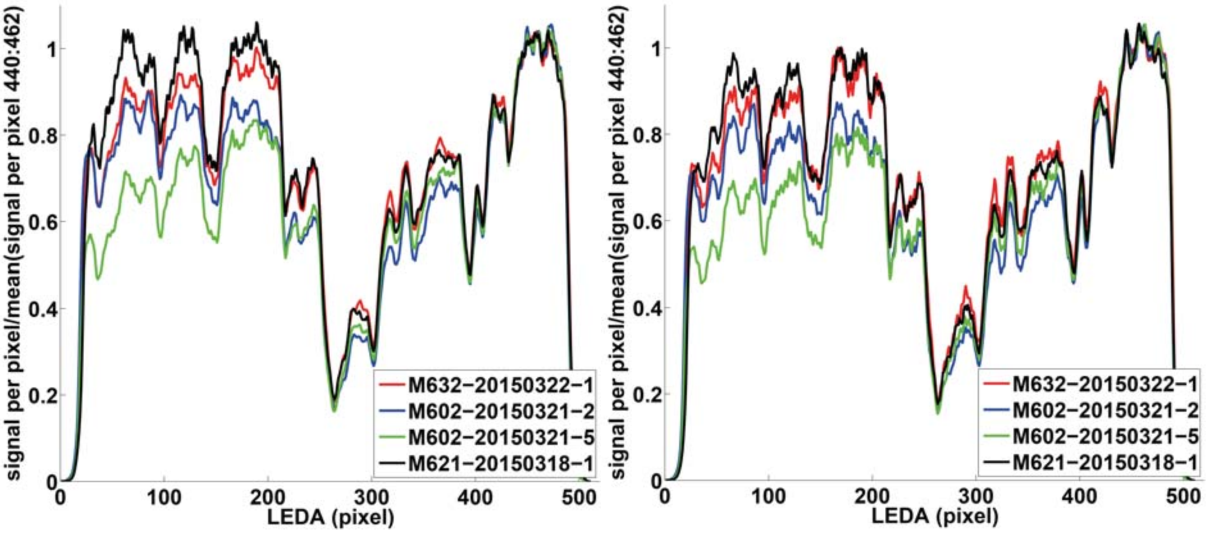

(a) Row A **(b)** Row B

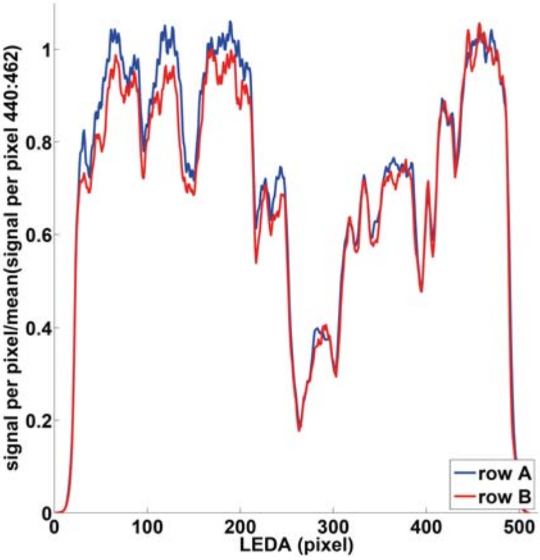

(c) M621-20150318-1

Fig. 3.4.21: Comparison of pixel gain factors for measurements with GS 11 executed between January 2015 and end March 2015. (a) and (b) show row A, B, respectively. The values have been determined following the nominal procedure and the selection of the best correction has been done in section C.3. In (c) a comparison of the individual pixel gain for row A and B is done for the measurement M621-20150318-1.

GS 12 was only once measured between March 18th and 22nd thus the two measurements from March 15th are used for a comparison done in fig. 3.4.22 (a) and (b). Both measurements from March 15th show an overlap over almost the entire range of the LEDA and differ from the measurement done on March 18th in two points; first they are not on the same level at the left border and second the shape and depth of the central dip around pixel 265 differs for both rows. In addition the depth differs for row B for the dips around pixel 325, 343, 395, 407, and 432, and the second measurement done at March 15th shows on row B between pixel 50 and 100 a disturbance due to a few bas spectra. Comparing row A and B for M601-20150322-1, see (c), reveals a different behavior than seen for the previous two gain steps because there are dips present (pixel 232 and 422) on row A which are not present on row B. Besides the different amount of dips the shape and the depth of the central dips around pixel 264 are not the same on both rows.

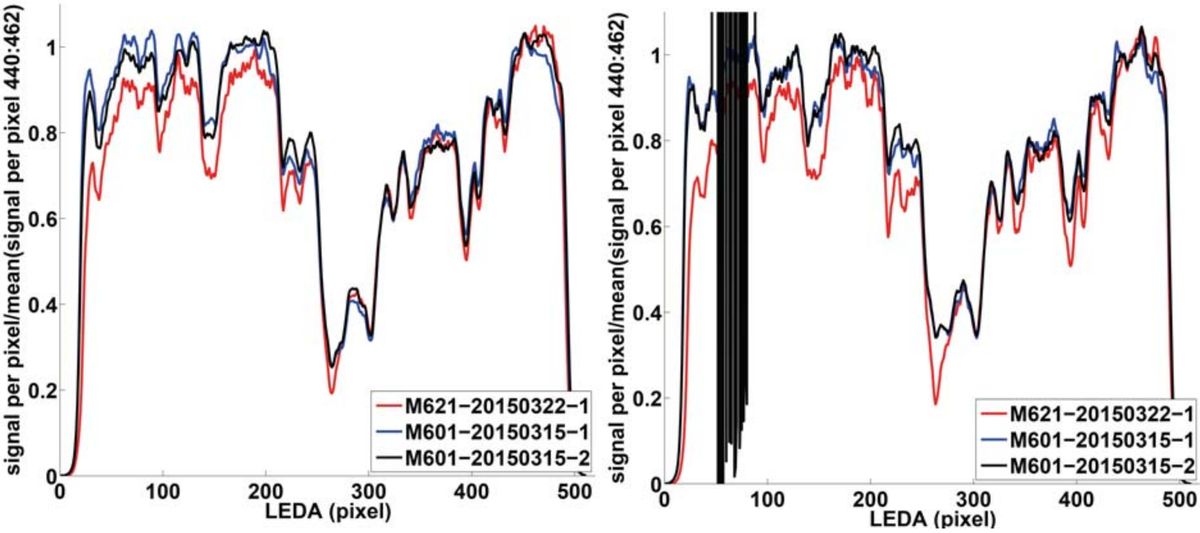

(a) Row A

(b) Row B

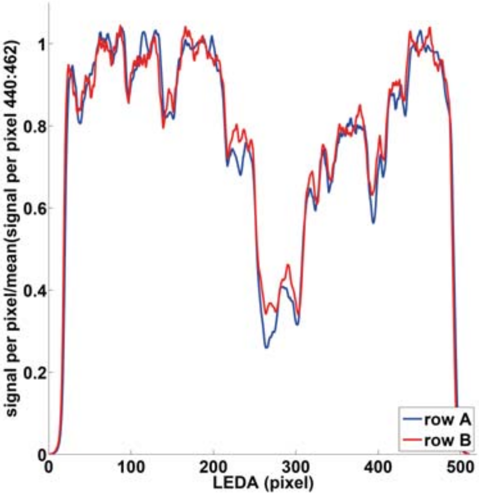

(c) M601-20150322-1

Fig. 3.4.22: Comparison of pixel gain factors for measurements with GS 12 executed between January 2015 and end March 2015. (a) and (b) show row A, B, respectively. The values have been determined following the nominal procedure and the selection of the best correction has been done in section C.3. In (c) a comparison of the individual pixel gain for row A and B is done for the measurement M601-20150322-1.

For GS 13 6 different measurements are available between March 18th and 22nd measured with 5 different measurement modes. From fig. 3.4.23 (a) and (b) it can be seen that they differ only slightly and the maximum spread is between pixel 32 and 194 with a maximal difference among the curves at pixel 30 of ~0.14 on row A and a difference at pixel 30 of ~0.20 on row B. The additional dip for M631-20150322-1 around pixel 275 for both rows is due to a missing spectra. From the direct comparison of row A and B of the measurement M601-20150322-2 done in (c) one can learn that: i) similar to gain step 12 the dip depth is not the same on both rows, and ii) overall the LEDA row B has higher values than row A for the individual pixel gain.

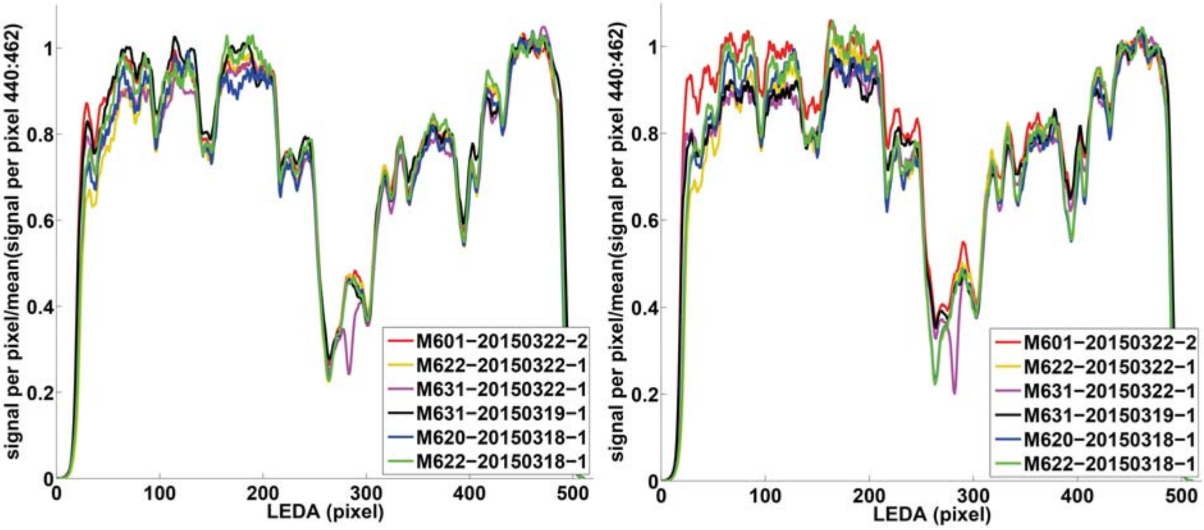

(a) Row A

(b) Row B

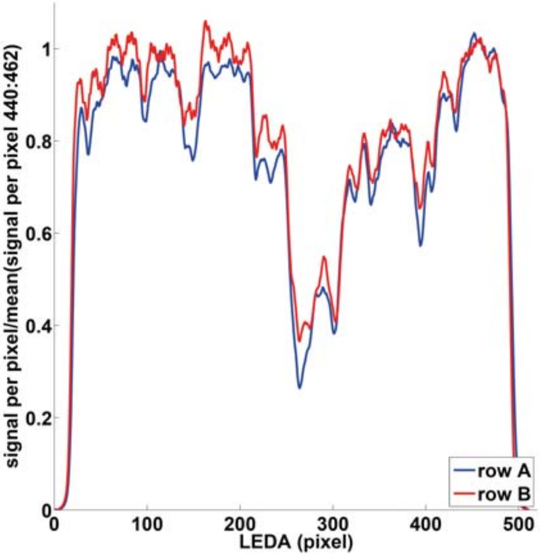

(c) M601-20150322-2

Fig. 3.4.23: Comparison of pixel gain factors for measurements with GS 13 executed between January 2015 and end March 2015. (a) and (b) show row A, B, respectively. The values have been determined following the nominal procedure and the selection of the best correction has been done in section C.3. In (c) a comparison of the individual pixel gain for row A and B is done for the measurement M601-20150322-2.

For GS 14 two measurements were done during the period from March 18th to 22nd with two different modes, M620 and M601, respectively. For the comparison done in (a) and (b) fig. 3.4.22 the measurement from beginning of February has been included. All three measurements show a slope over the LEDA but not in the same extend and the dip around pixel 125 of M620 is due to a missing spectra of the sweep. The direct comparison of row A and B in (c) reveals a difference in shape and dip depth of the central dip, a difference in level around pixel 26 - 52, 107 - 245, and 332 - 445, and a difference in the smoothness of the overall curve.

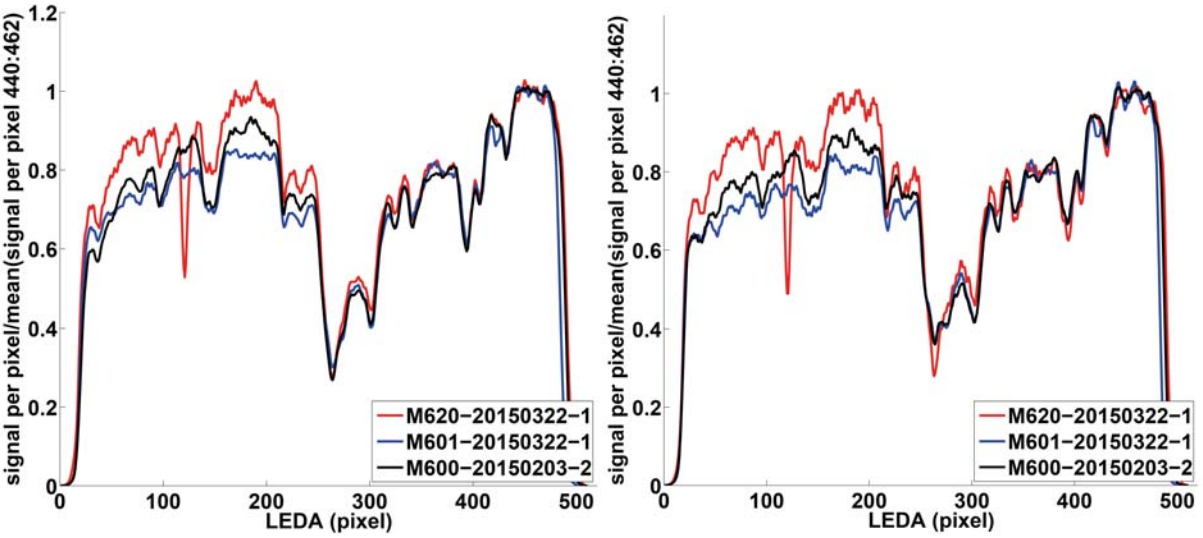

(a) Row A **(b)** Row B

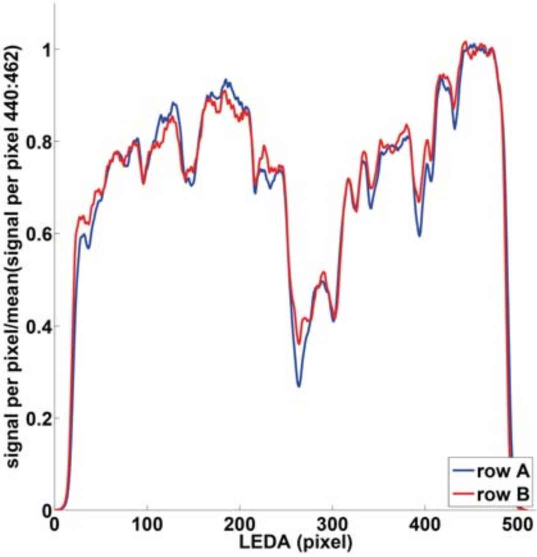

(c) M600-20150203-2

Fig. 3.4.24: Comparison of pixel gain factors for measurements with GS 14 executed between January 2015 and end March 2015. (a) and (b) show row A and B, respectively. The values have been determined following the nominal procedure and the selection of the best correction has been done in section C.3. In (c) a comparison of the individual pixel gain for row A and B is done for the measurement M600-20150203-2.

From beginning of 2015 till March 2015 five time pixel gain measurements with GS 16 were performed and except for one (M630-20150318-1) M600 was always used. In fig. 3.4.25 (a)-(b) a comparison of the individual pixel gain based on those measurements is done for row A and B, respectively. Remarkably M600-20150322-2 and M600-20150103-1 show both a similar slope over the entire LEDA while the other three data sets seem to have twice a slope; one going from around pixel 30 - 190 and the second one from around pixel 316 - 450. The comparison of row A and B done with the data set M600-20150322-1 shows a difference in the level in the first half of the LEDA and a different shape and dip depth of the central peak around pixel 256.

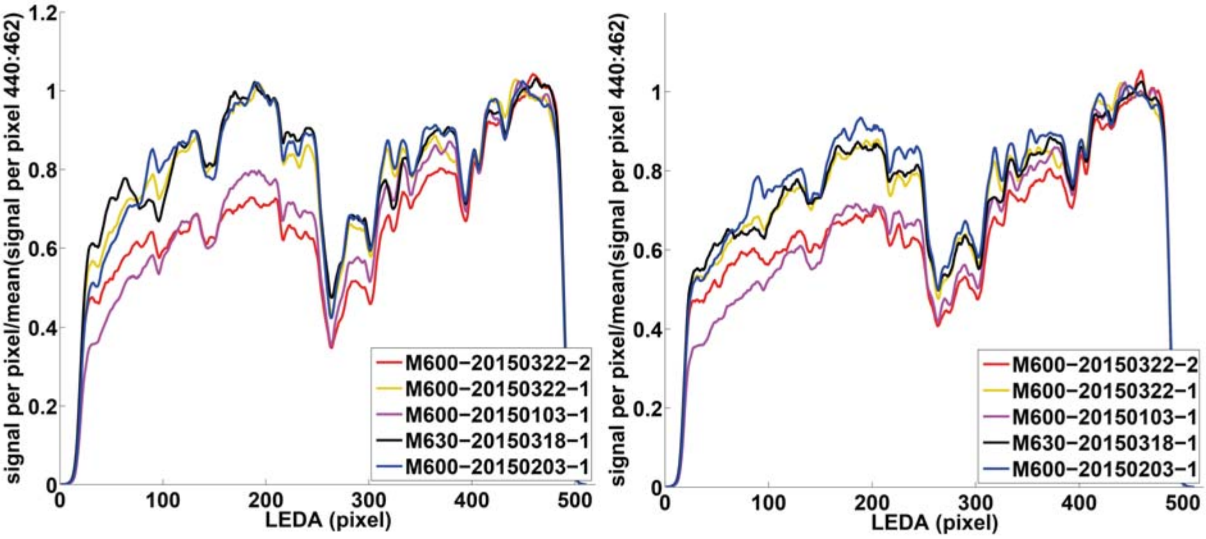

(a) Row A **(b)** Row B

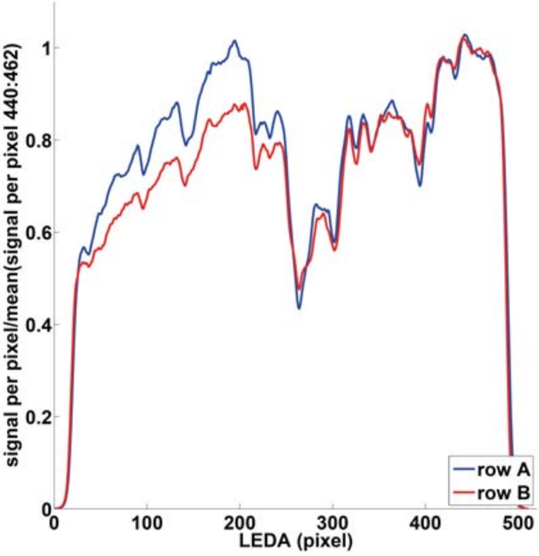

(c) M600-20150322-1

Fig. 3.4.25: Comparison of pixel gain factors for measurements with GS 16 executed between January 2015 and end March 2015. (a) and (b) show row A, B, respectively. The values have been determined following the nominal procedure and the selection of the best correction has been done in section C.3. In (c) a comparison of the individual pixel gain for row A and B is done for the measurement M600-20150322-1.

In order to do a comparison of the individual pixel gain among the gain steps the most likely to be true had to be selected. Since pixel gain measurements done before Rosetta was in the vicinity of 67P did not show a slope overall the LEDA, as it is present for FM, it is assumed that undepleted regions should be around 1. Based on this assumption a selection of the measurements acquired between begin of 2015 and mid March 2015 has been done. The list of the selected measurements is given in table 3.4.3 and for GS 14 and GS 16 two measurements were selected because the comparison did not yield a distinct measurement to be the best. Therefore the two most likely ones were chosen. And thus could be compared to the individual pixel gain before the encounter with 67P in August 2014. Then the individual pixel gain factors were determined for GS 12, 15, and 16. The comparison for GS 12 has already been done in fig. 3.4.17 and a change of depletion of 12% could be determined. Unfortunately no measurements were performed at GS 15 since then and the comparison can be done only for GS 16. This is done in fig. 3.4.26 with the individual pixel gain factors acquired in July 2014 and March 2015. From the graph it can be seen that the depletion around pixel 264 increased from ~0.62 to ~0.42 which is a change in the depletion of 20%. The discussion of the resulting values for the change in depletion will be discussed later as first the individual pixel gain factors at different gain steps in March are compared.

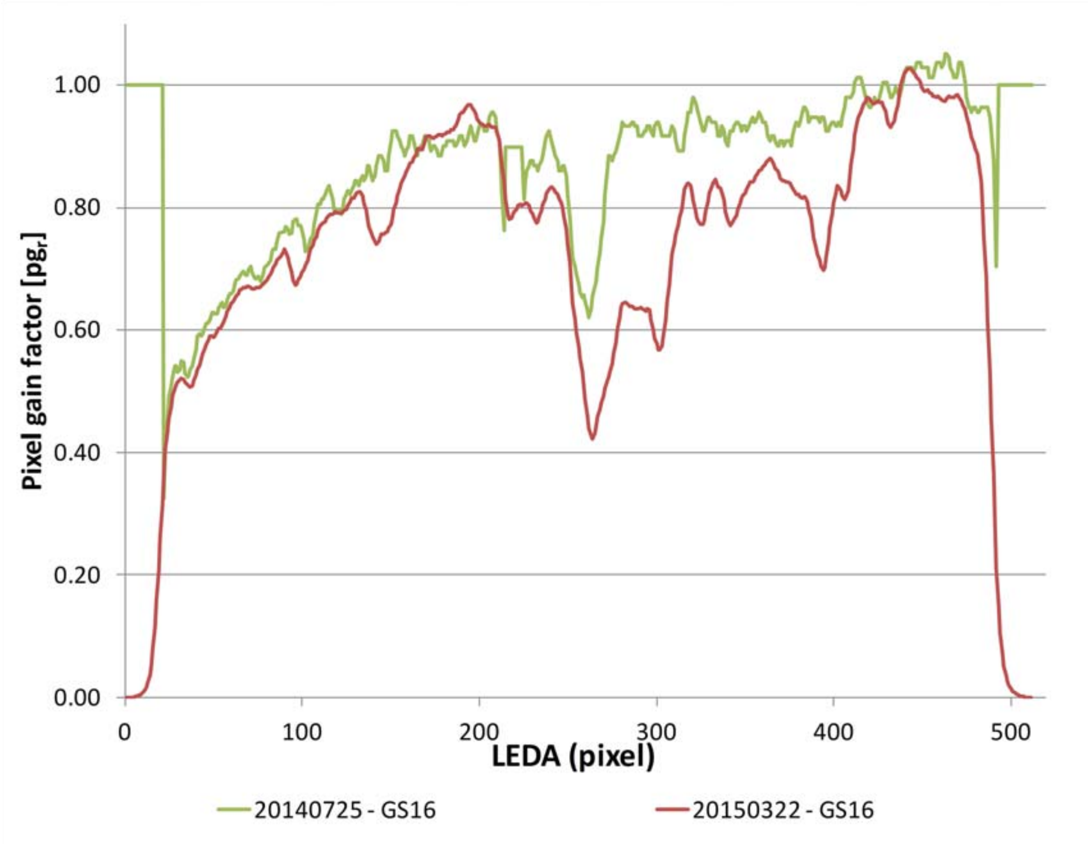

Fig. 3.4.26: Comparison of individual pixel gain factors at GS16 due to data acquired in July 2014 and March 2015.

Table 3.4.3: Selection of gain steps which are supposed to be closest to the real individual pixel gain.

Gain step	measurement
9	M602-20150203-1
10	M602-20150321-6
11	M621-20150318-1
12	M601-20150315-1
13	M601-20150322-2
14-1	M620-20150322-1
14-2	M600-20150203-2
16-1	M600-20150322-1
16-2	M600-20150203-1

On the two following pages a graphical comparison of all GS based on the selection is presented. The graphs are arranged as follows: the x axis represents the 512 pixels of the LEDA,the y axis is the individual pixel gain normalized to the rightmost pixels, the colors go from blue to red with increasing gain step. The upper panel shows row A while the lower one shows row B. Figure 3.4.27 (a) shows the version with GS 14-1 and GS 16-1 while in (b) GS 14-2 is used. From the lower panel of (a) (row B) several important observations can be made:

i GS 16 shows significant difference from the other gain steps in the level for the supposedly almost undepleted pixels between the dips up to pixel 200.

ii The spread among gain steps in the regions with out a dip is up to 0.4.at the leftmost pixels while in average it is about 0.2.

iii Above pixel 300 the lowest gain step has the highest values for the pixel gain factors besides the dips and below pixel 200 it is the opposite.

iv There is a dip for GS 14 around pixel 120 that is not present for the other gain steps.

v Between pixel 225 and 425 the dip depth is more or less correlated with the gain step meaning the lower the gain step the larger the depletion. However, at the dip around pixel 264 GS 14 is out of alignment and shows the largest depletion for all gain steps.

vi Below pixel 200 the order of gain steps at the dips is not any more preserved.

There are two major differences between the two row in (a). First the shape of the dip at pixel 256 differs. For Row A for most of the gain steps it looks like one dip while for row B there is like a step on the right side. Second the order of gain steps below pixel 200 for both the dips and the regions in between is not the same for A and B. The likely causes are presented in the discussion.

In fig. 3.4.27 (b) gain step 14 has been exchanged by another measurement which has a lower level on the left side for both rows and for row B a different shape and depth of the central dip around pixel 264. Like this GS 14 doe not show a larger depletion at pixel 264 and pixel 302 for row B than for GS 12 and 13. However, this in not the case for row A, where GS 13 and 14 show the same depletion at pixel 264, and for most of the other dips spread over the LEDA . In addition the dip around pixel 120 is vanished with using GS14-2. Moreover the individual pixel gain factors of GS 14 lay mostly below the ones of the lower gain steps in the range up to 200 pixels.

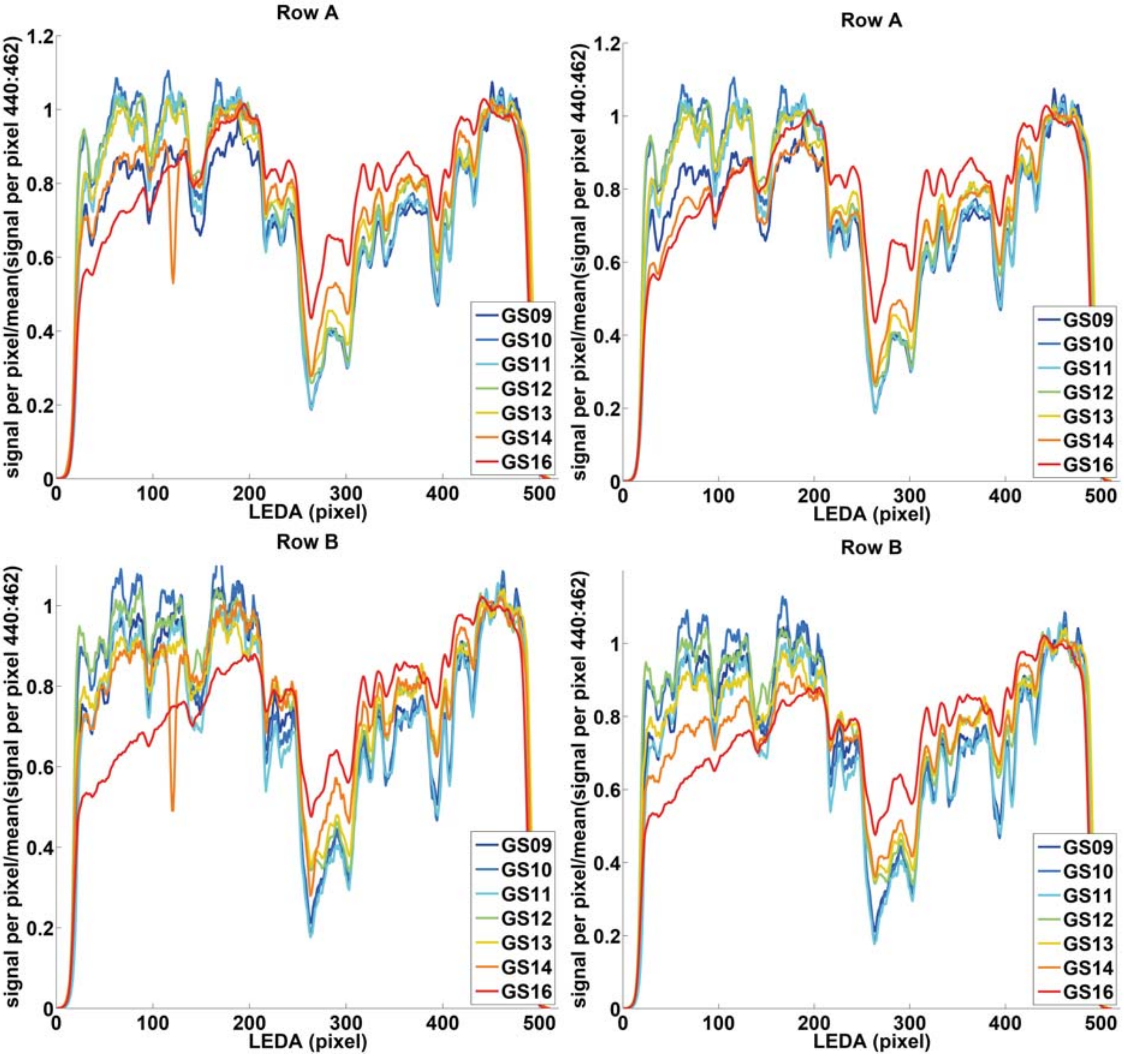

(a) GS14-1 & GS16-1 **(b)** GS14-2 & GS16-1

Fig. 3.4.27: Comparison of different gain steps measured at FS between begin of February 2015 and end March 2015. For (a) the set with GS14-1 and GS16-1 has been used while for (b) GS14-1 has been exchanged with GS14-2 (for more details see table 3.4.3). Both graphs show in the upper panel the individual pixel gain factors for row A and in the lower panel for row B.

In figure 3.4.28 (a) gain step 14-1 and 16-2 have been used for the comparison. GS16-1 and 16-2 differ mostly in the allover slope over the LEDA and the level height for regions besides the dips. The sole change is that the spread between the gain steps did slightly decrease. For the sake of completeness the version with GS14-2 and GS16-2 is shown in fig. 3.4.28 (b) and no further knowledge can be gained from it.

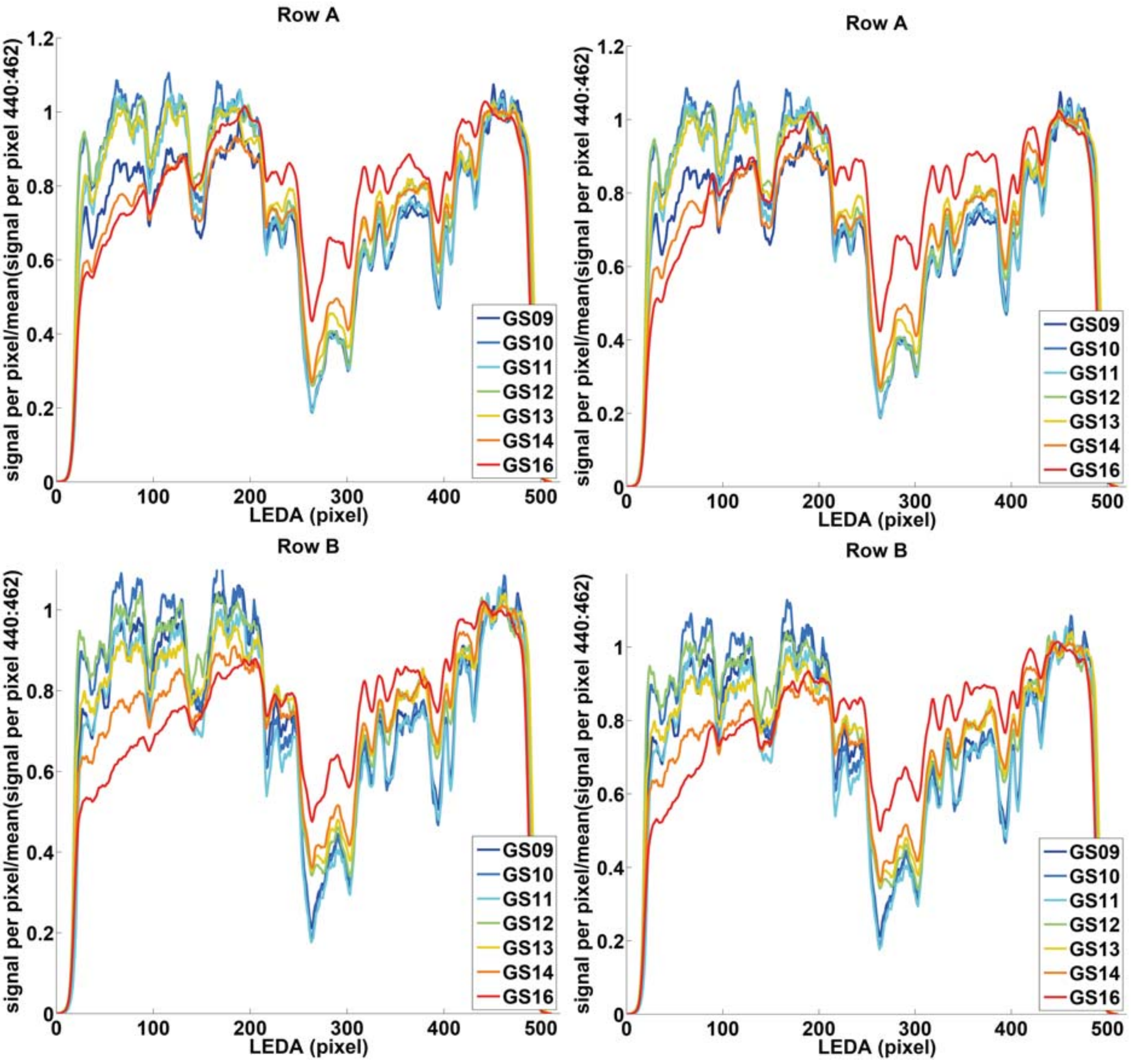

(a) GS14-1 & GS16-2

(b) GS14-2 & GS16-2

Fig. 3.4.28: Comparison of different gain steps measured at FS between begin of February 2015 and end March 2015. For (a) the set with GS14-1 and GS16-2 has been used while for (b) GS16-1 has been exchanged with GS16-2. Both graphs show in the upper panel the individual pixel gain factors for row A and in the lower panel for row B.

3.4.2.3 Manifestation of Depletion

Based on four selections done in the previous sub section the manifestation of depletion as it has been done for FM in section 3.4.2.3 can be examined. In essence it is again comparing the dip depth for one gain step relative to the dip depth of gain step 16. However for FS data the amount of dips is much higher and thus 12 dips have been evaluated. A list of the dip location is given in table 3.4.4 and in the following the results of the dip depth for the set with GS14-1 and GS16-1 will be presented.

Table 3.4.4: Dip locations present on both rows for FS mid March 2015.

Dip no.	Dip location (pixel)
1	37
2	98
3	149
4	216
5	233
6	264
7	302
8	323
9	342
10	395
11	407
12	433

In fig. 3.4.29 a comparison of the 12 dips are shown. In each subfigre the dip depth relative to the one of GS 16 with respect to the gain step is draw. The orientation of the triangle indicates which side of the shoulder next to the dip has been taken as reference (left-handed (LH) and right-handed (RH)) while row A is colored in blue and B in red. In addition the fit functions deduced from FM for row A FM (black), row B FM (gray) both right and left handed (1, 2,resp.) are included.
The graph of the dip no. 1 in (a) reveals first for LH a difference in dip depth more than a factor of 10, second the difference between LH and RH is for both rows about a factor of 5, and third it seems that GS 9 - GS 11 group and GS 12 - GS 14 group. The same groups can be seen for dip no. 2 for RH while while LH shows a an increase of dip depth of a factor of 4 for row A and a factor of 8 for row B. At dip no. 3 again the same grouping can be seen for both LH and RH. For no. 4 only LH has been calculated and it lays within the fit functions deduced at FM. In addition a clustering into the two groups is present. For dip no. only LH has been calculated and unlike for the previous presented dips the relative dip depth lays within corresponding fit of the FM. For the large central dip (no. 6) around pixel 264 the relative dip depth seems to be chaotic for both rows. In contrast the that the RH relative dip depth for the dip around pixel 302 seem to lay for both rows on a similar curve as for the FM but with a different curvature between GS 11 and 16. At dip no. 8 the RH relative depths spread between in the area defined by the fit curves while the LH relative depths are scatter around 1. Although the relative dip depth of no.9 lays in the region of the FM functions no other correlation than the clustering into the two gain step groups can be seen. At dip no. 10 for row A all points except for GS 10 and 11 lay within the left handed functions for row A and B FM. In addition the clustering into two the gain groups is present for both rows and orientations. Similar to the dips at the left border the last two dips (no. 11 and 12) display chaotic pattern, the clustering into the two gain step groups, and an increase in relative dip depth up to a factor 4 with decreasing gain step.

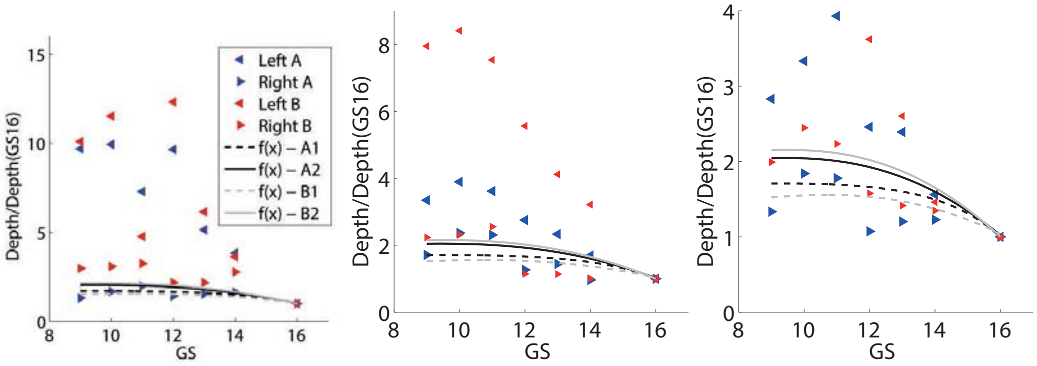

(a) Dip no. 1 **(b)** Dip no. 2 **(c)** Dip no. 3

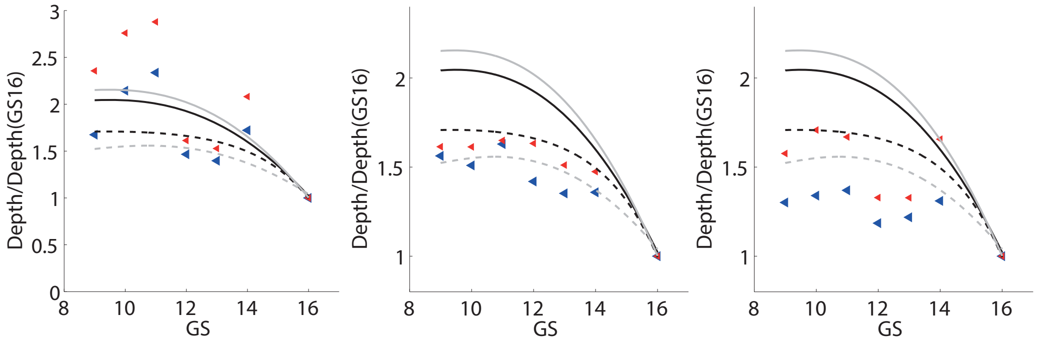

(d) Dip no. 4 **(e)** Dip no. 5 **(f)** Dip no. 6

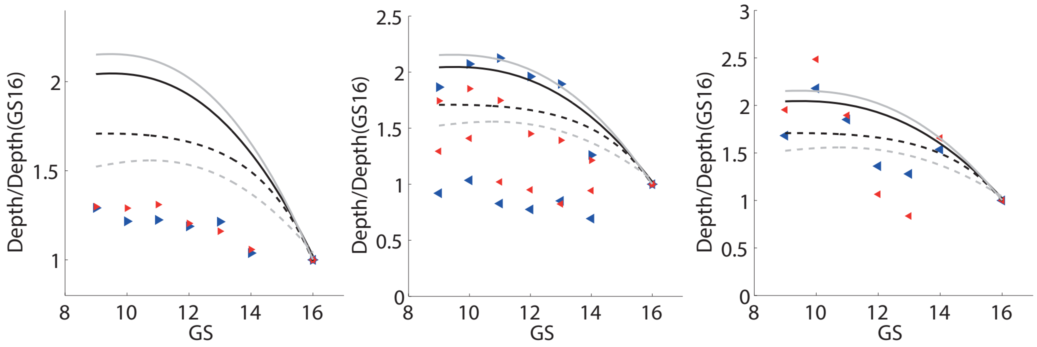

(g) Dip no. 7 **(h)** Dip no. 8 **(i)** Dip no. 9

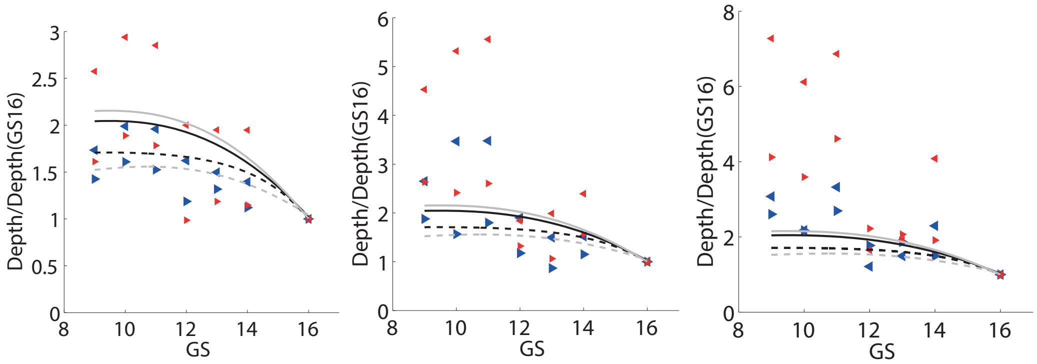

(j) Dip no. 10 **(k)** Dip no. 11 **(l)** Dip no. 12

Fig. 3.4.29: Relative dip depth of FS pixel gain acquired between begin February 2015 and end March 2015 with GS14-1 and GS16-1. (a) to l) show the relative dip depth of 12 selected dips present in the individual pixel gain data (see fig. 3.4.27); in blue row A, in red row B, and the orientation of the triangle gives the direction to the reference point. In addition the functions derived for FM for the relative dip depth are displayed (see fig. 3.4.6).

The influence on the relative dip depth by using a different set is shown exemplarily for the dips no. 6, 7, and 8 since they are the most important ones for high resolution measurements. In fig. 3.4.30 each sub figure is composed of three graphs using GS 14-1 and 16-1 (left panel), GS 14-2 and GS 16-1 (mid panel), and GS 14-1 and GS 16-2 (right panel).

Exchanging GS14-1 with GS14-2 at the dip no. 6, see mid panel of (a), reduced the relative dip depth from ~1.7 to ~1.2 and as a consequence GS 12 to GS 14 lay closer together. An exchange of GS 16-1 with GS 16-2 ((a) right panel) decreases all points for row A for about 0.2 and for row B for about 0.1. Exchanging GS 14-1 with GS 14-2 at the dip no. 7 ((b) mid panel) lifts the data point at GS 14 up to ~1.2 and as a consequence the relative dip depth for GS 12 to GS 16 seems be more a linear relation than anything curved. Exchanging GS 16-1 with GS 16-2 ((b) right) leads not to a significant changes. An exchange of GS14-1 with GS14-2 at the dip no. 8 ((c) mid panel) leads to an increase of the LH data point for both rows at GS 14 which lay now between the fits for row A and B LH. Exchanging GS 16-1 with GS 16-2 ((a) right) only increases the level of the data points marginally.

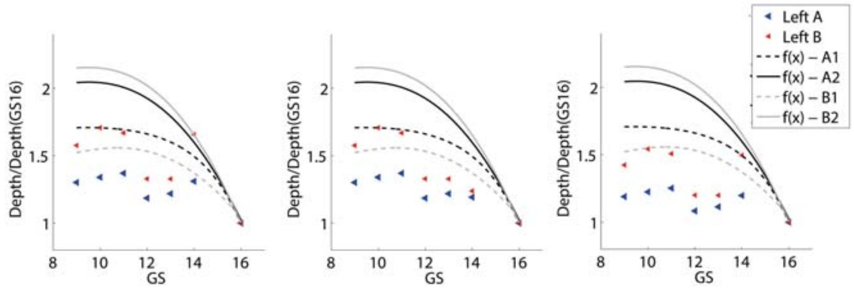

(a) Dip no. 6

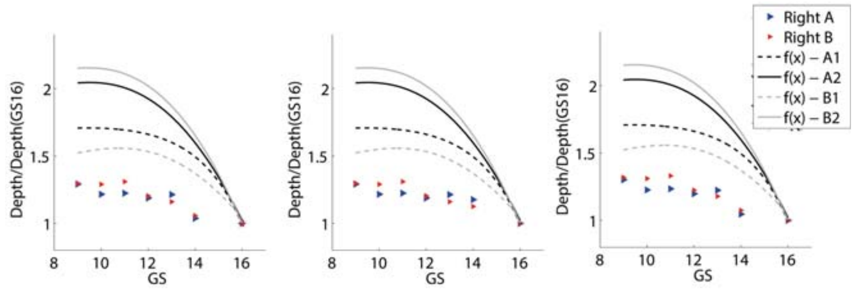

(b) Dip no. 7

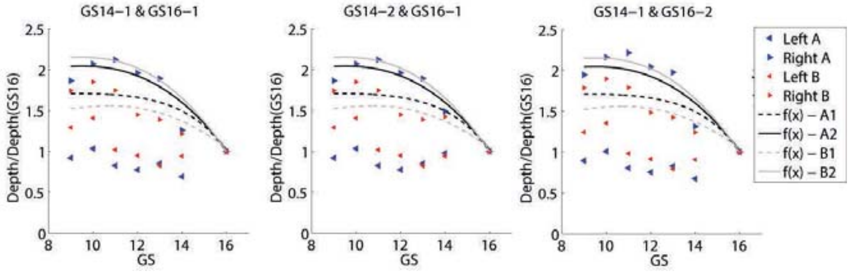

(c) Dip no. 8

Fig. 3.4.30: Comparison of relative dip depth of FS pixel gain determined for the sets GS14-1 and GS16-1 (first column), GS14-2 and GS16-1 (second column), and GS14-1 and GS16-2 (third column). It is shown exemplarily for dips no. 6 to 8.

Different from FM the FS pixel gain data show more dip features and some superimpose such as the two large dips in the center or around pixel 400 where two dips lay very close together. For the first example it is clear that the elevation in between the dips shows some sort of degradation and does not represent the pristine individual pixel gain. For the second example it is not clear how much degradation the region between the two dips experienced. As a consequence the relative dip depth for the two main dips have been determined with other reference points and the results for the selection with GS 14-1 and GS 16-1 are presented in fig. 3.4.31 (b) and (d). As reference on the left side of the dips the shoulder before the fourth dip around pixel 210 has been used and on the right side the right shoulder after the eleventh dip around pixel 410. The resulting dip depth for both sides and rows at dip no. 6 do not follow the functions derived at FM and again a clustering into gain step groups is present. In contrast the change of reference points for dip no. 7 increases RH values and the LH values lay for row B around the RH fits for both rows at FM while for row A they seem to scatter around the LH fit for row A at FM.

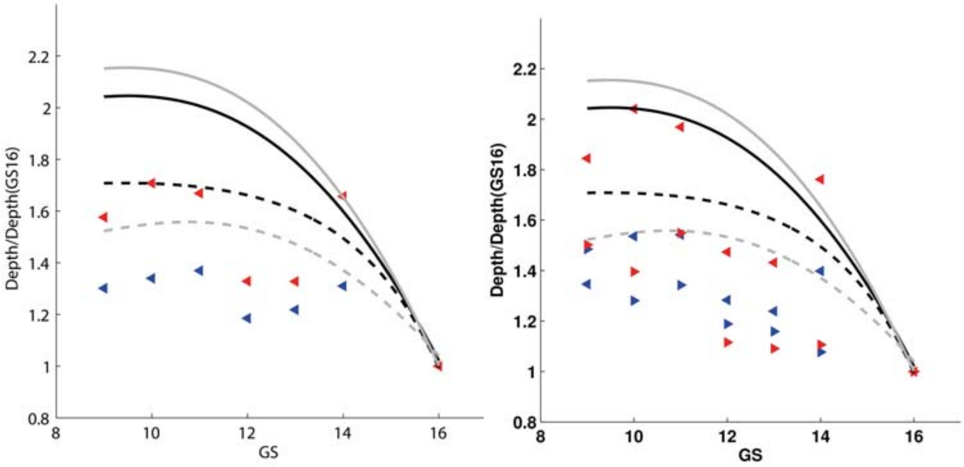

(a) Dip no. 6 **(b)** Dip no. 6a

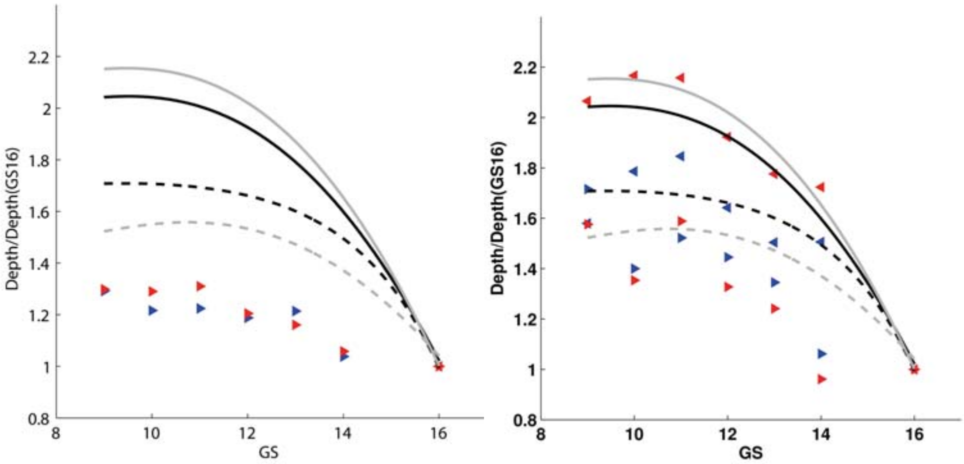

(c) Dip no. 7 **(d)** Dip no. 7a

Fig. 3.4.31: Comparison of relative dip depth of FS pixel gain determined exemplarily for dip 6 and 7 with different reference points. The values in (a) and (c) were calculated using the maximum value on either the left or the right side of the dip. The values in (b) and (d) were calculated by using the shoulder before the fourth dip around pixel 210 and the shoulder after the eleventh dip around pixel 410.

3.4.2.4 Influence of a Bias in the Pixel Gain Factors

From all work done so far concerning the determination of the individual pixel gain it is thought that not yet the true values are known. The values reported here have a bias which is estimated to be up to 10% in certain regions of the LEDA, in particular between pixel 1 and 200. Consequently the questions of how large the influence is on the resulting peak areas and how does it effect ratios of two peaks emerge. In the following a small study will be presented basing on the knowledge so far with the aim to give an upper limit for the introduced uncertainties.

Assuming that the individual pixel gain factors determined in November 2014 for GS 16 represent the true individual pixel gain for each pixel the effect adding the sum of a random error and a constant error to the assumed true values was to be checked. This was done by comparing the ratio of peak area of two identical peaks having their peak center (x_c) a few pixels apart. Like this slightly differing pixel gain factors were applied. the individual pixel gain factors determined in November 2014 at GS 16 have been used for the estimation because all presented space data in this study was measured on this gain step. The simulated individual pixel gain factors have the following structure:

$$pg_{16,Si}(x) = pg_{16}(x) \cdot (1 + \epsilon \cdot a_i - b_i) + c_i \tag{3.4.3}$$

where ϵ is an uniformly distributed number between 0 and 1 which is then transformed by a and b to the intervals ± 0.5 and ± 0.1 for $a = 0.1$ resp. while c is ± 0.05 or ± 0.1. The random part of equation (3.4.3) it thought to simulate the bias caused by no correct determination of the peak center, not equidistant steps, and changes in the water signal on short time scale i.e. between two spectra. The constant part it thought to simulate the bias due to a not correct water signal correction. The combination of those two ensures that there are pixels at which the maximal deviation is present and pixel were almost no deviation is present. In table 3.4.5 the different combination used for the study are presented.

Table 3.4.5: Parameter sets to calculate simulated pixel gain factors using equation (3.4.3).

$pg_{16,Si}(x)$	a_i	b_i	c_i
1	0.1	0.05	0.05
2	0.2	0.1	0.05
3	0.1	0.05	0.1
4	0.2	0.1	0.1
5	0.1	0.05	-0.05
6	0.2	0.1	-0.05
7	0.1	0.05	-0.1
8	0.2	0.1	-0.1

The resulting ratio of area between a peak with its center at x_c-Δx and a peak with its center at x_c is shown in fig. 3.4.32 and fig. 3.4.33 for Δx = 1-6 pixels using $pg_{16,Si}(x)$. The upper most panel of both graphs shows the peak area with respect to x_c for the true area and if simulated pixel gain factors were used. The six smaller panels show the deviation from the true peak area ratio for differences in peak center of Δx = 1-6 pixels. Only the section going from pixel 160 to 340 is showed because in HR mode the peaks lay within this range. First it can be observed that for $pg_{16,S1}(x)$ - $pg_{16,S4}(x)$ with Δx = 1-6 pixels the deviation from the true ratio does not exceed 8% and is predominantly below 4% while for $pg_{16,S5}(x)$ - $pg_{16,S8}(x)$ with Δx = 1-6 pixels the deviation from the true ratio does not exceed 10% and is predominantly below 5%. Second the largest spread is present for the simulated pixel gain factors with $c \pm 0.1$ and ϵ in the interval [-0.1,0.1] for all Δx while the smallest spread is present with $c \pm 0.05$ and $\epsilon \in$ [-0.1,0.1]. Third with increasing Δx the shape of the true pixel gain curve has an increasing influence. For $pg_{16,Si}(x)$ with positive c there is first a decrease and then an increase around pixel 256 and 300 while for $pg_{16,Si}(x)$ with having a negative c there is first an increase and then a decrease i.e. at Δx 6 the increase around pixel 256 is 4% followed by an decrease of 4% about 20 pixels afterwards.

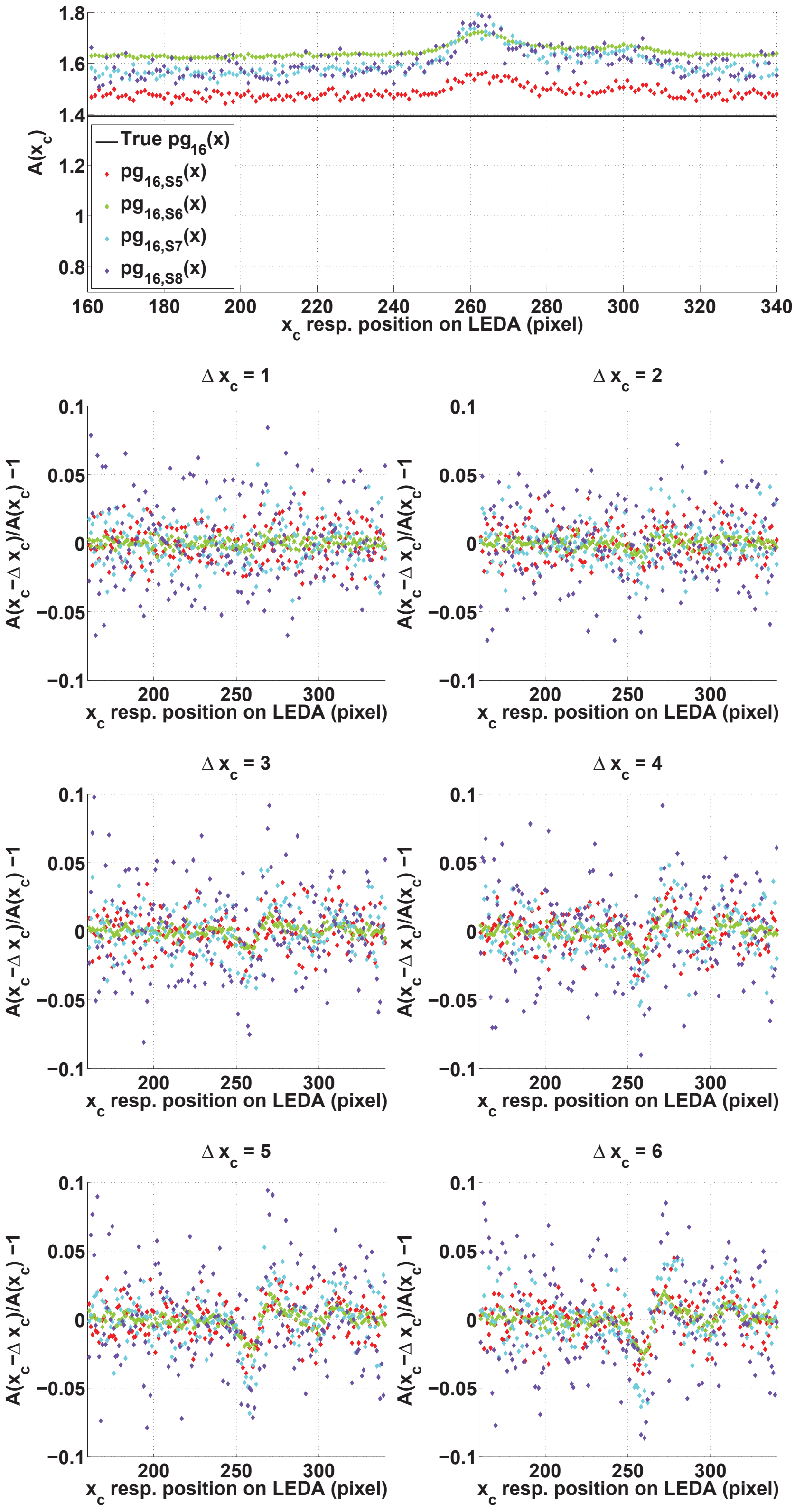

Fig. 3.4.32: The upper most panel shows the peak area with respect to the location on the LEDA for the assumed 'true' pixel gain factors and for the factors with a random uncertainty and a positive constant term added (for more details see table 3.4.5). The six lower panels the deviation from the 'true' signal ratio of two peaks with a difference in location between Δx 1 to 6 pixels.

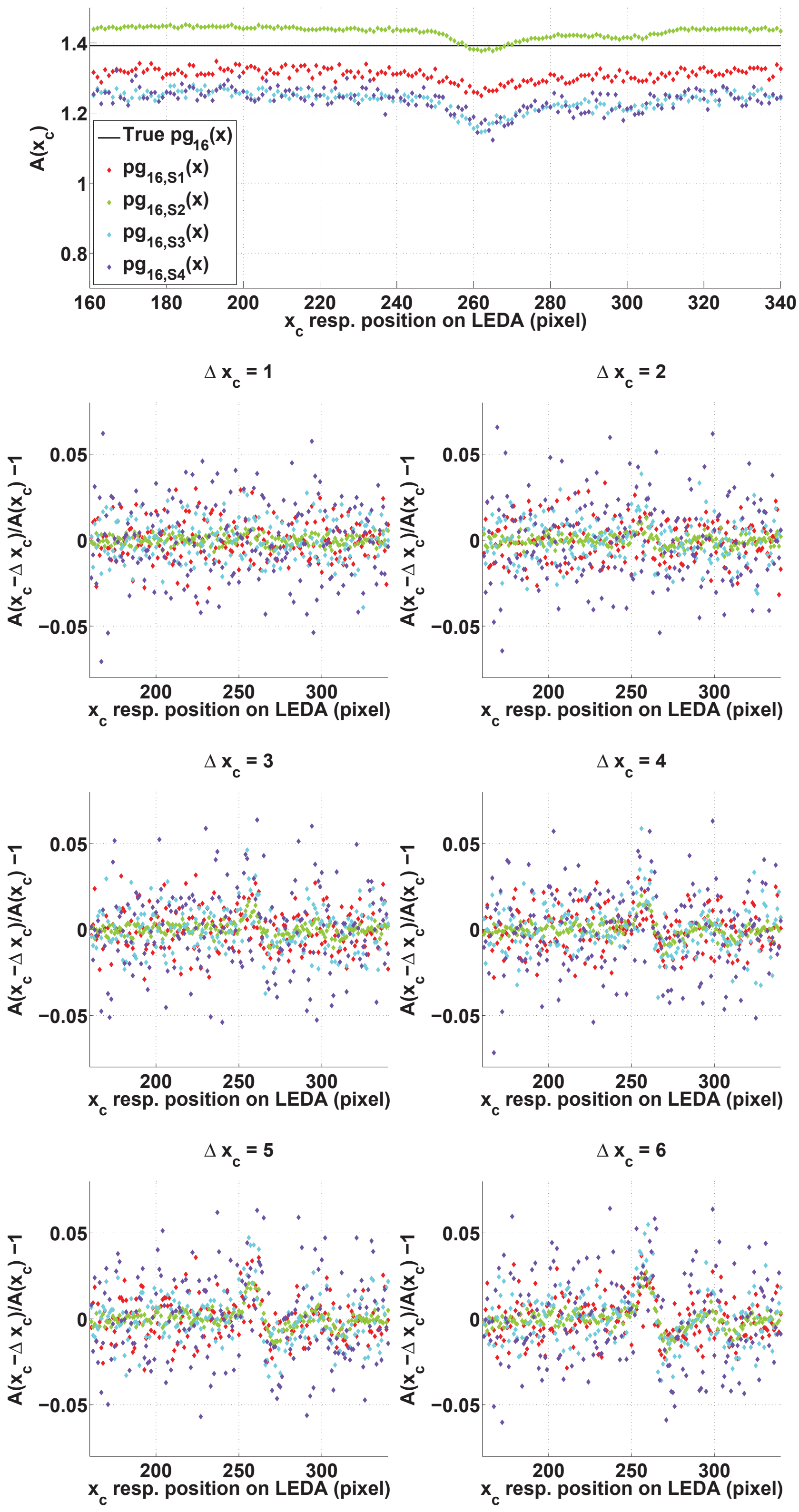

Fig. 3.4.33: The upper most panel shows the peak area with respect to the location on the LEDA for the assumed 'true' pixel gain factors and for the factors with a random uncertainty and a negative constant term added (for more details see table 3.4.5). The six lower panels the deviation from the 'true' signal ratio of two peaks with a difference in location between Δx 1 to 6 pixels.

3.4.3 Discussion

In the first half of this discussion the results of the individual pixel gain of DFMS FM are reviewed. Possible explanations for the linear slope over the LEDA correlated with the gain step and the manifestation of depletion will be given. Subsequent the obtained results for the numerous pixel gain measurements performed in space with DFMS FS will be discussed and the most likely causes for the inconsistencies seen in the results will be presented.

3.4.3.1 Flight Model

The compilation of GS 7 - GS 16 measured in 2015 showed the same correlation between gain step and steepness/orientation of linear slope over the LEDA as the 2012 set. In order to rule out the measurement procedure as cause GS 16 has been measured with inverted sweep direction. To rule out a bias due to the signal intensity measurements at GS 16 with a ten times lower signal were preformed. The linear slope is present in all three sets resulting pixel gain sets and therefore the measurement procedure can not be the cause. Comparing the peak height of each step in one sweep revealed that the signal intensity changes linearly with the step number thus the location of the peak on the LEDA. In addition the peak full width at half maximum (FWHM) decreases from pixel 1 to pixel 512 from ~3 to 2 pixels for all gain steps. Thus the change in signal and FWHM per step is not correlated otherwise the FWHM should increase with decreasing signal height. If the linear slope would be a characteristics of the MCP it is expected to show the same sign for the linear slope regardless gain step. As a consequence it has to be concluded that the total signal per step changes which can only be caused by the ion optics.

A side product of this investigation was the discovery of the differences in FWHM in the 2012 data that can be explained by the selection of the mass to charge ratio of the species used to perform the measurements. The decrease of peak width in pixel over the LEDA is cause by the decrease of resolution for increasing mass to charge ratio. In addition the comparison of the three resulting pixel gain factor sets for GS 16 showed that they vary in the range of 0.06 in particular were no strong depletion is present. The statistical error of the signal is smaller than the seen variation and could therefore be ruled out. The author is aware of three factors which might have caused the seen effect: first small variations in the pressure which has an uncertainty of 6%, second the impact of not having the peak center exactly on a pixel, and third the assumption that the peak center is at the location of the peak maximum. However it is not possible to quantify the impact for only one of the three factors and anyway the seen variation is most likely a combination of them. Consequently the individual pixel gain sets determined in 2015 have an uncertainty of 6%.

A direct comparison of each gain step between the results obtained in 2012 and 2015 revealed the presence of five new dips at pixel 85, 105, 393, 440, and 461. In addition there is a difference of the level with not significant depletion between the data from 2012 and 2015. The presence of new dips at the periphery of the LEDA is best explained by a depletion due to calibration in low resolution mode while the difference in level is due to the normalization. In the nominal data reduction procedure the signal per pixel is divided by the mean signal per pixel (

The correlation between gain step thus applied potential on the MCP and the dip depth relative to the dip depth of GS 16 can be described by $f(x) = a \cdot exp(-b \cdot x) + c \cdot x^2 + d$ that can fit both the decrease between GS 10 and GS 16 and the constant relative dip depth for gain steps smaller than 10. For both rows for the relative dip depth with reference point at the first local minimum at the left/right side a least square fit with $f(X)$ has been performed.

The differences in the parameters between the rows is not significant while the parameters differ for the two reference points. Leaving out the fit 'Row B - 1' which has an adjusted R^2 of 0.923 the fit for the left shoulder differs from the one for the right shoulder mainly in the parameters a, b, and c while for d no significant deviation is present. The difference in parameters manifests itself in the curvature of the fit function between gain step 11 and 16. However, the difference in relative dip depth is due to the selection of reference points and consequently the differences in the parameters for $f(x)$ should be regarded as irrelevant. It is thought that the curve shape is directly linked to the function principle and the material of the MCP which will be elucidated in the following. As it has been already explained the gain of the incoming signal is achieved with release a secondary electron avalanche in the tubes of the MCP. A consequence of this is the depletion since the released electrons can be replaced. Moreover to release further electrons from an atom needs more energy than it needed before thus the more used a MCP is the higher voltages have to be applied to achieve the same gain. The effect on the gain can be directly observed at the absolute dip depth which decreases with increasing potential. Consequently it is assumed that with increasing measurement time the relative dip depth reaches the same level as for the gain steps below 10. This decrease in relative dip depth is equatable to a decrease in the dynamic range.

In order to proof this hypothesis further measurements of the individual pixel gain are needed and the author suggest the following: to be able to detect the effect on a reasonable time scale a section of the MCP needs to be depleted strongly on purpose. To achieve the depletion it is suggested to do continuous measurements with a signal around pixel 100 or 450 where only a small depletion is present yet. The continuous measurements should be interrupted on a regularly bases with pixel gain measurements with at least the gain steps 7 to 16.

3.4.3.2 Flight Spare

Analyzing and interpret the pixel gain measurements in space is a demanding and complex task because besides one needs to be aware of the circumstances during the measurements of which not all are well documented such as the evolution of water to name the most important one. Nevertheless in this work an attempt has be done to determine the individual pixel gain factors in space and to constrain the uncertainties as far as possible.

Already the first measurements acquired in April and July 2014 were puzzling since for GS 15 and GS 16 there is a slope present between pixel 1 and 200 which is not there for GS 12 and GS 13 that has been measured in 2010. In addition the later two measurements show a small depression right after the central dip up to pixel 400 where the curves start to increase again. Besides the difference in curve shape which will be discussed later it is not possible to determine the change of the individual pixel gain between April 2010 and April 2014 because the measurements in April 2015 were not performed at the same gain step as in 2010. However, it is assumed to be almost zero since not much measurements were performed in the meantime. Nevertheless the depletion between April and July 2014 could be determined for GS 16 which increased is about 0.13 at pixel 255 and 0.19 at pixel 265 resulting in a depletion of ~36% and ~38%, respectively.

Unfortunately the data acquired in November 2014 results in individual pixel gain factors of less quality because a different data procedure had to be developed for those data sets (for more details see section 2.3.4). The decrease in quality is due to the linear interpolation between the peak maxima of two subsequent steps for the number of sampled pixel is smaller than nominally. In addition the peak maximum does not necessary be at the peak center and an additional bias is introduced. A comparison of the nominal computed individual factors and the once determined via interpolation of the peak maxima revealed a difference up to 10% for areas where no spectra was missing nor any inconsistency in the stepping was present. Therefore the November sets are assumed to have an uncertainty of 10%.

The compilation of GS 16 acquired from April to January 2015 revealed a significant change in the individual pixel gain curve between July and November. Moreover the change of depletion between November 2014 and January 2015 is difficult to quantify since the two curves show a difference in level for areas with small depletion. However, all four measurements show the increasing slope between pixel 1 and 200 implying that this is a real feature. Besides the change of the depletion at the main dip several new dips appeared between July and November 2014 that can be explained by the measurement modes and densities in this period as it can be seen from the upper panel of fig. 3.4.34. The graph shows the signal on the detector between May and December 2014 during high and low resolution measurements with MPC/LEDA. For the calculation only the peak intensities and not the entire peak area have been considered. The amount of signal per pixel is highly biased because it has not been corrected for the individual pixel gain nor its change with measurement time. In addition the signal has not been corrected for the sensitivity. However, from this graph it is clear that dips formed besides the center due to measurements and as well that most signal was acquired in October 2014. This can be concluded because despite the present depletion the size of the biased signal in October is still larger than for the months before.

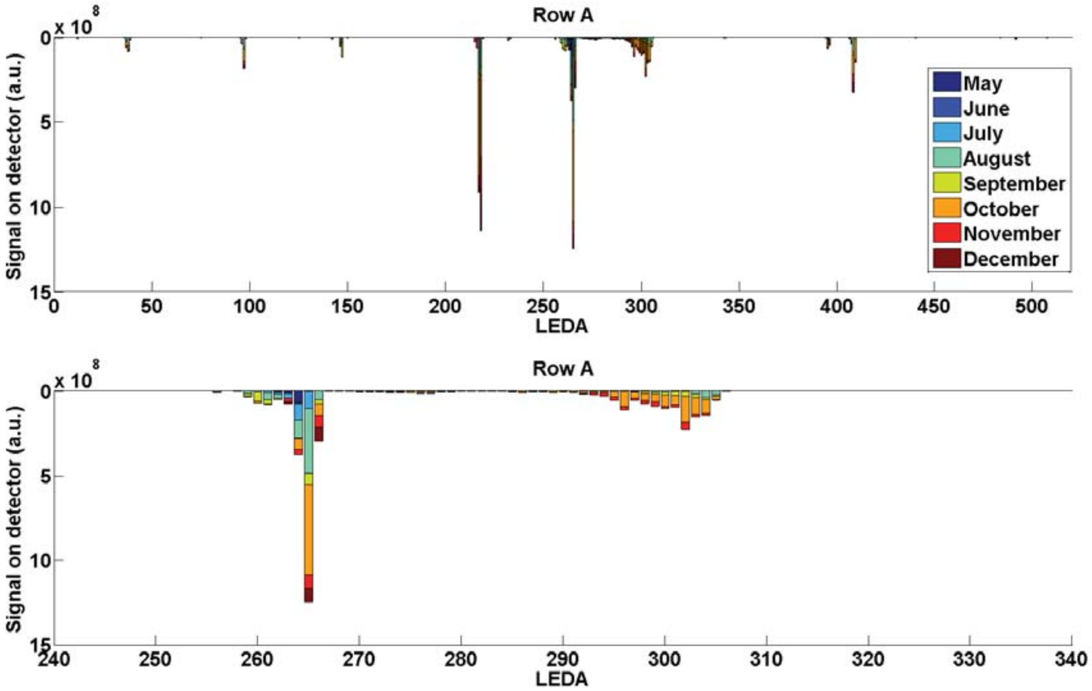

Fig. 3.4.34: Signal on detector during high and low resolution measurements with MCP/LEDA between May and December 2014. The signal is not corrected for the change of individual pixel gain over the measurement period and sensitivities of the measured species.

Beginning of February 2015 the individual pixel gain could be determined for the same gain steps as in November which are GS 9, 14, and 16. The comparison revealed a large difference regarding the level at which almost no depletion should be present while the overall curve shape seemed to be conserved (see fig. 3.4.15). Consequently a bias is implied in the analysis procedure and/or the measurement procedure. Therefore a measurement campaign with an adapted measurement procedure and additional measurement modes were been preformed in March 2015.
Between February 2015 and March 2015 the individual pixel gain could be determined for GS 9 - GS 14 and GS 16 at least once. Although is it no possible to determine the change in depletion accurately between November 2014 and March 2015 it can be done between the data sets of July 2014 and March 2015. The change in depletion basing on GS 12 is 0.12 around pixel 264 and the depletion is about 75%. In addition it could be done for GS 16 resulting in a change of depletion of 0.20 and the depletion in March was about 60% around pixel 264. It is not clear whether the change of depletion should be the same regardless the gain step or whether the observed difference between GS 12 and 16 is due to a bias in the individual pixel gain sets.

From the comparison of the different measurements at one gain step it could be seen that there is no correlation between overall curve shape and measurement mode as well as there is no correlation between LEDA the overall curve shape and the LEDA temperature. Hence the measurement procedure in a mode and a temperature dependence are ruled out to be the cause for the differences in level at less depleted areas seen between the individual pixel gain determined in November 2014 and February 2015. This leaves a not proper correction of the change in the water signal during the pixel gain mode as remaining possible cause. Therefore for each gain step the curve with the smallest slope

has been chosen for the comparison among gain steps (for more details see section C.3) From the comparison of individual pixel gain measured at different gain steps it could be seen that the further away from the center a dip lays the less the sequence among the gain steps is preserved, meaning the higher a gain step the smaller the dip depth. This implies that not all interferences due to a change in the water signal during the acquisition of one set are properly corrected.
Nevertheless it has been tried to quantify the manifestation of depletion and compare it with the results obtained with DFMS FM. Of the 12 examined dips none showed exactly the same behavior as it has been observed for the FM. For all dips except no. 5 and 7 the relative dip depth could be divided into two groups consisting of GS 9 - GS 11 and GS 12 - GS 15. The two groups are characterized by their small difference in dip depth within a group and the large difference in relative dip depth to the other group. This is thought to be as well a consequence of a not proper correction of the evolution of water. Exchanging GS 14 and GS 16 with other sets differing in the level for almost no depletion and changing the reference point for the dip depth calculation did no lead to further a convergence of the relative dip depths. As already mentioned the dips no. 5 and no. 7 are the odd once outs because no distinct grouping into the two groups is present and because they show the slightest spread in relative dip depth. For no. 5 the relative dip depth seems to follow more or less the function $f(x) = a \cdot exp(-b \cdot x) + c \cdot x^2 + d$ with the parameters of the fit Row A - 1, while the curvature for dip no. 7 between GS 12 and 16 is more shallow. Nonetheless for both dips the relative dip depth seems to be more or less constant between GS 9 and 12 and then it decreases towards GS 16. Consequently if the hypothesis about the evolution of the relative dip depth with measurement time is true the obtained results it would indicate that the MCP in space is more depleted than the one in lab in the central region and that with increasing measurement time. Thus the dynamic range would be lower than at the beginning of the mission. However, the evolution of the relative dip depth and how the evolution of water should be corrected are not yet understand to the level which would be needed to make substantial predictions about the functionality of the MCP in space.

In order to do a refinement of the existing individual pixel gain sets further measurements with the MCP in space are needed to investigate whether for GS 15 a slope is present as well between pixel 1 and 200. As soon as the nominal overall shape at a certain gain step is known the existing data can be corrected such that it fits this shape. Then it is suggested to determine again the manifestation of depletion for the existing data and compare it with the lab results.

The uncertainties introduced by using individual pixel gain sets of 2014 and March 2015 is assumed for signal ratios at the same gain step to be less than 10% and for ratios of signal obtained at different gain steps not more than 15%. The assumptions base on the study of the impact of a not correct individual pixel gain for a ratio and on the spread within one gain step in the data between February and March 2015 presented in section 3.4.2.4.

4. Sulfur Bearing Species at 67P/Churyumov-Gerasimenko

This chapter is dedicated to the presentation of the results for sulfur bearing volatiles seen at Churyumov-Gerasimenko during the 10 km orbits in October 2014. First the abundance of OCS, S_2, SO_2, and CS_2 relative to H_2S measured during one spacecraft terminator orbit will be presented followed by the first measurements of both δ^{33}S and δ^{34}S in cometary volatiles. In the beginning of the discussion first the obtained results of the abundances are compared to what has previously been published by Le Roy, L. et al. (2015) for 67P and a brief comparison with other comets will be done. The main part of the discussion is dedicated to proof that the determined sulfur isotopic ratios are not biased due to instrumental effects and they are discussed in context of sulfur isotopic ratios measured so far in other Solar System bodies.

All timings in this study are given in UTC and the sub satellite latitude are defined by Scholten et al. (2015). Except for H_2S non of the studied species was present in the spacecraft background measured in April 2014. The signal of H_2S in the spacecraft background is negligible compared to the cometary signal (spectra of m/z 34 u/e are shown in fig. D.0.1).

4.1 Results

4.1.1 Sulfur Bearing Species Compared to H_2S

The abundance of OCS, S_2, SO_2, and CS_2 relative to the main sulfur species H_2S are shown in fig. 4.1.1; in (a) with respect to the measurement time and (b) with respect to the sub satellite latitude. The values obtained by Le Roy, L. et al. (2015) are indicated for the summer hemisphere (negative latitudes) with a solid line and for the winter hemisphere (positive latitude) a dotted line. In addition to the period to calculate the isotopic ratios the same spectra used by Le Roy, L. et al. (2015) for SO_2 and S_2 have been analyzed; the data points are marked with an arrow and the corresponding season in (a). The uncertainties are due to the ion statistics, the fit to determine the peak area, and the pixel gain correction while the uncertainty for the sensitivity has been omitted since it can be up to 100% for OCS, S_2, SO_2, and CS_2 for which the sensitivity relation described in section 3.3 had to be used. For the winter hemisphere there is a good agreement with Le Roy, L. et al. (2015) for both S_2 and SO_2 but for the summer hemisphere only OCS is in good agreement while S_2 is about a factor 2.8 lower than the reported value and SO_2 is about a factor 1.3 to high.

The relative abundance of OCS between October 23rd and 27th is in the range $(0.66 - 7.8)\cdot10^{-2}$ relative to H_2S, S_2 is in the range of $(0.13 - 1.1)\cdot10^{-3}$, SO_2 is between $(3.2 - 6.5)\cdot10^{-2}$, and CS_2 ranges from $(0.18 - 2.2)\cdot10^{-2}$. Remarkably none of the species lays only in the range given by Le Roy, L. et al. (2015). In contrast SO_2 and S_2 lay mostly outside of the given ranges and both OCS and CS_2 spread in the given ranges between the 23rd and 25th while between the 25th and 27th they are significantly lower. For comparison in fig. 4.1.1 (b) are shown the same data with respect to the sub satellite latitude. From this graph it can be seen that the relative abundance of OCS and CS_2 is higher for negative latitudes and about a factor 3.6 lower for positive latitudes while between -20° and 20°

a decrease from the higher level to the lower level can be seen. For SO_2 and S_2 no clear correlation with the latitude can be seen. However, there is a cluster of points around 50° which have significant higher values than the majority of the S_2 values. The mean abundance relative to H_2S of OCS is $(2.98 \pm 1.92)\cdot 10^{-2}$, of S_2 is $(3.82 \pm 3.10)\cdot 10^{-4}$, of SO_2 is $(4.04 \pm 1.14)\cdot 10^{-2}$, and of CS_2 is $(6.18 \pm 3.30)\cdot 10^{-3}$ (1 σ). In addition, the mean abundances relative to H_2S has been calculated for sub satellite latitudes below -20° and above 20°. Below -20° the relative abundances of OCS is $(3.85 \pm 1.14)\cdot 10^{-2}$ and of CS_2 it is $(8.33 \pm 2.61)\cdot 10^{-3}$ while above 20° the relative abundances for OCS is $(1.60 \pm 0.73)\cdot 10^{-2}$ and for CS_2 $(2.77 \pm 0.79)\cdot 10^{-3}$. All values can be found in table 4.1.1.

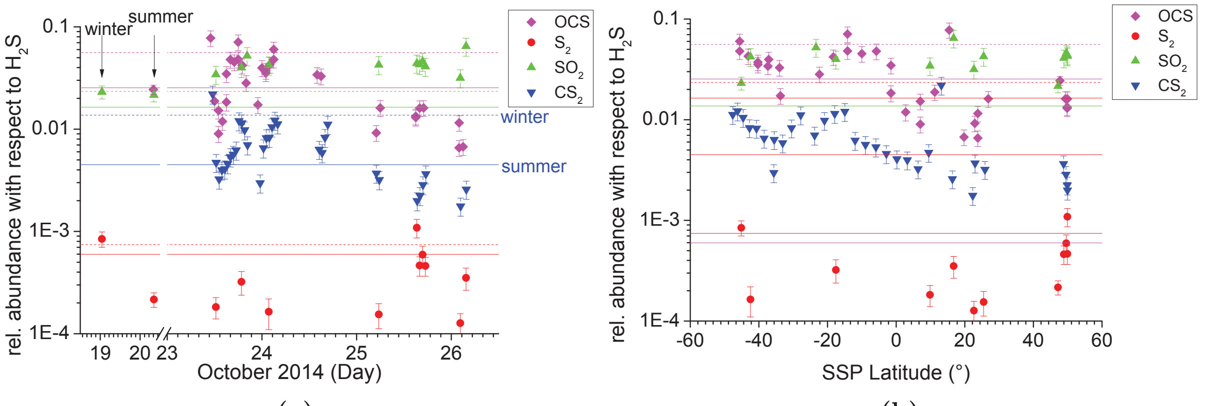

(a)

(b)

Fig. 4.1.1: Abundances for OCS, S_2, SO_2, and CS_2 relative to H_2S during the October 19th and 26th 2014 when Rosetta was within 10 km distance to 67P/Churyumov-Gerasimenko.

Table 4.1.1: Mean values (± 1 σ without considering the uncertainties due to the sensitivity) of the relative abundances of sulfur bearing species measured in October 2014 at 67P relative to H_2S. Beside the mean of all values the mean for measurements below -20° and above 20° sub satellite latitude are given.

	OCS/H_2S	S_2/H_2S	SO_2/H_2S	CS_2/H_2S
all	$(2.98 \pm 1.92)\cdot 10^{-2}$	$(3.82 \pm 3.10)\cdot 10^{-4}$	$(4.04 \pm 1.14)\cdot 10^{-2}$	$(6.18 \pm 3.30)\cdot 10^{-3}$
$\varphi <$ -20	$(3.85 \pm 1.14)\cdot 10^{-2}$	$(3.36 \pm 4.47)\cdot 10^{-4}$	$(4.60 \pm 8.64)\cdot 10^{-2}$	$(8.33 \pm 2.61)\cdot 10^{-3}$
$\varphi >$ 20	$(1.60 \pm 0.73)\cdot 10^{-2}$	$(4.43 \pm 3.35)\cdot 10^{-4}$	$(4.31 \pm 1.69)\cdot 10^{-2}$	$(2.77 \pm 0.79)\cdot 10^{-3}$

4.1.2 Isotopic Ratios of Sulfur Bearing Species

Basing on an exemplary mass spectrum acquired at a certain integer mass to charge ratio the typical signal during the observation period and the identified species are presented. Then the obtained isotope fractionation in ^{33}S and ^{34}S will be shown with respect to the sub satellite latitude in order to have framework for first observations. The sulfur three isotope plots will be presented in the discussion where the obtained results will be discussed in context of what is known about sulfur isotope fractionation in the Solar System.

4.1.2.1 H_2S

In figure 4.1.2 exemplary spectra for m/z 34, 35, and 36 u/e with the identification of the peaks are shown. For the spectra at m/z 34 u/e are unambiguously identified: ^{34}S a fragment of $H_2{}^{34}S$ and other S-bearing species, $H^{33}S$ as well most it expected to be a fragment of $H_2{}^{33}S$, H_2S, and H_2O_2. The right shoulder between H_2S and H_2O_2 could be due to PH_3, $^{18}O^{16}O$, or a mixture of both which has not been investigated in this study but the presence of a peak in the right shoulder has been taken into account at fitting the spectra. Figure 4.1.2 (b) shows the spectra at m/z 35 u/e and identified are: ^{35}Cl a fragment of at least HCl, $H^{34}S$ again main contributor is most likely a fragment of $H_2{}^{34}S$, and $H_2{}^{33}S$.

The discussion of the peak between $H_2{}^{33}S$ and 35 u/e follows after the presentation of the isotopic ratios of sulfur in H_2S. In figure 4.1.2 (c) one can see the peaks due to ^{36}Ar (not labeled) at the left foot of $H^{35}Cl$, $H_2{}^{34}S$ and C_3. All the listed peaks were taken into account at fitting the spectra in order to not under or overestimate the amount of measured H_2S isotopologues. $H_2{}^{36}S$, which is overlapped by $H^{37}Cl$, and its fragments could not be identified in the analyzed data.

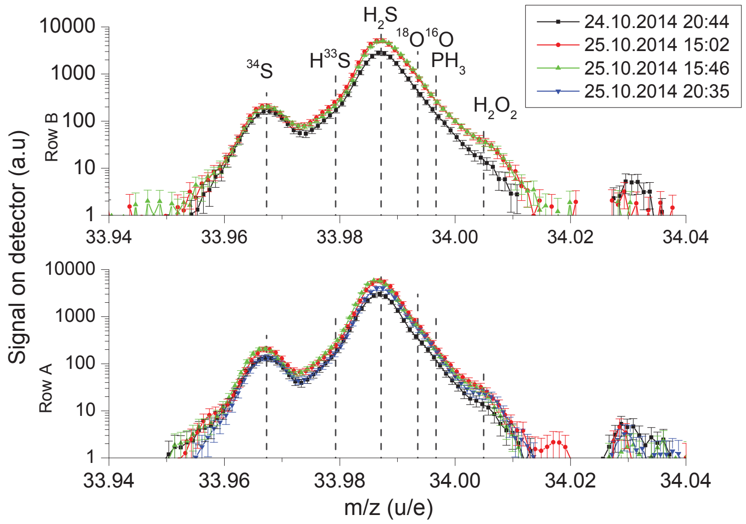

(a) m/z 34 u/e

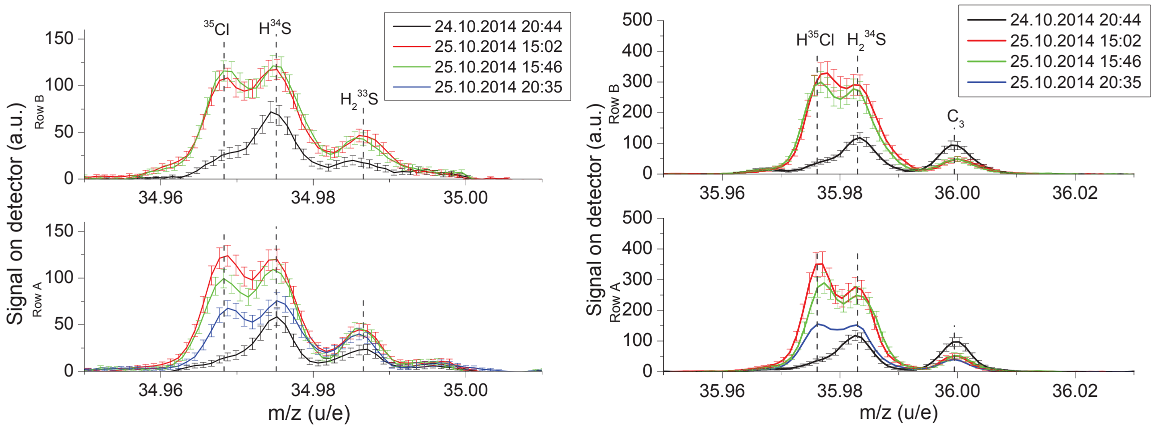

(b) m/z 35 u/e **(c)** m/z 36 u/e

Fig. 4.1.2: Exemplary spectra of H_2S isotopologues acquired at 10 km distance to the comet in October 2014.

In figure 4.1.3 δ^{34}S and δ^{33}S in H_2S are drawn with respect to the sub satellite latitude for the analyzed spacecraft terminator orbit in October 2014. Several points are remarkable in this plot; first the values do not scatter around 0, second there seems to be two subsets with boundary around 20°, third the coverage of δ^{33}S in the interval from -30° to 30° is not as good as for δ^{34}S. The gap between -10° to 10° is due to low signal intensity for $H_2{}^{33}S$ while the gap between 30° and 40° is due to a change in the measurement mode of DFMS. Based on this data set the weighted mean values can be calculated for all data points, the linked measurements for which H_2S, $H_2{}^{33}S$, and $H_2{}^{33}S$ were measured within 2 minutes, and for the two subsets. The weighted mean values of the linked data set are δ^{34}S = -50 ± 22‰ (1σ 92‰) and δ^{33}S = -306 ± 31‰ (1σ 114‰). The other values are given in the compilation in table 4.1.3 and will be discussed later.

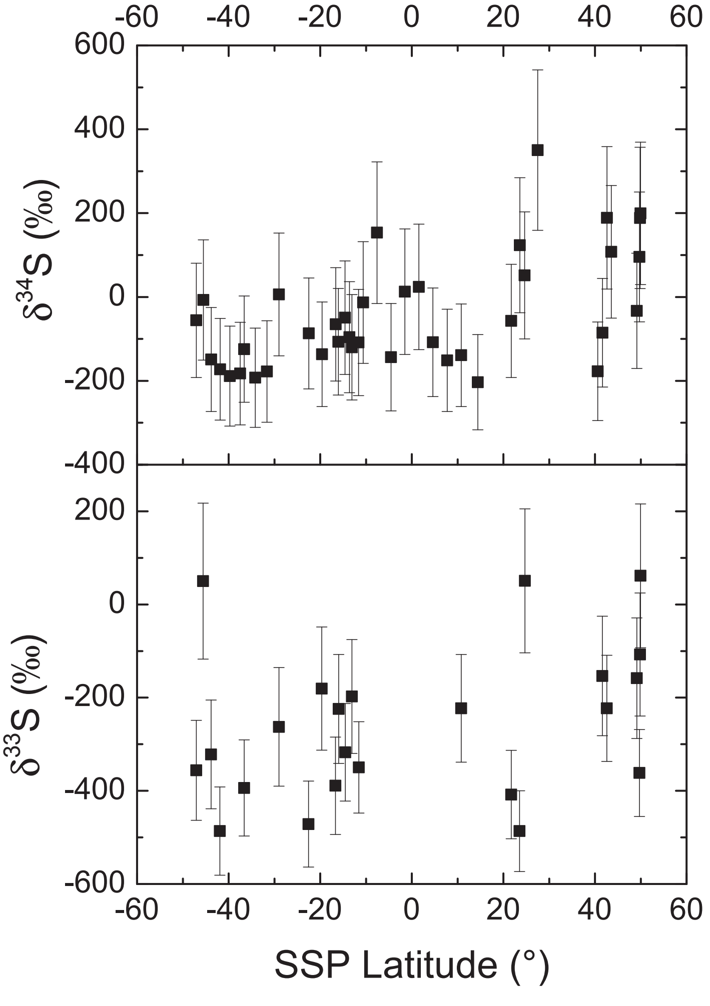

Fig. 4.1.3: In the upper and lower panel the isotope fractionation for ^{34}S and ^{33}S in H_2S with respect to the sub satellite latitude for one orbit at ~10 km distance to the center of Churyumov-Gerasimenko in October 2014 are shown. The δ values are given with respect to the Vienna Diablo Cañon Troilite (V-CDT) (Ding et al., 2001).

Since both δ^{33}S and δ^{34}S show an increase for latitudes larger than 20° a change in the relative amounts of signal between the species on m/z 34 u/e was thought to be likely. Therefore a comparison of spectra at different latitudes was done for row A at m/z 34 u/e. In figure 4.1.4 the signal normalized to H_2S for 6 different latitudes going from -42° to 50° is displayed. From the graph it can be seen that there are slight changes in the spectrum shape between the different latitudes. However, there is no correlation between overall curve shape and latitude. Solely the appearance of a new species could not be handled by the fit and would therefore result in biased peak areas. However, from fig. 4.1.4 it is evident that no additional peak appears at latitudes above 20°.

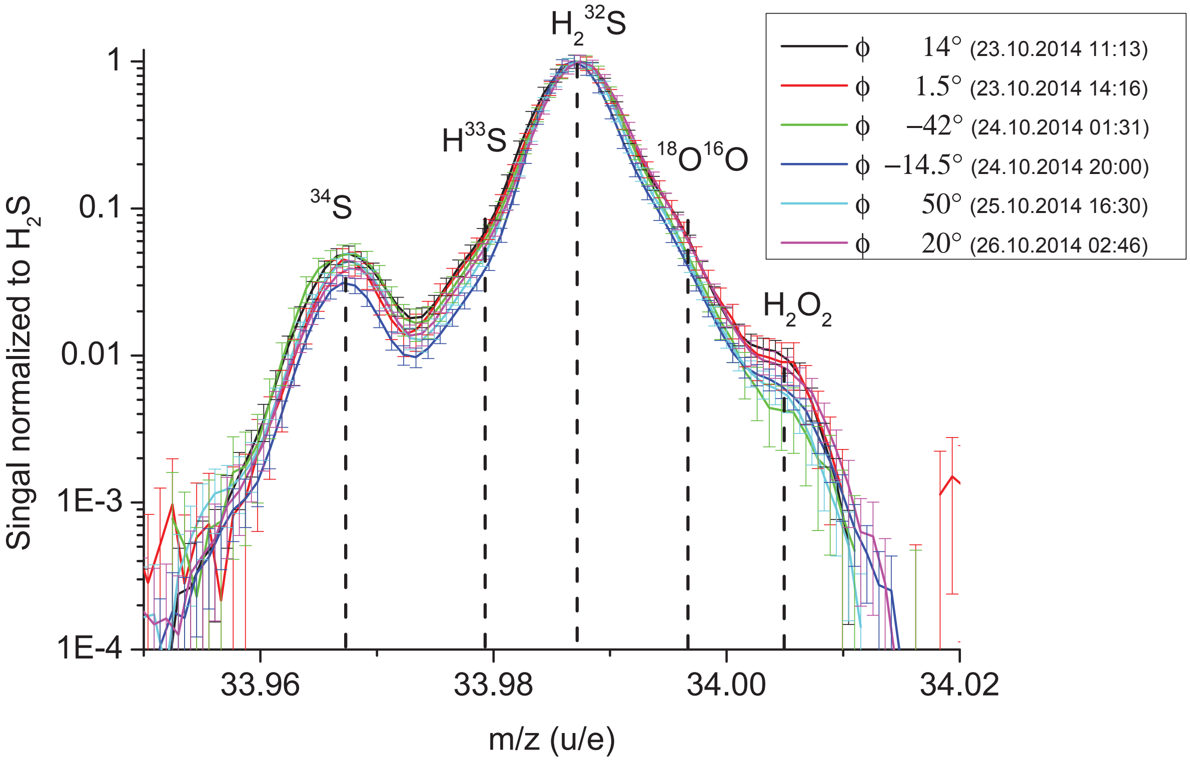

Fig. 4.1.4: Comparison of spectra at m/z 34 u/e for different latitudes during the selected period in October 2014.

To rule out depletion of the MCP as cause for the unexpected isotopic ratios measurements with a shift of the ion beam were done in space in order to measure at different locations of the MCP. Therefore two constraints had to be fulfilled: first the H_2S peak should lay on an area where no strong features are present and second the locations should be within pixel 200 - 300 because further away from the center of the LEDA the beam is less focused. Thus having all October measurements around pixel 270 - 300 (peak center of H_2S and its isotopologues) measurements with shifted ion beam to pixel ~240 and ~210 have been acquired on 8th and 10th of July 2015, respectively. The distance between Rosetta and the nucleus was around 150 km and the entire comet was in the field of view. Although ~20 measurements were done for each ion beam shift only 3 data sets had sufficient signal intensity to see both $H_2{}^{33}S$ and $H_2{}^{34}S$ in the spectra.

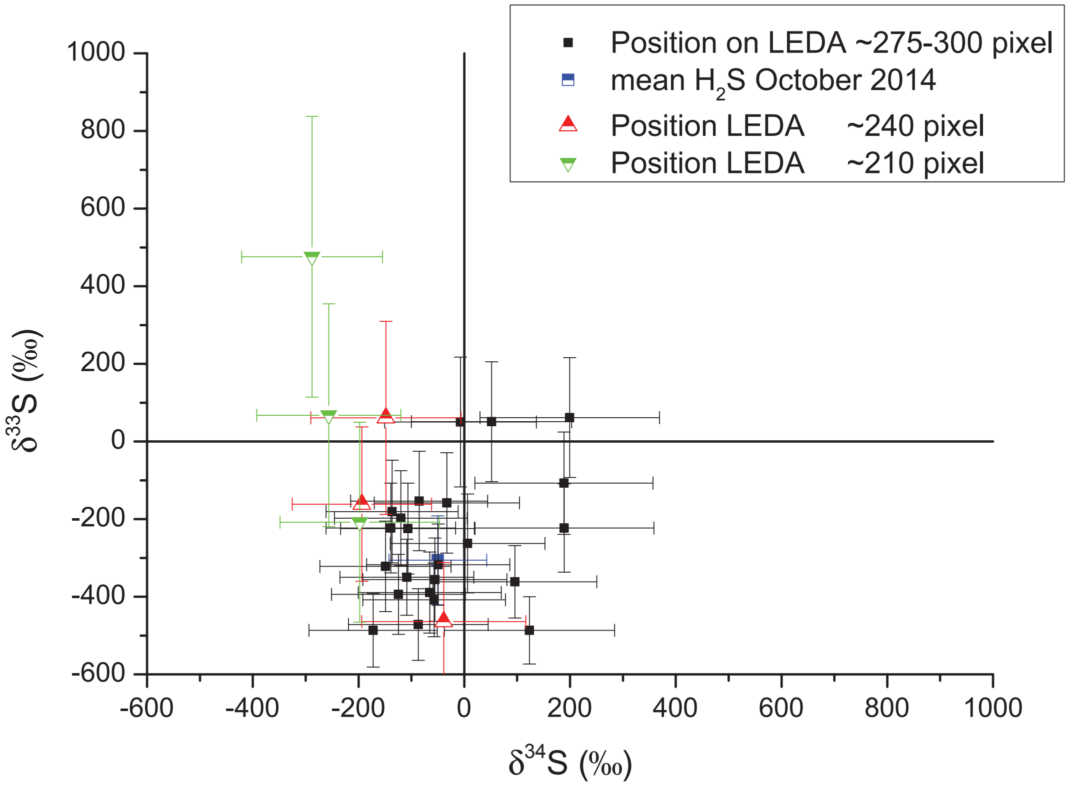

Fig. 4.1.5: Three isotope plot for H_2S with results from October 2014 when Rosetta was in 10 km orbit around the comet (black squares) and from July 2015 when measurements with a shifted ion beam were performed.

In figure 4.1.5 a comparison between the October 2014 and the July 2015 data sets is done. The first set from July 2015 with a shift of the H_2S peaks to pixel ~240 is drawn as half filed red triangles and the three results lay within the spread of the October data (black squares). The second set consists as well of three points drawn as half filled green up side down triangles. The peaks due to H_2S lay around pixel 210 and this data set has a clear outlier with $\delta^{34}S$ = -287 ± 133‰ and $\delta^{33}S$ = 476 ± 362‰. In figure 4.1.6 the used data sets to derive the isotopic ratios for the measurements with a shift of the ion beam are shown. From (a) one can see that the peak height is with ~400 counts roughly a factor of 10 smaller then what has been measured in October 2014. This is due to the over all smaller gas density around Rosetta in July 2015 compared to October 2014 [1]. Thus the signal of the heavier isotopologues of H_2S are as well roughly a factor of 10 lower as it can be seen in (b) and (c) for m/z 35 and 36 u/e, respectively. Because of the low count rate only spectra that had on one of the rows a peak above 5 counts were used. Due to the low signal for the heavier isotopologues of H_2S the uncertainties are rather large for the 6 selected mass spectra sets.

---

[1] The distance between Rosetta and 67P was several hundred kilometers and therefore the density could be lower than in October although the comet was close to its perihelion.

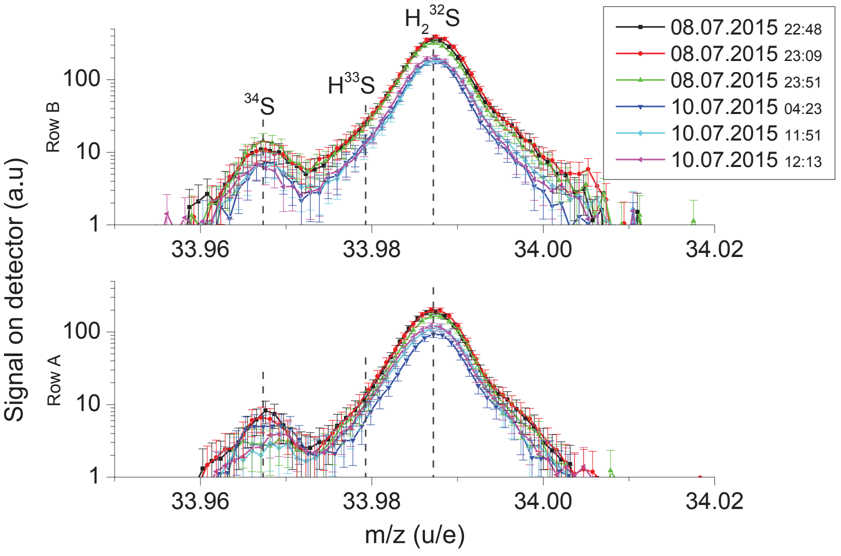

(a) m/z 34 u/e

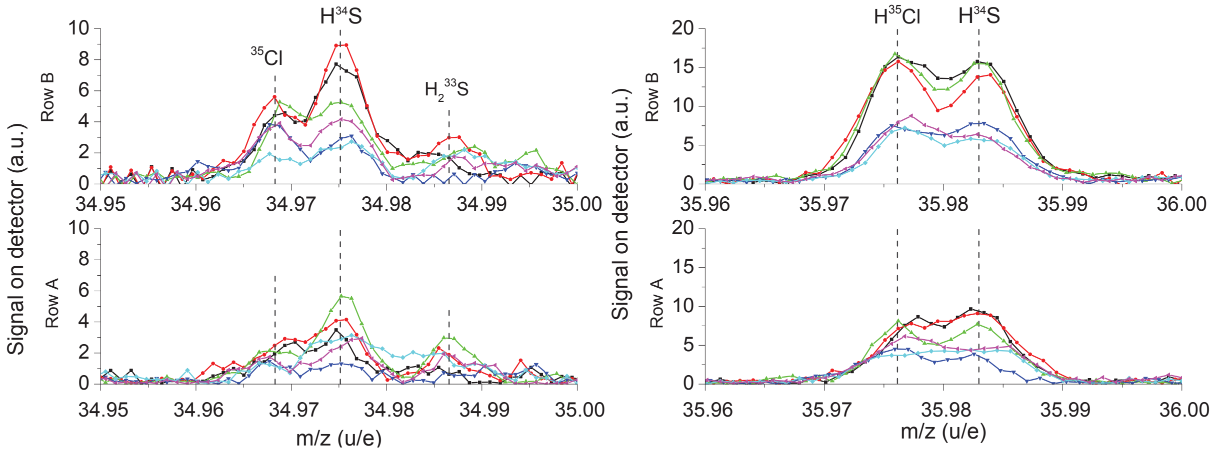

(b) m/z 35 u/e **(c)** m/z 36 u/e

Fig. 4.1.6: A compilation of the used data set with the shift in location on the LEDA. In (b) and (c) the statistical error bars are not drawn for better illustration.

In addition to the determination of sulfur isotopic ratios it has been tried to determine the D/H ratio in H_2S. However, here only a tentative value can be reported since there is an overlap of the HDS peak on m/z 35 u/e with most likely H_3S as it can be seen in fig. 4.1.7. The graph shows two mass spectra of m/z 37 u/e when H_2S had its peak abundance and the location of HDS and H_3S are indicated with dashed lines. One can learn from the graph that next to the peak due to $H_2{}^{33}S$ is a bump that has not the distinct peak shape for MCP/LEDA high resolution spectra and is around the location of HDS and H_3S. HDS and H_3S are too close together to be fitted with two peaks therefore the bump has been fitted with a single peak with the peak center and width as variables. The aim was to check if there are tendencies or if there is a correlation between the derived peak center (x_c) and the D/H ratio assuming that the entire bump is due to HDS. In addition, for the same time frame on m/z 37 u/e might be a peak present due to $HD^{34}S$ (fig. 4.1.8). The two spectra of row A have been used to calculated the D/H ratio under the assumption that the peak around 36.99 u/e is due to $HD^{34}S$ [2] solely.

---

[2] All spectra of m/z 37 u/e for the time stamps 25.10.2015 16:30 and 17:14 are in the appendix

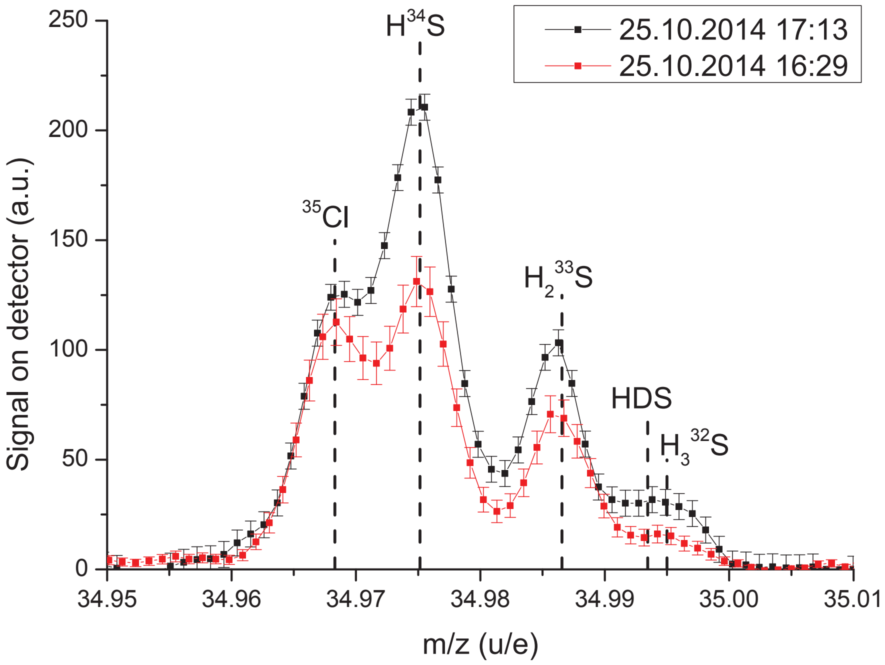

Fig. 4.1.7: Two mass spectra of row A at m/z 35 u/e during the period when H_2S had its peak abundance in October 2014. The location of ^{35}Cl, $H^{34}S$, $H_2{}^{33}S$, HDS, and H_3S are indicated by dashed lines.

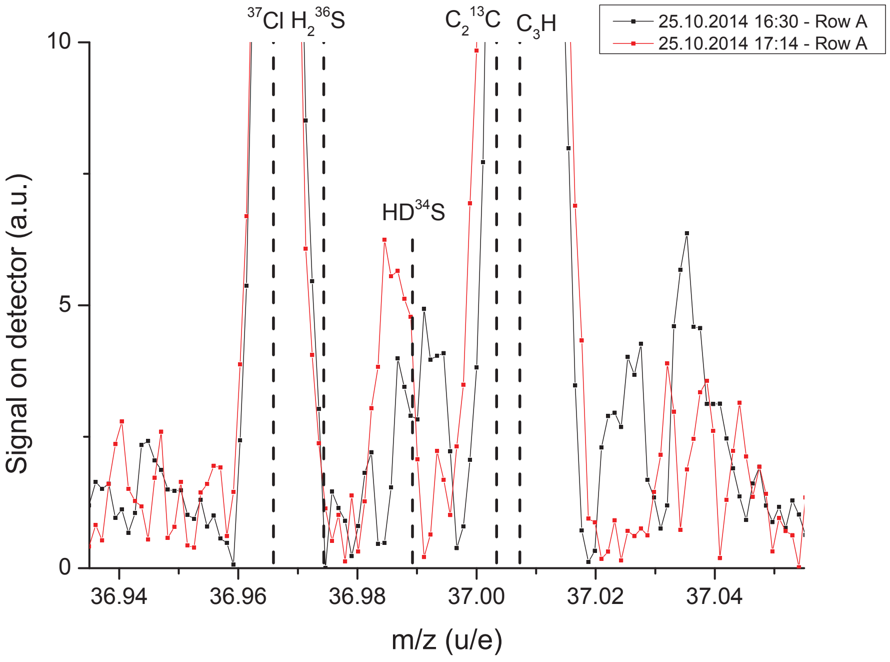

Fig. 4.1.8: Section of two mass spectra of row A at m/z 37 u/e acquired when H_2S had its peak abundance in October 2014. The locations of $H^{36}S$, $HD^{34}S$, $C_2{}^{13}C$, and C_3H are indicated with dashed lines.

(section D).

The resulting D/H ratio under the assumption that the bump on m/z 35 u/e is only HDS (red dots) and that on m/z 37 u/e $HD^{34}S$ (blue dots) relative to the sub satellite latitude are shown in the upper panel of fig. 4.1.9 together with the range for D/H in H_2O for 67P (pale blue box) while the lower panel shows the peak center due to the fit with error of the fit of the bump on m/z 35 u/e. In the upper panel three points are apparent. First except on point (around 24°) all data for the supposedly HDS are above the value D/H in water at 67P of $(5.3 \pm 0.7)\cdot 10^{-4}$ (Altwegg et al., 2015). Second the ratio for the peak at m/z 37 u/e is about a factor 2.7 lower than D/H in water and is therefore in the range of the terrestrial D/H ratio. Third there seems to be a correlation between the sub satellite latitude and the derived ratio; for negative latitudes the value is larger than for positive. The weighted mean for supposedly D/H in HDS is for latitudes smaller than -20° $(1.30 \pm 0.02)\cdot 10^{-3}$ ($1\ \sigma$), for latitudes above -20° $(9.98 \pm 0.07)\cdot 10^{-4}$, and the total weighted mean is $(9.64 \pm 0.19)\cdot 10^{-4}$.

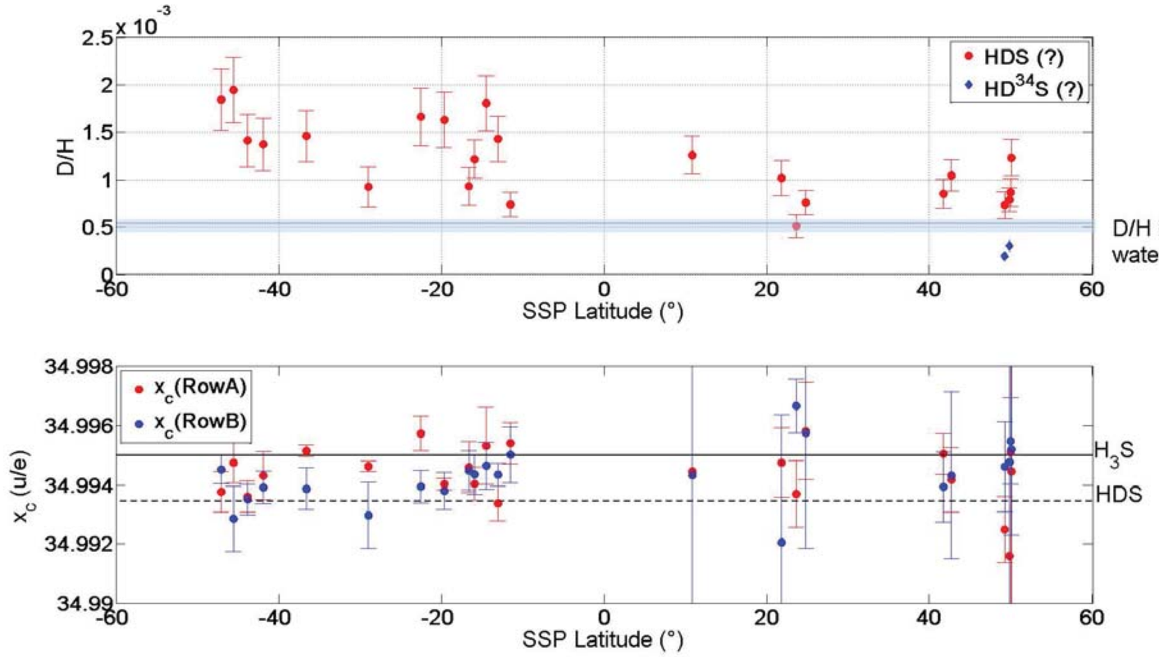

Fig. 4.1.9: The upper panel shows the D/H ratio assuming the peaks seen on m/z 35, and 37 u/e are solely due to deuterated H_2S (for more details see text). The lower panel shows the peak center of the bump m/z 34.95 u/e determined by fitting; in red are the results for row A and in blue for row B.

4.1.2.2 OCS

The identification of peaks is more difficult for OCS and its isotopologues than for H_2S. This is illustrated on an exemplary spectrum that is shown for m/z 60 u/e in fig. 4.1.10 and for m/z 62 u/e where several are shown in fig. 4.1.12. The data set in this figure represents the overall maximal measured amount of OCS till end of 2014 and the maximum during the previously selected period. The asymmetric peak shape implies that there is at least one additional peak around 59.975 u/e. The three most likely species are CHOP, C_2HCl, and N_2S (grey label) whereas CHFSi (59.9826u/e) is rather unlikely. To check which one is the most likely species one can search for the isotopologues or fragments on other masses. CHOP and C_2HCl are unlikely because COP and C_2Cl are not present on

59 u/e as it can be seen in fig. 4.1.11. For the remaining one, N_2S, the only way to check is to look for $N_2{}^{34}S$ on m/z 62 u/e.

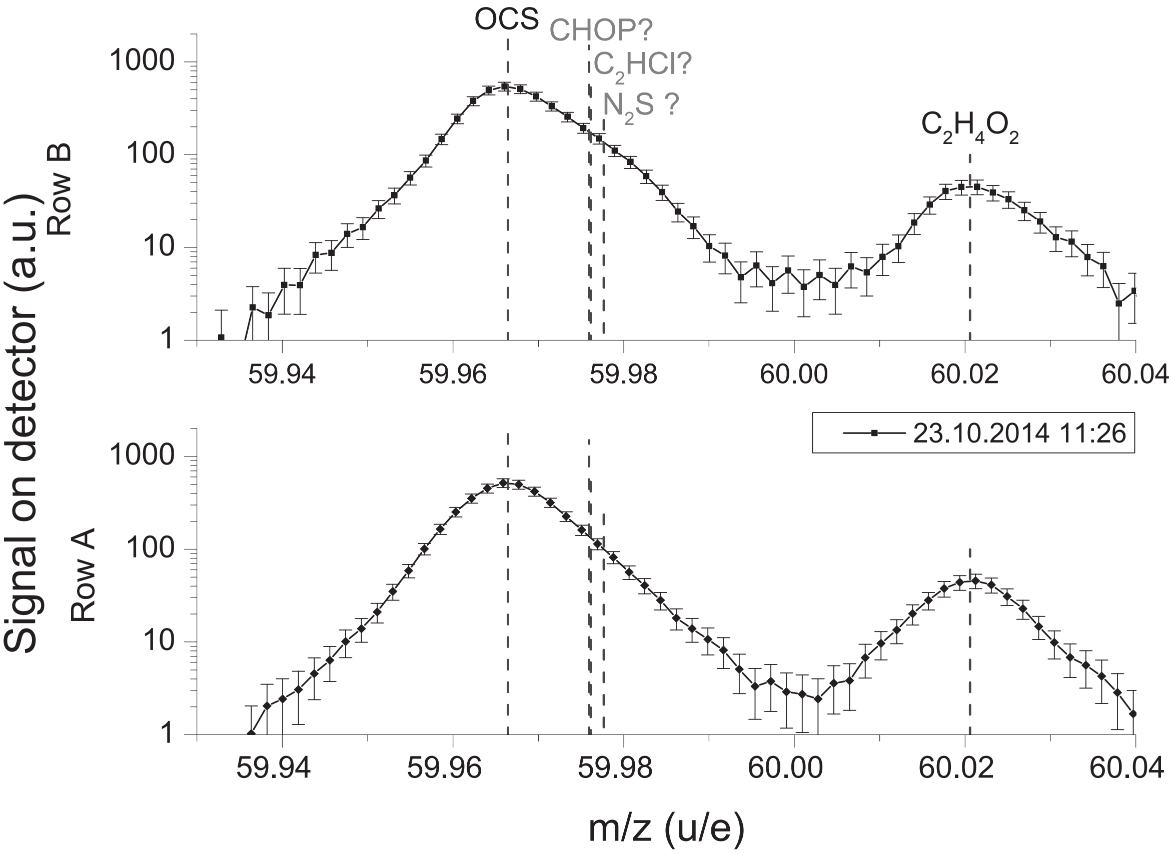

Fig. 4.1.10: Mass spectrum at m/z 60 u/e at peak intensity of OCS during October 2014. Identified species are displayed in black while unidentified are given in grey.

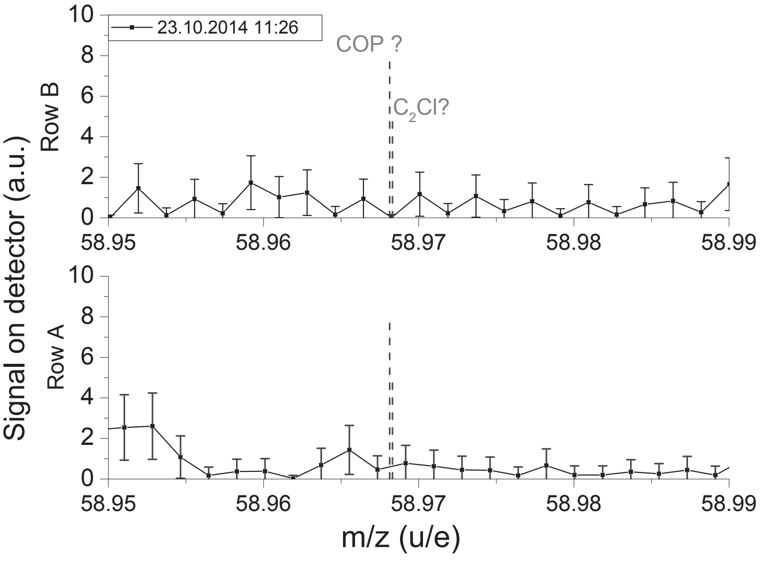

Fig. 4.1.11: Mass spectra at m/z 59 u/e at peak intensity of OCS during October 2014. The locations of COP and C_2Cl are indicated with a line.

In figure 4.1.12 the spectra of m/z 62 u/e used for the determination of δ^{34} are shown. As the peak of $OC^{34}S$ is asymmetric other species have to be present on the right side. If terrestrial isotopic ratios are assumed except of $OC^{34}S$ the shoulders on the right side should be due to $O^{13}C^{33}S$ and $^{17}O^{13}CS$ (for values see table 4.1.2) and $N_2{}^{34}S$. As it is not possible to unambiguous identify the peaks on the right side of $OC^{34}S$ for fitting this peaks width was set to the value obtained by fitting OCS.

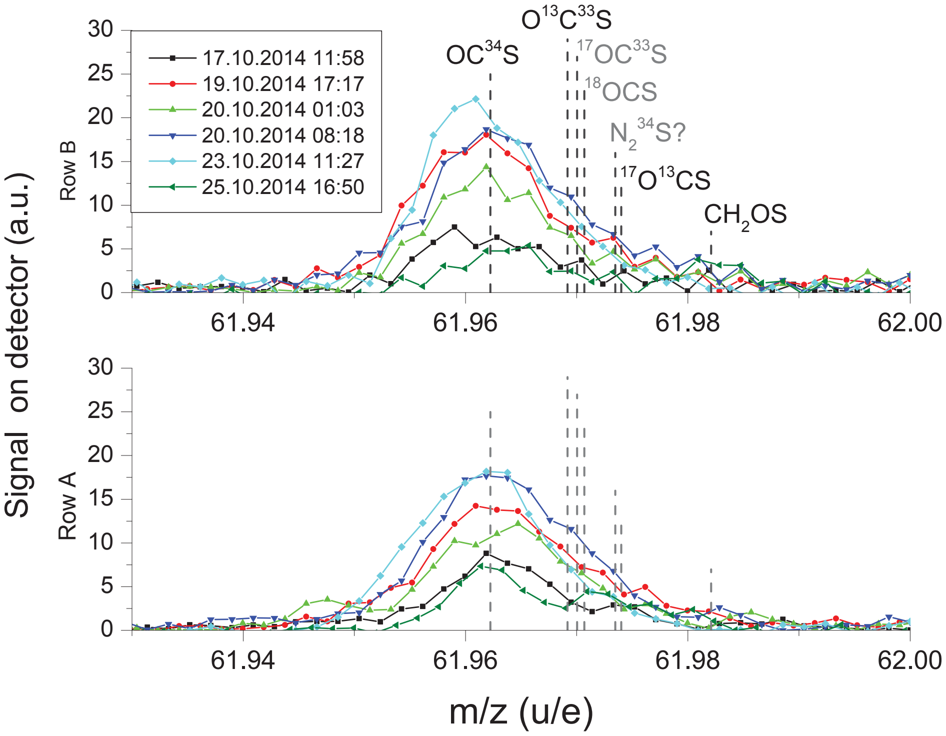

Fig. 4.1.12: Mass spectra of row A at m/z 62 u/e at peak intensity of OCS during October 2014 and 5 selected data sets (for more details see text). The location of the isotopologues of OCS, $N_2{}^{34}S$ and CH_2OS are indicated with a dashed line. Unlikely species are written in grey.

Table 4.1.2: Relative abundance of OCS isotopologues assuming $^{12}C/^{13}C$ to be VPDB and for oxygen isotopes SMOV isotopic ratios are assumed.

Molecule	Relative abundance
$OC^{34}S$	1
$O^{13}C^{33}S$	0.372
$O^{17}OC^{33}S$	0.057
$O^{18}OCS$	0.059
$O^{17}O^{13}CS$	0.338

Unfortunately the signal of OCS was very low during the selected period and rarely a sufficient signal height was reached for the heavy isotopologues therefore the entire period in October when Rosetta was within 10 km distance to the center of the nucleus was scanned for high values of OCS. All together 41 sets were analyzed, 32 from the selected period and 11 around the diurnal maxima during the 10 km period. However, only with

5 data sets it was possible to determine the $^{32}S/^{34}S$ isotopic ratio. In fig. 4.1.12 the 5 spectra used to determine $OC^{34}S$ are shown and in addition the maximal signal on the 25.10.2014. From the graph it can be seen that not only $OC^{34}S$ is present for there is at least one other peak on the right side of $OC^{34}S$. Since it is already difficult to distinguish the two peaks in the data set of 17.10.2014 11:58 a lower limit for the peak height has been set; only data sets which have a peak height on either row A or B which is higher than 10 counts were taken into account for the calculation of $^{32}S/^{34}S$. The results with respect to sub satellite latitude are shown in fig. 4.1.14. The weighted mean for the linked measurements of $\delta^{34}S$ is -252 ± 39‰ (1σ 77 ‰), which is even a larger enrichment in ^{32}S than seen in H_2S.

For $^{32}S^{33}S$ in OCS only tentative values are given. The difficulties were that $OC^{33}S$ and $O^{13}CS$ can not be separated. In addition an unidentified species is present to the right of $O^{13}CS$. For illustration the mass spectrum of m/z 61 u/e at the peak intensity of OCS in October 2014 is shown in fig. 4.1.13. Since $OC^{33}S$ and $O^{13}CS$ can not be separated the total signal has been fitted with two peaks; one for the $OC^{33}S$ plus $O^{13}CS$, and the other one for the unidentified species. Then the ratio $^{12}C/^{13}C$ has been assumed to be terrestrial i.e. VDPB and the signal has been corrected for $O^{13}CS$. The resulting isotope fractionation for ^{33}S is displayed in fig. 4.1.14. From this graph it can be seen that the resulting values spread over almost 200% in $\delta^{33}S$ going from -803 ± 429‰ to 1199 ± 877‰. The weighted mean for the presumably isotope fractionation of ^{33}S is $\delta^{33}S$ = -858‰ ± 124‰ (1σ 215‰).

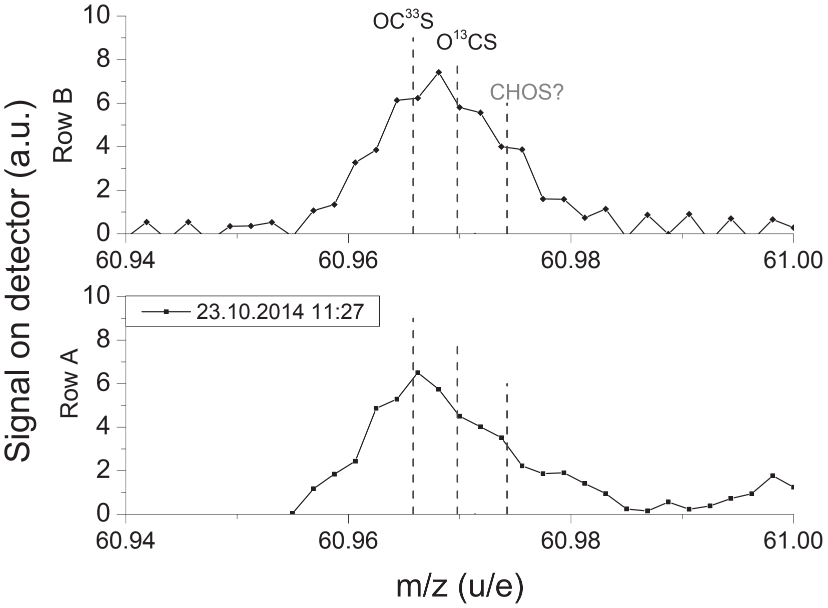

Fig. 4.1.13: Mass spectra of row A at m/z 61 u/e at peak intensity of OCS during October 2014. The location of the isotopologues of OCS and possible other species are indicated with a dashed line.

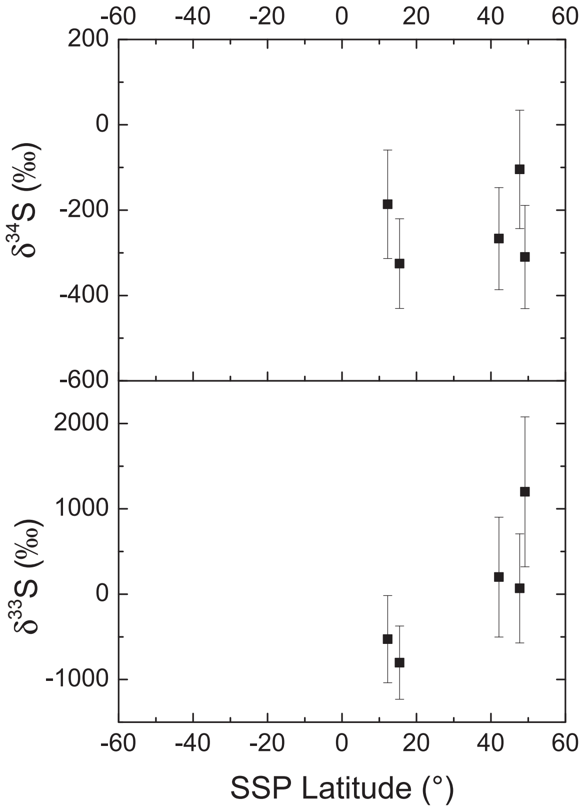

Fig. 4.1.14: In the upper the isotope fractionation for ^{34}S in OCS with respect to the sub satellite latitude for one orbit at ~10 km distance to the center of Churyumov-Gerasimenko in October 2014 is shown. The lower panel shows the tentative values ^{33}S in OCS assuming ^{12}C/^{13}C to be VPDB relative to the latitude.

4.1.2.3 S_2

Similar to OCS the signal of S_2 was during the selected period predominantly too small to determine the isotopic ratios of both ^{34}S and ^{33}S therefore the entire period when Rosetta was within 10 km orbit in October 2014 was scanned for data sets which could be used. The scan resulted in having seven data sets all acquired at positive latitudes which had on either row A or B for ^{33}S^{32}S a peak height of at least 2 counts. The mass spectra of the seven set are shown for m/z 65 u/e in fig. 4.1.15. Due to the low signal of S_2 and the low ratio S_2/SO_2 the peak shape is not distinct and only a bump can be seen which made determination of peak area of ^{33}S^{32}S difficult. Additionally there might be more peaks present then just the isotopologues of S_2 and SO_2 with ^{33}S as it can be seen in fig. 4.1.15. Due to the difficulties to determine the amount of measured ^{33}S^{32}S only tentative values for the isotopic fractionation are given. The supposedly δ^{33}S and the values for δ^{34}S are displayed in fig. 4.1.16 with respect to the sub satellite latitude. From the upper panel it can be seen that the majority of δ^{34}S seem to group between -750 and -55‰ while the remaining three values show an enrichment in ^{32}S of more than 500‰. For δ^{33}S the spread is even larger going from about 230‰ up to almost 12'000‰. However, the largest two deviations from V-CDT, measured both on October 20th at 12:47 and 14:24 UTC, show the largest uncertainties and have a low signal to noise ratio as it can be seen from fig. 4.1.15.

The weighted mean of the linked measurements is -357 ± 145‰ (1σ 207 ‰) for δ^{34}S while for δ^{33}S the tentative value is 682 ± 423‰ (1σ 670‰).

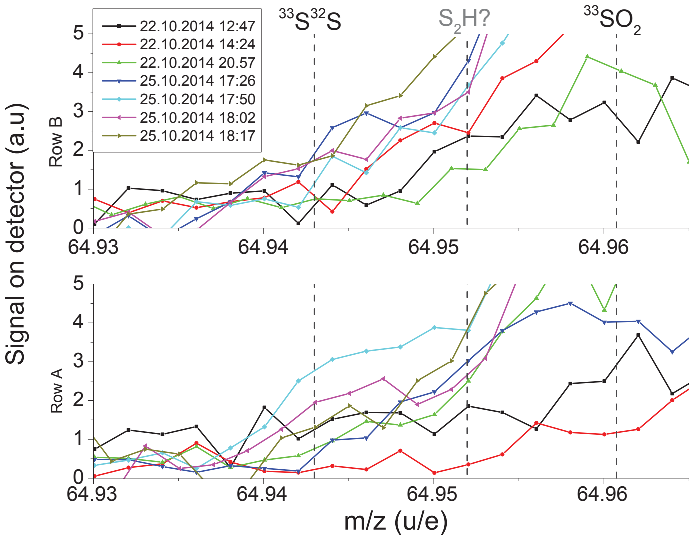

(a) m/z 65 u/e

Fig. 4.1.15: Shown is a section of the mass spectra at m/z 65 u/e used to calculate δ^{33}S during the selected orbit in October 2014.

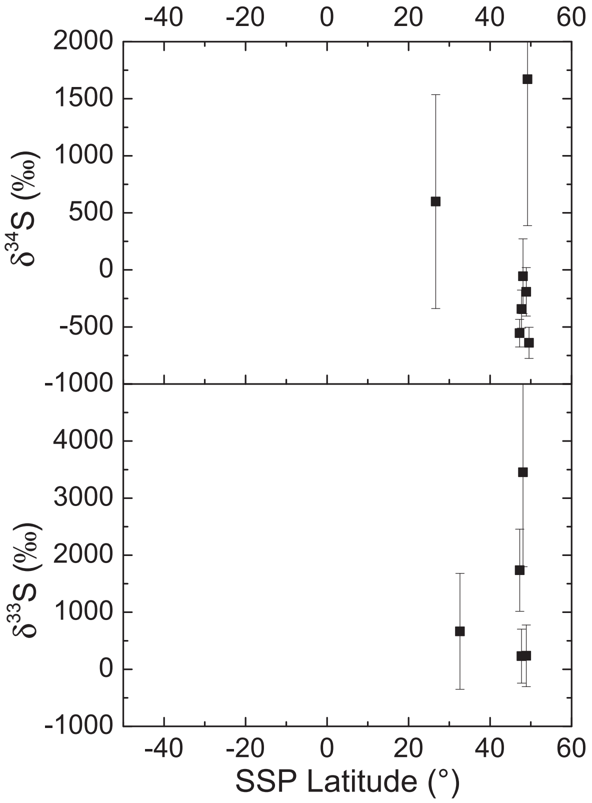

Fig. 4.1.16: The upper panel shows the isotope fractionation ^{34}S in S_2 while in the lower panel only tentative values for the fractionation of ^{33}S are given. Both δvalues are give with respect to the sub satellite latitude for one orbit at 10 km distance to the center of Churyumov-Gerasimenko in October 2014.

4.1.2.4 SO_2

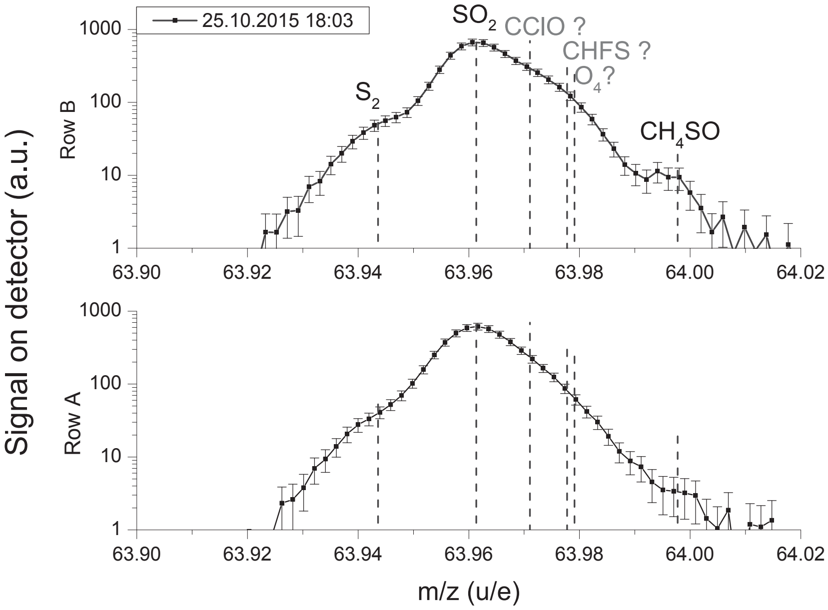

(a) m/z 64 u/e

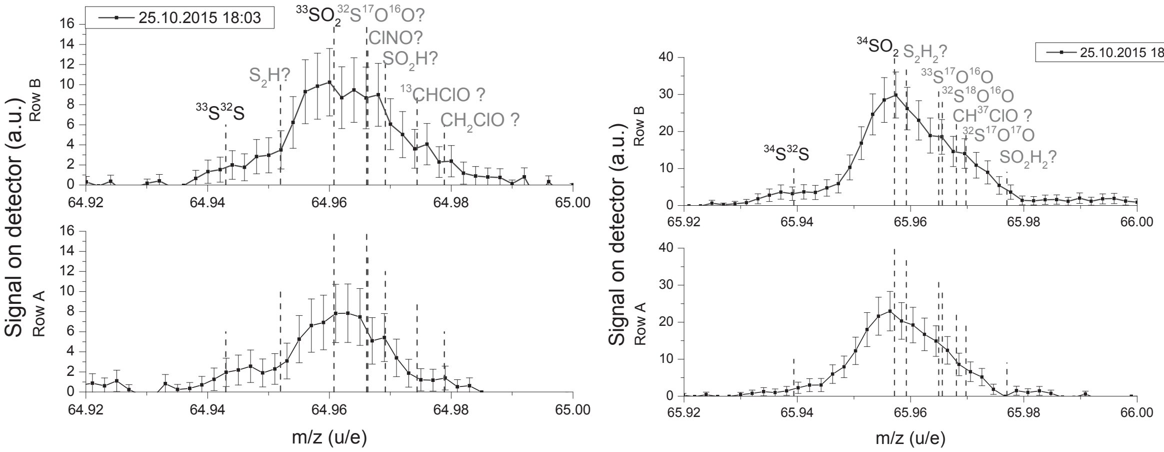

(b) m/z 65 u/e

(c) m/z 66 u/e

Fig. 4.1.17: Exemplary spectra of m/z 64 - 66 u/e during the 10 km orbit in October 2014. The location of an ion is indicated with a dashed line while identified peaks are labeled in black and ambiguous peaks are labeled in grey.

Figure 4.1.17 (a)-(c) show the exemplary mass spectra for SO_2 and its isotopologues with ^{33}S and ^{34}S at m/z 64 u/e - 66 u/e. In each spectrum the identified peaks are labeled in black while the ambiguous ones are labeled in grey. First the seen features for m/z 64 - 66 u/e will be described basing on the graphs in fig. 4.1.17 and then the ambiguous peaks will be discussed.

On m/z 64 u/e is a large peak present due to SO_2 while on its left side the peak due to S_2 is visible. In addition, there is an elevation at about 63.97 u/e which might be due to CHFSO or O_4 and on both rows a small signal which is due to CH_4SO. Comparing row A and B it can be seen that for row A the features due to S_2 and CH_4SO, and the elevation in the right shoulder are less distinct than in the spectra of row B.

On m/z 65 u/e the maximal signal height is 10 counts. In order to fit this signal more peaks have to be present than only $^{33}S^{32}S$, $^{33}SO_2$, and $^{32}S^{17}O^{16}O$.
The maximal signal on m/z 66 u/e is due to $^{34}SO_2$ and accounts for about 30 counts. Besides $^{34}S^{32}S$ and $^{34}SO_2$ there have to be at least two more peaks present besides $^{34}S^{32}S$ and $^{34}SO_2$ in this spectra considering the signal shape.

The mass to charge ratio of the unidentified peak on m/z 64 u/e points to CHFS or O_4 even though both seem to be unlikely. First O_4 is not known to be stable. Second there is no peak present on m/z 63 u/e at the location for CFS, a fragment of CHFS, as it can be seen from fig. 4.1.19. As well a bias due to the LEDA and due to pixel gain correction can be ruled out since the feature is present in spectra acquired at different locations of the LEDA as it can be seen in fig. 4.1.18. In this figure four measurements of m/z 64 u/e acquired at two different days with different location of the center of the ion beam (x_0) on the LEDA are shown. The first two data sets have x_0 ~284 for row A while the other two have x_0 ~274; for row B it is x_0 ~285 and x_0 ~274, respectively. A difference of 10 pixels on m/z 64 u/e is equivalent to ~0.02 u/e and if the peak around m/z 63.98 u/e is due to the LEDA or the pixel gain correction one would expect to have a peak around m/z 64 u/e for the latter two measurements. Since all four measurements show the same curve shape the pixel gain and the LEDA are ruled out to be the cause of the described feature. The location of CHClO is indicated for the discussion of m/z 65 u/e.

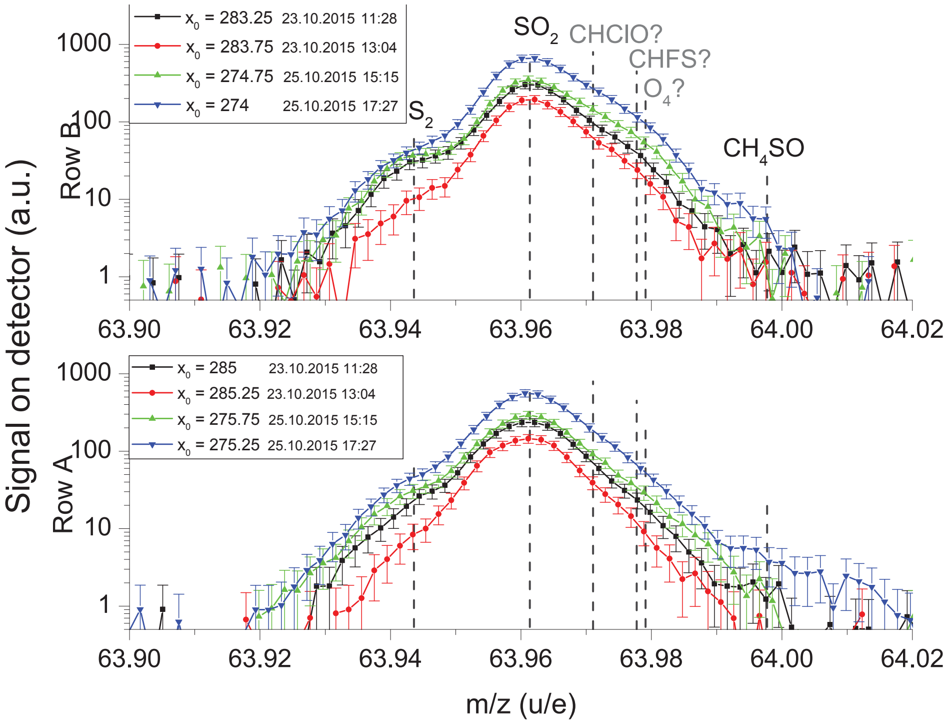

Fig. 4.1.18: Four different measurements of m/z 64 u/e are shown for row A and B in the lower and the upper panel, respectively. The first two and last two measurements were acquired at two different days and were measured with different locations of the ion beam center (x_0) on the LEDA. Identified peaks are labeled in black while for ambiguous features the likely species are indicated in grey.

In (b) between $^{33}S^{32}S$ and $^{33}SO_2$ the curve decreases not as strong as one would expect from having only those two peaks indicating that in between them a signal due to another

species is present. The species best fitting the location of this additional feature is S_2H however it can not be unambiguously identified.
On the right side of $^{33}SO_2$ $^{32}S^{17}O^{16}O$ is located. However, assuming terrestrial ratio for oxygen isotopic ratios the signal should be about 0.5 counts. The signal at 64.97 u/e has a similar height as the peak due to $^{33}SO_2$ thus is significantly higher than 0.5 counts and therefore it seems unlikely to be due to $^{32}S^{17}O^{16}O$. Considering the mass to charge ratio possible other species are ClNO and SO_2H.
The signal at the right most edge of the spectrum could be explained by the presence of either $^{13}CClO$ or CH_2ClO. However, for all of the four species mass spectra below and above m/z 65 u/e have to be checked for the identification. Going back to m/z 64 u/e one can see that it is not possible to see a signal due to CHClO however it might be hidden by SO_2 and the unidentified peak at 63.97 u/e. Assuming the ratio $^{37}Cl/^{35}Cl$ to be terrestrial the signal on m/z 67 u/e would be for ClNO only about 1.7 counts and for CH_2ClO even smaller therefore again the peak can not be unambiguously identified.
For $^{34}SO_2$ a similar situation is present as for $OC^{34}S$ because next to the peak of $^{34}SO_2$ are other peaks which might be due to isotopologues of SO_2 but they can not be resolved and unambiguously identified. Assuming $^{32}S/^{34}S$ to be similar to what has been measured in H_2S and the oxygen isotopic ratios to be terrestrial the abundance of $^{33}S^{17}O^{16}O$ would be about 0.1‰ relative to $^{34}SO_2$, of $^{32}S^{18}O^{16}O$ it would be 8.5%, and of $^{32}S^{17}O_2$ it would be 1.6%. As a consequence those isotopologues are ruled out to be the cause for the signal seen between 65.96 and 65.98 u/e. Based on the mass to charge ratio the peaks would need to create the seen curve shape the possible molecules are S_2H_2, $CH^{37}ClO$, and SO_2H_2. However, again they can not be unambiguously unidentified.

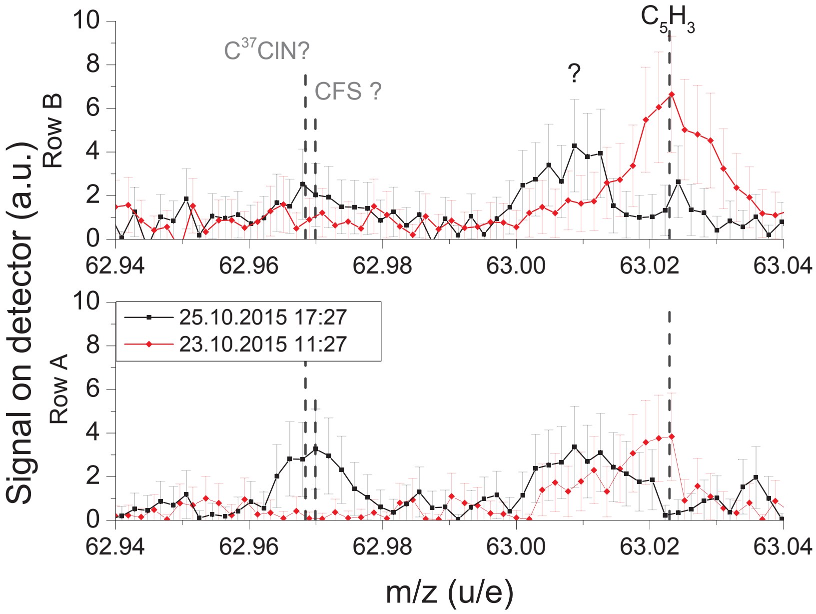

Fig. 4.1.19: Exemplary spectra of m/z 63 u/e. At m/z 63.02 u/e C_5H_3 has been identified while the location of CFS and $C^{37}ClN$ are indicated with dotted lines. For better illustrations statistical error bars are not drawn.

Since not all features seen in the mass spectra of m/z 64 u/e - 66 u/e could be linked to a species the features have been fitted with the peak center as a variable. As a consequence on m/z 64 u/e it was assumed to have four peaks - S_2, SO_2, CH_4SO, and an unidentified peak, on m/z 65 u/e as well the fit was done assuming four peaks - besides $^{33}S^{32}S$ and $^{33}SO_2$ a peak was assumed to be between the two and one in the shoulder of $^{33}SO_2$, and on m/z 66 u/e again four peaks were assumed - besides $^{34}S^{32}S$ and $^{34}SO_2$ two peaks were assumed to be on the right side of $^{34}SO_2$.

In figure 4.1.20 the isotope fractionation of ^{34}S and ^{33}S in SO_2 are shown in the upper and the lower panel on the left side, respectively. In addition, the left two panels show the section of the right panels between sub satellite latitude 40° and 55°. As for H_2S, OCS and S_2 the highest signal was between 40° - 60° sub satellite latitudes. Though four data sets $\delta^{34}S$ could be derived for sub satellite latitudes below 40°. All values for δ^{34} lay within -320‰ and 300‰. The spread for data measured above 40° ranges from -169‰ to 242‰ and is smaller than the overall spread. δ^{33} could only be determined for latitudes larger than 20° and they range from -437 to 219‰. However, more than two third of the data lay between -169 and -42 ‰.
The weighted mean of δ^{34} is -68 ± 44‰ (1σ 130‰) and of δ^{33} it is -131 ± 53‰ (1σ 119‰).

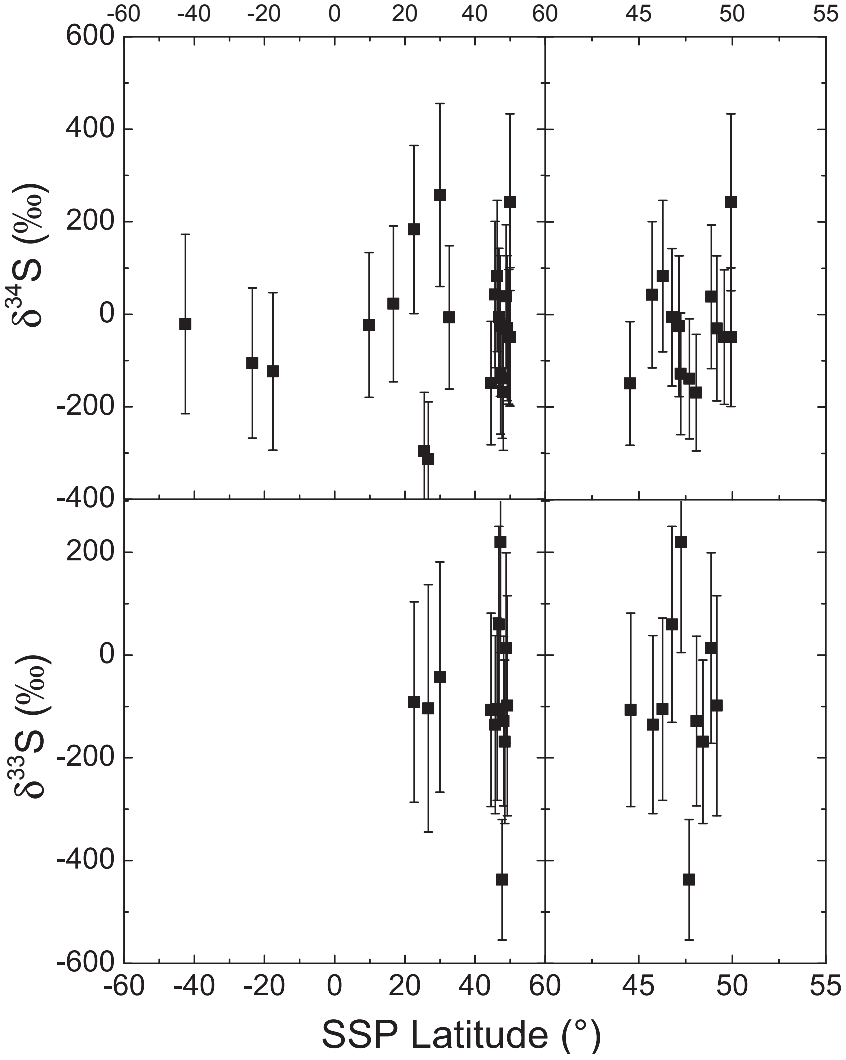

Fig. 4.1.20: Shown are the isotope fractionation for ^{34}S and ^{33}S resp. in SO_2 with respect to the sub satellite latitude during the 10 km orbit around Churyumov-Gerasimenko in October 2014. The left panels show the entire latitude range while the right panels display a section ranging from 40° to 55°.

4.1.2.5 CS_2

Figure 4.1.21 (a)-(c) show exemplary spectra of m/z 76, 77, and 78 u/e resp. which were acquired on the 23rd of October in 2014 at 11:33 UTC and at 15:59 UTC. The difference in signal height is roughly a factor of 10 and they represent the minimal and the maximal signal in the selected period. The determination of the mass scale is more difficult for m/z larger than 69 u/e because the post acceleration increases from -50 V to -1000 V for HR mode and the anode on which it is applied is highly asymmetric (for more details see section 1.9.3). However, it is still possible to identify molecules due to their fragmentation pattern and only for few peaks an unambiguous identification is not possible yet.
On m/z 76 u/e could be identified CS_2, C_5O, and C_6H_4. In addition, there seems to be an unidentified peak around 76.90 u/e. On m/z 77 u/e are the peaks present due to $C^{33}S^{32}S$, $^{13}CS_2$, C_5OH, C_6H_5, and there might be an unidentified peak around 77.06 u/e. On m/z 78 u/e peaks are present due to $CS^{34}S$, C_5H_2O, and C_6H_6.

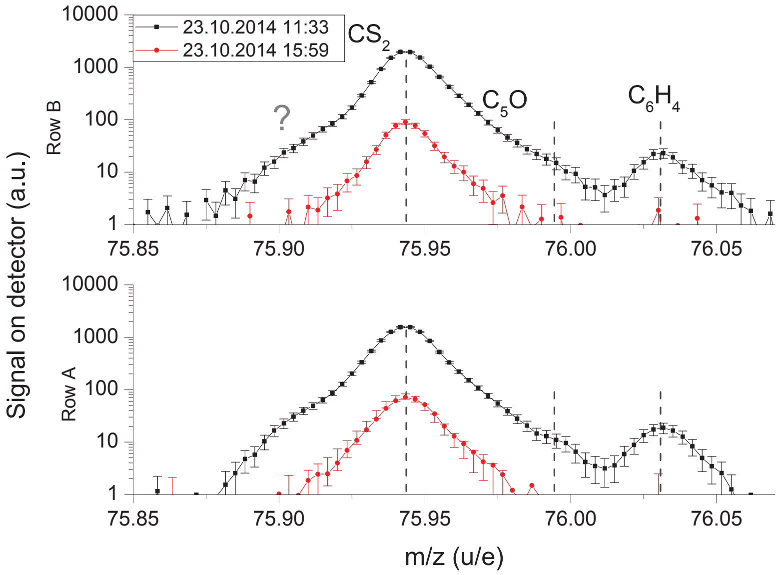

(a) m/z 76 u/e spectrum

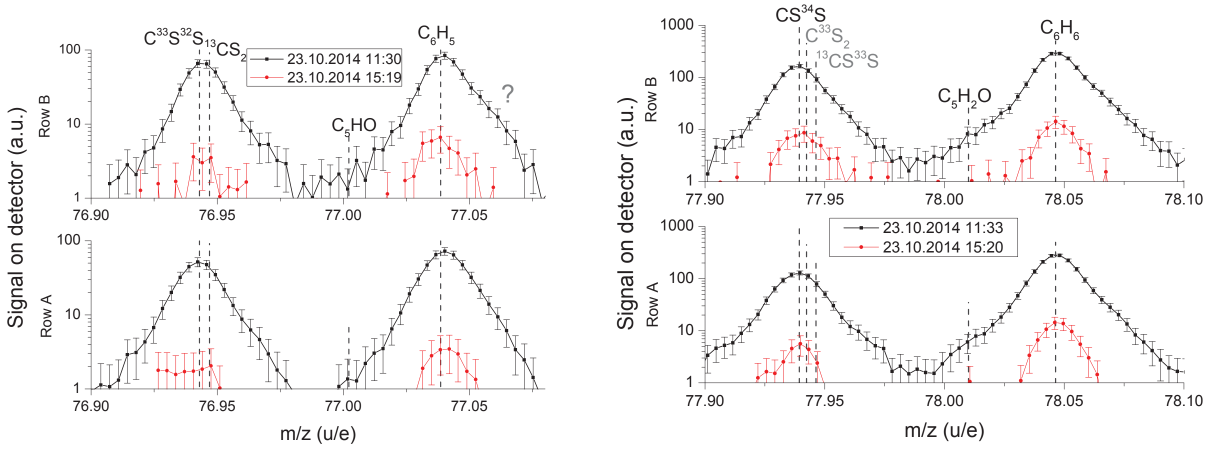

(b) m/z 77 u/e spectrum

(c) m/z 78 u/e spectrum

Fig. 4.1.21: Exemplary spectra of CS_2. (a)-(c) show exemplary mass spectra for m/z 76 - 78 u/e acquired in the period when Rosetta was within 10 km distance to Churyumov-Gerasimenko. Species unambiguously identified are labeled in black and the other in grey.

The molecule with the closest mass to charge ratio to the unidentified peak on m/z 76 is AsH with 75.92887 u/e which gives a difference in m/z between the peak and the species of ~0.03 u/e and therefore AsH has been ruled out. On m/z 77 u/e the peaks of $C^{33}S^{32}S$ and $^{13}C^{32}S_2$ overlap which can not be resolved with a fit. Fortunately this is the sole interference at this mass. Theoretically on m/z 78 u/e there should be the isotopologues $CS^{34}S$, $C^{33}S_2$, and $^{13}C^{32}S^{33}S$. However, assuming $^{12}C/^{13}C$ to be VPDB and $^{32}S/^{33}S$ as it has been seen in H_2S at 67P the abundances of $C^{33}S_2$ and $^{13}C^{32}S^{33}S$ relative to $CS^{34}S$ are 0.04% and 0.15%, respectively. Therefore their contribution to the peak is negligible. As a consequence the signal on 76 u/e has been fitted with two peaks in order to take into account the unidentified peak while for the signal on m/z 77 and 78 u/e only a single peak was fitted. To counteract the interference of $^{13}C^{32}S_2$ for $C^{33}S^{32}S$ the ratio $^{12}C/^{13}C$ has been assumed to be like VPDB since no significant depletion of C is known for comets.

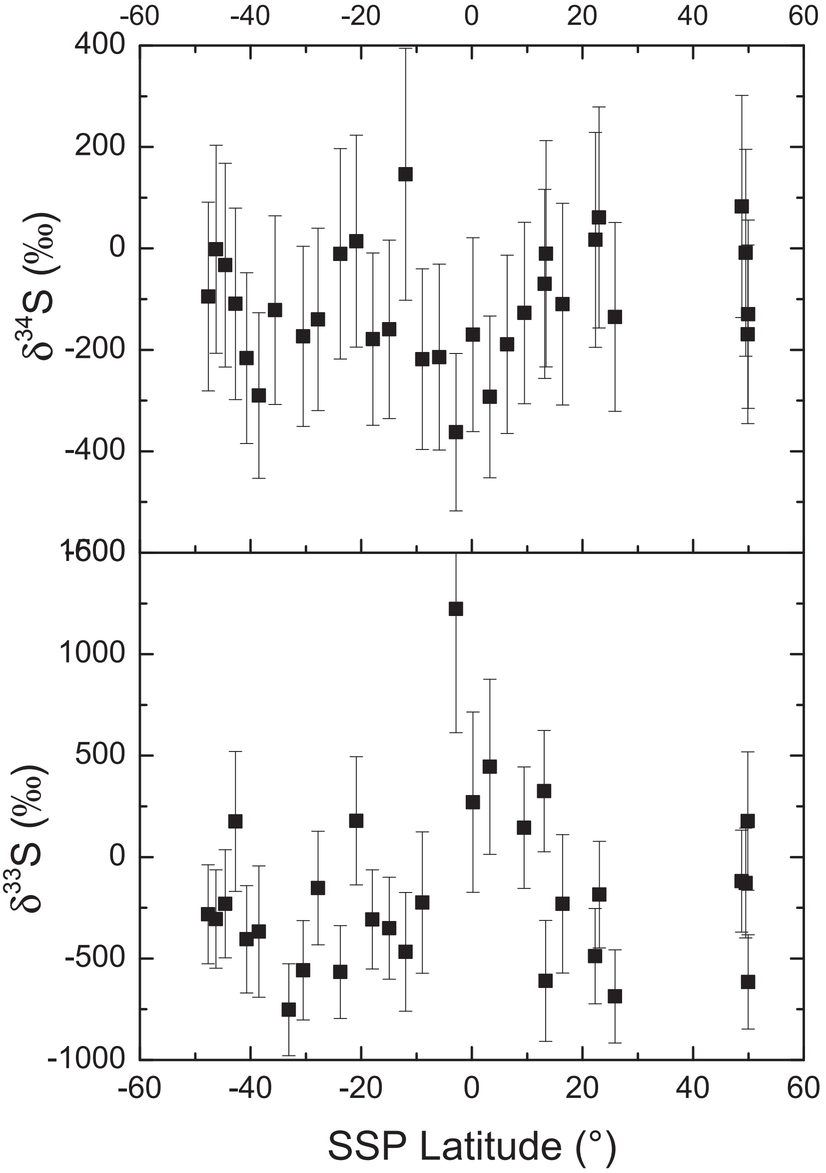

Fig. 4.1.22: In upper and the lower panel the isotope fractionation for ^{34}S and ^{33}S resp. in CS_2 are shown with respect to the sub satellite latitude during the 10 km orbit around Churyumov-Gerasimenko in October 2014.

The resulting isotope fractionation for ^{33}S and ^{34}S with respect the sub satellite latitudes are shown in fig. 4.1.22. Similar to H_2S the signal intensity for the heavy isotopologues of CS_2 was high enough over a wide range during one spacecraft terminator orbit in October 2014 to be detected. Only between 30° - 50° data is missing because DFMS was sampling another mass range. The resulting values for δ^{34}S spread between -400 and 200‰ while the spread of δ^{33}S is even larger going from -800 to 500‰ omitting the outlier at δ^{33}S 1223 ± 610‰. From the upper panel of fig. 4.1.22 one can learn that δ^{34}S is for latitudes below 0° around -100‰ while for latitudes above 10° the values seem to scatter around 0. In contrast all values for δ^{33}S except a group between 0°-10° scatters around -400‰. The mean value of linked measurements except the outlier in the selected period is $\delta^{34}S = -276 \pm 55$ ‰ (1σ 238‰) and $\delta^{33}S = -114 \pm 21$ ‰ (1σ 90‰).

Table 4.1.3: Compilation of weighted mean sulfur isotopic ratios and deviations from V-CDT for H_2S, OCS, S_2, SO_2, and CS_2 for linked data sets and all available data in this study. As well those values were calculated for the two sub sets of H_2S and CS_2.

Species	$^{32}S/^{34}S \pm \sigma_{mean}$	1σ	$^{32}S/^{33}S \pm \sigma_{mean}$	1σ	$\delta^{34}S \pm \sigma_{mean}$	1σ	$\delta^{33}S \pm \sigma_{mean}$	1σ
H_2S - linked	23.8 ± 0.5	2.3	183 ± 8.1	30	-50 ± 22	92	-306 ± 31	114
H_2S - all	24.4 ± 0.5	2.6	183 ± 8.1	30	-71 ± 19	99	-306 ± 31	114
Set 1 - all (φ>20)	25.0 ± 0.4	2.3	180 ± 9.4	35	79 ± 43	148	-198 ± 64	192
Set 2 - all (φ<20)	21.0 ± 0.8	2.9	158 ± 13	38	-92 ± 16	84	-295 ± 37	138
OCS - linked	30.3 ± 1.6	3.1	-	-	-252 ± 39	77	-	-
S_2 - linked	35.2 ± 8.0	11.4	-	-	-357 ± 145	207	-	-
S_2 - all	40.1 ± 8.8	14.8	-	-	-436 ± 124	208	-	-
SO_2 - linked	24.3 ± 1.2	3.4	146 ± 9	20	-67 ± 40	130	-130 ± 53	119
SO_2 - all	24.3 ± 0.8	3.0	147 ± 8	19	-66 ± 30	116	-134 ± 48	114
CS_2 - linked	25.6 ± 0.6	2.6	175 ± 13	58	-114 ± 21	90	-276 ± 55	238
CS_2 - all	25.8 ± 0.6	2.6	182 ± 15	64	-121 ± 19	87	-301 ± 27	247
Set 1 - linked	25.2 ± 0.7	2.6	184 ± 12	46	-102 ± 25	94	-310 ± 46	171
Set 2 - linked	26.5 ± 1.1	2.6	103 ± 3	7	-145 ± 37	84	231 ± 38	87

4.2 Discussion

4.2.1 Relative Abundance of S Bearing Molecules

From the comparison of the abundances of OCS, S_2, SO_2, and CS_2 relative to H_2S it can be learned that for CS_2 and OCS there is a difference between northern and southern hemisphere thus between summer and winter. In addition, a transition zone is present between $\pm 20°$ for CS_2 and H_2S while S_2 and SO_2 do not show any correlation regarding the sub satellite latitude. The difference between relative abundance of the summer and winter hemisphere, omitting the transition zone, is for OCS about a factor 0.5 and for CS_2 about a factor 0.45. The results of this study differ from the results presented by Le Roy, L. et al. (2015) where for OCS a factor of about 0.17 and for CS_2 of about 0.13 were reported between summer and winter hemisphere. The difference can be explained by recalling that Le Roy, L. et al. (2015) had one time stamp while the results of this work base on one spacecraft terminator orbit and therefore more latitudes were sampled. No conclusion can be drawn basing on this data set whether the seen variation between the summer and winter hemisphere reflects a pristine difference or whether is it due to different evolution of the hemispheres caused by their different exposure to the sun. The inconsistency for S_2 and SO_2 between this work and Le Roy, L. et al. (2015) is most likely caused by a difference in the determination of the area which would affect SO_2 only little while S_2 would be strongly effected.

Here we forgo a comparison of the abundances relative to sulfur in different comets because first only in the two long period comets Hale-Bopp and Hyakutake some of them are determined and second because the abundances of OCS, SO_2, S_2, and CS_2 have an uncertainty up to 100% introduced by the sensitivity based on the relation presented in section 3.3.

4.2.2 Isotopic Ratios in Sulfur Bearing Species at 67P

See that the resulting sulfur isotope ratios for the five analyzed species is significant different from terrestrial values an unexpected bias caused by the instrument or the data reduction has to be discussed first.

4.2.3 Instrumental Bias

There are two possible sources of instrumental bias for the achieved sulfur isotopic results which will be discussed in the subsequent paragraphs; the individual pixel gain and the mass dependence of the sensitivities.

4.2.3.1 Influence of Individual Pixel Gain Factor

As it has been explained in section 1.9.5 the MCP has an individual pixel gain for each pixel. Those factors are dependent on the manufacturing of the MCP and the amount of ions that impinged on the MCP yet. It is not reasonable to measure those factors after every spectrum or for every day since the measurements take for one GS ~1 1/2 hour and the measurement requires a signal as stable as possible. Thus pixel gain measurements are performed based on the activity and the variability of the cometary signal. As a

consequence it can happen that a distinct change of the individual pixel gain, due to the sampling possibilities, is not well resolved in time. A way to estimate the impact of not correct individual pixel gain factors is to compare the position on the LEDA of the isotopologues for a species. This is done in fig. 4.2.1 - fig. 4.2.3. Each figure is composed of three panels; the uppermost panel shows the individual pixel gain curve, in the mid panel is the slope of the curve displayed, and in the bottom panel the spectra (row A only) of the molecule and its isotopologues are drawn. Going from top to bottom H_2S, SO_2, and CS_2 are shown. S_2 will not be discussed because it behaves the same way as SO_2 for they have the same integer mass to charge ratio for all isotopologues. OCS will not be discussed in detail because the influence of the not well defined peak shape and the statistical uncertainties are expected to be larger than the influence of small changes in the individual pixel gain factors.
A comparison of the distance in pixel on the LEDA between peak centers of main isotopologue and minor isotopologues shows that it is largest for H_2S and smallest for CS_2, which is due to the decreasing mass resolution. From figure 4.2.1 one can learn that the difference in position between H_2S and $H_2{}^{33}S$ is ~2-3 pixels and for $H_2{}^{34}S$ ~5-6 pixels while the change of $pg_{GS16}(x)$ is ~0.02. Since the peaks of H_2S and $H_2{}^{33}S$ have a difference in location of not more than 1 pixel the bias is supposed to be marginal.

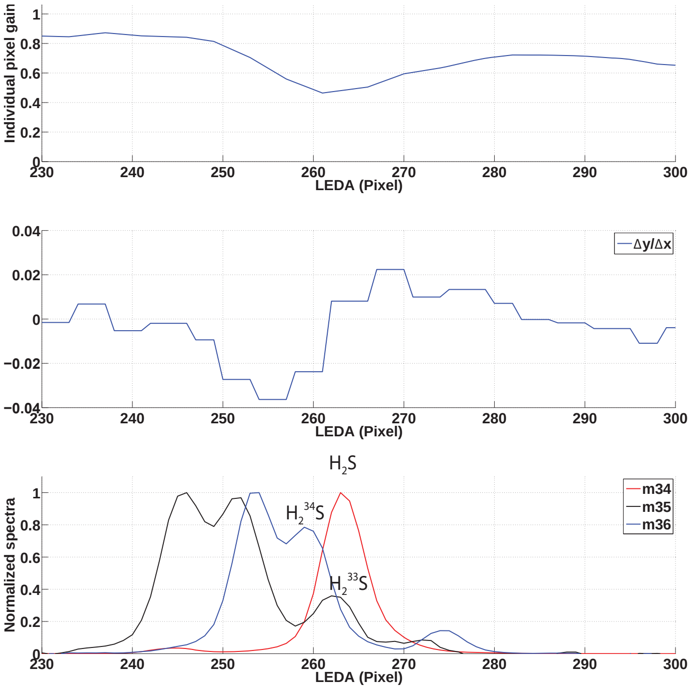

Fig. 4.2.1: Comparison of individual pixel gain curve (GS16 - Nov-2014), its change, and the location of the isotopologues of H_2S on the LEDA.

Figure 4.2.2 shows the positions of SO_2 and its heavier isotopologues on the LEDA. The difference between peak center of SO_2 and ${}^{33}SO_2$ or ${}^{34}SO_2$ resp. is for both heavier isotopologues about 2-3 pixels while the change of $pg_{GS16}(x)$ is ~0 and 0.01, respectively. For CS_2 the influence of a different position on the LEDA is the smallest as it can be seen in fig. 4.2.3.
The difference in position on the LEDA is ~1 pixel for both $CS^{33}S$ and $CS^{34}S$, thus the difference of $pg_{GS16}(x)$ is ~0.01. The individual pixel gain is not expected to show large deviations from the true values on the scale of pixels. The reason is that in average

the change in water signal is not occurring rapidly during one mode. In addition, the changes on a short time scale do not have in general large amplitudes (for more details see section C.3). Since the peak center among the isotopologues do not differ more than 6 pixels from each other the effect of a not correct pixel gain correction is expected to be marginal.

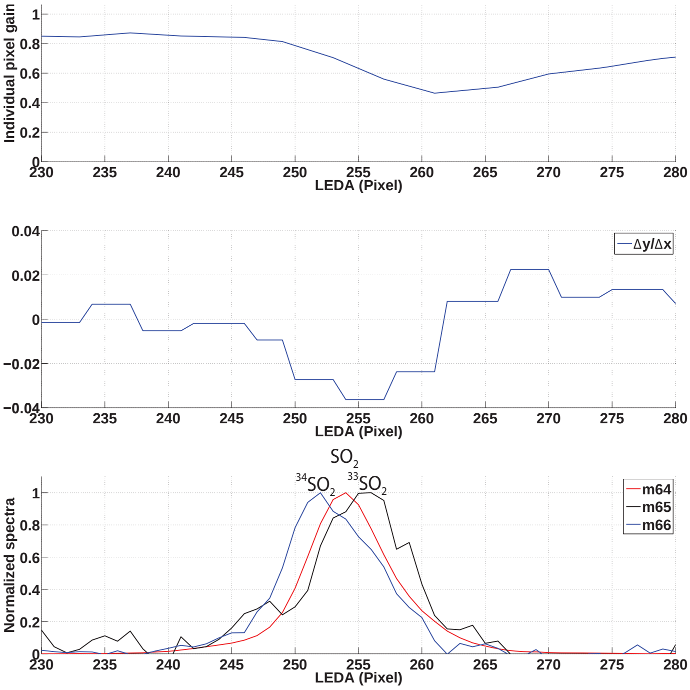

Fig. 4.2.2: Comparison of individual pixel gain curve, its change, and the location of the isotopologues of SO_2 on the LEDA.

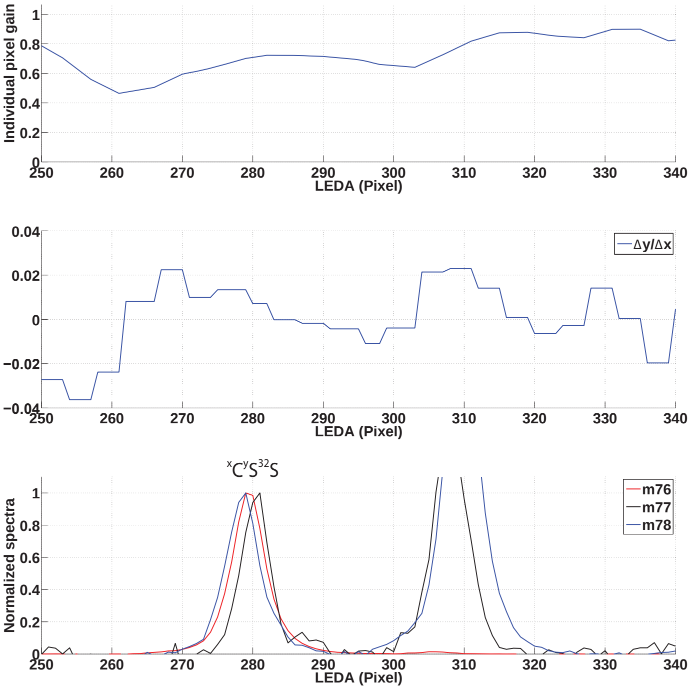

Fig. 4.2.3: Comparison of individual pixel gain curve (GS16 - Nov-2014), its change, and the location of the isotopologues of CS_2 on the LEDA.

Although deviations in the individual pixel gain factor could lead to marginal bias for one pixel the influence on the entire peak area has to be considered and quantified which has already been discussed in section 3.4.2.4. For two peaks differing up to 6 pixels in location the deviation from the true peak area ratio is predominantly below 5% in the simulated cases. This gives an upper limit introduced via the pixel gain correction. Nevertheless the bias is assumed to be smaller. First because $^{32}S/^{33}S$ in H_2S has a larger deviation from the standard than $^{32}S/^{34}S$ although $H_2{}^{33}S$ and H_2S lay only one pixel apart. Second because CS_2 shows large isotope fractionation for both ^{33}S and ^{34}S resp. although the three peaks lay almost on the same pixel. Consequently the seen isotope fractionation can not be caused by the pixel gain correction.

4.2.3.2 Influence of Mass Dependent Sensitivity

Due to construction of the mass analyzer and the detector the sensitivity is dependent on the energy of analyzed particles which is equivalent to m/z. Theoretically one has a $1/\sqrt{m/z}$ dependency from both mass analyzer and detector but an empirically retrieved relation based on noble gas measurements lead to relation of $1/m^{0.82}$ instead of $1/m$ for masses between 13 - 69 u/e as it has been shown in section 3.3. With this relation the relative sensitivity for the masses of interest can be calculated and compared (see table 4.2.2). Thus the bias due to different sensitivities is supposed to be largest for the ratio $^{32}S/^{34}S$ with 7% for H_2S, OCS, S_2, and SO_2 while the bias could be up to 4% for $^{32}S/^{33}S$.

For m/z larger than 69 u/e the dependency changes because DFMS applies an additional acceleration voltage to obtain a higher sensitivity. The bias is smaller, based to the empirical curve, for $^{32}S/^{34}S$ and $^{32}S/^{33}S$ in CS_2 with 1% and 3%, respectively. However, from the discussion of the empirical curve in section 3.3 it is clear that the above made estimations have large uncertainties and therefore the discussion of a possible bias can not base only on this relation. Fortunately for H_2S calibrations measurements have been done and the resulting isotope fractionation $\delta^{34}S$ in S and H_2S are given in table 4.2.1 with respect to V-CDT. However, the values show large variations that are thought to be due to interferences with other species on the considered mass to charge ratio (for more details see section 3.2). Considering only the results achieved for 200 µA at $6.13 \cdot 10^{-8}$ mbar for which the peak shape of $H_2{}^{34}S$ was more distinct a depletion in ^{34}S of 7% is not present.

Table 4.2.1: isotope fractionation of ^{34}S of the calibration measurements of H_2S (for more details see section 3.2).

Emission	H_2S partial pressure (Pa)	$\delta^{34}S$ (‰)	
		S	H_2S
200 µA	$6.13 \cdot 10^{-8}$	-14 ± 90	-72.6± 72.5
200 µA	$2.13 \cdot 10^{-8}$	-7 ± 123	420 ± 123
20 µA	$6.13 \cdot 10^{-8}$	-367 ± 94	298 ± 115
20 µA	$2.13 \cdot 10^{-8}$	-255 ± 157	-361 ± 97

Table 4.2.2: For the species of interest the relative sensitivity has been calculated based on the empirical relation deduced in section 3.3. Additionally the result of the ratio between the relative sensitivity of the minor isotopologues and the main isotopologues is given.

m/z	S_{relative}	$\frac{S_{\text{relative,minor isotopologue}}}{S_{\text{relative,main isotopologue}}}$
H_2S		
34	0.55	1
35	0.53	0.96
36	0.51	0.93
OCS		
60	0.22	1
62	0.20	0.93
SO_2 & S_2		
64	0.189	1
65	0.182	0.96
66	0.175	0.93
CS_2		
74	0.97	1
75	0.96	0.99
76	0.94	0.97

4.2.4 Isotopic Ratios in Context

First the obtained isotopic ratios for sulfur in H_2S, SO_2, OCS, CS_2, and S_2 will be discussed in this order and are then put into context with what is known about sulfur isotope fractionation in the Solar System. Afterward the tentative values for D/H in H_2S will be discussed. Mean values will always given with the error of the mean while for single data points 1σ will be given. A compilation of all determined mean values can be found in table 4.1.3.

The figures 4.2.4 (a) and (b) show the three isotope plots for H_2S and SO_2 for which the isotopologues with ^{33}S and ^{34}S could be identified unambiguously. For H_2S one can see from fig. 4.2.4 (a) that first the sulfur isotopic ratios do not spread symmetrically around their mean of $\delta^{34}S = -50 \pm 22‰$ and $\delta^{33}S = -306 \pm 31‰$. Second for one third of the values an enrichment in ^{33}S and/or ^{34}S is present with a maximal enrichment of $\delta^{34}S = 199 \pm 170‰$ and $\delta^{33}S = 61 \pm 154‰$. Interestingly all data points of the latter population were measured at sub satellite latitudes higher than 30° as it can be seen from fig. 4.2.4 (c). The weighted means of the population measured at latitudes below 20° are $\delta^{34}S = 79 \pm 43‰$ and $\delta^{33}S = -198 \pm 97‰$ and for the second population with latitudes above 20° they are $\delta^{34}S = -92 \pm 16‰$ and $\delta^{33}S = -295 \pm 37‰$. In addition, it can be seen from fig. 4.2.4 (c) that there seems to be on a large scale a correlation between isotopic ratio and sub satellite latitude. However, it is not possible to deduce from the measured heterogeneity in sulfur isotopic ratios whether those are the result of an evolutionary process occurring after the comets formation or whether it indicates a different formation location of the two lobes of 67P/Churyumov-Gerasimenko because at a distance of 10 km to the comet the area that lies in DFMS large field of view is with about 1.76 km x 1.76 km too large

to sample distinct regions or lobes.
Similar as for H_2S the spread in SO_2 shown in fig. 4.2.4 (b) is not radial symmetric around the weighted means of $\delta^{34}S$ = -67 ± 40‰ and $\delta^{33}S$ = -130 ± 53‰ and an elongation in $\delta^{34}S$ is present. In addition, there are two data points that fall out of alignment for the isotope fractionation of ^{33}S with $\delta^{33}S$ = 220 ± 215‰ and $\delta^{33}S$ = -437 ± 117‰. Unlike H_2S data the signal height of the minor isotopologues of SO_2 were sufficient only for latitudes above 20° to determine the isotope fractionation therefore the spread can not be linked to differences in latitude.

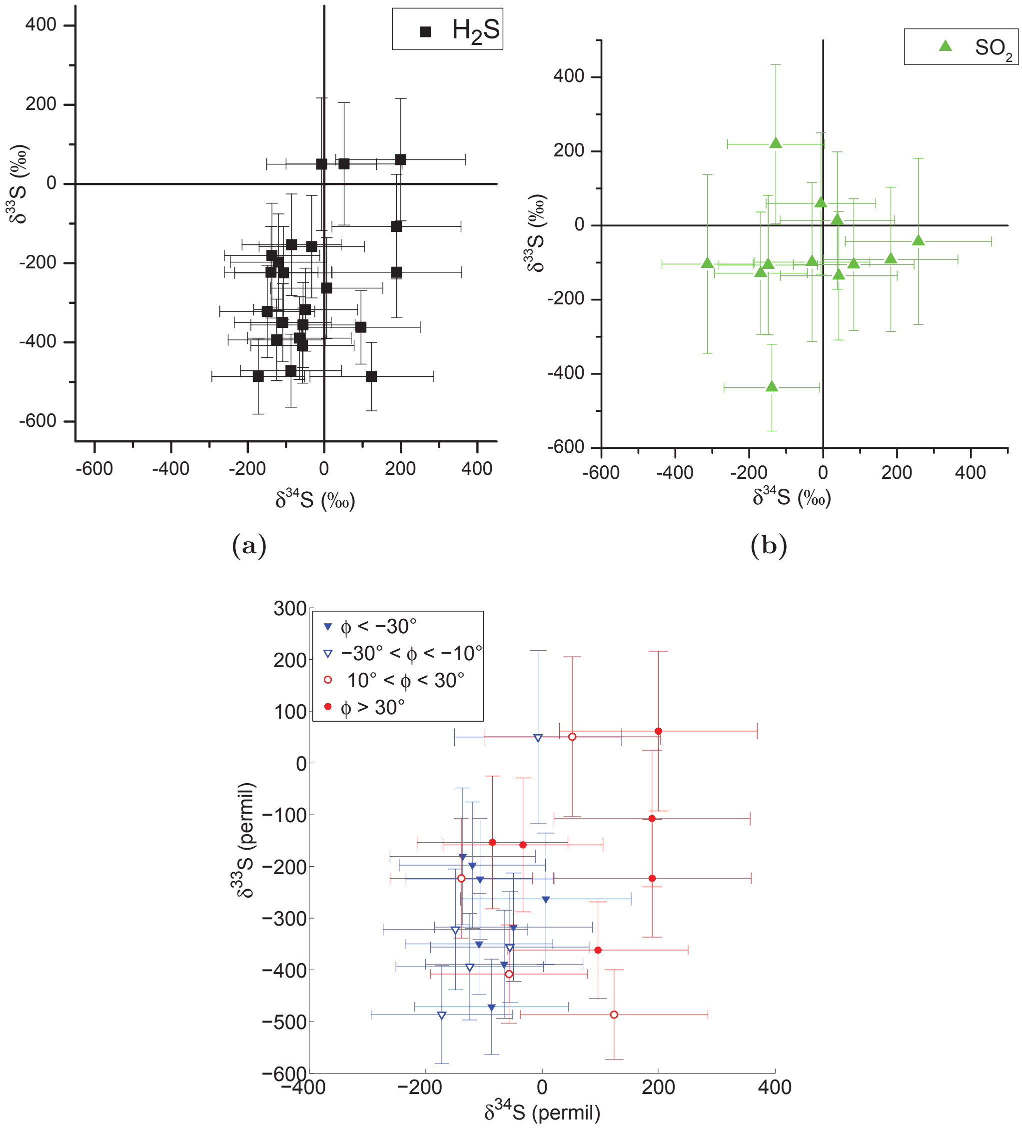

(a) (b)

(c)

Fig. 4.2.4: (a) and (b) show the isotope fractionation of ^{34}S and ^{33}S seen in H_2S and SO_2 during October 2014 when Rosetta was in a 10 km orbit around Churyumov-Gerasimenko. (c) shows the isotope fractionation in H_2S sorted by sub satellite latitudes.

The interpretation of the isotopic ratios for OCS and CS_2 is more difficult because the isotopologues with ^{13}C and ^{33}S overlap and can not be distinguished. As a first step $^{12}C/^{13}C$ was assumed to be terrestrial, thus VPDB, resulting in large scale asymmetric spread in $\delta^{33}S$ for both OCS and CS_2 for which the three isotope plots are shown in

fig. 4.2.5 (a) and (b). For OCS only for 5 measurements the isotopic ratio could be determined for both ^{33}S and ^{34}S, respectively. Therefore and because of the enormous spread in δ^{33}S no further knowledge about OCS can be deduced from the three isotope plot. In consequence two conclusions can be drawn; first that the assumption of a terrestrial ^{12}C/^{13}C ratio might not be valid for OCS and second that the peak on m/z 61 u/e is not likely to be due to only O^{13}CS and OC^{33}S.
In contrast the three isotope plot for CS_2 (fig. 4.2.5 (b)) reveals a large spread in δ^{33}S which seems to be grouped in 2 populations and an outlier, that has been already discussed in section 4.1.2.5. The larger of the two populations spreads more or less symmetrically around δ^{34}S = -102 ± 25‰ and δ^{33}S = -340 ± 46‰ while the smaller population has a larger spread in δ^{33}S than in δ^{34}S. In addition, the weighted mean shows an enrichment of ^{33}S with δ^{34}S = -145 ± 37‰ and δ^{33}S = 231 ± 38‰ omitting the outlier. Like H_2S CS_2 had a sufficient high signal over one cometary rotation to determine isotopic ratios and separating the data for the sub satellite latitude which did not reveal any correlation as it can be seen from fig. 4.2.5 (c).

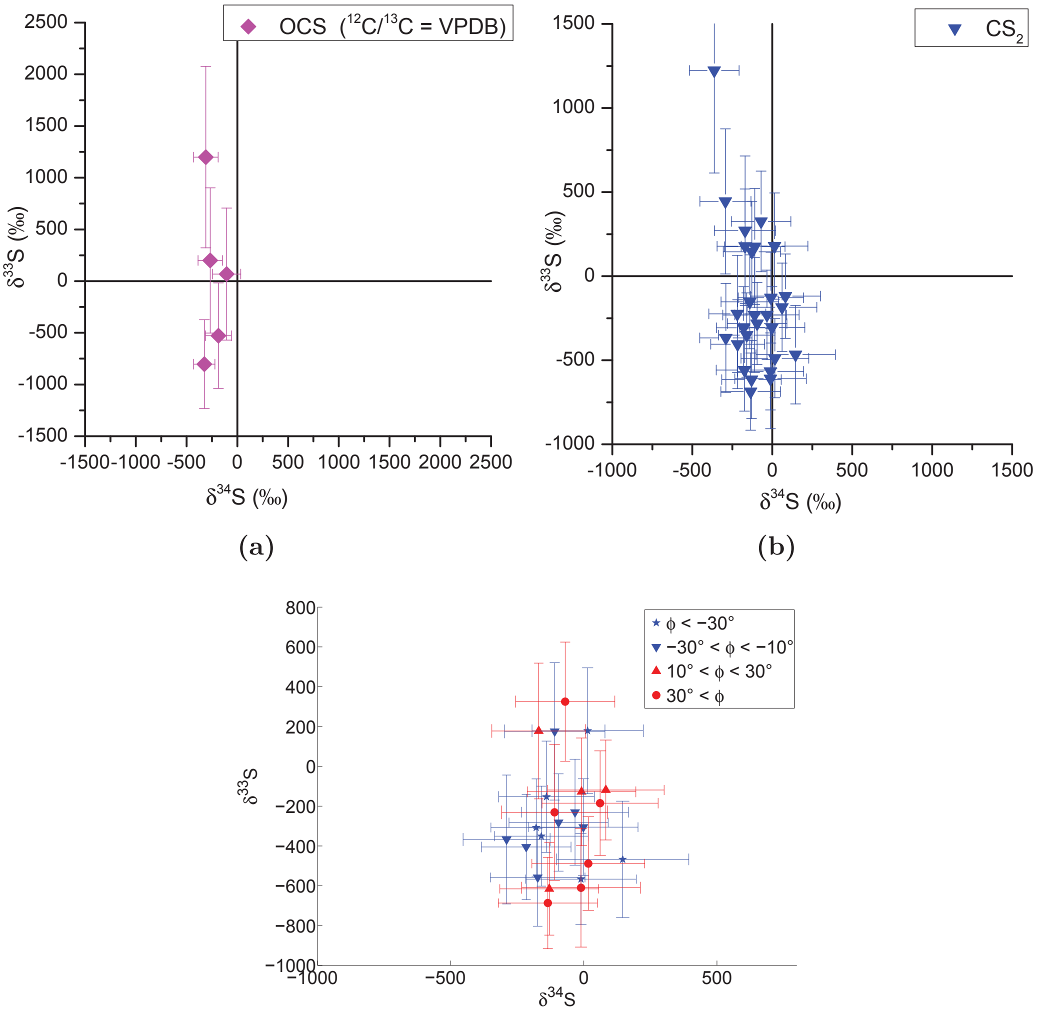

(a) (b)

(c)

Fig. 4.2.5: (a) and (b) show the isotope fractionation of sulfur ^{34}S and ^{33}S seen in OCS and CS_2 during October 2014 when Rosetta was in a 10 km orbit around Churyumov-Gerasimenko. (c) shows the sulfur isotope fractionation in CS_2 sorted by sub satellite latitudes.

A cause of the size and type of spread in ^{33}S for CS$_2$ could be the assumption of terrestrial ^{12}C/^{13}C which might not be valid for all data points. Thus based on the mean values of the two subsets the ^{12}C/^{13}C ratio can be calculated for all CS$_2$ measurements. In the upper panel of fig. 4.2.6 are drawn δ^{34}S versus ^{12}C/^{13}C together with VPDB while the lower panel shows the sulfur three isotope plot. For illustration the error bars in δ^{34}S are not drawn in both panels. The half filled blue squares represent the ^{12}C/^{13}C ratio for δ^{33}S = -310‰ whereas the half filed blue rhombuses represent the result when δ^{33}S is assumed to be 231‰. For the later case five resulting values are negative and therefore not displayed in the upper panel of fig. 4.2.6. In addition in this case the majority of the values show a significant enrichment in ^{12}C and ^{12}C/^{13}C goes up to 836 ± 1551. Consequently assuming δ^{33}S to be -310‰ leads to a spread around VPDB for the large population which spreads in ^{12}C/^{13}C from 43.3 ± 6.4 to 191 ± 66. The interesting points to look at are the ones belonging to the small population. For those points the ^{12}C/^{13}C ratio lays below the standard at 89 meaning an enrichment of ^{13}C.

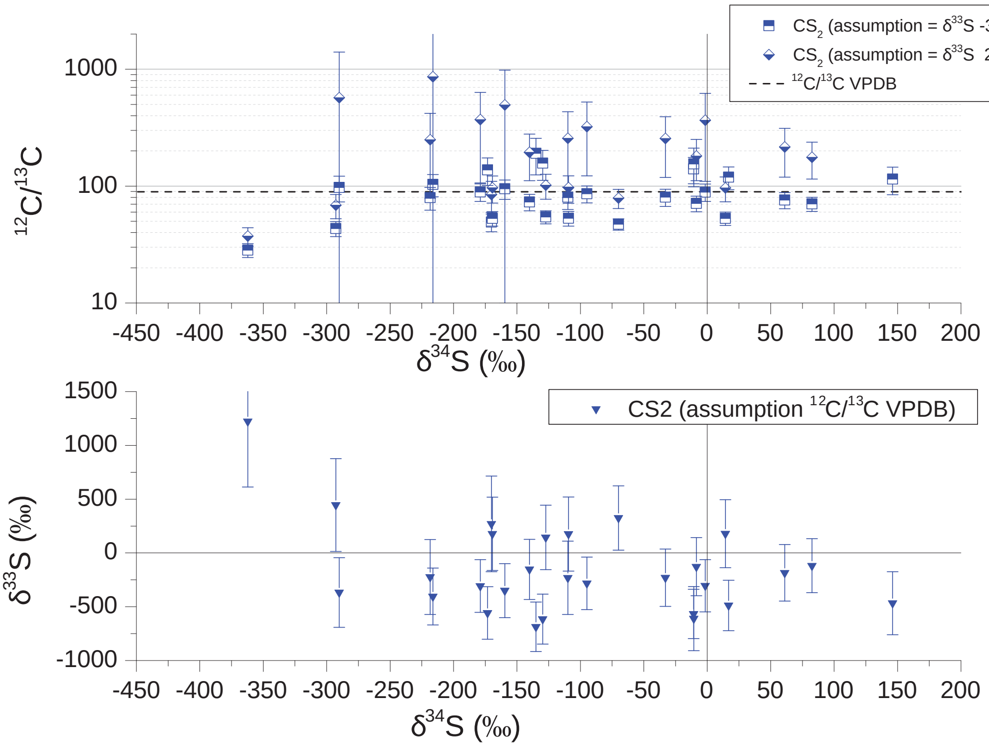

Fig. 4.2.6: The upper panel shows ^{12}C/^{13}C in CS$_2$ assuming δ^{33}S = -310‰ (half filled squares) and assuming δ^{33}S = 231‰ (half filled rhombuses). The lower panel shows the sulfur 3 isotope plot of CS$_2$. For illustration the error bars in δ^{34}S are not drawn.

For S_2 the three isotope plot is shown in fig. 4.2.7 (a) and a section of it in (b). As it has been already discussed in section 4.1.2.3 for both $\delta^{33}S$ and $\delta^{34}S$ a large spread is present which is most likely due to the low signal to noise ratio for both $^{32}S^{33}S$ and $^{32}S^{34}S$. As a consequence only the weighted mean of $\delta^{34}S$ = -357± 145‰ will be used for further discussions since it shows a smaller spread.

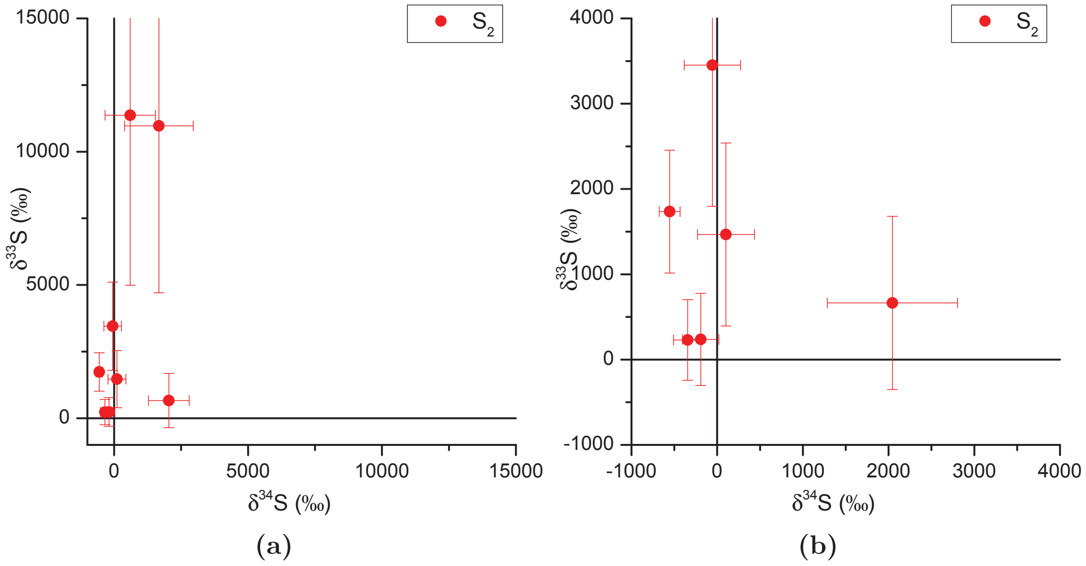

(a) **(b)**

Fig. 4.2.7: Shown are the isotope fractionation of sulfur ^{34}S and ^{33}S in S_2 during October 2014 when Rosetta was in a 10 km orbit around Churyumov-Gerasimenko; in (a) the entire data set is shown and in (b) the section closest to zero is enlarged.

In order to see the unexpected results in a scientific context a compilation of the main results of this study (weighted mean ± 1σ), impact of photodissociation processes on sulfur isotopic ratios, previous results of sulfur isotopes in comets, sulfur isotopic ratio in the interstellar medium (ISM) and a carbon star, the isotopic ratio in massive stars ending in supernovae Type II modeled by Rauscher et al. (2002), and a compilation of SiC grains data is done in fig. 4.2.8. The results of numerous studies on the sulfur isotopic ratios in meteorites and the results of dust originating from comet Wild 2 are not contained in this compilation since the range for isotope fractionation in different types of meteorites does not exceed ± 10‰ in $\delta^{33}S$ and ± 5‰ in $\delta^{34}S$ while for dust impact craters from comet Wild 2 on stardust the reported values show no significant deviation from the terrestrial value for $^{32}S/^{34}S$. In addition, no results are available on the isotope fractionation of sulfur in so called interplanetary dust grains nor about the isotope fractionation in solar wind measured by Genesis.

From the compilation in fig. 4.2.8 it can be seen that:

i H_2S, SO_2, and CS_2 do not lay on the slope of mass dependent fractionation nor on the slope for photodissociation for none of the above mentioned species but they overlap with what has been measured in SiC grains.

ii Non of the measured species lays within 1 σ of terrestrial isotopic ratio for ^{33}S but H_2S and SO_2 lay within 1 σ of terrestrial isotopic ratio for ^{34}S.

iii Except S_2 all measured species lay in the range of the previous measurements of $^{32}S/^{34}S$ in comets.

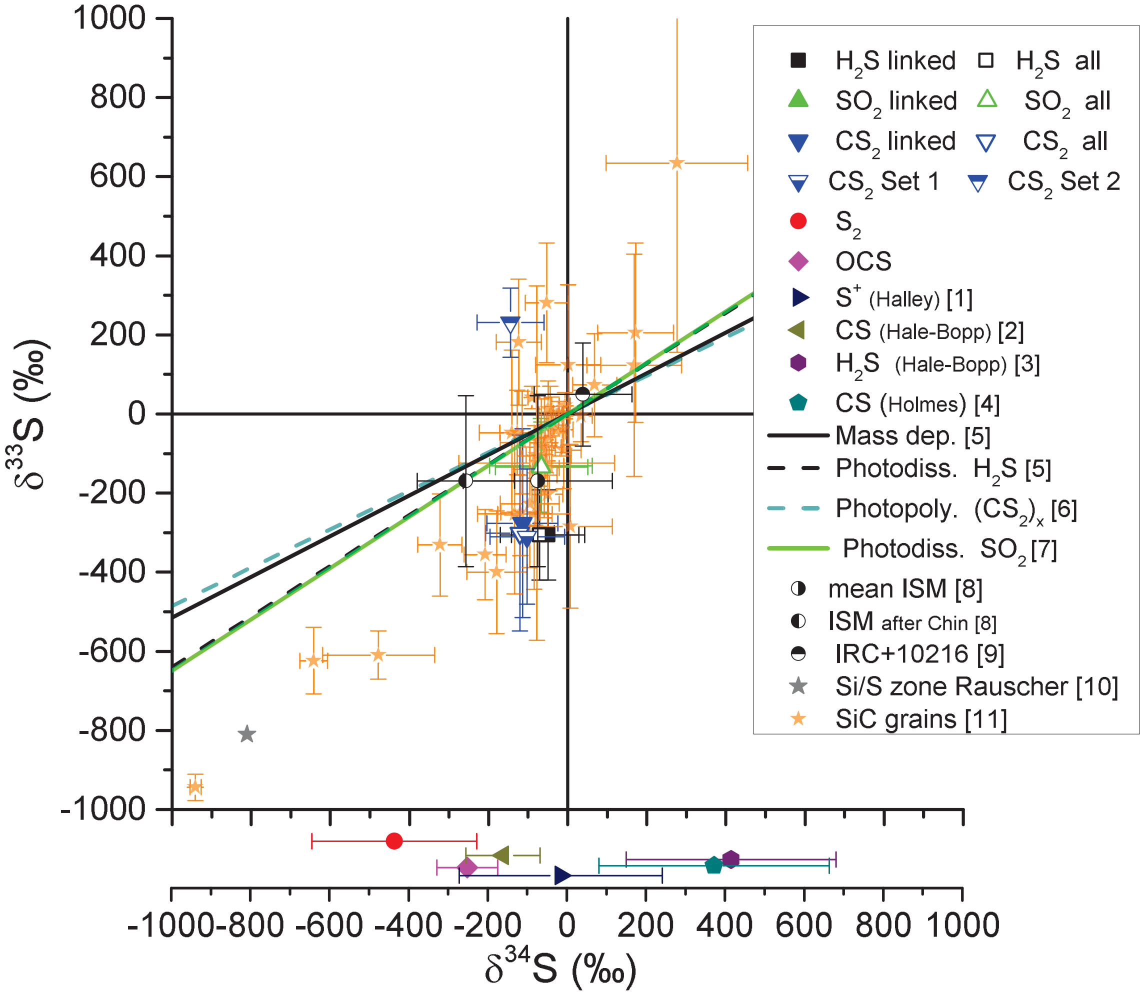

Fig. 4.2.8: Sulfur three isotope plot comparing the results of this work with the state of art knowledge concerning sulfur isotopic fractionation in Solar System bodies and beyond. Compared are this work with other comets ([1] (Altwegg, 1996), [2] (Jewitt et al., 1997), [3] (Crovisier et al., 2004), [4] (Biver et al., 2008)), mass dependent and independent fractionation ([5] (Chakraborty et al., 2013), [6] (Zmolek et al., 1999), [7] (Farquhar et al., 2000)), a carbon star ([8] (Mauersberger et al., 2004)), the ISM ([9] (Chin et al., 1996), [10] after (Chin et al., 1996): $^{32}S/^{34}S = (3.3 \pm 0.5) \cdot d + (4.1 \pm 3.1)$ with distance of the Sun to the center of the galaxy d 8 kpc), a model of massive stars ending in supernovae Type II ([11] (Rauscher et al., 2002)), and SiC grains ([12] (Xu et al., 2015), (Hoppe et al., 2015), (Gyngard et al., 2010), (Orthous-Daunay et al., 2012), (Hoppe et al., 2012)).

The fact that neither H_2S nor SO_2 or CS_2 lay on the slope due to their photodissociation via UV basing on laboratory work (for more details see section 1.6.1) rules out photodissociation as sole cause. In addition it indicates that there was none or very little mixture in the formation region of 67P material between the inner Solar System were H_2S is assumed to be affected by photodissociation during the suns T-Tauri phase and the outer regions of the protoplanetary nebula because of the large deviation from V-CDT and the line for photodissociation for H_2S. On the other hand having an overlap between the weighted means of H_2S, SO_2, and CS_2 and the population of diverse SiC grains points to a link between SiC grains and those three species - so refractory phase and gas phase. However, it would go beyond the scope of this work to investigate which processes are the cause for the seen overlap in ^{33}S and ^{34}S sulfur isotopic ratios between cometary volatiles and SiC grains.

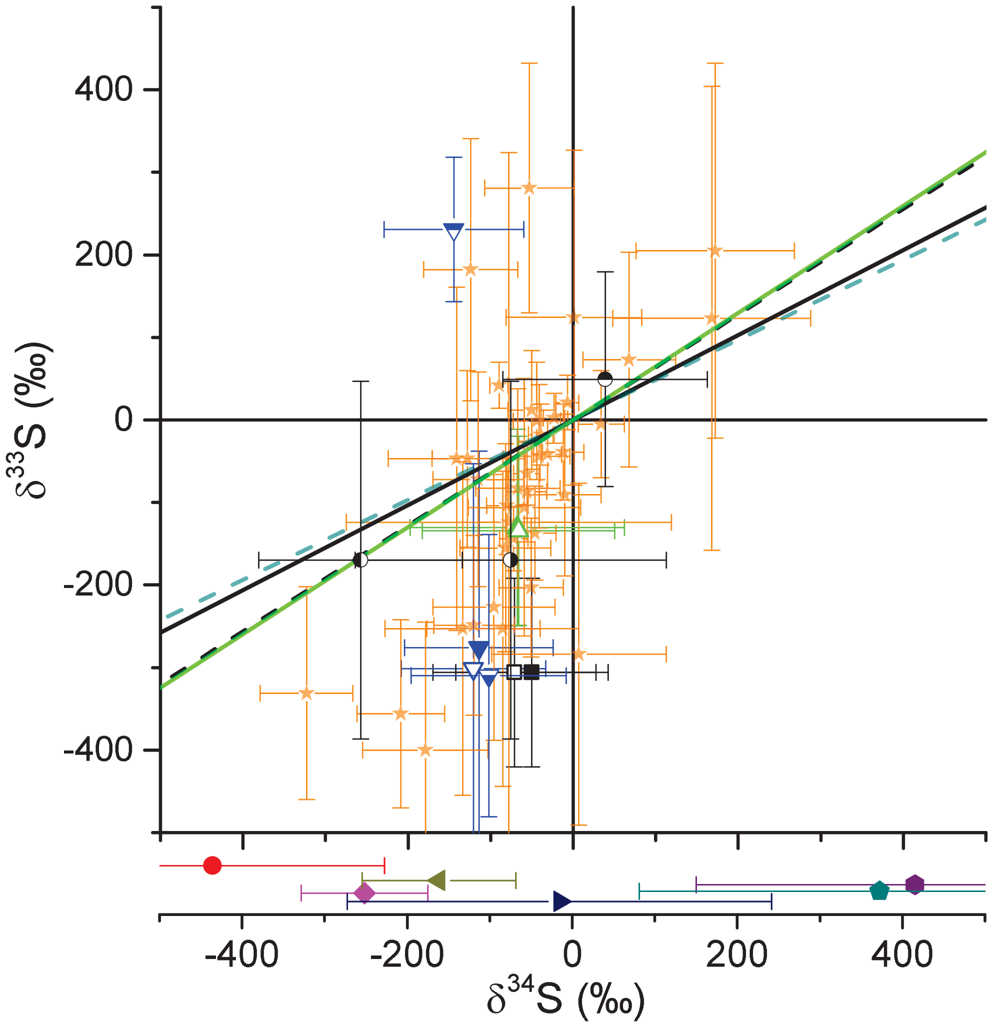

Fig. 4.2.9: Section of fig. 4.2.8 with focus on the center.

Nevertheless further conclusions can be drawn having a closer look at the graph without knowing the origin of the seen isotope fractionation in H_2S, SO_2, and CS_2 - therefore the a section of the center is shown in fig. 4.2.9. First the overlap of the weighted means of H_2S and CS_2 indicates that the weighted mean of the sub set 1 is more likely to represent the bulk isotope fractionation of ^{33}S in CS_2. Consequently the sub set 2, that had positive

values for δ^{33}S, can not have a terrestrial ^{12}C/^{13}C ratio but needs to have an enrichment in ^{13}C as it has been shown already in section 4.1.2.5. Since for sulfur ^{33}S and ^{34}S the isotope fractionation seen in CS_2 is similar to what has been measured in SiC grains a comparison of the carbon isotopic ratio relative to δ^{34}S in those grains and CS_2 is done in fig. 4.2.10. The different SiC grains are sorted by their type and the parent body is given in the legend, the results for CS_2 assuming δ^{33} to be -341‰ are given in grey squares, and the standard for C is indicated by the black dashed line. From the graph it can be seen that for CS_2 two third of the data points are below VPDB and that CS_2 overlap with the SiC grains. No further conclusion can be drawn because the SiC data set is scarce since in not many grains both ^{12}C/^{13}C and ^{32}S/^{34}S have been determined.
Second the depletion in ^{34}S in S_2 and the enrichment in ^{34}S seen in H_2S at Hale-Bopp and in CS at comet Holmes seem to fall out of alignment because all other measurements of ^{32}S/^{34}S in comets lay in the range going from -251 to -37.9‰. It might be that the so far reported values for ^{32}S/^{34}S represent other populations due to different chemistry or due to different location of formation of the parent body. Unfortunately no possible explanation has bee given for the enrichment of ^{34}S seen in ^{34}S Hale-Bopp and Holmes.

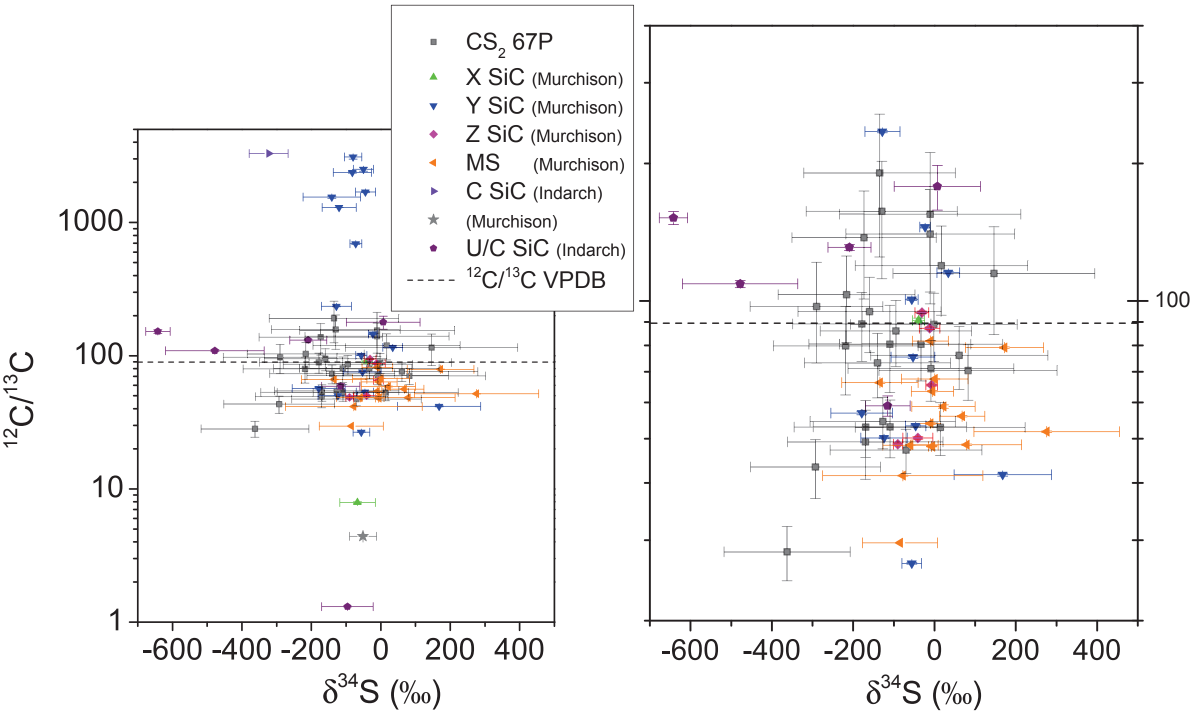

Fig. 4.2.10: Compilation of ^{12}c/^{13}c relative to δ^{34}S of different types of SiC grains and the tentative values obtained from CS_2 assuming δ^{33}S = 231‰ in the coma of 67P in October 2014. SiC Data: X - Z SiC (Murchison) (Xu et al., 2015) , MS (Hoppe et al., 2015), C SiC (Indarch) (Gyngard et al., 2010) , (Murchison) (Orthous-Daunay et al., 2012), U/C SiC (Indarch) (Hoppe et al., 2012)

The discovered significant deviation of ^{32}S/^{33}S and ^{32}S/^{34}S in cometary volatiles from V-CDT leads to two fundamental questions. First how could the sulfur in SiC grains be linked to sulfur in those volatile species? Second if there is no link to SiC grains which type of process could lead to the measured isotope fractionation?

Although there is no scientific proof whether there is a link between cometary volatiles and SiC grains a hypothesis will be presented in the next paragraph.

What if H_2S has been formed on SiC grains using the sulfur in the grains, in the form of MGS as suggested by Hoppe et al. (2015), and therefore transmit the isotopic fingerprint or at least part by grain surface chemistry. This fingerprint could then be transferred to other sulfur bearing molecules when H_2S ice covered SiC grains warm up and H_2S sublimates. Again a change in the fingerprint is assumed to happen since isotopologues do not behave exactly the same in chemical reactions. In addition, sublimation could lead as well to some sort of fractionation and thus alter the fingerprint. However, the mass dependent and the photodissociation induce isotopic fractionation leads to small changes compared to the fractionation seen in SiC grains. Thus those effects are expected to alter the SiC fingerprint not significantly. Due to a lack of concepts about how sulfur bearing molecules could be formed in the interstellar medium or molecular clouds no further hypothesis with respect on the formation can be presented by the author.
However, the scenario can be developed further without knowing the exact cause of the isotope fractionation in sulfur because there is still the deviation between what has been detected in different types of meteorites and this work. Assuming the isotope fractionation seen in H_2S, SO_2, and CS_2 are of presolar nature and that the obtained results represent the bulk comets further questions arise. First why do they differ significantly from what is thought to be the pristine isotope fractionation in sulfur in the protoplanetary disk? Second what is the carrier of the enrichment in ^{33}S and ^{34}S that would be needed to have at the end of the mixing between this carrier and cometary sulfur bearing molecules again the up to date solar isotope fractionation? The author sees two possibilities either the thought pristine value for isotope fractionation represented by V-CDT is already the product of chemistry occurring in the protoplanetary disk or the mixing of two reservoirs occurred.

Leaving the puzzling S isotopic ratios the tentative D/H values in H_2S will be discussed in the following paragraph. Based on the mass spectra it is clear that there has to be an additional peak to HDS on m/z 35 u/e as it has been already discussed in section 4.1.2.1 and the question emerging is; what could it be. Due to the peak shape it has to be a species with almost the same mass to charge ratio as HDS. Considering only this H_3S is a suitable candidate which would be formed most likely in the ion source of DFMS due to the presence of water. Luckily the abundance of H_2S relative to the water background in CASYMIR was about a factor 1.7 - 3.7 higher during the calibration measurements where no signal due to H_3S could be detected. Therefore chemistry in the ion source could be ruled out as origin of the supposedly H_3S. At any rate the presence of an additional peak makes it difficult to properly interpret the determined D/H ratios because the mixing ratio of HDS and supposedly H_3S is not known. An attempt to get an idea what the fraction of HDS could be has been done by comparing the peak centers obtained by the fit and solely a correlation between the sub satellite latitude and the tentative D/H value could be seen while there is no correlation between the peak center and D/H. Consequently no further conclusion can be drawn about the mixing between HDS and the additional peak which is supposedly H_3S and therefore the obtained mean of $9.64 \pm 0.19\ 10^{-4}$ gives an upper limit for D/H in HDS. In addition, the tentative value in $HD^{34}S$ of $(2.5 \pm 0.8) \cdot 10^{-4}$ is about a factor of 5 lower and does not help to confine D/H in H_2S.
So far two upper limits for D/H in H_2S have been reported; for Hale-Bopp the limit is $2 \cdot 10^{-1}$ (Crovisier et al., 2004) and for comet Holmes it is $8 \cdot 10^{-3}$ (Biver et al., 2008). The

upper limit obtained in this work is lower than what has been reported for both Hale-Bopp and Holmes.

For D/H in HS_2 outside of the Solar System one value has been reported yet. HDS has been observed in the protobinary source IRAS 16293-2422 by van Dishoeck et al. (1995) with the James Clerk Maxwell Telescope. They report a D/H of 0.10 with an uncertainty of about 50%. This value is compared to the terrestrial value given by the VSMOV highly enriched in D which is thought to be caused by grain surface chemistry. After the formation of the molecules in a cold molecular cloud, that goes together with the deuteration, it is thought that the volatiles are released from grains due to the collapse of the cloud (van Dishoeck et al., 1995). The upper limit for D/H in H_2S at 67P is compared to the value found by van Dishoeck et al. (1995) two orders of magnitude lower and it is about a factor two larger than D/H in water at 67P (Altwegg et al., 2015).

5. Conclusion and Perspectives

The beginning of the conclusion is dedicated to the characterization of DFMS FM and FS while in the second half the results for the sulfur isotopic ratios in the five most abundant sulfur bearing species in the coma of the comet Churyumov-Gerasimenko and the implications are summarized.

5.1 Characterization of DFMS FM and FS

It has been shown that for low resolution measured with MCP/LEDA the actual mass to charge ratio deviates from the theoretical one calculated via:

$$m(x) = m_0 \cdot e^{(x-x_0)\frac{s}{D\cdot z}} \tag{5.1.1}$$

where m_0 is the commanded mass, x_0 the pixel on which m_0 lays, the distance between two pixel s = 25 µm/pixel, D the dispersion factor 127'000 µm (Wüthrich, 2007), and z the zoom factor (for more details see section 2.3.1). The deviation dm is dependent on the location of the signal relative to the location of the center (x_0) and the commanded mass m_0 which is supposed to lay in the center of the LEDA. It is assumed that the cause is a change in dispersion. The cause for the change in dispersion and therefore in the dm is most probably due to asymmetric electrical fields in the vicinity of the detector as well as an angle between the plane of the detector and the ion optical focus plane. In addition, for $m_0 > 69$ u/e a further distortion is added that causes larger deviations. The cause of the additional distortion is the applied so-called post acceleration which changes from -50 to -1000 V between 69 and 70 u/e. The deviation is for m_0 around 45 u/e between 0.02 to 0.05 u/e while for masses below it was not possible to be determined. For m_0 around 65 u/e dm lays between -0.01 and 0.09 u/e depending on the peak location. For m_0 around 83 u/e dm lays between 0.01 and 0.15 u/e and for m_0 132 u/e dm is between -0.2 to 0.3 u/e. Since the deviations are significant it is necessary to give always uncertainties for the mass scale of low resolution spectra and it is suggested to continue the study about the deviation in order to find an empirical function to correct for the observed distortion of the mass scale.

For both, NH_3 and H_2S, the density is linearly correlated with the ratio of ion current to emission current. Therefore a linear least square fit was applied to determine the sensitivity. For both calibrated species the sensitivity is inverse proportional to the emission current meaning the lower the emission the higher the sensitivity. A comparison of the sensitivity corrected for the electron impact ionization with the result presented by Hässig (2013) for species with similar mass revealed some inconsistencies. First the relation between emission and sensitivity was not present for all results obtained by Hässig (2013) and second the relation among the sensitivities for one species is not constant. Clearly further investigations are need to ascertain whether this is a peculiarity of DFMS or a bias in the calibrated sensitivities so far.

The calibration of H_2S and NH_3 showed both some inconsistencies for the fragmentation pattern in particular for the ratios N/NH_3 and S/H_2S. In addition, the ratio of N/NH_3 showed a correlation with pressure of the calibration gas therefore it is assumed that in the case of NH_3 an additional source of N was present. A likely species is N_2 as source.

Furthermore, the ratio of NH_2/NH_3 and NH/NH_2 indicate a correlation between the amount of fragments and the emission current. As a consequence it is suggested to review the so far calibrated species with focus on this possible correlation.
The isotopic ratio could be determined for NH_3 in NH_2 only because of overlapping peaks for the isotopologues of NH_3 and NH and the missing signal for 15N. For all three emission at two pressures the isotopic ratio has been determined and it ranges from 0.8 to 2 relative to the standard (nitrogen air). The most likely cause for this variation is a not proper peak fit. For sulfur the ratio of ^{34}S/^{32}S could be determined in S and H_2S for 200 and 20 µA and it ranges from 0.6 to 1.4 relative to the Vienna Cañon Diablo Troilite (V-CDT). Similar to NH_3 the most accurate values are obtained at the highest pressure for the highest emission therefore it is assumed that the variation in the isotopic ratios is due to the data treatment and not a characteristic of DMFS. However, this needs to be verified and thus it is suggested to redo measurements with MCP/LEDA at total pressure relative to N_2 of $1{\cdot}10^{-7}$ mbar and $5{\cdot}10^{-7}$ mbar for both species.
Despite the variations seen in the fragmentation pattern and the isotopic ratio the sensitivities are considered to be correct within their uncertainties because the sum of the fragments and the isotopologues were taken into account.

It is not possible to calibrate every species seen at a comet because some are lethal like HCN and some would damage the calibration facility like HCl. Therefore it has been attempted to find an empirical function for the correlation between mass of a species and their sensitivity for MCP/LEDA and CEM for high and low resolution. Difficulties in doing so were the dependence of ionization and detection efficiency on the species, and the absence of correction factors for the pressure of some species (mostly hydrocarbons). It has been tried to correct for some of those dependencies which did not result in a clear correlation. Therefore the data set has been reduced to the noble gases because for them the pressure correction was known, they do not have fragments, they were assumed to show similar detection efficiency (not taking into account the dependence in detection efficiency on the particles energy), for both neutrals and ions calibration measurements were done. The results are a power law ($f(x) = a \cdot e^{-b \cdot x} + c$) with different parameters for neutrals measured with MCP/LEDA, neutrals measured with CEM, and ions measured with MCP/LEDA constrained to m_0 between 13 and 69 u/e. For larger m_0 the available data was scarce and a linear fit has been done. For all fits high and low resolution data were combined in order to raise the number of data points for the fit. Despite the large uncertainties, going up to 100% depending on the mass to charge ratio, the resulting relations between mass to charge and sensitivity are assumed to be correct since they show all the expected decrease ~1/m. Nevertheless it is suggested to refine the parameters as soon as a larger set of calibrated data is available.

To follow and characterize the depletion of the MCP it is essential for doing calibration measurements in the lab and to interpret the results in space as it has been explained in section 1.9.5. Thus a new set of the individual pixel gain has been ascertained for FM in 2015 and based on this set it has been tried to find an empirical function describing the relation between gain step and dip depth. However, this was complicated by particularities of DFMS FM and the data reduction procedure. First the presence of a linear slope over the LEDA depending on the gain step had to be understood and second the individual pixel gain factors for different gains steps do not have a common level for regions were almost no depletion should have occurred. The linear slope and its orientation could be referred to the ion optics while the absence of a common level 1 is due to the nominal normalization procedure. To avoid a bias of those two effects the manifestation of depletion was determined for the dip depth relative to the dip depth of GS 16. The resulting relative dip depths seemed to be more or less constant for gain steps between 7 and 11 followed by a decrease for increasing gain step. This could be fit best by combination of a polynomial second order and exponential function - $f(x) = a \cdot e^{-b \cdot x} + c \cdot x^2 + d$. In addition, a change in depletion around pixel 260 between spring 2012 and spring 2015 at GS 7 from 0.298 to 0.183 relative to the mean individual pixel gain an increase in depletion of 0.115 could be observed. In addition, at least five new dips, spread over the LEDA, are present in the 2015 pixel gain set.

The determination of the individual pixel gain factors in space has been proved to be a difficult task to undertake because of the varying measurement circumstances. Here the main results and the conclusion will be presented and for further details it is referred to section 3.4.2 and section 3.4.3. Between April and July 2014 the depletion in the center of the MCP increased from about 20% to ~40% for GS 16. In the following months severe changes of the individual pixel gain factors occurred which can be seen in the individual pixel gain set from November 2014. First the depletion in the center increased again to ~50% for GS 16, second another large dip appeared in the center around pixel 300, and third at least 10 new dips are present spread all over the LEDA. The change in the individual pixel gain factors can be explained with the measured signal as it has been shown in section 3.4.3.2.
Beginning of 2015 it became apparent that the data reduction procedure used so far did not correct all dependencies in the data because a comparison of the pixel gain factors for the same gain step revealed differences in the level height for regions besides the dips. Thus it has been concluded that the so far used correction of the change in water signal is not yet adequate. Consequently the change in depletion between November 2014 and February 2015 can not be quantified with the needed accuracy. However, it is assumed that no significant change occurred since the signal densities were at least a factor 10 lower than in October 2014 and because the increase in depletion slows down in already depleted regions.
In March 2015 numerous pixel gain measurements were performed following an adapted measurement procedure with the aim to measure the individual pixel gain on several gain steps. On the basis of the resulting pixel gain factors the change in depletion between July 2014 and begin of March 2015 could be determined for GS 16 and 12 which increased from ~0.62 to ~0.42 and from about 0.37 to 0.25, respectively. Based on this set of individual pixel gain factors it has been tried to determine the manifestation of depletion for FS. However, no substantial conclusions with respect to the dip depth relative to the gain step could be drawn because the present pixel gain sets are thought to be still biased from the evolution of water signal. In addition, the difference in the change of depletion for GS 12 and GS 16 between July 2014 and March 2015 is supposed to be biases as well. Best would be to refine the existing individual pixel gain data sets but before some ambiguity have to be removed. First is there a presence of a slope for GS 15 and 16 between pixel 1 and 200 due to the MCP? Second can it be justified to assume that the regions between two dips in the first half of the MPC lay at 1, thus do not show any depletion? Third is there a pristine change of level between pixel 350 and 400 or is this a remnant of not proper correction for water in the data acquired before April 2014? The first of those questions might be answered within the next months since several pixel gain measurements were performed in July 2015 on GS 15 and GS 16. However, in order to answer the other two question further investigations are needed.
Despite the bias present in the pixel gain it has been shown that for ratios of peak areas

acquired at the same gain step and within a difference in peak center up to 6 pixels the introduced uncertainty is smaller than 10%. If the signal was acquired at different gain steps the uncertainty due to the individual pixel gain factors is assumed to be smaller than 15%.

For the further mission it is suggested to shift the signal to a region of the MCP which shows less depletion e.g. around pixel 220 and to do more frequent pixel gain measurements when the density around Rosetta is similar or higher than what it was in October 2104 when Rosetta was within 10 km distance to the nucleus.

5.2 Isotopic Ratios in Sulfur Bearing Species at 67P

Comparing abundances of OCS, SO_2, S_2, and CS_2 relative to H_2S with other comets does not lead to a gain of knowledge since the uncertainties are too large. However, a correlation between the sub satellite latitude and the relative abundance of CS_2 and OCS was seen in 67P in October 2014 indicating either a seasonal effect or a result of different evolution of the two hemispheres due to different insolation.

In this study isotope fractionation of ^{34}S are reported in H_2S, OCS, SO_2, S_2, and CS_2 and of ^{33}S in H_2S, SO_2 while a tentative value is given for CS_2. With weighted means for linked measurements of -50 ± 22‰ and -306 ± 31‰ for $\delta^{34}S$ and $\delta^{33}S$ resp. H_2S shows a significant depletion in both ^{34}S and ^{33}S. In contrast SO_2 shows with -67 ± 40‰ and -130 ± 53‰ for $\delta^{34}S$ and $\delta^{33}S$ resp. the smallest deviation from V-CDT. Furthest away in the sulfur three isotope space lays CS_2 with -114 ± 21‰ and -276 ± 55‰ for $\delta^{34}S$ and $\delta^{33}S$, respectively. For OCS and S_2 only $\delta^{34}S$ could be determined accounts for -252 ± 77‰ and -357 ± 145‰.

For H_2S, SO_2, and CS_2 three different types of spread are identified in the three isotope plot. H_2S has most of its values around the weighted mean however one third show an enrichment in ^{33}S and/or ^{34}S. In addition, there seems to be on a large scale a correlation between sub satellite latitude and isotope fractionation meaning the more negative the latitude the stronger the enrichment in ^{32}S and vice versa. Unfortunately the data set is too small to give significant results regarding the sub satellite latitude dependence. Furthermore, the the distance to the comet was still too large to determine the footprint for the measured region in the coma on the nucleus. Thus no further conclusion could be drawn. The data set of SO_2 is scarce and besides two outliers only a spread in $\delta^{34}S$ was present. Since for all results of SO_2 the data used was acquired at latitudes above 20° no further knowledge about a potential correlation between isotope fractionation and latitude could be obtained. In contrast to HS_2 and SO_2 CS_2 shows a large spread in $\delta^{33}S$ resulting in two sub sets one close to the mean of H_2S and the other one around -145 ± 37‰ and 231 ± 38‰ for $\delta^{34}S$ and $\delta^{33}S$, respectively. The spread in $\delta^{33}S$ is supposed to be caused by the assumption of terrestrial $^{12}C/^{13}C$ for the correction of the signal seen on m/z 77 u/e. Similar as for H_2S the isotope fractionation for ^{33}S and ^{34}S could be determined over a wider range of latitudes but no correlation between isotope fractionation and location of the spacecraft in the coma is present in this data set.

The unexpected considerable deviation from the standard V-CDT led to a small study considering an instrumental bias to be the cause for the seen deviations. However, a bias through the individual pixel gain factors and the sensitivity relation for MCP/LEDA could be ruled out as cause.

The obtained isotopic compositions in this study show first that comets differ significantly from sulfur isotopic ratios measured in other solar system bodies like meteorites, second that photo dissociation is unlikely to be the sole cause for this heterogeneity, and third that there might be a similarity to SiC grains. Surprisingly the weighted means for H_2S, SO_2, and CS_2 lay within the so far obtained data of SiC grains found in mainly Murchison meteorite. Nevertheless it is not known whether this is a coincidence, the indication of common evolution which led to similar isotope fractionation or whether this indicates a direct link between SiC grains and the volatile sulfur bearing species in 67P/Churyumov-Gerasimenko.

For H_2S a tentative upper value for D/H of $(9.64 \pm 0.19) \cdot 10^{-4}$ is reported which is almost a factor two larger than what has been reported by Altwegg et al. (2015) for D/H in water for the same comet. So far only two upper limits have been given for D/H in H_2S, one for Hale-Bopp where the limit is $2 \cdot 10^{-1}$ (Crovisier et al., 2004) and for comet Holmes it is $8 \cdot 10^{-3}$ (Biver et al., 2008). Besides this the D/H has been determined so far only for one object outside of the Solar System namely the protobinary source IRAS 16293-2422. The value obtained by van Dishoeck et al. (1995) for D/H is 0.10 with about 50% uncertainty. The upper limit of D/H in HDS for comet 67P is significantly lower than the two upper limits reported so far and it is about a factor of 100 lower from what has been observed in IRAS 16293-2422.

A. Dispersion - FM

In this chapter the deviation *dm*, occurring in low resolution mode, for measurements of CO_2, Kr, and Xe are shown with respect to the dispersion and to the location on the LEDA. For more details see section 3.1.

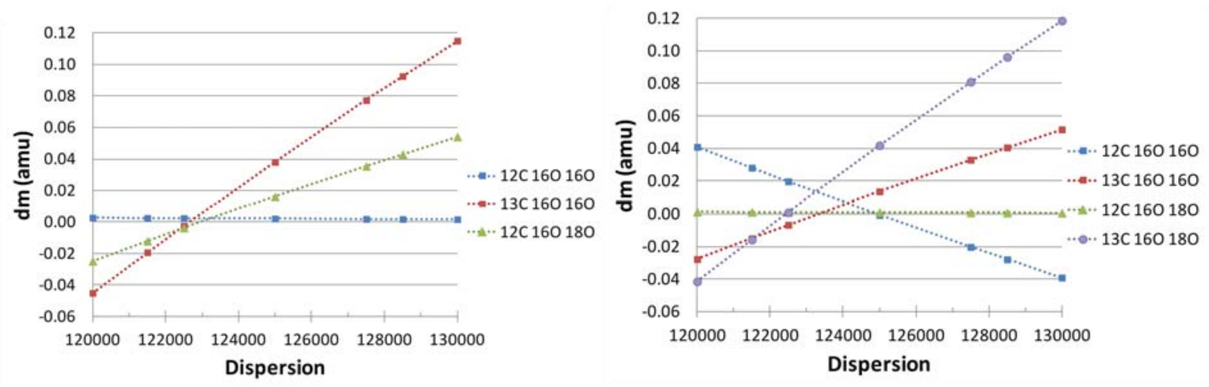

(a) m/z 44 u/e **(b)** m/z 45 u/e

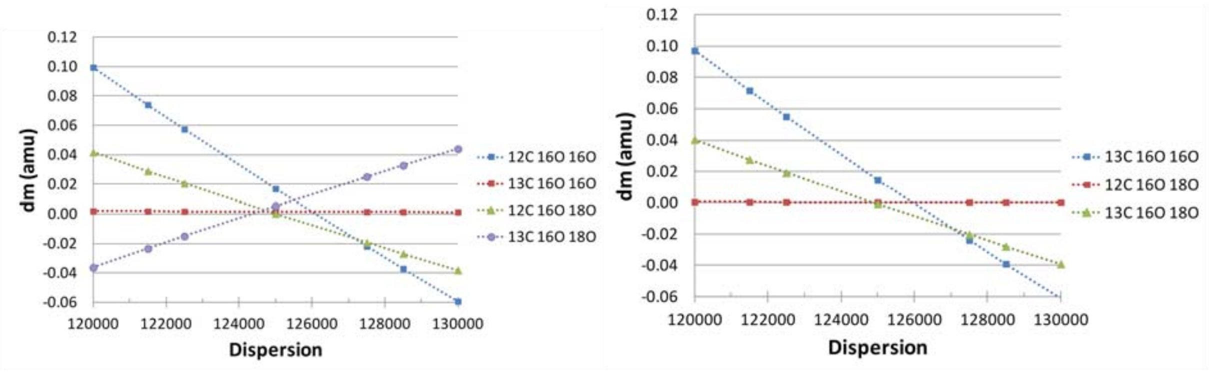

(c) m/z 46 u/e **(d)** m/z 47 u/e

Fig. A.0.1: Relation between dispersion and deviation (*dm*) in mass for CO_2 for MCP/LEDA low resolution spectra.

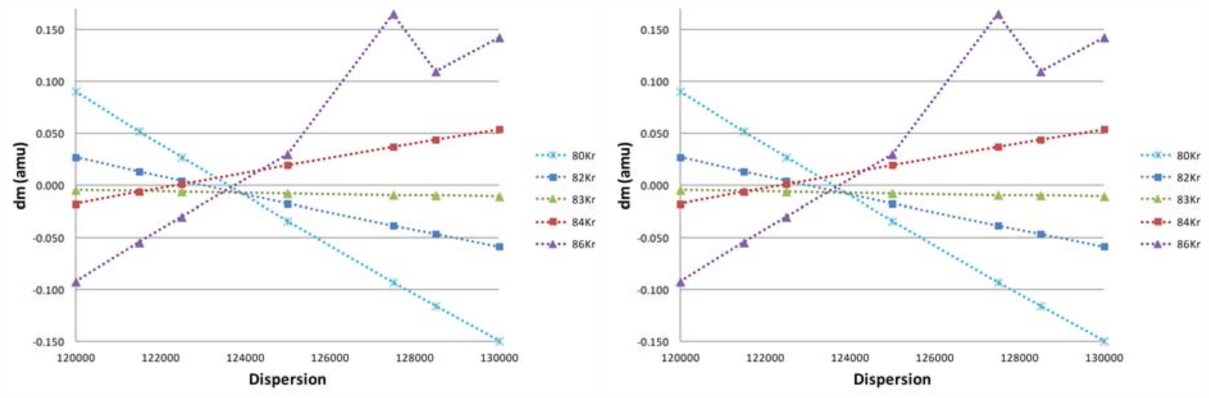

(a) m/z 83 u/e **(b)** m/z 84 u/e

Fig. A.0.2: Relation between dispersion and deviation (*dm*) in mass for Kr for MCP/LEDA low resolution spectra.

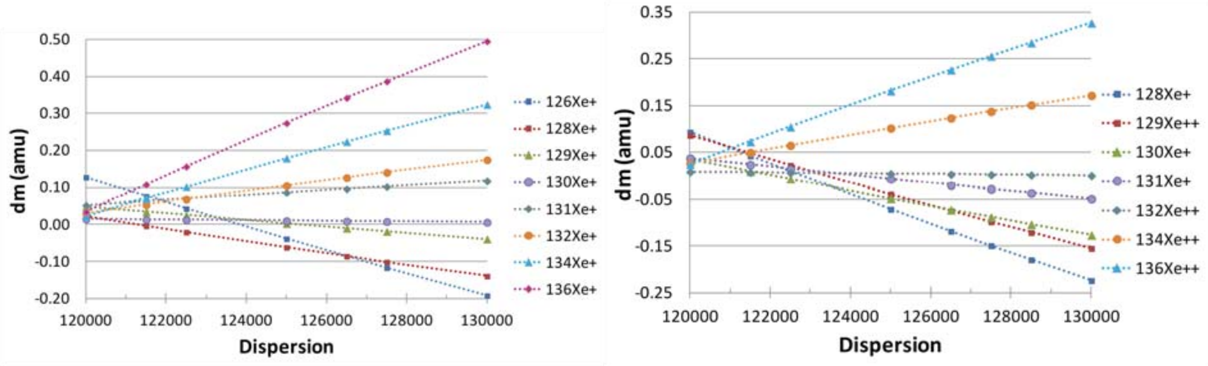

(a) m/z 130 u/e **(b)** m/z 132 u/e

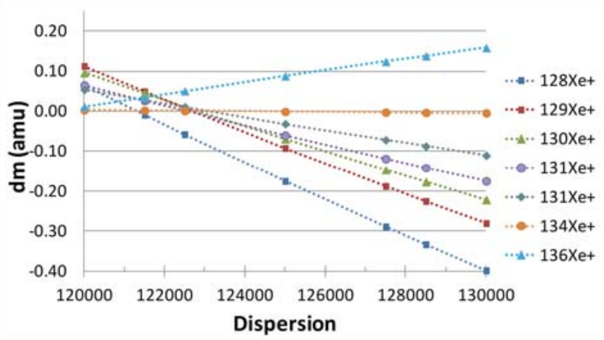

(c) m/z 134 u/e

Fig. A.0.3: Relation between dispersion and deviation (*dm*) in mass for Xe for MCP/LEDA low resolution spectra.

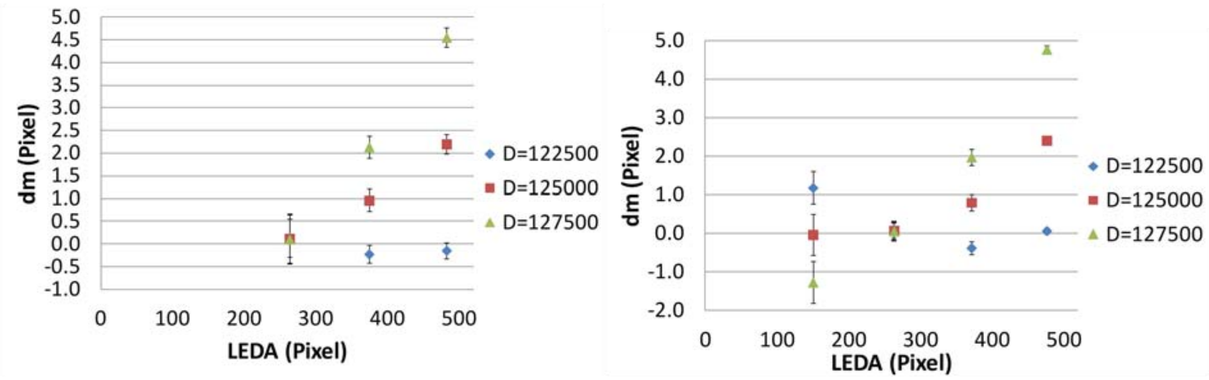

(a) m/z 44 u/e

(b) m/z 45 u/e

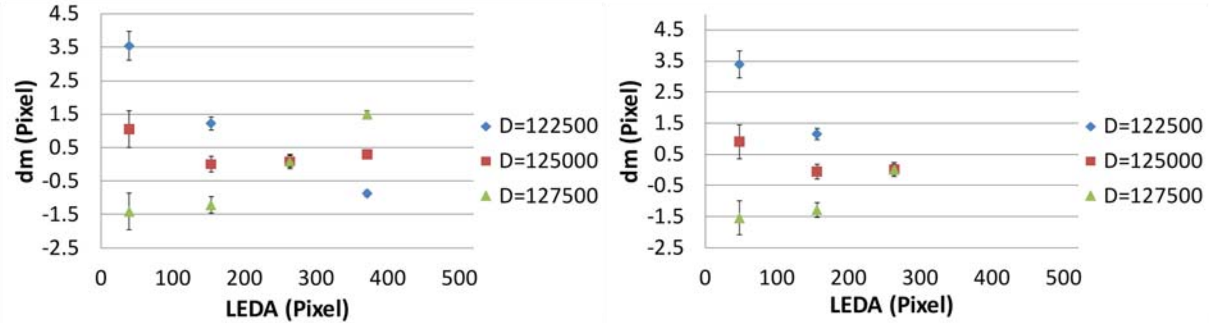

(c) m/z 46 u/e

(d) m/z 47 u/e

Fig. A.0.4: Relation between location on the LEDA and deviation in mass (*dm*) given in pixel for CO_2 in MCP/LEDA for low resolution spectra.

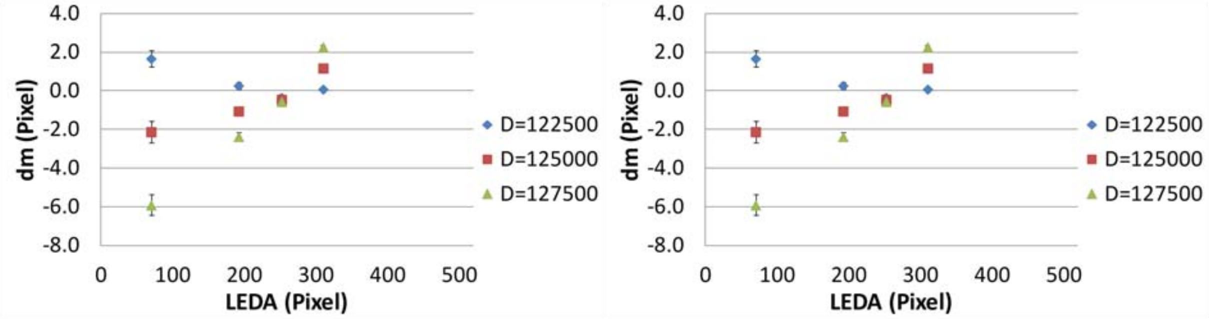

(a) m/z 83 u/e

(b) m/z 84 u/e

Fig. A.0.5: Relation between location on the LEDA and deviation in mass (*dm*) given in pixel for Kr in MCP/LEDA for low resolution spectra.

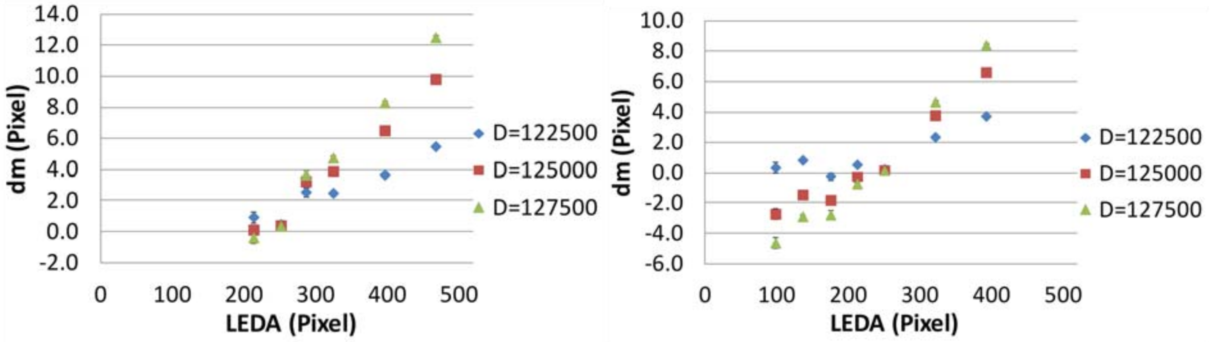

(a) m/z 130 u/e **(b)** m/z 132 u/e

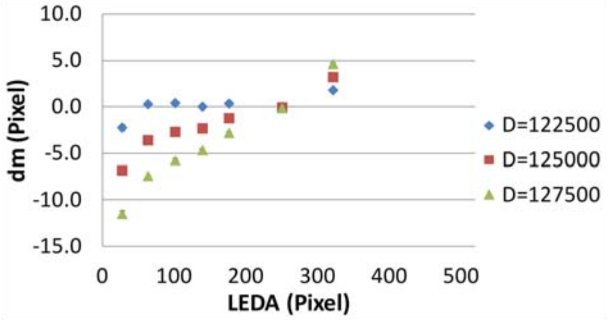

(c) m/z 134 u/e

Fig. A.0.6: Relation between location on the LEDA and deviation in mass (*dm*) given in pixel for Xe in MCP/LEDA for low resolution spectra.

Table A.0.1: Resulting fit parameters and fit function for the deviation *dm* around m_0 132 u/e. For more details see section 3.1

$$\begin{gathered} fit(x,y) = p00 + p10 \cdot x + p01 \cdot y \\ +p20 \cdot x^2 + p11 \cdot x \cdot y \\ +p30 \cdot x^3 + p21 \cdot x^2 \cdot y \\ +p40 \cdot x^4 + p31 \cdot x^3 \cdot y \\ p50 \cdot x^5 + p41 \cdot x^4 \cdot y \end{gathered}$$

where x is normalized by mean -26.71 and std 96.81

Fit parameters		95% confidence bounds	
		lower bound	upper bound
p00	-0.01083	-0.01551	-0.006153
p10	0.07447	0.0578	0.09114
p01	-0.01921	-0.02436	-0.01405
p20	0.05627	0.04272	0.06981
p11	0.0687	0.06047	0.07692
p30	0.0001457	-0.02758	0.02787
p21	0.0006109	-0.01204	0.01327
p40	-0.01637	-0.02402	-0.008723
p31	-0.0007997	-0.006404	0.004804
p50	0.003025	-0.006561	0.01261
p41	0.000554	-0.004877	0.005985

B. Calibration

In this chapter first the mass spectra acquired with MCP/LEDA at 200 µA are shown for the calibration of NH_3 and H_2S. Second it is explained how sensitivities can be calculated for MCP/LEDA for species which could not be calibrated. There is no procedure yet for the CEM sensitivities because the obtained fits in section 3.3 base on a scarce data set.

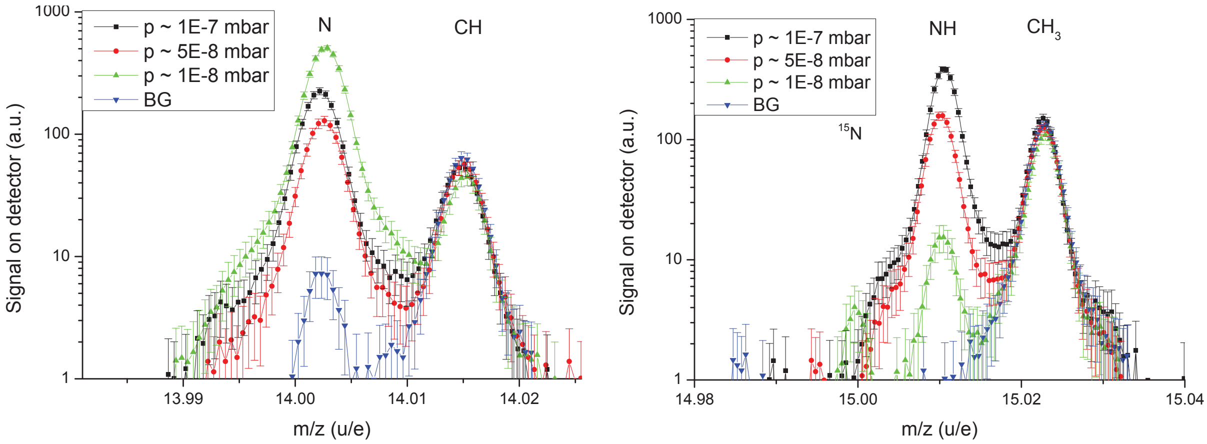

(a) m/z 14 u/e

(b) m/z 15 u/e

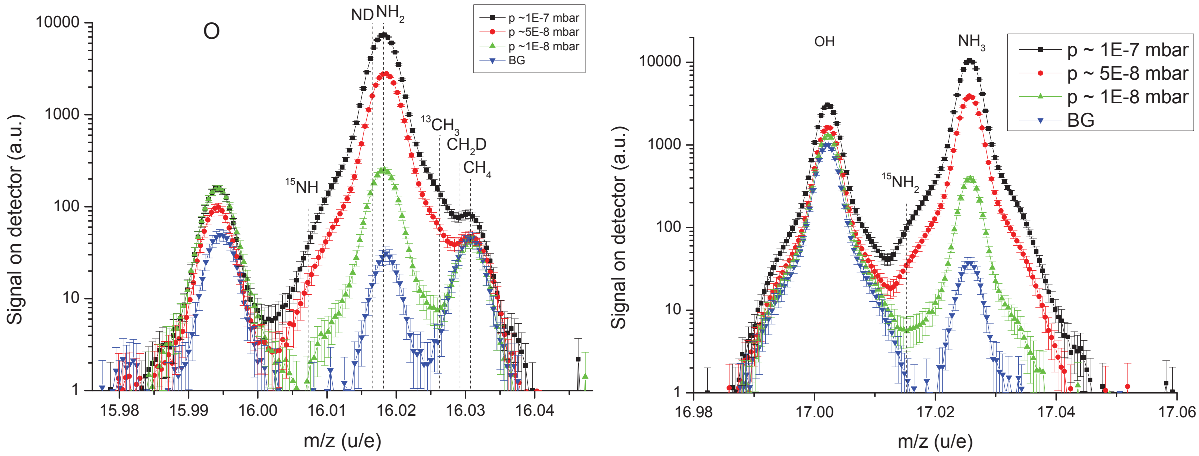

(c) m/z 16 u/e

(d) m/z 17 u/e

Fig. B.0.1: Mass spectra of MCP/LEDA row A measured with an emission of 200 µA at three pressure ranges plus background pressure.

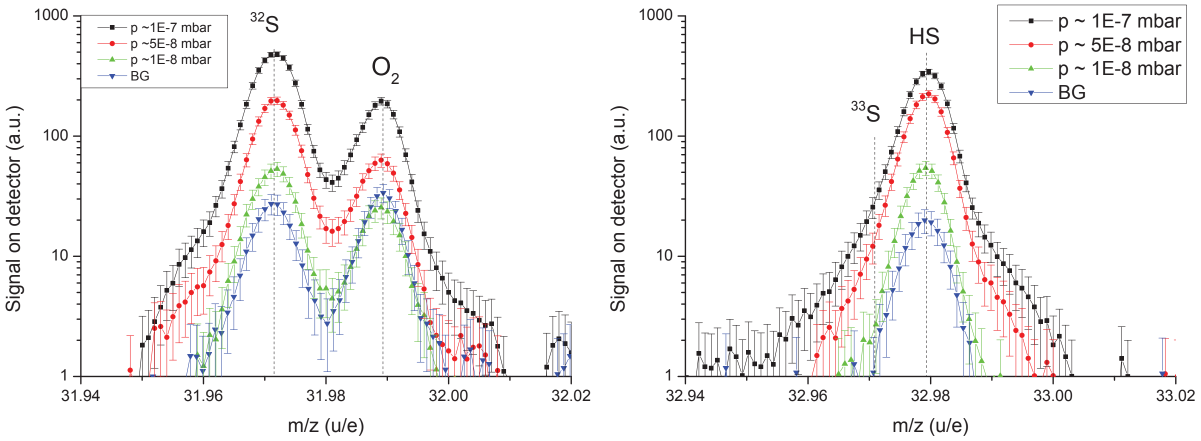

(a) m/z 32 u/e **(b)** m/z 33 u/e

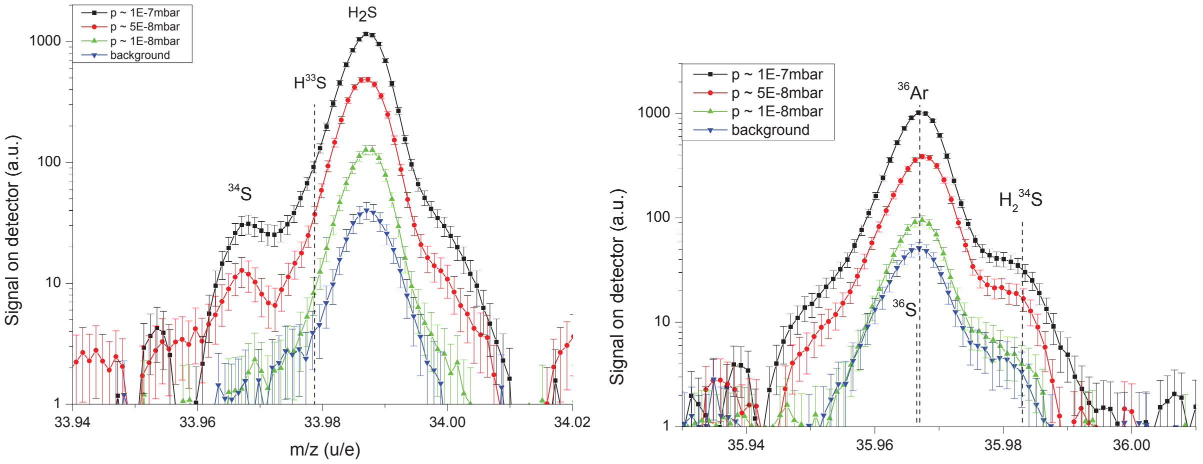

(c) m/z 34 u/e **(d)** m/z 36 u/e

Fig. B.0.2: Mass spectra of MCP/LEDA row A measured with an emission of 200 µA at three pressure ranges plus background pressure.

B.1 How to Handle Sensitivities which have not been Measured for MCP/LEDA

First it will be explained how the sensitivity for a neutral species can be estimated based on the relation obtained in section 3.3. Afterward it will be explained for ions. However, for those the empirical sensitivity can be calculated only up to 69 u/e because no calibration measurements have been done for ions with post acceleration PA = -1000V.

Neutrals For mass to charge ratios lower than 70 u/e and neutral mode the sensitivity for a species at mass i will be calculated the following:

1. Calculate $\mathrm{S}_{\mathrm{relative,emission}}$ via:

$$S_{relative,i} = (16 \pm 40) \cdot x^{(-0.82 \pm 1.19)-(0.34 \pm 1.37)} \tag{B.1.1}$$

2. Calculated $\mathrm{S}_{\mathrm{absolute,i,emission}}(\mathrm{cm}^{-3})$ using $\mathrm{S}_{\mathrm{relative,emission}}$ and $_{\mathrm{corr,Ne,emission}}$ that are given in table B.1.1:

$$S_{\mathrm{absolute,i,emission}}(cm^{-3}) = S_{\mathrm{relative,i}} \cdot S_{\mathrm{corr,Ne,emission}} \cdot \sigma_{EII}(45eV) \tag{B.1.2}$$

Table B.1.1: Neon sensitivities of MCP/LEDA corrected for ionization efficiency.

	$\mathrm{S}_{\mathrm{corr,Ne}}$ (cm^{-1})
HR - 2uA	9.57E-03 ± 1.51E-03
HR - 20uA	4.03E-03 ± 6.38E-04
HR - 200uA	1.42E-03 ± 2.24E-04

For masses equal and higher than 70 u/e with post acceleration PA = -1000 V the following has to be done:

$$S_{\mathrm{relativ,i,emission}} = S_{\mathrm{relativ,Kr,emission}} + (m/z - 84) * slope_{\mathrm{emission}} \tag{B.1.3}$$

with values given in Table B.1.2 and then the step 2 of the procedure for masses lower than 70 has to be performed.

Table B.1.2: Krypton sensitivities relative to neon for MCP/LEDA. Both Ne and Kr are corrected for the ionization efficiency.

	$\mathrm{slope}_{\mathrm{emission}}$	$\mathrm{S}_{\mathrm{relativ,Kr,emission}}$
HR - 2uA	-5.02E-03 ± 6.91E-02	3.03E-01 ± 6.77E-02
HR - 20uA	-1.14E-02 ± 2.24E-01	6.78E-01 ± 1.52E-01
HR - 200uA	-1.26E-02 ± 2.55E-01	8.43E-01 ± 1.88E-01

Ions For mass to charge ratios lower than 70 u/e with nominal post acceleration (PA = -50 V) the following has to be done:

1. Calculate $\mathrm{S}_{\mathrm{relative,emission}}$ via:

$$S_{relative,i} = (15 \pm 8.7) \cdot x^{(-0.776 \pm 0.254)-(0.47 \pm 0.29)} \tag{B.1.4}$$

2. Determine the sensitivity for the mass to charge ratio i and energy corresponding to the grid value. The values for the absolute sensitivties for Ne for different energies and both resolutions are given in table B.1.3.

$$S_{\text{absolute,i,energy}} = S_{\text{absolute,Ne,energy}} \cdot S_{\text{relative,i}} \tag{B.1.5}$$

Table B.1.3: The uncertainties for the values are estimated to be 20% (Schläppi, 2011).

	$\mathrm{S}_{\text{absolut,Ne,Ion}}$ (Ion/s)
HR - 5eV	4.78E-04
HR - 10eV	6.34E-03
HR - 20eV	1.46E-04
LR - 5eV	1.74E-03
LR - 10eV	1.40E-04
LR - 20eV	1.93E-03

C. Individual Pixel Gain - FS

In this appendix first the Matlab code for the evaluation of the pixel gain measurements in the lab is presented. The code for FS deviates only in the application of the three types of corrections form the one of FM. Then for all measurements performed in March 2015 the resulting pixel gain factors calculated nominal and via interpolation of the peak maxima are shown. The values are not corrected for COPS or the evolution of water and bad stepping points are indicated with a cross. Afterward all pixel gain measurements performed between January and end of March 2015 a compilation of all corrections is shown for both nominal calculated and via interpolation of the peak maxima. In between always the corresponding COPS nude gauge measurement are shown in order to give an flavor of the measurement conditions during the pixel gain measurements. The graphs are composed to be self explaining and in the caption it is explained which correction and why has been chosen for giving the values thought to be closest to the true ones.

C.1 Matlab Code

Filename: Pixelgain_V4.m

```
clear all;
close all;

% Initialization & Data upload
%--------------------------

PixelgainFactor = zeros(511,2);
Files           = zeros(138,1);
PosMax          = zeros(138,2);
Diff            = zeros(138,2);
ValueMax        = zeros(138,2);
Indexbla        = zeros(138,2);
IndexBad        = zeros(138,2);
PeakSum         = zeros(511,2);
Hit             = zeros(138,2);
DATA_C          = zeros(511,2);
Summe           = zeros(511,2);
Summe_U         = zeros(511,2);

delimeterIn = ',';
headerLines = 129;
plotindex = 1 ;
x = linspace(1,511,511);

% load data
%-----------

FileList = importdata('Path_GS16_3_backwards.txt');
GS = 16;

pp = 1;
for ii = 1:size(FileList,1)
```

```
    Files(ii) = ii;
%     Temp = importdata(FileList{ii},delimeterIn,headerLines);
    for jj = 1:2
        Temp = importdata(FileList{ii},delimeterIn,headerLines);
        if(jj==1)
           [peakLoc, peakMag] = peakfinder(Temp.data(15:511,jj+1),500,1300);
%            [peakLoc, peakMag] = peakfinder(Temp.data(15:511,jj+1),1300,1300);
%comment for measurements LR & mass fourty four => 1/3
        elseif(jj==2)
            [peakLoc, peakMag] = peakfinder(Temp.data(15:511,jj+1),1500,1200);
%             [peakLoc, peakMag] = peakfinder(Temp.data(15:511,jj+1),1300,1200);
%comment for measurements LR & mass fourty four  => 1/3
        end
        index = ii;
        peakLoc = peakLoc + 15;
        groessePeakLoc = size(peakLoc,1);

        bloed = peakLoc ;

        % comment for measurements LR & mass fourty four
        %--------------------------------------
        if(size(peakLoc,1) > 4)
            continue
        end
        if(size(peakLoc,1) == 4)
            for ww = 1 : 3
                PeakPos(ii,ww) = peakLoc(ww,1);
                PeakMax(ii,ww) = peakMag(ww,1);
            end
        end
        %--------------------------------------

        % uncomment for measurements LR & mass fourty four => 2/3
%         %--------------------------------------
%         if(size(peakLoc,1) == 4)
%             for ww = 1 : 4
%                 PeakPos(ii,ww) = peakLoc(ww,1);
%                 PeakMax(ii,ww) = peakMag(ww,1);
%             end
%         end
%         if(size(peakLoc,1) == 5)
%             for ww = 1 : 5
%                 PeakPos(ii,ww) = peakLoc(ww,1);
%                 PeakMax(ii,ww) = peakMag(ww,1);
%             end
%         end
%         if(size(peakLoc,1) > 5)
%             continue
%         end
        %--------------------------------------

        if(size(peakLoc,1) == 3)
            for ww = 1 : 3
                PeakPos(ii,ww) = peakLoc(ww,1);
                PeakMax(ii,ww) = peakMag(ww,1);
            end
        elseif(size(peakLoc,1) == 2)
            for ww = 1 : 2
```

```
                PeakPos(ii,ww) = peakLoc(ww,1);
                PeakMax(ii,ww) = peakMag(ww,1);
            end
        elseif(size(peakLoc,1) == 1)
            for ww = 1 : 1
                PeakPos(ii,ww) = peakLoc(ww,1);
                PeakMax(ii,ww) = peakMag(ww,1);
            end
        elseif(size(peakLoc,1) == 0)
            continue
        end

        if(jj==1)
            [cf_ ft_]    = FitbgA(Temp.data(5:511,1),Temp.data(5:511,jj+1) ...
                        ,PeakPos(ii,:));
%              [cf_ ft_]    = %FitbgAm44(Temp.data(5:511,1) ...
%,Temp.data(5:511,jj+1),PeakPos(ii,:)); %  => 3/3
            Data_A(:,ii) = Temp.data(:,jj+1) -  polyval(coeffvalues(cf_),x)';
            bg_A(:,ii)   = polyval(coeffvalues(cf_),x)';
            clear cf_
            clear ft_
        elseif(jj==2)
            [cf_ ft_]    = FitbgB(Temp.data(20:511,1),Temp.data(20:511,jj+1) ...
                        ,PeakPos(ii,:));
%              [cf_ ft_]    = %FitbgBm44(Temp.data(20:511,1) ...
%,Temp.data(20:511,jj+1),PeakPos(ii,:)); %  => 3/3
            Data_B(:,ii) = Temp.data(:,jj+1) -  polyval(coeffvalues(cf_),x)';
            bg_B(:,ii)   = polyval(coeffvalues(cf_),x)';
            clear cf_
            clear ft_
        end

        [c index]= max(PeakMax(ii,:));

        PosMax(ii,jj)   = PeakPos(ii,index);
        ValueMax(ii,jj) = c;

        pp = pp +1;
%          clear Temp
        clear index
        clear c
        clear PeakPos
        clear PeakMax
    end

end

% Check step width (nominal = 4 pixel)
% ----------------------------
for ii = 1:size(PosMax,1)-1
    for jj = 1:2
        Indexbla(ii,jj) = ii;
        Diff(ii,jj)        = (PosMax(ii+1,jj)-PosMax(ii,jj)) - 4;
                % 4 is the nominal step widt/ so Diff is the deviation
                % of the nominal position for the step ii

        if(ii >= 2 && Diff(ii-1,jj)~=0 && Diff(ii,jj)~=0)    % Here further
        %distinctions are needed for the case one side has ==0
```

```
        %but the other not!
            Hit(ii,jj)      = 1;
            IndexBad(ii,jj) = ii;
        end
    end
end

% Select the data to be used
%----------------------------

% if this is a a straigth line the selection is ok else change i in the
% loop above
figure(1)
plot(Files,PosMax(:,1),'+r',Files,PosMax(:,2),'+b','MarkerSize',10)
legend('Row A','Row B')
set(findall(figure(1), '-property', 'FontSize'), 'FontSize', 20, 'fontWeight', ...
% 'bold')
set(gcf,'PaperUnits','Normalized','PaperPosition',[0 0 1.5 1])
print('PxGain-Ne20150612_GS16_3_backwards_Peakposition','-depsc2')

xfit  = linspace(1,511,511);

Gain = [1.41E-1, 3.88E-1, 1.01, 2.79, 7.63, 2.20E1, 6.48E01, 1.94E02, 5.97E02, ...
 1.90E03, 6.41E03, 2.25E04, 7.84E04, 2.89E05,1.02E06, 2.78E06];

ConversionToIons = 1/(Gain(GS))*2.5/(2^12-1)*4.22*10^-12/(1.60217646*10^-19);

DATA_A          = zeros(511,130);
DATA_B          = zeros(511,130);

StartLoop = 12;
EndLoop   = 129;
for i = StartLoop:EndLoop

    % Calculate the amount of signal each detector pixel got
    % The signal is corrected for the COPS pressure
    %-------------------------------------------------------
    if(PosMax(i,1) > 20 && PosMax(i,1) < 491) % first attempt is to only
        %calculate the values for the middle of the MCP
        for(kk =(PosMax(i,1) - 20):(PosMax(i,1) + 20))
            DATA_C(kk,1) = kk;
            DATA_C(kk,2) = i;
            DATA_A(kk,i) = Data_A(kk,i)*ConversionToIons;
            DATA_B(kk,i) = Data_B(kk,i)*ConversionToIons;

            Uncertainty_A(kk,i) =  sqrt(abs(Data_A(kk,i))*ConversionToIons);
            Uncertainty_B(kk,i) =  sqrt(abs(Data_B(kk,i))*ConversionToIons);

            Summe_U(kk,1) = Summe_U(kk,1) + Uncertainty_A(kk,i)^2;
            Summe_U(kk,2) = Summe_U(kk,2) + Uncertainty_B(kk,i)^2;

            Summe(kk,1) = Summe(kk,1) + Data_A(kk,i)*ConversionToIons;
            Summe(kk,2) = Summe(kk,2) + Data_B(kk,i)*ConversionToIons;
        end


        yfitnA = (DATA_A(PosMax(i,1)-20:PosMax(i,1)+20,i) - ...
                mean(DATA_A(PosMax(i,1)-20:PosMax(i,1)+20,i)))/ ...
```

```
                std(DATA_A(PosMax(i,1)-20:PosMax(i,1)+20,i));
        xfitnA = (xfit(PosMax(i,1)-20:PosMax(i,1)+20) - ...
                mean(xfit(PosMax(i,1)-20:PosMax(i,1)+20)))/ ...
                std(xfit(PosMax(i,1)-20:PosMax(i,1)+20));
        [sigmaA,muA,AA]=mygaussfit(xfitnA,yfitnA,0);
        width(i,1) = PosMax(i,1);
        width(i,2) = ValueMax(i,1)*ConversionToIons;
        width(i,3) = sigmaA * std(xfit(PosMax(i,1)-20:PosMax(i,1)+20));


        yfitnB = (DATA_B(PosMax(i,2)-20:PosMax(i,2)+20,i) - ...
                mean(DATA_B(PosMax(i,2)-20:PosMax(i,2)+20,i)))/ ...
                std(DATA_B(PosMax(i,2)-20:PosMax(i,2)+20,i));
        xfitnB = (xfit(PosMax(i,2)-20:PosMax(i,2)+20) - ...
                mean(xfit(PosMax(i,2)-20:PosMax(i,2)+20)))/ ...
                std(xfit(PosMax(i,2)-20:PosMax(i,2)+20));
        [sigmaB,muB,AB]=mygaussfit(xfitnB,yfitnB,0);
        width(i,4) = PosMax(i,2);
        width(i,5) = ValueMax(i,2)*ConversionToIons;
        width(i,6) = sigmaB * std(xfit(PosMax(i,2)-20:PosMax(i,2)+20));

    end
end

Summe_U(:,1) = Summe_U(:,1).^(1/2);
Summe_U(:,2) = Summe_U(:,2).^(1/2);

figure(6)
subplot(3,1,1)
hold on
plot(width(:,1),width(:,3),'+r','MarkerSize',10)
plot(width(:,4),width(:,6),'+b','MarkerSize',10)
ylim([mean(width(:,3))*0.6 mean(width(:,3))*1.6])
hold off
title('Ne20150612 GS16_3_backwards')
legend('Row A','Row B')
ylabel('\sigma narrow Gauss (pixel)')
subplot(3,1,2)
hold on
plot(width(:,1),width(:,2),'+r','MarkerSize',10)
plot(width(:,4),width(:,5),'+b','MarkerSize',10)
ylim([mean(width(:,2))*0.2 mean(width(:,5))*2])
hold off
ylabel('Total peak height (Ions)')
subplot(3,1,3)
hold on
plot(width(:,1),width(:,2)./width(:,3),'+r','MarkerSize',10)
plot(width(:,4),width(:,5)./width(:,6),'+b','MarkerSize',10)
hold off
xlabel('LEDA')
ylabel('h_{peak}/\sigma (Ions/pixel)')
set(findall(figure(6), '-property', 'FontSize'), 'FontSize', 20, 'fontWeight', ...
% 'bold')
set(gcf,'PaperUnits','Normalized','PaperPosition',[0 0 1.5 1])
print('PxGain-Ne20150612_GS16_3_backwards_peakwidth','-depsc2')

figure(4)
hold all
```

```
plot(DATA_A)
hold off
xlabel('LEDA (pixel)')
ylabel('Signal on LEDA (Ions)')
title('Signal on LEDA - Row A')
xlim([0 520])
ylim([0 max(max(DATA_A(:,15),DATA_A(:,120)))*1.4])
set(findall(figure(4), '-property', 'FontSize'), 'FontSize', 20, 'fontWeight', ...
% 'bold')
set(gcf,'PaperUnits','Normalized','PaperPosition',[0 0 1.5 1])
print('PxGain-Ne20150612_GS16_3_backwards_Peak_RowA','-depsc2')

figure(5)
hold all
plot(DATA_B)
hold off
xlabel('LEDA (pixel)')
ylabel('Signal on LEDA (Ions)')
title('Signal on LEDA - Row B')
xlim([0 520])
ylim([0 max(max(DATA_B))*1.1])
set(findall(figure(5), '-property', 'FontSize'), 'FontSize', 20, 'fontWeight', ...
% 'bold')
set(gcf,'PaperUnits','Normalized','PaperPosition',[0 0 1.5 1])
print('PxGain-Ne20150612_GS16_3_backwards_Peak_RowB','-depsc2')

for jj = 1:2
   Factor_nominal(:,jj) = Summe(:,jj)./mean(Summe(21:491,jj));
end

% Plot results
%---------------

dlmwrite('PxGain-Ne20150612_GS16_3_backwards.txt',Factor_nominal,'delimiter', ...
%'\t','precision',10)

figure(3)
plot(x,Factor_nominal(:,1),x,Factor_nominal(:,2),'LineWidth',2)
legend('Row A','Row B','Location','Best')
xlim([0 520])
ylim([0 max(Factor_nominal(:,2))*1.2])
set(findall(figure(3), '-property', 'FontSize'), 'FontSize', 20, 'fontWeight', ...
% 'bold')
set(gcf,'PaperUnits','Normalized','PaperPosition',[0 0 1.5 1])
print('PxGain-Ne20150612_GS16_3_backwards','-depsc2')

tt(:,1) = Files;
tt(:,2:3) = PosMax;
tt(:,4:5) = ValueMax;
dlmwrite('PxGain-Ne20150612_GS16_3_backwards_ValueMax.txt',tt,'delimiter', ...
%'\t','precision',10);

www(:,1:2) = IndexBad;
www(:,3:4) = PosMax;
www(:,5:6) = Hit;
dlmwrite('PxGain-Ne20150612_GS16_3_backwards_BadSteppingPoints.txt',www, ...
% 'delimiter','\t','precision',10)

```

```
dlmwrite('PxGain-Ne20150612_GS16_3_backwards_DataTreated_A.txt',DATA_A, ...
%'delimiter','\t','precision',10)
dlmwrite('PxGain-Ne20150612_GS16_3_backwards_DataTreated_B.txt',DATA_B, ...
%'delimiter','\t','precision',10)
dlmwrite('PxGain-Ne20150612_GS16_3_backwards_width.txt',width, ...
%'delimiter','\t','precision',10)

dlmwrite('PxGain-Ne20150612_GS16_3_backwards_Uncertainty_A.txt', ...
%Uncertainty_A,'delimiter','\t','precision',10)
dlmwrite('PxGain-Ne20150612_GS16_3_backwards_Uncertainty_B.txt', ...
%Uncertainty_B,'delimiter','\t','precision',10)

dlmwrite('PxGain-Ne20150612_GS16_3_backwards_Summe.txt',Summe, ...
%'delimiter','\t','precision',10)
dlmwrite('PxGain-Ne20150612_GS16_3_backwards_Summe_U.txt',Summe_U, ...
%'delimiter','\t','precision',10)
```

C.2 Comparison Between Nominal Calculation and Interpolation of the Maximum

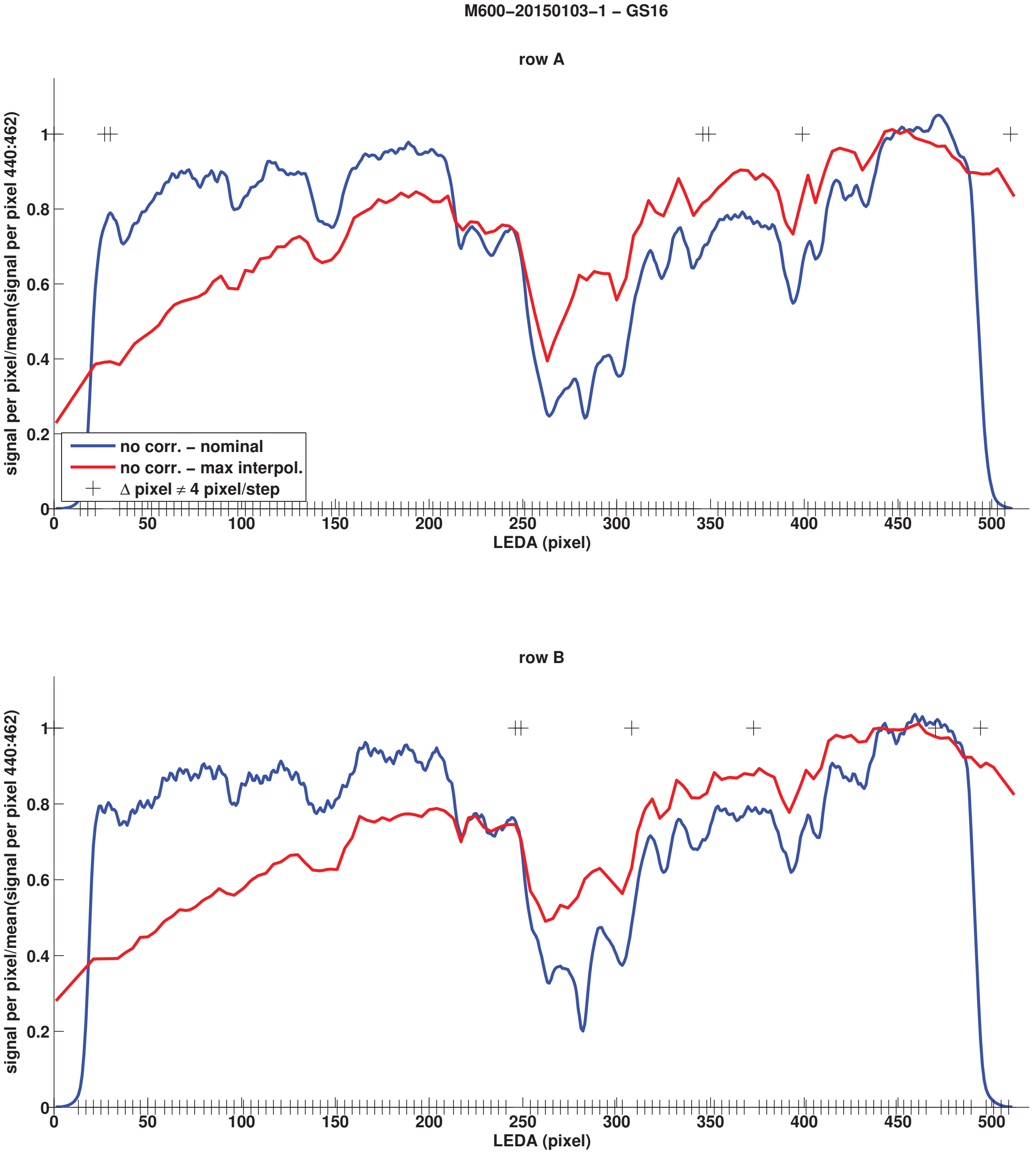

Fig. C.2.1: Pixel gain of the measurement M600-20150103-1-GS16 nominal calculated (blue), calculated by linear interpolation between the maxima (red), and the location of bad stepping points indicated by black crosses.

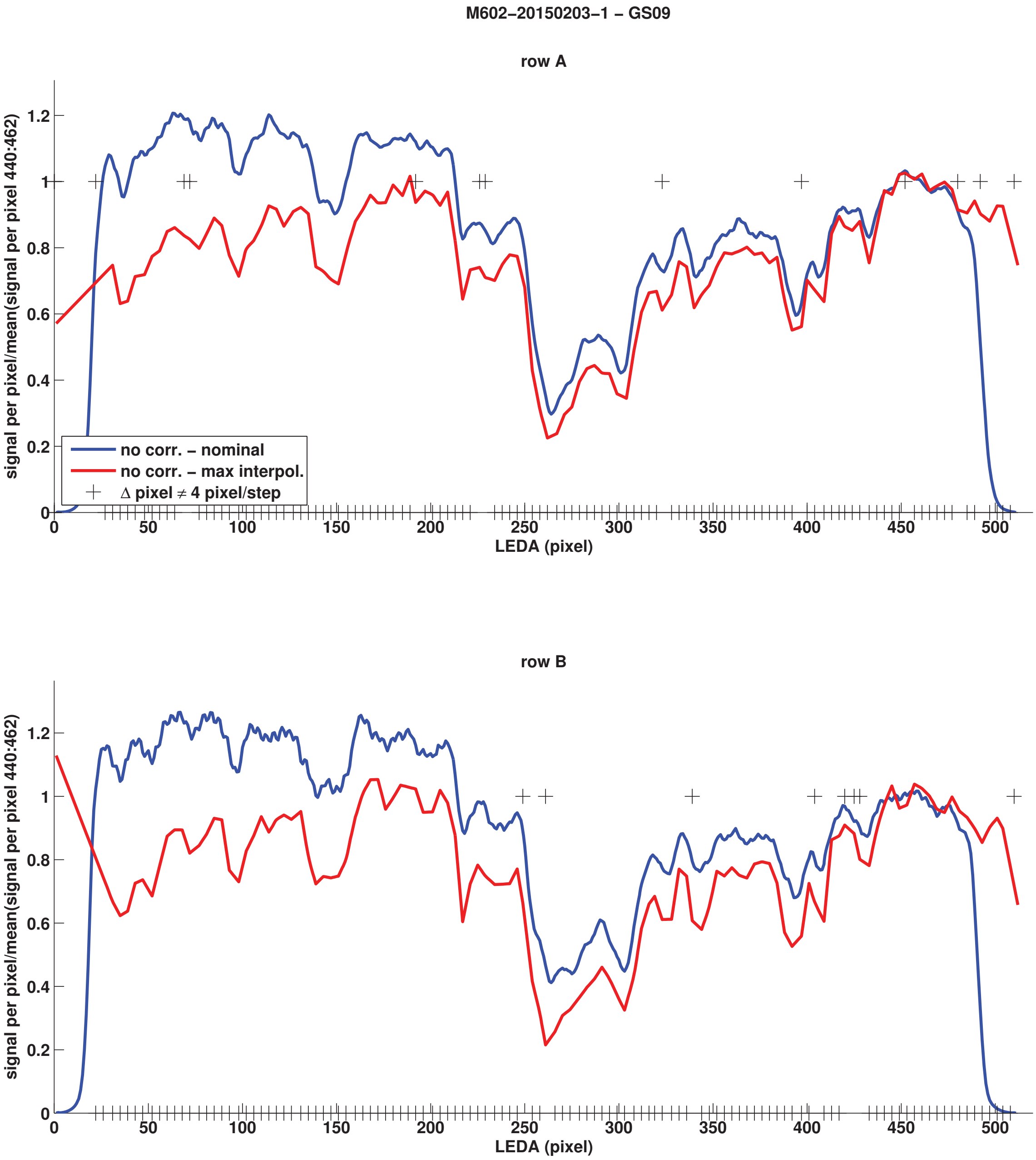

Fig. C.2.2: Pixel gain of the measurement M602-20150203-1-GS09 nominal calculated (blue), calculated by linear interpolation between the maxima (red), and the location of bad stepping points indicated by black crosses.

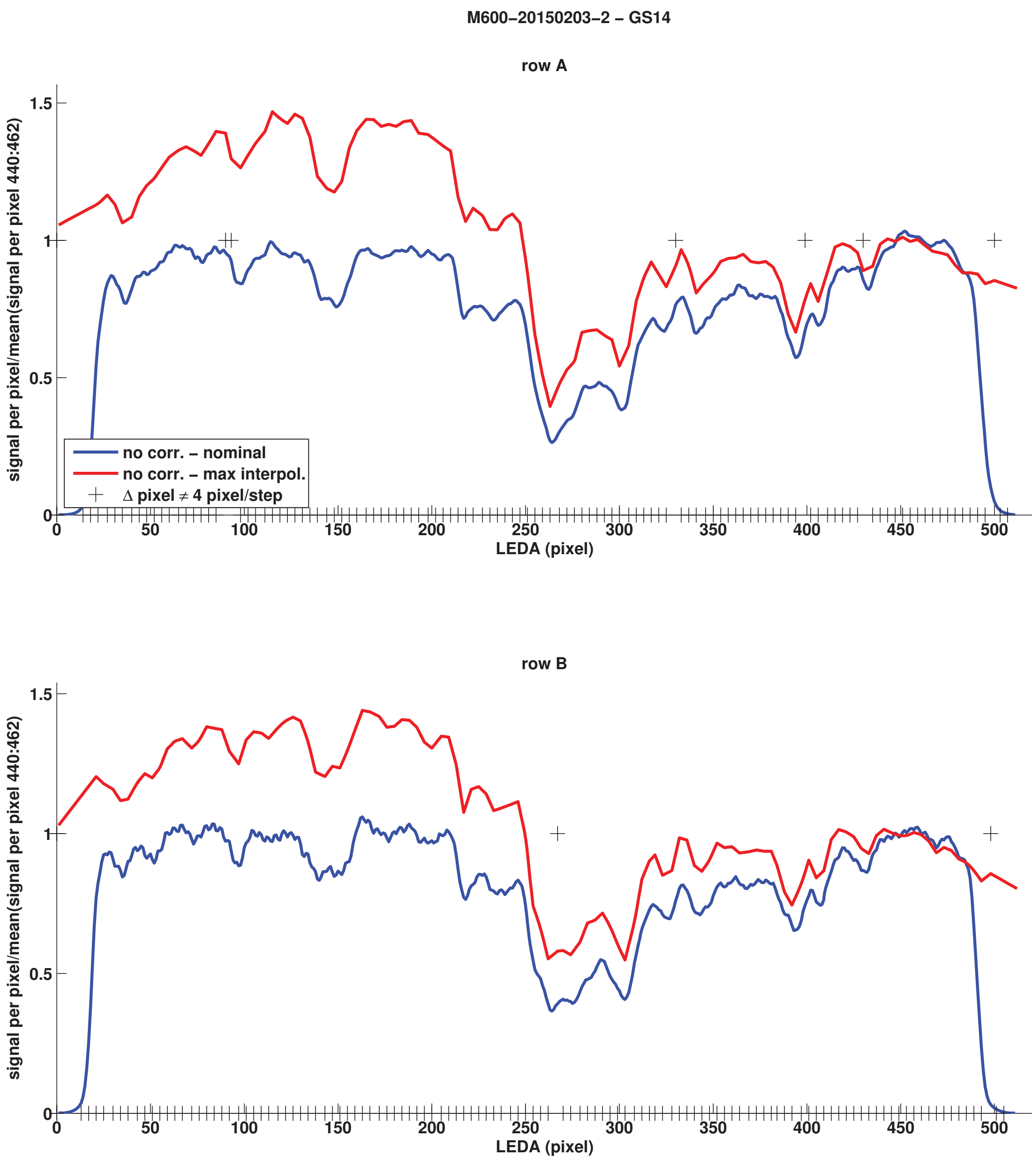

Fig. C.2.3: Pixel gain of the measurement M600-20150203-2-GS14 nominal calculated (blue), calculated by linear interpolation between the maxima (red), and the location of bad stepping points indicated by black crosses.

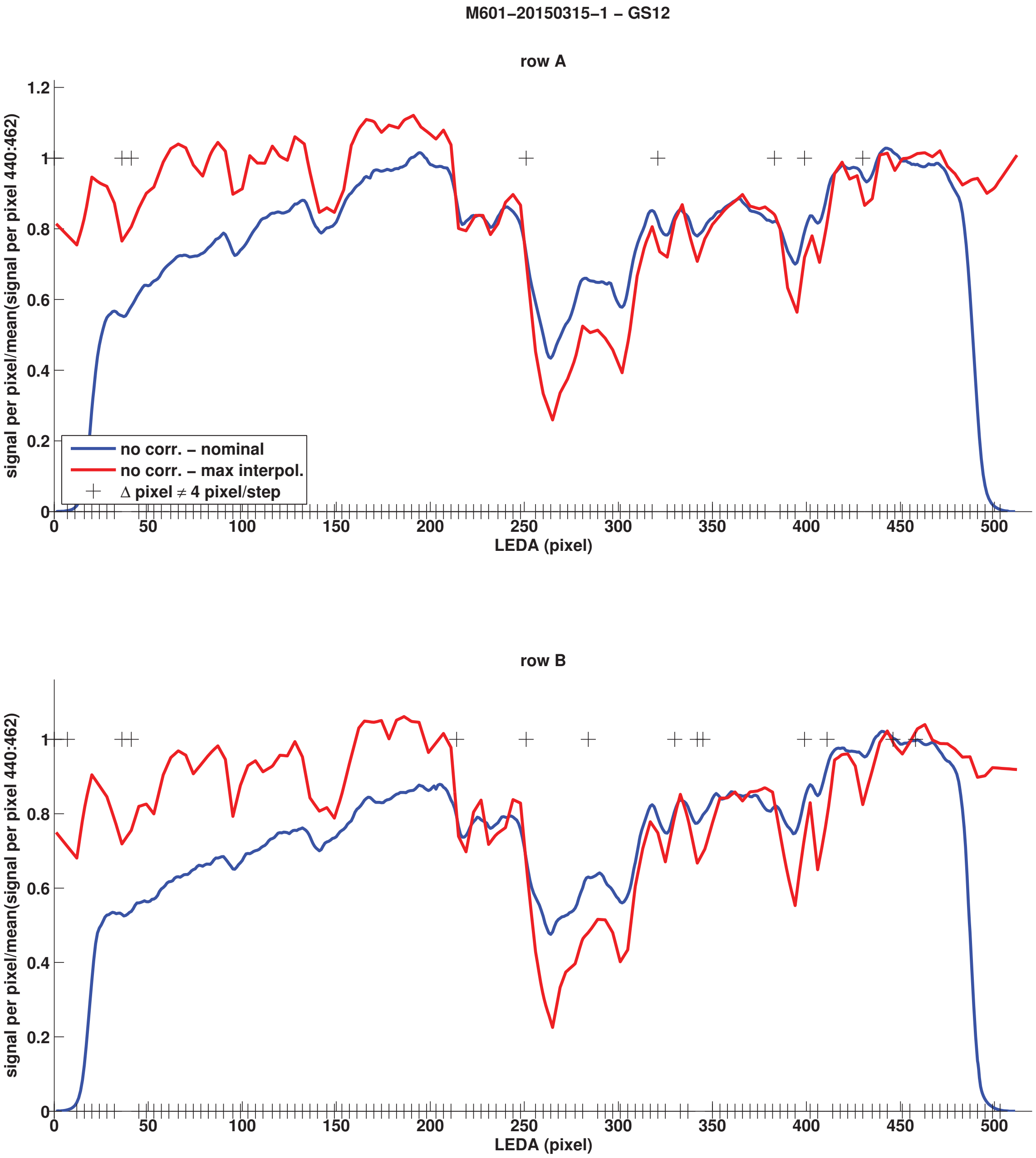

Fig. C.2.4: Pixel gain of the measurement M601-20150315-1-GS12 nominal calculated (blue), calculated by linear interpolation between the maxima (red), and the location of bad stepping points indicated by black crosses.

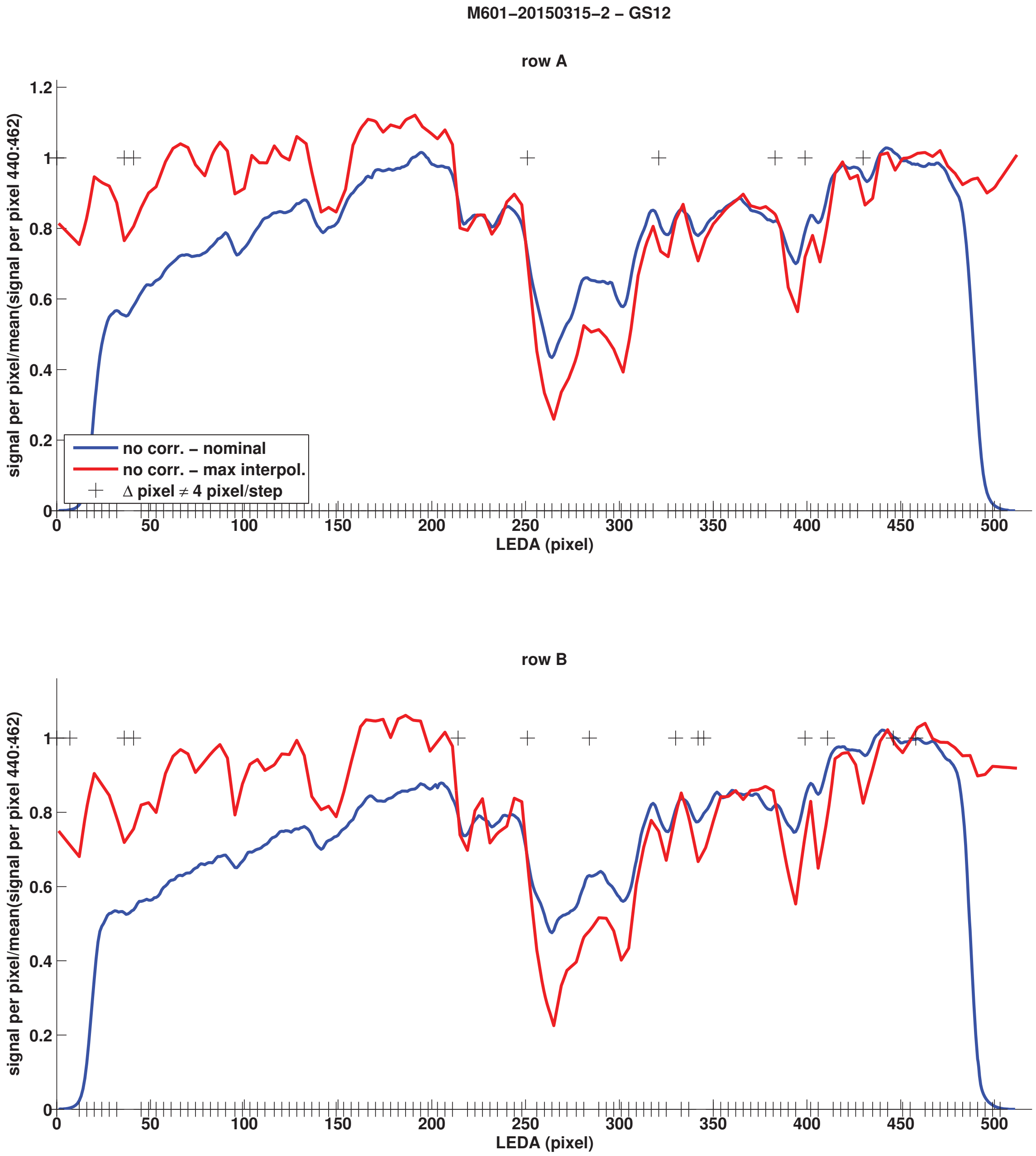

Fig. C.2.5: Pixel gain of the measurement M601-20150315-2-GS12 nominal calculated (blue), calculated by linear interpolation between the maxima (red), and the location of bad stepping points indicated by black crosses.

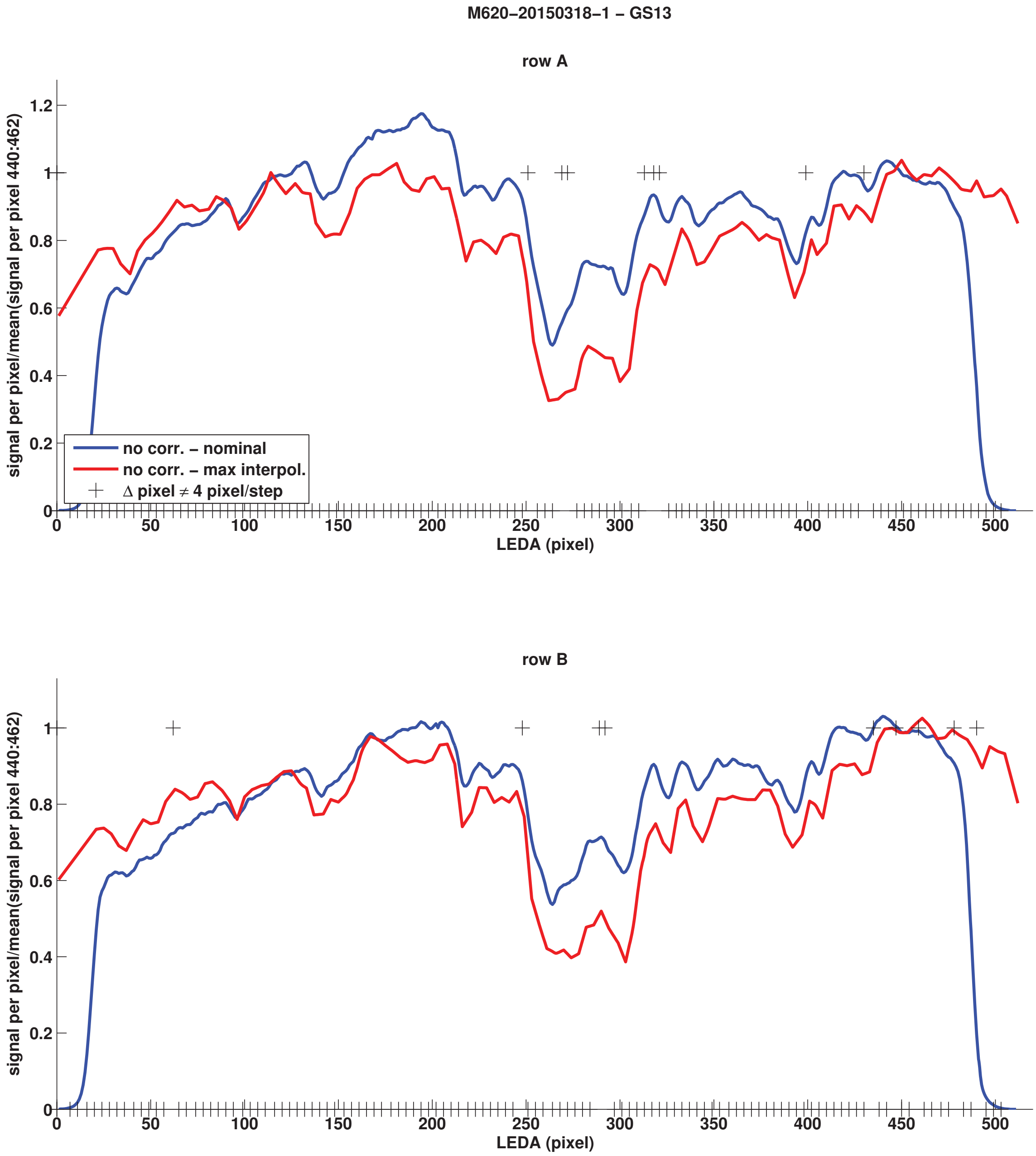

Fig. C.2.6: Pixel gain of the measurement M620-20150318-1-GS13 nominal calculated (blue), calculated by linear interpolation between the maxima (red), and the location of bad stepping points indicated by black crosses.

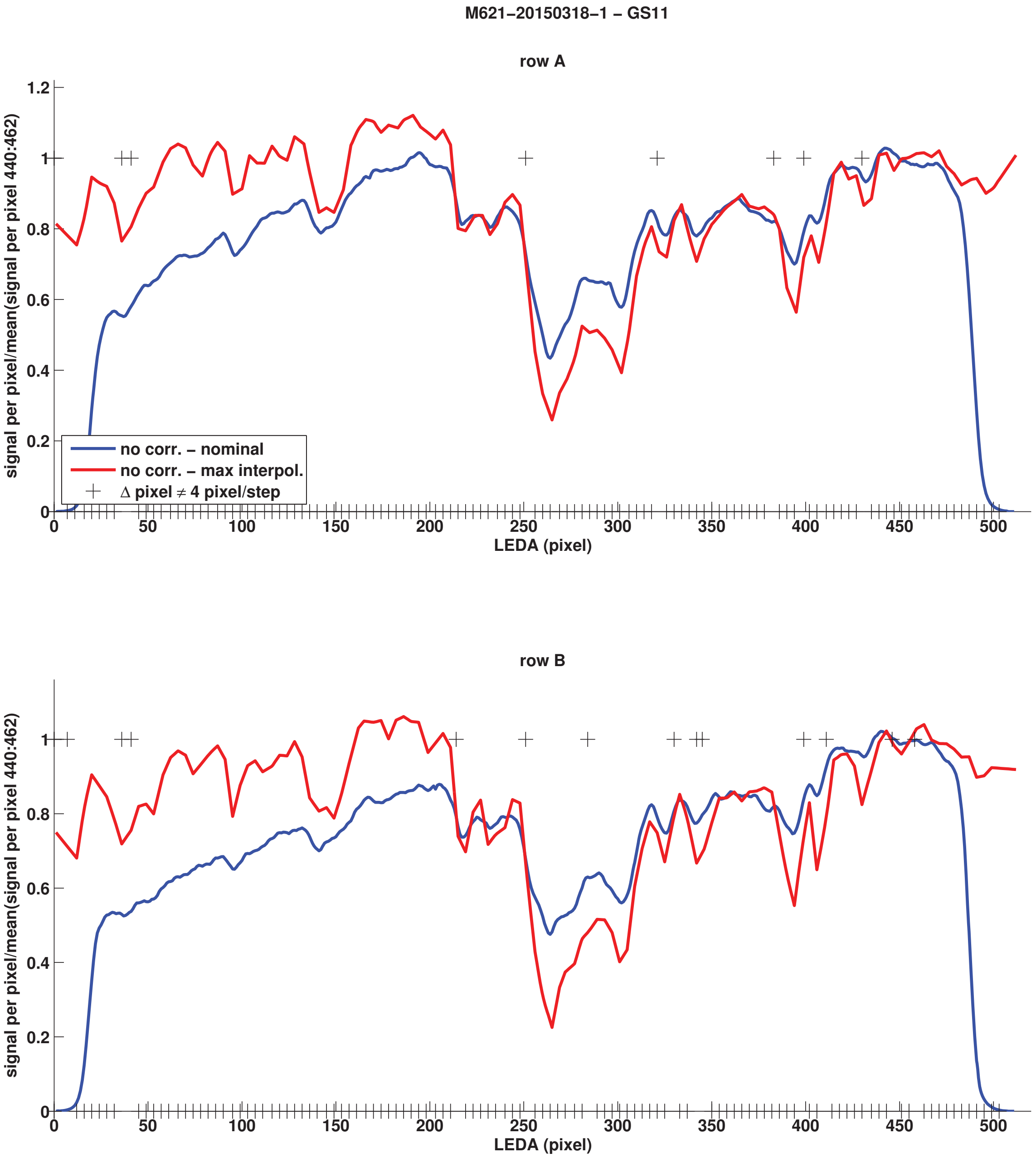

Fig. C.2.7: Pixel gain of the measurement M621-20150318-1-GS11 nominal calculated (blue), calculated by linear interpolation between the maxima (red), and the location of bad stepping points indicated by black crosses.

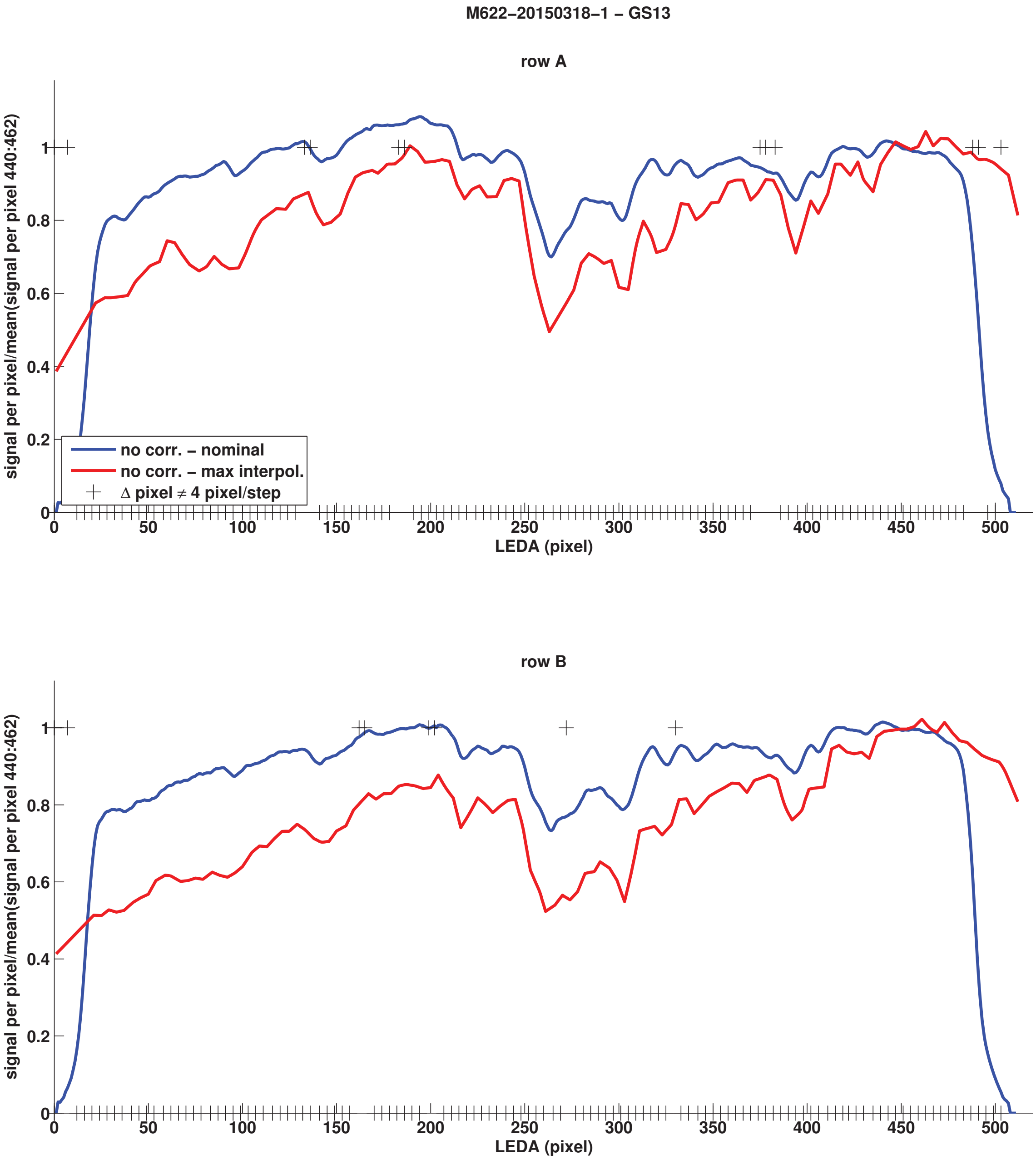

Fig. C.2.8: Pixel gain of the measurement M622-20150318-1-GS13 nominal calculated (blue), calculated by linear interpolation between the maxima (red), and the location of bad stepping points indicated by black crosses.

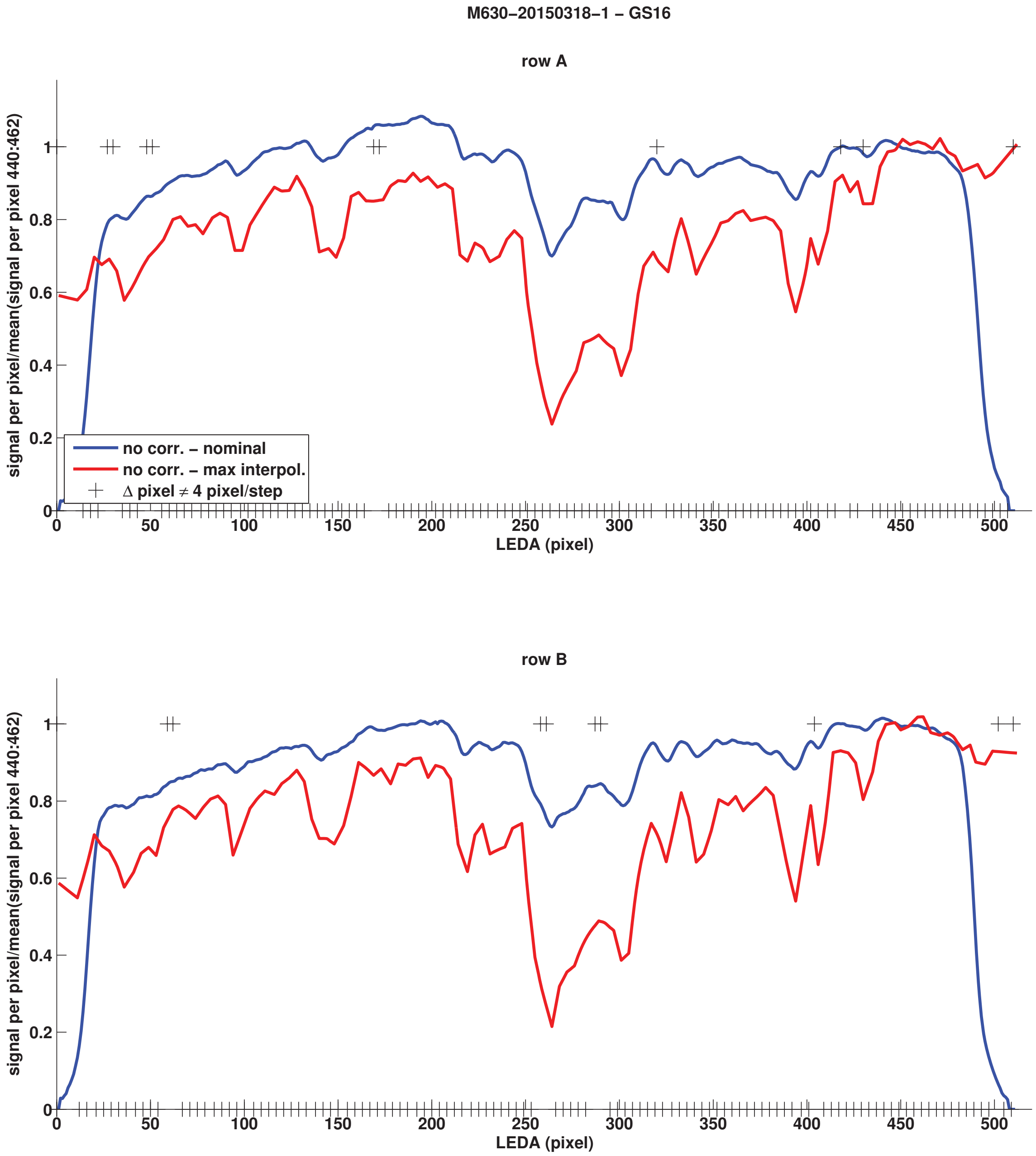

Fig. C.2.9: Pixel gain of the measurement M630-20150318-1-GS16 nominal calculated (blue), calculated by linear interpolation between the maxima (red), and the location of bad stepping points indicated by black crosses.

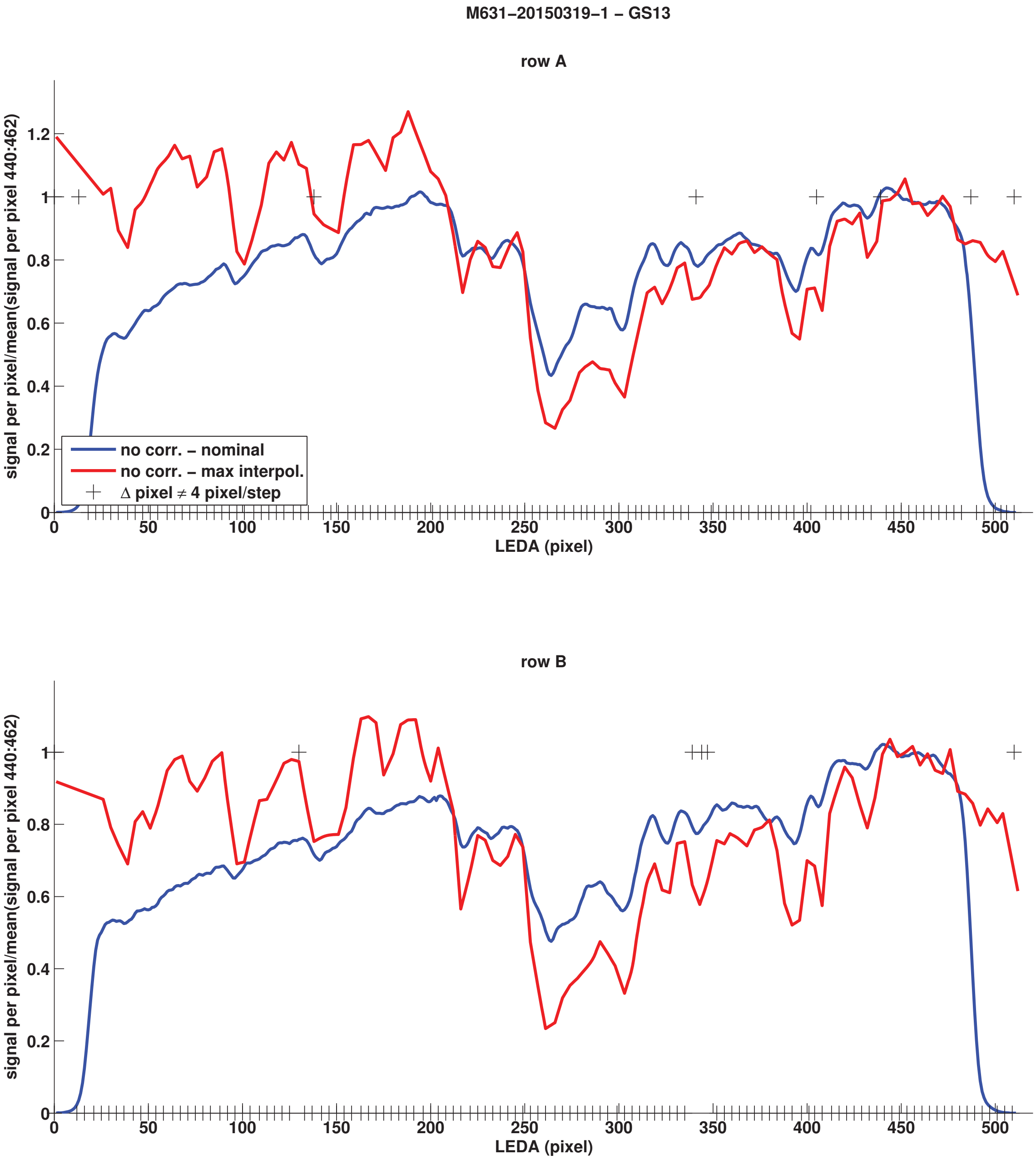

Fig. C.2.10: Pixel gain of the measurement M631-20150319-1-GS13 nominal calculated (blue), calculated by linear interpolation between the maxima (red), and the location of bad stepping points indicated by black crosses.

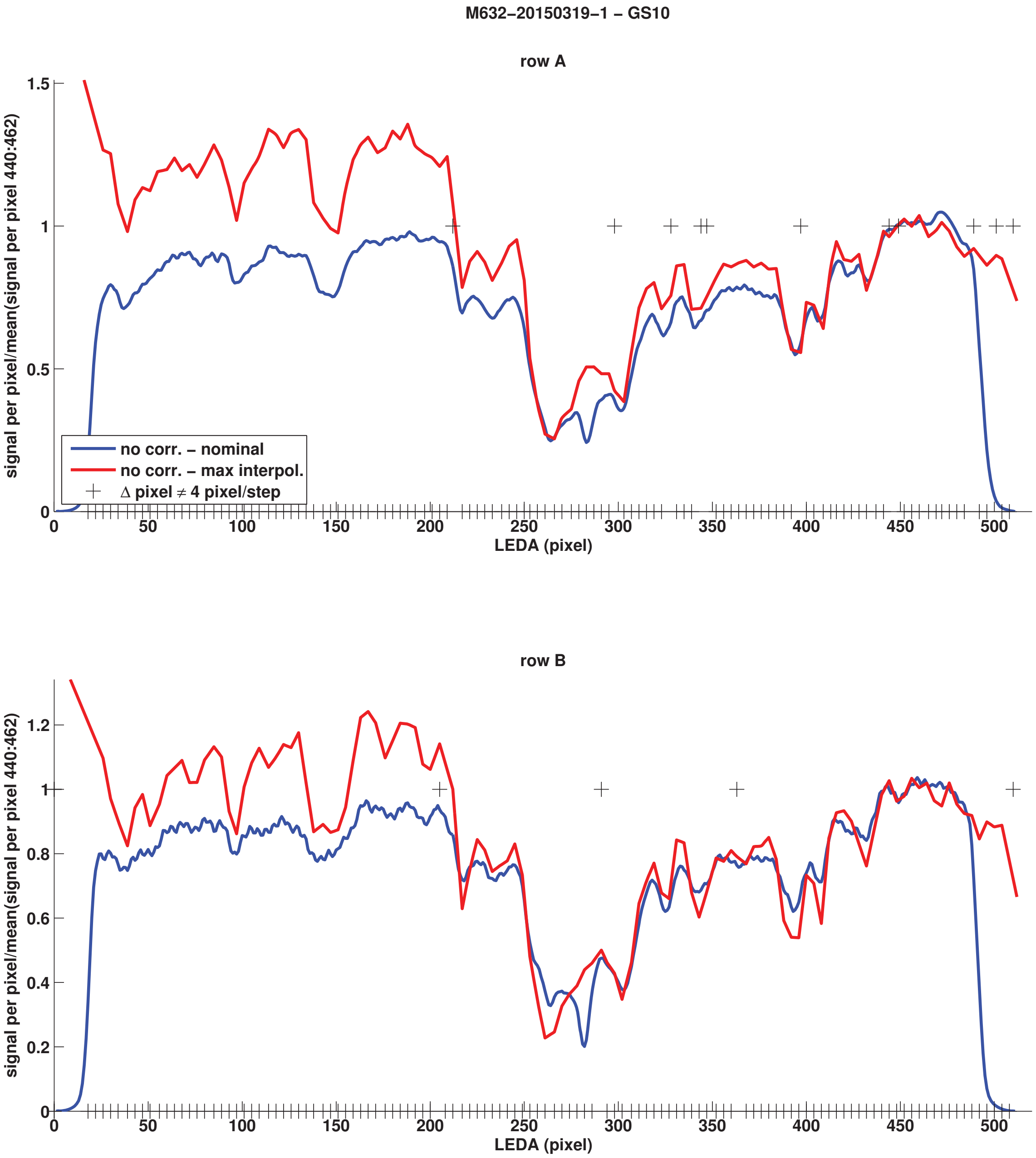

Fig. C.2.11: Pixel gain of the measurement M632-20150319-1-GS10 nominal calculated (blue), calculated by linear interpolation between the maxima (red), and the location of bad stepping points indicated by black crosses.

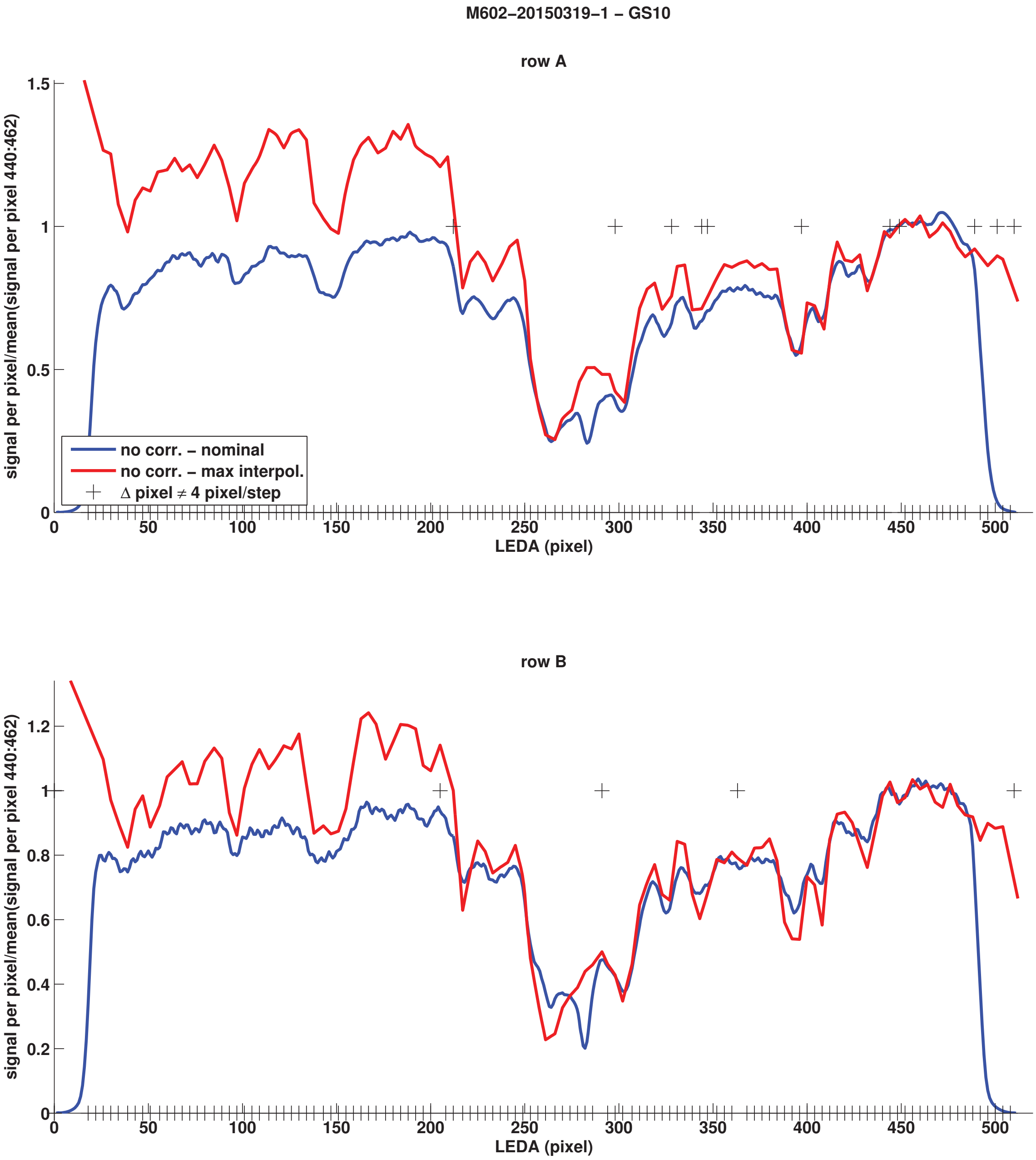

Fig. C.2.12: Pixel gain of the measurement M602-20150319-1-GS10 nominal calculated (blue), calculated by linear interpolation between the maxima (red), and the location of bad stepping points indicated by black crosses.

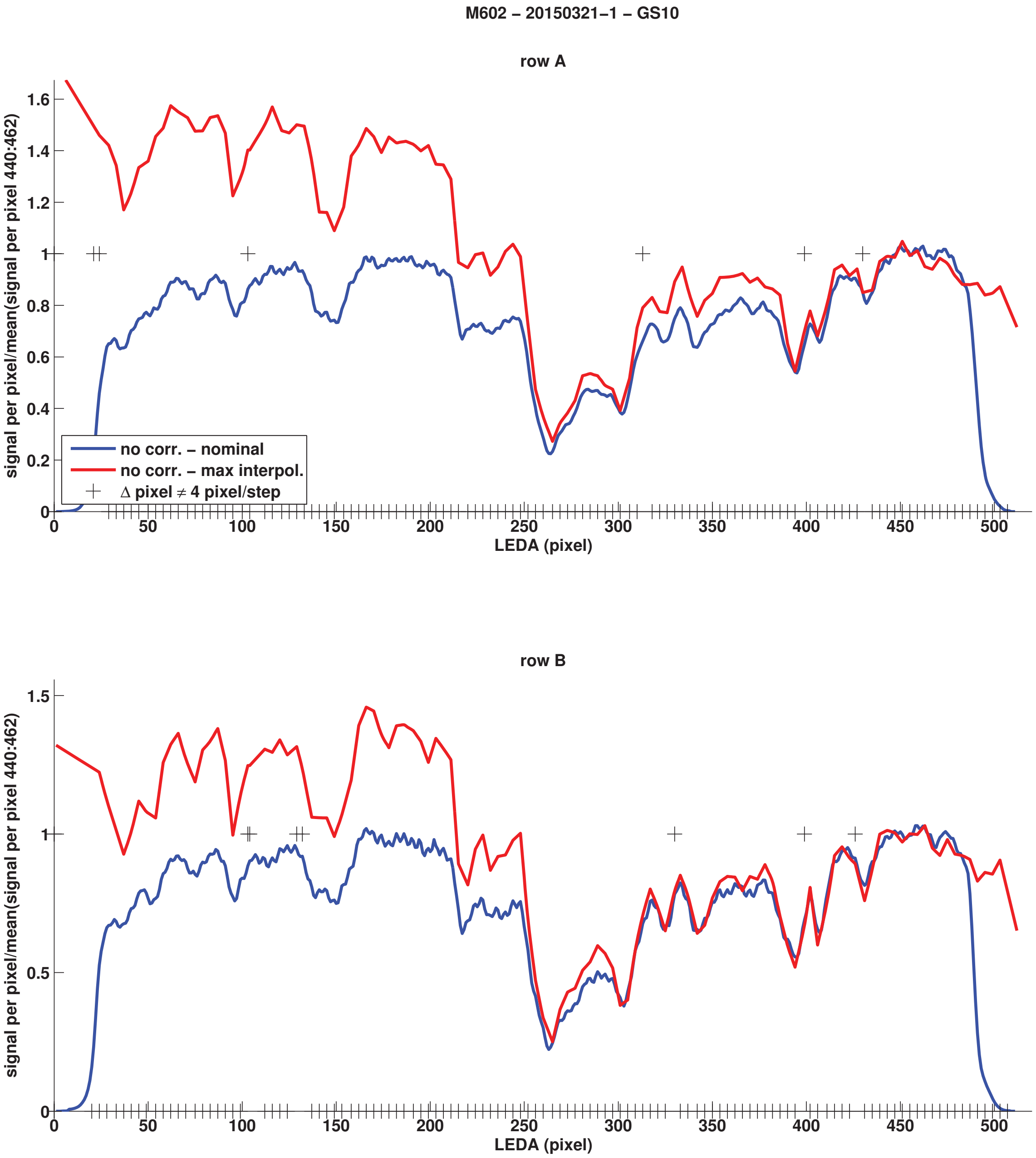

Fig. C.2.13: Pixel gain of the measurement M602-20150321-1-GS10 nominal calculated (blue), calculated by linear interpolation between the maxima (red), and the location of bad stepping points indicated by black crosses.

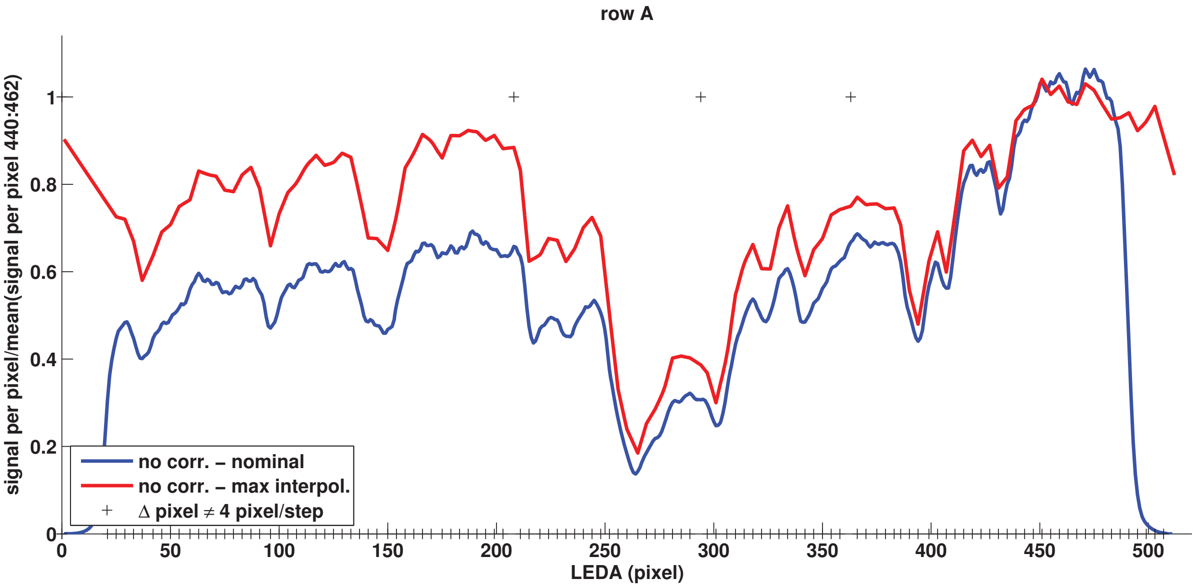

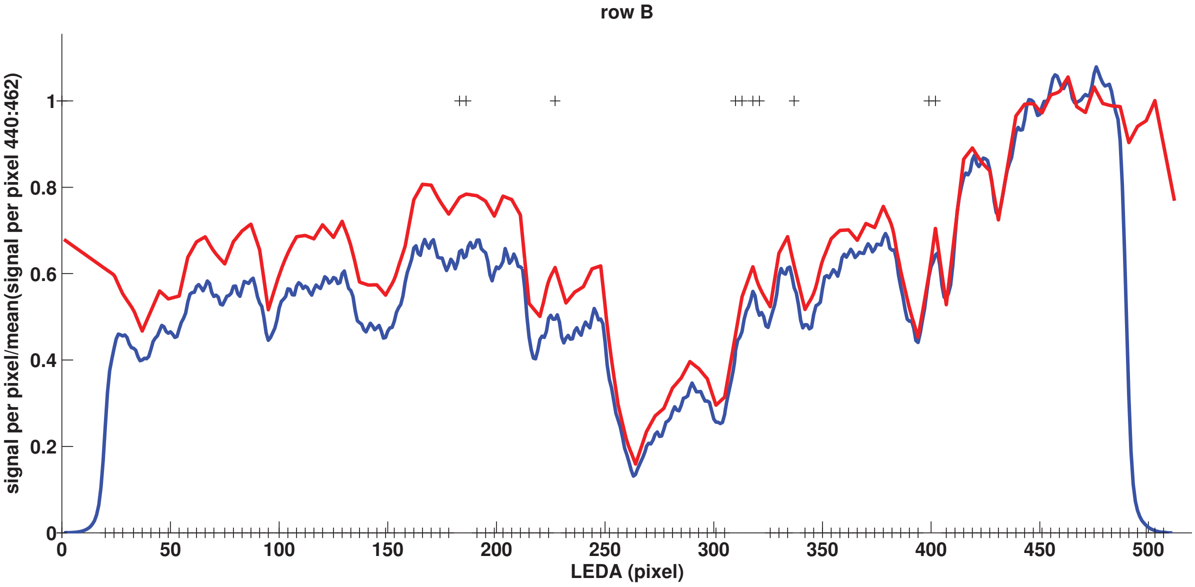

Fig. C.2.14: Pixel gain of the measurement M602-20150321-2-GS11 nominal calculated (blue), calculated by linear interpolation between the maxima (red), and the location of bad stepping points indicated by black crosses.

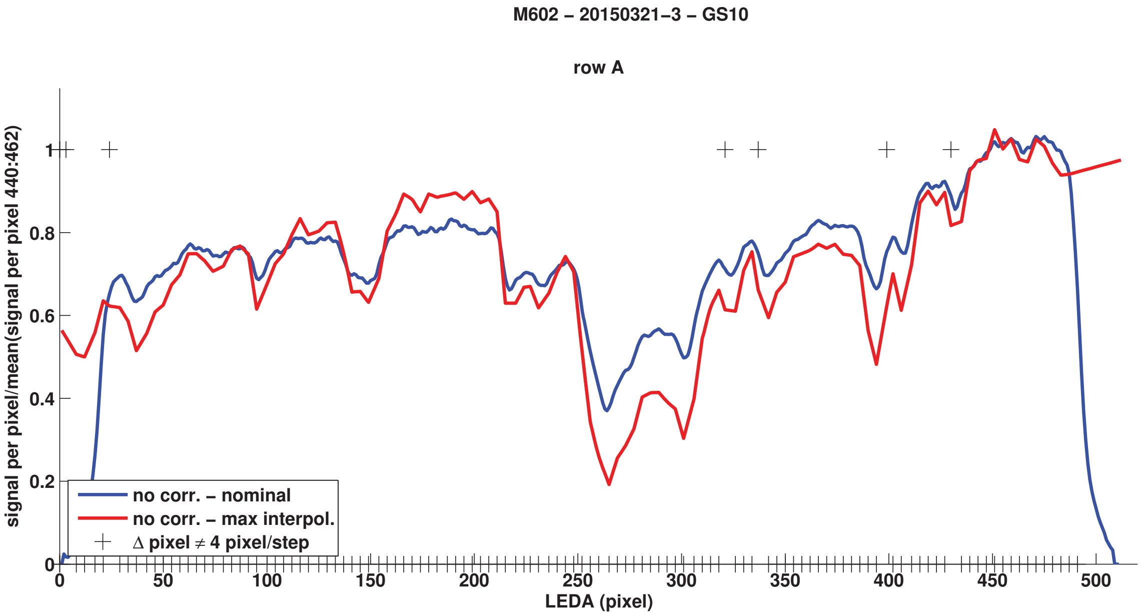

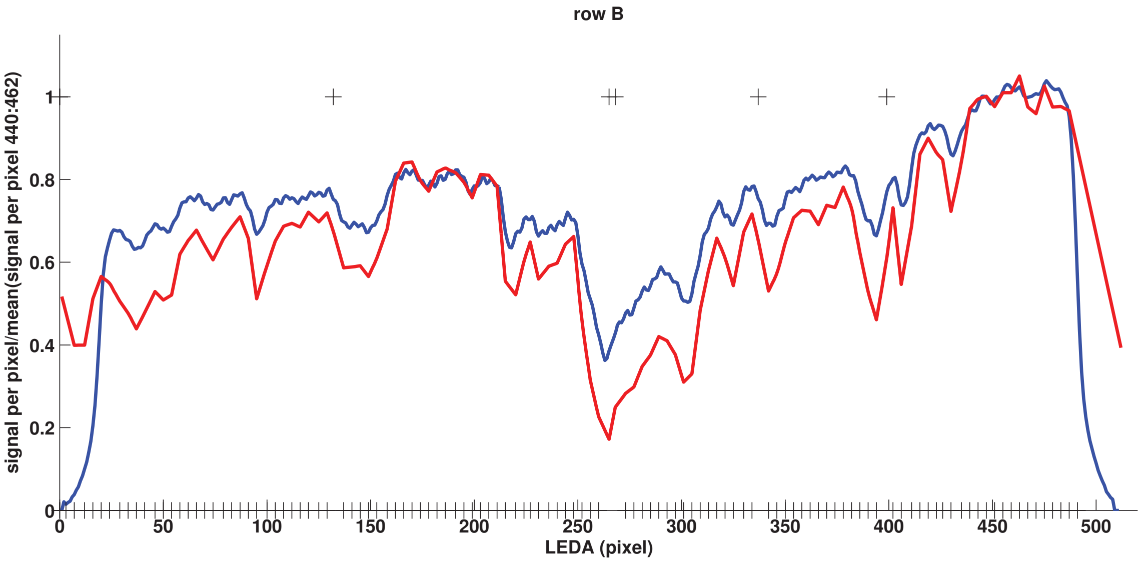

Fig. C.2.15: Pixel gain of the measurement M602-20150321-3-GS10 nominal calculated (blue), calculated by linear interpolation between the maxima (red), and the location of bad stepping points indicated by black crosses.

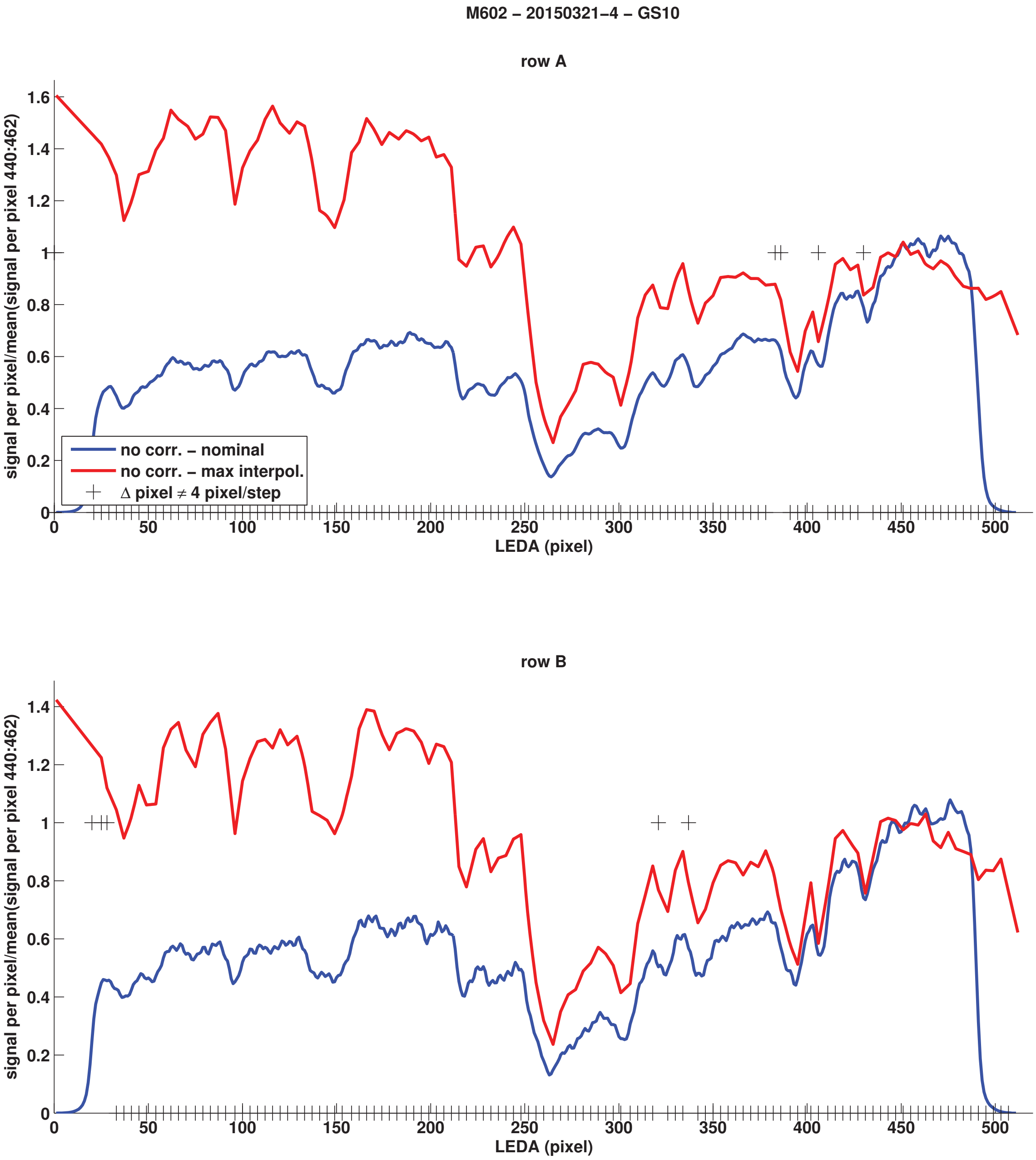

Fig. C.2.16: Pixel gain of the measurement M602-20150321-4-GS10 nominal calculated (blue), calculated by linear interpolation between the maxima (red), and the location of bad stepping points indicated by black crosses.

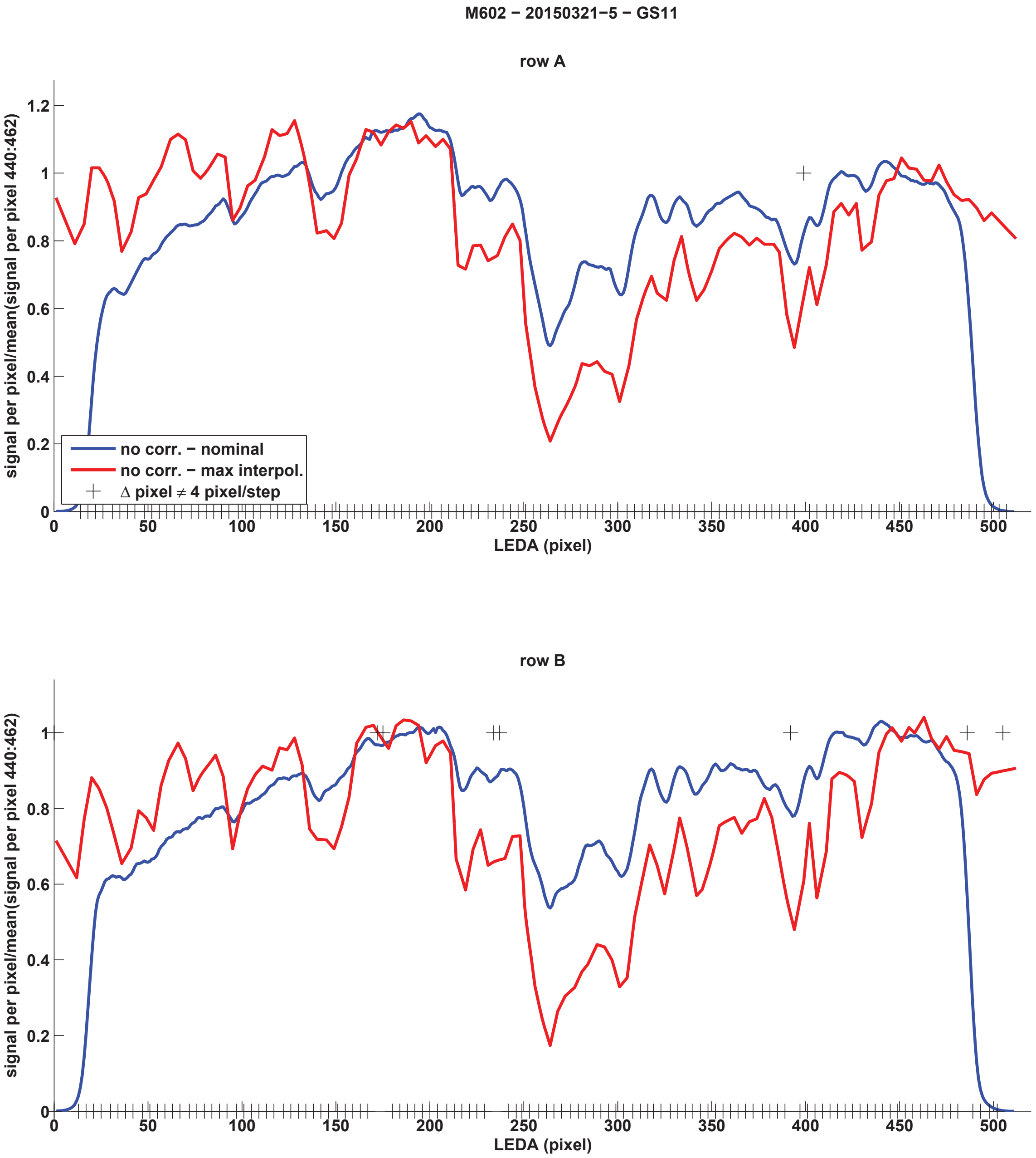

Fig. C.2.17: Pixel gain of the measurement M602-20150321-5-GS11 nominal calculated (blue), calculated by linear interpolation between the maxima (red), and the location of bad stepping points indicated by black crosses.

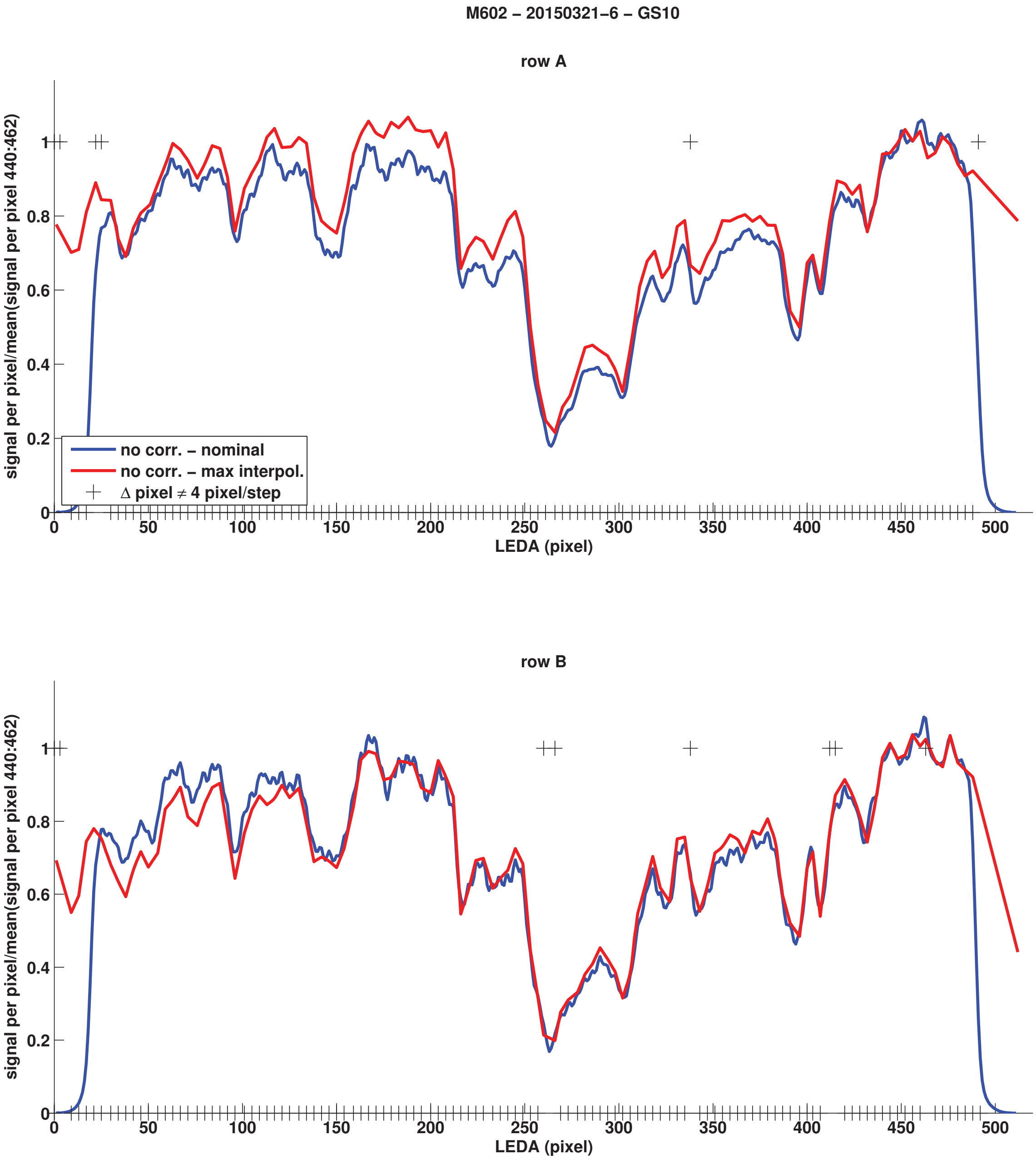

Fig. C.2.18: Pixel gain of the measurement M602-20150321-6-GS10 nominal calculated (blue), calculated by linear interpolation between the maxima (red), and the location of bad stepping points indicated by black crosses.

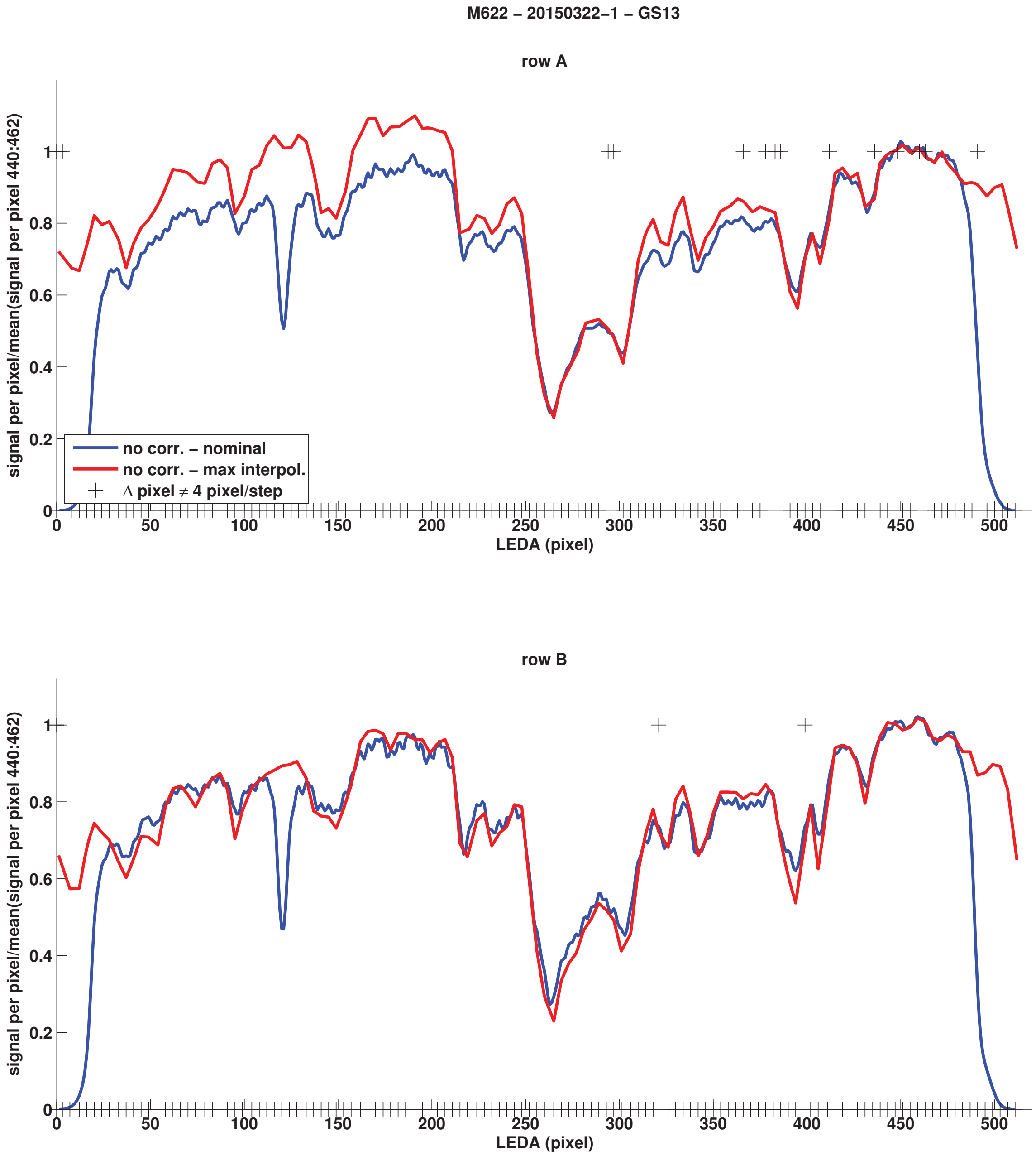

Fig. C.2.19: Pixel gain of the measurement M622-20150322-1-GS13 nominal calculated (blue), calculated by linear interpolation between the maxima (red), and the location of bad stepping points indicated by black crosses.

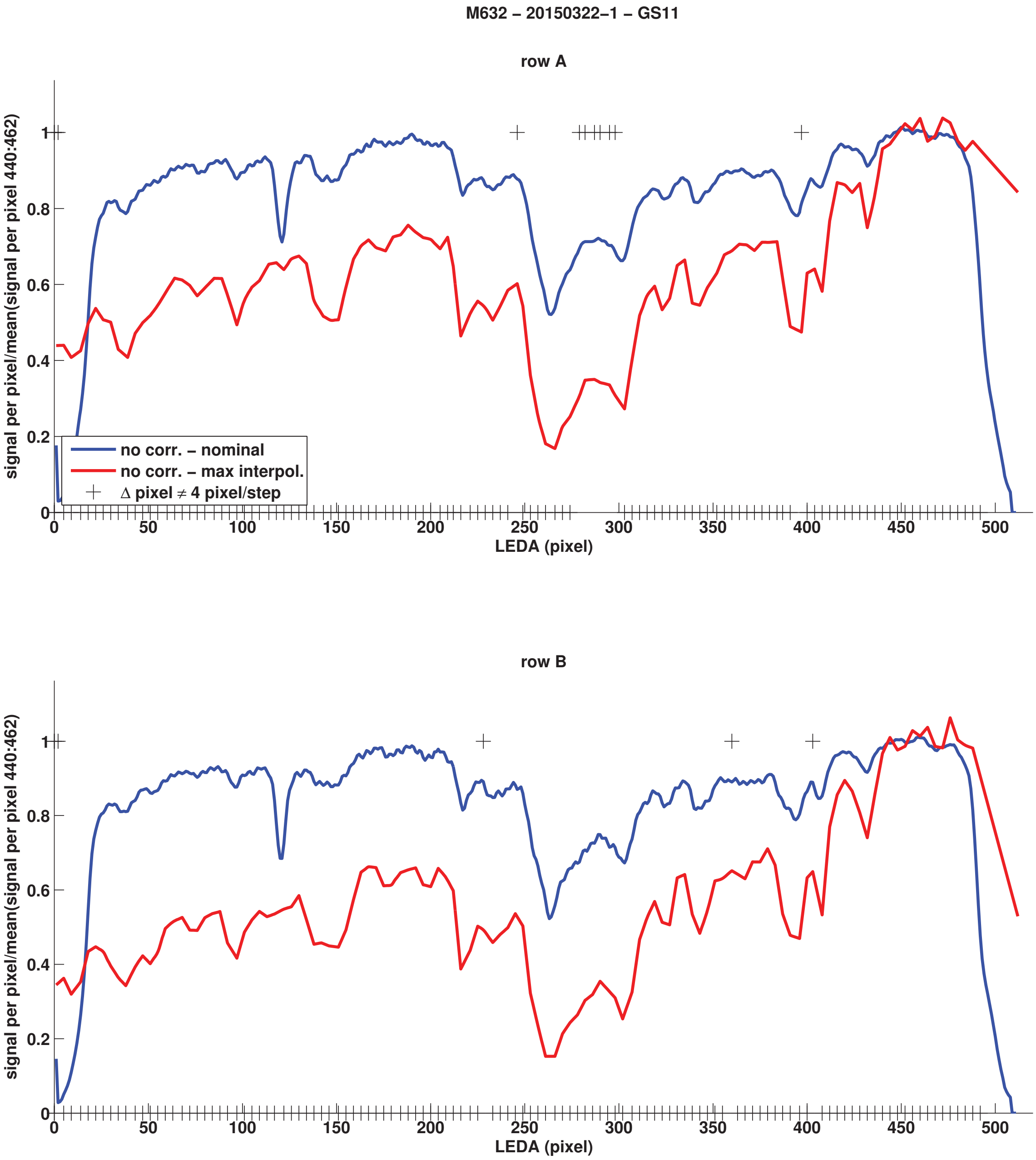

Fig. C.2.20: Pixel gain of the measurement M632-20150322-1-GS11 nominal calculated (blue), calculated by linear interpolation between the maxima (red), and the location of bad stepping points indicated by black crosses.

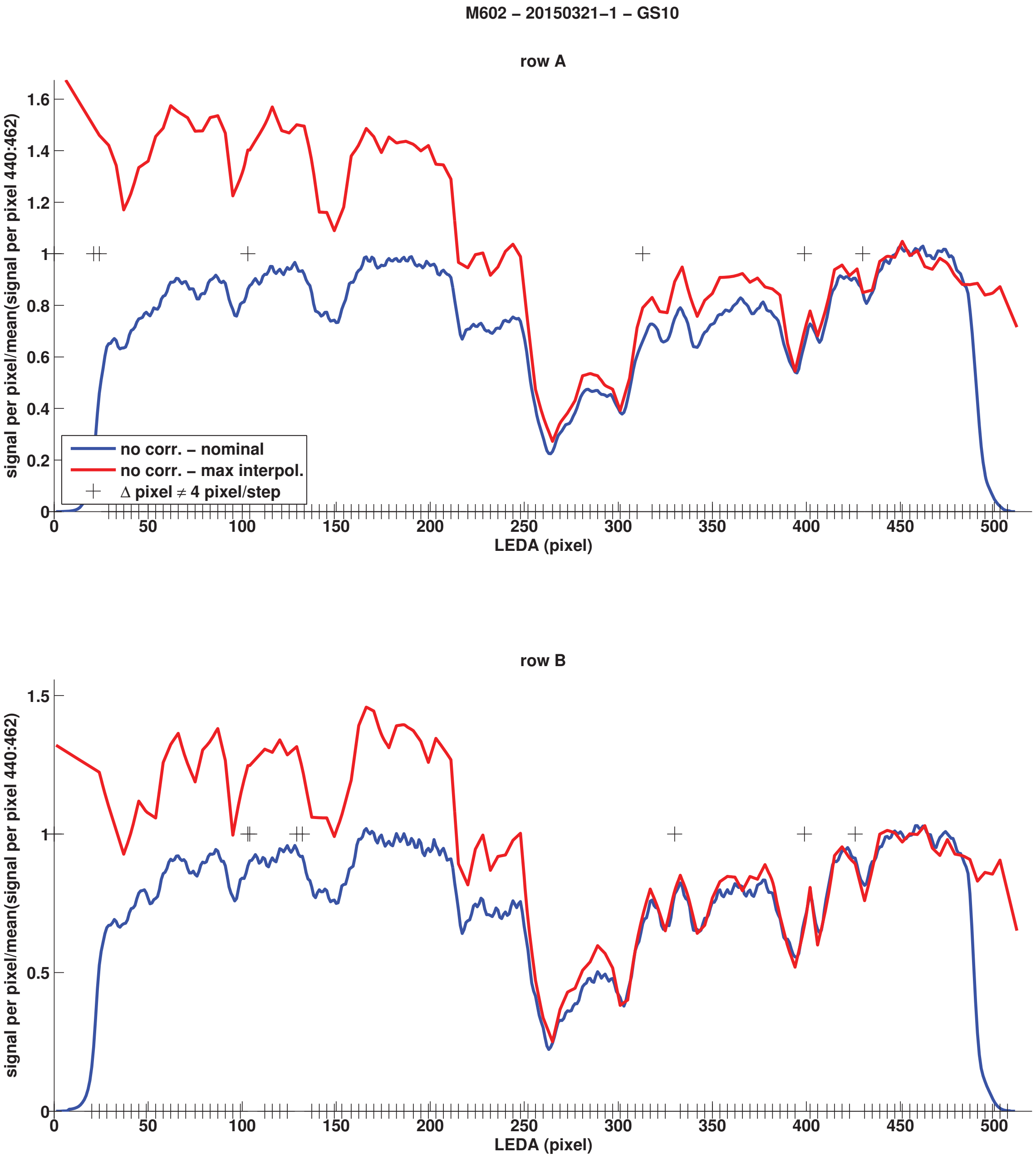

Fig. C.2.21: Pixel gain of the measurement M602-20150322-1-GS10 nominal calculated (blue), calculated by linear interpolation between the maxima (red), and the location of bad stepping points indicated by black crosses.

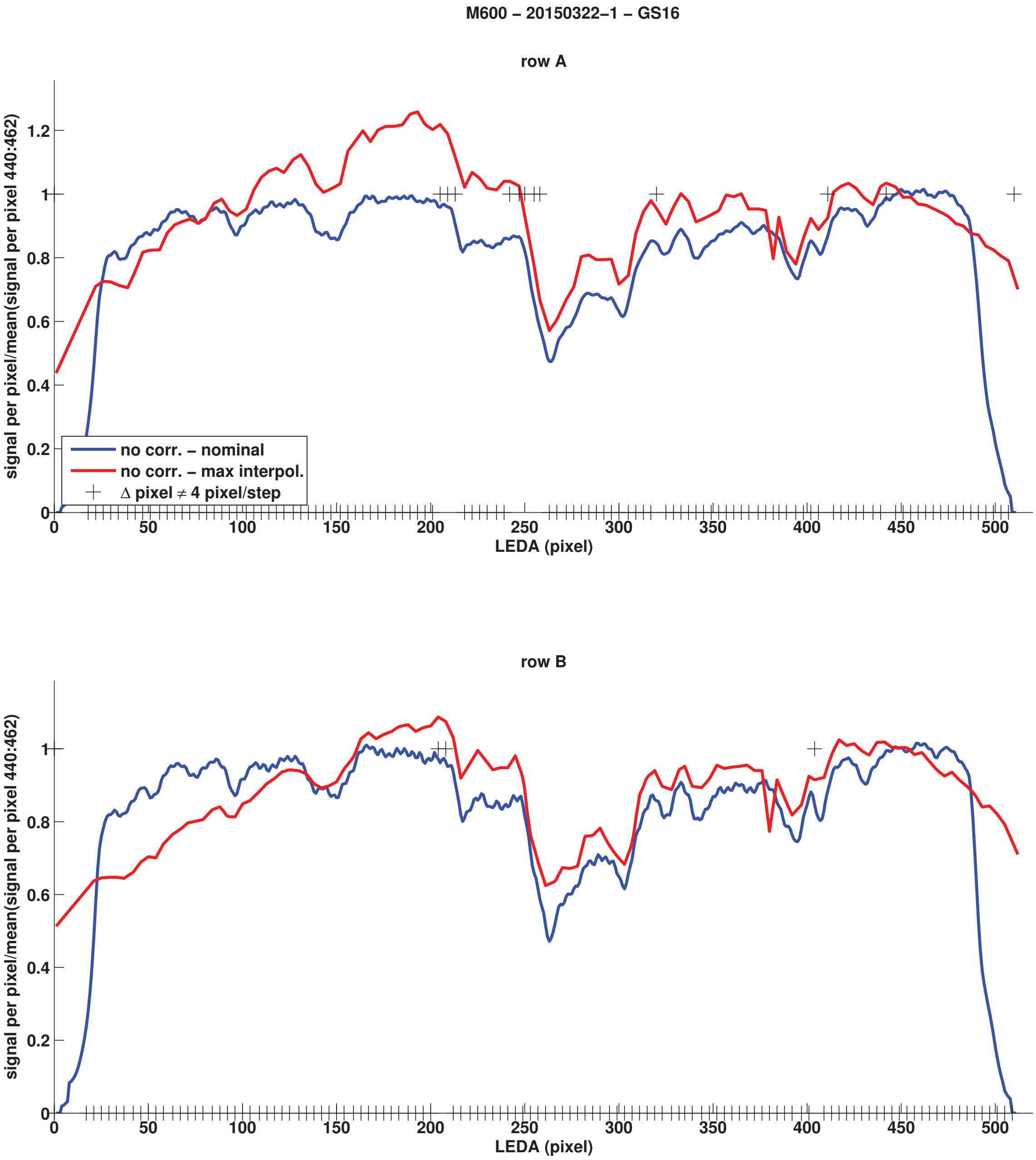

Fig. C.2.22: Pixel gain of the measurement M600-20150322-1-GS16 nominal calculated (blue), calculated by linear interpolation between the maxima (red), and the location of bad stepping points indicated by black crosses.

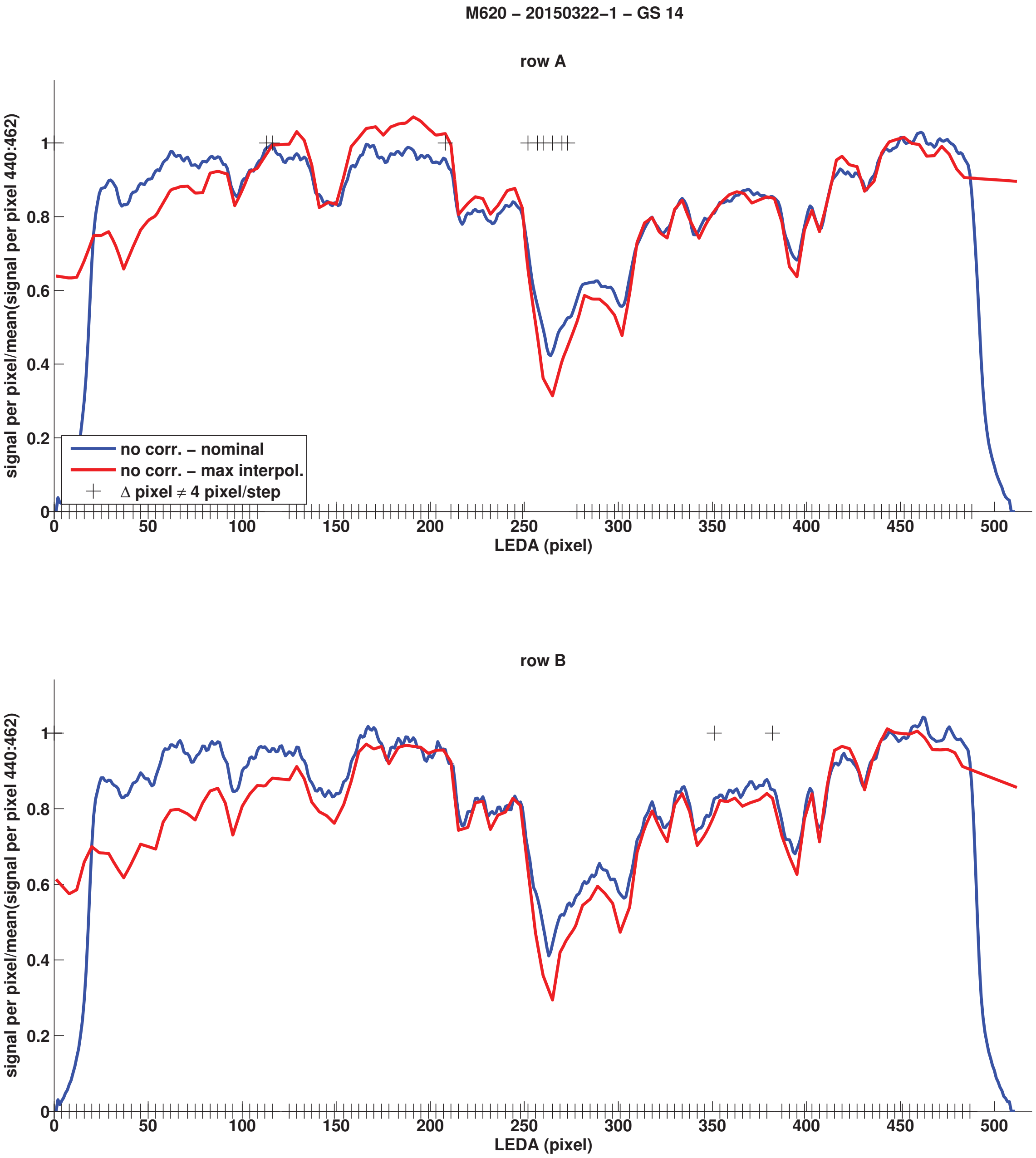

Fig. C.2.23: Pixel gain of the measurement M620-20150322-1-GS14 nominal calculated (blue), calculated by linear interpolation between the maxima (red), and the location of bad stepping points indicated by black crosses.

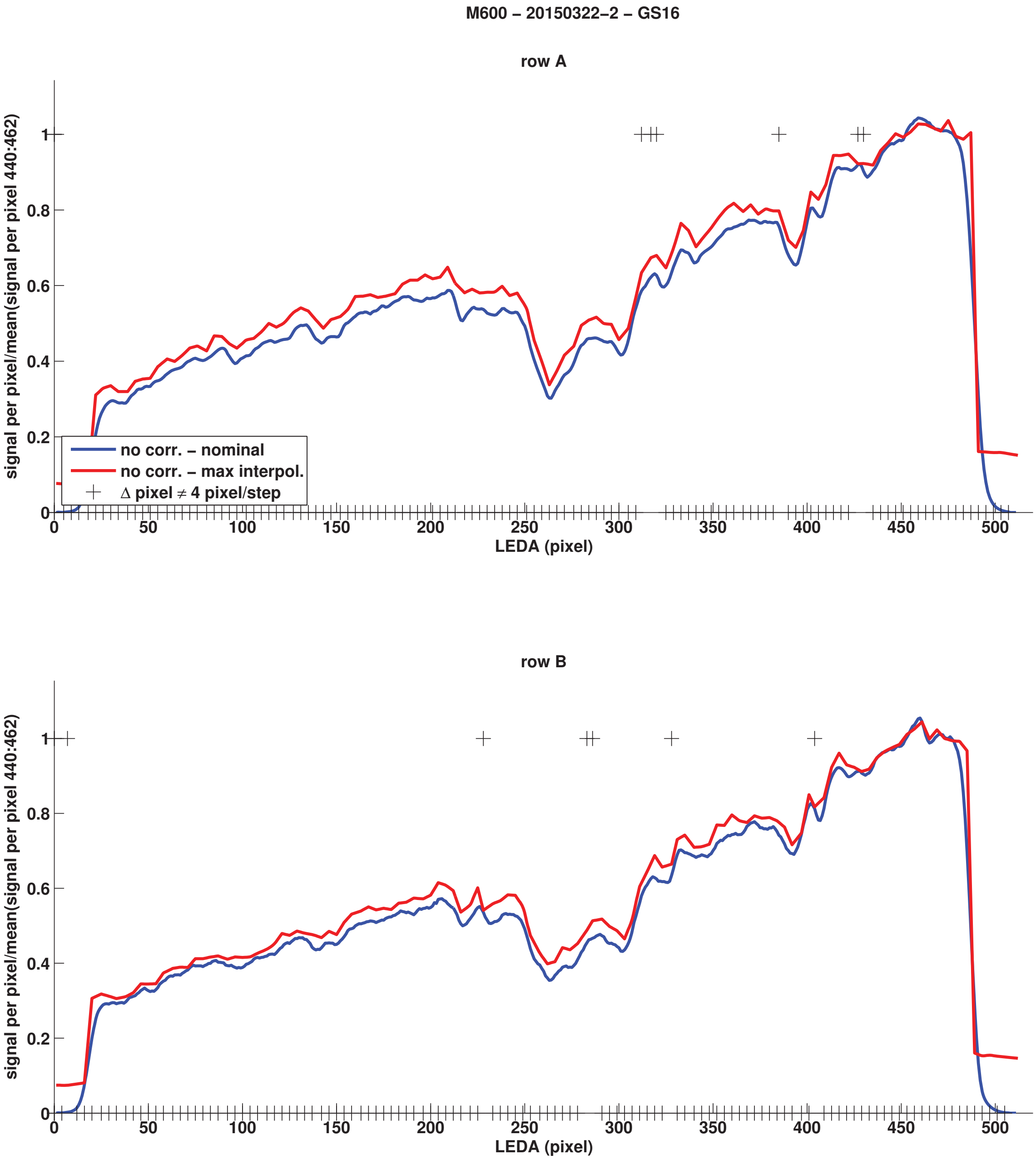

Fig. C.2.24: Pixel gain of the measurement M600-20150322-2-GS16 nominal calculated (blue), calculated by linear interpolation between the maxima (red), and the location of bad stepping points indicated by black crosses.

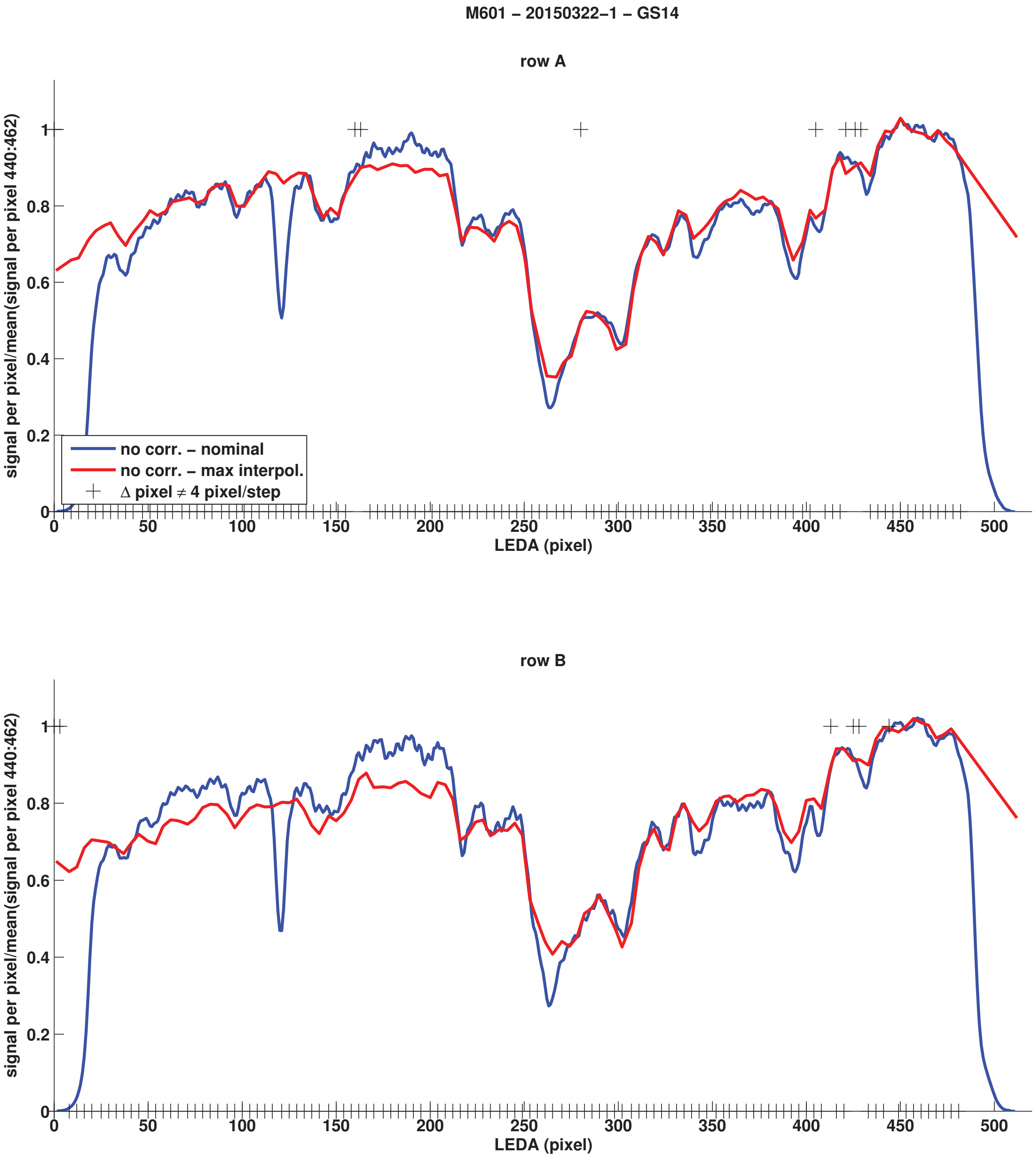

Fig. C.2.25: Pixel gain of the measurement M601-20150322-1-GS14 nominal calculated (blue), calculated by linear interpolation between the maxima (red), and the location of bad stepping points indicated by black crosses.

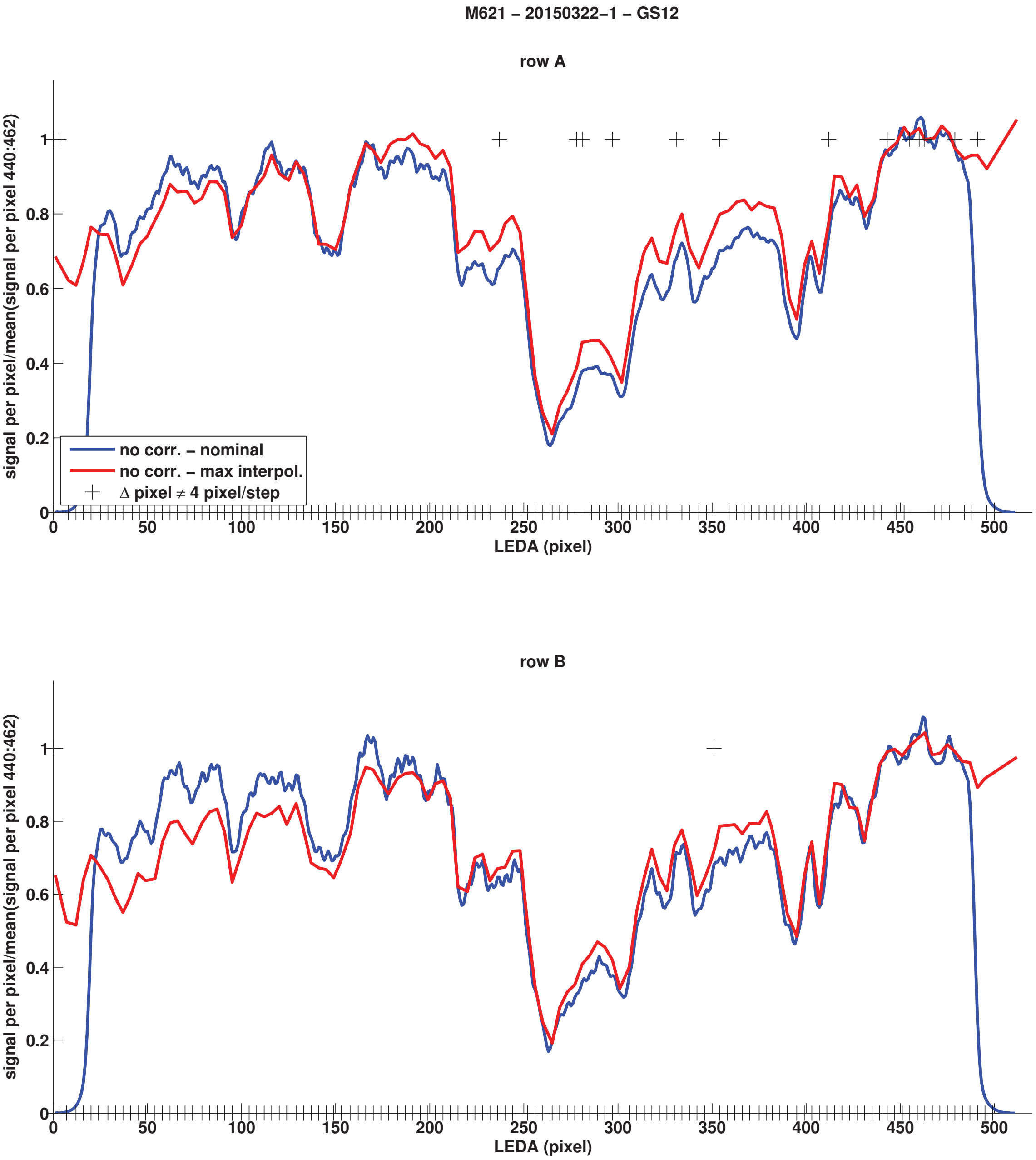

Fig. C.2.26: Pixel gain of the measurement M621-20150322-1-GS12 nominal calculated (blue), calculated by linear interpolation between the maxima (red), and the location of bad stepping points indicated by black crosses.

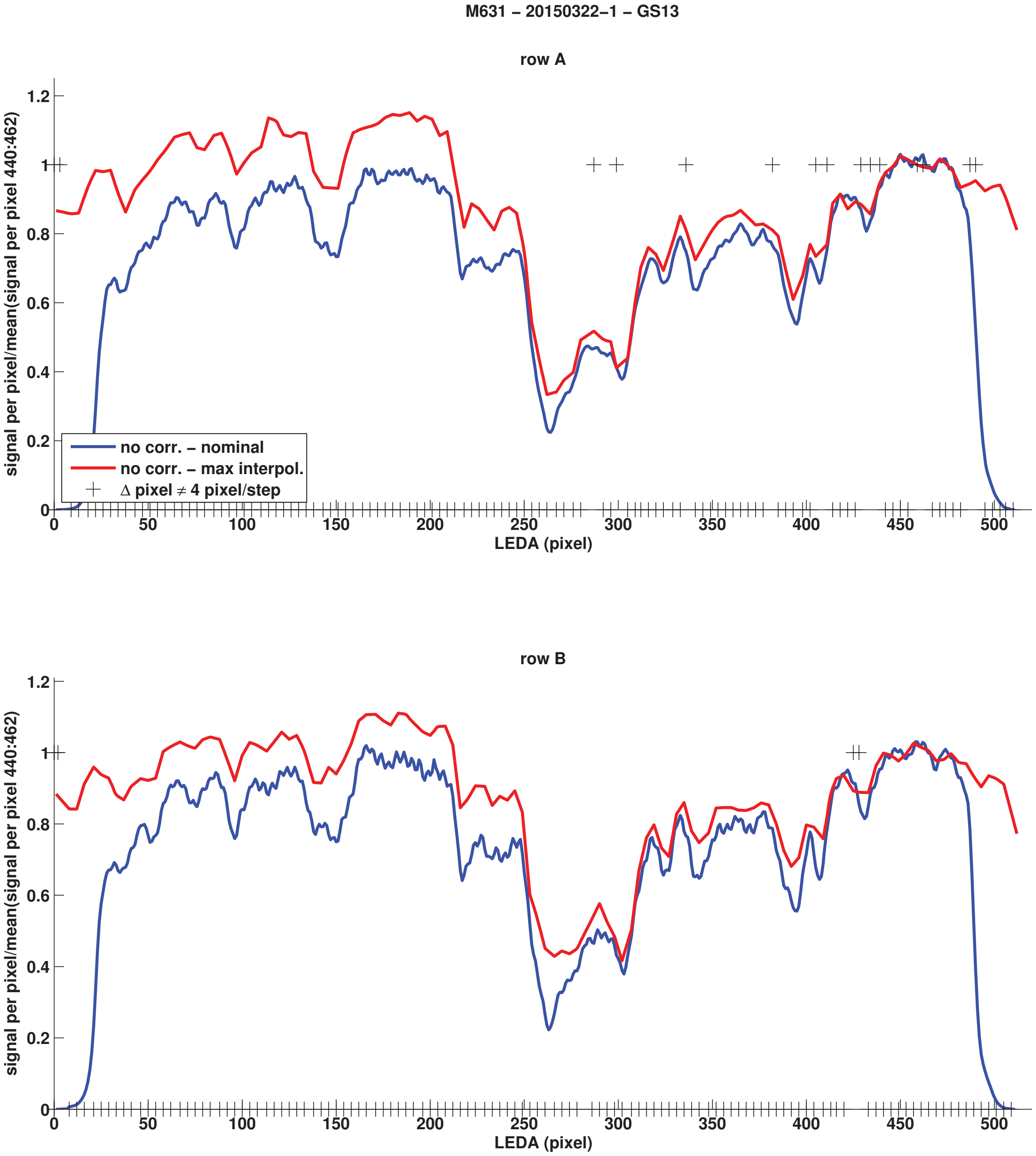

Fig. C.2.27: Pixel gain of the measurement M631-20150322-1-GS13 nominal calculated (blue), calculated by linear interpolation between the maxima (red), and the location of bad stepping points indicated by black crosses.

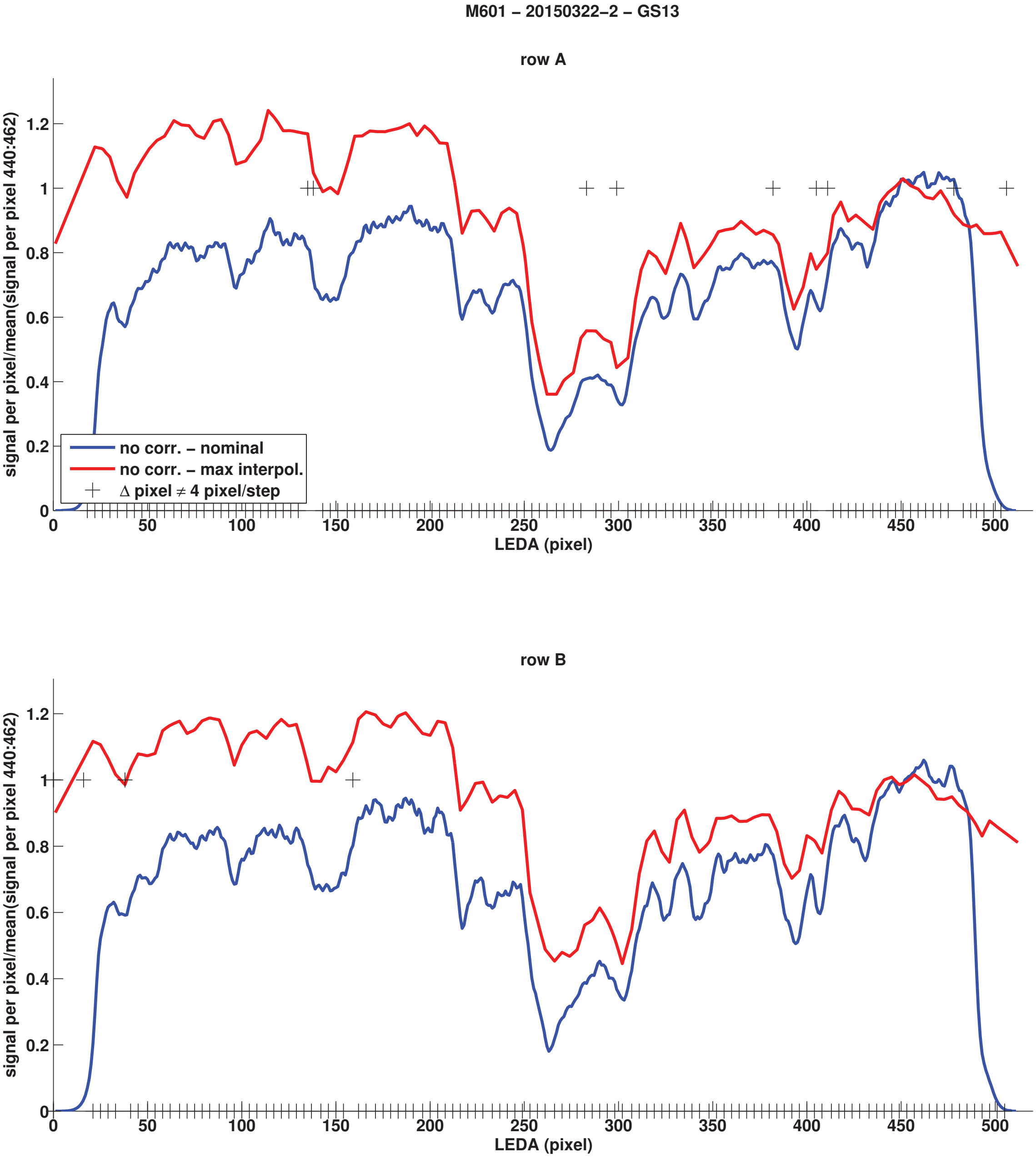

Fig. C.2.28: Pixel gain of the measurement M601-20150322-2-GS13 nominal calculated (blue), calculated by linear interpolation between the maxima (red), and the location of bad stepping points indicated by black crosses.

C.3 Comparison of Different Correction Types - 2015

The following graphs have all the same structure which is: the upper two sub figures show row A and the lower to row B, in the first column the individual pixel gain has been normed to the right edge and in the second row it has been normed to the mean of the signal for all pixel, and the title of the graph contains the information about the measurement mode, time and its gain step. Depending of availability the data was corrected for COPS pressure, evolution of water, and evolution of ratio of main species. A head of the graphs showing the different corrections for the individual pixel gain calculation is always a graph with the variation of COPS nude gauge density during the period of interest.

1. **No overlap of the four curves** The curve which has the smallest slope on the left side and which has values closest to 1 is chosen.

2. **Mostly overlap between correction for COPS and m18** In this case correction COPS is taken because the overlap indicates that water was the dominate species and for such cases the evolution of water is documented by the COPS measurements.

3. **Mostly overlap between no correction and m18** Here no correction was chosen because the overlap indicates that water signal was fairly constant.

4. **Mostly overlap between no correction and correction COPS** This overlap implies first that water was the dominate species, second that it stayed fairly constant and third that the correction of m18 is not correct. Therefore no correction is used.

5. **At least two corrections overlap mostly and have unusual steep slopes** The curve which has the smallest slope over the LEDA and which has values closest to 1 is chosen.

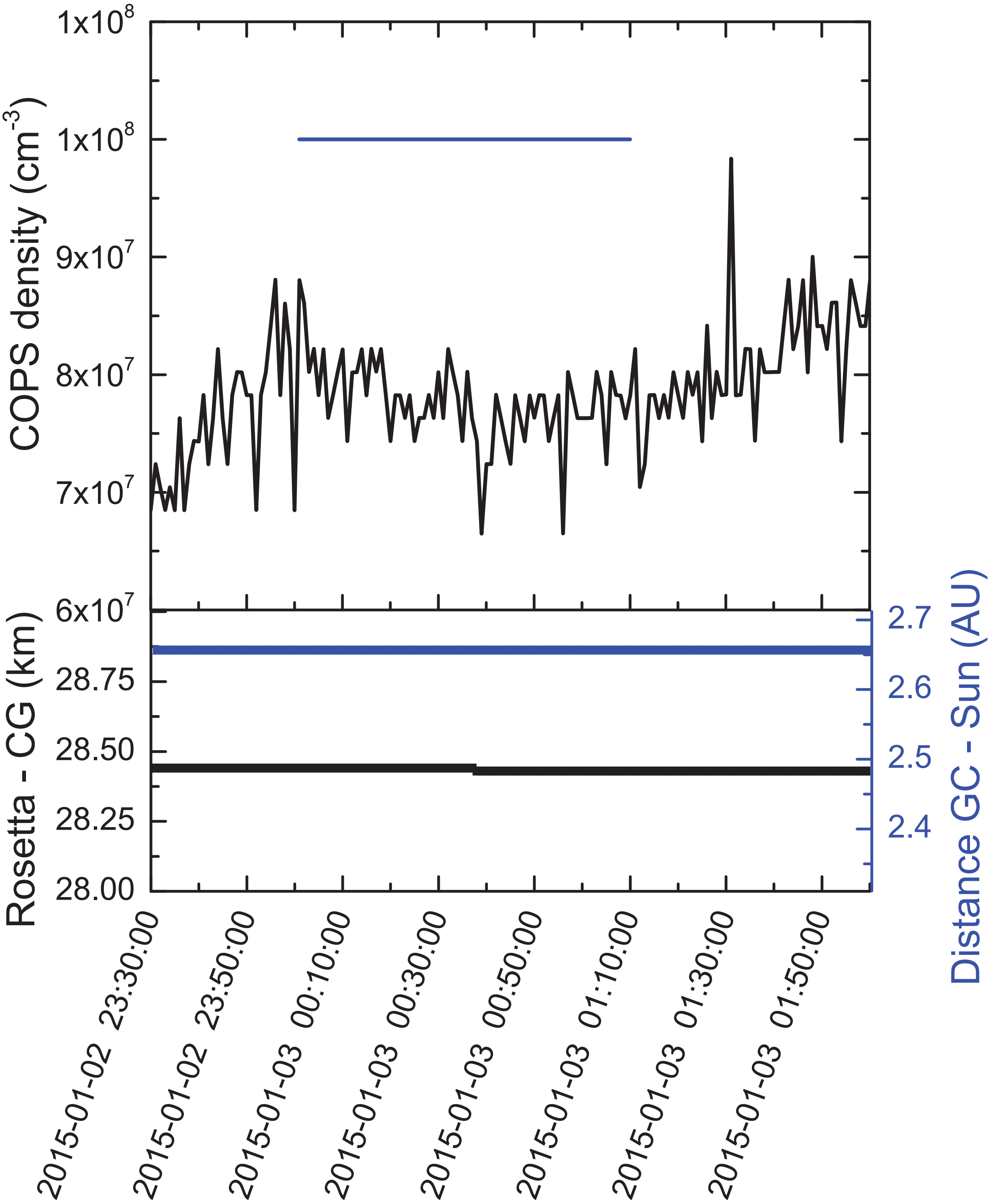

Fig. C.3.1: The upper panel shows the variation in nude gauge density and the lower panel shows the cometary and heliocentric distance of Rosetta. The duration of the pixel gain mode M600 is indicated by the red bar in the upper panel. As one can see there is no dramatic change in COPS nude gauge density.

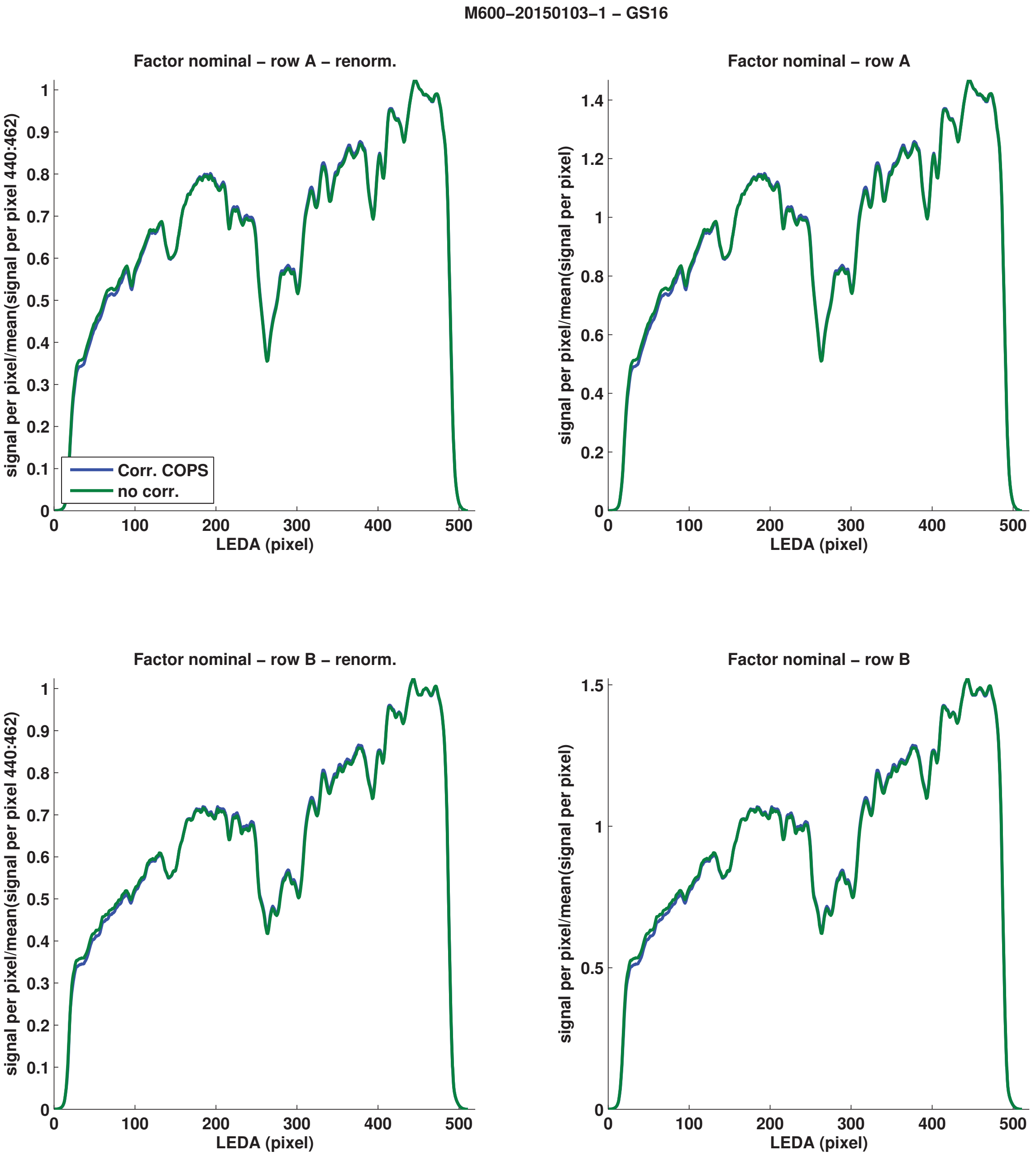

Fig. C.3.2: As a consequence of the overlap between no correction and correction COPS the first one is chosen.

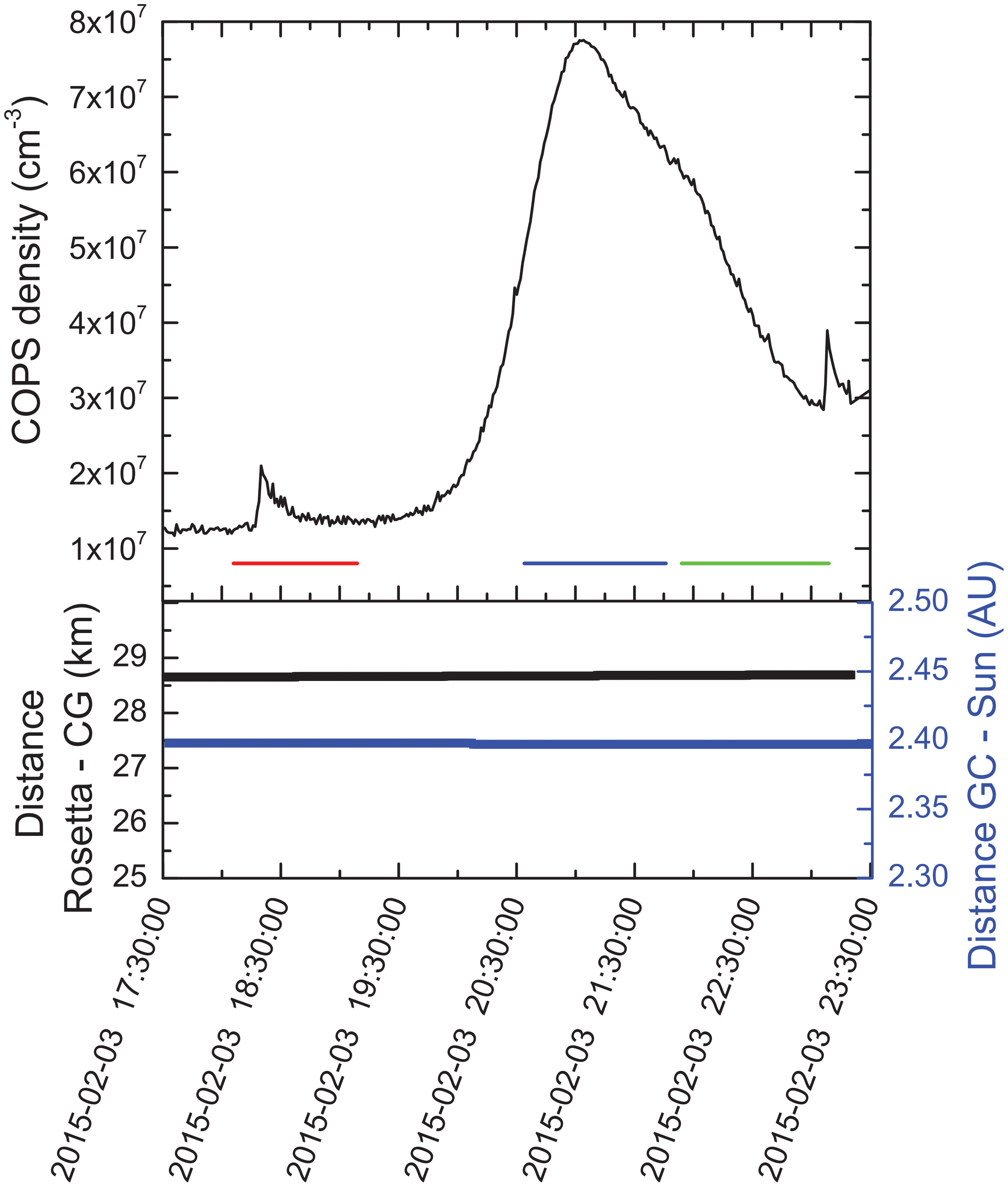

Fig. C.3.3: The upper panel shows the variation in nude gauge density and the lower panel shows the cometary and heliocentric distance of Rosetta. The duration of the pixel gain measurements is indicated by colored bar in the upper panel. In red is M600-1, in blue is M602, and in green is M600-2. For none of the pixel gain measurements the density is constant however this does not reflect the change of water density but the change of the coma density.

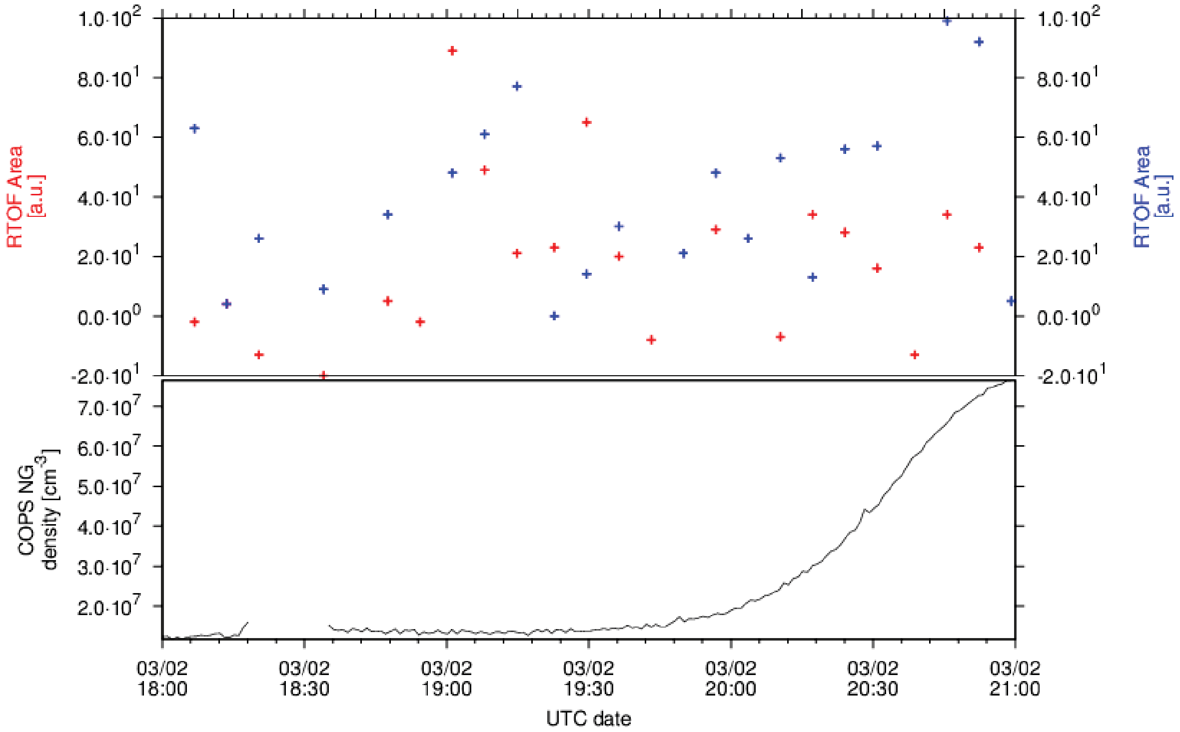

Fig. C.3.4: The upper panel shows the variation in nude gauge density and the lower panel shows the cometary and heliocentric distance of Rosetta. The duration of the pixel gain measurements is indicated by colored bar in the upper panel. In red is M600-1, in blue is M602, and in green is M600-2. For none of the pixel gain measurements the density is constant however this does not reflect the change of water density but the change of the coma density.

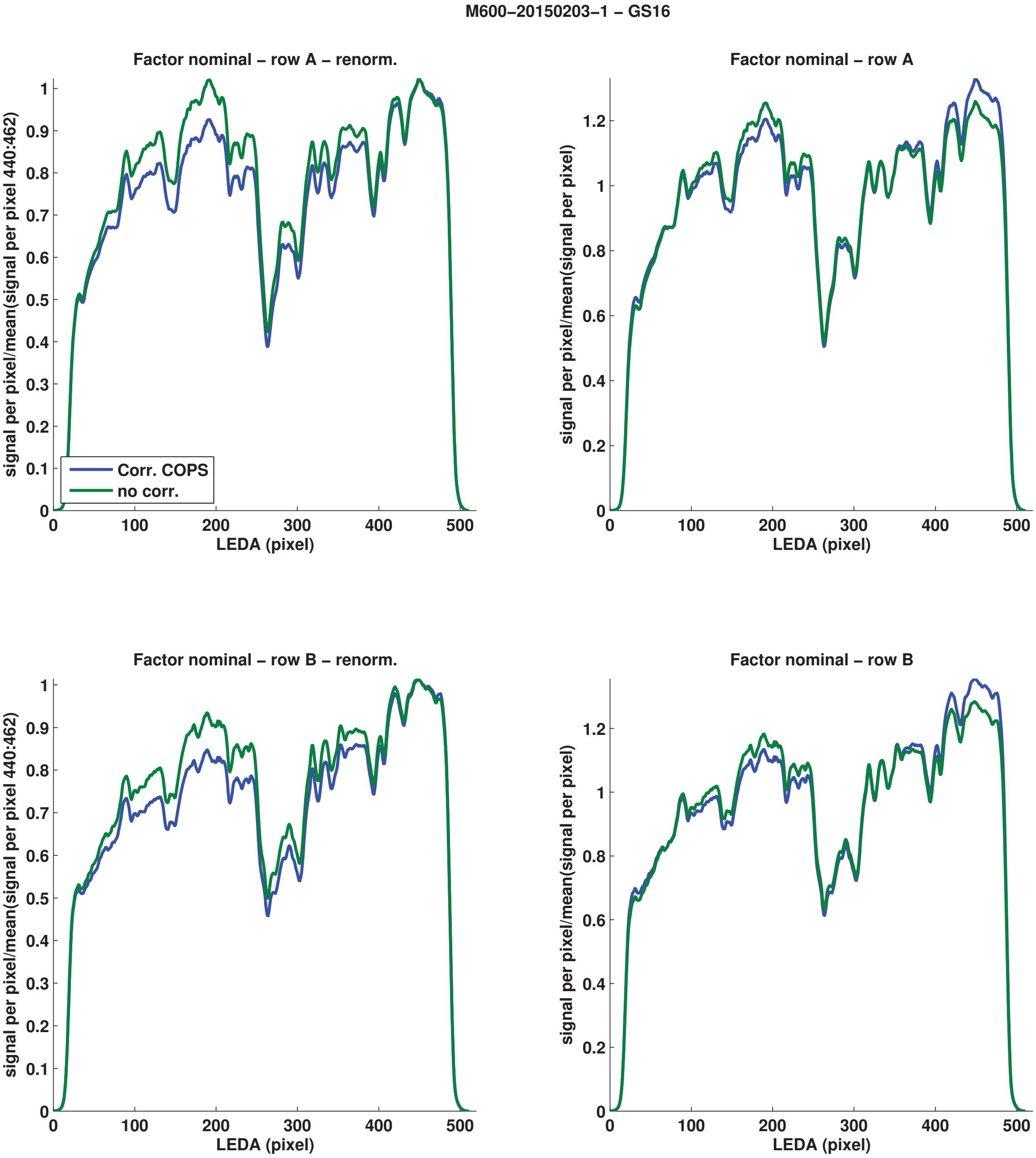

Fig. C.3.5: For this measurement no overlap between the two types of correction is present thus rule 1 applies and no correction is assumed to be the most likely one.

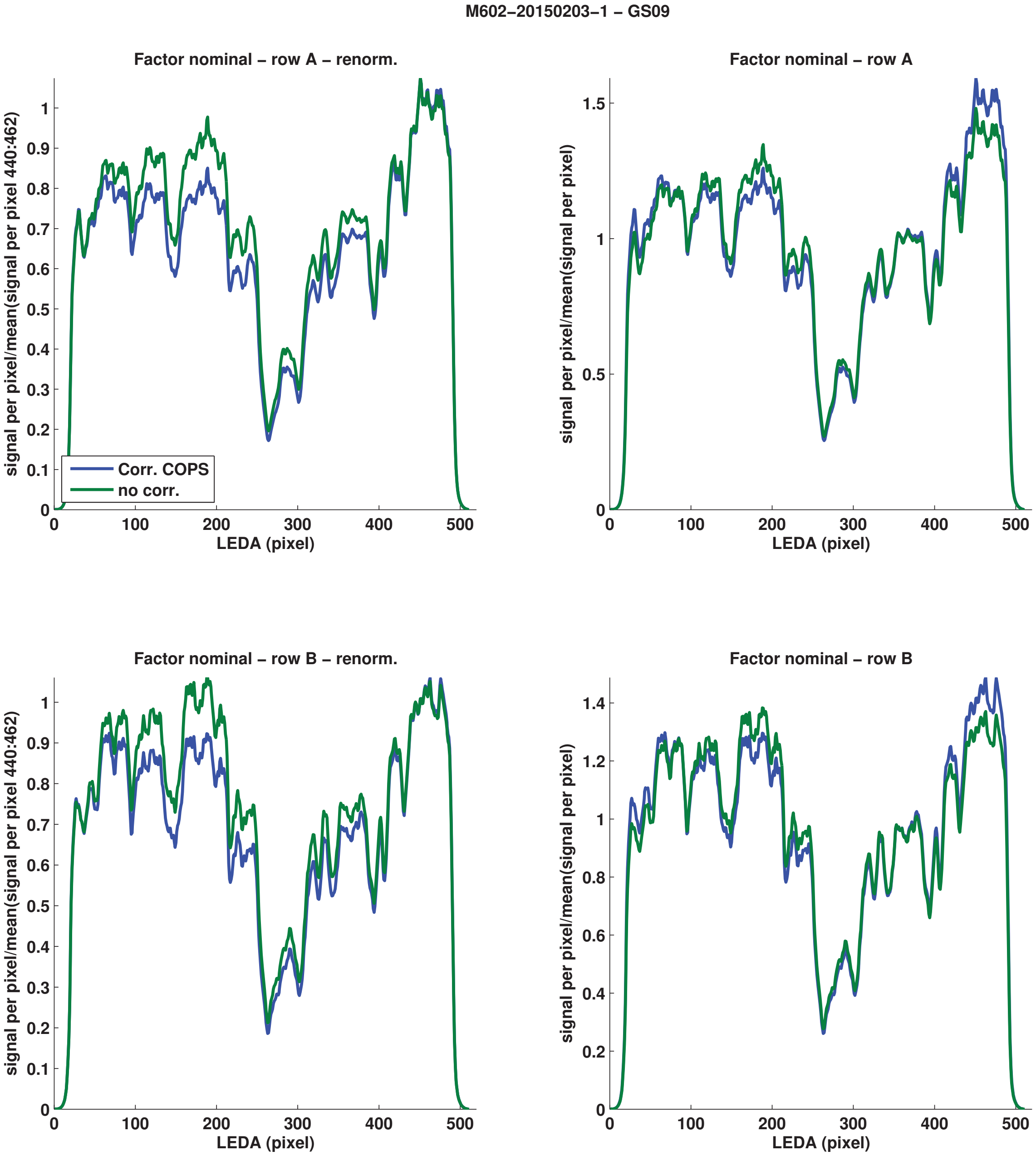

Fig. C.3.6: There is some overlap between the two types of correction but only for roughly 1/3 of the LEDA thus rule 1 applies and no correction has been chosen. However the difference in level between the left and right side implies that the some correction would be needed but COPS does not provide the correct signal.

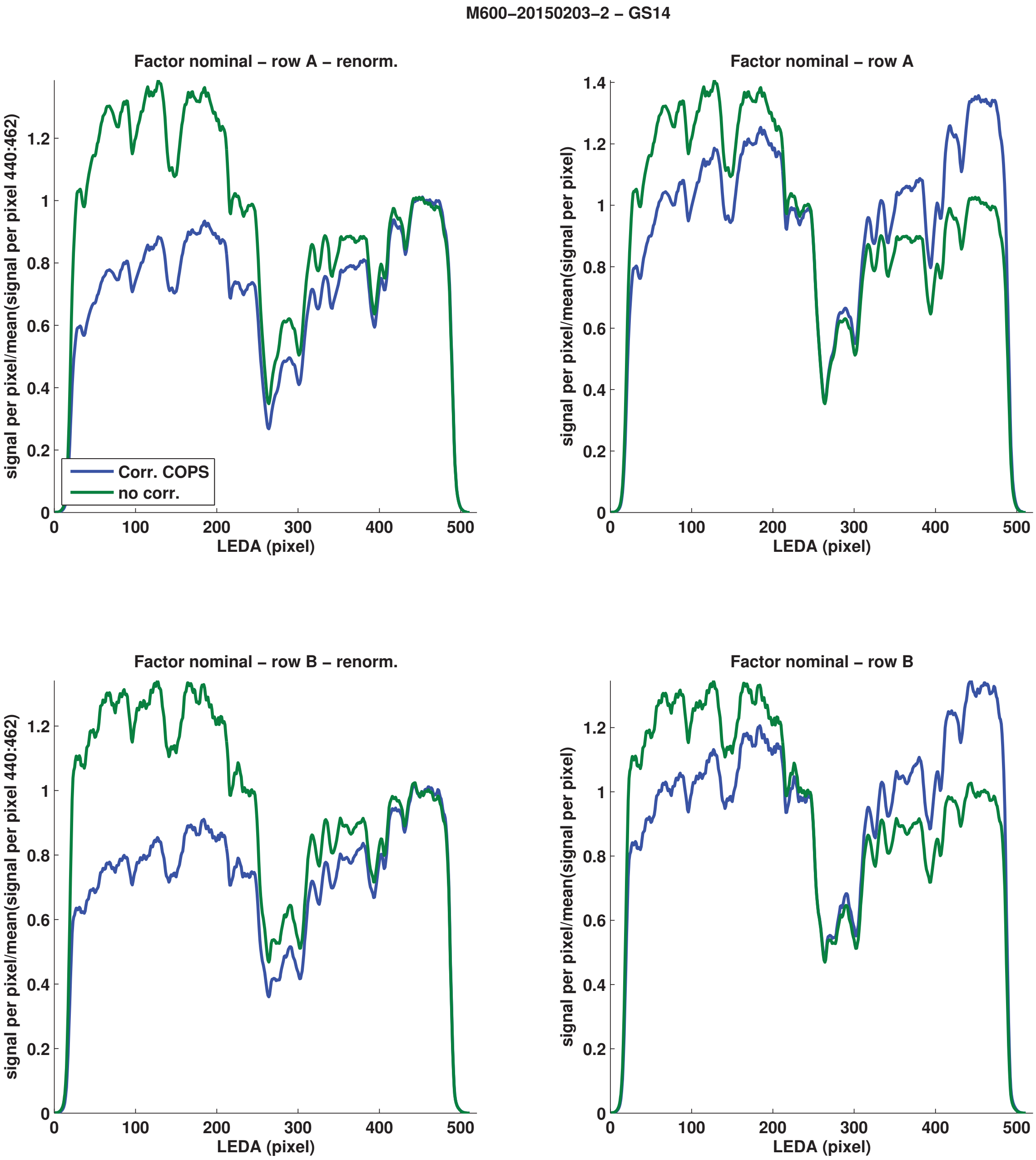

Fig. C.3.7: Again there is no overlap between the two types of correction and based on rule 1 correction COPS is chosen.

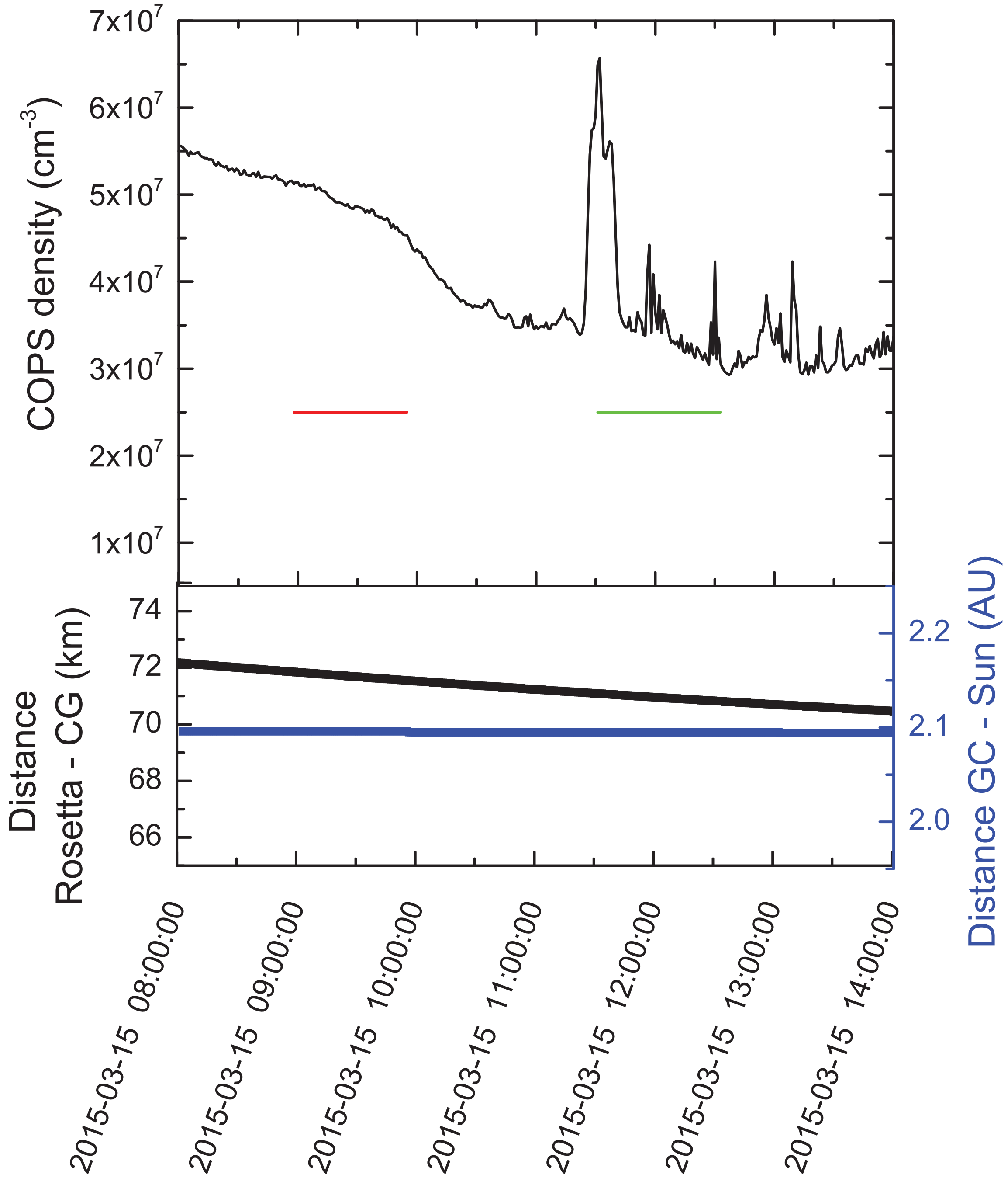

Fig. C.3.8: The upper panel shows the variation in nude gauge density and the lower panel shows the cometary and heliocentric distance of Rosetta. The duration of the pixel gain measurements are indicated by colored bars in the upper panel. In red is M601-1 and in blue M601-2. For both the nude gauge density is not constant however a correction of the first one seems more feasible than for the later one since for the later one the density changed in a short time scale for a factor of ~4.

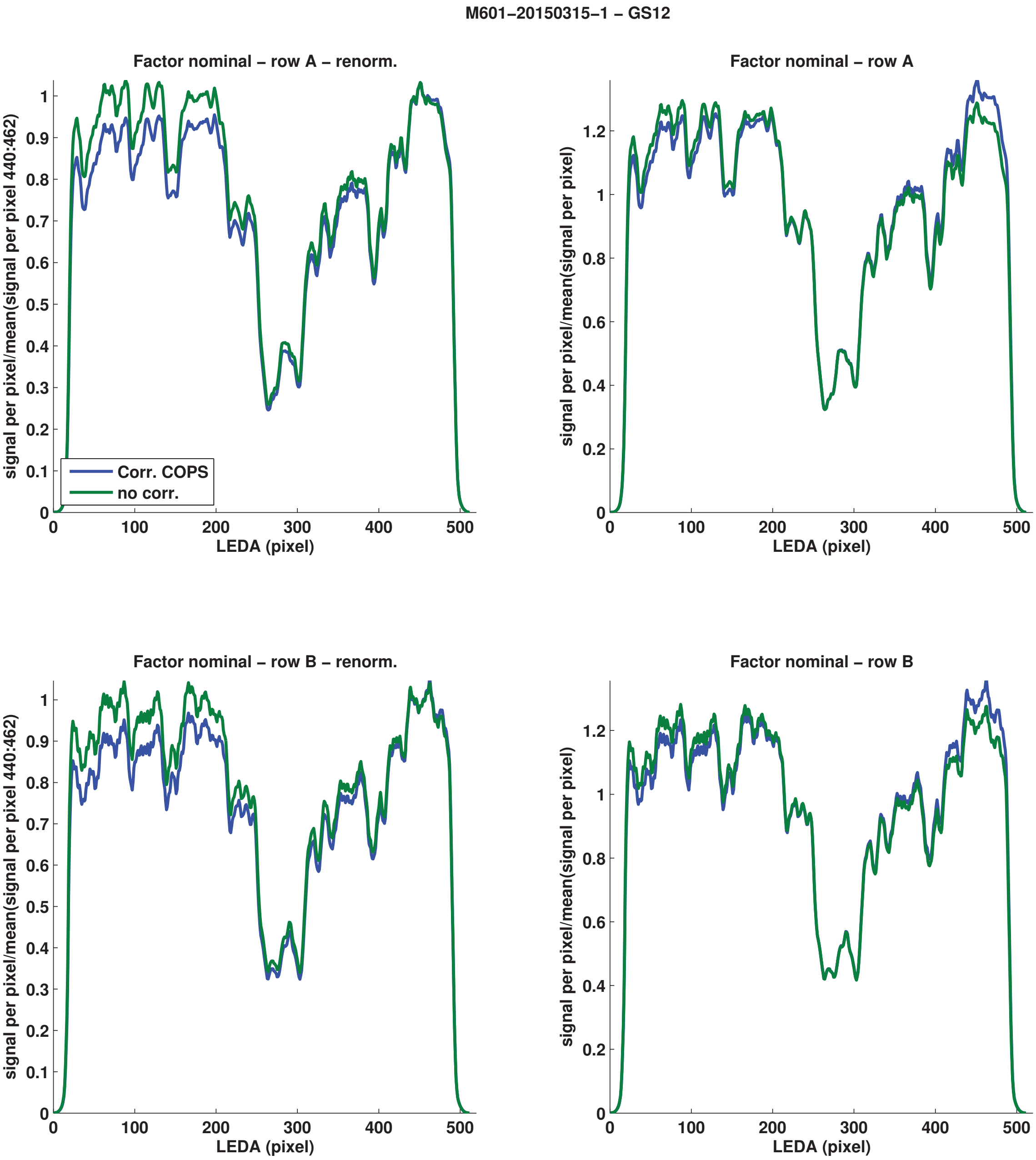

Fig. C.3.9: Based on rule 1 no correction is assumed to be the most likely one because it has almost no change in level of both sides of the central dips.

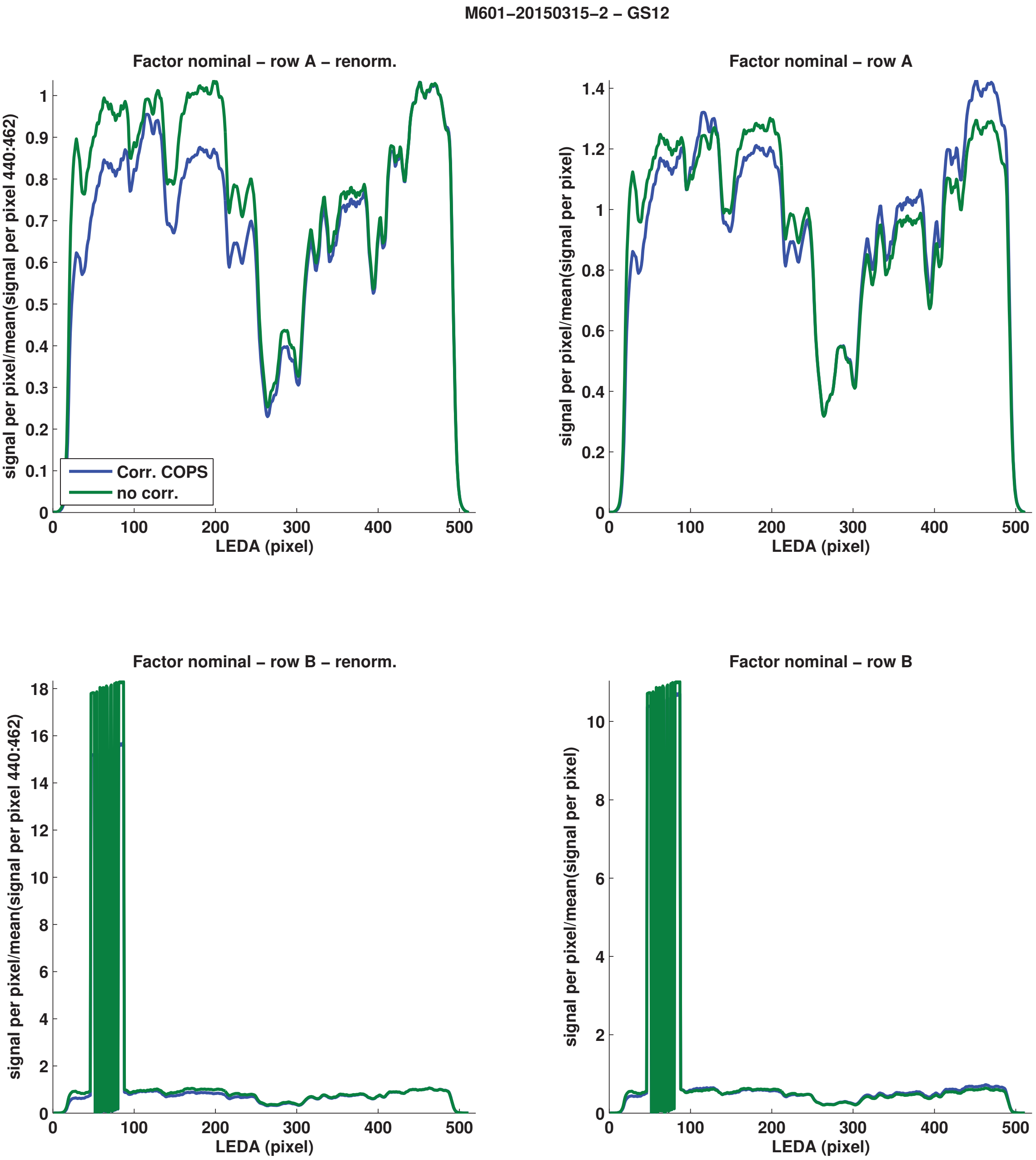

Fig. C.3.10: Based on rule 1 no correction is assumed to be the most likely one because it has almost no change in level of both sides of the central dips.

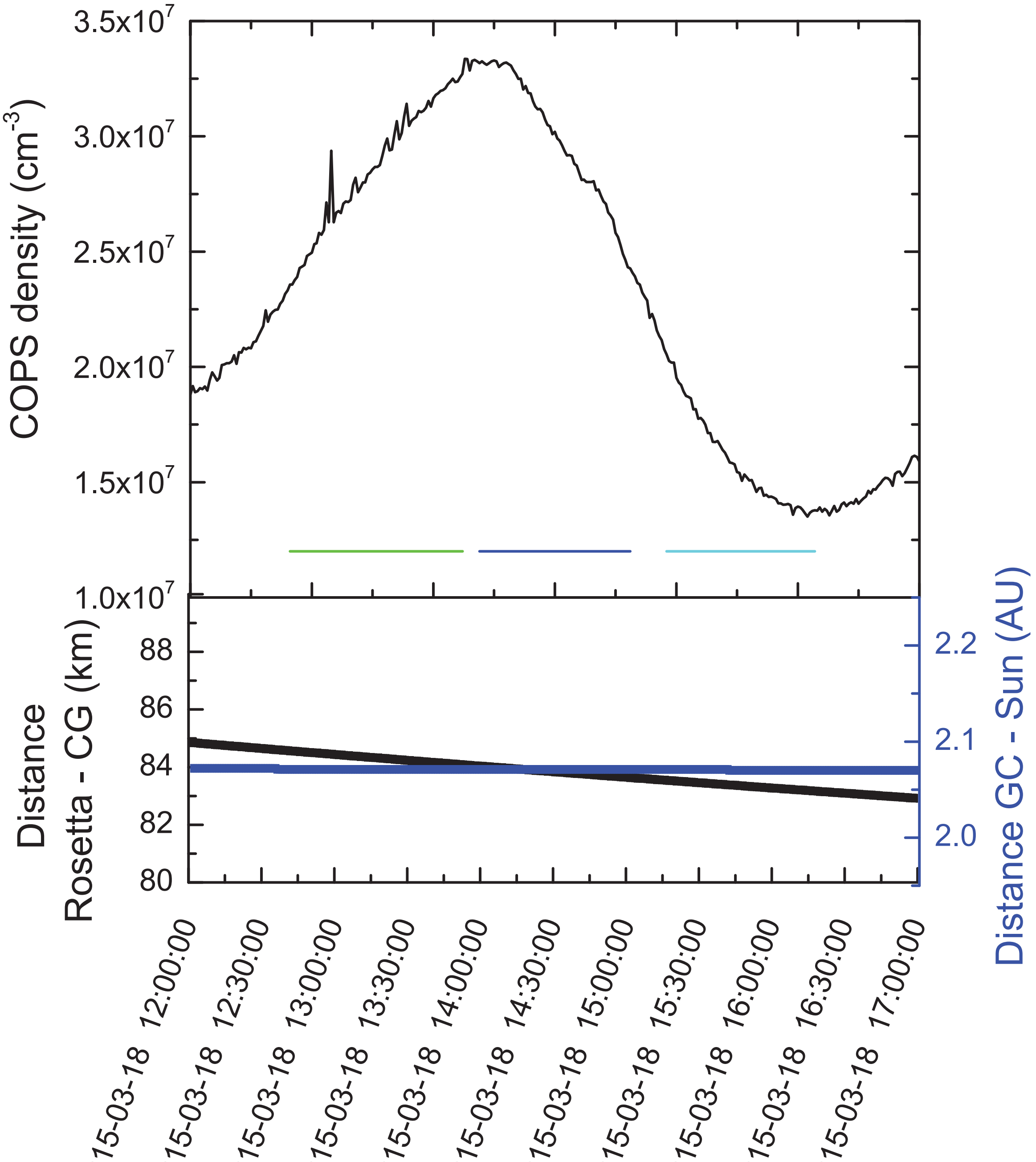

Fig. C.3.11: The upper panel shows the variation in nude gauge density and the lower panel shows the cometary and heliocentric distance of Rosetta. The duration of the pixel gain measurements are indicated with colored bars in the upper panel. In red is M620, in blue is M621,and in green is M622.

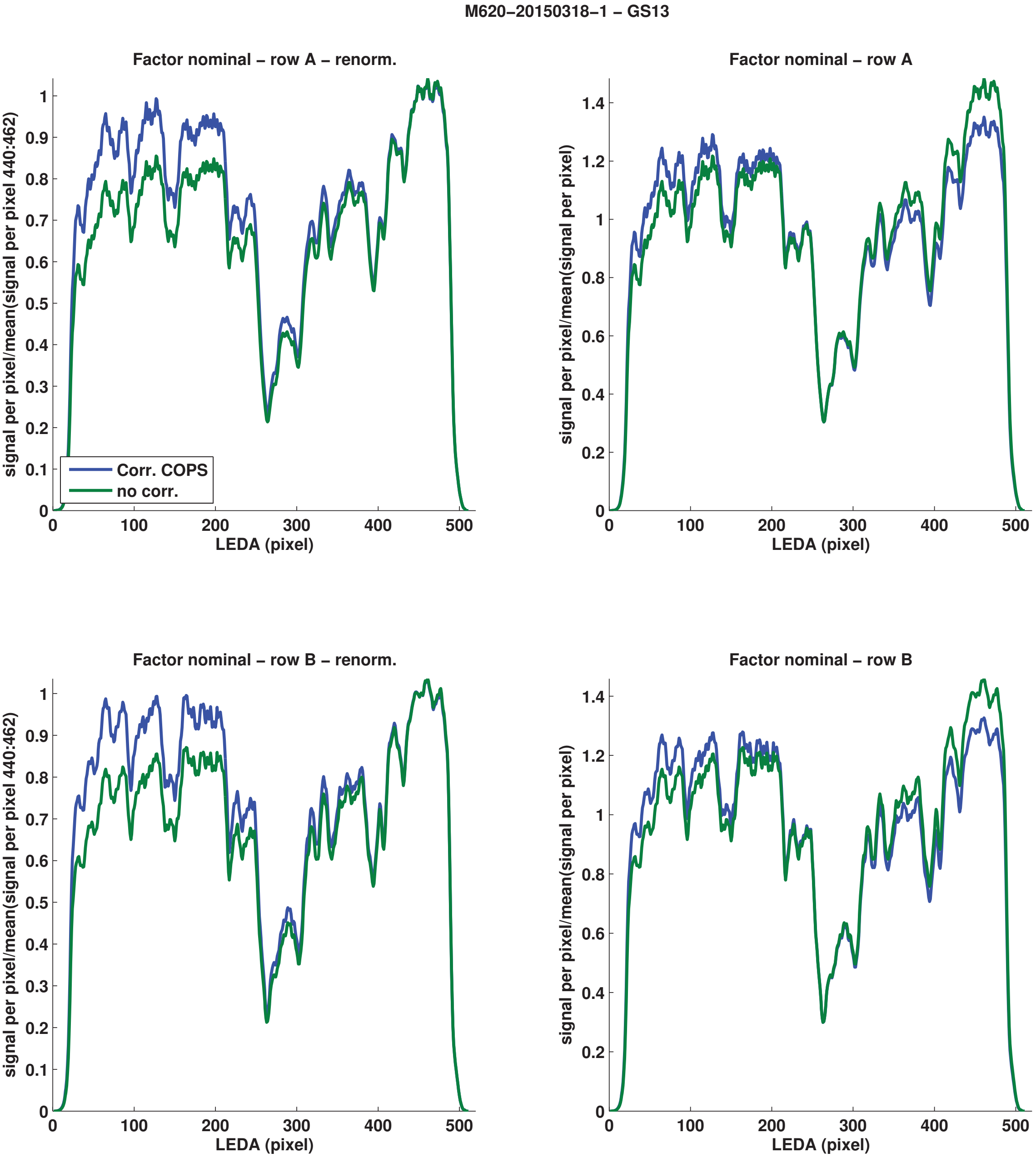

Fig. C.3.12: As a consequence of non overlapping curves rule 1 applies and no correction is selected to be the most realistic one.

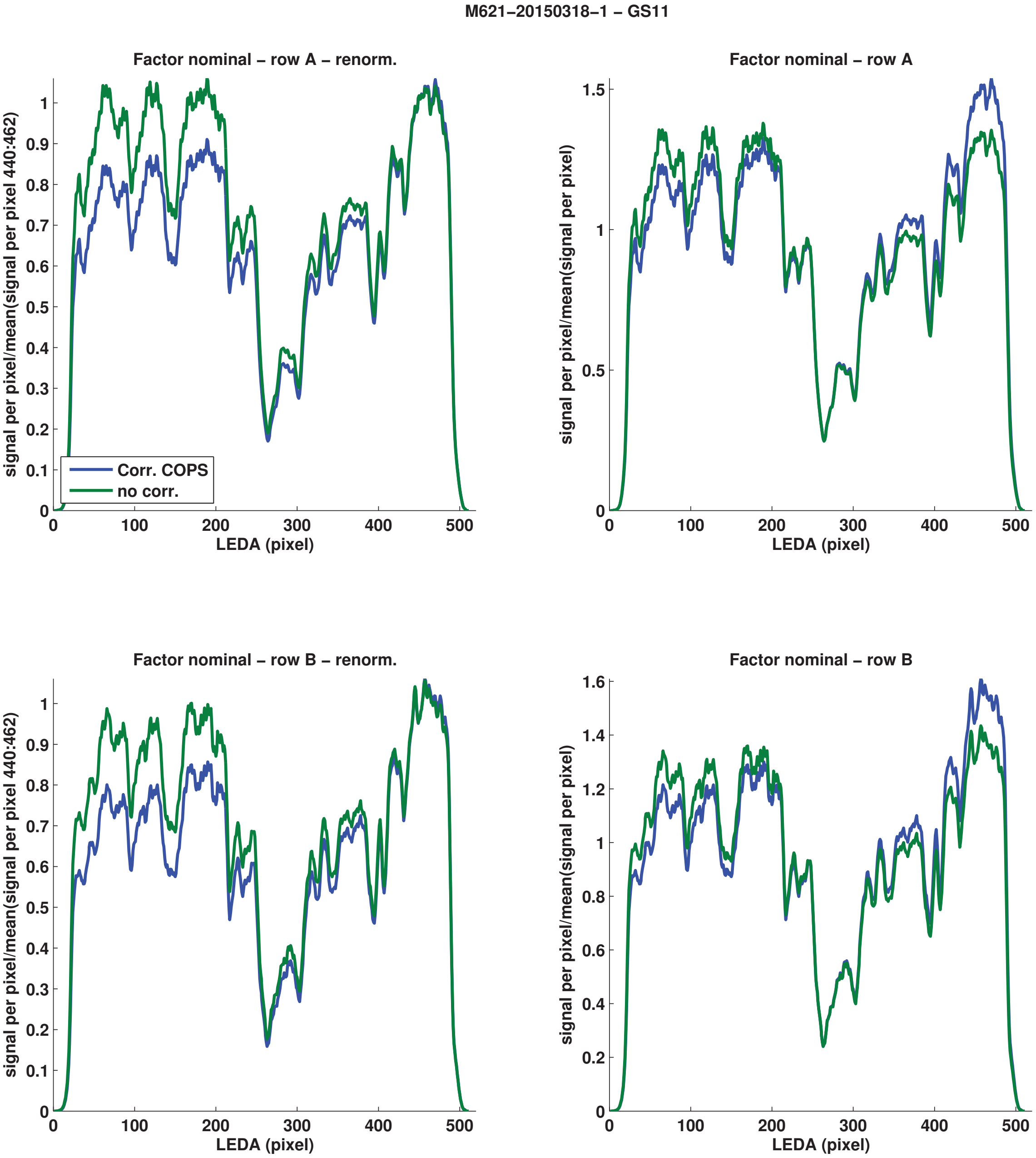

Fig. C.3.13: As a consequence of non overlapping curves rule 1 applies and no correction is selected to be the most realistic one.

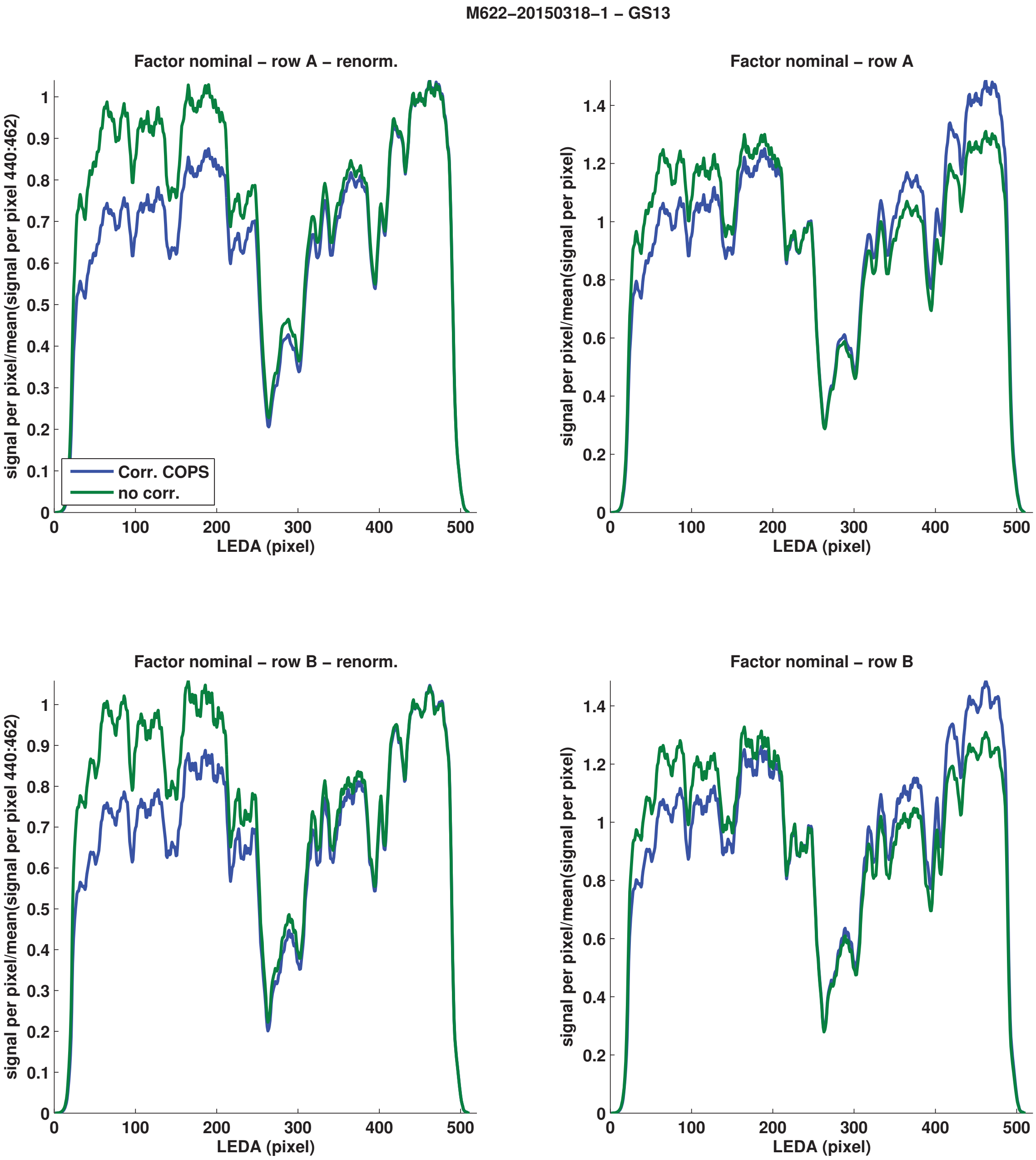

Fig. C.3.14: As a consequence of non overlapping curves rule 1 applies and correction COPS is selected to be the most realistic one.

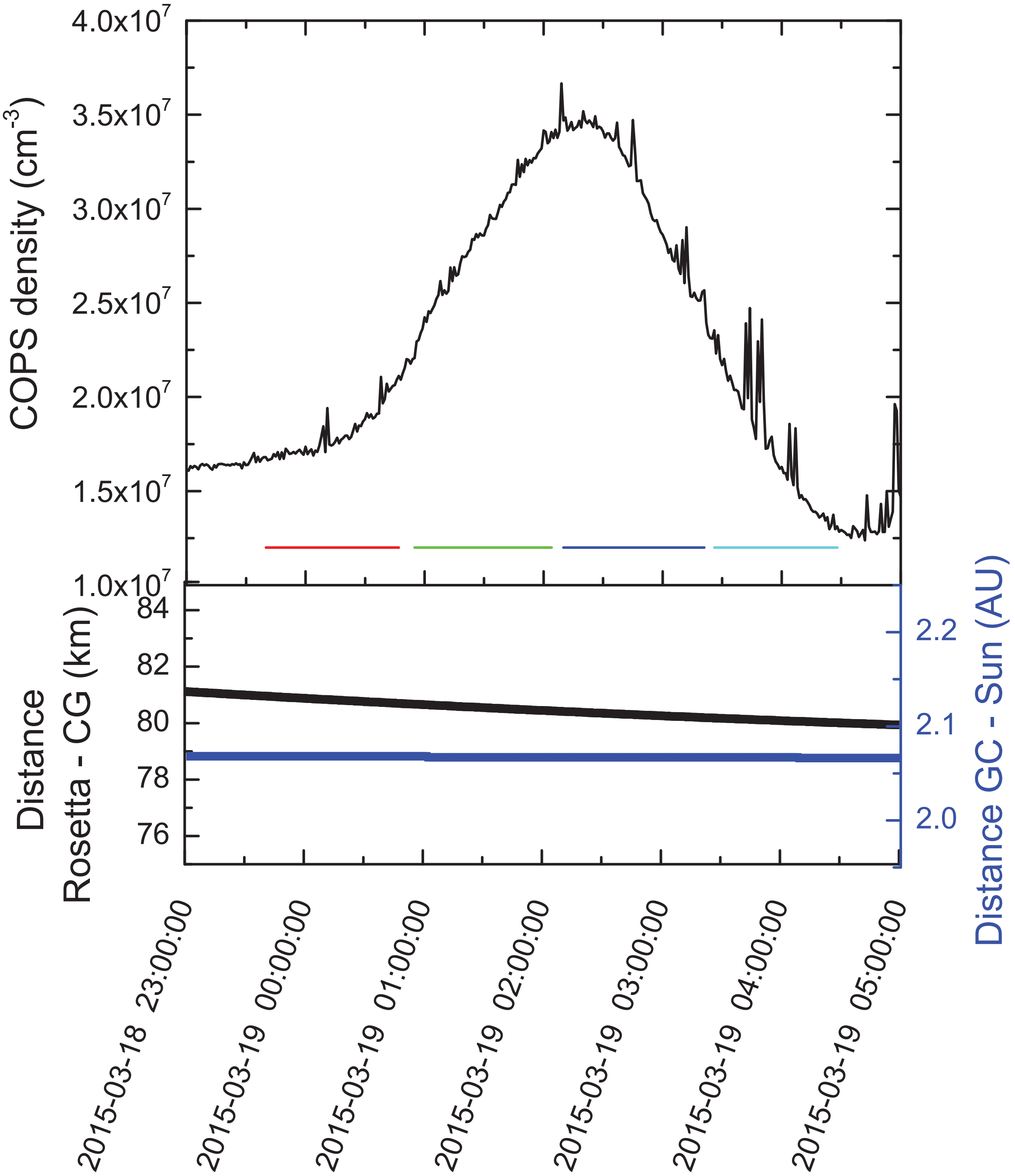

Fig. C.3.15: The upper panel shows the variation in nude gauge density and the lower panel shows the cometary and heliocentric distance of Rosetta. The duration of the pixel gain measurements are indicated with colored bars in the upper panel. In red is M630, in blue is M631, in green is M632, and in violet is M602. Although the overall shape of the COPS nude gauge density should be easily fitted by a polynomial the spikes seen in particular for the last two pixel gain measurements will not be taken into account by this fit and thus might lead to a not proper correction for part of the pixel gain measurement of one mode.

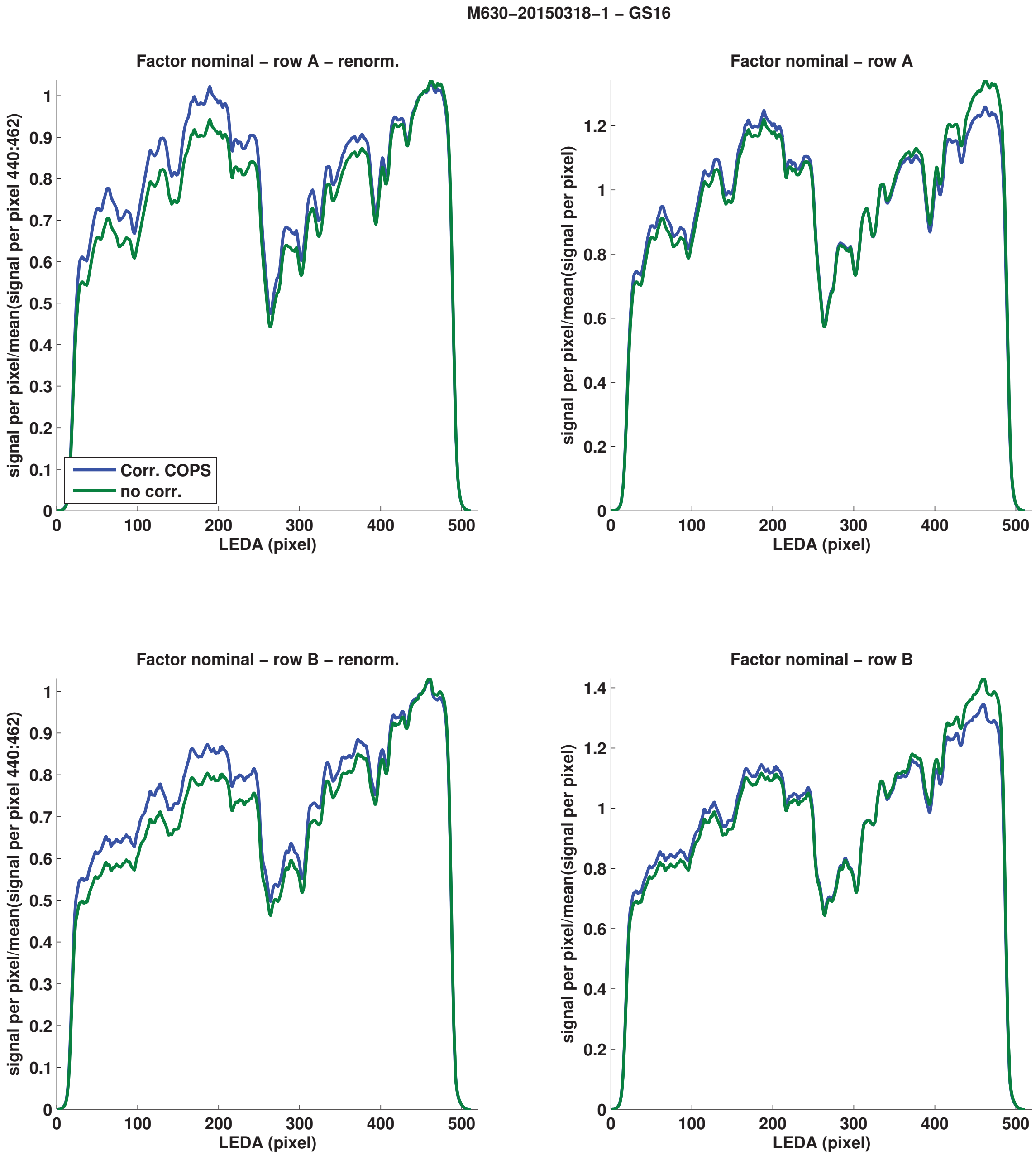

Fig. C.3.16: Although the curves for both corrections lay close together rule 1 is applied and correction COPS is selected because of having the highest level point before and after the central part at the same value.

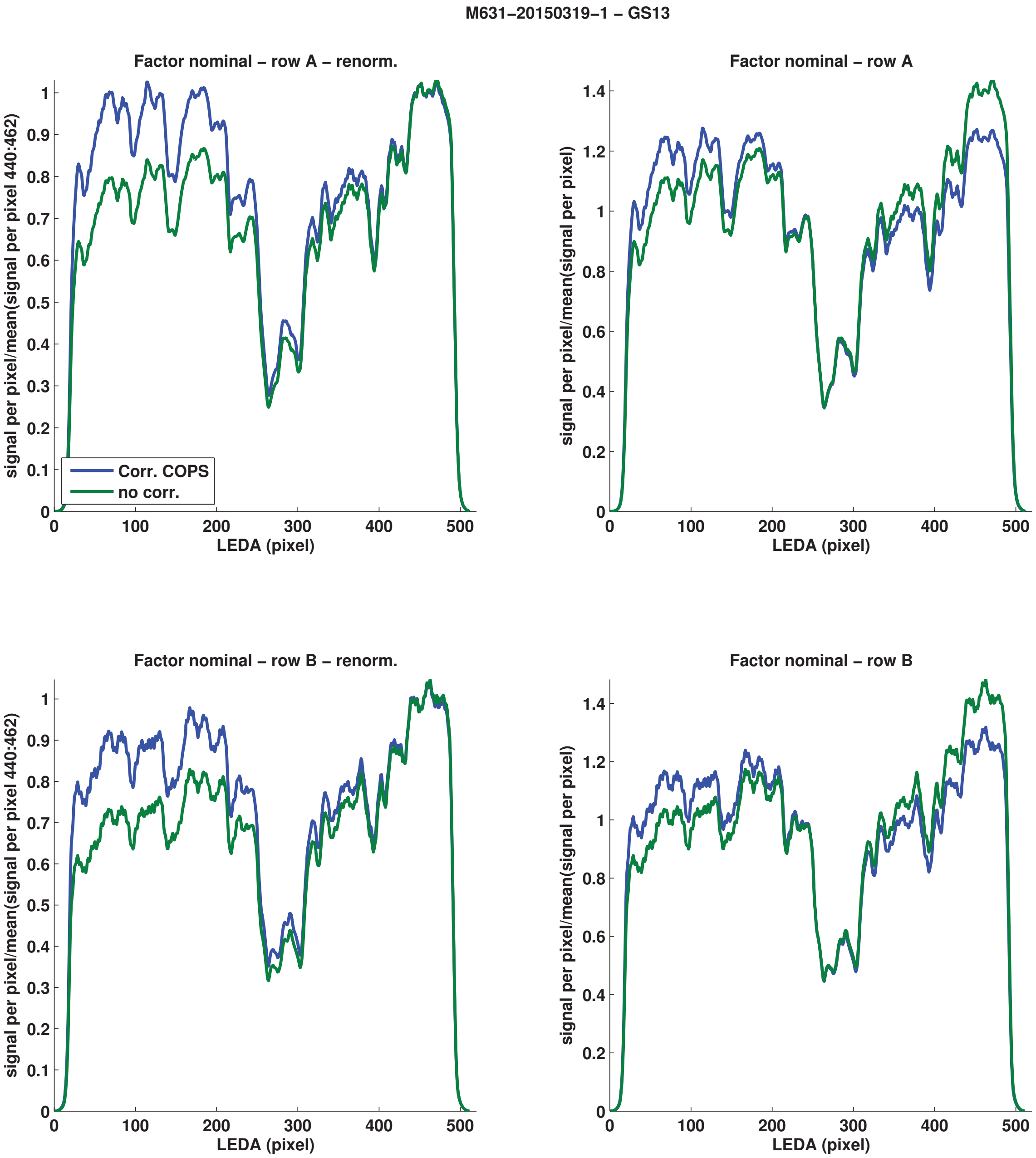

Fig. C.3.17: There is almost no overlap between the two types of corrections and thus rule 1 applies and correction COPS is selected because of having the highest level point before and after the central part at the same value.

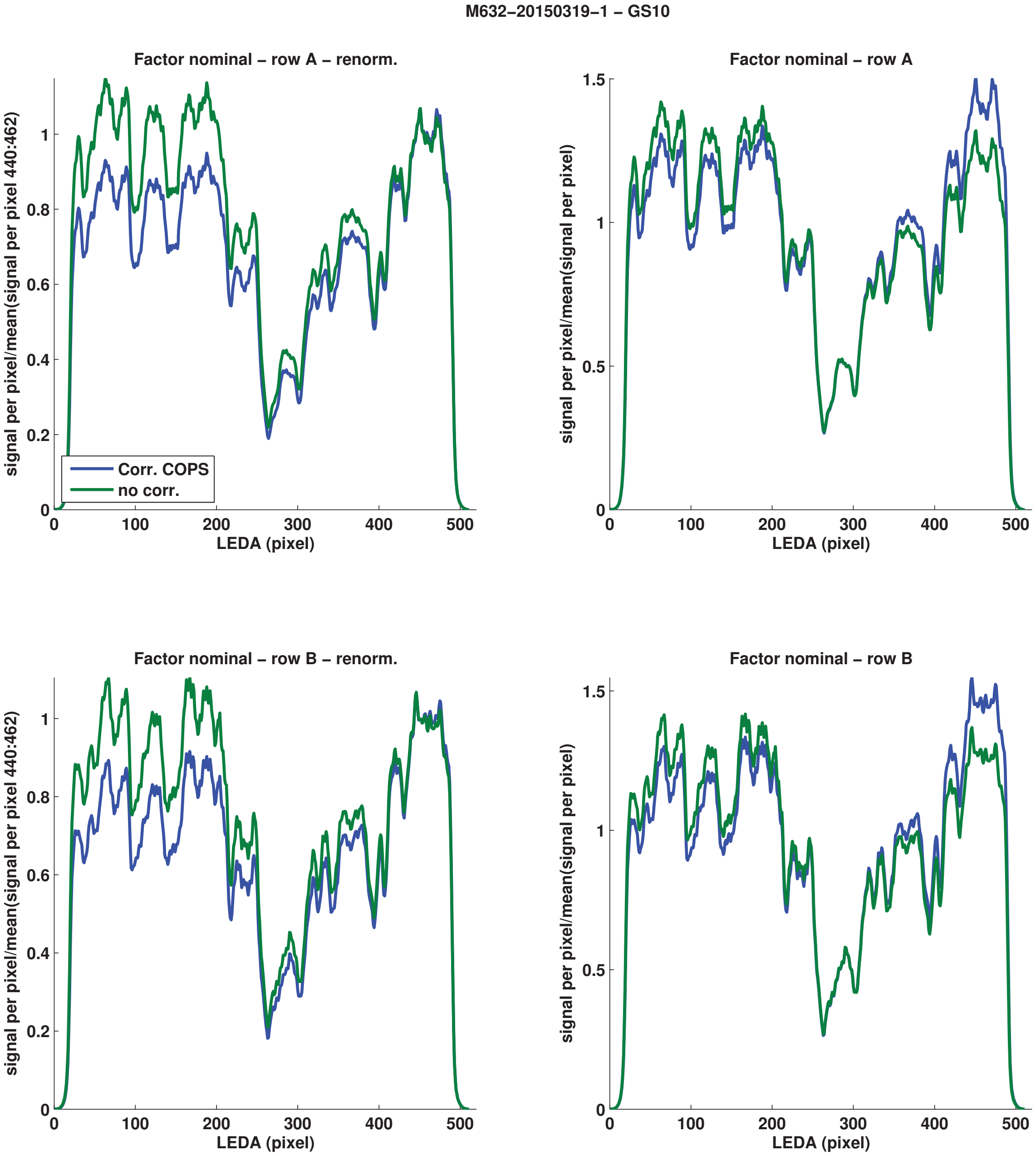

Fig. C.3.18: Here no overlap is present between the two types of corrections and rule 1 applies however both show not a slope in the level and it seems as correction COPS is slightly over corrected and no correction is slightly under corrected. As a consequence no correction has been selected.

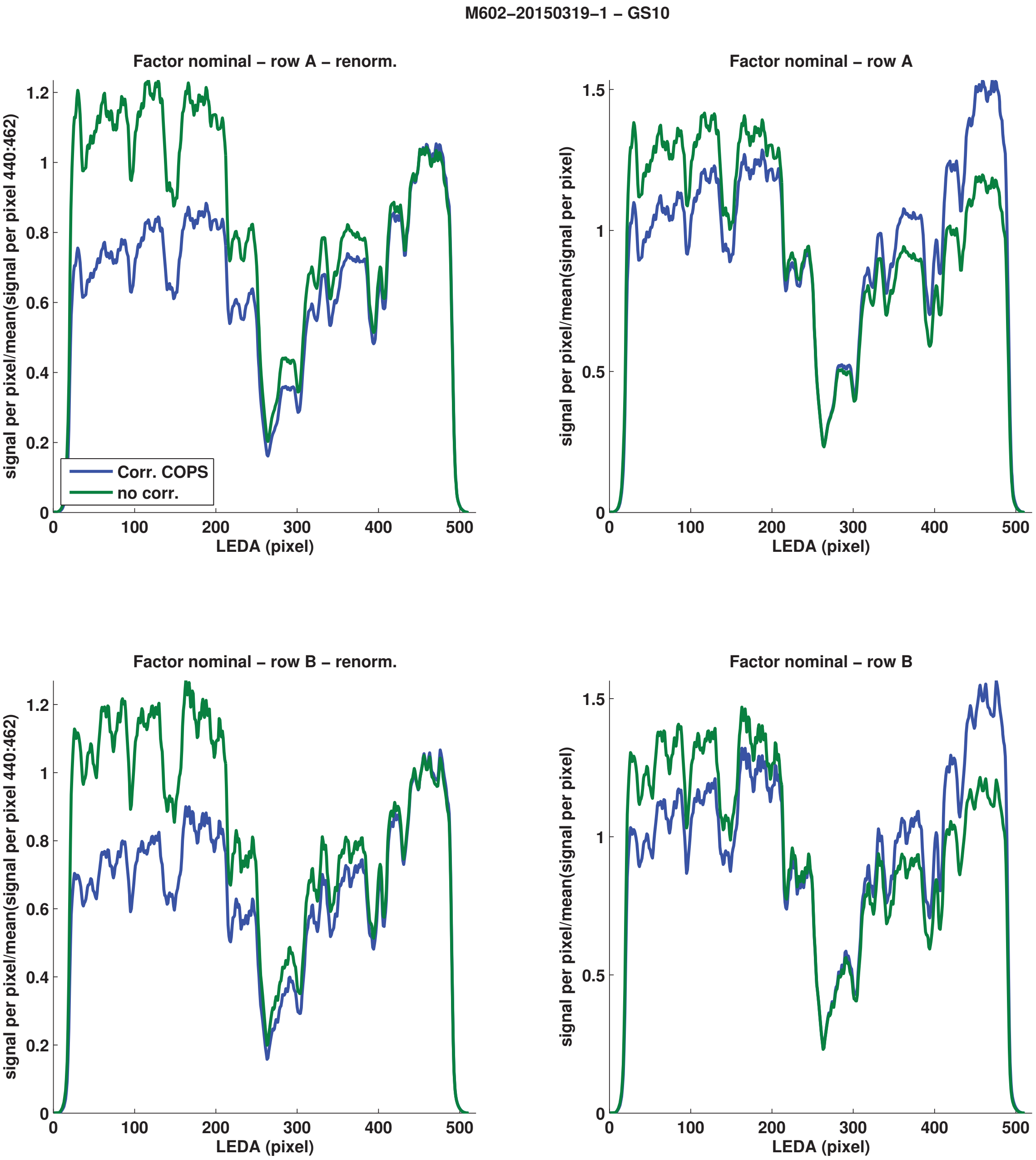

Fig. C.3.19: Again no overlap is present and rule 1 applies. However the selected correction COPS shows a slight increasing slope implying that water was not the dominate species and further corrections are needed.

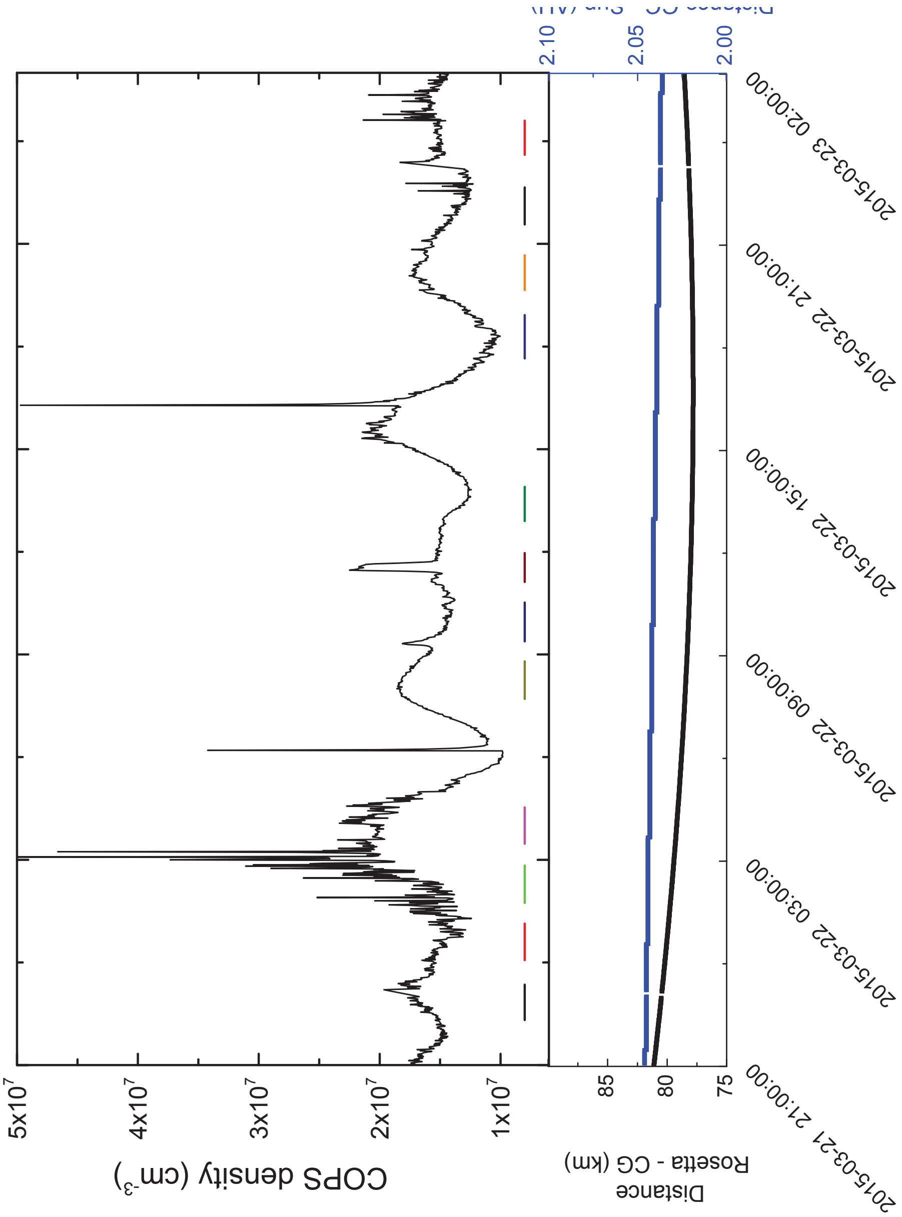

Fig. C.3.20: The upper panel shows the variation in nude gauge density and the lower panel shows the cometary and heliocentric distance of Rosetta. The duration of the pixel gain measurements are indicated with colored bars and label in the upper panel.

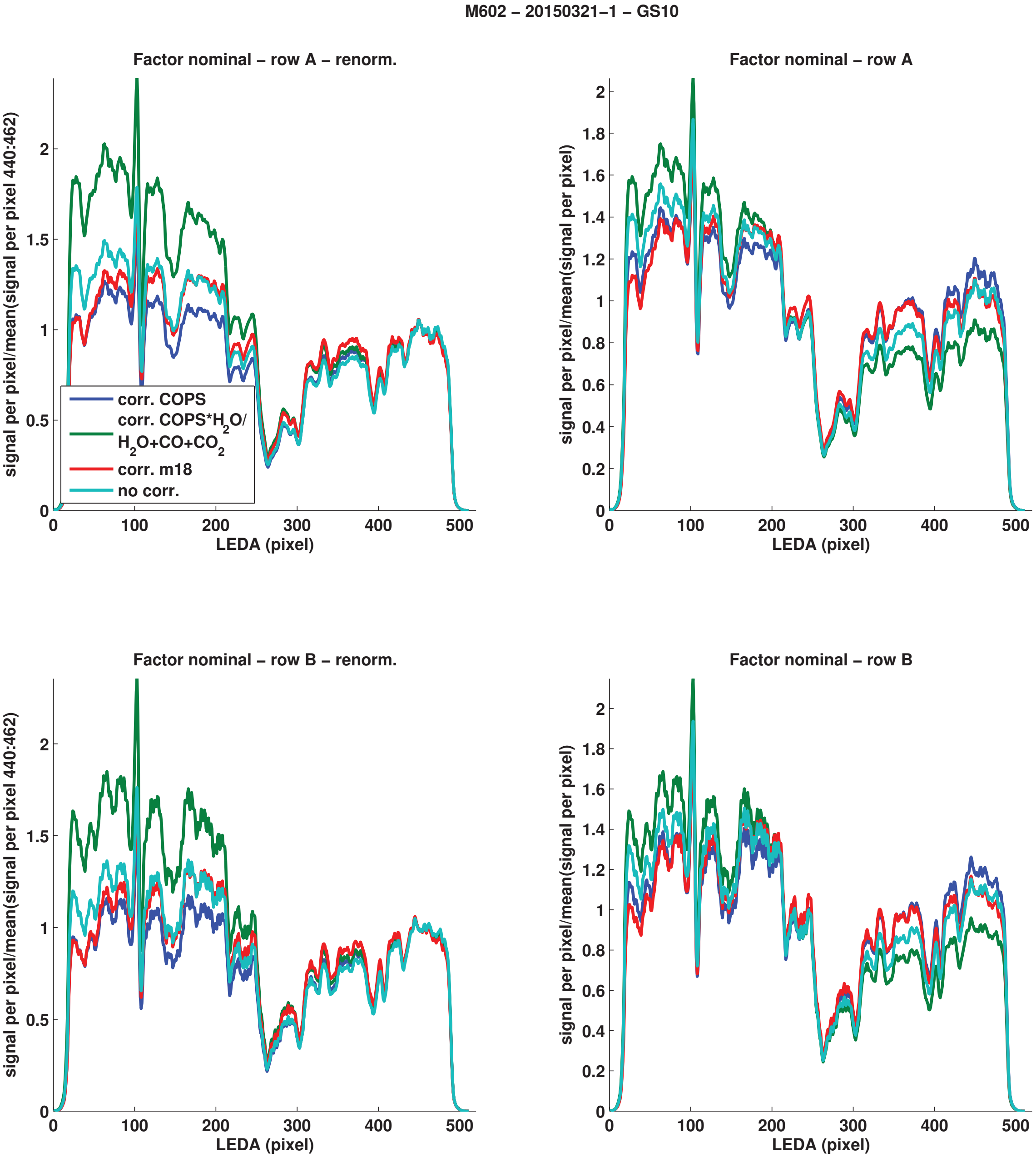

Fig. C.3.21: First of all there is noe overlap between at least two types for the majority of the LEDA thus the first rule is applied and correction COPS is chosen to be the closest to the real factors. The spike after pixel 100 is due to a missing step.

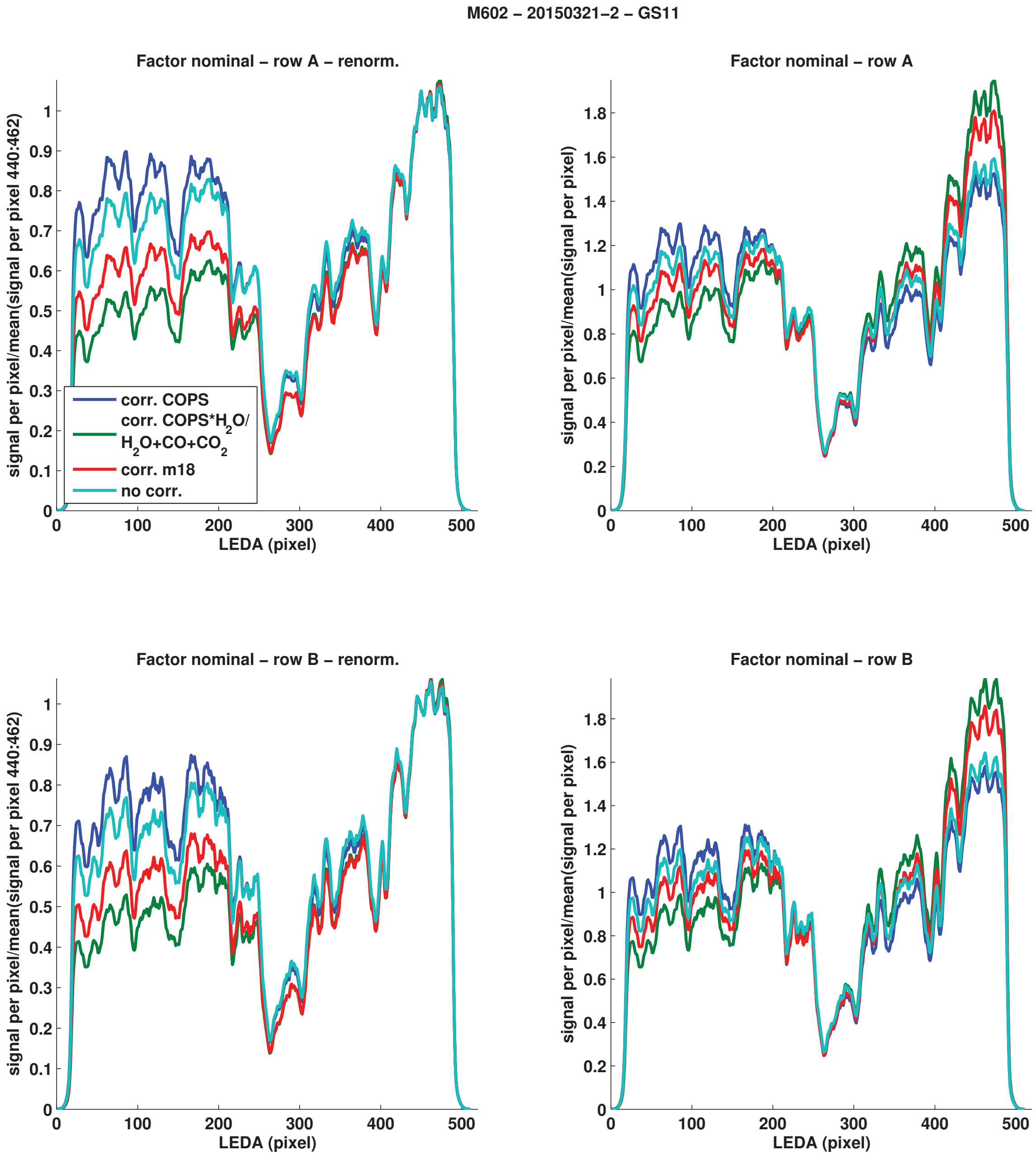

Fig. C.3.22: There is no overlap at all between the four types of corrections besides the central part thus rule 1 applies and correction COPS is chosen.

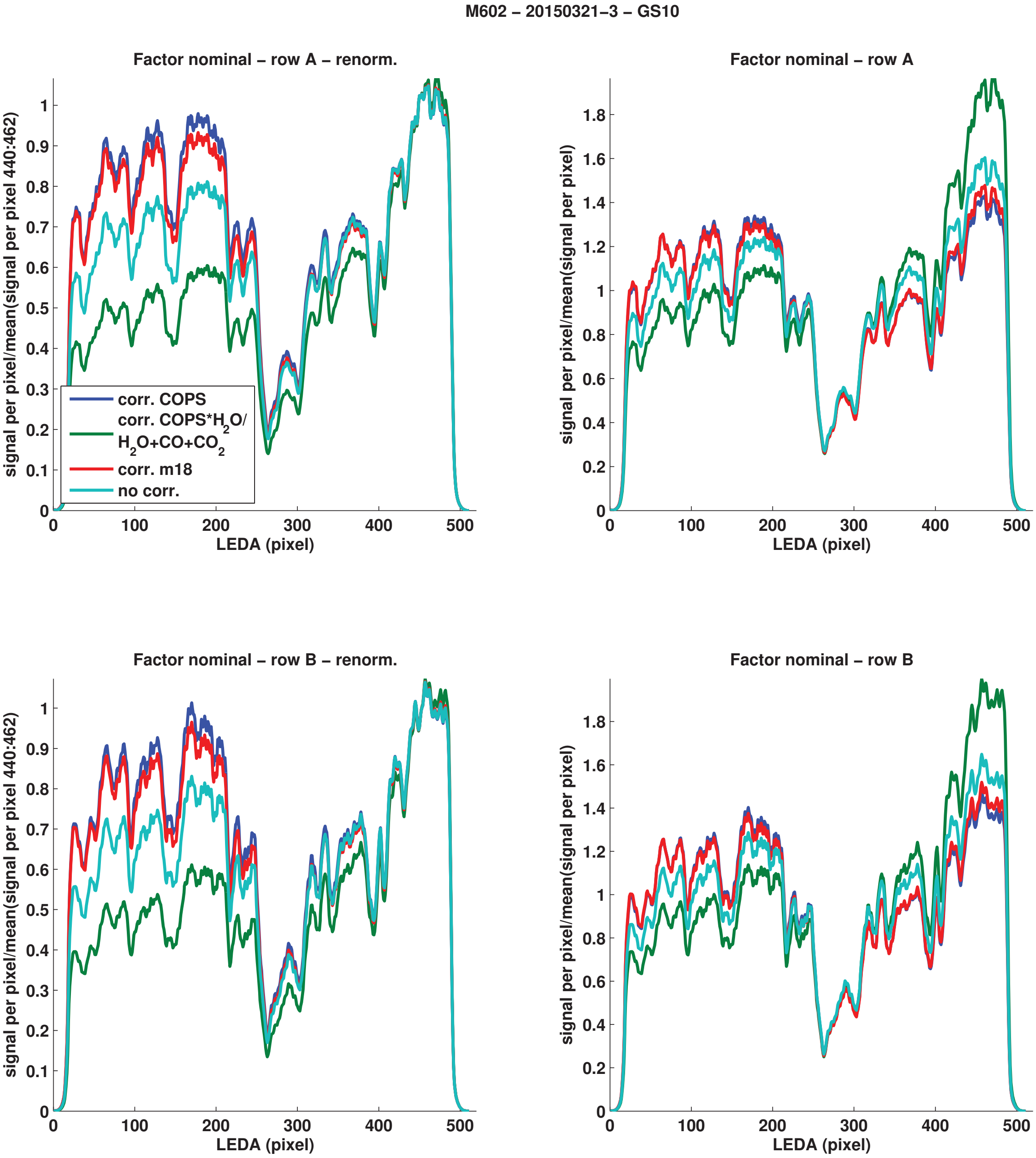

Fig. C.3.23: Here correction m18 and correction COPS show the most overlap implying that water was the major species and that the interpolation of water is close to reality. In consequence rule 2 applies and correction COPS is chosen.

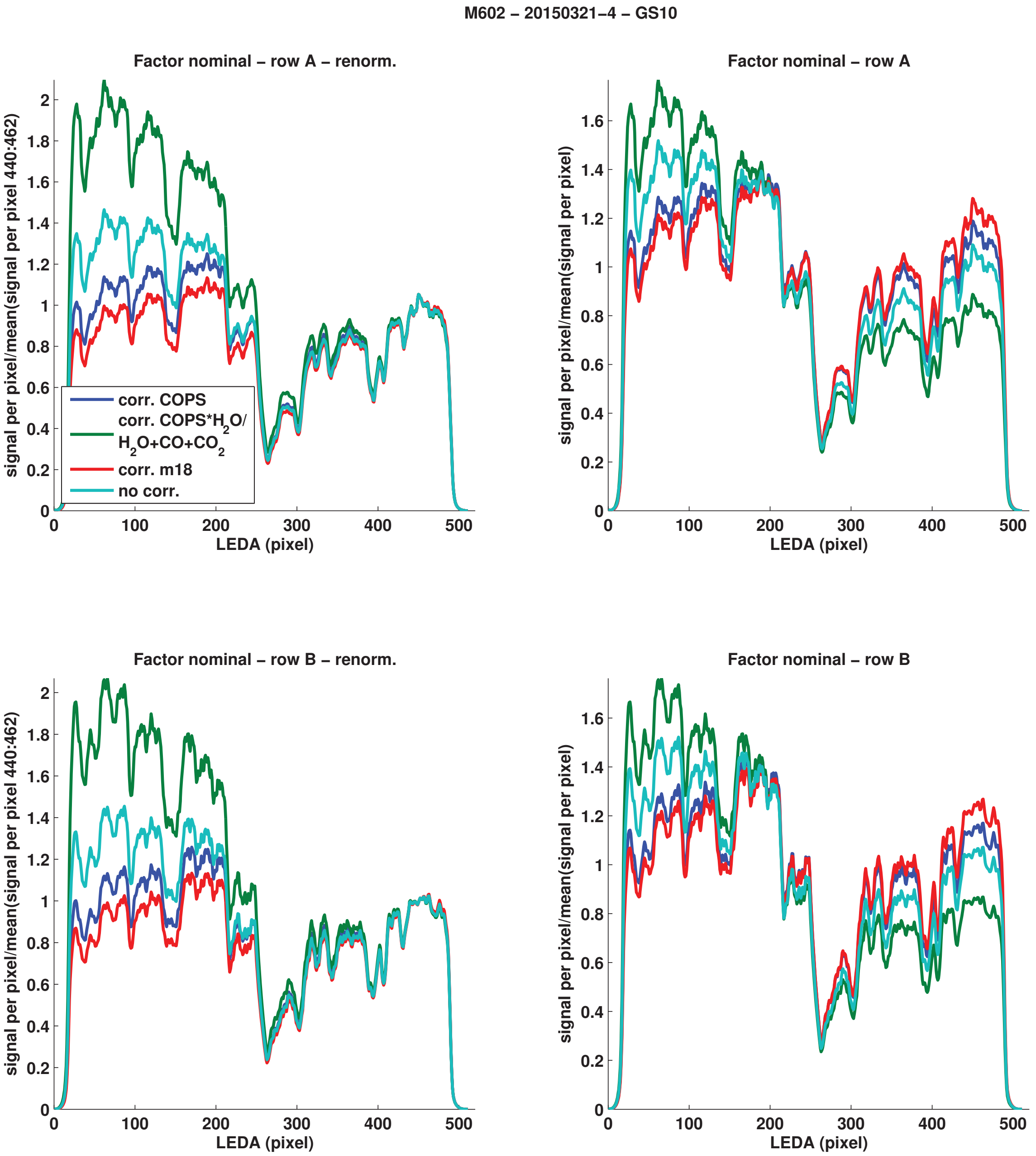

Fig. C.3.24: As for M602-20150321-3-GS10 correction m18 and correction COPS show the most overlap for the majority of the LEDA and thus following rule 2 correction COPS should be taken. However the change in level between the first half and the second half of the LEDA for correction COPS implies a change a change of relative level of water in the coma thus correction m18 is taken.

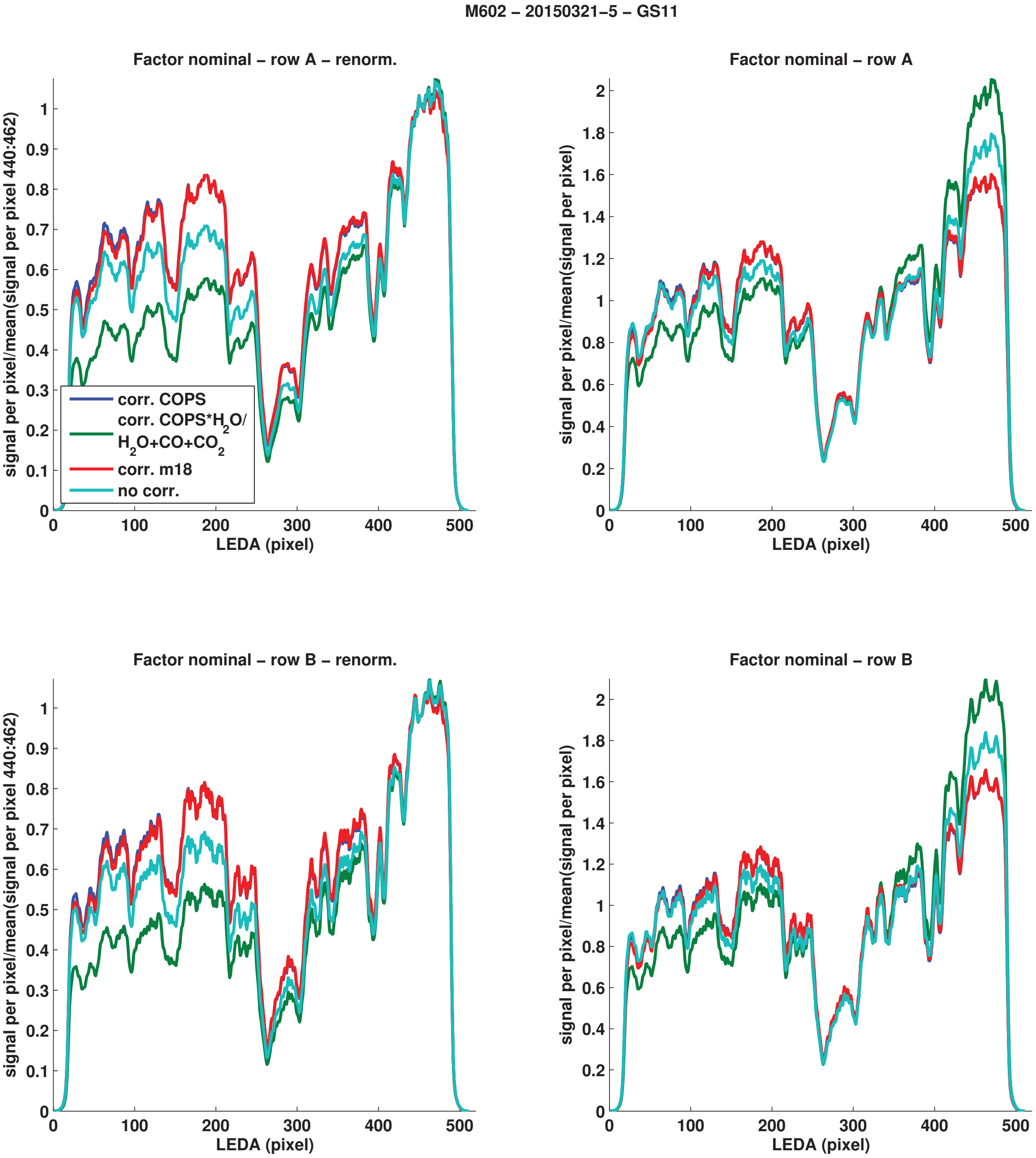

Fig. C.3.25: The most overlap show correction m18 and correction COPS and following rule 2 correction COPS is taken.

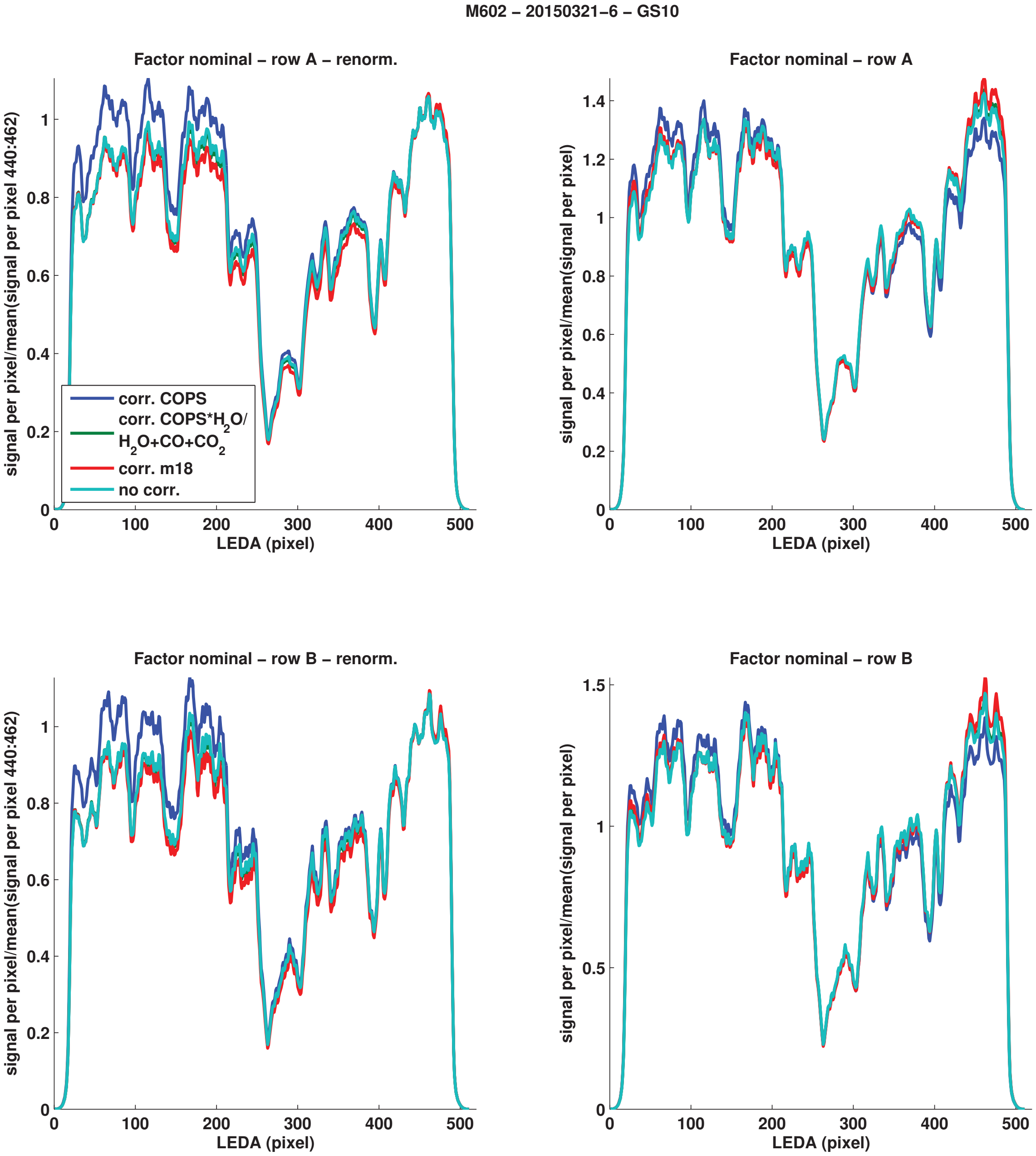

Fig. C.3.26: Here correction of ration main species and no correction overlap while correction of water is below and correction COPS shows almost no change of level over the LEDA thus rule 5 takes effect and correction COPS is chosen.

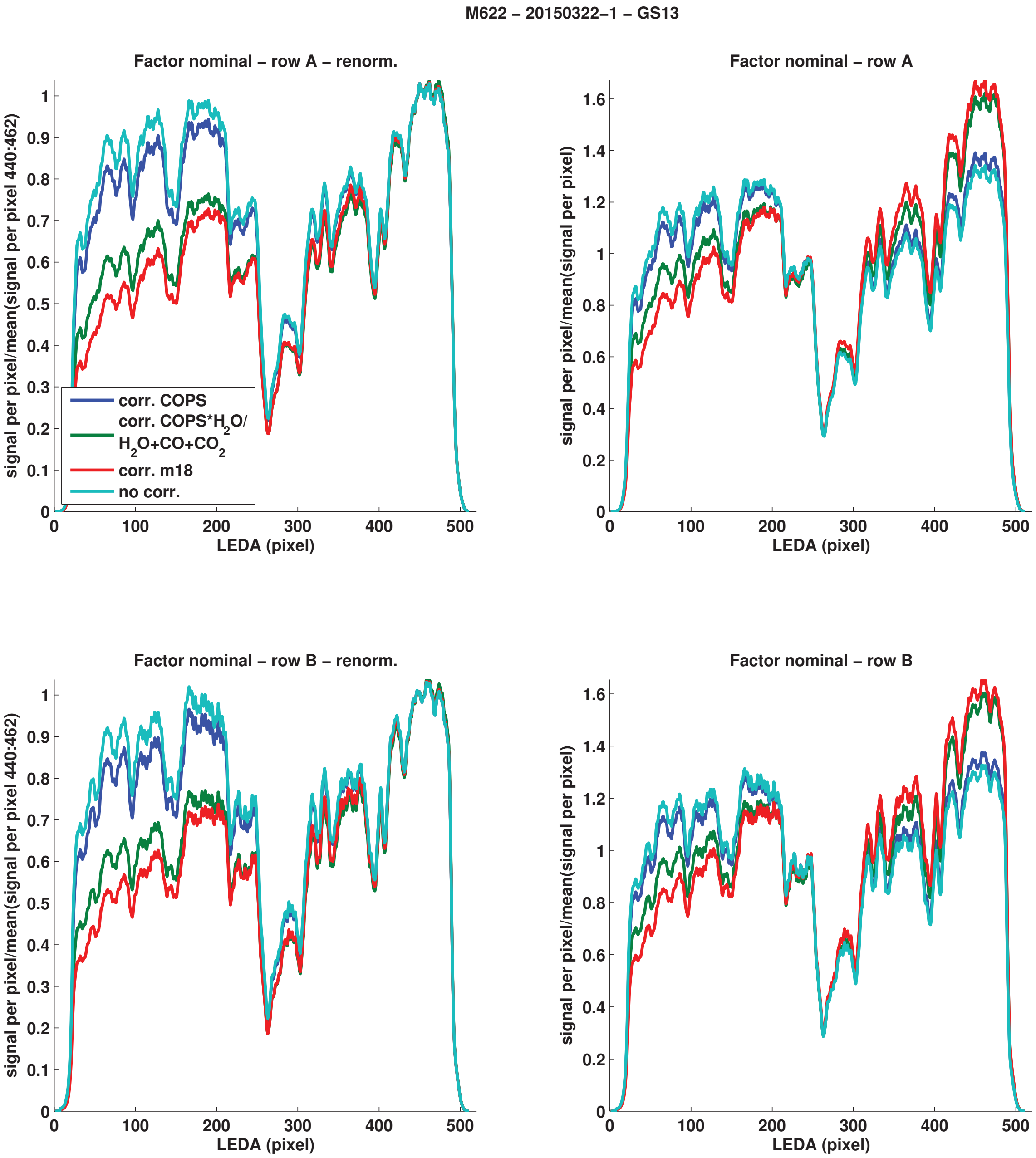

Fig. C.3.27: Here the corrections are divided into two groups first no correction together with correction COPS and second into correction m18 and correction of the main species combined with COPS. Since the first group shows the more shallow slope of the level rule 4 applies and no correction is taken.

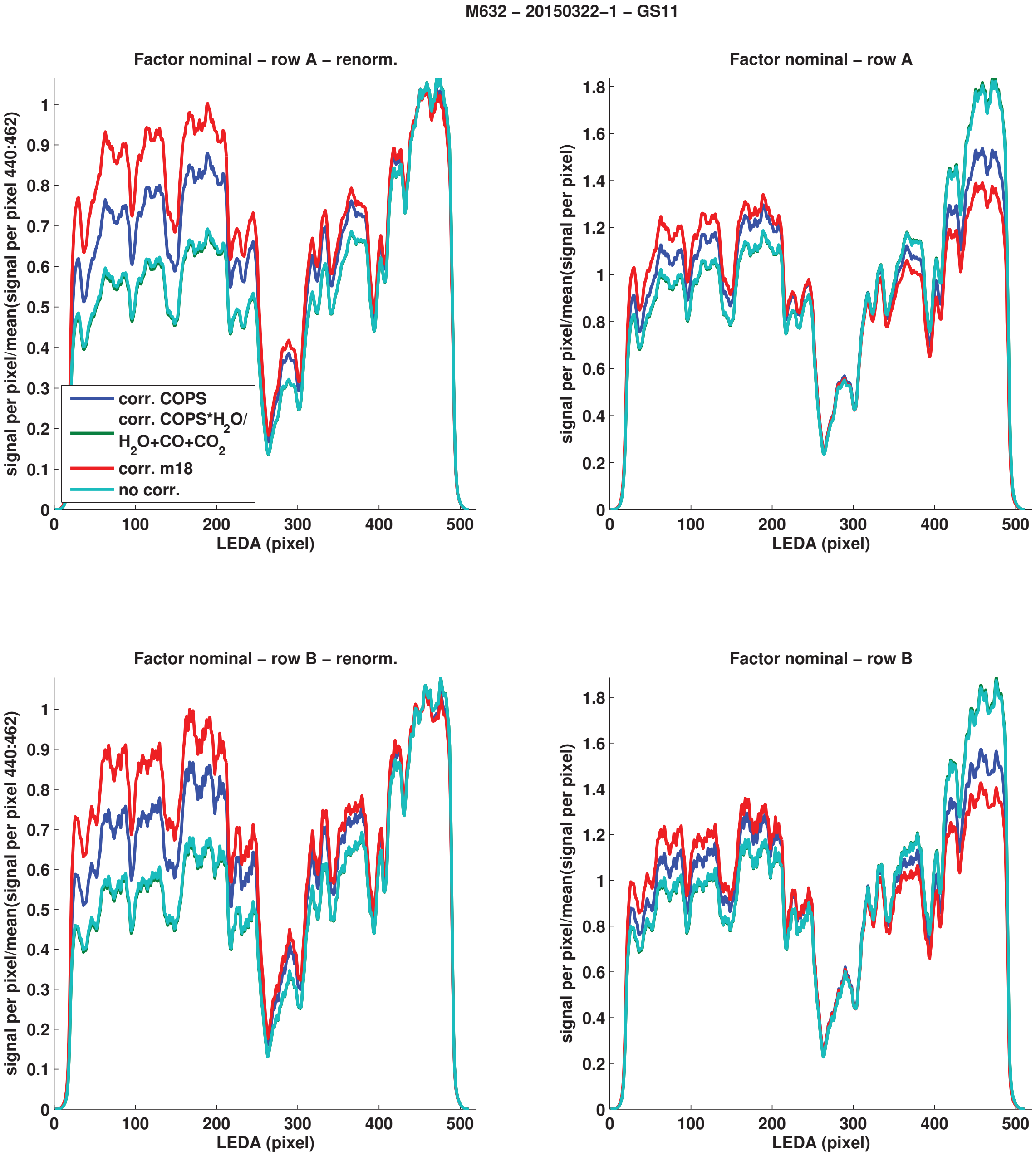

Fig. C.3.28: As a consequence of no overlap of two types of corrections correction m18 is taken to be the most likely one (rule 1).

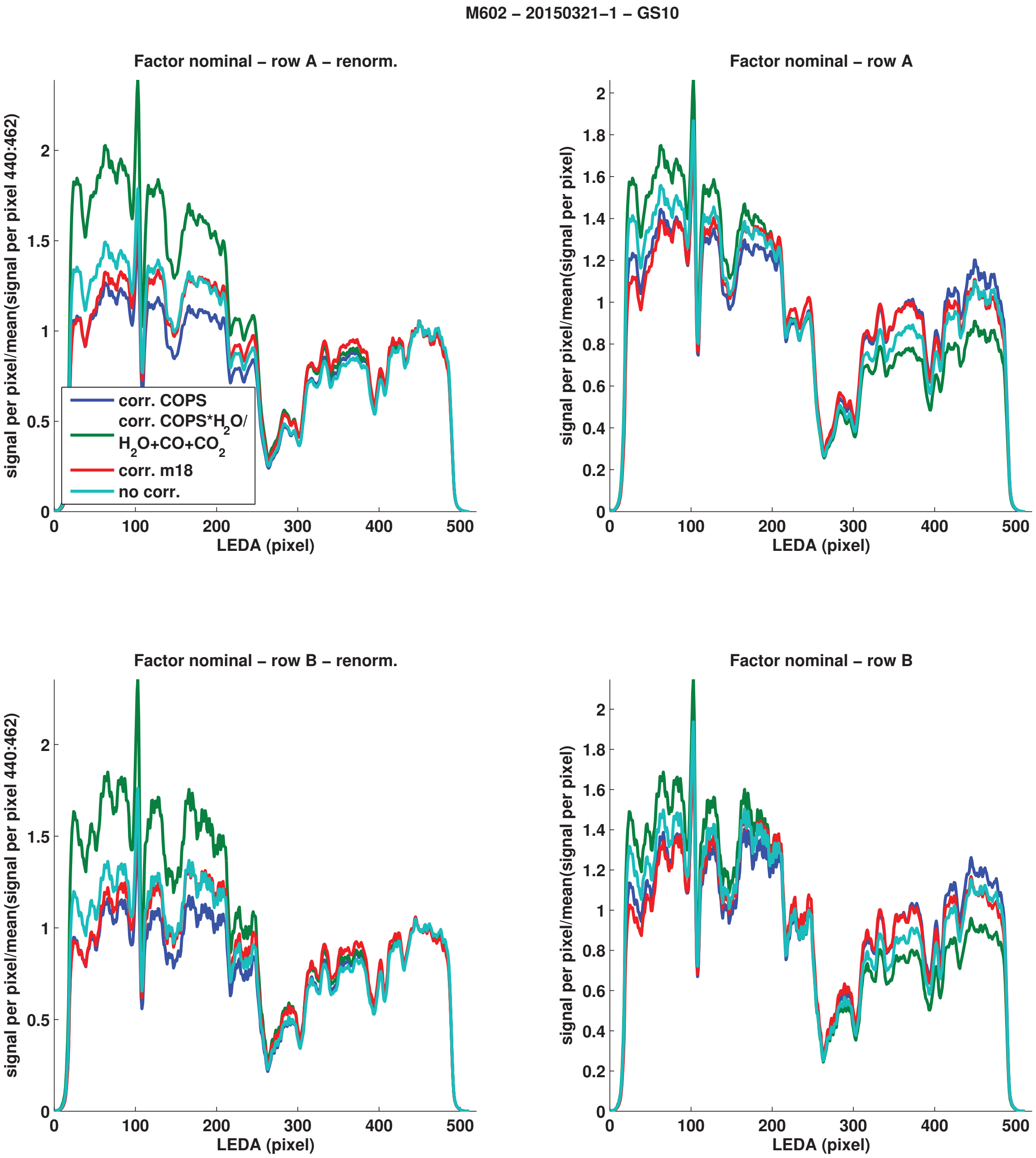

Fig. C.3.29: For this measurement correction COPS and no correction show the largest overlap while correction m18 is off. Based on rule 4 no correction is chosen. That correction m18 is off can be easily understood when one is checking COPS nude gauge signal during this period (Referenz). The space craft did a small slew which is taken into account for the correction COPS but not for correction m18.

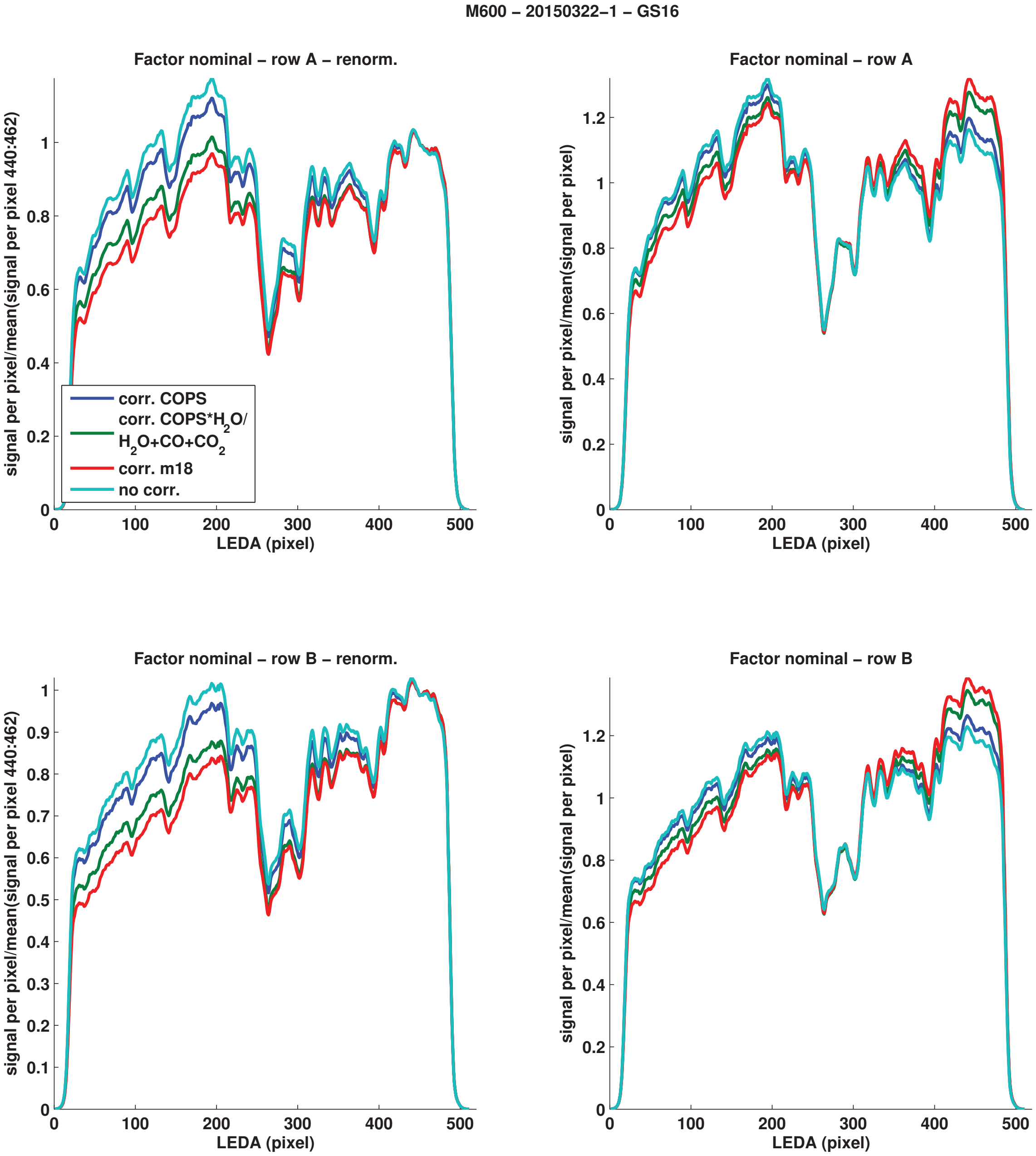

Fig. C.3.30: Here the corrections group in two and both have a different type of all over slope thus rule 5 has to be applied and correction ratio of the main species combined with COPS is chosen.

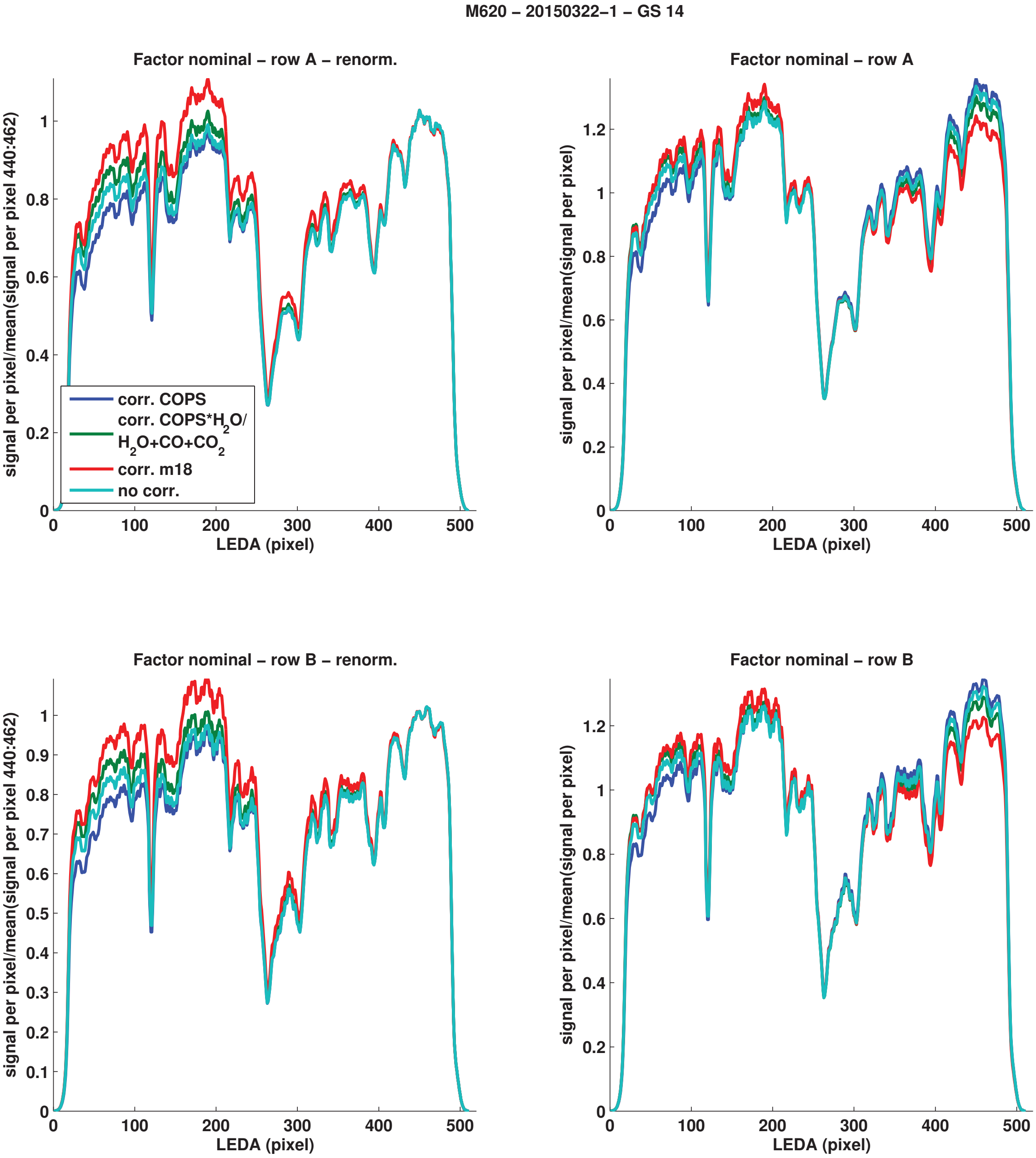

Fig. C.3.31: There is no overlap of two types of corrections for both sides of the central dip thus rule 1 applies and correction for the ratio of the main species is chosen to be the closest.

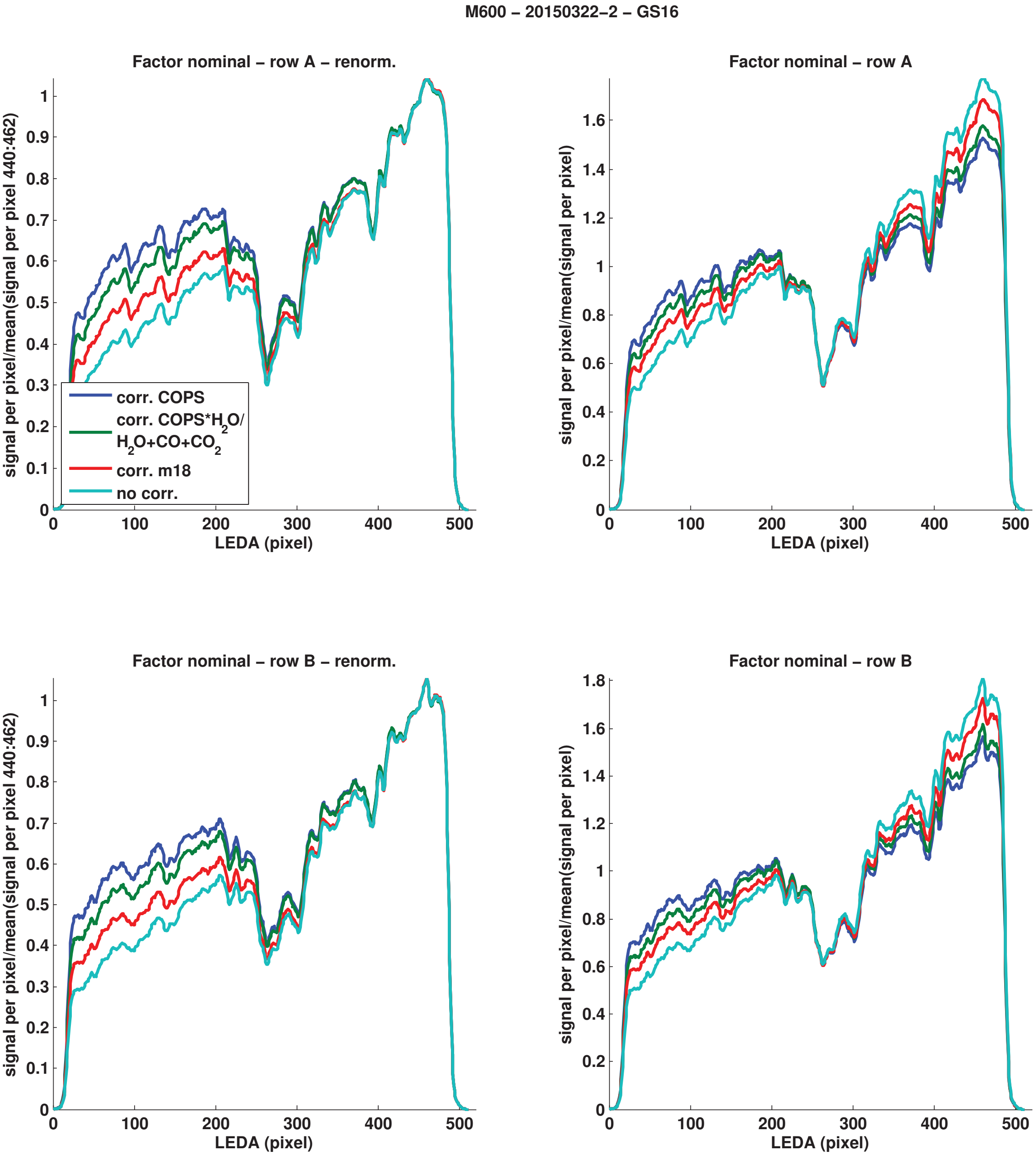

Fig. C.3.32: No overlap besides the central dips is apparent thus according to the rules corr. COPS is taken as the most likely.

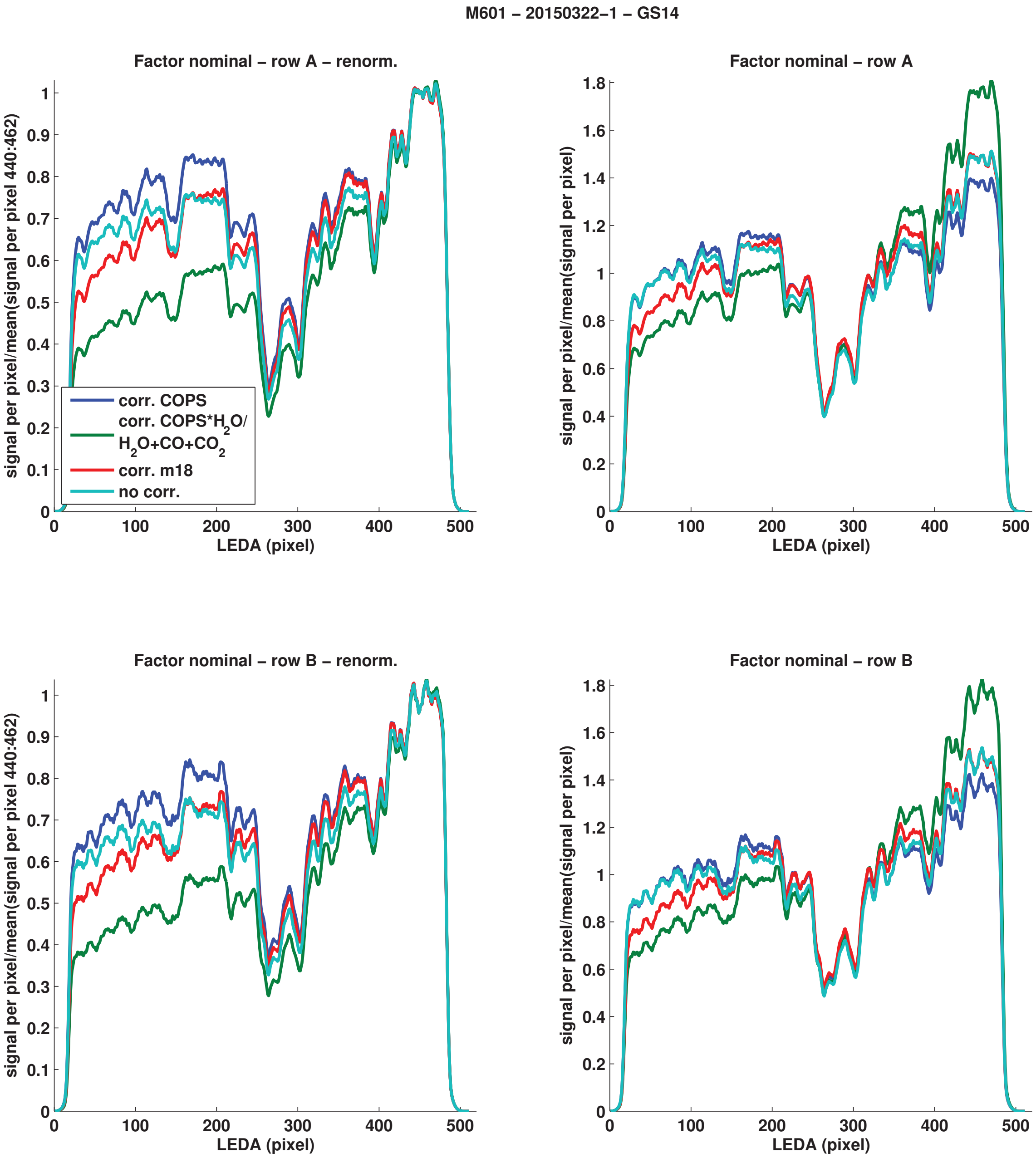

Fig. C.3.33: Here no overlap between two corrections is present for the major part of the LEDA. Between pixel 0-100 no correction and COPS correction overlap, followed by a section of no overlap of the four curves, and after the central dip first again no correction and COPS correction overlap but around pixel 400 m18 and no correction overlap. In consequence the first rule applies and correction COPS is chosen to be the most likely.

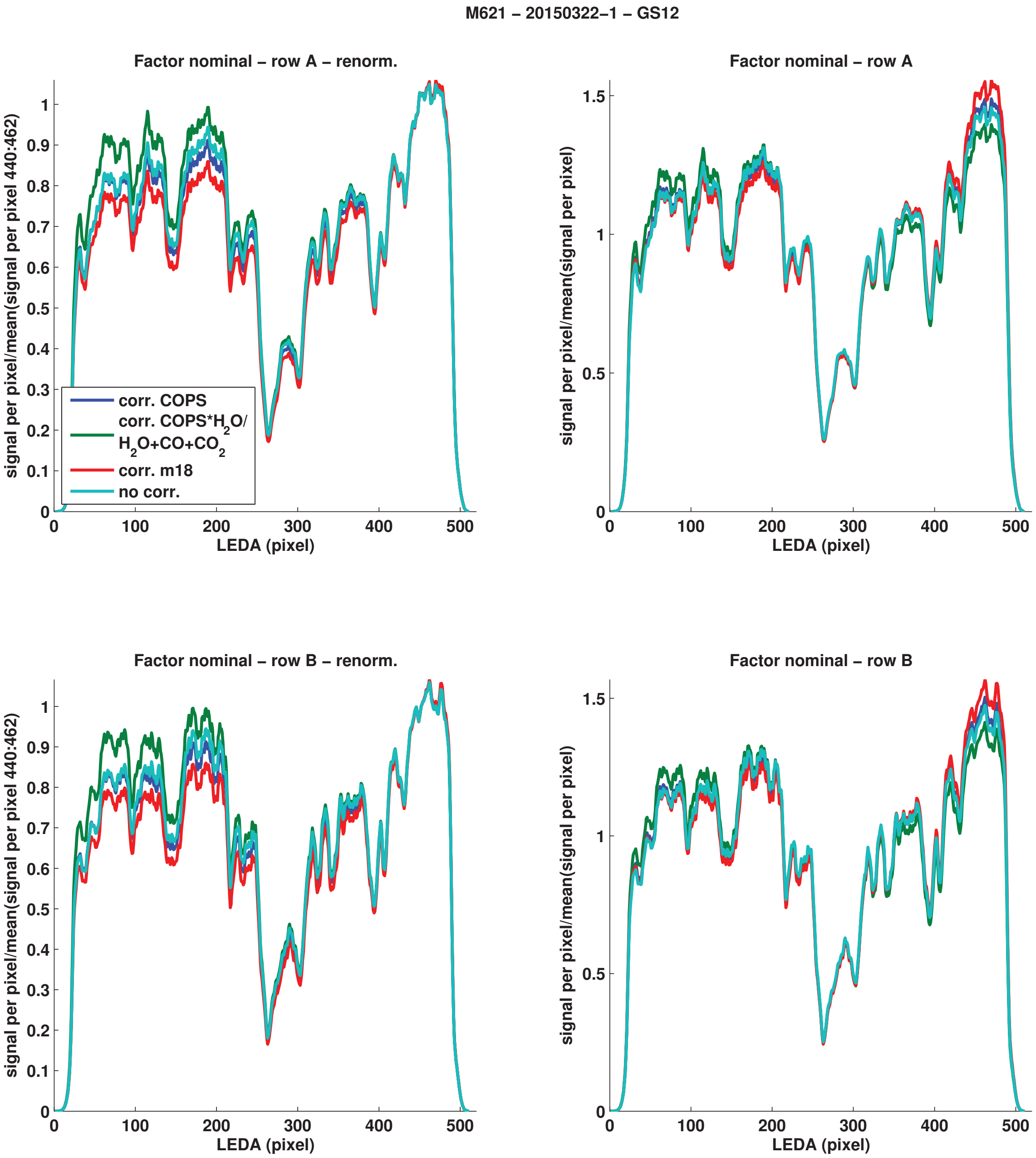

Fig. C.3.34: Here rule 5 applies because correction COPS and no correction show the largest overlap but correction for the main species combined with COPS has the smallest slope over the LEDA.

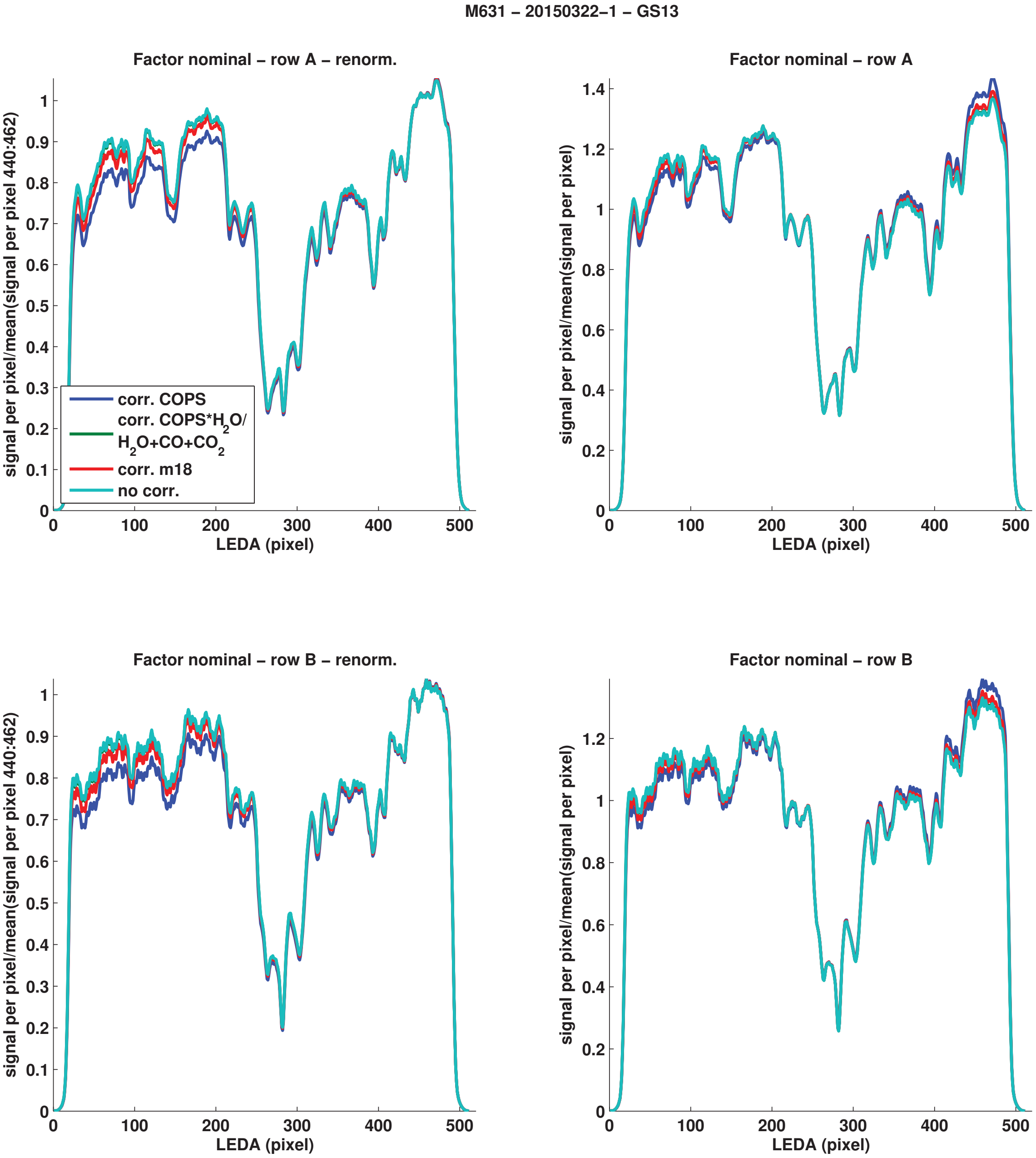

Fig. C.3.35: For this measurement no correction, correction m18, and correction of main species combined with COPS are overlapping thus no correction is taken following rule 3.

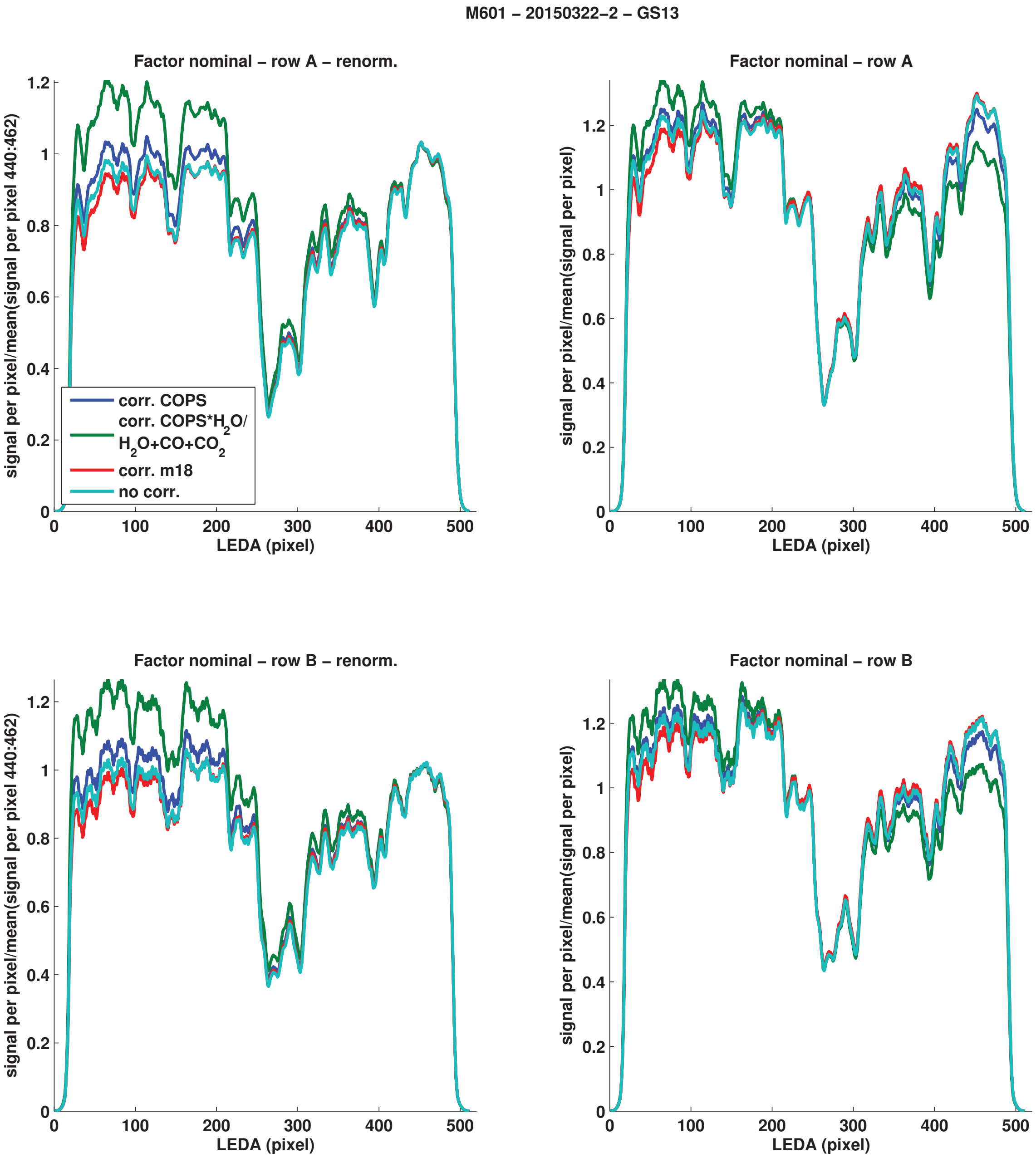

Fig. C.3.36: For almost the entire LEDA correction m18 and no correction overlap and thus no correction is chosen to be the most likely applying rule 3.

D. Sulfur Bearing Species in the Coma of 67P

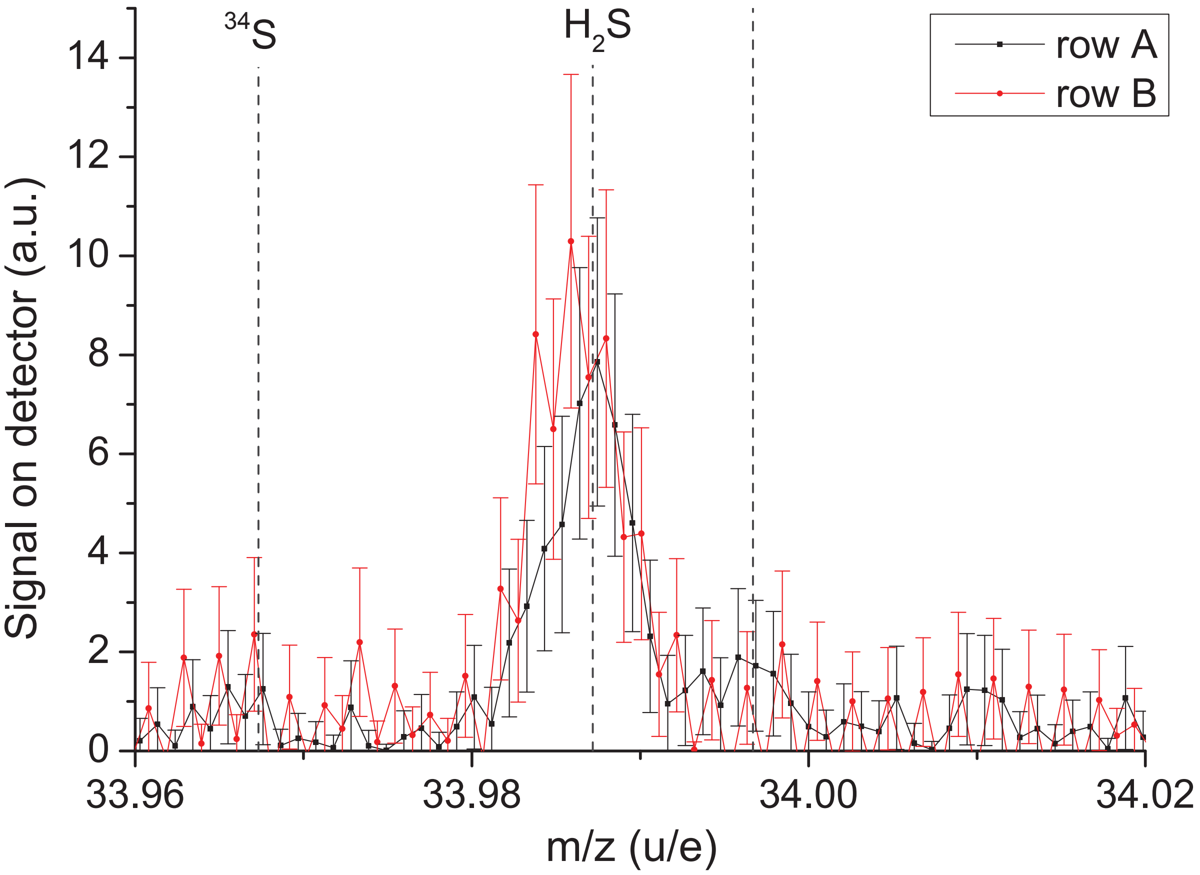

Fig. D.0.1: Mass spectra m/z 34 u/e in April 2014 for which the signal is expected to be due to the spacecraft background. The locations of ^{34}S and H_2S are indicated with dashes lines.

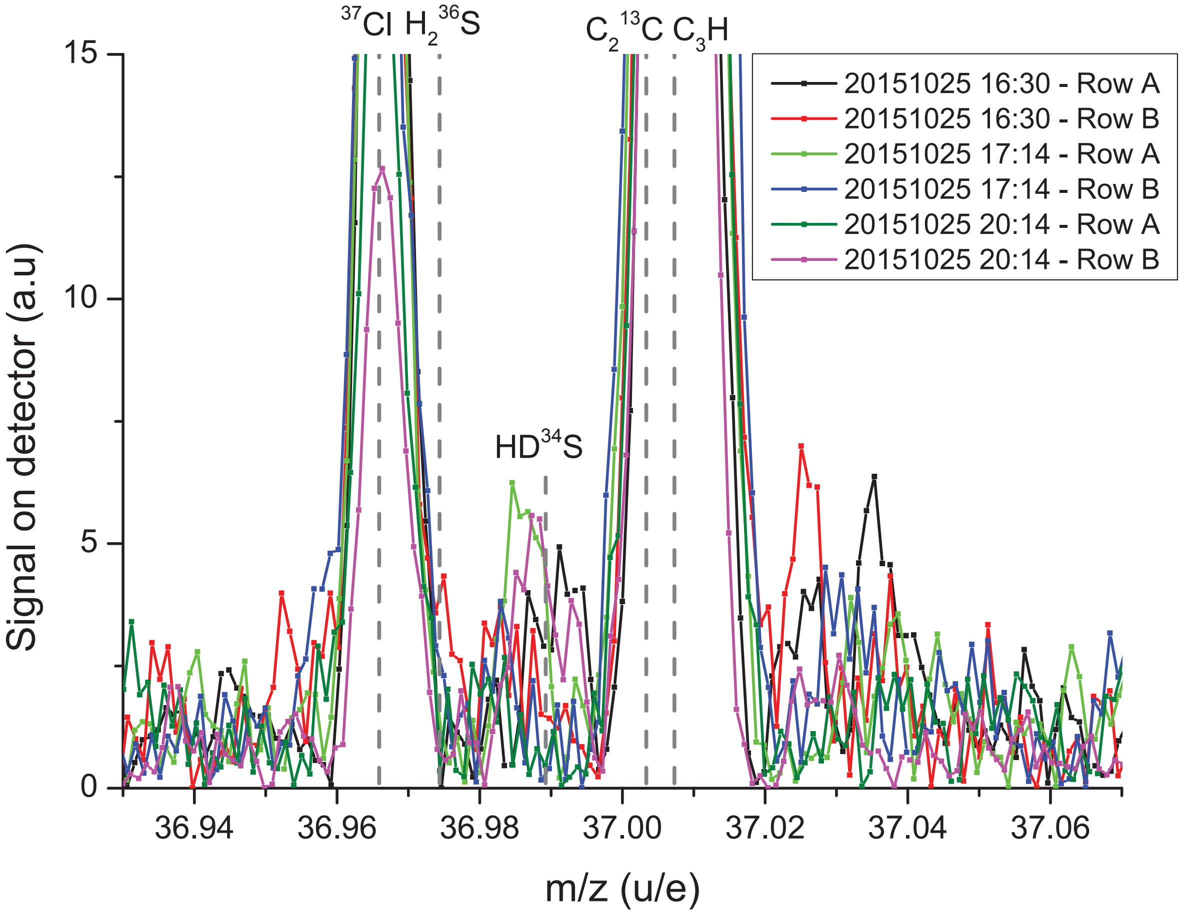

Fig. D.0.2: Mass spectrum of m/z 37 u/e acquired in October 2014 when Rosetta was at a cometary distance of 10 km to Churyumov-Gerasimenko. Shown are the mass spectra with the supposedly HD^{34}S signal. The locations of H^{35}S, H^{36}S, HD^{34}S C$_2$^{13}C, and C$_3$H are indicated by the dashed line.

Bibliography

M. F. A'Hearn, R. C. Millis, D. O. Schleicher, D. J. Osip, and P. V. Birch. The ensemble properties of comets: Results from narrowband photometry of 85 comets, 1976-1992. *Icarus*, 118:223–270, December 1995. doi: 10.1006/icar.1995.1190.

K. Altwegg, H. Balsiger, A. Bar-Nun, J. J. Berthelier, A. Bieler, P. Bochsler, C. Briois, U. Calmonte, M. Combi, J. De Keyser, P. Eberhardt, B. Fiethe, S. Fuselier, S. Gasc, T. I. Gombosi, K.C. Hansen, M. Hässig, A. Jäckel, E. Kopp, A. Korth, L. LeRoy, U. Mall, B. Marty, O. Mousis, E. Neefs, T. Owen, H. Rème, M. Rubin, T. Sémon, C.-Y. Tzou, H. Waite, and P. Wurz. 67p/churyumov-gerasimenko, a jupiter family comet with a high d/h ratio. *Science*, 347(6220), 2015. doi: 10.1126/science.1261952.

Kathrin Altwegg. *Sulfur in the coma of comet Halley from in situ measurements*. PhD thesis, University of Bern, 1996.

S. Amari, P. Hoppe, E. Zinner, and R. S. Lewis. Trace-element concentrations in single circumstellar silicon carbide grains from the Murchison meteorite. *Meteoritics*, 30:679, November 1995.

Michael A. Antonelli, Sang-Tae Kim, Marc Peters, Jabrane Labidi, Pierre Cartigny, Richard J. Walker, James R. Lyons, Joost Hoek, and James Farquhar. Early inner solar system origin for anomalous sulfur isotopes in differentiated protoplanets. *Proceedings of the National Academy of Sciences*, 111(50):17749–17754, 2014. doi: 10.1073/pnas.1418907111. URL `http://www.pnas.org/content/111/50/17749.abstract`.

Brooks Automation. *Granville-Phillips Series 370 Stabil-Ion Vacuum Measurement Controller*, 2007.

H. Balsiger, K. Altwegg, P. Bochsler, P. Eberhardt, J. Fischer, S. Graf, A. Jäckel, E. Kopp, U. Langer, M. Mildner, et al. Rosina-rosetta orbiter spectrometer for ion and neutral analysis. *Space Science Reviews*, 128(1-4):745–801, 2007.

H. Balsiger, K. Altwegg, A. Bar-Nun, J. J. Berthelier, A. Bieler, P. Bochsler, C. Briois, U. Calmonte, M. Combi, J. De Keyser, P. Eberhardt, B. Fiethe, S. A. Fuselier, S. Gasc, T. I. Gombosi, K. C. Hansen, M. Hässig, A. Jäckel, E. Kopp, A. Korth, L. Le Roy, U. Mall, B. Marty, O. Mousis, T. O.wen, H. Rème, M. Rubin, T. Sémon, C.-Y. Tzou, J. H. Waite, and P. Wurz. Detection of argon in the coma of comet 67p/churyumov-gerasimenko. *Science Advances*, 1(8), 2015. doi: 10.1126/sciadv.1500377.

A. Besmehn and P. Hoppe. A NanoSIMS study of Si- and Ca-Ti-isotopic compositions of presolar silicon carbide grains from supernovae. , 67:4693–4703, December 2003. doi: 10.1016/S0016-7037(03)00239-4.

A. Bieler, K. Altwegg, H. Balsiger, A. Bar-Nun, J.-J. Berthelier, P. Bochsler, C. Briois, U. Calmonte, M. Combi, J. De Keyser, E. F. van Dishoeck, B. Fiethe, S. A. Fuselier, S. Gasc, T. I. Gombosi, K. C. Hansen, M. Hassig, A. Jackel, E. Kopp, A. Korth, L. Le Roy, U. Mall, R. Maggiolo, B. Marty, O. Mousis, T. Owen, H. Reme, M. Rubin, T. Semon, C.-Y. Tzou, J. H. Waite, C. Walsh, and P. Wurz. Abundant molecular oxygen in the coma of comet 67p/churyumov-gerasimenko. *Nature*, 526(7575):678–681, Oct 2015. ISSN 0028-0836. URL `http://dx.doi.org/10.1038/nature15707`. Letter.

N. Biver, D. Bockelée-Morvan, H. Wiesemeyer, J. Crovisier, R. Peng, D. C. Lis, T. Phillips, J. Boissier, P. Colom, E. Lellouch, and R. Moreno. Composition and Outburst Follow-Up Observations of Comet 17P/Holmes at the Nançay, IRAM and CSO Radio Observatories. *LPI Contributions*, 1405:8146, 2008.

D. Bockelée-Morvan, U. Calmonte, S. Charnley, J. Duprat, C. Engrand, A. Gicquel, M. Hässig, E. Jehin, H. Kawakita, B. Marty, S. Milam, A. Morse, P. Rousselot, S. Sheridan, and E. Wirström. Cometary isotopic measurements. *Space Science Reviews*, pages 1–37, 2015. ISSN 0038-6308. doi: 10.1007/s11214-015-0156-9. URL `http://dx.doi.org/10.1007/s11214-015-0156-9`.

D. Bockelée-Morvan. An Overview of Comet Composition. In J. Cernicharo and R. Bachiller, editors, *IAU Symposium*, volume 280 of *IAU Symposium*, pages 261–274, December 2011. doi: 10.1017/S1743921311025038.

Bronstein, Semendjajew, Musiol, and Mühlig. *Taschenbuch der Mathematik*. Harri Deutsch, 5 edition, 2001.

D. Brownlee, P. Tsou, J. Aléon, C. M. O. '. Alexander, T. Araki, S. Bajt, G. A. Baratta, R. Bastien, P. Bland, P. Bleuet, J. Borg, J. P. Bradley, A. Brearley, F. Brenker, S. Brennan, J. C. Bridges, N. D. Browning, J. R. Brucato, E. Bullock, M. J. Burchell, H. Busemann, A. Butterworth, M. Chaussidon, A. Cheuvront, M. Chi, M. J. Cintala, B. C. Clark, S. J. Clemett, G. Cody, L. Colangeli, G. Cooper, P. Cordier, C. Daghlian, Z. Dai, L. D'Hendecourt, Z. Djouadi, G. Dominguez, T. Duxbury, J. P. Dworkin, D. S. Ebel, T. E. Economou, S. Fakra, S. A. J. Fairey, S. Fallon, G. Ferrini, T. Ferroir, H. Fleckenstein, C. Floss, G. Flynn, I. A. Franchi, M. Fries, Z. Gainsforth, J.-P. Gallien, M. Genge, M. K. Gilles, P. Gillet, J. Gilmour, D. P. Glavin, M. Gounelle, M. M. Grady, G. A. Graham, P. G. Grant, S. F. Green, F. Grossemy, L. Grossman, J. N. Grossman, Y. Guan, K. Hagiya, R. Harvey, P. Heck, G. F. Herzog, P. Hoppe, F. Hörz, J. Huth, I. D. Hutcheon, K. Ignatyev, H. Ishii, M. Ito, D. Jacob, C. Jacobsen, S. Jacobsen, S. Jones, D. Joswiak, A. Jurewicz, A. T. Kearsley, L. P. Keller, H. Khodja, A. L. D. Kilcoyne, J. Kissel, A. Krot, F. Langenhorst, A. Lanzirotti, L. Le, L. A. Leshin, J. Leitner, L. Lemelle, H. Leroux, M.-C. Liu, K. Luening, I. Lyon, G. MacPherson, M. A. Marcus, K. Marhas, B. Marty, G. Matrajt, K. McKeegan, A. Meibom, V. Mennella, K. Messenger, S. Messenger, T. Mikouchi, S. Mostefaoui, T. Nakamura, T. Nakano, M. Newville, L. R. Nittler, I. Ohnishi, K. Ohsumi, K. Okudaira, D. A. Papanastassiou, R. Palma, M. E. Palumbo, R. O. Pepin, D. Perkins, M. Perronnet, P. Pianetta, W. Rao, F. J. M. Rietmeijer, F. Robert, D. Rost, A. Rotundi, R. Ryan, S. A. Sandford, C. S. Schwandt, T. H. See, D. Schlutter, J. Sheffield-Parker, A. Simionovici, S. Simon, I. Sitnitsky, C. J. Snead, M. K. Spencer, F. J. Stadermann, A. Steele, T. Stephan, R. Stroud, J. Susini, S. R. Sutton, Y. Suzuki, M. Taheri, S. Taylor, N. Teslich, K. Tomeoka, N. Tomioka, A. Toppani, J. M. Trigo-Rodríguez, D. Troadec, A. Tsuchiyama, A. J. Tuzzolino, T. Tyliszczak, K. Uesugi, M. Velbel, J. Vellenga, E. Vicenzi, L. Vincze, J. Warren, I. Weber, M. Weisberg, A. J. Westphal, S. Wirick, D. Wooden, B. Wopenka, P. Wozniakiewicz, I. Wright, H. Yabuta, H. Yano, E. D. Young, R. N. Zare, T. Zega, K. Ziegler, L. Zimmerman, E. Zinner, and M. Zolensky. Comet 81p/wild 2 under a microscope. *Science*, 314:1711–, December 2006. doi: 10.1126/science.1135840.

D. E. Brownlee. *Comets*, pages 335–363. 2014.

Emma S. Bullock, Kevin D. McKeegan, Matthieu Gounelle, Monica M. Grady, and Sara S. Russel. Sulfur isotopic composition of fe-ni sulfide grains in ci and cm carbonaceous chondrites. *Meteoritics & Planetary Science*, 45(5):885–898, 2010. ISSN 1945-5100. doi: 10.1111/j.1945-5100.2010.01052.x. URL `http://dx.doi.org/10.1111/j.1945-5100.2010.01052.x`.

U. Calmonte. A flag mechanism to separate spacecraft background from tenuous atmospheres. Master's thesis, University of Bern, 2011.

C. Ceccarelli, P. Caselli, D. Bockelée-Morvan, O. Mousis, S. Pizzarello, F. Robert, and D. Semenov. Deuterium Fractionation: The Ariadne's Thread from the Precollapse Phase to Meteorites and Comets Today. *Protostars and Planets VI*, pages 859–882, 2014. doi: 10.2458/azu_uapress_9780816531240-ch037.

Subrate Chakraborty, Teresa L Jackson, Mushaid Ahmed, and Mark H. Thiemens. Sulfur isotopic fractionation in vacuum uv photodissociation of hydrogen sulfide and its potential relevance to meteorite analysis. *Proceedings of the National Academy of Sciences*, 110: 17650–17655, 2013.

Y.-N. Chin, C. Henkel, J. B. Whiteoak, N. Langer, and E. B. Churchwell. Interstellar sulfur isotopes and stellar oxygen burning. *Astronomy and Astrophysics*, 305:960, January 1996.

A. L. Cochran, E. S. Barker, T. F. Ramseyer, and A. D. Storrs. The McDonald Observatory Faint Comet Survey - Gas production in 17 comets. *Icarus*, 98:151–162, August 1992.

T. B Coplen and H. R. Krouse. Sulphur isotope data consistency improved. *Nature*, 1998.

D. Crovisier, D. Bockelee-Morvan, P. Colom, N. Biver, D. Despois, D. C. Lis, and the Team for target-of-opportunity radio observations of comets. The composition of ices in comet c/1995 o1 (hale-bopp) from radio spectroscopy. *Astronomy & Astrophysics*, 418 (3):1141–1157, 2004. doi: 10.1051/0004-6361:20035688. URL `http://dx.doi.org/10.1051/0004-6361:20035688`.

T. Ding, S. Valkiers, H. Kipphardt, P. De Bièvre, P. D. P. Taylor, R. Gonfiantini, and R. Krouse. Calibrated sulfur isotope abundance ratios of three iaea sulfur isotope reference materials and v-cdt with a reassessment of the atomic weight of sulfur. *Geochimica et Cosmochimica Acta*, 65:2433–2437, September 2001. doi: 10.1016/S0016-7037(01)00611-1.

M. Duncan, H. Levison, and L. Dones. *Dynamical evolution of ecliptic comets*, pages 193–204. 2004.

James Farquhar, Teresa L. Jackson, and Mark H. Thiemens. A 33s enrichment in ureilite meteorites: evidence for a nebular sulfur component. *Geochimica et Cosmochimica Acta*, 64(10):1819 – 1825, 2000. ISSN 0016-7037. doi: http://dx.doi.org/10.1016/S0016-7037(00)00356-2. URL `http://www.sciencedirect.com/science/article/pii/S0016703700003562`.

H. B. Franz, J. Farquhar, and A. J. Irving. Acid Volatile Sulfur Isotopic Composition of Seven Shergottites from Northwest Africa. In *Lunar and Planetary Science Conference*, volume 41 of *Lunar and Planetary Science Conference*, page 2341, March 2010.

X. Gao and M. H. Thiemens. Systematic study of sulfur isotopic composition in iron meteorites and the occurrence of excess s-33 and s-36. *Geochimica et Cosmochimica Acta*, 55:2671–2679, September 1991. doi: 10.1016/0016-7037(91)90381-E.

X. Gao and M. H. Thiemens. Isotopic composition and concentration of sulfur in carbonaceous chondrites. *Geochimica et Cosmochimica Acta*, 57:3159–3169, July 1993a. doi: 10.1016/0016-7037(93)90300-L.

X. Gao and M. H. Thiemens. Variations of the isotopic composition of sulfur in enstatite and ordinary chondrites. *Geochimica et Cosmochimica Acta*, 57:3171–3176, July 1993b. doi: 10.1016/0016-7037(93)90301-C.

Karl-Heinz Glassmeier, Hermann Boehnhardt, Detlef Koschny, Ekkehard Kührt, and Ingo Richter. *The ROSETTA Mission: Flying Towards the Origin of the Solar System*, chapter 1, pages 1–20. Springer-Verlag New York, 2009.

F. Gyngard, L. R. Nittler, and E. Zinner. Presolar sic grains of type c. *Meteoritics and Planetary Science Supplement*, 73:5242, September 2010.

P. Hartogh, D. C. Lis, D. Bockelée-Morvan, M. de Val-Borro, N. Biver, M. Küppers, M. Emprechtinger, E. A. Bergin, J. Crovisier, M. Rengel, R. Moreno, S. Szutowicz, and G. A. Blake. Ocean-like water in the Jupiter-family comet 103P/Hartley 2. , 478: 218–220, October 2011. doi: 10.1038/nature10519.

M. Hässig. *Sensitivity and framentation calibration of the ROSINA Double Focusing Mass Spectrometer.* PhD thesis, University of Bern, 2013.

M. Hässig, K. Altwegg, H. Balsiger, A. Bar-Nun, J. J. Berthelier, A. Bieler, P. Bochsler, C. Briois, U. Calmonte, M. Combi, J. De Keyser, P. Eberhardt, B. Fiethe, S. A. Fuselier, M. Galand, S. Gasc, T. I. Gombosi, K. C. Hansen, A. Jäckel, H. U. Keller, E. Kopp, A. Korth, E. Kührt, L. Le Roy, U. Mall, B. Marty, O. Mousis, E. Neefs, T. Owen, H. Rème, M. Rubin, T. Sémon, C. Tornow, C.-Y. Tzou, J. H. Waite, and P. Wurz. Time variability and heterogeneity in the coma of 67P/Churyumov-Gerasimenko. *Science*, 347(1):aaa0276, January 2015. doi: 10.1126/science.aaa0276.

P. R. Heck, P. Hoppe, and J. Huth. Sulfur four isotope nanosims analysis of comet-81p/wild 2 dust in impact craters on aluminum foil c2037n from nasa's stardust mission. *Meteoritics and Planetary Science*, 47:649–659, April 2012. doi: 10.1111/j.1945-5100.2012.01362.x.

J. Hoefs. *Stable Isotope Geochemistry.* Number 6. Springer-Verlag Berlin Heidelberg, 2009.

P. Hoppe, J. Leitner, E. Gröner, K. K. Marhas, B. S. Meyer, and S. Amari. Nanosims studies of small presolar sic grains: New insights into supernova nucleosynthesis, chemistry, and dust formation. *The Astrophysical Journal Letters*, 719:1370–1384, August 2010. doi: 10.1088/0004-637X/719/2/1370.

P. Hoppe, W. Fujiya, and E. Zinner. Sulfur molecule chemistry in supernova ejecta recorded by silicon carbide stardust. *The Astrophysical Journal Letters*, 745:L26, February 2012. doi: 10.1088/2041-8205/745/2/L26.

P. Hoppe, K. Lodders, and W. Fujiya. Sulfur in presolar silicon carbide grains from asymptotic giant branch stars. *Meteoritics and Planetary Science*, 50:1122–1138, June 2015. doi: 10.1111/maps.12449.

K. M. Hynes and F. Gyngard. The Presolar Grain Database: http://presolar.wustl.edu/˜pgd. In *Lunar and Planetary Science Conference*, volume 40 of *Lunar and Planetary Science Conference*, page 1198, March 2009.

E. Jehin, J. Manfroid, D. Hutsemékers, C. Arpigny, and J.-M. Zucconi. Isotopic Ratios in Comets: Status and Perspectives. *Earth Moon and Planets*, 105:167–180, September 2009. doi: 10.1007/s11038-009-9322-y.

David C. Jewitt, Henry E. Matthews, Tobias Owen, and Roland Meier. Measurements of 12c/13c, 14n/15n and 32s/34s ratios in comet hale-bopp (c/1995 o1). *Science*, 278: 90–93, 1997.

Johnson, E. and Nier, A. Angular Abberations in sector shaped electromagnetic lenses for focusin beasm of charged particels. *Astronomy and Astrophysics*, 19:10–17, 1953.

I. R. Kaplan and J. R. Hulston. The isotopic abundance and content of sulfur in meteorites. , 30:479–496, May 1966. doi: 10.1016/0016-7037(66)90059-7.

A.N. Krot, K. Keil, E.R.D. Scott, C.A. Goodrich, and M.K. Weisberg. 1.05 - classification of meteorites. In Heinrich D. HollandKarl K. Turekian, editor, *Treatise on Geochemistry*, pages 1 – 52. Pergamon, Oxford, 2007. ISBN 978-0-08-043751-4. doi: http://dx.doi.org/10.1016/B0-08-043751-6/01062-8. URL `http://www.sciencedirect.com/science/article/pii/B0080437516010628`.

P. L. Lamy, I. Toth, H. Weaver, L. Jorda, and M. Kaasalainen. The Nucleus of Comet 67P/Churyumov-Gerasimenko, the New Target of the Rosetta Mission. In *AAS/Division for Planetary Sciences Meeting Abstracts #35*, volume 35 of *Bulletin of the American Astronomical Society*, page 970, May 2003.

P. L. Lamy, I. Toth, H. A. Weaver, L. Jorda, M. Kaasalainen, and P. J. Gutiérrez. Hubble Space Telescope observations of the nucleus and inner coma of comet 67P/Churyumov-Gerasimenko. *Astronomy and Astrophysics*, 458:669–678, November 2006. doi: 10.1051/0004-6361:20065253.

P. L Lamy, I. Toth, B. J. R. Davidsson, O. Groussin, P. Gutierrez, L. Jorda, M. Kaasalainen, and S. C. Lowry. *The Nucleus of Comet 67P/Churyumov-Gerasimenko*, chapter 2, pages 21–54. Springer-Verlag New York, 2009.

U. Langer. Dfms-fm calibration report static mode. Technical report, University of Bern, 2003a.

U. Langer. Dfms-fm calibration report static mode. Technical report, University of Bern, 2003b.

Le Roy, L., Altwegg, K., Balsiger, H., Berthelier, J.-J., Bieler, A., Briois, C., Calmonte, U., Combi, M. R., De Keyser, J., Dhooghe, F., Fiethe, B., Fuselier, S. A., Gasc, S., Gombosi, T. I., Hässig, M., Jäckel, A., Rubin, M., and Tzou, C.-Y. The inventory of the volatiles on comet 67p/churyumov-gerasimenko from rosetta/rosina. *Astronomy and Astrophysics*, 2015. doi: 10.1051/0004-6361/201526450. URL `http://dx.doi.org/10.1051/0004-6361/201526450`.

Y. Lin, M. S. Sim, and S. Ono. Multiple-sulfur isotope effects during photolysis of carbonyl sulfide. *Atmospheric Chemistry & Physics Discussions*, 11:14233–14258, May 2011. doi: 10.5194/acpd-11-14233-2011.

S. Lowry, S. R. Duddy, B. Rozitis, S. F. Green, A. Fitzsimmons, C. Snodgrass, H. H. Hsieh, and O. Hainaut. The nucleus of Comet 67P/Churyumov-Gerasimenko. A new shape model and thermophysical analysis. *Astronomy and Astrophysics*, 548:A12, December 2012. doi: 10.1051/0004-6361/201220116.

Andrew L. Masterson, James Farquhar, and Boswel A. Wing. Sulfur mass-independent fractionation patterns in the broadband uv photolysis of sulfur dioxide: Pressure and third body effects. *Earth and Planetary Sciences Letters*, 306:253–260, 2011.

R. Mauersberger, U. Ott, C. Henkel, J. Cernicharo, and R. Gallino. The abundance of ^{36}s in irc+10216 and its production in the galaxy. *Astronomy and Astrophysics*, 426: 219–227, October 2004. doi: 10.1051/0004-6361:20040451.

Harry Y. McSween, Lee R. Riciputi, and Bruce A. Paterson. Fractionated sulfur isotopes in sulfides of the kaidun meteorite. *Meteoritics & Planetary Science*, 32(1):51–54, 1997. ISSN 1945-5100. doi: 10.1111/j.1945-5100.1997.tb01239.x. URL `http://dx.doi.org/10.1111/j.1945-5100.1997.tb01239.x`.

R. Meier and P. Eberhardt. Velocity and ion species dependece of the gain of microchannel plates. *International Journal of Mass Spectrometry and Ion Processes*, 123:19–27, 1993.

J. Monster, E. Anders, and H. G. Thode. ^{34}S/ ^{32}S ratios for the different forms of sulphur in the Orgueil meteorite and their mode of formation. , 29:773–779, July 1965. doi: 10.1016/0016-7037(65)90030-X.

M. J. Mumma and S. B. Charnley. The Chemical Composition of Comets - Emerging Taxonomies and Natal Heritage. , 49:471–524, September 2011. doi: 10.1146/annurev-astro-081309-130811.

E. Neefs, J.-M. Illiando, and D. Nevejans. Dfms mcp-leda detector calibration in casyms and flight spare model. Technical report, Belgian Institute for Space Aeronomy (BIRA-IASB), 2002a.

E. Neefs, J.-M. Illiando, and D. Nevejans. Dfms mcp-leda detector calibration in casyms and flight model. Technical report, Belgian Institute for Space Aeronomy (BIRA-IASB), 2002b.

D. Nevejans, E. Neefs, S. Kavadias, P. Merken, and Chris Van Hoof. The leda512 integrated circuit anode array for the analog recording of mass spectra. *International Journal of Mass Spectrometry*, 215(1?):77 – 87, 2002. ISSN 1387-3806. doi: http://dx.doi.org/10.1016/S1387-3806(01)00549-8. URL `http://www.sciencedirect.com/science/article/pii/S1387380601005498`. Detectors and the Measurement of Mass Spectra.

F.-R. Orthous-Daunay, F. Gyngard, F. Moynier, and E. Zinner. Multi-element isotopic compositions of presolar sic grains from the indarch meteorite. In *Lunar and Planetary Science Conference*, volume 43 of *Lunar and Planetary Inst. Technical Report*, page 2679, March 2012.

V. K. Rai, Teresa L. Jackson, and M. H. Thiemens. Photochemical mass-independent sulfur isotopes in achondritic meteorites. *Science*, 309(5737):1062–1065, 2005. doi: 10.1126/science.1112954. URL `http://www.sciencemag.org/content/309/5737/1062.abstract`.

T. Rauscher, A. Heger, R. D. Hoffman, and S. E. Woosley. Nucleosynthesis in massive stars with improved nuclear and stellar physics. *The Astrophysical Journal*, 576:323–348, September 2002. doi: 10.1086/341728.

T.-E. Riesen. *Calibration of the ROSINA DFMS in a static and dynamic environment*. PhD thesis, University of Bern, 2007.

P. Rousselot, O. Pirali, E. Jehin, M. Vervloet, D. Hutsemékers, J. Manfroid, D. Cordier, M. A. Martin-Drumel, S. Gruet, C. Arpigny, A. Decock, and O. Mousis. Toward a unique nitrogen isotopic ratio in cometary ices. *The Astrophysical Journal Letters*, 780(2):L17, 2014. URL `http://stacks.iop.org/2041-8205/780/i=2/a=L17`.

M. Rubin, K. Altwegg, H. Balsiger, A. Bar-Nun, J.-J. Berthelier, A. Bieler, P. Bochsler, C. Briois, U. Calmonte, M. Combi, J. De Keyser, F. Dhooghe, P. Eberhardt, B. Fiethe, S. A. Fuselier, S. Gasc, T. I. Gombosi, K. C. Hansen, M. Hässig, A. Jäckel, E. Kopp, A. Korth, L. Le Roy, U. Mall, B. Marty, O. Mousis, T. Owen, H. Rème, T. Sémon, C.-Y. Tzou, J. H. Waite, and P. Wurz. Molecular nitrogen in comet 67P/Churyumov-Gerasimenko indicates a low formation temperature. *Science*, 348:232–235, April 2015. doi: 10.1126/science.aaa6100.

B. Schläppi. *Characterization of the ROSINA Double Focusing Mass Spectrometer*. PhD thesis, University of Bern, 2011.

B. Schläppi, K. Altwegg, H. Balsiger, M. Hässig, A. Jäckel, P. Wurz, B. Fiethe, M. Rubin, S. A. Fuselier, J. J. Berthelier, J. De Keyser, H. Rème, and U. Mall. Influence of spacecraft outgassing on the exploration of tenuous atmospheres with in situ mass spectrometry. *Journal of Geophysical Research: Space Physics*, 115(A12):n/a–n/a, 2010. ISSN 2156-2202. doi: 10.1029/2010JA015734. URL `http://dx.doi.org/10.1029/2010JA015734`. A12313.

D. G. Schleicher. Compositional and physical results for Rosetta's new target Comet 67P/Churyumov Gerasimenko from narrowband photometry and imaging. *Icarus*, 181:442–457, April 2006. doi: 10.1016/j.icarus.2005.11.014.

F. Scholten, F. Preusker, L. Jorda, and S Hviid. Reference frames and mapping schemes of comet 67p/c-g ro-c-multi-5-67p-shape-v1.0:cheops_ref_frame_v1. *NASA Planetary Data System and ESA Planetary Science Archive*, 2015.

R. Schulz, J. A. Stüwe, and H. Boehnhardt. Rosetta target comet 67P/Churyumov-Gerasimenko. Postperihelion gas and dust production rates. *Astronomy and Astrophysics*, 422:L19–L21, July 2004. doi: 10.1051/0004-6361:20040190.

R. Schulz, M. Hilchenbach, Y. Langevin, J. Kissel, J. Silen, C. Briois, C. Engrand, K. Hornung, D. Baklouti, A. Bardyn, H. Cottin, H. Fischer, N. Fray, M. Godard, H. Lehto, L. Le Roy, S. Merouane, F.-R. Orthous-Daunay, J. Paquette, J. Rynö, S. Siljeström, O. Stenzel, L. Thirkell, K. Varmuza, and B. Zaprudin. Comet 67P/Churyumov-Gerasimenko sheds dust coat accumulated over the past four years. , 518:216–218, February 2015. doi: 10.1038/nature14159.

C. Snodgrass, C. Tubiana, D. M. Bramich, K. Meech, H. Boehnhardt, and L. Barrera. Beginning of activity in 67P/Churyumov-Gerasimenko and predictions for 2014-2015. *Astronomy and Astrophysics*, 557:A33, September 2013. doi: 10.1051/0004-6361/201322020.

R. L. Summers. Emprical observations on the sensitivity of hot cathode ionization type vacuum gauges. Technical report, NASA, 1969.

E. F. van Dishoeck, G. A. Blake, D. J. Jansen, and T. D. Groesbeck. Molecular Abundances and Low-Mass Star Formation. II. Organic and Deuterated Species toward IRAS 16293-2422. *The Astrophysical Journal*, 447:760, July 1995. doi: 10.1086/175915.

M. Weiler, H. Rauer, and J. Helbert. Optical observations of Comet 67P/Churyumov-Gerasimenko. *Astronomy and Astrophysics*, 414:749–755, February 2004. doi: 10.1051/0004-6361:20031610.

R. A. Werner and W. A. Brand. Referencing strategies and techniques in stable isotope ratio analysis. *Rapid Communications in Mass Spectrometry*, 15(7):501–519, 2001. ISSN 1097-0231. doi: 10.1002/rcm.258. URL `http://dx.doi.org/10.1002/rcm.258`.

C.B. Westermann. *A Novel Calibration System for the Simulation of Cometary Atmospheres.* PhD thesis, University of Bern, 2000.

S. Wüthrich. *Characterization of the ROSINA DFMS Instrument by Numerical Modeling.* PhD thesis, University of Bern, 2007.

Y. Xu, E. Zinner, R. Gallino, A. Heger, M. Pignatari, and Y. Lin. Sulfur isotopic compositions of submicrometer sic grains from the murchison meteorite. *The Astrophysical Journal Letters*, 799:156, February 2015. doi: 10.1088/0004-637X/799/2/156.

E. Zinner. 1.02 - presolar grains. In Heinrich D. HollandKarl K. Turekian, editor, *Treatise on Geochemistry*, pages 1 – 33. Pergamon, Oxford, 2007. ISBN 978-0-08-043751-4. doi: http://dx.doi.org/10.1016/B0-08-043751-6/01144-0. URL `http://www.sciencedirect.com/science/article/pii/B0080437516011440`.

E. Zinner. 1.4 - presolar grains. In Heinrich D. HollandKarl K. Turekian, editor, *Treatise on Geochemistry (Second Edition)*, pages 181 – 213. Elsevier, Oxford, second edition edition, 2014. ISBN 978-0-08-098300-4. doi: http://dx.doi.org/10.1016/B978-0-08-095975-7.00101-7. URL `http://www.sciencedirect.com/science/article/pii/B9780080959757001017`.

P. Zmolek, X. Xu, T. Jackson, M. H. Thiemens, and W. C. Trogler. Large mass independent sulfur isotope fractionations during the photopolymerization of 12cs2 and 13cs2. *Physical Chemistry A*, 103:2477–2480, 1999.

Acknowledgements

This thesis would not have been possible without the support I got from several persons whom I owe my gratitude.

Almost 20 years ago I was fascinated by explorers like Vasco da Gama or Marco Polo who went to the edges of their ’world’ and beyond. It was then when I discovered my scientific curiosity and my desire to explore new worlds. The past four years I had the unique opportunity to work on an active space mission extending yet again the boundaries of our knowledge and I am deeply grateful to my supervisor Prof. Dr. Kathrin Altwegg for this. I appreciated in particular the fascinating discussions about space research and comets as well as about the mission itself. Furthermore, I am grateful for the moral support provided during trying times, e.g. when DFMS FM did not behave as we hope for.

Special thanks go to Prof. Dr. Bernard Marty from the Centre de Recherches Pétrographiques et Géochimiques at the Université de Lorraine in Nancy for refereeing this work.

Many thanks go to Prof. Dr. Nicholas Thomas of the University of Bern for being the examiner at my defense as well as for the good collaboration with him as a member of the OSIRIS team.

The daily work in the laboratory would not have been possible without the support from many individuals of the mechanical and the electronic workshop:

- Harald Mischler for the many times he helped to move DFMS for calibrations at CASYMIR as well as for his helping hands and knowledge concerning laboratory work in general.

- Adrian Etter for the many discussion about laboratory equipment and how to improve our test setups for DFMS. It was always a pleasure to work with you. In addition I am grateful for the hospitality so that I could spend my time in the Clean Room far away from grass and birch pollen.

- Jürg Jost and his team for the support concerning the GCU which caused troubles more than once.

Furthermore I owe many thanks to

- Dr. Myrtha Hässig for the detailed introduction into the mysteries of DFMS.

- Dr. Timm Riesen who answered questions concerning the work he did years ago and for sharing his knowledge about the peculiarities of DFMS.

- Dr. Björn Fiethe for his support regarding software issues of GSEOS and implementing new modes for the space instrument.

- Dr. Martin Rubin and Dr. Léna Le Roy for the fruitful discussions concerning 67P and DFMS. In addition for their constructive criticism of my thesis.

- Dr. Annette Jäckel with whom I was on duty week every fourth week operating ROSINA in space. I am indebted to you for sharing your considerable knowledge about ROSINA with me and I am thankful for the collaboration.
- Thierry Sémon who did many last minute changes in command files shortly before they were uploaded to the spacecraft.
- Dr. Thomas Smith for reading the section about the individual pixel gain measurements and giving feedback as a non-specialist.

I am grateful to my office mates Chia-Yu Tzou and Sébastien Gasc for their support be it with discussions about ROSINA or for their helping hands in the laboratory. They experienced at first hand my up and downs while working at my thesis and have been a moral support to me as well as provider of Ovomaltine chocolate - the fuel of the past few weeks.

I consider myself very lucky to be a ROSINA team member because of the team spirit during some challenging times since ROSINA has been active again after deep space hibernation.

I owe thanks to all of the people in the department of physics for their assistance in technical and administrative concerns. The pleasant work environment made my time here a real pleasure.

Moreover I thank my parents Therese and Toni who supported my scientific curiosity from an early age on. Since I was able to read I binge-read nonfiction and journals regardless of the field and discussed the findings with my father. Even today there is an active exchange of scientific journals among us which I highly appreciate. In addition I thank my siblings for their support and their interest in my work although it can be rather dry and complex for an outsider.

Finally many thanks to my partner Christoph who was a kingpin during the past few weeks and who made sure I would get enough distraction and recovery from work. In addition, I highly appreciate that I could discuss my ideas and my work with him. Being together with you makes the world brighter and more joyful.

This work was funded by the Swiss National Science Foundation, the Prodex Programm of the European Space Agency, and the Kanton of Bern.

Erklärung

gemäss Art. 28 Abs. 2 RSL 05

Name/Vorname: Ursina Calmonte

Matrikelnummer: 06-102-750

Studiengang: Physik

Bachelor ☐ Master ☐ Dissertation ☑

Titel der Arbeit: Sulfur Isotopic Ratios at 67P/Churyumov-Gerasimenko and Characterization of ROSINA-DFMS FM & FS

LeiterIn der Arbeit: Prof. Dr. Kathrin Altwegg

Ich erkläre hiermit, dass ich diese Arbeit selbständig verfasst und keine anderen als die angegebenen Quellen benutzt habe. Alle Stellen, die wörtlich oder sinngemäss aus Quellen entnommen wurden, habe ich als solche gekennzeichnet. Mir ist bekannt, dass andernfalls der Senat gemäss Artikel 36 Absatz 1 Buchstabe r des Gesetzes vom 5. September 1996 über die Universität zum Entzug des auf Grund dieser Arbeit verliehenen Titels berechtigt ist. Ich gewähre hiermit Einsicht in diese Arbeit.

Bern, 03.11.2015

Ort/Datum

Unterschrift

Curriculum Vitae

Personal Data

Name:	Calmonte
First Name	Ursina Maria

Education

1993 - 1998	Primarschule in Thierachern/BE
1999 - 1999	Primarschule in Thierachern/BE
1999 - 2002	Sekundarschule in Dotzigen/BE
2002 - 2006	Gymnasium Linde Biel/BE
2006	Matura at Gymnasium Linde Biel Schwerpunktfach: Biologie und Chemie Ergänzungsfach: Geschichte

Academic Record

2006 - 2010	Studies at the University of Bern in physics and astronomy
2009 - 2010	Bachelor's thesis in physics at the Physics Institute, University Bern, Division of Space Research and Planetary Sciences, entitled „Noble Gas Analysis and Exposure Ages Determination of Five Desert Ureilites“ Supervisor: PhD. Mariana Cosarinsky
2010	Bachelor of Science in Physics with special qualification in astronomy, University Bern,
2010 - 2011	Studies at the University of Bern in physics and astronomy
2010 - 2011	Master's thesis in physics at the Physics Institute, University Bern, Division of Space Research and Planetary Sciences, entitled „A Flag Mechanism to Separate Spacecraft Background from Tenuous Atmospheres“ Supervisor: Prof. Dr. Kathrin Altwegg
2011	Master of Science in Physics with special qualification in Applied/Experimental Physics, University Bern
2011 - 2015	PhD thesis in physics at the Physics Institute, University Bern, Division of Space Research and Planetary Sciences, entitled „Sulfur Isotopic Ratios at 67P/Churyumov-Gerasimenko and Characterization of ROSINA-DFMS FM & FS “ Supervisor: Prof. Dr. Kathrin Altwegg

Professional Training

2008 - 2015	Teaching assistant of physics laboratory class and exercises for student of physics and other branches.
2008	Internship at the Federal Institute of Metrology (METAS) (6 weeks)